Nonlinear dynamics and active/passive control of parametrically excited slender structures

A
Thesis Submitted in
Partial Fulfillment of the Requirements
for the Degree of

DOCTOR OF PHILOSOPHY

by

Rajidi Shashidhar Reddy
(Roll No: 166103022)

DEPARTMENT OF MECHANICAL ENGINEERING
INDIAN INSTITUTE OF TECHNOLOGY GUWAHATI,
GUWAHATI-781039, INDIA

August, 2022

Department of Mechanical Engineering
Indian Institute of Technology Guwahati
Guwahati-781039 INDIA

CERTIFICATE

It is certified that the work contained in the thesis entitled "**NONLINEAR DYNAMICS AND ACTIVE/PASSIVE CONTROL OF PARAMETRICALLY EXCITED SLENDER STRUCTURES**" submitted by **Rajidi Shashidhar Reddy (Reg. No. 166103022)** to the Indian Institute of Technology Guwahati for the award of the degree of Doctor of Philosophy has been carried out under my supervision in the Department of Mechanical Engineering, Indian Institute of Technology Guwahati. This work has not been submitted elsewhere for the award of any other degree or diploma.

(Dr. Satyajit Panda)
Professor
Department of Mechanical Engineering
Indian Institute of Technology Guwahati
Guwahati-781039
INDIA

Declaration

I Rajidi Shashidhar Reddy (Roll no: 166103022) declare that the present written submission is my thoughts in my own words. I have adequately cited and referenced the original sources, where others ideas have been involved. I also declare that I have adhered to all principles of academic honesty and integrity and have neither fabricated nor falsified any idea/data/fact/source in my submission. I understand that any violation of the above will be cause for disciplinary action by the Institute and can also evoke penal action from the sources which have thus not been properly cited or from whom proper permission has not been taken when needed.

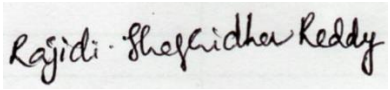

(**Rajidi Shashidhar Reddy**)

Date: 25-08-2022

Roll No: 166103022

Dedicated to

My family

Acknowledgments

The work presented in this thesis has been possible with my close association with several people. I would like to express my heartfelt gratitude and appreciation towards all those who made this Ph.D. thesis possible.

First and foremost, I must express my deepest sense of appreciation and respect for my thesis supervisor Prof. Satyajit Panda, who has been a remarkable mentor for me. His continuous support and encouragement have immensely helped me to gain good research experience and for the effective completion of this thesis. I am really pleased to be associated with him.

I am also thankful to Prof. Debabrata Chakraborty, Dr. Bhaskar kumar and Dr. Raghavendra Gupta for their careful review and suggestions in their capacity as doctoral committee members. I am also grateful to past and present departmental heads Prof. S. K. Dwivedy, Prof. S. Senthilvelan and Prof. K.S.R. Krishna Murthy for providing me enough facilities during my Ph. D. program.

The financial support provided by the Ministry of Education, Government of India for research work at IIT Guwahati is gratefully acknowledged.

I express deepest gratitude to my father Sri Gajender Reddy, mother Smt. Srilatha, brother Vamshidhar and sister-in-law Divya for their constant love, support and encouragement towards my research work.

Finally, I would be the grateful to my dearest friends Dr. Manish, Dr. Abhay, Sunku Prasad and Dr. Vishwanth for their emotional support, continuous encouragement and fruitful discussions. Also, I want to thank other friends Dr. Pavan, Dr. Ambesh, Dr. Praneeth, Dr. Vishal, Nitin, Rahul and Anil, who helped me in several situations.

Above all, I am thankful to the Almighty God.

Date: 25-08-2022

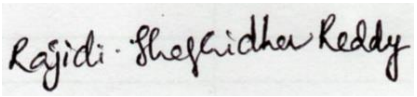

(**Rajidi Shashidhar Reddy**)

Abstract

This dissertation deals with the nonlinear dynamics and active/passive control of parametrically excited beam-like slender structures using piezoelectric actuators, viscoelastic damping materials and functionally graded materials (FGMs). First, the dynamics of smart slender beams is studied where the main focus is to investigate the usefulness of shear mode and extensional mode piezoelectric actuators in active control of complex nonlinear dynamics of the smart beams. Two smart beams are considered for separate use of the two different kinds of piezoelectric actuators; however, these beams are considered to operate under the transverse or axial compressive harmonic load while the actuators are activated by supplying the external electric field according to the velocity feedback control law. The dynamics of the smart beams is analysed by deriving the geometrically nonlinear electro-elastic incremental equations of motion in the finite element (FE) framework. The FE equations of motion are solved using Bathe time-integration method for evaluation of the transient responses, while the frequency responses are evaluated by implementing the harmonic balance method (HBM) in conjunction with a numerical continuation technique. The results for the transverse harmonic load reveal that both the actuators are capable of attenuating the large amplitude vibration of the smart beams; however, the application of the shear/extensional mode actuator is mainly limited to a certain extent of the load-amplitude. Under the axial compressive harmonic load, the dynamics of the smart beams in the pre-buckled state appears through the parametric instabilities. However, once the buckling occurs, the smart beams exhibit complex nonlinear dynamics due to the appearance of the snap-through periodic motion and the chaotic motion through the symmetry breaking, period-doubling/demultiplying and saddle-node bifurcations. The presented results mainly reveal the suitability of the shear mode and extensional mode piezoelectric actuators in active control of such dynamic instabilities and the associated complex motion of the smart beams.

The subsequent study is carried out to investigate the usefulness of viscoelastic damping materials in passive control of complex dynamics of parametrically excited beams. The viscoelastic damping materials are used through the constrained-layer damping (CLD) arrangement and modelled using fractional Zener constitutive relation. The corresponding dynamic analysis is carried out by deriving full-order nonlinear FE models (FOMs) of CLD treated beams in the time and frequency domains, where the HBM is employed for the derivation of frequency-domain FOM. However, to achieve reduced computational time in evaluating nonlinear transient/frequency responses, the nonlinear FOMs are subsequently reduced to reduced-order FE models (ROMs).

The nonlinear FOM in the time-domain is derived following the conventional formulation methodologies. However, the derivation of the nonlinear FOM in the frequency domain using HBM involves a tedious formulation mainly because of (a) an arbitrary number of harmonic terms in HBM and (b) the involvement of temporal derivative of stress/strain in the viscoelastic constitutive relation. Presently, this formulation of the HBM-based FOM is eased somewhat by introducing three new strategies, namely (a) a special factorization of the nonlinear strain-displacement matrix, (b) exploitation of orthogonality of Fourier basis functions and (c) reduction of various viscoelastic constitutive relations into a generalized mathematical form for the time-periodic stress/strain. The subsequent formulation of nonlinear ROMs is carried out at the elemental level without involving the full-order system matrices/vectors, where the primary contribution lies in the formulation of the nonlinear memory-load vector. It is observed that the present formulation of nonlinear ROMs at the elemental level yields a significant reduction of the computational time in the evaluation of nonlinear responses of CLD treated beams. Besides the reduced computational time, the accuracy of the nonlinear ROMs is achieved by proposing a new methodology for computation of appropriate reduced basis vectors (RBVs) using normal vibration modes (NMs), static modal derivatives (MDs) and proper orthogonal decomposition (POD) method. It is observed that the present RBVs are robust ones in

providing sufficient accuracy of the nonlinear ROMs, especially for accurate theoretical estimation of complex motion and dynamic bifurcations of CLD treated beams under the parametric excitation.

Using these ROMs, the usefulness of CLD treatment in passive control of complex nonlinear dynamics of parametrically excited beams is investigated, where the CLD treatment is configured in three different viscoelastic layered beams, namely (a) PCLD treated beam, (b) three-layered viscoelastic beam and (c) five-layered viscoelastic beam. The corresponding dynamic analysis reveals very complex motion of these viscoelastic layered beams involving various dynamic instabilities and chaotic oscillations. Besides, these beams also undergo the large-amplitude vibration through the snap-through periodic oscillation with respect to the zero equilibrium state. The CLD treatment is capable of attenuating this complex dynamics as well as large-amplitude vibration through the three/five-layered configuration. However, the PCLD configuration is not a suitable one for controlling this complex dynamics although it possesses greater static stability in comparison to the other two layered beams.

Finally, an FGM is taken as the material of a beam-like slender structure, where the main focus is to investigate the influence of graded material properties of the slender FGM structure on its nonlinear dynamic characteristics under the parametric excitation. This study is performed considering a pinned-pinned vertical/inclined FG pipe conveying hot fluid with the steady/pulsatile flow velocity. The FG pipe is comprised of metal and ceramic constituents with the inner ceramic rich surface to withstand the high temperature of internal hot fluid. The equation of motion of the FG pipe is derived based on the Euler-Bernoulli beam theory and plug-flow model, and that is subsequently solved using Galerkin discretization in conjunction with the HBM/Runge-Kutta method. First, the divergence of the FG pipe is investigated where it is mainly revealed that the inclination of the pipe with the vertical axis yields buckling at a higher temperature while the type of the associated bifurcation changes from pitchfork to saddle-node bifurcation. On the basis of this static instability, the pre-buckled and post-buckled equilibrium states of the FG pipe are identified, and its nonlinear dynamics associated with each of these equilibrium states is subsequently studied based on the variations of some system parameters, namely inclination angle, temperature, graded exponent of FG material, mean flow velocity, amplitude of pulsatile flow velocity and material damping. The corresponding results reveal some notable nonlinear dynamic characteristics of the vertical/inclined FG pipe like the appearance of both the principal primary and secondary parametric resonances in the pre-buckled state, exchange between softening and hardening structural behavior through period doubling/period demultiplying/fold bifurcation, movement of saddle periodic orbit with temperature leading to the unequal domains of attraction over the post-buckled equilibrium states and appearance of higher order parametric resonances at low material damping. However, the graded exponent of FGM and inclination angle may be utilized as the tuning parameters to alleviate static/dynamic instabilities and the associated complex motion of the FG pipe.

Table of Contents

Abstract
List of Figures
List of Tables
List of Symbols

Chapter 1 **Introduction**

1.1 Mechanical resonances in slender structures 2

1.2 Dynamics/instability of parametrically excited slender structures 5

1.2.1 Literature on dynamics of slender beams under periodic axial load in the pre-buckled state 7

1.2.2 Literature on dynamics of slender beams under periodic axial load in the post-buckled state 9

1.2.3 Literature on the dynamics of slender pipes conveying steady/pulsatile fluid 11

1.2.3.1 Instability of pipes conveying fluid with steady flow velocity 11

1.2.3.2 Dynamics of pipes conveying pulsatile fluid 12

1.2.4 Thermal effect on the stability of slender structures 15

1.3 Vibration/instability control of parametrically excited slender structures 17

1.3.1 Passive control of vibration/instability of parametrically excited slender structures using viscoelastic materials 18

1.3.2 Piezoelectric actuators in active control of vibration/instability of parametrically excited slender structures 20

1.3.3 Functionally graded materials (FGMs) in control of instability of parametrically excited slender structures 23

1.4 Methodologies for theoretical analysis of parametrically excited slender structures 26

1.4.1 HBM-based FE formulation for evaluation of nonlinear frequency responses of structural elements 27

1.4.2 Reduced-order FE models for evaluation of time/frequency responses of structural elements 28

1.5 Motivation and objectives of the present research 31

1.6 Contributions 35

1.7 Organization of the thesis 37

Chapter 2 **Nonlinear dynamics and active control of smart beams using shear/extensional mode piezoelectric actuators**

2.1 Introduction 40

2.2 Present smart beams 41

2.3 Mathematical formulation 43

2.4 Active control strategy 48

2.5 Implementation of the harmonic balance method 50

2.6 Local stability analysis 52

2.7 Results and discussion 54

2.7.1 Active control of nonlinear vibration of the smart beams under a direct excitation 58

2.7.2 Active control of the smart beams under parametric excitation 61

2.7.2.1 Dynamics and active control of smart beams in the pre-buckled state 61

2.7.2.2 Nonlinear dynamics and control of smart beams in the post-buckled state 67

2.8 Summary 75

Chapter 3 **A generalized finite element formulation for nonlinear frequency response analysis of slender viscoelastic beams using harmonic balance method**

3.1 Introduction 78

3.2 Mathematical modelling of a viscoelastic sandwich beam 81

3.3 Present HBM formulation 84

3.3.1 Reduction of time-domain constitutive relations for periodic stress/strain using HBM 85

3.3.2 Derivation of the governing equation of motion by exploiting the orthogonality of Fourier basis functions 89

3.3.3 Derivation of finite element model 91

3.4 Governing equation of motion in the time-domain 97

3.5 Results and discussion 99

3.5.1 Verification of the present FE formulation in the time/frequency domain 99

3.5.2 Computational efficiency of present FE formulation using HBM 102
3.5.3 Study on the simplified formulation of the tangent stiffness matrix 103
3.5.4 Nonlinear frequency responses of the sandwich beam using different viscoelastic constitutive models 105
3.6 Summary 107

Chapter 4 **Reduced-order finite element formulation for the geometrically nonlinear dynamic analysis of slender viscoelastic beams**

4.1 Introduction 109
4.2 Derivation of reduced-order FE model in the time domain 111
4.3 Derivation of the reduced-order FE model in the frequency domain 115
4.4 Enrichment of basis vectors 121
4.5 Results and discussion 124
4.5.1 Computational efficiency and accuracy of the present ROMs using enriched RB 125
4.5.2 Comparative study 130
4.6 Summary 135

Chapter 5 **Constrained layer damping treatment of post-buckled beams under parametric excitation: a theoretical study using reduced-order finite element formulation**

5.1 Introduction 138
5.2 Configuration of beams with CLD treatment 139
5.3 Formulation of incremental governing equation of motion 140
5.4 Nonlinear reduced-order FE models in time/frequency domain 144
5.4.1 Computation of reduced basis vectors (RBVs) 145
5.4.2 Derivation of the reduced-order FE model in the time domain 146
5.4.3 Derivation of the reduced-order FE model in the frequency domain 149
5.5 Results and discussion 151
5.5.1 Verification of present ROMs in the estimation of complex dynamics 152

5.5.2 Passive control of nonlinear dynamics of post-buckled beams 158
5.6 Summary 167

Chapter 6 **Nonlinear dynamics of functionally graded pipes conveying hot fluid**

6.1 Introduction 169
6.2 System model and governing equation of motion 172
6.3 Solution method 176
6.4 Local stability analysis 178
6.5 Numerical results and discussion 179
6.5.1 Verification of the present formulation 181
6.5.2 Static/dynamic characteristics of the vertical FG pipe conveying hot fluid 182
6.5.2.1 Stability of the vertical FG pipe conveying hot fluid with the constant flow velocity 183
6.5.2.2 Parametric instability of the vertical FG pipe conveying hot fluid with pulsatile flow velocity 184
6.5.2.3 Nonlinear frequency responses of the vertical FG pipe conveying pulsatile fluid 186
6.5.2.3.1 Nonlinear frequency responses of the FG pipe at the post-buckled state 187
6.5.2.3.2 Nonlinear frequency responses of the vertical FG pipe at the pre-buckled equilibrium state 188
6.5.2.3.3 Nonlinear frequency responses of the vertical FG pipe at the transition state 190
6.5.2.3.4 Global bifurcation diagrams 193
6.5.2.3.4.1 Global dynamics of the vertical FG pipe with respect to the frequency of pulsatile flow velocity 194
6.5.2.3.4.2 Global dynamics of the vertical FG pipe with respect to the pulsation 198

velocity-amplitude

6.5.3 Static/dynamic characteristics of the inclined FG pipe conveying hot fluid 199

6.5.3.1 Nonlinear response of the inclined FG pipe conveying hot fluid with constant flow velocity 200

6.5.3.2 Nonlinear dynamic response of inclined FG pipe conveying pulsatile hot fluid 202

6.5.3.2.1 Effect of temperature 203

6.5.3.2.2 Effect of the graded exponent of FGM 209

6.5.3.2.3 Effect of the mean flow velocity and amplitude of the pulsatile fluid 212

6.5.3.2.4 Effect of material damping of FGM 214

6.6 Summary 215

Chapter 7 **Conclusions and scope of future work**

7.1 Conclusions 218

7.2 Scope of future work 225

References 227

List of Publications 252

List of Figures

Fig. 1.1	A typical parametric instability region in the two-dimensional domain of excitation frequency and dynamic load parameter.	5
Fig. 1.2	A schematic diagram for pitchfork bifurcation of zero equilibrium position of a slender structure with respect to static load parameter.	6
Fig. 1.3	Schematic diagrams of (a) undeformed and (b) deformed states of substrate layer integrated with UCLD layer; (c) undeformed and (d) deformed states of substrate layer integrated with CLD/PCLD layer.	18
Fig. 1.4	Schematic diagrams of the (a) extensional mode and (b) shear mode piezoelectric actuators.	21
Fig. 2.1	Schematic diagrams of (a) a substrate beam integrated with extensional mode actuator patches (EMA beam) and (b) a sandwich beam having the shear mode actuator patches at the core (SMA beam).	42
Fig. 2.2	Verification of the present FE formulation in handling the electromechanical coupling in the extensional mode or shear mode piezoelectric actuators (SMA: shear mode actuation; EMA: extensional mode actuation) (Ref. (Sun and Zhang, 1995)).	57
Fig. 2.3	Verification of the present solution for nonlinear frequency response of clamped-clamped beams under the transverse harmonic point-load (Ω_n is the fundamental natural frequency) (Ref. (Ribeiro, 2004)).	58
Fig. 2.4	(a), (c) Controlled nonlinear frequency responses of the clamped-clamped SMA/EMA beam; (b),(d) the corresponding variations of the externally applied electric field (E_z).	59
Fig. 2.5	Variation of the applied electric field (E_z) corresponding to the peak displacement-amplitude for different values of the load-amplitude (p_t^o) (k_{sd} = 400, k_{ed} = 400).	60
Fig. 2.6	Convergence study for deciding the value of in the evaluation of the parametric instability regions for the (a) SMA beam and (b) EMA beam; (c) verification of the present FE solution for the evaluation of the parametric instability region (Ref. (Iwatsubo et al., 1973)).	62
Fig. 2.7	Parametric instability regions for (a) SMA beam with p_r = 0.3, (b) SMA beam with p_r = 0.7, (c) EMA beam with p_r = 0.3, (d) EMA beam with p_r = 0.7.	63
Fig. 2.8	Variations of (a) the origin (λ_o) of instability and (b) the width of instability ($\Delta\Omega$ at $\lambda = 0.2$) with the control gain (k_{sd} or k_{ed}).	64

Fig. 2.9 (a), (c) Frequency responses of the SMA and EMA beams under the principal primary parametric resonance; (b), (d) the corresponding variations of the applied electric field (E_z); (1: k_{sd} = 535, 2: k_{sd} = 530, 3: k_{sd} = 500; 1': k_{ed} = 138, 2': k_{ed} = 135, 3': k_{ed} = 125). 65

Fig. 2.10 (a), (c) Transient responses of the SMA (Ω =390 rad/s, k_{sd} =500) and EMA beams (Ω =305 rad/s, k_{ed} =125) for different initial transverse displacements (w_{it}); (b), (d) the corresponding variations of the applied electric field (p_r =0.3, λ =0.2). 67

Fig. 2.11 (a), (c) Frequency responses of SMA beam in its post-buckled state (p_r = 1.05, λ = 0.02, (a) k_{sd} = 3500, (c) k_{sd} = 500); (b), (d) the corresponding variations of the applied electric field ((b) k_{sd} = 3500, (d) k_{sd} = 500). 68

Fig. 2.12 (a) Global bifurcation diagram corresponding to the critical zones (KN, QR) in Fig. 2.11(a); (b) the corresponding variation in the applied electric field (E_z). 69

Fig. 2.13 Responses of SMA beam at different excitation frequencies (p_r =1.05, λ=0.02, k_{sd}=500); transient responses at (a) Ω = 49 rad/s, (b) Ω = 121.9 rad/s; phase plots at (c) Ω = 49 rad/s, (d) Ω = 121.9 rad/s, (e) Ω = 71.2 rad/s, (f) Ω = 71.2 rad/s, (g) Ω = 72.8 rad/s; frequency spectrums at (h) Ω = 131.18 rad/s, (i) Ω = 131.5 rad/s, (j) Ω = 136.8 rad/s. 70

Fig. 2.14 (a) Frequency response of SMA beam in its post-buckled state (p_r = 1.05, λ = 0.02, k_{sd} =900) and (b) the corresponding variations of the applied electric field (E_z). 71

Fig. 2.15 (a), (c) Frequency responses of the EMA beam in its post-buckled state (p_r = 1.05, λ = 0.02, (a) k_{ed} = 100, (c) k_{ed} = 500); (b), (d) the corresponding variations of the applied electric field ((b) k_{ed} = 100, (d) k_{ed} = 500). 72

Fig. 2.16 (a) Global bifurcation diagram corresponding to the critical zones (KN, QR) in Fig. 2.15(a); (b) the corresponding variation of the applied electric field (E_z). 73

Fig. 2.17 (a) Frequency responses of the EMA beam at its post-buckled state (p_r = 1.05, λ = 0.02) for different values of the control gain (k_{ed}), (b) the corresponding variations of the applied electric field (E_z). 73

Fig. 2.18 (a), (c) Frequency responses of the EMA beam in its post-buckled state (p_r = 1.05, λ = 0.2, (a) k_{ed} = 500, (c) k_{ed} = 3500); (b), (d) the corresponding variations of the applied 74

electric field ((b) k_{ed} = 500, (d) k_{ed} = 3500).

Fig. 2.19 (a), (c) Frequency responses of the EMA beam in its post-buckled state (p_r = 1.1, λ = 0.2, (a) k_{ed} = 500, (b) k_{ed} = 3000); (b), (d) the corresponding variations of the applied electric field ((b) k_{ed} = 500, (d) k_{ed} = 3000). 75

Fig. 3.1 Schematic diagram of a sandwich beam with the viscoelastic core. 81

Fig. 3.2 Verification of the present FE code for evaluation of transient responses of the sandwich beam based on the fractional Zener model (Ref. (Galucio et al., 2004)). 99

Fig. 3.3 (a) Convergence study for an appropriate number (H) of harmonic terms in implementation of HBM (p_t^o = 4000 N/m^2), (b) verification of the present FE formulation for nonlinear frequency response analysis of viscoelastic structures using HBM. 101

Fig. 3.4 Nonlinear frequency responses of the viscoelastic sandwich beam are evaluated using either conventional or present strategy in the implementation of HBM. 102

Fig. 3.5 Nonlinear frequency responses of the sandwich beam for three different thicknesses of the viscoelastic core using the simplified formulation of the tangent stiffness matrix (p_t^o = 4000 N/m^2). 104

Fig. 3.6 Fitted curves for time-domain viscoelastic constitutive models in the determination of their model parameters from the experimental data (Galucio et al., 2004); (a) storage modulus and (b) material loss factor. 106

Fig. 3.7 Frequency response of the sandwich beam using different viscoelastic constitutive models for the viscoelastic core (H = 7, p_t^o = 4000 N/m^2). 107

Fig. 4.1 Comparison of nonlinear transient responses evaluated using ROM#1, ROM#2 and full-order FE model. 127

Fig. 4.2 Comparison of frequency responses obtained from full-order FE model and ROM with or without simplified formulation of the tangent stiffness matrix (ROM is taken with the enriched RB (RB#II)). 128

Fig. 4.3 Comparison of frequency responses obtained from full-order FE model and ROM considering unenriched RB (RB#I) or enriched RB (RB#II). 129

Fig. 4.4 (a) Comparison of transient responses obtained from full-order FE model and ROM#2 considering the number (N_r) of enriched RBVs as 52 from different approaches, (b) corresponding displacement errors with respect to the 132

displacement solution of full-order FE model.

Fig. 4.5 Variation of mean displacement error with the number (N_r) of basis vectors in the enriched RB. 133

Fig. 4.6 Comparison of nonlinear frequency responses obtained from full-order FE model and ROM considering the number (N_r) of enriched RBVs as 52 through different approaches. 134

Fig. 4.7 Variation of the normalized displacement error for the nonlinear frequency responses presented in Fig. 4.6. 134

Fig. 4.8 Variation of the mean normalized displacement error with the number (N_r) of basis vectors within the enriched RB. 135

Fig. 5.1 Schematic diagrams of (a) a substrate beam with a PCLD layer, (b) a three-layered beam and (c) a five-layered beam operating under the axial compressive harmonic load (p_a^t). 140

Fig. 5.2 Comparison of frequency responses obtained from the time-domain/frequency-domain FOM and ROM considering unenriched RB or enriched RB. 153

Fig. 5.3 Accuracy of the frequency-domain ROM with reference to the full-order FE model (FOM) in the evaluation of a complex nonlinear frequency response of the thee-layered beam under the parametric excitation in the post-buckled state. 154

Fig. 5.4 Accuracy of the time-domain ROM with reference to the full-order FE model (FOM) in the evaluation of global bifurcation diagram of the parametrically excited three-layered beam in its post-buckled state. 155

Fig. 5.5 Verification of the present time-domain ROM in the evaluation of different kinds of transient responses with reference to FOM, ((a)-(b) transient responses; (c) phase portraits of chaotic response showing intermittent transition bifurcation; (d) phase portraits for dual period-2 responses; frequency spectrums showing the period-demultiplying bifurcation of global periodic attractors (e) period-8 response, (f) period-4 response, (g) period-2 response; phase portraits showing the period-demultiplying bifurcation of local periodic attractors (h) period-8 , (i) period-4 and (j) period-2 responses). 156

Fig. 5.6 Variation of the transverse deflection of the layered beams with the static counterpart of the parametric load, C#1: PCLD treated beam (Fig. 5.1(a)), C#2: Three-layered beam (Fig. 5.1(b)), C#3; Five-layered beam (Fig. 5.1(c))). 159

Fig. 5.7 (a), (b) Nonlinear frequency responses and (b), (d) global bifurcation diagrams of the PCLD treated beam under the parametric excitation (p_a^o = 320 N, λ = 0.1) in the post-buckled 161

state ((a), (b) for h_v = 0.5 mm and (c), (d) for h_v = 1.5 mm).

Fig. 5.8 (a), (b) Nonlinear frequency responses and (b), (d) global bifurcation diagrams of the three-layered beam under the parametric excitation (p_a^o = 320 N, λ = 0.1) in the post-buckled state ((a), (b) for h_v = 0.5 mm and (c), (d) for h_v = 1.5 mm). 162

Fig. 5.9 Frequency responses of the five-layered beam under the parametric excitation (p_a^o = 320 N, λ = 0.1) in the post-buckled state ((a), (b) for h_v = 0.5 mm and (c), (d) for h_v = 1.5 mm). 163

Fig. 5.10 Nonlinear frequency responses of the PCLD treated beam under the parametric excitation (p_a^o = 250 N, λ = 0.1) for two different values of thickness (h_v) of the constrained viscoelastic layer. 164

Fig. 5.11 (a), (c) Nonlinear frequency response and (b), (d) global bifurcation diagram of the three-layered beam under the parametric excitation (p_a^o = 250 N, λ = 0.1) for two different values of thickness (h_v) of the constrained viscoelastic layer. 165

Fig. 5.12 Nonlinear frequency response of the five-layered beam under the parametric excitation (p_a^o = 250 N, λ = 0.1) for two different values of total thickness (h_v) of the constrained viscoelastic layers. 166

Fig. 6.1 Schematic diagram of an inclined pinned-pinned FG pipe conveying hot fluid. 172

Fig. 6.2 Fig. 6.2. (a) Comparison of the static profile of an inclined isotropic pipe with that for an identical pipe in Ref: (Alfosail et al., 2017b), (b) comparison of nonlinear dynamic response of vertical isotropic pipe conveying pulsatile fluid with the similar response of an identical pipe in Ref: (Jin and Song, 2005). (RK: Runge-Kutta) 182

Fig. 6.3 Variation of the constant flow velocity (V_f, $\lambda = 0$) with temperature (T_i) corresponding to the onset of buckling of the FG pipe. 183

Fig. 6.4 Regions of parametric instability corresponding to the principal primary parametric resonance at the pre-buckled state of the FG pipe ($V_f = 5$ m/s), (a)-(d) for different temperatures (T_i (K), $n = 5$) and (e)-(f) for different values of the graded exponent (n, T_i = 335 K). 185

Fig. 6.5 Nonlinear frequency responses of the FG pipe at its post-buckled state, (a), (b), (d) for different temperatures (T_i) ($n=5$), and (c), (d), (e) for different values of the graded exponent (n) ($T_i = 380$ K). 187

Fig. 6.6 Fig. 6.6. Nonlinear frequency responses of the FG pipe at its post-buckled state ($n=5$, $T_i=360$ K); (a) $V_f=2$m/s or 5 m/s, $\lambda=0.5$; (b) $V_f=2$ m/s or 5 m/s, $\lambda=0.1$. 189

Fig. 6.7 Fig. 6.7. Frequency responses of the FG pipe corresponding to the principal primary parametric resonance when the FG pipe is in its pre-buckled state; (a) for different temperatures (T_i (K), $n=5$), (b) for different values of the graded exponent (n, $T_i=$ 335 K) ($V_f=5$ m/s, $\lambda=0.5$). 190

Fig. 6.8 Nonlinear frequency responses of the FG pipe for different temperatures near the critical buckling temperature ($n=5$, $V_f=5$ m/s, $\lambda=0.5$); (a) $T_i=337.2$ K, (b) $T_i=337.6$ K, (c) $T_i=$ 339 K, (d) $T_i=350$ K. 191

Fig. 6.9 Nonlinear frequency response of the FG pipe at its post-buckled state ($V_f=5$ m/s, $\lambda=0.5$, $T_i=350$ K, $n=8$). 192

Fig. 6.10 Nonlinear frequency responses of the FG pipe ($n=5$, $T_i=339$ K) for different values of the mean flow velocity (V_f) and pulsation velocity-amplitude (λ); (a) $V_f=4$ m/s, $\lambda=0.5$, (b) $V_f=5$ m/s, $\lambda=0.3$. 193

Fig. 6.11 Global bifurcation diagrams with respect to the frequency (Ω) of the pulsating flow velocity of the internal hot fluid ($n=5$, $V_f=5$ m/s, $\lambda=0.5$); (a), (b) for critical zone AB in Fig. 6.8(b) ($T_i=337.6$ K); (c), (d) for critical zones AB and CD in Fig. 6.8(c) ($T_i=339$ K). 194

Fig. 6.12 Responses of the veritcal FG pipe at different frequencies ($n=5$, $V_f=5$ m/s, $\lambda=0.5$, $T_i=337.6$ K); transient responses at (a) $\Omega=0.3402$, (b) $\Omega=0.3403$; phase plots at (c) $\Omega=0.3403$, (e) $\Omega=0.64$, (f) $\Omega=0.66$, (g) $\Omega=0.66$, (h) $\Omega=0.85$, (i) $\Omega=0.9$, (j) $\Omega=0.9$; Poincare map at (d) $\Omega=0.3403$. 195

Fig. 6.13 Responses of the vertical FG pipe at different frequencies ($n=5$, $V_f=5$ m/s, $\lambda=0.5$, $T_i=339$ K); phase plots at (a) $\Omega=2$, (b) $\Omega=4.77$, (d) $\Omega=4.785$, (e) $\Omega=4.79$, (f) $\Omega=4.8$; Poincare map at (c) $\Omega=4.77$; amplitude-frequency spectrums at (g) $\Omega=$ 196

4.785, (h) $\Omega = 4.79$, (i) $\Omega = 4.8$.

Fig. 6.14 Global bifurcation diagrams with respect to the pulsation velocity-amplitude ($n = 5, V_f = 5$ m/s, $\Omega = 1.23$) at different temperatures, (a) $T_i = 337.6$ K, (b) $T_i = 337.8$ K, (c) $T_i = 338$ K, (d) $T_i = 338.2$ K. 197

Fig. 6.15 Responses of the FG pipe ($n = 5, V_f = 5$ m/s, $\Omega = 1.23$) at different pulsation velocity-amplitudes; time response plots at (a) $\lambda = 0.2025$ ($T_i = 337.6$ K), (b) $\lambda = 0.203$ ($T_i = 337.6$ K), phase plots at (c) $\lambda = 0.203$ ($T_i = 337.6$ K), (d) $\lambda = 0.35$ ($T_i = 337.8$ K), (e) $\lambda = 0.38$ ($T_i = 337.8$ K), (f) $\lambda = 0.38$ ($T_i = 337.8$ K), (g) $\lambda = 0.4$ ($T_i = 337.8$ K), (h) $\lambda = 0.402$ ($T_i = 337.8$ K), (i) $\lambda = 0.403$ ($T_i = 337.8$ K), amplitude-frequency spectrums at (j) $\lambda = 0.4$ ($T_i = 337.8$ K), (k) $\lambda = 0.402$ ($T_i = 337.8$ K), (l) $\lambda = 0.403$ ($T_i = 337.8$ K). 198

Fig. 6.16 (a) Variation of static profile of FG pipe ($n = 4$) having the internal mass of fluid ($V_f = 0$) for different values of the inclination angle, (b) variation of maximum transverse deflection (η_m) of the inclined FG pipe ($\chi = 45^0$) with the steady flow velocity (V_f) of internal fluid for different values of the graded exponent (n) of FGM ($T_i = T_o = 300$ K). 201

Fig. 6.17 Variation of the maximum transverse deflection (η_m) of the inclined FG pipe with the temperature (T_i) of the internal fluid (V_f = 5 m/s). 202

Fig. 6.18 Nonlinear frequency responses of the vertical FG pipe ($\chi = 0$) at its (a) pre-buckled state ($T_i = 335$ K) and (b)-(c) post-buckled state ($T_i = 350$ K, 385 K), (d) global bifurcation diagram with respect to pulsation frequency at the neighborhood of bifurcation points A and A′ in Fig. 18b ($n = 4$, $V_f = 5$ m/s and $\lambda = 0.5$). 203

Fig. 6.19 Nonlinear frequency responses of the inclined FG pipe ($n = 4$, $\lambda = 0.5$, $V_f = 5$ m/s, $\chi = 25^0$) in the pre-buckled state for different temperatures; (a) $T_i = 300$ K, (b) $T_i = 335$ K. 205

Fig. 6.20 Nonlinear frequency responses of the inclined FG pipe ($n = 4$, $\lambda = 0.5$, $V_f = 5$ m/s) for (a) $\chi = 15^0$, $T_i = 350$ K and (b) $\chi = 45^0$, $T_i = 350$ K; (c) basin of attraction at a frequency of $\Omega = 9$ 207

corresponding to the frequency response in the case (a).

Fig. 6.21 Nonlinear frequency responses of the inclined FG pipe ($n=4$, $\lambda=0.5$, $V_f=5$ m/s, $\chi=25^0$) for different temperatures; (a) $T_i=344$ K, (b) $T_i=355$ K, (c) $T_i=385$ K and (d) $T_i=390$ K. 208

Fig. 6.22 Basin of attraction at a frequency of $\Omega=7.5$ ($n=4$, $\lambda=0.5$, $V_f=5$ m/s, $\chi=25^0$) for two different temperatures; (a) $T_i=355$ K and (b) $T_i=385$ K (green closed curves are limit cycle attractors and red closed curve is saddle periodic orbit). 209

Fig. 6.23 Nonlinear frequency responses of the inclined FG pipe ($V_f=5$ m/s, $\lambda=0.5$, $\chi=25^0$) for (a) $T_i=344$ K, $n=8$ and (b) $T_i=355$ K, $n=2$. 211

Fig. 6.24 Nonlinear frequency responses of the inclined FG pipe ($n=4$, $\lambda=0.5$, $\chi=25^0$) conveying pulsatile fluid with the flow velocity (V_f) of 3 m/s at two different temperatures; (a) $T_i=344$ K and (b) $T_i=355$ K. 212

Fig. 6.25 (a) Nonlinear frequency response of the inclined FG pipe at its pre-buckled state ($T_i=350$ K, $\chi=45^0$) for a low material damping of FGM ($r_\tau=0.00004$ s, $V_f=5$ m/s, $\lambda=0.5$) and (b) the corresponding global bifurcation diagram. 213

Fig. 6.26 (a) Nonlinear frequency response of the inclined FG pipe at its post-buckled state ($T_i=390$ K, $\chi=25^0$) for a low material damping of FGM ($r_\tau=0.00004$ s, $V_f=5$ m/s, $\lambda=0.5$) and (b) the corresponding global bifurcation diagram. 214

List of Tables

Table 2.1	Geometrical properties of the smart beams (Figs. 2.1(a)-(b)).	55
Table 2.2	Material properties of component materials in the smart beams (Figs. 2.1(a)-(b)).	55
Table 2.3	Transverse displacement amplitudes of SMA/EMA beam at the fundamental resonance under the direct excitation (p_t^o = 0.01 N) for different numbers (n_p) of actuator patch segments (SMA beam: k_{sd} =150 and w at $x = L/2$, $z = h$; EMA beam: k_{ed} =70 and w at $x = L/2$, $z = h - (h_p/2)$).	55
Table 3.1	Computational time for evaluation of nonlinear frequency responses in Fig. 3.4 using either the present strategy (t_{Pc}) or the conventional strategy (t_{Cc}) in the implementation of HBM.	103
Table 3.2	Computational time in the evaluation of nonlinear frequency responses (Fig. 3.5) by ignoring the viscoelastic part in the formulation of the tangent stiffness matrix (t_{Fc} for full tangent stiffness matrix; t_{Sc} for simplified tangent stiffness matrix).	104
Table 3.3	Constitutive model parameters for generalized Maxwell model of the viscoelastic material (3M ISD 112) for different numbers (n) of Maxwell elements (E_o = 1.5 MPa).	106
Table 4.1	Computational time in the evaluation of nonlinear transient responses (Fig. 4.1) using ROM#1, ROM#2 and full-order FE model.	127
Table 4.2	Computational time in the evaluation of frequency responses in Fig. 4.2.	128
Table 4.3	Computational time in the evaluation of frequency responses (Fig. 4.3) using the present ROM with the simplified formulation of the tangent stiffness matrix	129
Table 4.4	Present consideration of the number of enriched RBVs for different approaches (MSE, MSEC, MM, ICES, RKT and FSRK).	131
Table 5.1	Computational time in the evaluation of complex frequency response (Fig. 5.3) or transient response (at $\Omega = 110$ rad/s, Fig. 5.4) of the three-layered sandwich beam using the present ROMs and FOMs.	158
Table 5.2	Critical buckling load (p_{cr}) for the layered beams.	159

Table 6.1 Comparison of critical buckling temperatures of FG pipe ($r_o = 0.5$ mm, $r_i = 0.5 r_o$). 181

List of Symbols

List of symbols used throughout the thesis are listed. List of symbols less frequently used, or that have different meaning or different forms at different contexts, are defined where they are used.

L / L_p	Length of the beam or pipe/actuator patch
n_p / L_s	Number/length of uniform segments containing piezo patches along the span of beam
S_i	i^{th} velocity sensor
h_f / h_p	Thickness of substrate beam/piezo patch
h_{s1} / h_{s2} and h_v	Thicknesses of the bottom or top face layers and the core layer of sandwich beam
h	Thickness of overall beam
b	width of the beam
r_i / r_o	Internal /external radius of the pipe
χ	Inclination angle of pipe
v	Poisson's ratio
ρ	Mass density
p_{cr}	Critical buckling load
λ	Dynamic load parameter
p_a^o / p_r	Static load parameter
p_a^t	Axial compressive load
p_t / p_{tu}	Transverse point/uniformly distributed load
H	Number of harmonic terms
k_{sd}	Feedback control gain for SMA actuator
k_{ed}	Feedback control gain for EMA actuator
$\boldsymbol{d}$	Displacement vector
$\boldsymbol{I}_{N_f}$ / $\boldsymbol{I}_{N_r}$ / $\boldsymbol{I}_{18}$	Identity matrix of size $(N_f \times N_f)$/ $(N_r \times N_r)$ /(18×18)
$\boldsymbol{O}_{N_f}$ /$\boldsymbol{O}_{N_r}$ /$\boldsymbol{O}_{18}$	Null matrix of size $(N_f \times N_f)$/ $(N_r \times N_r)$/(18×18)
$\boldsymbol{L}$ / $\boldsymbol{L}_n$	Operator matrices
$\boldsymbol{M}_s$	Mass matrix
$\boldsymbol{K}_{sl}$ / $\boldsymbol{K}_{sn1}$ / $\boldsymbol{K}_{sn3}$ / $\boldsymbol{K}_{sn4}$ / $\boldsymbol{K}_{sn5}$	Linear stiffness matrices
$\boldsymbol{K}_{sn}$	Nonlinear stiffness matrix

$^{r}\bar{F}_{s1}$ / $^{r}\bar{F}_{s2}$	Reduced-order anelastic forces
K_{sa} / K_{sg}	Load-dependent/displacement-dependent geometric stiffness matrix
K_a / K_g	Overall load-dependent/displacement-dependent geometric stiffness matrix
K_{sm} / K_{st}	Stiffness/Tangent stiffness matrices
K	Tangent stiffness matrix for static deformation of beam
K_m / K_t	Overall stiffness/tangent stiffness matrix
N	Shape function matrix
B_l / B_n	Linear/Nonlinear strain-displacement matrices
d^e	Elemental nodal displacement vector
$\bar{P}_s$	Memory load vector
P_s / P_{su}	Load vectors corresponding to point/uniformly distributed loads
P_Ω / P_λ	Load vector per unit increment of Ω / λ ;
R_s	Residue vector
R / R_Ω / R_λ	Overall residue vector/ Load vector per unit increment of Ω / λ
X	Overall displacement vector
d	Global general displacement field vector
D	Electrical displacement field vector
E	Electric field vector
ϕ	State transition matrix
λ_q / Θ_q	Proper orthogonal value/mode for the q^{th} mode
$\Re$	Correlation matrix
Φ	Reduction basis
θ_p	p^{th} reduced-basis vector
φ_{pj}	Static derivative of p^{th} RBV (θ_p) with respect to the j^{th} reduced coordinate
$^{i}\Gamma^{k}$	Stress matrix at any point in k^{th} material for reference state
Γ_a^k	Pre-stress matrix
d_s^o / d_{sm}^c / d_{sm}^s	Displacement amplitude vectors corresponding to the constant, cosine and sine terms
V	Reduced coordinate vector

N_f / N_r	Number of degrees of freedom for full-order/reduced-order model
N_m	Number of reduced basis vectors
δT_t	Variation of total kinetic energy
δT_p	Variation of total potential energy
u , w	Displacements components in x and z directions
$\boldsymbol{\varepsilon}$	Strain vector
$\bar{\boldsymbol{\varepsilon}}$	Anealstic strain vector
$\varepsilon_l / \varepsilon_n$	Linear/Nonlinear strain vector
$\boldsymbol{\sigma}$	Stress vector
$\boldsymbol{\sigma}_a$	Pre-stress vector
Ω	Operating frequency
Ω_n	Fundamental natural frequency of vibration
$\varepsilon_x / \varepsilon_z$	Normal strain along x / z direction
γ_{xz} / τ_{xz}	Transverse shear strain/stress in the xz -plane
$\boldsymbol{C}^k$	Stiffness matrix for k^{th} material
E^k	Young's modulus for k^{th} material
E_o / E_∞	Relaxed/non-relaxed elastic moduli
ν^k	Poisson's Ratio for k^{th} material
σ_x / σ_z	Normal stress along x / z direction
E_z	Electric field component along z direction
$\boldsymbol{e}^k$	Electro-mechanical coupling coefficient matrix for k^{th} material
A^e / A^k	Area of an element/ k^{th} material
α	fractional-order time derivative
α_T	Thermal expansion coefficient
P_c / P_m	Properties of ceramic and metal constituents
P_{in}	Internal pressure of fluid
V_f	Mean flow velocity

Superscript:

e	Element

i	Reference State of vibration
R	Real
I	Imaginary
T	Transpose
$o / c / s$	Constant/cosine/sine terms
p / f	Pipe/fluid
r	Reduced-order

Subscript:

eq	Static equilibrium
q	q^{th} time-step
k	Material number

Abbreviations:

UCLD	Unconstrained layer damping
CLD	Constrained layer damping
PCLD	Passive constrained layer damping
ACLD	Active constrained layer damping
FE	Finite element
FGM	Functionally graded material
ROM	Reduced-order FE model
FOM	Full-order model
VEM	Viscoelastic material
HBM	Harmonic balance method
RBV	Reduced basis vector
RB	Reduction basis
ICES	Iterative complex eigen solution method
MM	Multi-model method
ERM	Enriched Ritz method
MSE	Modal strain energy
MSEC	MSE with first order corrective terms (MSEC)
RKT	Rational Krylov approach with Taylor expansion of complex modulus
FSRK	Frequency-dependent rational Krylov approach
EMA	Extensional mode actuator

SMA	Shear mode actuator
MD	Modal derivative
SD	Static derivative
VM	Vibration mode
POD	Proper orthogonal decomposition
POM	Proper orthogonal mode

Chapter 1

Introduction

Beam-like structural elements are essential components of various engineering systems, which appear in different forms like drill strings in deep hole drilling (Dunayevsky et al., 1993; Gupta and Wahi, 2018), vibrating screens in vibratory machines (Zahedi and Babitsky, 2016), drills in high-speed drilling and milling machines (Huang and Kuang, 2007a), work piece in lathe operations (Huang and Yang, 2009), turbine blades (Sinha, 2005), robotic manipulator arms, power transmission belts, marine risers, fluid conveying pipes (Marynowski and Kapitaniak, 2014), etc. In common practice, these slender structural elements operate under the transverse and axial harmonic forces that are customarily known as direct and parametric harmonic excitations, respectively (Abou-Rayan et al., 1993; Ewins and Inman, 2001). The direct harmonic excitation acting in the transverse direction causes periodic oscillation of a beam element through forced resonance (Ewins and Inman, 2001). In the other type of load, i.e. parametric harmonic excitation along the axial direction, a beam element undergoes periodic or quasi-periodic oscillation through parametric resonance/instability (Bolotin, 1964). However, the parametric resonance/instability is more critical than the forced resonance (Jia and Seshia, 2014; Zahedi and Babitsky, 2016) since the vibration amplitude grows exponentially with time under the parametric resonance. Moreover, a parametrically excited beam element may undergo complex dynamics once its buckling occurs due to the static counterpart of the parametric load (Abou-Rayan et al., 1993; El-Bassiouny, 2006; Emam and Abdalla, 2015). This complex dynamics of post-buckled beams appears with various dynamic instabilities and the associated complex motion, where chaotic oscillation may also arise depending on the amplitude/frequency of the parametric excitation (Abou-Rayan et al., 1993; El-Bassiouny, 2006; Emam and Abdalla, 2015).

However, this complex motion of a parametrically excited slender structure usually leads to improper functionality in an engineering system and even fracture/fatigue failure. Therefore, a great deal of research has been reported in the literature for active/passive control of parametrically excited beam-like slender structures using different kinds of active materials, viscoelastic damping materials and functionally graded materials (FGMs) (Chen et al., 2002; Dwivedy

et al., 2007; Hosseini and Fazelzadeh, 2011; Lacarbonara et al., 2007; Li and Liu, 2012; Lv et al., 2018; Mohanty et al., 2011; Pradhan et al., 2016; Ray and Kar, 1996a; Sheng and Wang, 2018, 2019; Yao et al., 2015). However, the utilization of these materials in controlling or stabilizing a parametrically excited slender structure poses its complex geometrical and material configuration, which is commonly handled using the finite element (FE) procedure for theoretical study (Balamurugan and Narayanan, 2002; Kumar and Panda, 2016; Trindade, 2007; Trindade et al., 2001). Here, the nonlinear dynamical analysis using FE models usually involves high computational time, especially for evaluating nonlinear frequency responses and global bifurcation diagrams. In this aspect, reduced-order FE models (ROMs) are recommended in a good number of available studies (Hollkamp et al., 2005; Mignolet et al., 2013; Touze et al., 2021).

In this introductory chapter, a brief introduction is first presented on the mechanical resonances and the associated nonlinear dynamics of slender structures operating under the direct/parametric excitation. Next, a literature review is presented on the nonlinear dynamics/instability of parametrically excited slender structures. Subsequently, a brief introduction on viscoelastic, piezoelectric and FGMs is furnished along with the available studies on their use in control of vibration/dynamic instability of parametrically excited slender structures. In the next section, a literature review on the FE models for the nonlinear dynamic analysis of slender structures is presented, where the development of ROMs is mainly focused. Based on this literature review, the scope of the present research has been identified, and the objectives of the present thesis are furnished. The contributions in the field of nonlinear dynamics and control of slender structures made towards the preparation of this dissertation are delineated thereafter. In the end, the organization of the thesis is outlined.

1.1. Mechanical resonances in slender structures

Mechanical resonance is a phenomenon where the maximum amount of work done by the external harmonic excitation is transferred to the system resulting in its large amplitude vibration. As mentioned above, the applied dynamic forces on a slender structure are commonly classified as direct and parametric excitations (Abou-Rayan et al., 1993). A direct harmonic excitation usually appears in the form of additive force within the governing equation of motion. A classical example of a governing equation of motion of a nonlinear system under direct harmonic excitation is given in Eq. (1.1a), known as the nonlinear Duffing equation.

$$\ddot{x} + 2\xi\Omega_n\dot{x} + \Omega_n^2 x + \alpha_2 x^2 + \alpha_3 x^3 = f\cos(\Omega t) \tag{1.1a}$$

$$x = c_1 \cos(\Omega_n t) + c_2 \sin(\Omega_n t) + \langle f/(2\Omega_n) \rangle t \sin(\Omega_n t) \tag{1.1b}$$

In Eq. (1.1a), x is the displacement of mass of the system; ξ and Ω_n are the damping ratio and natural frequency of the system, respectively; α_2 and α_3 are the quadratic and cubic nonlinear coefficients, respectively; f is the amplitude of harmonic excitation per unit mass, which appears as an additive force. Since it is an additive force, the oscillatory motion of the mass occurs at any frequency of excitation. However, the mechanical resonance of a linear undamped system appears when the frequency of excitation (Ω) is equal to the natural frequency (Ω_n) of the system, and it is known as direct/forced resonance. It results in the linear growth of amplitude of vibration with time, which can be observed through the response of the undamped linear system ($\alpha_2 = \alpha_3 = \xi = 0$, Eq. (1.1a)) at the resonant condition, as given in Eq. (1.1b) where c_1 and c_2 are the constants in terms of initial conditions. However, the damping (ξ) in the system limits the amplitude of vibration.

The parametric excitation usually appears through the time-varying parameters (mass, damping coefficient, stiffness) of a system. A classical example of the governing equation of motion of a parametrically excited nonlinear system is given in Eq. (1.2a), known as the nonlinear Mathieu equation (Bolotin, 1964).

$$\ddot{x} + 2\xi\Omega_n \dot{x} + \Omega_n^2 (1 - 2\lambda \cos(\Omega t)) x + \alpha_2 x^2 + \alpha_3 x^3 = 0 \tag{1.2a}$$

$$x = e^{\vartheta t} \{c_1 \cos(\Omega/2) t + c_2 \sin(\Omega/2) t\}, \quad \vartheta = \pm(\Omega_n/2\kappa)\sqrt{\lambda^2 - (1-\kappa^2)^2},$$

$$\kappa = \Omega/2\Omega_n \tag{1.2b}$$

In Eq. (1.2a), the parametric excitation is evident through time varying stiffness of the system. Here, λ is the dynamic counterpart of parametric excitation known as dynamic load parameter, while the natural frequency (Ω_n) is a function of static counterpart of parametric excitation known as static load parameter. Since the excitation appears in the form of a system parameter, the system remains at its static equilibrium. However, a sudden loss of stability of the system may occur, resulting in an oscillatory motion when the frequency (Ω) of excitation is in the vicinity of $2\Omega_n/r$ where r is a positive integer. This loss of stability is commonly known as parametric instability or parametric resonance. The corresponding amplitude of vibration grows exponentially with time, which can be observed through the response (Eq. (1.2b), (Bolotin, 1964)) of the undamped linear system ($\alpha_2 = \alpha_3 = \xi = 0$, Eq. (1.2a)) when $\lambda^2 > (1-\kappa^2)^2$. This condition provides a range of frequency for parametric instability/resonance, which increases with the rise in

the dynamic load parameter (λ). However, unlike the forced resonance, the amplitude of oscillation is not limited by the linear damping but it is restricted by the nonlinearity in system. Moreover, the linear damping eliminates the possibility of parametric instability/resonance at lower values of the dynamic load parameter (λ) (Bolotin, 1964).

However, for a multi-degree-of-freedom system, the parametric instability occurs in the vicinity of $({}_i\Omega_n \pm {}_j\Omega_n)/r$, where ${}_i\Omega_n$ is the i^{th} modal natural frequency of the linearized system. This kind of parametric instability is known as combinatory parametric resonance. Moreover, the frequency range of instability increases with the increasing dynamic load parameter (λ), resulting in a wide frequency range of instability where the loss of stability occurs with the exponential growth of vibration amplitude. In this concern, parametric resonance is said to be more critical than forced resonance.

The nonlinearity in the aforesaid systems (Eqs. (1.1a) and (1.2a)) mainly induces the variation of natural frequency with the amplitude of vibration, and it results in a wide frequency range of resonance. In the case of quadratic nonlinearity, the natural frequency decreases with the increase in the amplitude of vibration so that it is known as softening nonlinearity. Whereas cubic nonlinearity causes the rise of the natural frequency with the increase in the amplitude of vibration, and thus it is known as hardening nonlinearity. Further, the nonlinearity causes the appearance of mechanical resonance in a wide range of frequency (Ω) satisfying the condition $r\Omega = \sum_{i=1}^{N} \pm {}_i\Omega_n \, p_i$ ($p_i = 0,1,2,3,...,N$), (Amabili, 2008), where N is the number of degrees of freedom of the system. In addition, the resonance also occurs when different modal natural frequencies are commensurate or nearly commensurate (${}_i\Omega_n / {}_j\Omega_n \approx r$). It is known as internal resonance, which mainly leads to the energy transfer among the different modes.

However, in the case of slender structures under direct excitation, the governing equation of motion appears in a similar form, as given in Eq. (1.1a), where the commonly known mechanical resonances are primary (at $\Omega = {}_i\Omega_n$), super harmonic (at $\Omega = {}_i\Omega_n/r$) and internal (1:3, 1:2, 1:5, etc.) resonances. In the other case, i.e. for slender structures under parametric excitation, the corresponding governing equation of motion appears in a similar form, as given in Eq. (1.2a). The different mechanical resonances in this kind of dynamic system are (a) primary parametric resonance (at $\Omega = 2\,{}_i\Omega_n/r$, r =1, 3, 5…), (b) secondary

parametric resonance (at $\Omega = 2_i\Omega_n/r$, r =2, 4, 6 …), (c) combination resonance (at $\Omega = ({}_i\Omega_n\, p_i \pm {}_j\Omega_n\, p_j)/r$) and (d) internal resonances (1:3, 1:2, 1:5, etc.).

Among these different kinds of parametric resonances, principal primary parametric resonance (at $\Omega = 2_i\Omega_n$) is said to be most critical one (Bolotin, 1964), and it is commonly characterized by an instability region (Kumar et al., 2022) in the two-dimensional domain of dynamic load parameter and frequency of excitation. This instability region is parametrically described by instability boundaries, origin of instability and width of instability, as shown in Fig. 1.1. The origin of instability mainly indicates the minimum value of the dynamic load parameter, which is required for the onset of parametric instability/resonance. In the case of an undamped system, the origin of instability coincides with the zero value of the dynamic load parameter and the frequency of parametric resonance (Fig. 1.1) (Bolotin, 1964). However, the incorporation of damping in the system results in a shift of the instability region towards a high value of the dynamic load parameter. Thus, the damping stabilizes the system at lower values of the dynamic load parameter (Bolotin, 1964).

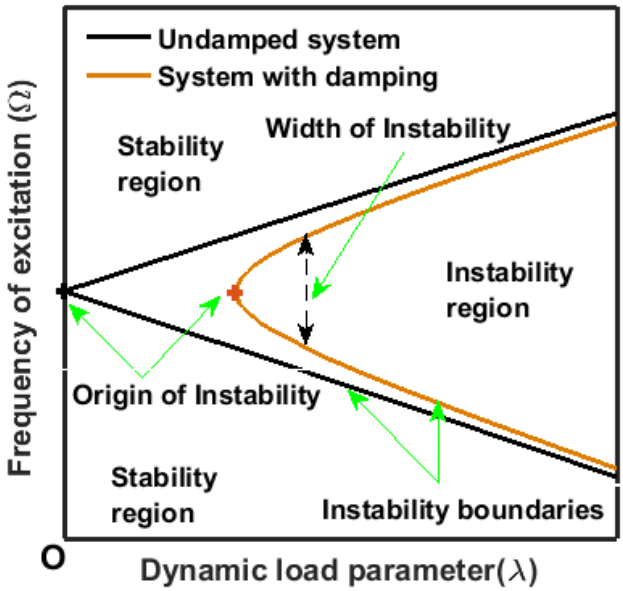

Fig. 1.1. A typical parametric instability region in the two-dimensional domain of excitation frequency and dynamic load parameter.

1.2. Dynamics/instability of parametrically excited slender structures

As mentioned in the previous section, the parametric excitation on a slender structure is commonly comprised of its static and dynamic counterparts that are known as static and dynamic parametric load parameters, respectively. Here, the

static load parameter induces compressive stress in a slender structure, which leads to a decrease in the effective stiffness of the structure. As a result, the slender structure undergoes static instability or divergence or buckling at a certain value of the static load parameter (Bolotin, 1964; Paidoussis, 2014). This limiting value of the static load parameter is called the critical buckling load. However, the static instability of a straight and slender member leads to the bifurcation of its zero equilibrium position through pitchfork bifurcation resulting in two stable buckled equilibrium states and the unstable zero equilibrium, as shown in Fig. 1.2. The corresponding equilibrium states of the slender structure before and after the bifurcation are called as the pre-buckled and post-buckled states, respectively.

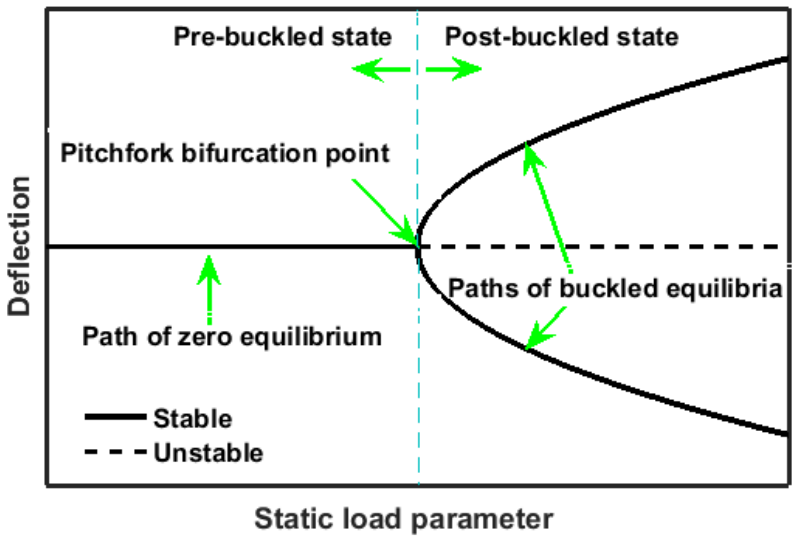

Fig. 1.2. A schematic diagram for pitchfork bifurcation of zero equilibrium position of a slender structure with respect to static load parameter.

Now, in any of the pre-buckled and post-buckled equilibrium states, a slender structure undergoes the aforesaid mechanical resonances due to the dynamic counterpart of the parametric load, where the associated motion of the structure appears in a complex manner depending on the value of static/dynamic load parameter, excitation frequency, material configuration, geometrical properties, boundary conditions, etc. A great deal of research has been addressed in the literature to explore complex motion of parametrically excited slender structures in both the pre-buckled and post-buckled states. Different kinds of practical slender structures are addressed in this available research, like beams, pipes, drill strings, twisted/untwisted drills, rods/cylinders, etc. Depending on the practical applications of these structures, different types of parametric excitations appear, namely periodic axial compressive load (Dunayevsky et al., 1993; Huang and Yang, 2009), axial excitation through supports (Lei et al., 2017;

Zhou et al., 2020), axially moving load (Gouskov et al., 2007), axially moving mass (Paidoussis, 2014; Pao, 1970), temperature (Kar and Sujata, 1988; Qian et al., 2009), etc. It shows a variety of slender structures and different types of parametric excitations, leading to a vast topic. However, in this thesis, the dynamics of two types of slender structural elements, namely beam and pipe, is focused for their operation under the parametric excitation in both the pre-buckled and post-buckled states. The corresponding available research towards the exploration of dynamics of these slender structures is furnished in the following subsections.

1.2.1. Literature on dynamics of slender beams under periodic axial load in the pre-buckled state

In the pre-buckled state, the dynamics of a parametrically excited slender beam commonly appears through the parametric resonance. The beam loses stability from its static equilibrium state and oscillates. Here, this instability/resonance appears mainly in three types, namely primary, secondary and combinatory parametric resonances depending on the dynamic load parameter, excitation frequency, geometrical/material properties and boundary conditions of a slender beam element. The corresponding oscillation of the beam element usually appears either in periodic or in quasi-periodic oscillations based on the type of parametric resonance/instability. However, in this concern of different types of parametric instabilities/resonances and the associated motion of slender beams, a good number of studies are available in the literature.

Initially, a study on the dynamic stability of a simply-supported beam subjected to periodic axial load was carried out by Utida and Sezawa (1940). Later, similar studies were also carried out by many other researchers (Ahuja and Duffield, 1975; Iwatsubo et al., 1972; Somerset and Evan-Iwanowski, 1964). These studies revealed the uncoupled Mathieu-Hill governing equations of motion and the existence of parametric resonance around $\Omega = 2\Omega_n / r$. At the same time, Iwatsubo et al. (1974, 1973) also carried out theoretical and experimental studies where they reported that the combination resonances do not occur for simply-supported boundary condition. But, in the cases of clamped-clamped/clamped-hinged boundary condition and cantilever beams, sum type $(\Omega = ({}_i\Omega_n + {}_j\Omega_n)/r)$ and sum/difference type $(\Omega = ({}_i\Omega_n \pm {}_j\Omega_n)/r)$ combination resonances appear, respectively, due to the corresponding coupled Mathieu-Hill governing equation of motion. It was also reported that the damping in the system leads to the reduction in the size of the instability region of simple parametric resonances. In

contrast, the enlargement or reduction of instability region appears for combination resonances depending on the ratio of modal damping coefficients of involved modes of vibration. Celep (1985) studied the dynamic stability of a pre-twisted beam and reported that combination resonances may appear for the twist of the beam even for the simply-supported boundary condition. Further, various instability regions were reported in an experimental study (Dufour and Berlioz, 1998) for the consideration of an additional constant or periodic torque to mimic the loading in drill string.

Ahuja and Duffield (1975) conducted experimental and theoretical studies on the parametric instability of a beam element having linearly varying cross-section under elastic foundation. These studies revealed that the slope factor of varying cross-section significantly influences the principal primary parametric instability region while the elastic foundation enhances the critical buckling load. Later, Mailybaev et al. (2004) addressed an optimal variation of the width of cross-section for the reduction of instability region. Further, Svensson (2001), Li et al. (2015) and Zajaczkowski (1981) conducted experimental and theoretical studies to investigate instability regions of a beam and found that the damping reduces the size of the instability region. Shastry and Rao (1986) studied the effect of two symmetrically placed intermediate supports on the parametric instability region of a simply-supported/clamped beam. It was found that the instability regions do not alter when the intermediate supports are placed at a distance equal to one-eighth of beam length from ends. Briseghella et al. (1998) presented a finite element (FE) formulation to evaluate the parametric instability region for beams and frames considering the effects of shear deformation, rotatory inertia, distributed axial loads, elastic soil, restraints and material damping.

All the aforesaid studies were carried out without considering the geometric nonlinearity of slender beams. However, Tezak et al. (1978) considered the geometric nonlinearity of slender beams and investigated nonlinear responses of hinged-clamped and hinged-hinged beams for the parametric excitation frequency near the twice/sum of the first two modal natural frequencies. It was revealed that internal (1:3) and combination resonances appear only for the hinged-clamped boundary condition. Corresponding to these resonances for hinged-clamped beams, Chin and Nayfeh (1999, 1997) reported complex dynamics including chaotic motion where they observed super critical Hopf/sub critical Hopf bifurcation, period-doubling bifurcation, cyclic-fold bifurcation and blue-sky catastrophes of equilibrium solutions. Zhang et al. (2005) considered the quintic nonlinearity of hinged-hinged beam subjected to the periodic axial load and observed local and codimension-3 degenerate bifurcations. Recently, Wang

and Zhu (2021a, 2021b) presented a study on the dynamic instability of hyperelastic beams and reported that the critical buckling load increases with the rise of Neo-Hookean material parameter. This variation of the material parameter also induces the transformation between softening and hardening structural behavior of the beams.

1.2.2. Literature on dynamics of slender beams under periodic axial load in the post-buckled state

In the post-buckled state of a slender beam, it has two stable and one unstable equilibrium states, as shown in Fig. 1.2. The corresponding dynamics of the beam under the parametric excitation appears through the aforesaid resonances/instabilities. However, this dynamics of the post-buckled beam appears in a complex manner mainly because of the coexistence of multiple stable/unstable static equilibrium states. A good number of studies have been addressed in the literature towards the exploration of complex nonlinear dynamics of post-buckled beams under the parametric excitation.

Initially, Szemplinska-Stupnicka et al. (1989), Zavodney and Nayfeh (1988) and Zavodney et al. (1990, 1989) studied the dynamic responses of a post-buckled beam near the fundamental and principal primary parametric resonances by considering a simplified one-degree-of-freedom system with quadratic and cubic nonlinearities. They found that the dynamics around double-well potentials involves period-doubling/demultiplying bifurcation and coexistence of periodic and/or chaotic attractors. In a similar work, Ariaratnam et al. (1989) and Ariaratnam and Namachchivaya (1986a) studied the characteristics of homoclinic orbits and chaotic dynamics of the same simplified system. The corresponding results were also qualitatively verified by conducting an experimental study on a buckled column by imposing periodic axial displacement at its ends.

Abou-Rayan et al. (1993) conducted a theoretical study to address the complex dynamics of a simply-supported buckled beam under the periodic axial load. The complex dynamics mainly involves periodic/chaotic snap-through oscillation, periodic doubling/demultiplying routes to chaos, period-3/period-6 attractors and coexistence of local and global periodic/chaotic attractors. Later, Chin et al. (1997) investigated the dynamics of a buckled beam considering fixed/hinged/sliding boundary conditions at the support ends. They reported the existence of two-to-one internal resonance. Also, the dynamics of the buckled beam involves different bifurcations (saddle-node, pitchfork, Hopf, symmetry-breaking, type-I intermittency), jumping phenomena over multiple attractors and crises phenomena. Ji and Hansen (2000) conducted an experimental study to

investigate the nonlinear dynamics of a clamped-sliding buckled beam under the periodic axial load. They reported the influence of dynamic load parameter and frequency of excitation on the local/global periodic and chaotic responses of the buckled beam. The same study also revealed the influence of sliding frictional damping on the parametric instability region and chaotic response.

Lestari and Hanagud (2001) presented exact solutions for the dynamics of a parametrically excited buckled beam with different types of end conditions. Later, Yabuno et al. (2003) conducted an experimental study on the parametric resonance at the second normal mode of a simply-supported buckled beam under the periodic axial load. They detected zero-to-one internal resonance between the first and second normal modes. El-Bassiouny (2006) investigated the dynamics of a post-buckled beam subjected to direct and parametric excitations, where the stability of the beam under different subharmonic resonances ($\Omega = r\Omega_n$, r =2, 3, 4, 5, 6) is mainly studied. Emam and Abdalla (2015) studied the nonlinear dynamics of a simply-supported buckled beam under the periodic axial load near the principal primary parametric resonance. In this study, all possible attractors are explored by constructing global bifurcation diagram with respect to dynamic load parameter. The same study also reveals complex dynamics of the buckled beam, which involves different types of bifurcations (period-doubling/demultiplying, symmetry breaking and cyclic-fold) and chaotic oscillations.

Apart from the aforesaid homogeneous straight/buckled beams, the nonlinear dynamics of many other kinds of beams under parametric excitation has also been reported in the literature, namely geometrically imperfect beams (Farokhi and Ghayesh, 2019), micro beams (Farokhi and Ghayesh, 2018, 2016; Ghayesh et al., 2015; Ghayesh and Farokhi, 2016, 2015; Gutschmidt and Gottlieb, 2010, 2012), functionally graded beams (Ke et al., 2013; Lu and Chen, 2020; Mohanty et al., 2012; Sheng and Wang, 2018), drill stings (Dunayevsky et al., 1993), axially oscillating cantilever beams with/without end mass (Anderson et al., 1996; Fey et al., 2011; Gurgoze, 1986; Hyun and Yoo, 1999; Zavodney and Nayfeh, 1989), axially moving beams (Marynowski and Kapitaniak, 2014), spinning pre-twisted beams/drills (Huang and Kuang, 2007b; Lee, 1995, 1994), etc. It is observed that the nonlinear dynamics of these beams appears almost similar to that for the parametrically excited straight/buckled beams. However, some changes in the dynamics due to the variation of different system parameters like material inhomogeneity, initial geometrical imperfection, size and geometry of structure, etc. are mainly identified and reported.

1.2.3. Literature on the dynamics of slender pipes conveying steady/pulsatile fluid

This section presents the dynamics/instability of another parametrically excited slender structure, i.e. a fluid conveying pipe. Pipes conveying fluid with the steady or pulsatile flow at moderate or high velocity are common elements in petrochemical industries, oil and gas industries, ocean mining, rocket and aircraft engines, power generating systems, etc. These flexible slender cylindrical elements are often susceptible to undergo instability due to flow-induced excitation. As it may lead to the failure of the associated engineering systems, their dynamic characteristics have been studied substantially by many researchers in the past four decades (Ibrahim, 2010; Paidoussis, 2014; Paidoussis and Li, 1993), and it is revealed that the dynamics of fluid conveying pipes appears through the interaction of inertia, elastic, centrifugal and Coriolis forces. The centrifugal and Coriolis forces arise from the internal fluid flow, and they are constant or time-varying forces depending on the steady or pulsatile flow velocity. The centrifugal force causes static/dynamic compressive stress in a pipe resulting in its static/dynamic instabilities. The static instability or buckling of a fluid conveying pipe usually occurs when the steady flow velocity exceeds a certain limiting value, and the pipe is supported through both ends. The internal fluid flow with steady flow velocity also causes the flutter instability of cantilever pipes. However, in many practical piping systems, the internal fluid flows with pulsatile velocity due to the bends, valves, pumps, change of cross-section, etc. This pulsatile fluid flow is usually attributed to a harmonic component of velocity over the mean flow velocity, and it induces dynamic compressive stresses in a pipe leading to the parametric resonance/instability of a pipe. However, in the following sections, the available research on the dynamics/instability of fluid conveying pipes is furnished separately for the steady and pulsatile flow velocity of internal fluid.

1.2.3.1. Instability of pipes conveying fluid with steady flow velocity

The initial studies on pipes conveying fluid with steady flow velocity were carried out to investigate their natural frequencies and the critical flow velocity for the onset of static instability/buckling (Ashley and Haviland, 1950; Chen and Rosenberg, 1971; Dimaggio and Li, 1964; Housner, 1952; Niordson, 1953; Paidoussis and Issid, 1974; Chen and Jendrzejczyk, 1985; Dodds and Runyan, 1965; Jendrzejczyk and Chen, 1985; Liu and Mote Jr, 1974; Long Jr, 1955; Naguleswaran and Williams, 1968). In these earlier studies, fluid conveying pipes

are considered to be supported at both ends, and it was found that Coriolis force induces the deviation of classical normal modes. However, the internal pressurization in the fluid causes axial compressive stresses resulting in divergence/buckling beyond a certain value of it.

The available studies on the linear analysis of fluid conveying pipes show the existence of coupled-mode flutter even though a fluid conveying pipe supported at both ends is a conservative gyroscopic system. However, the difference in the response due to the change of immovable end support to sliding support could not be traced by the linear analysis (Yoshizawa et al., 1985). These issues were sorted out by considering the geometric nonlinearity of the fluid conveying pipes (Holmes and Marsden, 1978; Holmes, 1978, 1977; Lunn, 1983; Thurman and Mote Jr, 1969; Yoshizawa et al., 1985), where it is revealed that pipes with supported ends cannot undergo flutter instability, and the linear analysis is not valid beyond the first divergence. However, various nonlinear models were addressed in the literature considering geometric nonlinearity due to stretching (Holmes, 1978, 1977), curvature (Thompson and Lunn, 1981), gravity, internal pressurization (Paidoussis, 2014; Semler et al., 1994), Poisson coupling (Gorman et al., 2000; Paidoussis, 2014), thermal effect, change in the cross sectional area (Olunloyo et al., 2007), etc. Modarres-Sadeghi and Paidoussis (2009) and Nikolic and Rajkovic (2006) derived nonlinear models of fluid conveying pipes and reported that clamped-clamped/hinged-hinged/hinged-clamped pipe loses stability similar to a slender beam via the supercritical pitchfork bifurcation where the buckled deflection of the pipe increases with the increase in the flow velocity. For the same boundary pairs, Sinir (2013) investigated the dynamic stability of a fluid conveying pipe in its different post-buckled configurations where it is revealed that buckled configurations of the pipe beyond the first mode of buckling are unstable ones. Wang et al. (2017a) investigated 3D post-buckling behaviour of a fluid conveying pipe by deriving a 3D theoretical model. They found that the first-mode natural frequency for the in-plane motion of buckled pipe increases with the increase in the flow velocity, but the first-mode natural frequency corresponding to the out-of-plane motion is equal to zero; However, the second-mode and third-mode natural frequencies for the in-plane motion are approximately equal to their counterparts of the out-of-plane motion and remain constant with the increasing flow velocity.

1.2.3.2. Dynamics of pipes conveying pulsatile fluid

The earlier studies on the dynamics of pipes conveying pulsatile fluid were carried out mainly to investigate the influence of flow parameters on the parametric

instability region (Chen and Rosenberg, 1971; Ginsberg, 1973; Paidoussis and Issid, 1974, 1976; Paidoussis and Sundararajan, 1975). In these studies, a pipe is supported at its both ends and conveys pulsatile fluid in the pre-buckled state. However, it was observed that the dynamic behaviour of the pipe is analogous to that for a beam under the periodic axial load while the instability region widens due to the increase in the mean flow velocity, pulsation velocity-amplitude and mass ratio (ratio of fluid mass to the total mass of system). Further, the parametric instability of a pipe may occur even when the pulsation of flow velocity is quite weak provided that the mean flow velocity is sufficiently high (Ariaratnam and Namachchivaya, 1986a). The same researchers (Ariaratnam and Namachchivaya, 1986b) also reported that damping in the pipe system is an essential requirement to stabilize it. Seo et al. (2005) presented an FE model in conjunction with Bolotin method to evaluate the parametric instability region of fluid conveying pipes.

Apart from the above linear analyses, nonlinear vibration of flexible pipes conveying pulsatile fluid was studied by many researchers (Gorman et al., 2000; Namachchivaya and Tien, 1989a, 1989b; Namchchivaya, 1989; Oz, 2001). These studies reveal that the pipes undergo periodic motion under subharmonic resonance and modulated periodic motion under combination resonance through subcritical/supercritical Hopf bifurcation. Later, Jin and Song (2005) reported that a pipe conveying pulsatile fluid undergoes different types of motions in association with combination resonance. Further studies were carried out by many researchers to explore the dynamics of clamped-clamped pipes conveying pulsatile fluid (Czerwinski and Luczko, 2018, 2012; Luczko and Czerwiński, 2017, 2016, 2015). These studies reveal that the vibration intensity of the pipe under parametric resonance increases with the increase of mean flow velocity, pulsation velocity-amplitude, length of hose and operating temperature. Also, the increase in the internal damping coefficient lessens the probability of the occurrence of parametric resonance. Further, Luczko and Czerwinski (2016) analyzed the dynamics of a clamped-clamped pipe conveying fluid with non-harmonic flow velocity in the form of the rectangular waveform. In this study, overlapping of secondary parametric resonances of various vibration modes was observed in the lower range of pulsation frequency, where the complex motion of pipes appears with the large vibration amplitude as well as the dynamic change of vibration modes.

Czerwinski and Luczko (2018) and Luczko and Czerwinski (2017) presented nonlinear dynamics of a horizontal clamped-clamped fluid conveying pipe considering its gravity-induced static deformation. It was observed that the pipe undergoes complex non-planar vibration under the combination resonances

while the vibration of the same pipe appears in a plane for subharmonic resonances. Recently, Li et al. (2018) investigated the dynamics of a simply-supported pipe conveying pulsatile fluid where a segment over the length of the pipe is made of soft material, and the rest is made of hard material. This study revealed that the probability of parametric instability reduces for decreasing length of the soft segment or if the soft and hard segments are taken with the clamped and pinned boundary conditions, respectively.

Unlike the conventional simply-supported beams, the modal coupling coefficients do not vanish for simply-supported fluid conveying pipes resulting in the possibility of internal resonance. In this concern, Panda and Kar (2008, 2007) addressed the appearance of 1:3 internal resonance associated with the first two normal modes of a pipe conveying pulsatile fluid. They also reported the appearance of periodic, quasiperiodic and chaotic responses associated with the saddle-node and Hopf bifurcations, jump phenomena and beating effect. Further, Mcdonald and Namachchivaya (2005a, 2005b) addressed the presence of 0:1 internal resonance associated with the first two normal modes of a pipe for some flow velocities near the critical flow velocity. Wang (2009) studied the nonlinear dynamics of a simply-supported pipe conveying pulsatile fluid where the motion of the pipe in the transverse direction is constrained by a cubic spring at its middle point. This study revealed the rich dynamics of the pipe involving quasi-periodic motion and chaotic motion.

The aforesaid studies were carried out considering the horizontal or vertical orientation of a pipe conveying pulsatile fluid. However, in many industrial piping systems, similar fluid conveying pipes are laid in the inclined orientation (Alfosail et al., 2017; Lee and Kim, 1999; Lips and Meyer, 2011; Vigneaux et al., 1988; Wang and Bloom, 2001). In this aspect, Lee et al. (1995), Wang (2003) and Wang and Bloom (2001) studied linear dynamics of inclined pipes conveying pulsatile fluid and reported that the inclination angle with the vertical axis does not have much effect on the stability of a piping system. It may be due to the fact that the pipes possess sufficient rigidity against their static deformation under the gravitational force that arises due to the inclination angle with the vertical axis. However, Gan et al. (2015) considered a flexible cantilever pipe inclined with the vertical axis and studied its dynamics under the steady flow velocity of the internal fluid. They found that the inclination of the cantilever pipe can significantly affect its dynamic behavior. Later, Peng et al. (2019) presented a three-dimensional dynamic analysis of an inclined pinned-pinned flexible pipe conveying pulsatile fluid. In this study, it was found that the motion of the pipe not only changes from

planar to non-planar but also involves complexity with various dynamic instabilities when the inclination angle with the horizontal/vertical axis increases.

All the aforesaid studies on the dynamics of pipes conveying pulsatile fluid were carried out in the pre-buckled equilibrium state. However, a few studies are reported in the literature towards the exploration of dynamics of similar fluid conveying pipes in their post-buckled equilibrium state. Jayaraman and Narayanan (1996) investigated the nonlinear dynamic behaviour of a post-buckled pipe conveying pulsatile fluid. They found the appearance of a weak chaotic behaviour of the pipe for a small pulsation amplitude through the period-doubling bifurcation of local periodic motion, and this chaotic motion coexists with a global period-2 motion. However, as the pulsation amplitude increases, a sequence of symmetry breaking and period doubling bifurcation of global period-2 motion occurs resulting in a strong chaotic motion. Later, Zhang and Chen (2014) and Zhou et al. (2017) investigated steady-state response of post-buckled pipe near 2:1 internal resonance associated with the first two normal modes. They reported that the oscillation amplitude involves the greater contribution of the second mode than the first mode. Also, the presence of the internal resonance leads to the subharmonic, superharmonic and sum/difference type combination resonances.

Apart from the aforesaid studies, the research in this line has also been extended to investigate the change in the dynamics of a fluid conveying pipe due to the variation of different system parameters, namely boundary conditions (Askarian et al., 2017; Ghayesh et al., 2013), variable cross-section (Olunloyo et al., 2007), curvature of slender pipes (Czerwinski and Luczko, 2018; Li and Yang, 2017), geometrical periodicity (Singh and Mallik, 1979; Yu et al., 2013, 2008), corrugated pipes (Wang et al., 2019), material damping (Deng et al., 2017a; Tang et al., 2018; Vassilev and Djondjorov, 2006), elastic constraints (Ghayesh et al., 2011; Zhang et al., 2016), motion-limiting constraints (Peng et al., 2018; Wang, 2009; Wang et al., 2017b), lumped mass (Ghayesh et al., 2011; Modarres-Sadeghi et al., 2007; Zhang et al., 2016), attached nozzles (Firouz-Abadi et al., 2013), elastic foundation (Vassilev and Djondjorov, 2006; Wang and Ni, 2008) and support vibration (Zhang and Chen, 2013; Zhou et al., 2020).

1.2.4. Thermal effect on the stability of slender structures

In many engineering systems like steam generators, heat exchangers, liquid propellant rocket engines, helicopter rotor blades, rotor blades in turbo machinery, industrial robotic structures, etc., beam-like slender structures operate in the thermal environment. The corresponding thermally induced stress within the structure may yield its thermo-elastic instability and/or enhance its

vibration while operating under a dynamic force. In this line, Raju and Rao (1984a, 1984b) and Rao and Raju (1984) investigated the effect of the geometry of a beam on its thermal buckling characteristics. Later, Kar and Sujata (1988) studied the effect of thermal load on the dynamic stability of a beam under periodic axial load and found that the increasing temperature causes the reduction in the buckling load and the rise in the size of the parametric instability region. Similar studies are also addressed by Parida and Dash (2016) and Pradhan et al. (2016). However, Pradhan et al. (2016) presented static and dynamic stability analysis of an asymmetric sandwich beam and reported that symmetric beam has a better resistance against static buckling. Gao et al. (2017) investigated the dynamic buckling of Euler–Bernoulli beam–column considering the constant velocity of ends such that the compressive force in the beam increases gradually with time. From this study, it is revealed that the temperature rise decreases the time of buckling. Further, Manoach and Ribeiro (2004) studied the dynamics of a beam under the forced excitation and an applied thermal load through a time-varying ram function of heat flux. This study revealed that thermal load increases the amplitude of vibration, especially for constant total heat flux. The short duration heat flux produces large amplitude vibration. However, Warminska et al. (2014) studied the influence of the thermal load on the nonlinear dynamics of a beam under forced excitation. In their study, it was found that additional resonances appear at the low-frequency region while the increase in temperature may cause complex motion involving chaotic attractors. Further, the effect of thermal load on the nonlinear dynamics of a buckled axially moving beam under the forced excitation was studied by Kazemirad et al. (2013). It was observed that the increase in the amplitude of excitation results in the bifurcation of the periodic response of the beam into complex motion involving multi-periodic, quasi-periodic and chaotic responses. However, with the rise in temperature, the complex motion reduces to periodic motion for a wide range of amplitude of excitation. A similar study was also conducted by Ghayesh and Amabili (2015) considering the pre-buckled state of an axially moving beam. They reported that the increase in temperature causes the increase of hardening nonlinear behaviour of the beam and the appearance of additional resonant peaks in the frequency response due to the energy transfer between different modes.

In many engineering systems like heat exchangers, steam generators, nuclear reactors, etc., a fluid-conveying pipe operates in the thermal environment where the thermally induced compressive stress arises in the pipe material in addition to the similar stress due to fluid flow. In this line, Qian et al. (2009) and Gu et al. (2017) investigated the effect of thermal load on the critical flow velocity

for static instability of a fluid conveying pipe by considering linear/quadratic stress-temperature relation. It was found that the critical flow velocity greatly decreases with the increase in the temperature. Further, Zhao et al. (2015) conducted a similar study considering pulsatile fluid flow in a pipe and reported the possibility of chaotic oscillation of the pipe around a buckled equilibrium position.

1.3. Vibration/instability control of parametrically excited slender structures

The static/dynamic instabilities and the corresponding large amplitude vibration of slender structures commonly cause their improper functionality and/or fracture/fatigue failure. Therefore, a great deal of research has been reported in the literature for control of such parametrically exited slender structures using different types of active materials like magnetorheological materials (Hoseinzadeh and Rezaeepazhand, 2020; Yeh and Shih, 2006), magnetostrictive materials (Kumar et al., 2003), piezoelectric actuators (Chen et al., 2002; Lacarbonara et al., 2007; Reddy et al., 2021; Yao et al., 2015), electrorheological materials (Tabassian and Rezaeepazhand, 2013; Yeh et al., 2004; Yeh and Chen, 2005), shape memory alloy (Roslan et al., 2019; Tsai and Chen, 2002; Yusof et al., 2020), etc. Among these different kinds of active materials, piezoelectric materials have drawn the special interest of researchers because of their advantages of high actuation capability, low power requirement, capability in directional actuation, wide frequency range of application, etc. (Chen et al., 2002; Lacarbonara et al., 2007; Li and Liu, 2012; Yao et al., 2015). However, besides these active materials, the use of passive damping materials like viscoelastic polymers has also been reported in the literature for control of dynamic instability and the associated vibration of parametrically excited slender structures (Dwivedy et al., 2007; Lv et al., 2018; Pradhan et al., 2016; Ray and Kar, 1996b). Apart from these active and passive damping materials, the utilization of functionally graded materials (FGMs) has also been addressed in a good number of available studies (Hosseini and Fazelzadeh, 2011; Mohanty et al., 2012, 2011; Sheng and Wang, 2019, 2018) for stabilizing parametrically excited slender structures operating in the thermal environment. However, in this line, the present study is focused on the utilization of viscoelastic damping materials, piezoelectric actuators and FGMs in control of static/dynamic instability and the associated motion of slender structures. A corresponding literature review is delineated in the following subsections.

1.3.1. Passive control of vibration/instability of parametrically excited slender structures using viscoelastic materials

Viscoelastic materials (VEMs) are homogeneous and isotropic materials, exhibiting both elastic and viscous damping properties during their time-dependent deformation. However, the damping properties of viscoelastic materials are immensely exploited for vibration attenuation of thin-walled flexible structures. The commonly used VEMs in structural damping applications are Paracril-BJ, Polymer Blend, butyl rubber, Viton-B, Styrene-butadiene rubber (SBR), Soundcoat N5, 3M-467, LD-400, etc. (Jones, 2001). These damping materials are commonly used through two different damping mechanisms in vibration control of thin-walled flexible structures, namely unconstrained layer damping (UCLD) (Baz, 2019; Cortes and Elejabarrieta, 2007; Lumsdaine and Scott, 1998; Ungar and Kerwin Jr, 1964) and constrained layer damping (CLD) or passive constrained layer damping (PCLD) (Baz, 2019; Kung and Singh, 1998; Plunkett and Lee, 1970). In the UCLD, a viscoelastic layer is freely attached to the surface of a host structure (substrate layer), as shown in Fig. 1.3(a). During bending deformation of the overall structure, the viscoelastic layer undergoes extensional deformation, as shown in Fig. 1.3(b). In the CLD/PCLD, the viscoelastic layer is constrained by a stiff constraining layer, as shown in Fig. 1.3 (c), leading to the shear deformation of the viscoelastic layer during the bending deformation of the overall structure, as shown in Fig. 1.3(d). This extensional/shear deformation of the viscoelastic layer causes energy dissipation during the transient deformation of the overall structure.

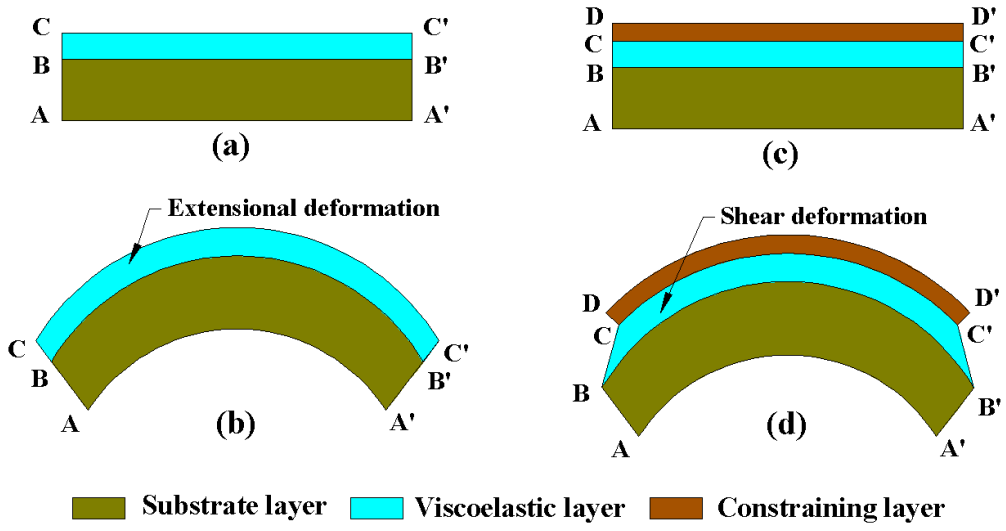

Fig. 1.3. Schematic diagrams of (a) undeformed and (b) deformed states of substrate layer integrated with UCLD layer; (c) undeformed and (d) deformed states of substrate layer integrated with CLD/PCLD layer.

However, among these two viscoelastic damping techniques, the energy dissipation capability of CLD/PCLD treatment is significantly more than that for the UCLD treatment (Plunkett and Lee, 1970). So, viscoelastic damping materials are mostly utilized through CLD/PCLD treatment in vibration control of different kinds of structures operating under direct excitation (Baz, 2019; Gupta et al., 2020; Li et al., 2020; Tomlinson, 1990; Zheng et al., 2006). Besides, the application of CLD treatment for parametrically excited structures has also been reported in the open literature.

In an early work, Stevens and Evan-Iwanowski (1969) investigated the effect of material viscoelasticity on the principal primary parametric resonance of a column structure operating under a dynamic compressive load. It was observed that the material viscoelasticity significantly reduces the size of the instability region and also shifts the instability region towards a high value of the dynamic load parameter. Later, a similar study was carried out by Saito and Otomi (1979), considering simple and combination parametric resonances. Ray and Kar (1995) and Dwivedy et al. (2007) utilized CLD treatment for passive control of parametric instability of a symmetric sandwich beam for different boundary conditions, where it was revealed that the parametric instability region reduces significantly with the rise of damping in the beam by means of increasing the thickness of the constrained viscoelastic layer in the CLD arrangement. Ray and Kar (1996b, 1996a) also studied the dynamic instability of multi-layered beams with constrained viscoelastic layers and beams with partial CLD treatment. These studies revealed the possibility of reduced parametric instability region and also improved stability against static compressive load by the use of CLD treatment. Pradhan et al. (2016) analyzed the dynamic instability of a CLD treated asymmetric sandwich beam and reported that the dynamic stability of the beam improves with the increasing material loss factor as well as the ratio of moduli of viscoelastic and substrate layers. In all the aforesaid studies, the viscoelastic material is modelled using Kelvin-Voigt model or frequency-independent properties. However, considering the frequency-dependent viscoelastic properties, Shih and Yeh (2005) proposed a solution methodology to find the parametric instability region of the viscoelastic beam where it was observed that the parametric instability region reduces with the increase in the viscoelastic beam length.

In a few other studies (Lv et al., 2018; Zhu et al., 2018), the nonlinear dynamics of a parametrically excited axially moving symmetric viscoelastic sandwich beam with simply supported ends was analyzed where the parametric excitation appears through the axial velocity of the beam. Here, Lv et al. (2018)

mainly observed that the frequency range of trivial solution corresponding to the principal primary parametric resonance decreases first and then increases with the increase in the thickness of the viscoelastic layer. However, in the other study (Zhu et al., 2018), the nonlinear dynamics of the beam is investigated considering an additional periodic axial load, and it was observed that the complex motion of the beam arises involving periodic, quasi-periodic and chaotic responses.

1.3.2. Piezoelectric actuators in active control of vibration/instability of parametrically excited slender structures

Piezoelectric materials belong to a special class of ceramics, which possess an important property of energy conversion from mechanical to electric field or vice versa. This property is exploited in the development of sensors and actuators, particularly for the shape/vibration control of flexible structures. In 1880, Curie brothers (Jacques and Pierre) first demonstrated the piezoelectricity phenomenon in natural materials such as quartz and Rochelle salt. It was observed that when the mechanical strain is imposed on these materials, they produce an electrical output. This property is known as the direct piezoelectric effect. Further, in 1881, Gabriel Lippmann theoretically proposed the converse piezoelectric effect, where an electrical input produces mechanical strain in these materials. However, the existence of the converse piezoelectric effect in the piezoelectric crystals was experimentally confirmed by Curie brothers. A detailed description of piezoelectric constitutive behaviour is available in (Arnau, 2004; Cady, 2018; Heywang et al., 2008; Qin, 2012). However, the linear constitutive relations of piezoelectric ceramics under constant temperature are expressed in terms of some field parameters like stress ($\boldsymbol{\sigma}$), strain ($\boldsymbol{\varepsilon}$), electric displacement ($\boldsymbol{D}$) and electric field ($\boldsymbol{E}$). Based on these field parameters ($\boldsymbol{\sigma}$, $\boldsymbol{\varepsilon}$, $\boldsymbol{D}$, $\boldsymbol{E}$), thermodynamic potentials like internal energy (U), enthalpy (H), Helmholtz free energy (F) and Gibbs free energy (G) can be defined, as given in Eq. (1.3) (Chee, 2000).

$$dH = \boldsymbol{\sigma}\, d\boldsymbol{\varepsilon} - \boldsymbol{D}\, d\boldsymbol{E}\,,\quad dU = \boldsymbol{E}\, d\boldsymbol{D} + \boldsymbol{\sigma}\, d\boldsymbol{\varepsilon}\,,$$
$$dF = \boldsymbol{E}\, d\boldsymbol{D} - \boldsymbol{\varepsilon}\, d\boldsymbol{\sigma}\,,\quad dG = -\boldsymbol{\varepsilon}\, d\boldsymbol{\sigma} - \boldsymbol{D}\, d\boldsymbol{E} \tag{1.3}$$

These piezoelectric constitutive formulations (Eq. (1.3)) are utilized depending on the natural variables. For structural application, the natural variables are commonly considered as strain ($\boldsymbol{\varepsilon}$) and electric field (E). Accordingly, the constitutive relations are expressed using the thermodynamic potential H as (Chee, 2000),

$$\boldsymbol{\sigma} = \boldsymbol{C}\,\boldsymbol{\varepsilon} - \boldsymbol{e}\,\boldsymbol{E} \tag{1.4}$$

$$\boldsymbol{D} = \boldsymbol{e}^{\mathrm{T}}\boldsymbol{\varepsilon} + \in \boldsymbol{E} \tag{1.5}$$

where, $\boldsymbol{C}$ is the stiffness matrix for a constant electric field ($\boldsymbol{E}$); $\boldsymbol{e}$ is the piezoelectric matrix for the constant strain ($\boldsymbol{\varepsilon}$) or the constant electric field ($\boldsymbol{E}$); $\in$ is the electrical permittivity matrix for the constant strain ($\boldsymbol{\varepsilon}$). Here, Eq. (1.4) represents the converse piezoelectric effect, while the direct piezoelectric effect is represented by Eq. (1.5). These converse (Eq. 1.4) and direct (Eq. 1.5) piezoelectric effects are utilized in the development of piezoelectric actuators and sensors, respectively, for structural applications (Thakkar and Ganguli, 2004).

Some examples of piezoelectric ceramics are lead zirconate titanate (PZT), barium titanate, lead niobrate, lead lanthanum zirconate titanate (PLZT), ammonium dihydrogen phosphate, lithium sulfate, polyvinylidene fluoride (PVDF or PVF2), etc. However, for structural applications, piezoelectric actuators are usually made in the form of a thin wafer, as shown in Fig. 1.4, where a piezoelectric wafer is poled (P) either vertically (Fig. 1.4(a)) or horizontally (Fig. 1.4(b)). These piezoelectric actuators are usually activated by the application of an external electric field (E_z) through their top and bottom fully electrode surfaces. Here, for the vertically poled piezoelectric wafer (Fig. 1.4(a)), the primary actuation forces appear as the electrically induced normal stresses in the plane of the wafer. So, it is called as the extensional mode piezoelectric actuator (Sun and Zhang, 1995). In another type, i.e. for the horizontally poled piezoelectric wafer (Fig. 1.4(b)), the primary actuation forces appear as the electrically induced shear stresses in the transverse (xz or yz) planes of the wafer. Thus it is known as the shear mode piezoelectric actuator (Sun and Zhang, 1995).

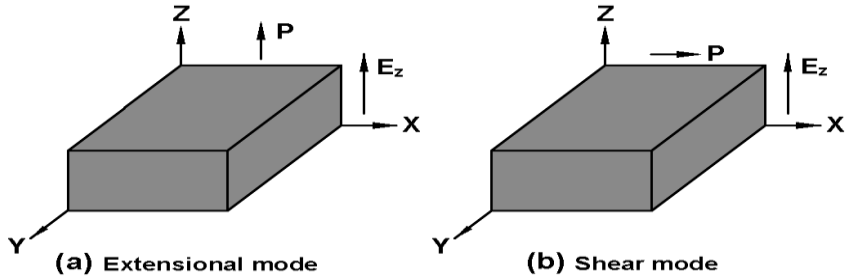

Fig. 1.4. Schematic diagrams of the (a) extensional mode and (b) shear mode piezoelectric actuators.

The extensional mode piezoelectric actuators are usually mounted over the surface of a host structure to provide the extensional actuation force against the bending deformation of the overall structure (Trindade, 2011, 2007; Kitio Kwuimy, 2015; Giri et al., 2021). On the other hand, the shear mode piezoelectric actuators are commonly embedded in a host structure through the sandwich structural configuration, where the actuator at the core provides shear actuation force to

counteract the bending deformation of the sandwich structure (Baillargeon and Vel, 2005; Trindade, 2011, 2007; Trindade et al., 1999; Trindade and Maio, 2008).

However, the extensional mode and shear mode piezoelectric actuators are extensively utilized for active control of flexible structures operating under the direct excitation (Baz, 2019; Belouettar et al., 2008; Li et al., 2016; Rechdaoui and Azrar, 2010; Yao et al., 2015; Batra and Geng, 2002; Benjeddou, 2007; Benjeddou et al., 1999; Raja et al., 2002; Sun and Zhang, 1995; Trindade et al., 1999; Zhang and Sun, 1996; Trindade, 2007; Karagiannis et al., 2016). In parallel, the active control of parametrically excited beams has also been reported in the literature using extensional mode piezoelectric actuators, where linear (Chen et al., 2009; Ghandchi Tehrani and Kalkowski, 2016), nonlinear (Alhazza et al., 2008; Oueini and Nayfeh, 1999) and experimental (Alhazza et al., 2008; Chen et al., 2009; Ghandchi Tehrani and Kalkowski, 2016; Yabuno et al., 2001) analyses are presented to investigate the actuation capability of extensional mode piezoelectric actuators in control of parametric instability region and vibration of cantilever beams. These studies revealed that the extensional mode piezoelectric actuators are capable of stabilizing the beams in a wide range of the amplitude and frequency of parametric excitation. Similar studies for simply-supported beams under the axial harmonic load have also been presented by Chen et al. (2002), Lacarbonara et al. (2007), Li and Liu (2012) and Yao et al. (2015).

Chen et al. (2002) investigated the parametric instability of a fiber-reinforced composite beam and reported that a thin piezoelectric actuator could significantly reduce the size of the instability region. Li and Liu (2012) carried out a similar study on isotropic beams and reported that the active damping provided by the piezoelectric actuator shifts the instability region towards a high value of the dynamic load parameter. Lacarbonara et al. (2007) conducted theoretical and experimental studies to propose an open-loop control technique using piezoelectric actuators for cancellation of principal primary parametric resonance associated with the skew-symmetric mode of a beam. Yao et al. (2015) investigated the effect of piezoelectric actuation on the modification of complex nonlinear vibration of a composite beam under combined axial and transverse harmonic loads. It was observed that the dynamics of the beam could be altered between chaotic and periodic motion using the piezoelectric actuation. All the aforesaid studies are carried out in the pre-buckled equilibrium state of flexible beams, where the capability of extensional mode piezoelectric actuators in controlling parametric instability is revealed. However, in this line, the usefulness of the shear mode actuators is not yet explored in the literature to the author's best knowledge.

1.3.3. Functionally graded materials (FGMs) in control of instability of parametrically excited slender structures

When a structure operates in the thermal environment, it would have sufficient strength/toughness to sustain the mechanical load in addition to the high temperature resistant property. To achieve all these properties in a single structure, one needs to look for a composite made of metal and ceramic. However, if this composite is made in layered form, the corresponding mismatch of material properties at the inter-layer surface of two different material layers leads to its (composite) failure through delamination, especially at the high-temperature operation. Based on this shortcoming, the concept of FGM emerged (Koizumi, 1993; Yamanouchi et al., 1990), where this composite material is made of metal and ceramic, but the volume fractions of the constituent materials vary smoothly from fully ceramic to fully metal in the desired direction. So, the properties of FGM change gradually from ceramic to metal properties in that direction. This gradual variation of material properties eliminates the possibility of delamination. At the same time, the ceramic constituent provides the high-temperature resistant property of the FGM, and the metallic constituent provides sufficient toughness in the composite (FGM) to sustain the mechanical load. An FGM is commonly characterized as an isotropic material where the material properties vary in the direction of continuous variation of the volume fractions of ceramic and metal constituents. Usually, the volume fractions of constituents are varied following a power-law, as given in Eq. (1.6) where V_c and V_m are the volume fractions of ceramic and metal constituents, respectively; h is the dimension of structure in z direction and n is the graded exponent of FGM.

$$V_c = \left(\frac{2z+h}{2h}\right)^n, \; V_m = (1-V_c) \tag{1.6}$$

The effective material properties of an FGM are usually determined following the rule of mixture. Accordingly, the material properties ($P(z)$) of the FGM vary along the desired direction (z) as (Reddy and Chin, 1998),

$$P(z) = P_m V_m(z) + P_c V_c(z) \tag{1.7}$$

where, P_c and P_m are the material properties of ceramic and metal constituents, respectively. However, having the aforesaid advantages of FGMs, these composites are extensively utilized for parametrically excited slender structures especially to improve their stability during operation in the thermal environment. Despite the recommended utilization of FGMs in the thermal environment, those are also used to improve the stability of slender structures operating at room temperature.

Ke et al. (2010), Mohanty et al. (2012, 2011) and Sheng and Wang (2018) addressed the advantage of thickness-wise graded properties of beams for their static/dynamic stability under the operation at room temperature. Similar studies have also been carried out by Arani et al. (2021) and Lu and Chen (2020) considering bidirectional graded properties of beam elements. These studies mainly reveal the improved static instability of a beam made of FGM. However, Mohanty et al. (2012, 2011) investigated the parametric instability of FG beams and sandwich beams with FG core for pinned-pinned ends. They found that the dynamic stability of FG beams composed of steel and aluminium improves when the bottom surface of the beams is made of steel instead of aluminium. Also, the dynamic stability of the sandwich beams improves as the thickness of the FG core increases.

Further, Sheng and Wang (2018) studied nonlinear dynamics of FG beams under parametric and direct excitations, where different periodic and chaotic oscillations are observed by changing some system parameters like graded exponent, material damping and load parameters**.** Later, considering bidirectional graded properties of FG beams, Arani et al. (2021) investigated their dynamic stability and reported that the influence of the material properties on dynamics of the beams increases when graded properties are taken in axial direction instead of the thickness direction. A similar observation was also reported by Lu and Chen (2020)**.** Vo et al. (2014) considered a sandwich beam with homogeneous hard/soft core and FG face layers. They reported that the natural frequencies and critical buckling load decrease for hard core and increase for soft core when the power-law index increases or core-thickness decreases. Later, considering the geometric nonlinearity, Lanc et al. (2015) addressed the critical buckling load and post-buckling responses of FG sandwich box beams.

Considering thermal loads, Li et al. (2006) presented the post-buckling behavior of an FG beam with thickness-wise graded properties, where it was reported that the post-buckled deflection and the extensional deformation of the FG beam increase with the increase in the power-law index for a given temperature rise. Later, Ma and Lee (2012, 2011) considered shear deformation of the FG beam with its temperature-dependent material properties and found that buckling through pitchfork bifurcation does not occur for simply-supported FG beams. This study also revealed that the critical buckling temperature of classical beams is higher than that of shear deformable beams. Further, the effect of temperature distribution across the thickness of an FG beam on its static/dynamic behavior was studied by Majumdar and Das (2018) and Paul and Das (2016). However, similar studies on the static stability of FG box columns and

FG sandwich beams with viscoelastic core were also reported by Bhangale and Ganesan (2006) and Ramkumar and Ganesan (2008).

Piovan and Machado (2011) studied the parametric instability of FG box beams and found that the size of the parametric instability region enlarges for the decrease in the graded exponent. Shen et al. (2017) presented nonlinear free vibration characteristics of FG beams. Recently, Sheng and Wang (2019) studied the nonlinear dynamics of parametrically excited FG beams operating in the pre-buckled state under the thermal environment. This study shows that the parametric resonance appears with the hardening nonlinear behavior of FG beams; however, the hardening nonlinearity reduces with the increase in the temperature. Further, in a few other studies (Alibeigloo, 2010; Bian et al., 2006; Gharib et al., 2008; Kiani et al., 2011; Li and Cheng, 2009), the piezoelectric actuators are attached to the surface of an FG beam, and the corresponding critical buckling temperature, as well as the static behavior of the beam, are investigated. It was observed that the critical buckling temperature increases due to the activated piezoelectric actuators. Besides, some available studies addressed the effect of linear/nonlinear elastic foundation on the stability of FG beams (Fallah and Aghdam, 2012, 2011; Komijani et al., 2014; Sun et al., 2016). These studies revealed that the critical buckling temperature increases due to the increase in the linear stiffness of the elastic foundation. However, the increase in the nonlinear stiffness of elastic foundation does not have much effect on the critical buckling temperature.

FGMs are also considerably utilized in the design of fluid conveying pipes. In this line, the linear stability analysis of FG pipes conveying fluid with steady flow velocity was presented by An and Su (2017), Maalawi and EL-Sayed (2011) and Tang and Yang (2018). However, in these studies, the thermal environment is not considered, and the FG pipe is taken with axially graded properties. Similar studies were also addressed considering the graded properties of FG pipes across the wall-thickness (Deng et al., 2017b; Wang and Liu, 2016). These available studies reveal that FGM improves the stability of a pipe while the graded exponent is an important parameter to regulate stability boundaries. However, Hosseini and Fazelzadeh (2011) considered the thermal load for a cantilever FG pipe conveying fluid with steady flow velocity. In the same line, Eftekhari and Hosseini (2016) reported a similar study on the thermo-mechanical stability of a cantilever FG pipe spinning about its longitudinal axis. These studies reveal an indicative improvement of thermo-mechanical stability of the pipe when it is made of FGM instead of conventional isotropic material. Recently, Dehrouyeh-Semnani et al. (2019) presented the nonlinear thermo-resonant behavior of a simply-supported

FG pipe conveying hot fluid under forced excitation. It was reported that the graded exponent regulates the backbone curve/frequency response. Also, the rise in temperature or fluid flow velocity causes augmented hardening structural behavior of the pipe.

1.4. Methodologies for theoretical analysis of parametrically excited slender structures

In the aforesaid literature on the instability/dynamics of parametrically excited slender structures, the corresponding theoretical analyses are carried out by deriving linear/geometrically nonlinear mathematical models mostly by using the Galerkin method or the FE procedure. The linear mathematical models are limited to the pre-buckled state of a slender structure, which provide the estimation of the onset of static/dynamic instability depending on different system parameters. However, for the precise analysis of the corresponding motion of a slender structure, one needs to proceed with nonlinear mathematical models, since the motion of a slender structure associated with its parametric instabilities/resonances usually appears in a complex manner involving various nonlinear phenomena like hardening/softening nonlinear behavior, existence of multiple attractors associated with periodic and chaotic responses, jumping phenomena among the attractors, different kinds of bifurcation of dynamic response, etc. (Abou-Rayan et al., 1993; Chin and Nayfeh, 1999; El-Bassiouny, 2006; Emam and Abdalla, 2015; Jin and Song, 2005; Namachchivaya and Tien, 1989; Tezak et al., 1978). These complex dynamics are commonly analyzed by evaluating nonlinear frequency responses and global bifurcation diagrams in the Galerkin or FE framework. Here, the global bifurcation diagrams can be constructed by deriving the nonlinear equations of motion in the time domain. However, for the evaluation of nonlinear frequency responses, the nonlinear equations of motion are to be solved in conjunction with other analytical methods like the method of multiple scales, generalized method of averaging, Lindstedt-Poincare method, Krylov-Bogoliubov-Mitropolsky technique, homotopy perturbation method, etc. (Nayfeh, 2008; Yun and Temuer, 2015) or numerical methods like shooting method (Claeys et al., 2014; Ribeiro, 2004; Padmanabhan and Singh, 1995; Patel et al., 2009), orthogonal collocation method (Karkar et al., 2014) and harmonic balance method (HBM) (Detroux et al., 2015; Dimitriadis, 2008; Karkar et al., 2014). Among these various methods for evaluation of nonlinear frequency responses, HBM is the most popular one because of its robustness, computational efficiency and accuracy in the representation of strong

nonlinearity, especially for non-smooth or stiffer nonlinear systems (Detroux et al., 2015; Dimitriadis, 2008; Karkar et al., 2014).

Further, between the Galerkin and FE frameworks, the FE method is more robust one as it is capable of handling complex material configuration, geometry and boundary conditions in a structural problem. But, the major shortcoming of the FE procedure appears as a high computational time in the evaluation of nonlinear frequency responses and global bifurcation diagrams especially due to a large number of nodal degrees of freedom in the FE model. Another shortcoming with the FE procedure appears as the complexity in the formulation of the nonlinear FE model in conjunction with HBM, particularly for a complex mathematical form of material constitutive relation. However, looking into the robustness of FE procedure and HBM, a few studies in this dissertation are carried out using these methods while the aforesaid shortcomings are tackled following the corresponding available studies in the literature, as a review in these aspects is presented in the following two subsections.

1.4.1. HBM-based FE formulation for evaluation of nonlinear frequency responses of structural elements

For the evaluation of nonlinear frequency responses in the FE framework using HBM, first, the FE equations of motion are to be derived in the time domain. Next, the time-domain equations are to be converted for periodic responses by invoking Fourier expansion of nodal displacements. Subsequently, Galerkin method is to be applied to reduce the resulting equation within a time-period, which basically yields the equations of motion in the frequency domain for the periodic responses. However, the implementation of Galerkin method needs the time-integration of all HBM-based expanded matrices/vectors in the FE model over a time period. This computation is usually carried out using a conventional numerical time-integration method, which involves a good computational time (Blahoš et al., 2020; Chen et al., 2001; MS et al., 2016). So, in some available studies (Dou and Jensen, 2015; Lewandowski, 1997, 1992), the time-integration is carried out analytically to reduce the computational time. But, this analytical approach may be a cumbersome one, especially for handling a robust FE formulation using a good number of harmonic terms in HBM. Therefore, with the same objective of reduced computational time, fast Fourier transform or discrete Fourier transform is utilized in some other studies (Blahoš et al., 2020; Dimitriadis, 2008; LaBryer and Attar, 2010), where the evaluation of stiffness terms at a good number of sampling points within the time-period is required for the computation of Fourier coefficient matrices corresponding to the nonlinear stiffness matrix.

However, the implementation of HBM in the FE framework is well established for the nonlinear frequency response analysis of elastic and piezoelectric structures (Blahos et al., 2020; Chen et al., 2001; Ms et al., 2016). But, the implementation of HBM for a viscoelastic structure is not yet fully developed (Jacques et al., 2010; Litewka and Lewandowski, 2017a, 2017b), since the aforesaid procedure does not work due to the involvement of temporal derivative/integral of stress/strain in the viscoelastic constitutive relations (Baz, 2019) like fractional Zener model (Litewka and Lewandowski, 2017b), generalized Maxwell model (Amabili et al., 2019), Hereditary integral approach (Jacques et al., 2010), etc.

Initially, Bilasse et al. (2010) and Jacques et al. (2010) presented a FE formulation using Hereditary integral approach in conjunction with complex modulus approach for a viscoelastic material, where the harmonic form of displacement is taken in the complex domain. Later, Lewandowski and Wielentejczyk (2017), Litewka and Lewandowski (2017b, 2017a) and Wielentejczyk and Lewandowski (2017, 2019) presented FE formulations using fractional Zener model of viscoelastic materials. However, in these available studies, the FE formulation appears in a complex manner where HBM is implemented before FE discretization because of the temporal derivative/integral of stress/strain in the viscoelastic constitutive relation. Also, the HBM is implemented using one or two harmonic terms, which may not be sufficient to produce accurate nonlinear frequency responses of a viscoelastic structure.

1.4.2. Reduced-order FE models for evaluation of time/frequency responses of structural elements

The evaluation of nonlinear frequency responses and global bifurcation diagrams in the FE framework usually involves a high computational time because of a large number of nodal degrees of freedom in the FE model. In this concern, the reduced-order FE model (ROM) is recommended in the literature. For the derivation of a ROM, one needs to select appropriate reduced basis vectors (RBVs). The subsequent construction of ROM involves the Galerkin projection of FE equations of motion onto the subspace spanned by RBVs. The resulting FE equations of motion appear in terms of the reduced-order linear/nonlinear system matrices/vectors, where a large number of degrees of freedom in the full-order FE model reduces to a small number of reduction coordinates corresponding to the RBVs (Hollkamp et al., 2005; Jain, 2019; Mignolet et al., 2013; Rutzmoser, 2018; Tiso et al., 2013). This reduction of the number of degrees of freedom in the FE model facilitates the computation of dynamic responses with a reduced

computational time; however, the accuracy of the ROM is an important concern that depends on the selection of RBVs. A great deal of research has been addressed in the literature for the development of ROM in the time domain for elastic structures (Allen et al., 2020; Cho et al., 2020; Dimitriu et al., 2017; Hollkamp et al., 2005; Jain, 2019; Jain and Tiso, 2018; Kumar et al., 2021; Mahdiabadi et al., 2021; Mignolet et al., 2013; Tiso et al., 2013; Touze et al., 2014; Vizzaccaro et al., 2020). Further, the implementation of HBM over a time-domain ROM has been addressed by Givois et al. (2019), Lazarus et al. (2012) and Weeger et al. (2014). Also, the reduction of frequency-domain full-order FE model based on HBM is addressed (Praveen Krishna and Padmanabhan, 2011) by using mode superposition, dynamic substructuring and component mode synthesis methods.

These available studies mainly addressed the selection of RBVs and the subsequent construction of ROM. Accordingly, the basic RBVs available in the literature for the linear analysis of elastic structures are tangent eigen modes/vibration modes (VMs), Ritz vectors, Krylov vectors, etc. (Allen et al., 2020; Rutzmoser, 2018; Teunisse et al., 2017; Tiso et al., 2013). However, as these RBVs are originally proposed for linear analysis of an elastic structure, those may not produce accurate solutions in the geometrically nonlinear analysis of the same structure since it involves various nonlinear phenomena like bending-stretching coupling, bending-twist coupling, coupling between lower and higher vibration modes, etc. (Rutzmoser, 2018; Teunisse et al., 2017). However, this inaccuracy in the solution appears mainly due to the absence of relevant higher-order modes in RBVs (Hollkamp et al., 2005; Rutzmoser, 2018), which are required to capture the aforementioned nonlinear phenomena. So, the aforesaid RBVs are usually enriched with different kinds of basis vectors like companion/dual modes (Hollkamp et al., 2005), modal derivatives (MDs) (Jain and Tiso, 2018; Mahdiabadi et al., 2021; Witteveen and Pichler, 2014), proper orthogonal modes (POMs) (Lu et al., 2019), etc.

However, in a nonlinear ROM, generally, the reduced-order linear system matrices/vectors do not involve much computational cost, while the reduced-order nonlinear system matrices/vectors are to be formed repeatedly from the corresponding full-order system matrices/vectors for solving the reduced-order nonlinear equations of motion through an iterative solution procedure. So, the computational cost in a nonlinear ROM mainly arises for the computation of the reduced-order nonlinear system matrices/vectors (Jain, 2019; Rutzmoser, 2018; Tiso et al., 2013). To reduce this computational cost, as a first step, the RBVs can be taken in the elemental level to compute the reduced-order elemental system matrices/vectors, while the elemental quantities are summed over all elements

(Jain, 2015; Touze et al., 2014). It provides the advantage of significantly low computational cost, and also the computation can be carried out with low computer memory. Further, hyper reduction methods were proposed in some studies (Allen et al., 2020; Cho et al., 2020; Dimitriu et al., 2017; Jain, 2019; Jain and Tiso, 2018).

However, for geometrically nonlinear structures, the system matrices/vectors in the nonlinear ROM can be derived completely in terms of the reduction coordinates without involving the full-order solution corresponding to the full-order FE model. A procedure in this direction is introduced by Jain (2015) and Touze et al. (2014). However, such a method is usually called as direct or intrusive method (Touze et al., 2014). Alternatively, taking advantage of a polynomial system of equations in the ROM of a geometrically nonlinear problem, non-intrusive methods were also proposed. In these methods, the reduced-order linear/nonlinear stiffness coefficients are evaluated through a set of static full-order solutions by enforcing a specific set of displacements or forces without accessing FE framework (Hollkamp et al., 2005; Vizzaccaro et al., 2020).

The aforesaid ROMs are developed mainly for the linear/nonlinear dynamic analysis of elastic structures. These methods can be utilized for the derivation of ROMs for viscoelastic structures, but the RBVs would be derived considering the frequency-dependent material properties of viscoelastic structures (Rouleau et al., 2017). For this derivation of RBVs for viscoelastic structures, various methods have been proposed in the literature like iterative complex eigen solution method (ICES) (Lin and Lim, 1996; Vasques et al., 2010), multi-model (MM) method (Balmes, 1997), enriched Ritz method (ERM) (Boumediene et al., 2014; De Lima et al., 2010), modal strain energy (MSE) method (Johnson and Kienholz, 1982), iterative MSE (Trindade et al., 2000; Zhang and Chen, 2006), modified MSE (Hu et al., 1995; Merlette, 2006), MSE with first-order corrective terms (MSEC) (Plouin and Balmès, 2000), rational Krylov approach with Taylor expansion of complex modulus (RKT) (Xie et al., 2018) and frequency-dependent rational Krylov approach (FSRK) (Jith and Sarkar, 2020). Using these RBVs, the derivation of ROMs for linear analysis of viscoelastic structures has been addressed in a good number of available studies (Bilasse and Oguamanam, 2013; De Lima et al., 2010; Ding et al., 2018; Jith and Sarkar, 2020; Kuether, 2019; Rouleau et al., 2017; Song et al., 2016; Xie et al., 2018; Zghal et al., 2015).

However, besides the linear ROM of viscoelastic structures, a geometrically nonlinear ROM was reported by Song et al. (2016) using a non-intrusive method, where the nonlinear ROM of a viscoelastic beam is derived using Kelvin-Voigt

model. Further study on the development of nonlinear ROM for viscoelastic structures is not yet available in the literature to the author's best knowledge.

1.5. Motivation and objectives of the present research

From the aforesaid literature survey, it is clear that a great deal of research has already been reported towards the exploration of nonlinear dynamics of parametrically excited slender beams and fluid conveying pipes. Further, a good number of studies have also been reported on the active/passive control of static/dynamic instabilities and the associated complex motion of these slender structural elements using piezoelectric actuators, viscoelastic damping materials and FGMs. Besides, various mathematical models of the parametrically excited slender structures have also been addressed to analyze their instabilities and the associated nonlinear dynamics.

However, in the context of active control of parametrically excited slender structures using piezoelectric actuators, the available literature (Section 1.3.2) shows an extensive application of extensional mode piezoelectric actuators (Fig. 1.4(a)), where these actuators are utilized to stabilize the slender structures in the pre-buckled equilibrium state. It is observed that the extensional mode piezoelectric actuators are capable of stabilizing slender structures in a wide range of the amplitude of parametric excitation. However, in this line, the usefulness of the other one, i.e. shear mode piezoelectric actuator (Fig. 1.4(b)), is not yet explored in the open literature although this kind of piezoelectric actuator is commercially available and possesses various advantages over the extensional mode piezoelectric actuator (Sun and Zhang, 1995; Zhang and Sun, 1996). So, the first objective of this study is decided to investigate the control capability of the shear mode piezoelectric actuators in control of parametric instability and the associated dynamics of a flexible beam in the pre-buckled state with reference to that for the extensional mode piezoelectric actuators.

Besides the parametric instability of a flexible beam in the pre-buckled state, the same beam may also undergo complex nonlinear dynamics once its static instability/buckling appears under the parametric excitation. Here, different kinds of dynamic instabilities associated with the static instability cause the critical motion of the flexible beam along with the large amplitude vibration (Abou-Rayan et al., 1993; Emam and Abdalla, 2015). However, the usefulness of the extensional mode and shear mode piezoelectric actuators in control of such critical nonlinear dynamics of flexible beams in the post-buckled state is not yet reported in the available literature. Therefore, it is also included within the first objective of this study.

For passive control of parametrically excited beam-like slender structures using viscoelastic damping materials, the available literature (Section 1.3.1) shows a good number of studies on the utilization of CLD treatment for controlling parametric instabilities of beams in the pre-buckled equilibrium state (Dwivedy et al., 2007; Lv et al., 2018; Pradhan et al., 2016; Ray and Kar, 1996a, 1996b, 1995; Shih and Yeh, 2005). Good effectiveness of the CLD treatment in the control of parametric instability at the pre-buckled state of beam-like structures is observed in these available studies. However, further research on this viscoelastic damping treatment for attenuation of complex nonlinear dynamics of a slender structure under the parametric excitation in the post-buckled state is not yet reported in the literature to the best knowledge of the author. Therefore, the second objective of the present study is to investigate the effectiveness of the CLD treatment in passive control of nonlinear dynamics of a parametrically excited beam, especially when it undergoes buckling or static instability.

However, for accurate estimation of passive damping in the CLD treatment, the corresponding viscoelastic material is to be modelled using an advanced material constitutive model like fractional Zener model, generalized Maxwell model, Hereditary integral approach, etc. (Amabili et al., 2019; Baz, 2019; Galucio et al., 2004; Litewka and Lewandowski, 2017b; McTavish and Hughes, 1992; Zhou et al., 2016). Now, these material constitutive models involve temporal derivative/integral of stress/strain so that the derivation of the corresponding mathematical model of a viscoelastic structure for its nonlinear analysis in the time/frequency domain appears in a complex manner. Moreover, a high computational cost arises when modelling through FE procedure in handling complex material configuration, loading, etc. Here, the derivation of the nonlinear FE model in the time domain is somewhat straightforward, as observed in the literature (Bahraini et al., 2012; Baz, 2019; Payette and Reddy, 2013; Sahoo and Ray, 2019). But the derivation of the nonlinear FE model in the frequency domain involves complexity because of the associated solution methodologies like shooting method (Claeys et al., 2014; Ribeiro, 2004; Padmanabhan and Singh, 1995), orthogonal collocation method (Karkar et al., 2014) and harmonic balance method (HBM) (Detroux et al., 2015; Dimitriadis, 2008; Karkar et al., 2014). Here, HBM is the most popular one because of its robustness, computational efficiency and accuracy in the representation of strong nonlinearity, especially for non-smooth or stiffer nonlinear systems (Detroux et al., 2015; Dimitriadis, 2008; Karkar et al., 2014).

Now, in the use of HBM for FE modelling of a viscoelastic structure in the frequency domain, the HBM is to be implemented before the FE discretization

because of the temporal derivative of stress/strain in the constitutive relation (Jacques et al., 2010; Lewandowski and Wielentejczyk, 2017; Litewka and Lewandowski, 2017b). It poses a long expression of nonlinear stress vector associated with the Fourier basis functions, which complicates the subsequent formulation of the nonlinear stiffness matrix of the system. So, the available studies in this line are carried out considering one/two harmonic terms in the implementation of HBM (Jacques et al., 2010; Lewandowski and Wielentejczyk, 2017; Litewka and Lewandowski, 2017a; Wielentejczyk and Lewandowski, 2019). But, for the accurate modelling of nonlinear dynamic characteristics of a viscoelastic structure in the frequency domain, one needs to consider a sufficient number of harmonic terms in the implementation of HBM, and it poses (i) the difficulty in handling a long and complex expression of nonlinear stiffness matrix, (ii) a high computational cost especially due to the requirement of numerical time-integration of system matrices/vectors in the implementation of HBM and (iii) separate FE formulations for different viscoelastic constitute models. In order to ease these three difficulties, the third objective of this study is decided to present a generalized FE formulation for nonlinear frequency-response analysis of viscoelastic structures using HBM.

Although this generalized FE formulation is expected to provide reduced computational time, the nonlinear frequency responses are to be evaluated using the full-order FE model. So, the concern of computational time still remains. The same concern also lies in the full-order FE model of a viscoelastic structure in the time domain especially for the construction of global bifurcation diagrams to study various dynamic instabilities and the associated motion of a viscoelastic structure. In this issue, the option is to formulate nonlinear ROMs of viscoelastic structures in the time and frequency domains.

However, the formulation of ROM of viscoelastic structures has been demonstrated in a good number of available studies using various approaches in deriving the reduced basis vectors (RBVs) (Bilasse and Oguamanam, 2013; De Lima et al., 2010; Ding et al., 2018; Jith and Sarkar, 2020; Kuether, 2019; Rouleau et al., 2017; Song et al., 2016; Xie et al., 2018; Zghal et al., 2015). But all these available approaches in the derivation of RBVs are developed for linear analysis of a viscoelastic structure. So, these RBVs may not provide a nonlinear ROM with sufficient accuracy especially to model different nonlinear phenomena like bending-stretching coupling, bending-twist coupling, coupling between different vibration modes, etc. Therefore, further study on the enrichment of these RBVs is needed towards the development of ROM for the nonlinear analysis of viscoelastic structures.

Besides this concern of accuracy, another important issue is the reduced computational time that may be achieved appreciably by deriving the ROM through the elemental level computation of reduced-order system matrices/vectors completely in terms of reduced coordinates without involving the full-order solution (Jain, 2015; Touze et al., 2014). But, this elemental level computation involves difficulty, mainly for the formulation of (i) the reduced-order nonlinear memory-load vector in the time-domain ROM and (ii) the HBM based expended form of reduced-order nonlinear stiffness matrix in the frequency-domain ROM. However, with these concerns, a fruitful formulation for nonlinear ROM of viscoelastic structures in the time/frequency domain is not yet available in the open literature. Therefore, the fourth objective of this study is to develop a methodology for enrichment of the aforesaid RBVs for nonlinear ROM of viscoelastic structures and also to present a fruitful elemental level formulation of the corresponding reduced-order system matrices/vectors.

In many engineering systems like steam generators, heat exchangers, liquid propellant rocket engines, helicopter rotor blades, rotor blades in turbomachinery, industrial robotic structures, etc., beam-like slender structures operate under the thermal environment. The corresponding thermally induced stress within the structure may yield its thermo-elastic instability and/or enhance its vibration while operating under a dynamic force. A similar circumstance can be observed in pipes conveying hot pulsatile fluid, where the thermally induced compressive stress in a pipe is significantly more than the similar stress due to the flow velocity of fluid. So, the pipe undergoes static instability/buckling even at a very low velocity of the fluid. Therefore, the thermal environment hampers the functionality of the pipe. In this concern, the utilization of FGM made of ceramic and metal has been addressed in a few studies in the open literature (Section 1.3.3), where the hot surface of the pipe is made of ceramic to withstand a high temperature of the fluid and the material properties vary gradually from ceramic to metal across the pipe wall thickness. From these available studies, it is observed that the pipes have significantly improved thermo-elastic stability due to the use of FGM. However, further study on the various dynamic instabilities and the associated complex motion of FGM pipes in both the pre-buckled and post-buckled states is not yet addressed in the open literature. But this study is an obvious need for having knowledge in the practical design of FGM pipes. In this aspect, the last objective of this study is to explore the static/dynamic instabilities and the corresponding critical motion of vertical/inclined FGM pipes conveying a hot pulsatile fluid.

On the basis of the aforesaid five objectives, the following studies are carried out in this dissertation.

(a) Nonlinear dynamics and active control of smart beams using shear/extensional mode piezoelectric actuators.

(b) A generalized finite element formulation for nonlinear frequency response analysis of slender viscoelastic beams using harmonic balance method.

(c) Reduced-order finite element formulation for the geometrically nonlinear dynamic analysis of slender viscoelastic beams.

(d) Constrained layer damping treatment of post-buckled beams under parametric excitation: a theoretical study using reduced-order finite element formulation.

(e) Nonlinear dynamics of functionally graded pipes conveying hot fluid.

1.6. Contributions

The following contributions in the field of nonlinear dynamic analysis and control of parametrically excited slender structures have been made towards the preparation of the dissertation.

1. The usefulness of shear mode piezoelectric actuators in active control of parametric instability of a slender beam is investigated and presented.

2. The actuation capability of shear mode and extensional mode piezoelectric actuators in control of complex nonlinear dynamics of slender beams under parametric excitation in the post-buckled equilibrium state is investigated and presented.

3. A new generalized FE formulation is presented for geometrically nonlinear frequency response analysis of viscoelastic slender structures using HBM and various material constitutive models as Kelvin-Vogt model, Maxwell model, fractional Zener model, generalized Maxwell model and Heredity integral approach. The special features of this new formulation are as follows.

    (a) All types of viscoelastic material models are reduced to a single mathematical form by implementing HBM for the time-periodic stress/strain. It facilitates a common HBM-based FE formulation for all types of viscoelastic material models.

(b) A special factorization of the nonlinear strain-displacement matrix is introduced to ease the formulation of HBM based expanded forms of nonlinear stiffness matrix and tangent stiffness matrix.

(c) The orthogonality of Fourier basis functions is exploited not only to reduce the number of terms in the HBM based expanded form of system matrices/vectors but also to decrease the computational time for time-integration in the implementation of HBM.

4. A reduced-order FE model of viscoelastic slender structures is presented for their geometrically nonlinear analysis in the time domain based on the fractional Zener constitutive model. The contributions here are as follows.

   (a) A methodology for the enrichment of reduced basis vectors is proposed for sufficient accuracy of nonlinear ROMs of viscoelastic structures.

   (b) The elemental level computation of reduced-order system matrices and vectors is introduced through a special factorization of the nonlinear strain-displacement matrix. The reduced-order system matrices can be computed without involving the full-order solution. It facilitates a significant reduction of computational time and the requirement of computer memory.

   (c) A special formulation of nonlinear reduced-order memory-load vector based on the fractional Zener model is presented by introducing two new anelastic forces especially to reduce computational time.

5. A reduced-order FE model of viscoelastic slender structures is formulated for their geometrically nonlinear analysis in the frequency domain using HBM.

6. A comparative study is presented to address the best one among the MSE, MSEC, MM, ICES, RKT and FSRK approaches in selection and enrichment of reduced basis vectors for deriving nonlinear ROMs of viscoelastic structures.

7. The performance CLD treatment in passive control of complex nonlinear dynamics of parametrically excited slender structures in the post-buckled equilibrium state is investigated and presented.

8. The nonlinear dynamics of a slender FG pipe conveying steady/pulsatile hot fluid is thoroughly investigated in its pre-buckled and post-buckled

states. This study reveals the utility of FGM to mitigate the static and dynamic instabilities of fluid conveying slender pipes.

9. The nonlinear dynamics of an inclined slender FG pipe conveying hot pulsatile fluid is also investigated thoroughly and presented. This study reveals the effect of inclination of a fluid conveying pipe on its static/dynamic instabilities and the associated complex motion.

1.7. Organization of the thesis

In Chapter 1, a brief introduction of various mechanical resonances and the associated nonlinear dynamics of slender structures operating under the parametric excitation is presented. This is accompanied by a literature review on the nonlinear dynamics/instability of parametrically excited slender structures. Subsequently, a brief introduction on viscoelastic, piezoelectric and FGMs is furnished along with the available studies on their use in the control of dynamics/instability of parametrically excited slender structures. Next, a literature review on the FE models for the nonlinear dynamic analysis of slender structures is presented where the development of reduced-order FE models is mainly focused. On the basis of this literature review, the scope of the present research has been identified, and the objectives of the present thesis are furnished.

Chapter 2 deals with the nonlinear dynamic analysis and active control of parametrically excited smart beams using shear mode and extensional mode piezoelectric actuators. First, the geometrically nonlinear electro-elastic incremental FE equations of motion are derived based on the velocity feedback control law, and then the HBM is implemented to evaluate the nonlinear frequency responses under the transverse/axial harmonic load. Subsequently, a methodology for the local stability analysis in the FE framework is presented using Floquet theory. Next, the numerical results are illustrated to explore the nonlinear dynamics of the smart beams in both the pre-buckled and post-buckled states where the active control capabilities of shear mode and extensional mode piezoelectric actuators are mainly focused.

Chapter 3 presents a generalized FE formulation for nonlinear frequency-response analysis of viscoelastic structures using HBM. The HBM-based FE formulation is presented considering a viscoelastic sandwich beam and an arbitrary number of harmonic terms in HBM. This formulation is carried out by introducing three new strategies especially to ease the implementation of HBM in the FE framework, which are: (i) a special factorization of nonlinear strain-

displacement matrix, (ii) exploitation of orthogonality of Fourier basis functions and (iii) reduction of various mathematical forms for viscoelastic constitutive behaviour into a generalized form for periodic stress/strain. The fruitfulness of this formulation is subsequently verified through the numerical illustrations.

In Chapter 4, the nonlinear ROMs are derived in the time and frequency domains for the geometrically nonlinear FE analysis of viscoelastic structures using the fractional Zener constitutive model. First, the ROM is derived in the time domain, where the nonlinear memory-load vector is formulated in terms of two new anelastic forces, especially to enable the formulation of all reduced-order system matrices/vectors in the elemental level without involving the full-order solution. Subsequently, the ROM is derived in the frequency domain using HBM. Next, a methodology for the enrichment of RBVs that are utilized in literature for linear ROM of a viscoelastic structure is presented. Successively, the fruitfulness of the ROMs in achieving accurate results with less computational time is demonstrated through the numerical illustrations. Also, a comparative study is presented for a suitable approach in the selection of RBVs and the corresponding enrichment for the nonlinear analysis of viscoelastic structures with frequency-dependent material properties.

Chapter 5 presents a study on the passive damping capability of CLD treatment in the control of nonlinear dynamics of a parametrically excited beam, especially when it undergoes buckling or static instability. The theoretical analysis is carried out by considering the CLD treatment in three different layered beam configurations. For all these configurations, the nonlinear ROMs are first derived in the time and frequency domains. Subsequently, the numerical results are illustrated, where the fruitfulness of the ROMs in the estimation of very complex dynamics of the CLD treated layered beams under the parametric excitation at the post-buckled state is first verified. Next, the effectiveness of the CLD treatment in attenuation of these complex dynamics is investigated.

Chapter 6 presents a study on the static/dynamic instabilities and the corresponding critical motion of vertical/inclined FGM pipes conveying hot pulsatile fluid. The geometrically nonlinear governing equation of motion of a pinned-pinned inclined FG pipe conveying hot pulsatile fluid is derived based on the Euler-Bernoulli beam theory and plug-flow model, and the solutions are obtained using Galerkin discretization in conjunction with the incremental HBM/Runge-Kutta method. In the numerical results, first, the effects of temperature, graded exponent of FGM and flow velocity on the static instability of the FG pipe are illustrated. Next, the effects of the same system parameters on the dynamic instabilities, as well as the associated motion, of the FG pipe are

investigated in both the pre-buckled and post-buckled states. Subsequently, the effect of the inclination of the FG pipe on its dynamics is presented.

Finally, the important conclusions from the work carried out, and the future scope of the present thesis work are outlined in Chapter 7. The list of references is provided at the end of the thesis.

Chapter 2

Nonlinear dynamics and active control of smart beams using shear/extensional mode piezoelectric actuators

2.1. Introduction

The literature survey in the previous chapter shows a substantial number of studies on the active control of vibration/instability of smart beams under direct/parametric excitation (Section 1.3.2). It is observed from this literature review that the extensional mode piezoelectric actuators are capable of controlling both the linear and large amplitude vibration of flexible beams under direct excitation. On the other hand, the available studies on the control capability of shear mode piezoelectric actuators are limited to the linear dynamics of slender beams (Batra and Geng, 2002; Raja et al., 2002; Trindade et al., 1999), where it is revealed that shear mode actuator exhibits better control capability than that for the extensional mode actuator in control of cantilever beams and higher bending modes of vibration of beams with end supports. However, the attenuation of large amplitude vibration using shear mode actuator may be somewhat difficult since the geometrically nonlinear stiffness of flexible beams and the externally applied electric field to the actuator increase with the rise in the amplitude of vibration. An investigation in this concern is performed at present to explore the utility of the shear mode piezoelectric actuator in comparison to that of the extensional mode piezoelectric actuator for active control of large amplitude vibration of flexible beams operating under the direct excitation.

Besides the direct excitation, a few studies in the available literature addressed the control of parametrically excited flexible beams using extensional mode piezoelectric actuators, where the actuators are used to control the parametric instability of slender beams in the pre-buckled state (Chen et al., 2009; Lacarbonara et al., 2007; Yabuno et al., 2001; Yao et al., 2015). In these studies, it is observed that the active damping provided by the extensional mode piezoelectric actuator significantly reduces the parametric instability region, thus stabilizing the beams in a wide range of the amplitude of parametric excitation. However, in this line, the usefulness of the shear mode piezoelectric actuator is not yet explored in the literature to the best knowledge of this researcher. Apart from the parametric instability of a flexible beam in the pre-buckled state, the same beam may undergo complex nonlinear dynamics once its static

instability/buckling appears under the parametric excitation (Section 1.2.2). However, the usefulness of the extensional mode and shear mode piezoelectric actuators in control of such complex dynamics in the post-buckled state of a flexible beam is not yet reported in the open literature.

Therefore, in this chapter, the usefulness of shear mode and extensional mode piezoelectric actuators in active control of dynamics of a clamped-clamped beam is investigated where the beam is considered to operate under the direct/parametric excitation in the pre-buckled or post-buckled equilibrium state. The main concerns of the overall study are as follows.

(a) A comparative study on the active control capabilities of shear mode and extensional mode piezoelectric actuators in attenuation of large amplitude vibration of the clamped-clamped beam operating under the direct excitation.

(b) Active control capability of shear mode piezoelectric actuators in comparison to that of the extensional mode piezoelectric actuators for controlling parametric instability of the clamped-clamped beam in its pre-buckled state.

(c) Usefulness of shear mode and extensional mode piezoelectric actuators in active control of complex dynamics of the clamped-clamped beam under the parametric excitation in the post-buckled state.

In the following sections, first, the geometrical configurations of two smart beams are described (Section 2.2) for the separate use of the extensional mode and shear mode piezoelectric actuators. Section 2.3 is devoted to the derivation of a geometrically nonlinear incremental finite element (FE) model of the smart beams. Section 2.4 contains the presently used active control strategies and their implementation for a closed-loop FE model of the smart beams. Section 2.5 presents the implementation of the harmonic balance method (HBM) for the analysis of nonlinear dynamics of the smart beams in the frequency domain. The procedure for local stability analysis of the nonlinear frequency responses is furnished in Section 2.6. Section 2.7 presents the numerical results corresponding to the aforesaid investigation on the control capabilities of the extensional mode and shear mode piezoelectric actuators. Finally, in Section 2.8, the observations from this study are summarized.

2.2. Present smart beams

The extensional mode piezoelectric actuators are usually attached to the surface of a host structure for the actuation of bending deformation of the overall smart structure (Sun and Zhang, 1995; Trindade, 2007). Accordingly, for active control of a substrate beam using extensional mode actuators, a smart beam is

configured as shown in Fig. 2.1(a). The length (L) of the beam is divided into a number (n_p) of uniform segments having the length of L_s. In every segment, two identical actuator patches are attached to the top and bottom surfaces of the substrate beam (Fig. 2.1(a)). The length of the actuator patches is denoted by L_p, and they are located centrally within the span of a segment. These actuator patches are poled in the vertical direction, and the external electric field is applied across their top and bottom fully electrode surfaces according to a closed-loop control strategy presented in Section 2.4. For the implementation of this control strategy, the velocity sensors (S_i, i = 1, 2, 3...) are located following the length (L_s) of segments as shown in Fig. 2.1(a).

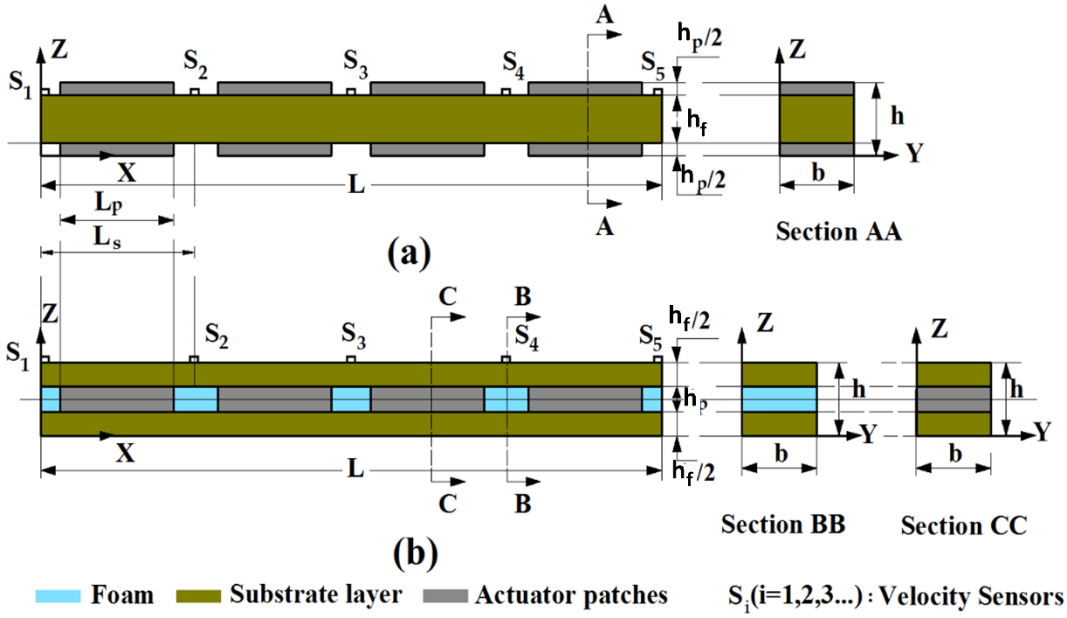

Fig. 2.1. Schematic diagrams of (a) a substrate beam integrated with extensional mode actuator patches (EMA beam) and (b) a sandwich beam having the shear mode actuator patches at the core (SMA beam).

Unlike the extensional mode piezoelectric actuators, the shear mode piezoelectric actuators are usually located at the core of a thin-walled structure through the sandwich configuration (Sun and Zhang, 1995; Trindade, 2007). So, for the actuation of the beam using shear mode actuators, the smart beam is constructed in the sandwich configuration, as shown in Fig. 2.1(b) where an actuator patch is taken at the core of a segment (L_s), and the gap between the actuator patches at the core is filled by foam. The shear mode actuator patches are poled along the longitudinal direction of the substrate beam, and they are activated by supplying external electric field across their top and bottom fully

electrode surfaces according to a shear-based active control strategy as presented in Section 2.4.

However, for making a comparative study between these two kinds of piezoelectric actuators in active control of dynamics of a beam element, the shear mode actuator patches are arranged through the same number (n_p) of patch segments as that are taken for the extensional mode actuator patches. Also, the velocity sensors (S_i, $i = 1, 2, 3...$) for the sandwich beam are located in the same manner as that is for the extensional mode actuator patches. For the other geometrical dimensions, the total thickness (h_p) of the extensional mode actuator patches over a typical cross-section of the smart beam (Fig. 2.1(a)) is considered as equal to the thickness of the shear mode actuator patches (Fig. 2.1(b)). Also, the total thickness (h_f) of the substrate/face layers in the smart sandwich beam (Fig. 2.1(b)) equals to the thickness of the other substrate beam (Fig. 2.1(a)). Both the smart beams are taken with their clamped ends and operate under the same dynamic load.

The substrate layers are considered to be made of an isotropic material. The foam is also considered to have isotropic material properties. Further, the extensional and shear mode actuator patches are considered to be made of the same piezoelectric material. However, for the sake of simplicity in the presentation, the smart beam with extensional mode actuators is presently called as extensional mode actuated (EMA) beam while the other smart beam with shear mode actuators is named as shear mode actuated (SMA) beam.

2.3. Mathematical formulation

According to the aforesaid material properties of the component materials in the smart beams and the poling direction of piezoelectric actuator patches, the material properties of the smart beams do not vary along the y-direction (Fig. 2.1). Also, the transverse shear or extensional actuation force in the actuator patches do not vary in the y-direction. There is no applied mechanical force over the boundary surfaces of the smart beams in parallel to the xz-plane. Moreover, there is no body force in any direction of the reference coordinate system (xyz). Therefore, the smart beams may be considered as plane stress problems in the xz-plane (Fig. 2.1). Accordingly, the state of stress and the state of strain at any point in the xz-plane can be written as,

$$\boldsymbol{\varepsilon} = \{\varepsilon_x \quad \varepsilon_z \quad \gamma_{xz}\}^{\mathrm{T}}, \ \boldsymbol{\sigma} = \{\sigma_x \quad \sigma_z \quad \tau_{xz}\}^{\mathrm{T}} \tag{2.1}$$

where, ε_x/σ_x and ε_z/σ_z are the longitudinal and transverse normal strains/stresses, respectively; γ_{xz}/τ_{xz} is the transverse shear strain/stress in the xz-plane. The von Karman nonlinear strain-displacement relations at any point in the xz-plane can be written as,

$$\boldsymbol{\varepsilon} = (\boldsymbol{\varepsilon}_l + \boldsymbol{\varepsilon}_N), \quad \boldsymbol{\varepsilon}_l = \left\{ \frac{\partial u}{\partial x} \quad \frac{\partial w}{\partial z} \quad \frac{\partial w}{\partial x} + \frac{\partial u}{\partial z} \right\}^{\mathrm{T}}, \quad \boldsymbol{\varepsilon}_n = \left\{ \frac{1}{2}\left(\frac{\partial w}{\partial x}\right)^2 \quad 0 \quad 0 \right\}^{\mathrm{T}} \tag{2.2}$$

where, u and w are the displacements at any point in the xz-plane along the x and z directions, respectively. The constitutive relations for the substrate beam or foam under the plane stress assumption can be written as,

$$\boldsymbol{\sigma}^k = \boldsymbol{C}^k \boldsymbol{\varepsilon}, \ \boldsymbol{C}^k = E^k \boldsymbol{C}_b^k, \ k = 1,2$$

$$\boldsymbol{C}^k = \frac{1}{1-(\nu^k)^2}\begin{bmatrix} 1 & \nu^k & 0 \\ \nu^k & 1 & 0 \\ 0 & 0 & (1-\nu^k)/2 \end{bmatrix} \tag{2.3a}$$

where, the superscript k indicates the materials for the substrate beam, foam and actuator patches as per its value as 1, 2 and 3, respectively; E^k and ν^k ($k = 1,2$) are Young's modulus and Poisson's ratio, respectively. The top and bottom surfaces of the thin piezoelectric actuator patches are fully electrode surfaces. So, the electric field components E_x, E_y and E_z along the x, y and z directions, respectively, can be assumed as, $E_x \approx 0$, $E_y \approx 0$ and $E_z = -aV/h_p$ where V is the applied voltage across the top and bottom electrode surfaces, and a is equal to 2 or 1 for EMA or SMA beam, respectively. Accordingly, the constitutive relations for the piezoelectric actuator patches under the plane stress assumption can be written as (Trindade, 2007),

$$\boldsymbol{\sigma}^k = \boldsymbol{C}^k \boldsymbol{\varepsilon} - \boldsymbol{e}^k E_z, \ D_z^k = (\boldsymbol{e}^k)^{\mathrm{T}} \boldsymbol{\varepsilon} + \in_{33}^k E_z, \ k = 3$$

$$\boldsymbol{C}^k = \begin{bmatrix} \bar{C}_{11}^k - (\bar{C}_{12}^k)^2/\bar{C}_{22}^k & \bar{C}_{13}^k - (\bar{C}_{12}^k \bar{C}_{23}^k)/\bar{C}_{22}^k & 0 \\ \bar{C}_{13}^k - (\bar{C}_{12}^k \bar{C}_{23}^k)/\bar{C}_{22}^k & \bar{C}_{33}^k - (\bar{C}_{23}^k)^2/\bar{C}_{22}^k & 0 \\ 0 & 0 & \bar{C}_{55}^k \end{bmatrix}$$

$$\boldsymbol{e}^k = \left\{ 0 \quad 0 \quad \bar{e}_{35}^k \right\}^{\mathrm{T}} \text{ for shear mode actuator}$$

$$\boldsymbol{e}^k = \left\{ \bar{e}_{31}^k - (\bar{e}_{32}^k \bar{C}_{12}^k)/\bar{C}_{22}^k \quad \bar{e}_{33}^k - (\bar{e}_{32}^k \bar{C}_{23}^k)/\bar{C}_{22}^k \quad 0 \right\}^{\mathrm{T}} \text{ for extensional mode actuator} \tag{2.3b}$$

where, $\bar{C}_{ij}^{k}$ $(k=3)$ are the stiffness coefficients of the vertically or longitudinally poled piezoelectric actuators; $\bar{e}_{ij}^{k}$ $(k=3)$ are the piezoelectric coefficients; $\in_{33}^{k}$ $(k=3$) is the electrical permittivity along the z-direction and D_z^k $(k=3)$ is the electrical displacement along the z-direction.

The smart beams are considered to be subjected to an axial compressive load (p_a^t) through the support ends. Generally, the influence of this kind of load on the bending deformation of a beam is accounted by means of the pre-stress ($\boldsymbol{\sigma}_a$) in the beam (Chen et al., 2002; Ganesan and Kadoli, 2004; Lacarbonara et al., 2007). This pre-stress in the beam corresponds to its axial deformation only under the axial compressive load. Further, a beam element usually possesses a very high rigidity against its axial deformation. So, the linear axial deformation of the beam may be assumed where the corresponding pre-stress at any point in the beam varies linearly with the applied axial compressive load (p_a^t). Accordingly, the pre-stress ($\boldsymbol{\sigma}_a$) in the beam element can be written as follows,

$$\boldsymbol{\sigma}_a = \boldsymbol{\sigma}_0(x,z)\, p_a^t \tag{2.4}$$

where, $\boldsymbol{\sigma}_0$ is the state of stress at a point in the beam corresponding to its linear axial deformation under the unit value of the applied axial compressive load (p_a^t). However, introducing the axial compressive load in this form of the pre-stress, the first variation of the total potential energy of the smart beams can be written as,

$$\delta T_p = \sum_{k=1}^{3} \int_{A^k} \left\langle (\delta\boldsymbol{\varepsilon})^{\mathrm{T}} \boldsymbol{\sigma}^k + (\delta\boldsymbol{\varepsilon})^{\mathrm{T}} \boldsymbol{\sigma}_0\, p_a^t \right\rangle b\; dA^k - \int_{A^k} (\delta E_z) D_z^k b\; dA^k \Big|_{k=3} \tag{2.5}$$

where, δ is the operator for the first variation; A^k is the area of k^{th} material in the xz-plane of the smart beam. It may be noted here that the electric field (E_z) is specified at any instant of time in the use of the piezoelectric actuators, and thus $\delta E_z = 0$. Substituting Eqs. (2.3a), (2.3b) and (2.2) in Eq. (2.5), the resulting expression for δT_p can be obtained as,

$$\delta T_p = \sum_{k=1}^{3} \int_{A^k} \left\langle \begin{matrix} (\delta\boldsymbol{\varepsilon}_l + \delta\boldsymbol{\varepsilon}_n)^{\mathrm{T}} \boldsymbol{C}^k (\boldsymbol{\varepsilon}_l + \boldsymbol{\varepsilon}_n) \\ +(\delta\boldsymbol{\varepsilon}_l + \delta\boldsymbol{\varepsilon}_n)^{\mathrm{T}} \boldsymbol{\sigma}_0\, p_a^t \end{matrix} \right\rangle b\; dA^k - \int_{A^k} (\delta\boldsymbol{\varepsilon}_l + \delta\boldsymbol{\varepsilon}_n)^{\mathrm{T}} \boldsymbol{e}^k E_z b\, dA^k \Big|_{k=3} \tag{2.6}$$

Now, if the smart beams are considered to undergo vibration under the harmonically varying axial compressive load (p_a^t , Eq. (2.7)), then the first variation

of the total kinetic energy (δT_t) of the smart beams can be written as given in Eq. (2.8).

$$p_a^t = p_a^o(1+\lambda\cos\Omega t) \tag{2.7}$$

$$\delta T_t = \sum_{k=1}^{3} \int_{A^k} (\delta \dot{\boldsymbol{d}}_s)^{\mathrm{T}}\ \rho^k\, \dot{\boldsymbol{d}}_s\ b\, dA^k\ ,\ \boldsymbol{d}_s = \{u \quad w\}^{\mathrm{T}} \tag{2.8}$$

In Eqs. (2.7)-(2.8), p_a^o is the static counterpart of the axial compressive load (p_a^t); λ and Ω are the dynamic load parameter and excitation frequency, respectively; ρ^k is the mass density of k^{th} material in the smart beams; $\boldsymbol{d}_s$ is the displacement vector at any point in the xz-plane. The governing equation of motion of the smart beams can be derived by employing Hamilton's principle as,

$$\int_{t_1}^{t_2} (\delta T_p - \delta T_t)\, dt = 0 \tag{2.9}$$

Substituting Eqs. (2.6) and (2.8) in Eq. (2.9), the following simplified equation can be obtained,

$$\sum_{k=1}^{3} \int_{A^k} \left\langle \begin{array}{l} (\delta\boldsymbol{\varepsilon}_l + \delta\boldsymbol{\varepsilon}_n)^{\mathrm{T}} \boldsymbol{C}^k (\boldsymbol{\varepsilon}_l + \boldsymbol{\varepsilon}_n) + \\ (\delta\boldsymbol{\varepsilon}_l + \delta\boldsymbol{\varepsilon}_n)^{\mathrm{T}} \boldsymbol{\sigma}_0\, p_a^t + (\delta \boldsymbol{d}_s)^{\mathrm{T}} \rho^k \ddot{\boldsymbol{d}}_s \end{array} \right\rangle b\, dA^k - \int_{A^k} (\delta\boldsymbol{\varepsilon}_l + \delta\boldsymbol{\varepsilon}_n)^{\mathrm{T}} \boldsymbol{e}^k E_z\, b\, dA^k \Big|_{k=3} = 0 \tag{2.10}$$

For the sake of simplicity in the formulation, a dimensionless time unit (τ) is introduced as $\tau = \Omega t$, and all subsequent equations are expressed in terms of this dimensionless time unit (τ). However, a state of vibration ($\boldsymbol{d}_s, \Omega, \lambda$) of the smart beams can be expressed with respect to a reference state of vibration ($^i\boldsymbol{d}_s$, Ω_i, λ_i) through an incremental form as given in Eq. (2.11). Accordingly, the incremental forms of the strain vectors ($\boldsymbol{\varepsilon}_l, \boldsymbol{\varepsilon}_n$) are presented in Eq. (2.12) where $\boldsymbol{L}$, $\boldsymbol{L}_n$ and $\boldsymbol{L}_x^w$ are the operator matrices.

$$\boldsymbol{d}_s = (^i\boldsymbol{d}_s + \Delta\boldsymbol{d}_s)\ ,\ \Omega = (\Omega_i + \Delta\Omega)\ ,\ \lambda = (\lambda_i + \Delta\lambda) \tag{2.11}$$

$$\boldsymbol{\varepsilon}_l = (^i\boldsymbol{\varepsilon}_l + \Delta\boldsymbol{\varepsilon}_l)\ ,\ \boldsymbol{\varepsilon}_n = (^i\boldsymbol{\varepsilon}_n + \Delta\boldsymbol{\varepsilon}_{n1} + \Delta\boldsymbol{\varepsilon}_{n2})\ ,$$

$$^i\boldsymbol{\varepsilon}_l = \boldsymbol{L}\,{}^i\boldsymbol{d}_s\ ,\ \Delta\boldsymbol{\varepsilon}_l = \boldsymbol{L}\Delta\boldsymbol{d}_s\ ,\ ^i\boldsymbol{\varepsilon}_n = (1/2)\,{}^i\boldsymbol{L}_n\,{}^i\boldsymbol{d}_s\ ,$$

$$\Delta\boldsymbol{\varepsilon}_{n1} = {}^i\boldsymbol{L}_n\Delta\boldsymbol{d}_s\ ,\ \Delta\boldsymbol{\varepsilon}_{n2} = (1/2)\Delta\boldsymbol{L}_n\Delta\boldsymbol{d}_s\ ,$$

$$\boldsymbol{L} = \begin{bmatrix} \partial/\partial x & 0 & \partial/\partial z \\ 0 & \partial/\partial z & \partial/\partial x \end{bmatrix}^{\mathrm{T}}\ ,\ {}^i\boldsymbol{L}_n = \boldsymbol{L}_n(^i\boldsymbol{d}_s)\ ,\ \Delta\boldsymbol{L}_n = \boldsymbol{L}_n(\Delta\boldsymbol{d}_s)\ ,$$

$$\boldsymbol{L}_n(\boldsymbol{d}_s) = (\boldsymbol{L}_1^w\boldsymbol{d}_s)\,\boldsymbol{L}_x^w\ ,\ \boldsymbol{L}_1^w = \left[(\boldsymbol{L}_x^w)^{\mathrm{T}} \ \boldsymbol{O} \ \ \boldsymbol{O}\right]^{\mathrm{T}}\ ,\ \boldsymbol{L}_x^w = \{0 \quad \partial/\partial x\} \tag{2.12}$$

Introducing Eqs. (2.11) and (2.12) in Eq. (2.10), the incremental form of the governing equation of motion of the smart beams can be obtained as,

$$\sum_{k=1}^{3}\int_{A^k}\left\langle\begin{array}{l}(\delta\Delta\boldsymbol{\varepsilon}_l+\delta\Delta\boldsymbol{\varepsilon}_{n1})^{\mathrm{T}}\boldsymbol{C}^k({}^i\boldsymbol{\varepsilon}_l+{}^i\boldsymbol{\varepsilon}_n+\Delta\boldsymbol{\varepsilon}_l+\Delta\boldsymbol{\varepsilon}_{n1}+\Delta\boldsymbol{\varepsilon}_{n2})+\\(\delta\Delta\boldsymbol{\varepsilon}_{n2})^{\mathrm{T}}\boldsymbol{C}^k({}^i\boldsymbol{\varepsilon}_l+{}^i\boldsymbol{\varepsilon}_n)+(\Omega_i+\Delta\Omega)^2(\delta\Delta\boldsymbol{d}_s)^{\mathrm{T}}\rho^k({}^i\ddot{\boldsymbol{d}}_s+\Delta\ddot{\boldsymbol{d}}_s)\\+(\delta\Delta\boldsymbol{\varepsilon}_l+\delta\Delta\boldsymbol{\varepsilon}_{n1}+\delta\Delta\boldsymbol{\varepsilon}_{n2})^{\mathrm{T}}\boldsymbol{\sigma}_0\;\; p_a^o\left\langle 1+(\lambda_i+\Delta\lambda)\cos\tau\right\rangle\end{array}\right\rangle b\,dA^k -$$

$$\int_{A^k}(\delta\Delta\boldsymbol{\varepsilon}_l+\delta\Delta\boldsymbol{\varepsilon}_{n1}+\delta\Delta\boldsymbol{\varepsilon}_{n2})^{\mathrm{T}}\boldsymbol{e}^k E_z\,b\,dA^k\Big|_{k=3}=0 \qquad (2.13)$$

The FE model of the smart beams is derived by discretizing the xz-plane using nine-node isoparametric quadrilateral elements. The edges of a typical element are parallel to the reference coordinate axes in the xz-plane, and also a typical element is made of either of the three component materials ($k=1, 2, 3$) in the smart beams. However, the displacement and strain vectors (Eqs. (2.11)-(2.12)) at any point in a typical element can be expressed in terms of the shape function matrix ($\boldsymbol{N}$) and the elemental nodal displacement vectors (${}^i\boldsymbol{d}^e$, $\Delta\boldsymbol{d}^e$) as follows,

$$ {}^i\boldsymbol{d}_s=\boldsymbol{N}\,{}^i\boldsymbol{d}^e,\;\; \Delta\boldsymbol{d}_s=\boldsymbol{N}\,\Delta\boldsymbol{d}^e,$$

$$ {}^i\boldsymbol{\varepsilon}_l=\boldsymbol{B}_l\,{}^i\boldsymbol{d}^e,\;\; \Delta\boldsymbol{\varepsilon}_l=\boldsymbol{B}_l\Delta\boldsymbol{d}^e,\;\; {}^i\boldsymbol{\varepsilon}_n=(1/2)\,\boldsymbol{B}_n\,{}^i\boldsymbol{d}_I^e\,{}^i\boldsymbol{d}^e,$$

$$ \Delta\boldsymbol{\varepsilon}_{n1}=\boldsymbol{B}_n\,{}^i\boldsymbol{d}_I^e\Delta\boldsymbol{d}^e\;\;,\;\; \Delta\boldsymbol{\varepsilon}_{n2}=(1/2)\,\boldsymbol{B}_n\Delta\boldsymbol{d}_I^e\Delta\boldsymbol{d}^e,$$

$$ \boldsymbol{B}_l=\boldsymbol{L}\,\boldsymbol{N}\;,\;\; \boldsymbol{B}_n=\boldsymbol{B}_1^w\boldsymbol{R}_x^w,$$

$$ \boldsymbol{R}_x^w=\left(\boldsymbol{I}_{18}\otimes\boldsymbol{B}_x^w\right),\;\; \boldsymbol{B}_1^w=\boldsymbol{L}_1^w\boldsymbol{N}\;,\;\; \boldsymbol{B}_x^w=\boldsymbol{L}_x^w\,\boldsymbol{N} \qquad (2.14)$$

where, where $\boldsymbol{I}_{18}$ is the unity matrix of size (18×18) and the symbol $\otimes$ represents Kronecker product. Introducing Eq. (2.14) in Eq. (2.13), the linearized incremental governing equation of motion for a typical element can be obtained as,

$$\Omega_i^2\boldsymbol{M}_s^e\Delta\ddot{\boldsymbol{d}}^e+\boldsymbol{K}_{stm}^e\,\Delta\boldsymbol{d}^e=\boldsymbol{P}_m^e\,\Delta\Omega+\boldsymbol{P}_\lambda^e\,\Delta\lambda+\boldsymbol{R}_{sm}^e+\left\langle\boldsymbol{P}_E^e+({}^i\boldsymbol{d}_I^e)^{\mathrm{T}}\boldsymbol{C}_E^e+\boldsymbol{K}_E^e\Delta\boldsymbol{d}^e\right\rangle V,$$

$$\boldsymbol{K}_{stm}^e=\boldsymbol{K}_{sl}^e+\boldsymbol{K}_{sn1}^e\,{}^i\boldsymbol{d}_I^e+(\boldsymbol{K}_{sn1}^e\,{}^i\boldsymbol{d}_I^e)^{\mathrm{T}}+\boldsymbol{K}_{sn3}^e\,{}^i\boldsymbol{d}_I^e+(3/2)({}^i\boldsymbol{d}_I^e)^{\mathrm{T}}\boldsymbol{K}_{sn4}^e\,{}^i\boldsymbol{d}_I^e+$$

$$p_a^o(1+\lambda_i\cos\tau)\,\boldsymbol{K}_{sa}^e,\;\; \boldsymbol{P}_m^e=-2\Omega_i\boldsymbol{M}_s^e\,{}^i\ddot{\boldsymbol{d}}^e,$$

$$\boldsymbol{P}_\lambda^e=-p_a^o\cos(\tau)\left\langle\boldsymbol{P}_a^e+\boldsymbol{K}_{sa}^e\,{}^i\boldsymbol{d}^e\right\rangle,\;\; \boldsymbol{R}_{sm}^e=-p_a^o(1+\lambda_i\cos\tau)\,\boldsymbol{P}_a^e-\boldsymbol{K}_{sm}^e\,{}^i\boldsymbol{d}^e-\Omega_i^2\boldsymbol{M}_s^e\,{}^i\ddot{\boldsymbol{d}}^e,$$

$$\boldsymbol{K}_{sm}^e=\boldsymbol{K}_{sl}^e+(1/2)\,\boldsymbol{K}_{sn1}^e\,{}^i\boldsymbol{d}_I^e+(\boldsymbol{K}_{sn1}^e\,{}^i\boldsymbol{d}_I^e)^{\mathrm{T}}+(1/2)({}^i\boldsymbol{d}_I^e)^{\mathrm{T}}\boldsymbol{K}_{sn4}^e\,{}^i\boldsymbol{d}_I^e+p_a^o(1+\lambda_i\cos\tau)\boldsymbol{K}_{sa}^e \qquad (2.15)$$

In Eq. (2.15), the superscript e indicates the elemental quantities, and the various component matrices are given by,

$$\boldsymbol{M}_s^e = \int_{A^e} \boldsymbol{N}^{\mathrm{T}} \rho^k \boldsymbol{N}\, b\, dA^e \;,\; \boldsymbol{K}_{sl}^e = \int_{A^e} \boldsymbol{B}_l^{\mathrm{T}} \boldsymbol{C}^k \boldsymbol{B}_l\, b\, dA^e \;,$$

$$\boldsymbol{K}_{sn1}^e = \int_{A^e} \boldsymbol{B}_l^{\mathrm{T}} \boldsymbol{C}^k \boldsymbol{B}_n\, b\, dA^e \;,\; \boldsymbol{K}_{sn3}^e = \int_{A^e} (\boldsymbol{B}_1^w)^{\mathrm{T}} \boldsymbol{C}^k \boldsymbol{B}_l\, \boldsymbol{R}_x^w\, b\, dA^e \;,$$

$$\boldsymbol{K}_{sn4}^e = \int_{A^e} (\boldsymbol{B}_n)^{\mathrm{T}} \boldsymbol{C}^k \boldsymbol{B}_n\, b\, dA^e \;,\; \boldsymbol{K}_{sa}^e = \int_{A^e} (\boldsymbol{B}_x^w)^{\mathrm{T}} \boldsymbol{\sigma}_0 \boldsymbol{B}_x^w\, b\, dA^e \;,$$

$$\boldsymbol{P}_a^e = \int_{A^e} \boldsymbol{B}_l^{\mathrm{T}} \boldsymbol{\sigma}_0\, b\, dA^e \;,\; \boldsymbol{P}_E^e = \int_{A^e} (-a/t_p) \boldsymbol{B}_l^T \boldsymbol{e}^k b\, dA^e \;,$$

$$\boldsymbol{C}_E^e = \int_{A^e} (-a/t_p) \boldsymbol{B}_n^{\mathrm{T}} \boldsymbol{e}^k b\, dA^e \;,\; \boldsymbol{K}_E^e = \int_{A^e} (-a/t_p) (\boldsymbol{B}_x^w)^{\mathrm{T}} e_1^k\, \boldsymbol{B}_x^w b\, dA^e \;,$$

$$\boldsymbol{R}_x^w = \boldsymbol{I}_{18} \otimes \boldsymbol{B}_x^w \;,\; {}^i\boldsymbol{d}_I^e = {}^i\boldsymbol{d}^e \otimes \boldsymbol{I}_{18} \qquad (2.16)$$

where, the superscript k denotes the material of an element among the three kinds of materials ($k = 1,2,3$) in the smart beams; e_1^k is the first component of piezoelectric coefficient vector $\boldsymbol{e}^k$ (Eq. (2.3b)). Assembling the elemental equations (Eq. (2.15)), the governing equation of motion of the smart beams can be obtained as,

$$\Omega_i^2 \boldsymbol{M}_s\, \Delta\ddot{\boldsymbol{d}} + \boldsymbol{K}_{stm}\, \Delta\boldsymbol{d} = \boldsymbol{P}_m\, \Delta\Omega + \boldsymbol{P}_\lambda\, \Delta\lambda + \boldsymbol{R}_{sm} + \sum_{p=1}^{n_p} \left\langle \boldsymbol{P}_E^p + ({}^i\boldsymbol{d}_I)^T \boldsymbol{C}_E^p + \boldsymbol{K}_E^p \Delta\boldsymbol{d} \right\rangle V_p \qquad (2.17)$$

where, $\boldsymbol{d}$ is the global nodal displacement vector; $\boldsymbol{M}_s$ and $\boldsymbol{K}_{stm}$ are the global mass and tangent stiffness matrices, respectively; $\boldsymbol{P}_m$ / $\boldsymbol{P}_\lambda$ is the global load vector per unit increment of Ω / λ; $\boldsymbol{R}_{sm}$ is the global residue vector excluding the electro-elastic coupling effect in the actuators; V_p is the voltage applied to the actuator in the p^{th} segment; $\boldsymbol{P}_E^p$, $\boldsymbol{C}_E^p$ and $\boldsymbol{K}_E^p$ are the global matrices corresponding to the assembly of elemental matrices $\boldsymbol{P}_E^e$, $\boldsymbol{C}_E^e$ and $\boldsymbol{K}_E^e$, respectively, for the elements made of actuator material within the p^{th} segment.

2.4. Active control strategy

The piezoelectric actuator patches are presently utilized to counteract the bending deformation of the smart beams (Fig. 2.1). In the case of the SMA beam (Fig. 2.1(b)), every shear mode piezoelectric actuator patch is utilized to counteract the mechanically induced transverse shear stress (τ_{xz}) around its location. Now, this mechanical stress (τ_{xz}) changes its sign at the antinodes of any bending mode shape of vibration of the smart beam. So, every shear mode actuator patch is presently activated by the feedback of the slope of bending at its location since the slope of bending also changes its sign at the antinodes. Further, to utilize the

shear actuation force in the form of the active damping force, the electric field (E_z) is supplied to a shear mode actuator patch in proportion to the time-rate of change of the local slope of bending deformation of the smart beam. However, this velocity feedback control strategy is implemented by locating the velocity sensors over the ends of the actuator patch segments, as shown in Fig. 2.1(b). These sensors provide the transverse velocities at the ends of the actuator patch segments, which are used to supply the external voltage (V_p) to the p^{th} actuator patch segment according to Eq. (2.18a). In Eq. (2.18a), $\dot{w}_{S_p}$ and $\dot{w}_{S_{p+1}}$ are the transverse velocities at the left and right ends of the p^{th} actuator patch segment, respectively, and k_{sd} is the velocity feedback control gain.

$$V_p = -k_{sd}\frac{\dot{w}_{S_{p+1}} - \dot{w}_{S_p}}{L_s} \quad \text{for SMA beam} \tag{2.18a}$$

Similar to the shear mode actuator patches in the SMA beam (Fig. 2.1(b)), every extensional mode actuator patch in the EMA beam (Fig. 2.1(a)) also acts against the mechanically induced extensional stress (σ_x) around the location of the actuator patch. However, since the beam undergoes bending deformation, the sign of the mechanical stress (σ_x) changes from positive to negative or vice versa as one proceeds from the top to the bottom surface of the substrate beam over its any cross-section. Therefore, the direction of the extensional actuation force within the top actuator patch in any patch segment would be in opposition to that for the bottom actuator patch in the same patch segment. It can be achieved by reversing the direction of the applied electric field (E_z) over the top and bottom actuator patches in a segment while both the actuators are poled in the same vertical direction. Physically, this arrangement can be achieved by grounding the electrodes at the interlayer surface of substrate beam and actuator patches. However, in any patch segment, the electric field (E_z) is applied to the corresponding actuator patches by supplying the external voltage (V_p) in proportion to the transverse velocity over that patch segment. For implementing this velocity feedback control strategy, the velocity sensors are arranged similar to that for the SMA beam (Figs. 2.1(a)-(b)), where the average transverse velocity over a patch segment (say, p^{th} actuator patch segment) is taken as given in Eq. (2.18b).

$$V_p = -k_{ed}\frac{\dot{w}_{S_{p+1}} + \dot{w}_{S_p}}{2} \quad \text{for EMA beam} \tag{2.18b}$$

where, k_{ed} is the velocity feedback control gain. The transverse velocities ($\dot{w}_{S_p}$, $\dot{w}_{S_{p+1}}$) at the sensor points can be expressed in terms of the global nodal velocity vector ($\dot{\boldsymbol{d}}$) by introducing a transformation row matrix ($\boldsymbol{N}_{ST}^{p}$ / $\boldsymbol{N}_{ET}^{p}$). It yields the applied voltage (V_p) in terms of the velocity vector ($\dot{\boldsymbol{d}}$) as follows,

$$V_p = -\frac{k_{sd}}{L_s}\boldsymbol{N}_{ST}^{p}\,\dot{\boldsymbol{d}}\,,\ (\dot{w}_{S_{p+1}} - \dot{w}_{S_p}) = \boldsymbol{N}_{ST}^{p}\,\dot{\boldsymbol{d}} \quad \text{for SMA beam} \tag{2.18c}$$

$$V_p = -\frac{k_{ed}}{2}\boldsymbol{N}_{ET}^{p}\,\dot{\boldsymbol{d}}\,,\ (\dot{w}_{S_{p+1}} + \dot{w}_{S_p}) = \boldsymbol{N}_{ET}^{p}\,\dot{\boldsymbol{d}} \quad \text{for EMA beam} \tag{2.18d}$$

Using Eq. (2.18c) or Eq. (2.18d) in the Eq. (2.17), the simplified form of the governing equation of motion of the smart beams can be obtained as,

$$\Omega_i^2\boldsymbol{M}_s\,\Delta\ddot{\boldsymbol{d}} + \boldsymbol{K}_{st}\,\Delta\boldsymbol{d} + \Omega_i\boldsymbol{C}_s\,\Delta\dot{\boldsymbol{d}} = \boldsymbol{P}_\Omega\,\Delta\Omega + \boldsymbol{P}_\lambda\,\Delta\lambda + \boldsymbol{R}_s\,,$$

$$\boldsymbol{R}_s = \boldsymbol{R}_{sm} - \Omega_i\boldsymbol{C}_s\,{}^{i}\dot{\boldsymbol{d}}\,,\ \boldsymbol{K}_{st} = \boldsymbol{K}_{stm} + \Omega_i\boldsymbol{K}_N\,{}^{i}\dot{\boldsymbol{d}}_I^{s}\,,$$

$$\boldsymbol{C}_s = \boldsymbol{C}_l + ({}^{i}\boldsymbol{d}_I)^{\mathrm{T}}\boldsymbol{C}_N\,,\ \boldsymbol{P}_\Omega = \boldsymbol{P}_m - \boldsymbol{C}_s\,{}^{i}\dot{\boldsymbol{d}}\,,$$

$$\boldsymbol{C}_l = \sum_{p=1}^{n_p}\boldsymbol{P}_E^{p}\,\boldsymbol{f}_c\,,\quad \boldsymbol{C}_N = \sum_{p=1}^{n_p}\boldsymbol{C}_E^{p}\,\boldsymbol{f}_c\,,$$

$$\boldsymbol{K}_N = \left[\boldsymbol{K}_E^{1}\quad (\boldsymbol{K}_E^{1} + \boldsymbol{K}_E^{2})\quad (\boldsymbol{K}_E^{2} + \boldsymbol{K}_E^{3})\quad \ldots\quad (\boldsymbol{K}_E^{n_p-1} + \boldsymbol{K}_E^{n_p})\quad \boldsymbol{K}_E^{n_p}\right],$$

$${}^{i}\dot{\boldsymbol{d}}_I^{s} = ({}^{i}\dot{\boldsymbol{d}}^{s} \otimes \boldsymbol{I}_{N_f})\,,\ {}^{i}\dot{\boldsymbol{d}}^{s} = \left[\dot{w}_{S_1}\ \dot{w}_{S_2}\ \dot{w}_{S_3}\ldots\dot{w}_{S_{n_p}}\right],$$

$$\boldsymbol{f}_c = \frac{k_{sd}}{L_s}\boldsymbol{N}_{ST}^{p} \text{ for SMA beam},\ \boldsymbol{f}_c = \frac{k_{ed}}{2}\boldsymbol{N}_{ET}^{p} \text{ for EMA beam} \tag{2.19}$$

In Eq. (2.19), $\boldsymbol{C}_s$ and $\boldsymbol{K}_{st}$ are the global damping and tangent stiffness matrices, respectively; $\boldsymbol{P}_\Omega$ / $\boldsymbol{P}_\lambda$ is the global load vector per unit increment of Ω / λ; $\boldsymbol{R}_s$ is the global residue vector; $\boldsymbol{I}_{N_f}$ is the identity matrix of size ($N_f \times N_f$) where N_f is the number of nodal degrees of freedom. It may also be noted here that the matrices $\boldsymbol{K}_N$ and $\boldsymbol{C}_N$ are null matrices for the SMA beam.

2.5. Implementation of the harmonic balance method

For the evaluation of frequency responses of the smart beams, the governing equation of motion (Eq. (2.19)) is expressed in the frequency domain by implementing the HBM. According to this method, the solution ($\boldsymbol{d}$) can be assumed following the Fourier series with the finite number (H) of harmonic terms as follows,

$$\boldsymbol{d} = \boldsymbol{S}\,\boldsymbol{X}\ ,$$

$$\boldsymbol{S} = \boldsymbol{Q} \otimes \boldsymbol{I}_{N_f}\ ,\quad \boldsymbol{Q} = \{1\ \ \boldsymbol{Q}_c\ \ \boldsymbol{Q}_s\}\ ,$$

$$\boldsymbol{Q}_c = \{\cos(\tau/2)\ \cos(2\tau/2)\ \cos(3\tau/2) \ldots\ \cos(H\tau/2)\}\ ,$$

$$\boldsymbol{Q}_s = \{\sin(\tau/2)\ \sin(2\tau/2)\ \sin(3\tau/2) \ldots\ \sin(H\tau/2)\}\ ,\quad \boldsymbol{X} = \left\{(\boldsymbol{d}^0)^{\mathrm{T}}\ (\boldsymbol{d}^c)^{\mathrm{T}}\ (\boldsymbol{d}^s)^{\mathrm{T}}\right\}^{\mathrm{T}} \tag{2.20}$$

where, $\boldsymbol{d}^0$, $\boldsymbol{d}^c$ and $\boldsymbol{d}^s$ are the nodal displacement amplitude vectors corresponding to the constant, cosine and sine terms, respectively. Substituting this solution (Eq. (2.20)) in Eq. (2.19) and then using the Galerkin method, the linearized incremental governing equation of motion in the frequency domain can be obtained as,

$$\boldsymbol{K}_t \Delta\boldsymbol{X} = \boldsymbol{R}_{\Omega}\Delta\Omega + \boldsymbol{R}_{\lambda}\Delta\lambda + \boldsymbol{R}$$

$$\boldsymbol{K}_t = \int_0^{4\pi} \boldsymbol{S}^{\mathrm{T}}\left(\Omega_i^2 \boldsymbol{M}_s\ \ddot{\boldsymbol{S}} + \Omega_i \boldsymbol{C}_s\ \dot{\boldsymbol{S}} + \boldsymbol{K}_{st}\ \boldsymbol{S}\right) d\tau\ ,\quad \boldsymbol{R} = \int_0^{4\pi} \boldsymbol{S}^{\mathrm{T}}\ \boldsymbol{R}_s\ d\tau\ ,$$

$$\boldsymbol{R}_{\Omega} = \int_0^{4\pi} \boldsymbol{S}^{\mathrm{T}}\ \boldsymbol{P}_{\Omega}\, d\tau\ ,\quad \boldsymbol{R}_{\lambda} = \int_0^{4\pi} \boldsymbol{S}^{\mathrm{T}}\ \boldsymbol{P}_{\lambda}\, d\tau \tag{2.21}$$

The solution of Eq. (2.21) provides the frequency responses of the smart beams when the beams operate under the harmonically varying axial compressive load (Eq. (2.7)). However, presently the frequency responses of the smart beams are also evaluated by applying a transverse harmonic point-load (p_t) in the form as given in Eq. (2.22) where p_t^o is the load-amplitude.

$$p_t = p_t^o \cos\Omega t = p_t^o \cos\tau \tag{2.22}$$

The first variation of the external workdone (δW) by this point-load can be written as,

$$\delta W = \delta w\big|_{(x_l, z_l)}\ p_t \tag{2.23}$$

where, the transverse harmonic point-load (p_t) is applied at a node having the coordinates as x_l and z_l. The first variation of the corresponding nodal displacement ($\delta w\big|_{(x_l, z_l)}$) under the point-load (p_t) can be expressed in terms of the global nodal displacement vector ($\boldsymbol{d}$) through a transformation column vector ($\boldsymbol{P}_s$). Accordingly, the first variation of the external workdone (δW) can be written as,

$$\delta W = \delta \boldsymbol{d}^T \boldsymbol{P}_t\ ,\quad \boldsymbol{P}_t = (\boldsymbol{P}_s\, p_t)\ ,\ \delta w\big|_{(x_l, z_l)} = \delta \boldsymbol{d}^T \boldsymbol{P}_s \tag{2.24}$$

The governing equation of motion of the smart beams under this transverse harmonic point-load can be obtained by adding the corresponding global nodal load vector ($\boldsymbol{P}_t$, Eq. (2.24)) over the right-hand side of Eq. (2.17) while the effect of the applied axial load can be removed by assigning its zero-value (p_a^t = 0). The subsequent formulation remains the same as presented previously, and the resulting governing equation of motion (Eq. (2.21)) can then be solved for the frequency responses of the smart beams under the transverse harmonic point-load.

2.6. Local stability analysis

For the local stability analysis of a steady-state response, a small perturbation is to be provided over that response. If this perturbation vanishes with time, then the response is said to be a stable one; otherwise, it is an unstable response. However, for the specified dynamic load parameter (λ) and excitation frequency (Ω), the corresponding steady-state solution can be obtained by solving Eq. (2.21), and this solution also satisfies Eq. (2.19). Accordingly, for this known steady-state solution ($^i\boldsymbol{d} = \boldsymbol{S}\,\boldsymbol{X}$, Eq. (2.20)) at the specified load parameter (λ) and excitation frequency (Ω) as λ_i and Ω_i, respectively, Eq. (2.19) can be written as,

$$\Omega_i^2 \boldsymbol{M}_s\, \Delta\ddot{\boldsymbol{d}} + \boldsymbol{K}_{st}\, \Delta\boldsymbol{d} + \Omega_i \boldsymbol{C}_s\, \Delta\dot{\boldsymbol{d}} = \boldsymbol{0} \tag{2.25}$$

where, the matrices $\boldsymbol{K}_{st}$ and $\boldsymbol{C}_s$ are the functions of Ω_i, λ_i and $^i\boldsymbol{d}$ (Eqs. (2.19) and (2.15)). Equation (2.25) represents the linear differential equations with the periodic coefficients, and thus the stability of the steady-state response ($^i\boldsymbol{d}$) can be obtained using Floquet theory by expressing Eq. (2.25) in the state-space form as,

$$\dot{\boldsymbol{F}} = \boldsymbol{Q}_t(\tau)\boldsymbol{F}\,,$$

$$\boldsymbol{F} = \left\{\Delta\boldsymbol{d} \;\; \Delta\dot{\boldsymbol{d}}\right\}^{\mathrm{T}},\; \boldsymbol{Q}_t(\tau) = \begin{bmatrix} \boldsymbol{O}_{N_f} & \boldsymbol{I}_{N_f} \\ -\dfrac{1}{\Omega_i^2}(\boldsymbol{M}_s)^{-1}\boldsymbol{K}_{st} & -\dfrac{1}{\Omega_i}(\boldsymbol{M}_s)^{-1}\boldsymbol{C}_s \end{bmatrix} \tag{2.26}$$

where, $\boldsymbol{O}_{N_f}$ is the null matrix of size $(N_f \times N_f)$. According to Floquet theory, the stability characteristics of the steady-state solution can be obtained from the eigenvalues of the monodromy matrix or state transition matrix ($\boldsymbol{\phi}$) that can be derived by satisfying $\boldsymbol{F}(\tau + T) = \boldsymbol{\phi}\,\boldsymbol{F}(\tau)$ where T is the time period of the steady-state response. This monodromy matrix can be computed by the solution of Eq. (2.26) following the standard procedure (Peletan et al., 2013) in conjunction with

a numerical time-integration method. However, it involves a high computational cost because of a large number of nodal degrees of freedom in the FE model of the smart beams. In this concern, the local stability analysis can be carried out by deriving a reduced-order model of the system (Eq. (2.25)) without significant loss of accuracy. For this model reduction, the basis vectors are presently chosen from the proper orthogonal modes ($\boldsymbol{\Theta}_q$) that can be evaluated by solving an eigenvalue problem, as illustrated in Eq. (2.27a).

$$\left(\mathfrak{R} - \lambda_q \boldsymbol{I}_{N_f}\right)\boldsymbol{\Theta}_q = 0$$

$$\mathfrak{R} = \frac{1}{N_l}\left(\boldsymbol{\Psi}\,\boldsymbol{\Psi}^T\right),\ \boldsymbol{\Psi} = \left[\boldsymbol{d}_1 \quad \boldsymbol{d}_2 \quad \boldsymbol{d}_3 \quad . \quad . \quad \boldsymbol{d}_{N_l}\right] \tag{2.27a}$$

In Eq. (2.27a), $\mathfrak{R}$ is the correlation matrix; λ_q and $\boldsymbol{\Theta}_q$ are the proper orthogonal value (POV) and proper orthogonal mode (POM), respectively, for the q^{th} mode (Rizzi and Przekop, 2008). Here, the snapshot matrix ($\boldsymbol{\Psi}$) is composed of nodal displacement vectors ($\boldsymbol{d}_i, i = 1,2,...N_l$), where a nodal displacement vector can be taken at any instant of time from the steady-state transient response of a smart beam at an excitation frequency. Presently, the displacement vectors in the snapshot matrix are considered for different excitation frequencies that are chosen arbitrarily within the operating frequency range. However, a transformation matrix ($\boldsymbol{\Phi}$, Eq. (2.27b)) can be formed by choosing a suitable number of proper orthogonal modes ($\boldsymbol{\Theta}_q$, $j = 1,2,...N_r$) for the coordinate transformation (Eq. (2.27c)) from the nodal ($\Delta\boldsymbol{d}$) to modal ($\Delta\boldsymbol{V}$) coordinates.

$$\boldsymbol{\Phi} = \left[\boldsymbol{\Theta}_1 \quad \boldsymbol{\Theta}_2 \quad \boldsymbol{\Theta}_3 \quad . \quad . \quad \boldsymbol{\Theta}_{N_r}\right] \tag{2.27b}$$

$$\Delta\boldsymbol{d} = \boldsymbol{\Phi}\,\Delta V \tag{2.27c}$$

Now, the differential system (Eq. (2.25)) is projected over the basis ($\boldsymbol{\Phi}$) to obtain the reduced-order state-space form of Eq. (2.25) as follows,

$${}^r\dot{\boldsymbol{F}} = {}^r\boldsymbol{Q}_t(\tau)\,{}^r\boldsymbol{F}\ ,$$

$${}^r\boldsymbol{F} = \left\{\Delta V^{\mathrm{T}} \quad \Delta\dot{V}^{\mathrm{T}}\right\}^{\mathrm{T}},\quad {}^r\boldsymbol{Q}_t(\tau) = \begin{bmatrix} \boldsymbol{O}_{N_r} & \boldsymbol{I}_{N_r} \\ -\frac{1}{\Omega_i^2}\left\langle ({}^r\boldsymbol{M}_s)^{-1}\,{}^r\boldsymbol{K}_{st}\right\rangle & -\frac{1}{\Omega_i}\left\langle ({}^r\boldsymbol{M}_s)^{-1}\,{}^r\boldsymbol{C}_s\right\rangle \end{bmatrix}$$

$${}^r\boldsymbol{M}_s = (\boldsymbol{\Phi}^{\mathrm{T}}\boldsymbol{M}_s\,\boldsymbol{\Phi}),\ {}^r\boldsymbol{K}_{st} = (\boldsymbol{\Phi}^{\mathrm{T}}\boldsymbol{K}_{st}\,\boldsymbol{\Phi}),\ {}^r\boldsymbol{C}_s = (\boldsymbol{\Phi}^{\mathrm{T}}\boldsymbol{C}_s\,\boldsymbol{\Phi}) \tag{2.28}$$

where, $\boldsymbol{O}_{N_r}$ and $\boldsymbol{I}_{N_r}$ denote the null matrix and identity matrix, respectively, with the size of $(N_r \times N_r)$; the pre-superscript r denotes the reduced-order system matrices or vectors. Now, the reduced-order monodromy matrix ($^r\boldsymbol{\phi}$) can be computed by the solution of Eq. (2.28) following the standard procedure (Peletan et al., 2013), where the numerical time-integration is presently carried out using Bathe time integration method (Bathe, 2006). The steady-state frequency response ($^i\boldsymbol{d}$) is said to be stable one when all moduli of eigenvalues of the monodromy matrix ($^r\boldsymbol{\phi}$) are less than 1; otherwise, the solution is an unstable one.

2.7. Results and discussion

In this section, the suitability of the shear mode and extensional mode piezoelectric actuators in control of nonlinear vibration of the smart beams (Figs. 2.1(a)-(b)) is investigated by evaluating the nonlinear dynamic responses of the beams in both the frequency and time domain. For the evaluation of dynamic responses in the frequency domain, the governing equation of motion (Eq. (2.19)) is first expressed in the frequency domain by implementing HBM, and then the resulting equation (Eq. (2.21)) is solved using a numerical continuation method (Cheung et al., 1990). However, a convergence study is first carried out to decide an appropriate number of elements in the FE model and also a suitable number of harmonic terms in the HBM, especially to achieve the results with sufficient numerical accuracy. This study is carried out through the evaluation of the peak displacement amplitude of the smart beams by increasing the number of harmonic terms, while, for each step of the increase in the number of harmonic terms, the number of elements in the FE model are increased for both the substrate layers and actuator patches. It is observed that a minimum number of 200 elements (100 element divisions in $x-$direction and 2 element divisions in $z-$direction) for the substrate layers and a minimum number of 16 elements (8 element divisions in $x-$direction and 2 element divisions in $z-$direction) for every actuator patch provide sufficient numerical accuracy in the result for any number of harmonic terms. Besides, for the implementation of HBM, the sufficient numerical accuracy in the results is achieved for the first six harmonic terms ($H = 1,2,..,6.$, Eq. (2.20)) in the case of the parametric excitation and the first six even harmonic terms ($H = 2,4,6, \ldots,12.$, Eq. (2.20)) in the case of the direct excitation. The subsequent numerical results are evaluated following this

convergence study. The local stability of the nonlinear frequency responses is analyzed using Floquet theory as it is described in the previous section where the reduced-order model is derived by choosing a suitable number of proper orthogonal modes (POMs). Usually, a higher proper orthogonal value (POV) indicates greater contribution of the corresponding POM to the response (Rizzi and Przekop, 2008). So, POMs are first arranged according to the corresponding POVs in descending order, and then the first nine POMs ($N_r = 9$) are taken based on a convergence study. However, for the evaluation of dynamic responses in the time domain, the equation of motion (Eq. (2.19) is solved using Bathe time integration method (Bathe, 2006). Here, the time-domain responses are mainly used for the construction of global bifurcation diagrams where the Poincare sections are selected at the intervals of the time-period ($2\pi/\Omega$) of excitation.

Table 2.1
Geometrical properties of the smart beams (Figs. 2.1(a)-(b)).

Substrate beam/face layers of sandwich beam	L = 0.6 m, b = 3 mm, h_f = 2 mm
Piezoelectric actuator patches	h_p = 1 mm, L_p/L_s = 0.8

Table 2.2
Material properties of component materials in the smart beams (Figs. 2.1(a)-(b)).

Material properties	PZT5H (Erturk and Inman, 2011)	Aluminum	Foam (Raja et al., 2002)
Elastic properties	$\bar{C}_{11}$ = 127 GPa, $\bar{C}_{33}$ = 117.84 GPa, $\bar{C}_{12}$ = 80.21 GPa, $\bar{C}_{13}$ = 84.67 GPa, $\bar{C}_{44}$ = 22.99 GPa, $\bar{C}_{66}$ = 23.47 GPa	E = 70 GPa, ν = 0.3	E =35.3 MPa, ν = 0.3822
Electromechanical coefficients	$\bar{e}_{31}$ = -6.6228 C/m^2, $\bar{e}_{33}$ = 23.24 C/m^2, $\bar{e}_{24}$ = 17.03 C/m^2	--	--
Density (ρ)	7500 kg/m^3	2700 kg/m^3	32 kg/m^3

The geometrical properties of the smart beams (Figs. 2.1(a)-(b)) are given in Table 2.1. The substrate beam (Figs. 2.1(a)) and the face layers of the sandwich beam (Figs. 2.1(b)) are considered to be made of Aluminum. The piezoelectric actuators are considered to be made of PZT5H (Erturk and Inman, 2011). The material properties for all component materials in the smart beams are given in Table 2.2. With these material and geometrical properties of the smart beams, their controlled nonlinear frequency responses under the direct excitation (p_t^0 =

0.01 N, Eq. (2.22)) are evaluated for different numbers (n_p) of actuator patch segments over the length of a smart beam. The corresponding variation in the peak transverse displacement-amplitude at the fundamental resonance is illustrated in Table 2.3 for each of the SMA and EMA beams. Here, the increase in the number (n_p) of actuator patch segments over the length of a smart beam yields their reduced length (L_s), while the volume fraction of actuator patch in a typical patch segment is kept with a constant value (L_p/L_s = 0.8). It is achieved by reducing the length (L_p) of actuator patches without alteration of total volume of actuator material in a smart beam. Also, for any number of actuator patch segments, the velocity sensors are located following the boundaries of the patch segments according to the aforesaid control strategy. However, it may be observed from the second column of Table 2.3 that the change in the number of actuator patch segments over the length of the SMA beam does not have much effect on the controlled vibration amplitude. In the third column of Table 2.3, similar results for the EMA beam show that the controlled vibration amplitude decreases slowly with the increasing number of actuator patch segments, and this change appears insignificantly as the number of actuator patch segments is more than 8.

Table 2.3
Transverse displacement amplitudes of SMA/EMA beam at the fundamental resonance under the direct excitation (p_t^o = 0.01 N) for different numbers (n_p) of actuator patch segments (SMA beam: k_{sd} =150 and w at $x = L/2$, $z = h$; EMA beam: k_{ed} =70 and w at $x = L/2$, $z = h-(h_p/2)$).

n_p	SMA beam w/h	EMA beam w/h
4	0.687	0.650
6	0.654	0.520
8	0.638	0.481
10	0.630	0.465

These results imply that the controlled response of a smart beam does not vary significantly when the number (n_p) of actuator patch segments is altered according to the aforesaid strategy. So, the number of patch segments may be increased for reducing the length of piezoelectric actuator patches particularly to avoid possible breakage of these actuator patches during the large amplitude vibration of the smart beams. But it poses the requirement of a large number of velocity sensors leading to the complexity in the feedback control arrangement. In

view of these aspects, a suitable number of actuator patch segments would be considered for attenuation of large amplitude vibration of a smart beam, and it may be decided through experimental study by observing the appearance of breakage of piezoelectric actuator patches for a reduced number of patch segments.

However, in the present theoretical study, the maximum transverse displacement-amplitude of a smart beam is considered around the thickness (h) of the beam, where four actuator patch segments (n_p = 4) are taken and the actuator patches are assumed to operate without their breakage. The control gains (k_{sd}^i, $i=1,2,3,....n_p$; k_{ed}^i, $i=1,2,3,....n_p$) can be assigned with their different values over the actuator patch segments. However, for the sake of simplicity, presently all actuator patches in the SMA or EMA beam are considered to be activated with the uniform control gain ($k_{sd}^i = k_{sd}$; $k_{ed}^i = k_{ed}$). The ends of the smart beams are considered as fully clamped ends while they operate under the transverse harmonic point-load (Eq. (2.22)) or axial harmonic load (Eq. (2.7)).

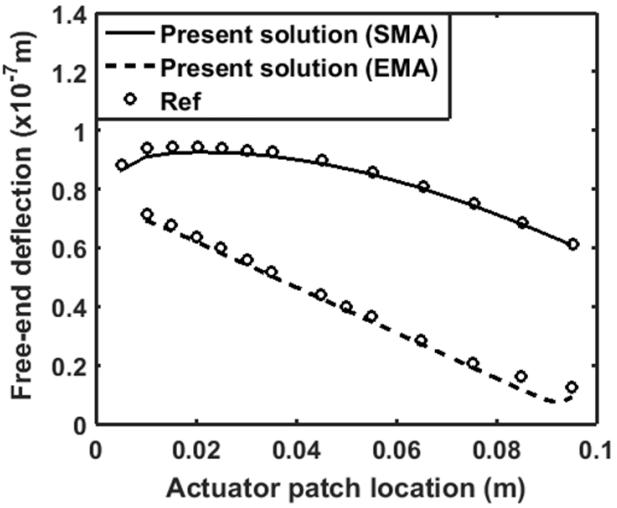

Fig. 2.2. Verification of the present FE formulation in handling the electromechanical coupling in the extensional mode or shear mode piezoelectric actuators (SMA: shear mode actuation; EMA: extensional mode actuation) (Ref. (Sun and Zhang, 1995)).

In order to verify the present FE formulation for handling the electromechanical coupling in the piezoelectric actuator patches, the reference results are taken from Sun and Zhang (1995) for the static analysis of two smart cantilever beams. In the first one, an extensional mode piezoelectric actuator patch is mounted on the surface of the substrate beam while the second one is a sandwich beam with a shear mode piezoelectric actuator patch at the core. For each of these smart cantilever beams, the location of the activated piezoelectric

actuator patch is varied over the length of the beam, and the corresponding change in the transverse deflection at the free end of the beam is computed. These results are illustrated in Fig. 2.2 along with similar reference results (Sun and Zhang, 1995). It may be observed from Fig. 2.2 that the present results are in good agreement with the similar reference results, thus verifying the present FE formulation in handling electromechanical coupling in the extensional mode and shear mode piezoelectric actuators.

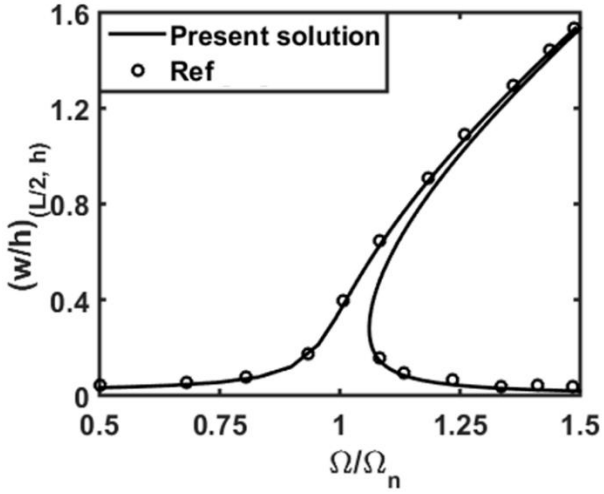

Fig. 2.3. Verification of the present solution for nonlinear frequency response of clamped-clamped beams under the transverse harmonic point-load (Ω_n is the fundamental natural frequency) (Ref. (Ribeiro, 2004)).

2.7.1. *Active control of nonlinear vibration of the smart beams under a direct excitation*

In this section, the control capability of the shear mode actuators is compared to that of the extensional mode actuators when the smart beams undergo large-amplitude vibration under a transverse harmonic point-load (p_t, Eq. (2.22)) at the middle point (x_l, z_l) of the beams ($x_l = L/2$, $z_l = h_L$; $h_L = h$ for the SMA beam and $h_L = h - (h_p/2)$ for the EMA beam). The corresponding nonlinear frequency responses of the smart beams are evaluated by the solution of Eq. (2.21) for the transverse harmonic point-load only. However, Eq. (2.21) is solved using a numerical continuation method (Cheung et al., 1990), and this solution is first verified considering the smart beams with the negligibly thin ($h_p \approx 0$) and deactivated ($k_{sd} = 0, k_{ed} = 0$) actuator patches. The nonlinear frequency response at the middle point of these clamped-clamped beams is evaluated for the aforesaid transverse harmonic point-load. This result is plotted in Fig. 2.3 along with the similar result for an identical clamped-clamped isotropic beam analyzed in

(Ribeiro, 2004). For this verification, the length (L), width (b) and thickness (h) of the beam are considered as 406 mm, 20 mm and 2 mm, respectively. The beam is considered to be made of Aluminum (E = 71.72 GPa, ν = 0.33, ρ =2800 kg/m^3) while the load-amplitude (p_t^o) is taken with a value as 0.134 N. It may be observed from Fig. 2.3 that the present result is in good agreement with the similar reference result (Ribeiro, 2004). This comparison verifies the present derivation of Eq. (2.21) for the transverse harmonic point-load and also the implementation of the numerical continuation method (Cheung et al., 1990).

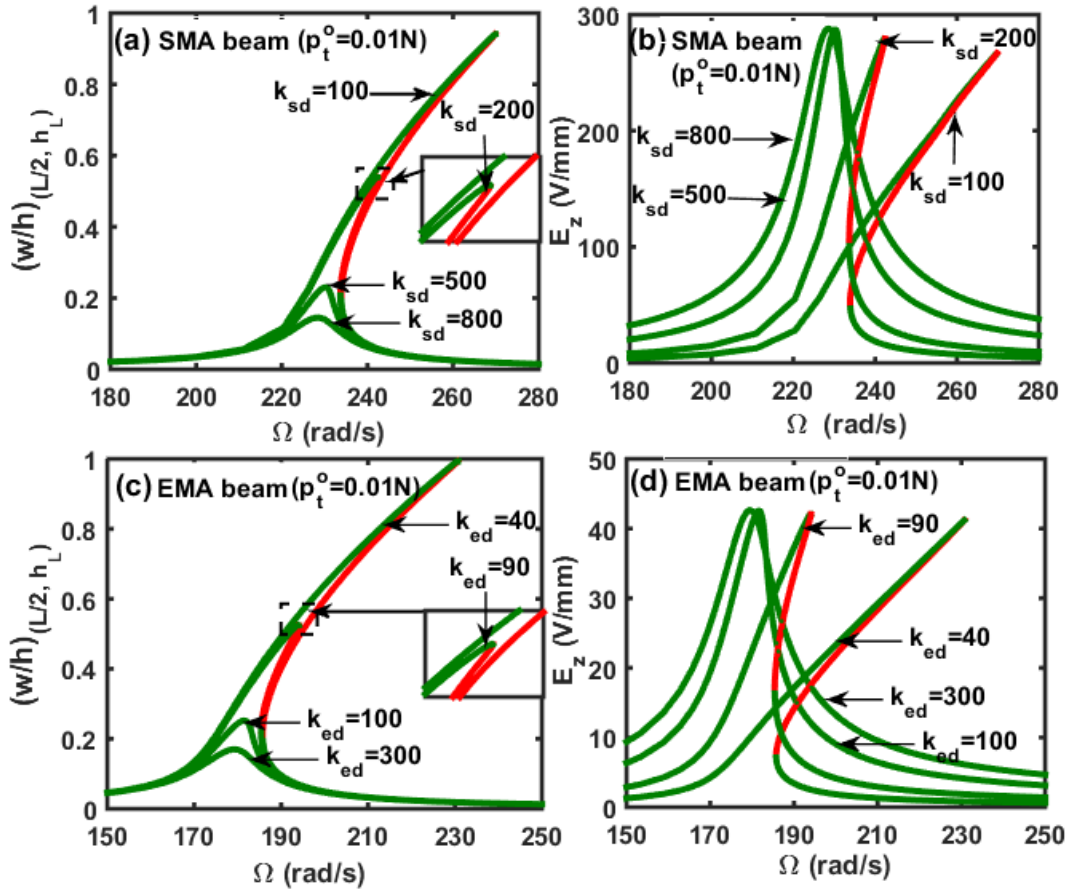

Fig. 2.4. (a), (c) Controlled nonlinear frequency responses of the clamped-clamped SMA/EMA beam; (b),(d) the corresponding variations of the externally applied electric field (E_z).

Figures 2.4(a) and 2.4(c) illustrate the nonlinear frequency responses of the SMA and EMA beams, respectively, for different values of the control gain (k_{sd} / k_{ed}). The corresponding variations of the externally applied electric field (E_z) is also shown in Figs. 2.4(b) and 2.4(d). The green and red points over a response curve indicate stable and unstable responses of the smart beams, respectively. These responses are evaluated within a frequency range around the fundamental

natural frequency while the load-amplitude (p_t^o) is taken with a value as 0.01 N. Also, for every point on a response curve in Figs. 2.4(a) and 2.4(c), the corresponding electric field amplitudes over the actuator patches in a smart beam are computed, and the maximum one is plotted in Figs. 2.4(b) and 2.4(d).

It may be observed from Fig. 2.4(a) that the peak displacement-amplitude of the SMA beam can be attenuated effectively by increasing the control gain (k_{sd}). A similar observation is also obtained for the extensional mode actuators in controlling the large-amplitude vibration of the EMA beam (Fig. 2.4(c)). However, it is important to notice from the results in Figs. 2.4(a)-(d) that, for almost the same value of the peak displacement-amplitude, the corresponding applied electric field for the shear mode actuators is significantly more than that for the extensional mode actuators. This observation implies greater control capability of the extensional mode actuators. The results in Figs. 2.4(a)-(d) also show that the peak displacement-amplitude is attenuated by increasing the control gain (k_{sd} / k_{ed}), but the corresponding applied electric field (E_z) does not change significantly. This advantage can be obtained for any value of the load-amplitude (p_t^o).

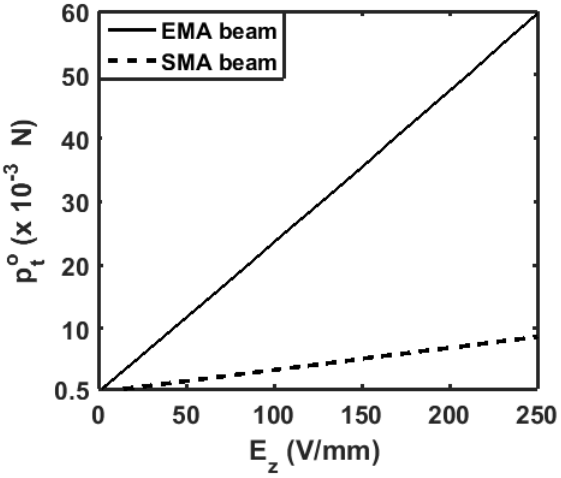

Fig. 2.5. Variation of the applied electric field (E_z) corresponding to the peak displacement-amplitude for different values of the load-amplitude (p_t^o) (k_{sd} = 400 and k_{ed} =400).

However, if the load-amplitude rises for any value of the control gain (k_{sd} / k_{ed}), then the applied electric field (E_z) corresponding to the peak displacement amplitude increases significantly (Fig. 2.5). But, it is known that the functionality of piezoelectric actuators is restricted to a certain permissible value of the applied electric field. So, these results indicate that the application of the shear mode and

extensional mode actuators is mainly limited by the load-amplitude (p_t^o), where extensional mode actuators are capable of working up to a large extent of the load-amplitude in comparison to that for the shear mode actuators (Fig. 2.5).

2.7.2. Active control of the smart beams under parametric excitation

In this section, the nonlinear dynamics and active control of smart beams are investigated when they operate under the harmonically varying axial compressive load (Eq. (2.7)). Here, the smart beams lie either in the pre-buckled or in the post-buckled equilibrium state depending on the value of the static counterpart (p_a^o) of the axial load with reference to the critical buckling load (p_{cr}). However, the critical buckling load does not appear with the same value for both the SMA and EMA beams. So, the pre-buckled and post-buckled equilibrium states of the smart beams are presented in a uniform manner by specifying the static axial compressive load (p_a^o) with reference to the corresponding critical buckling load (p_{cr}) through a static load parameter as $p_r = p_a^o / p_{cr}$. For a value of the static load parameter (p_r) as less than 1, the smart beams would lie in the pre-buckled equilibrium state. Otherwise, the smart beams lie in the post-buckled equilibrium state. However, for any of these equilibrium states, the smart beams may undergo vibration through the parametric resonances or instabilities due to the dynamic counterpart (λp_a^o) of the axial load (Eq. (2.7)). The corresponding dynamics and active control of the smart beams are explored in the following subsections.

2.7.2.1. Dynamics and active control of smart beams in the pre-buckled state

Generally, the parametric instability of a beam element appears in three types, namely primary, secondary and combinatory parametric instabilities. All the three kinds of parametric instabilities may appear in the pre-buckled equilibrium state of the smart beams depending on the range of excitation frequency. However, the principal primary parametric instability is the most critical one that appears at the twice of the natural frequency of a beam ($2\Omega_n$) (Bolotin, 1964). So, the dynamics and control of the smart beams in the pre-buckled equilibrium state are presently analyzed corresponding to the principal primary parametric instability. This kind of parametric instability of a beam element is usually characterized by an instability region in the two-dimensional domain of excitation frequency (Ω) and dynamic load parameter (λ), and it is presently evaluated by solving Eq. (2.21). For obtaining the boundary of this parametric instability region,

the numerical continuation method (Cheung et al., 1990) is employed in solving Eq. (2.21) with the constraint of a very small value of the Euclidian norm (A_0) of the nodal amplitude vector ($\boldsymbol{X}$). It may be noted here that a similar method is addressed in Pierre and Dowell (1985) for evaluation of the parametric instability region.

However, a convergence study is presently carried out for the consideration of a small value of A_0, where the principal primary parametric instability regions for the SMA and EMA beams are evaluated by gradually decreasing the value of A_0. These results are illustrated in Figs. 2.6(a)-(b). From these results, it is clear that a small value of A_0 may be taken as 10^{-6} for the evaluation of the instability region. With this small value of A_0, the present FE solution is verified by taking the reference results from Iwatsubo et al. (1973) for the principal primary parametric instability region of a clamped-clamped isotropic beam. These reference results and the presently computed FE results are illustrated in Fig. 2.6(c). It may be observed from Fig. 2.6(c) that the present FE results are in good agreement with the similar reference results (Iwatsubo et al., 1973), and this comparison verifies the present FE solution for evaluation of the parametric instability region.

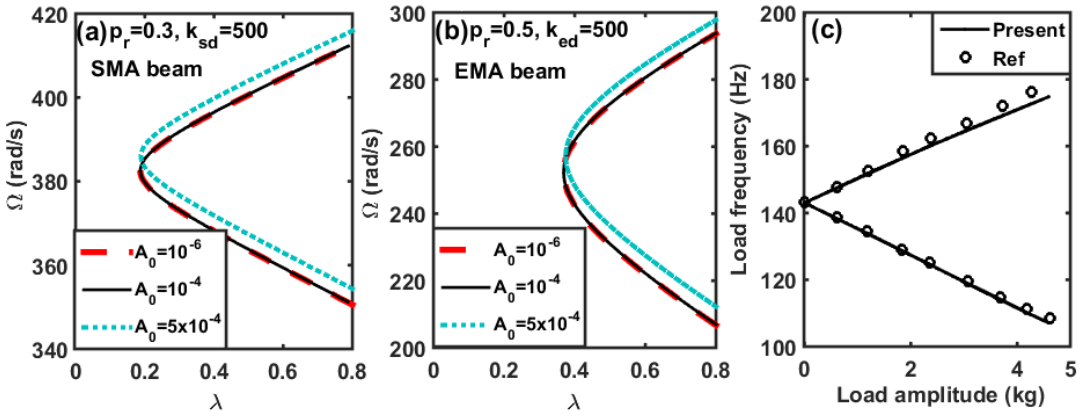

Fig. 2.6. Convergence study for deciding the value of A_0 in the evaluation of the parametric instability regions for the (a) SMA beam and (b) EMA beam; (c) verification of the present FE solution for the evaluation of the parametric instability region (Ref. (Iwatsubo et al., 1973)).

Figures 2.7(a) and 2.7(b) illustrate the principal primary parametric instability regions for the SMA beam where two different values of the static load parameter (p_r = 0.3, 0.7) are taken, and also the value of the control gain (k_{sd}) is varied. Similar responses for the EMA beam are also illustrated in Figs. 2.7(c)-(d).

For any value of the static load parameter (p_r), it may be observed from Figs. 2.7(a)-(d) that the instability region reduces significantly for the increase in the control gain (k_{sd} / k_{ed}). So, both the shear mode and extensional mode actuators are capable of retaining the initial undeformed state of the smart beams by avoiding the oscillation through parametric resonance. However, for a constant value of the control gain (k_{sd} / k_{ed}), the instability region enlarges as the static load parameter (p_r) increases. So, the active control capability of the actuators decreases with the increase in the static load parameter (p_r). It may also be observed from Figs. 2.7(a)-(b) or Figs. 2.7(c)-(d) that the shape of the instability region deviates significantly when the value of the static load parameter (p_r) approaches 1 or the static axial compressive load (p_a^o) approaches the critical buckling load (p_{cr}). This may be due to the influence of higher-order parametric instability regions that appear close to the principal primary parametric instability region when the static load (p_a^o) approaches the critical buckling load (p_{cr}).

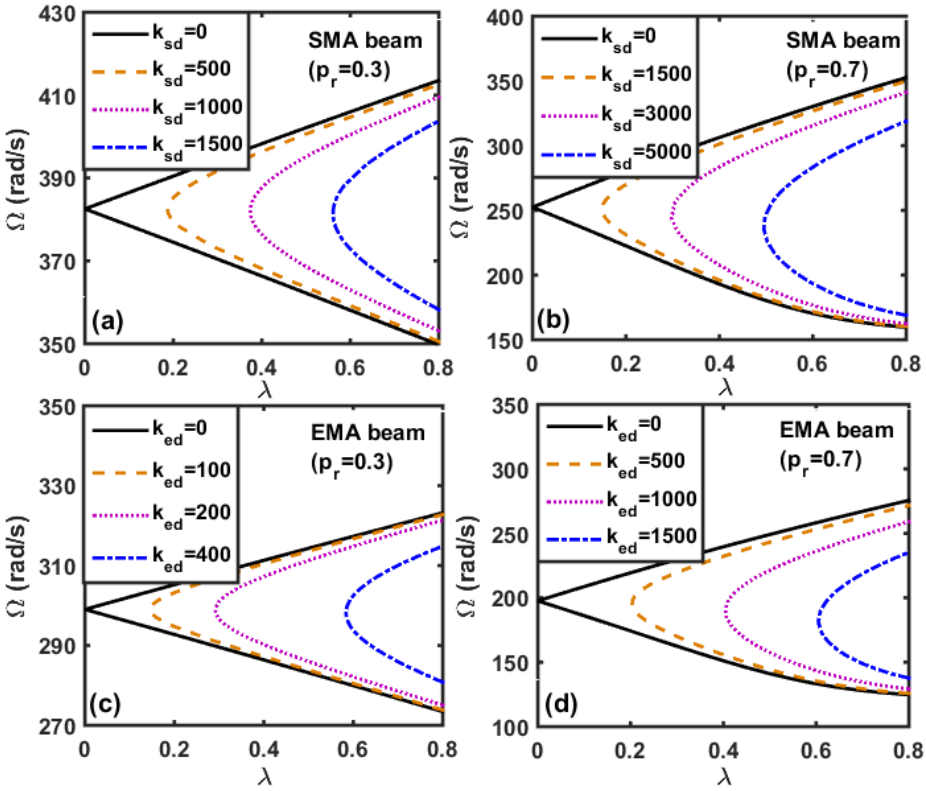

Fig. 2.7. Parametric instability regions for (a) SMA beam with p_r = 0.3, (b) SMA beam with p_r = 0.7, (c) EMA beam with p_r = 0.3, (d) EMA beam with p_r = 0.7.

Usually, a parametric instability region is characterized by its width of instability ($\Delta\Omega$) and the origin of the instability (λ_o). The width of instability ($\Delta\Omega$

) is basically a frequency range over the instability region at a given value of the dynamic load parameter (λ). The origin of instability is a point on the boundary of the instability region where the dynamic load parameter (λ) arises with its minimum value (λ_o). However, from the results in Fig. 2.7, it seems that the width of instability ($\Delta\Omega$) can sufficiently be reduced and the origin of instability (λ_o) can also be shifted beyond a desired value of the dynamic load parameter (λ) by increasing the control gain (k_{sd} / k_{ed}). It is clarified in Figs. 2.8(a)-(b) by plotting the variations of λ_o and $\Delta\Omega$ with the control gain (k_{sd} / k_{ed}) where a value of λ is considered as 0.2 for the measurement of $\Delta\Omega$. It may be observed from Figs. 2.8(a)-(b) that $\Delta\Omega$ significantly decreases and even approaches zero-value as the control gain increases. Concurrently, the origin of instability (λ_o) shifts linearly towards a high value of the dynamic load parameter (λ). However, the results in Figs. 2.8(a) reveal the minimum value of the control gain (k_{sd} / k_{ed}) for shifting the origin of instability (λ_o) to a desired value of λ so that the smart beams can be stabilized within this desired value of λ. For instance, the minimum value of the control gain is 270 or 70 to stabilize the SMA or the EMA beam for any value of the dynamic load parameter (λ) less than 0.1 (points T, T', in Figs 2.8(a)).

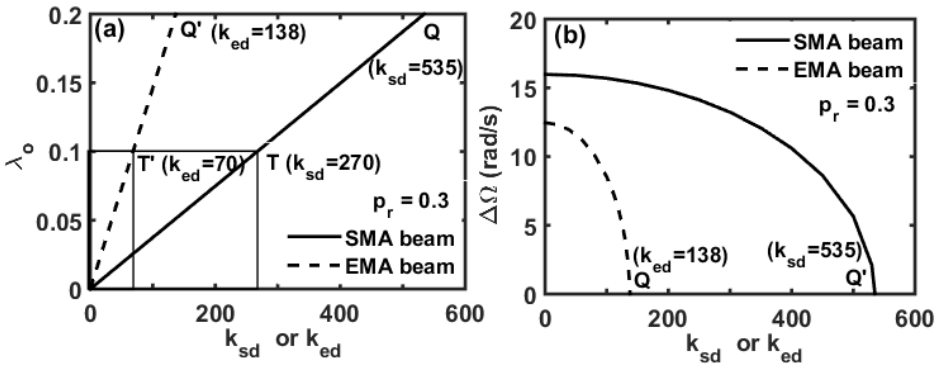

Fig. 2.8. Variations of (a) the origin (λ_o) of instability and (b) the width of instability ($\Delta\Omega$ at $\lambda = 0.2$) with the control gain (k_{sd} / k_{ed}).

According to this observation, the minimum value of the control gain (k_{sd} / k_{ed}) at a given value of λ may be marked as its (k_{sd} / k_{ed}) threshold value for indicating the appearance of the parametric instability of the smart beams beyond that value of λ. If the control gain is assigned a value that is greater than its threshold value, then the parametric instability of the smart beams would not arise. Otherwise, the smart beams may undergo vibration due to the parametric instability as the corresponding nonlinear frequency responses of the smart

beams are illustrated in Figs. 2.9(a) and 2.9(c) for three different values of the control gain (k_{sd} / k_{ed}). In these results, the dynamic load parameter (λ) is taken with a value as 0.2 where the threshold value of the control gain appears as k_{sd} =535 or k_{ed} =138 to stabilize the SMA or the EMA beam (points Q and Q' in Fig. 2.8(a)). However, it may be observed from these results (Figs. 2.9(a) and 2.9(c)) that there is no vibration of the smart beams for the threshold value of the control gain (k_{sd} / k_{ed}). As the control gain decreases from its threshold value, the smart beams vibrate through the parametric resonance, and the corresponding peak amplitude of vibration significantly increases with the decreasing control gain. The corresponding variations in the applied electric field are illustrated in (Figs. 2.9(b) and 2.9(d)) where the maximum value of the applied electric field is computed and plotted in the same manner as described for the results in Fig. 2.4. However, the results in Figs. 2.9(b) and 2.9(d) show that a small decrease in the control gain yields a significant increase in the applied electric field, particularly for the shear mode actuators. It may also be observed that the shear mode actuators need significantly more applied electric field than that for the extensional mode actuators even though the peak amplitude of vibration remains almost the same for both the SMA and EMA beams. Therefore, the extensional mode actuators are more capable of controlling the parametric instability of a smart beam than the shear mode actuators.

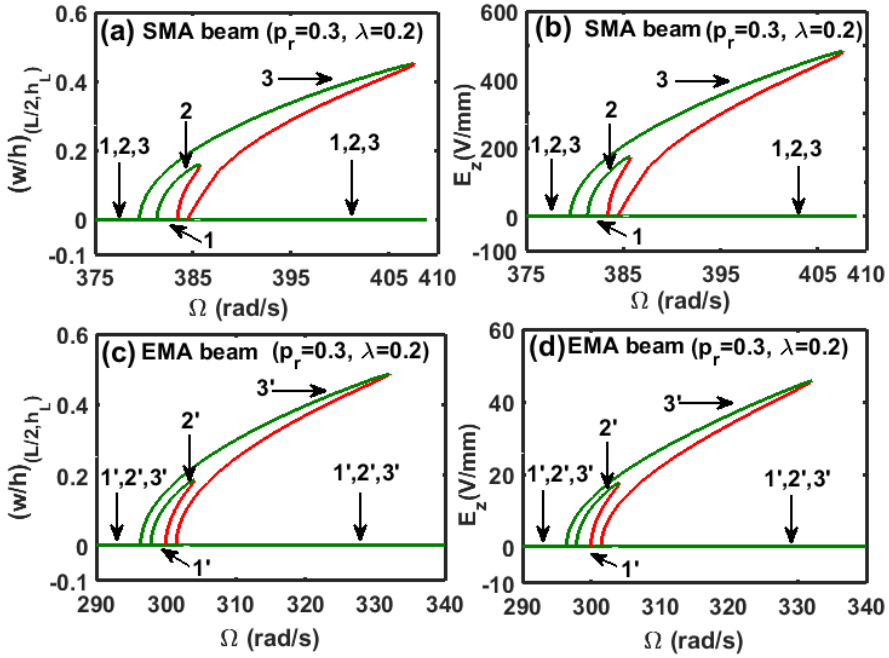

Fig. 2.9. (a), (c) Frequency responses of the SMA and EMA beams under the principal primary parametric resonance; (b), (d) the corresponding variations of the applied electric field (E_z); (1: k_{sd} = 535, 2: k_{sd} = 530, 3: k_{sd} = 500; 1': k_{ed} = 138, 2': k_{ed} = 135, 3': k_{ed} = 125).

In the case where the control gain is lesser than its threshold value at a given value of λ, the parametric instability of the smart beams would appear if the excitation frequency (Ω) lies within the width of instability ($\Delta\Omega$) at that given value of λ. So, for any excitation frequency (Ω) outside of this width of instability ($\Delta\Omega$), the smart beams are supposed to be stable ones. However, it may not always be true because of the hardening nonlinear structural behaviour of the smart beams. In order to corroborate this phenomenon, the SMA beam is taken with the dynamic load parameter (λ) as 0.2. The control gain (k_{sd}) is taken as 500 that is lesser than its threshold value (k_{sd} = 535). The excitation frequency (Ω) is considered as 390 rad/s that lies outside of the width of instability ($\Delta\Omega$ at $\lambda = 0.2$, Figs. 2.9(a) and 2.7(a)). So, the SMA beam is supposed to be stable under these values of the parameters (λ, Ω, k_{sd}). Now, an external disturbance is provided to the SMA beam as an initial transverse displacement in the form of the fundamental bending mode shape of the smart beam, and the corresponding transient responses are evaluated for different values of the maximum transverse displacement (w_{it}) in this mode shape. These transient responses and the corresponding variations of the applied electric field are illustrated in Figs. 2.10(a)-(b). Here, the applied electric field (E_z) is plotted corresponding to an actuator patch where it (E_z) appears with its maximum value. However, similar transient responses for the EMA beam are also shown in Figs. 2.10(c)-(d) where the aforesaid parameters (λ, Ω, k_{ed}) are taken with their values as, λ = 0.2, Ω = 305 rad/s and k_{ed} = 125.

It may be observed from these transient responses (Figs. 2.10(a) and 2.10(c)) that the SMA/EMA beam exhibits unstable response for a high value of the initial transverse deflection or disturbance, and the corresponding amplitude of vibration arises in the same manner as that appears in the frequency responses (Figs. 2.9(a) and 2.9(c)). So, the SMA/EMA beam may undergo parametric instability depending on the disturbance even though these beams are supposed to be stable for the aforesaid specified values of the parameters (λ, Ω, k_{sd} or k_{ed}). This observation implies that the parametric instability of the smart beams is not only confined to the origin of instability (λ_o) and width of instability (Ω) but also dependent on the disturbance that ensues large amplitude vibration of the smart beams. However, for stable responses, it may also be noted from Figs. 2.10(a)-(d) that the shear actuators need a very high electric field to stabilize the SMA beam in comparison to that for the extensional actuators in the EMA beam.

It again shows significantly greater control capability of the extensional mode actuators than that of the shear mode actuators.

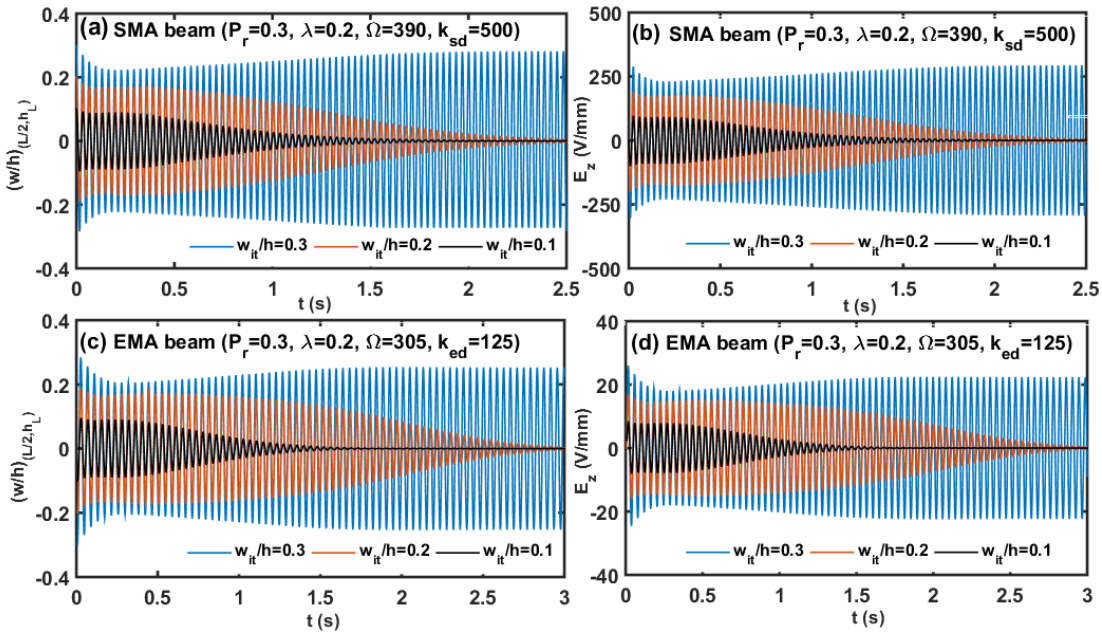

Fig. 2.10. (a), (c) Transient responses of the SMA (Ω=390 rad/s, k_{sd} =500) and EMA beams (Ω=305 rad/s, k_{ed}=125) for different initial transverse displacements (w_{it}); (b), (d) the corresponding variations of the applied electric field (p_r=0.3, λ =0.2).

2.7.2.2. *Nonlinear dynamics and control of smart beams in the post-buckled state*

In this section, the nonlinear dynamics and control of the buckled ($p_r > 1$) smart beams are analyzed mainly by varying the control gain (k_{sd} / k_{ed}). The post-buckled equilibrium state of the smart beams is considered with a value of the static load parameter (p_r) as 1.05 while the dynamic load parameter (λ) is taken with a value as 0.02. Figure 2.11(a) shows the corresponding frequency response of the SMA beam for the control gain (k_{sd}) as 3500. It may be observed from this figure that the stable and unstable dynamic responses of the SMA beam are associated with the three possible static equilibrium states, namely two post-buckled equilibrium states (AB and A'B', Fig. 2.11(a)) and the initial undeformed equilibrium state ($w/h=0$, OM, Fig. 2.11(a)). It may be recalled here that stable and unstable responses are indicated by green and red colour, respectively. However, at a post-buckled equilibrium state, the SMA beam undergoes stable period-1 oscillation mainly through the fundamental resonance, where the oscillation with a fundamental frequency of Ω/m is denoted by period-m oscillation. This periodic oscillation of the SMA beam is depicted here by the

corresponding maximum (1, 1', Fig. 2.11(a)) and minimum (2, 2', Fig. 2.11(a)) deflections of the beam during oscillation, where it is clear that two local periodic attractors or limit cycles appear with reference to the post-buckled equilibrium states. The corresponding variations in the applied electric field (E_z) are demonstrated in Fig. 2.11(b). Here, the applied electric fields over the actuator patches are computed for every solution point on a response curve (Fig. 2.11(a)), and the maximum one is plotted. However, the results in Fig. 2.11(b) indicate the requirement of a high value of the applied electric field to activate the shear mode actuators, particularly at the peak amplitude of vibration. So, the dynamics of the SMA beam at a low value of the control gain (k_{sd} = 500) is also investigated subsequently, where the frequency response and the corresponding variation of the applied electric field are illustrated in Figs. 2.11(c) and 2.11(d), respectively.

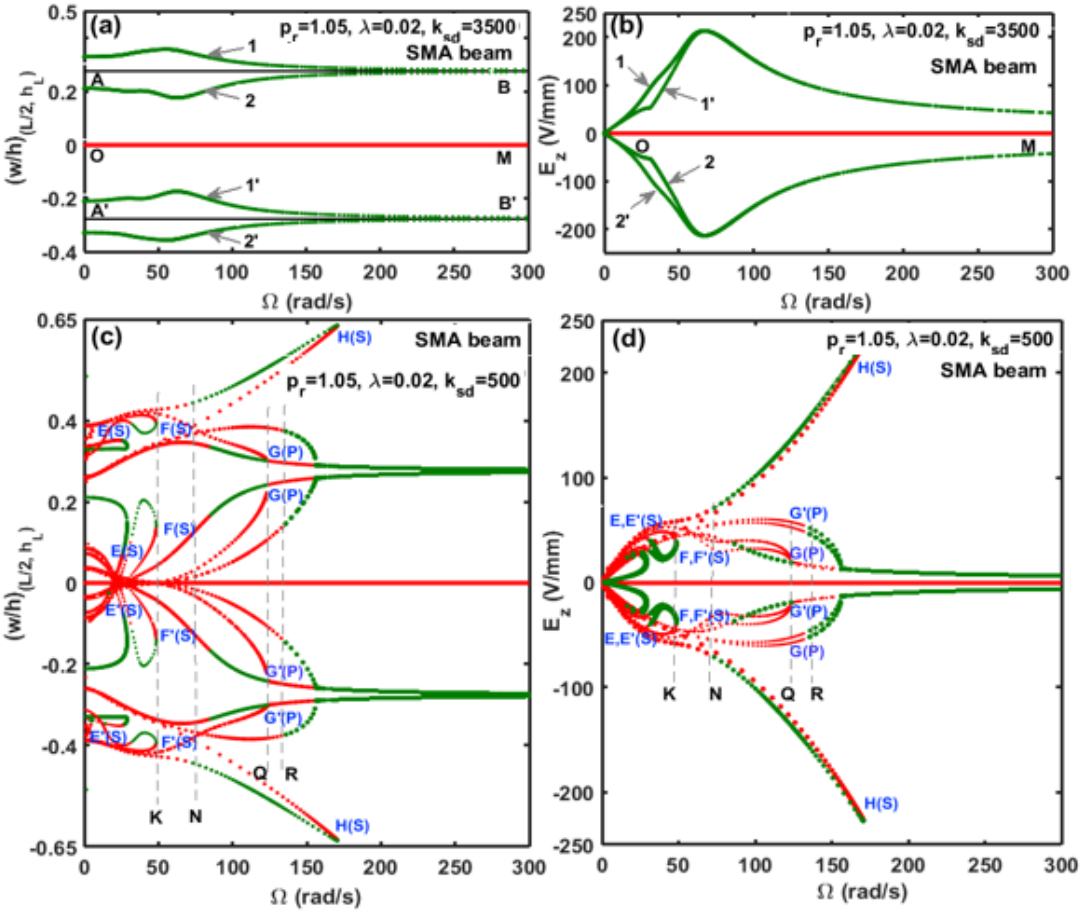

Fig. 2.11. (a), (c) Frequency responses of SMA beam in its post-buckled state (p_r = 1.05, λ = 0.02, (a) k_{sd} = 3500, (c) k_{sd} = 500); (b), (d) the corresponding variations of the applied electric field ((b) k_{sd} = 3500, (d) k_{sd} = 500).

It may be observed from Fig. 2.11(c) in comparison to Fig. 2.11(a) that the SMA beam undergoes complex motion as the control gain (k_{sd}) reduces. This

complex motion of the SMA beam appears through three types of local periodic attractors (E, E' (period-1); F, F' (period-1); G,G' (period-2); Fig. 2.11(c)) corresponding to the post-buckled equilibrium states and a global periodic attractor (H, Fig. 2.11(c)) with reference to the initial undeformed state of the SMA beam. The local attractors mainly involve principal primary parametric (period-2, G, G', Fig. 2.11(c)) and secondary parametric/fundamental (period-1, F, F', Fig. 2.11(c)) resonances at the frequencies $2\Omega_n$ and Ω_n, respectively, where Ω_n is the fundamental natural frequency. One higher-order parametric resonance (superharmonic resonance, period-1 oscillation, E, E', Fig. 2.11(c)) at $\Omega_n/2$ is also observed. However, the global attractor appears with the snap-through motion of the SMA beam, and it continues from the principal primary parametric resonance (period-2) at the pre-buckled state of the SMA beam (Fig. 2.9). It may be noted here that the local fundamental resonance, local higher-order resonance and global snap-through motion appear through saddle-node (S) bifurcation while the

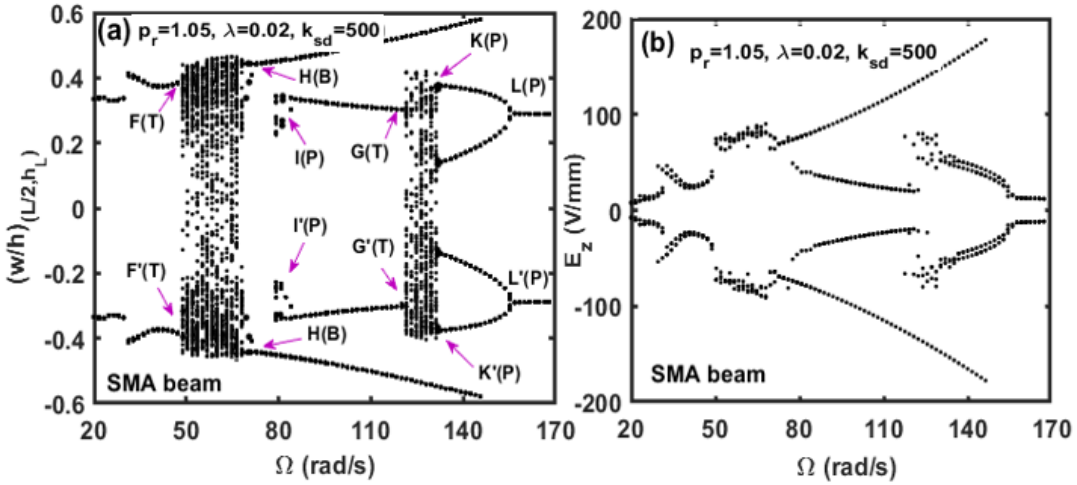

Fig. 2.12. (a) Global bifurcation diagram corresponding to the critical zones (KN, QR) in Fig. 2.11(a); (b) the corresponding variation in the applied electric field (E_z).

local principal primary parametric resonance appears through the period-doubling bifurcation (P) (Fig. 2.11(c)). However, Fig. 2.11(c) shows two critical zones (KN and QR) where there is no stable response of the SMA beam. It may be due to the fact that the solution (Eq. (2.20)) is taken with the limited number of harmonic terms (H = 1,2,3,...6) so that the other kinds of responses like aperiodic, chaotic and higher-order subharmonic responses (period-4, period-8, etc.) may not appear by this solution (Eq. (2.20), H = 1,2,...6). So, the motion of the SMA beam within these critical zones is investigated by evaluating the global bifurcation diagram, as shown in Fig. 2.12(a). In this construction of the global

bifurcation diagram, the Poincare sections are taken at the intervals of the time period of excitation ($2\pi/\Omega$) while the initial transients of the time response are ignored for the first 200 cycles of harmonic excitation, and the subsequent 50 cycles are considered.

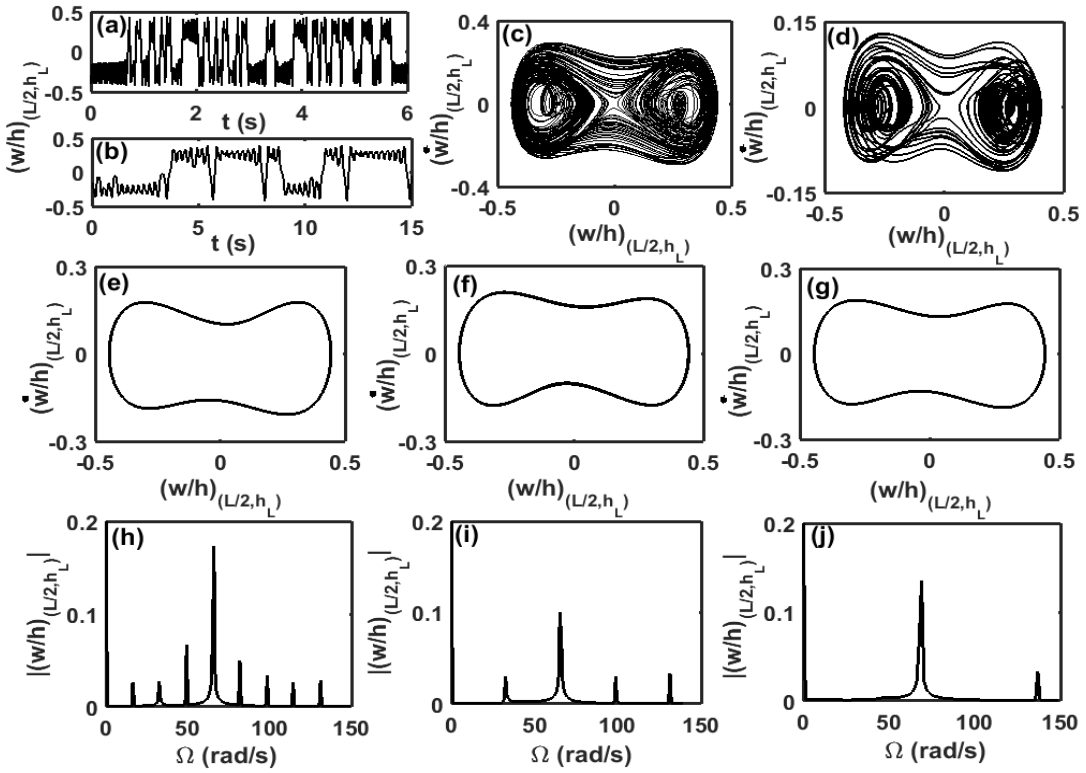

Fig. 2.13. Responses of SMA beam at different excitation frequencies (p_r =1.05, λ=0.02, k_{sd} =500); transient responses at (a) Ω = 49 rad/s, (b) Ω = 121.9 rad/s; phase plots at (c) Ω = 49 rad/s, (d) Ω = 121.9 rad/s, (e) Ω = 71.2 rad/s, (f) Ω = 71.2 rad/s, (g) Ω = 72.8 rad/s; frequency spectrums at (h) Ω = 131.18 rad/s, (i) Ω = 131.5 rad/s, (j) Ω = 136.8 rad/s.

It may be observed from Fig. 2.12(a) that the local period-1 response of the SMA beam appears at the low-frequency region till Ω = 49 rad/s (Point F/F'), where chaotic motion (KN) evolves through the intermittent transition bifurcation (T). This bifurcation can be seen clearly through the transient response in Fig. 2.13(a) and phase plot in Fig. 2.13(c) at a frequency Ω = 49 rad/s. This phenomenon occurs due to the disappearance of the stable solution after the cyclic-fold bifurcation at Ω = 49 rad/s (Point F/F', Fig. 2.11(c)). With the increase in the frequency, the inverse symmetry breaking bifurcation (B) occurs around a frequency Ω = 71 rad/s (point G/G', Figs. 2.11(c) and 2.12(a)), and the chaotic motion (KN, Fig. 2.11(c)) gradually reduces to snap-through motion (period-2). This bifurcation phenomenon can be observed through the phase plots in Fig.

2.13(e)-(g). However, besides the snap-through motion (period-2), the local period-1 attractor also evolves at a frequency Ω = 85.6 rad/s (Point I/I', Fig. 2.12(a)) through the period-demultiplying bifurcation (P). For further increase in the frequency, the chaotic attractor (QR, Fig. 2.11(c)) arises from the local period-1 attractor at a frequency Ω = 121.9 rad/s (point G/G', Figs. 2.11(c) and 2.12(a)) through the intermittent transition bifurcation (T). This bifurcation can be seen clearly by the transient response and phase plot in Figs. 2.13(b) and 2.13(d), respectively. However, with the increase in the frequency, period-demultiplying bifurcation (P) appears at a frequency Ω = 131.2 rad/s (point K/K', Fig. 2.12(a)), and the chaotic attractor (QR, Fig. 2.11(c)) reduces to the local period-2 attractor where the corresponding frequency spectrums (Figs. 2.13(h)-(j)) reveal period-8, period-4 and period-2 responses at Ω = 131.18 rad/s, Ω = 131.5 rad/s, Ω = 136.8 rad/s, respectively.

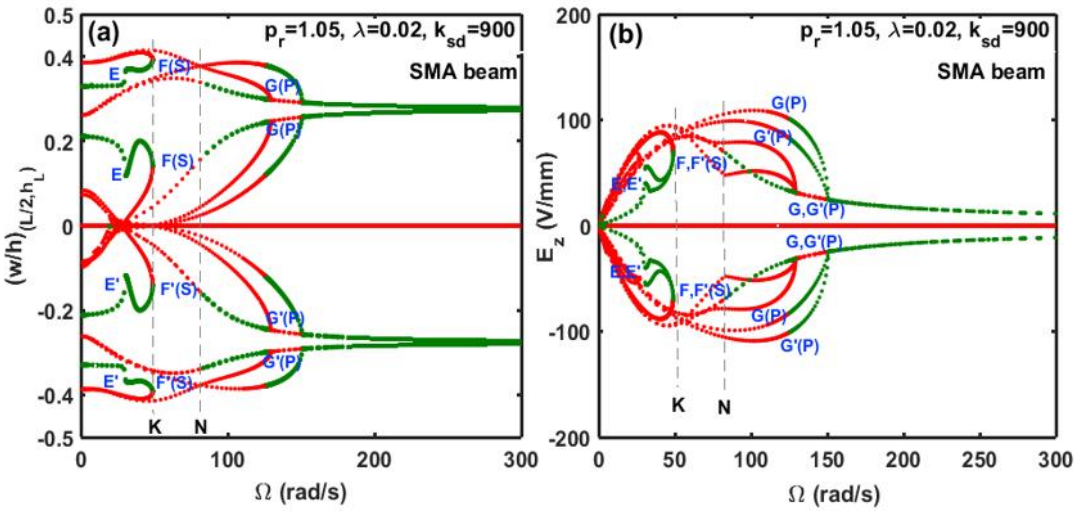

Fig. 2.14. (a) Frequency response of SMA beam in its post-buckled state (p_r = 1.05, λ = 0.02, k_{sd} =900) and (b) the corresponding variations of the applied electric field (E_z).

For this complex motion of the SMA beam, the corresponding variation in the applied electric field (E_z) is illustrated in Fig. 2.12(b). Here, for every attractor, the electric fields supplied to the actuators are computed over the aforesaid 50 cycles of oscillation at every excitation frequency, and the corresponding maximum and minimum values of the supplied electric field are plotted. It may be observed from Fig. 2.12(b) that the chaotic motion of the SMA beam does not cause the requirement of a high value of the applied electric field. However, from the previous results (Figs. 2.11 and 2.12), it may be noted here that a high value of the control gain is to be assigned for reducing the complex motion of the SMA

beam. But, the corresponding applied electric field may exceed its permissible value for the shear mode piezoelectric actuators (Fig. 2.11(b)). So, the control gain is to be reduced, and it yields complex motion of the SMA beam (Fig. 2.11(c)), where a high electric field may again appear due to the global snap-through periodic motion (H, Fig. 2.11(d)) of the SMA beam. In this issue, an adjustment in the value of the control gain may be needed for the disappearance of the global snap-through periodic motion (H, Fig. 2.11(d)) within a reasonable value of the applied electric field, as a similar dynamic response of the SMA beam is shown in Figs. 2.14(a)-(b). But, the corresponding complexity in the dynamic responses may not reduce. Therefore, the shear mode piezoelectric actuator may not be capable of reducing the complex motion of smart beams.

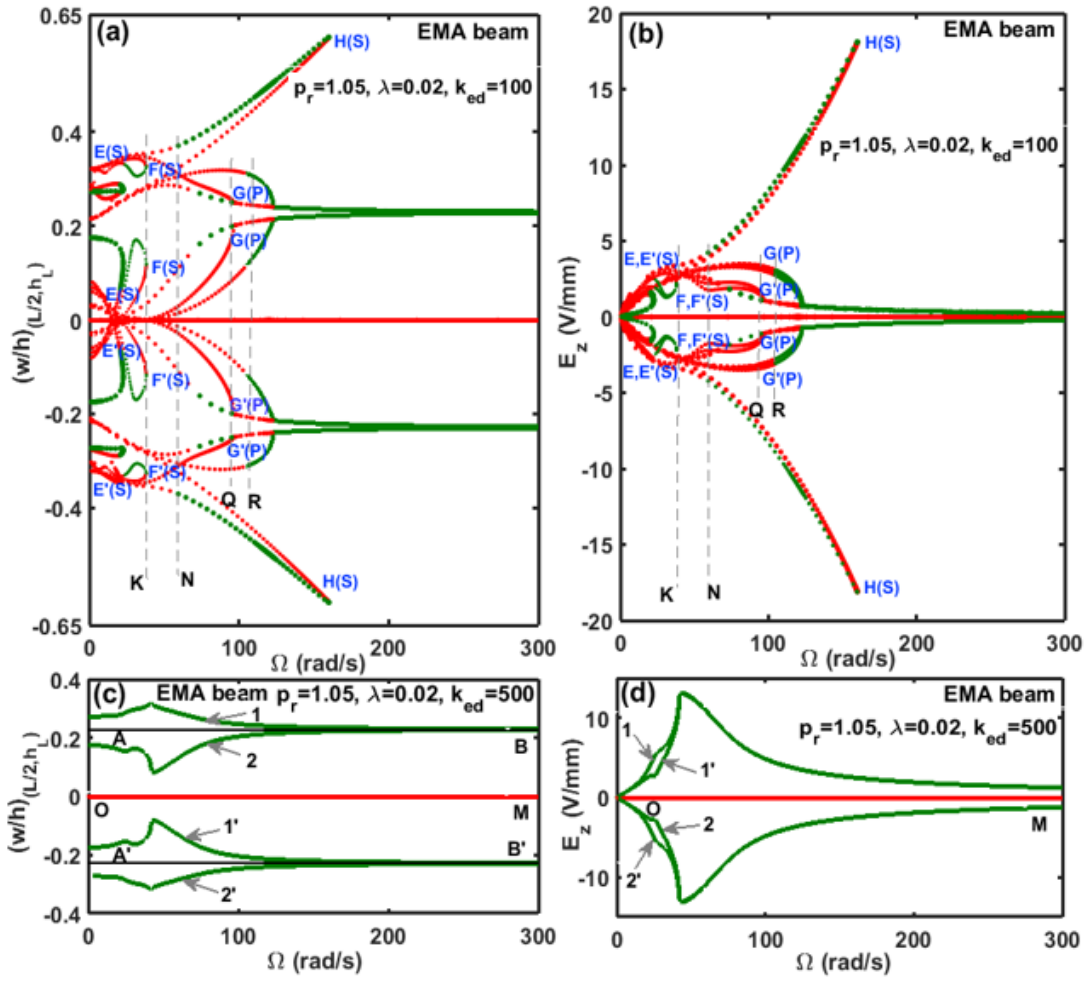

Fig. 2.15. (a), (c) Frequency responses of the EMA beam in its post-buckled state (p_r = 1.05, λ = 0.02, (a) k_{ed} = 100, (c) k_{ed} = 500); (b), (d) the corresponding variations of the applied electric field ((b) k_{ed} = 100, (d) k_{ed} = 500).

Figures 2.15(a)-(d) illustrate the frequency responses of the buckled EMA beam for two different values of the control gain (k_{ed}). In these responses, the

motion of the EMA beam within the critical zones (KN and QR, Fig. 2.15(a)) is explained through the bifurcation diagram in Fig. 2.16. However, it is important to observe from the results in Figs. 2.11, 2.12, 2.15 and 2.16 that the frequency responses of EMA beam are almost similar to that for the SMA beam. But, the maximum value of the required electric field is significantly higher for the shear mode actuators than that for the extensional mode actuators. Also, the complex motion of a smart beam can be reduced by applying a low electric field when the extensional mode actuators are used instead of the shear mode actuators. This requirement of the low electric field for extensional mode actuators provides the scope for further increase in the control gain (k_{ed}) towards the low amplitude of vibration besides the reduction of complex motion, as it is clear from Fig. 2.17.

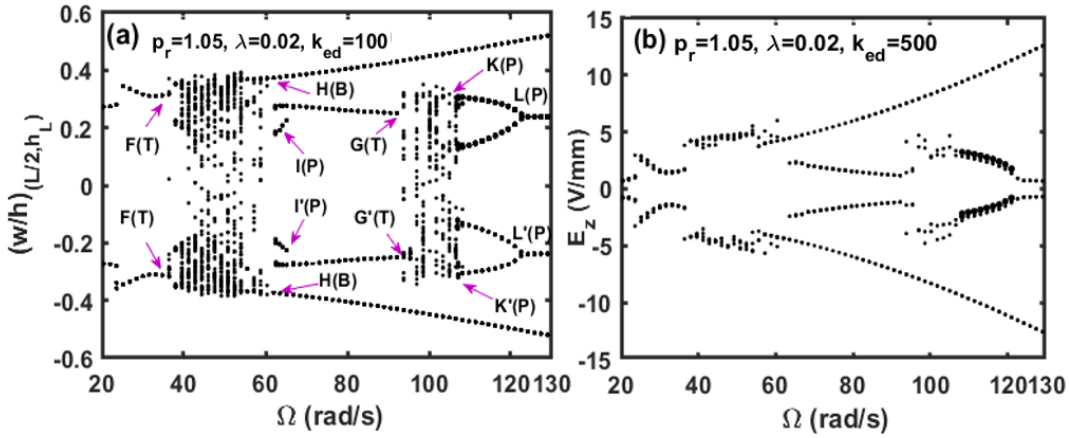

Fig. 2.16. (a) Global bifurcation diagram corresponding to the critical zones (KN, QR) in Fig. 2.15(a); (b) the corresponding variation of the applied electric field (E_z).

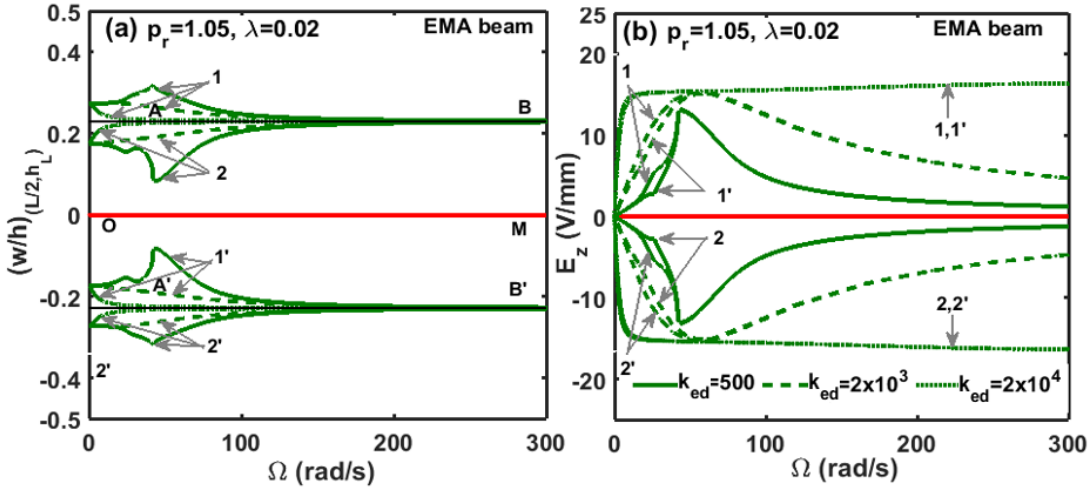

Fig. 2.17. (a) Frequency responses of the EMA beam at its post-buckled state (p_r = 1.05, λ = 0.02) for different values of the control gain (k_{ed}), (b) the corresponding variations of the applied electric field (E_z).

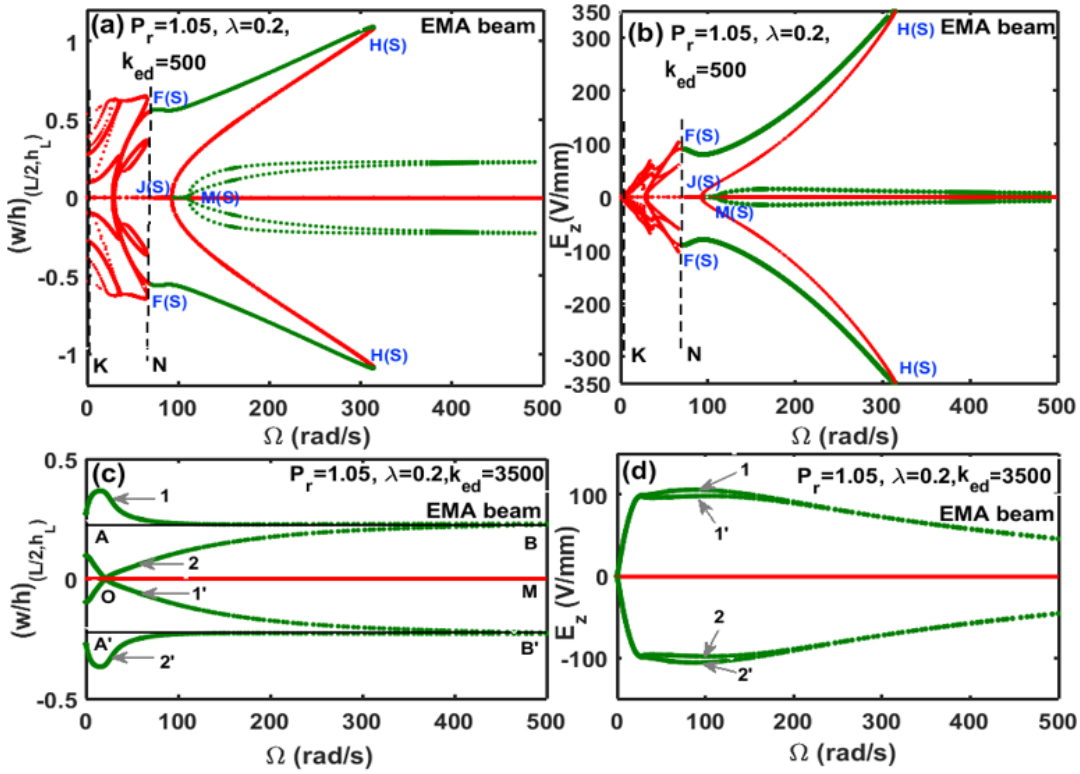

Fig. 2.18. (a), (c) Frequency responses of the EMA beam in its post-buckled state (p_r = 1.05, λ = 0.2, (a) k_{ed} = 500, (c) k_{ed} = 3500); (b), (d) the corresponding variations of the applied electric field ((b) k_{ed} = 500, (d) k_{ed} = 3500).

Although these observations imply the suitability of the extensional mode actuators in control of smart beams, it is further verified by increasing the static (p_r) and dynamic (λ) load parameters. Figure 2.18 illustrates the nonlinear frequency responses of the EMA beam for two different values of the control gain (k_{ed}) when the dynamic load parameter (λ) is increased to a value of 0.2. Figure 2.19 also illustrates similar frequency responses of the EMA beam when the static load parameter (p_r) is increased to a value of 1.1. However, it may be observed from these responses (Figs. 2.18(a) and 2.19(a)) in comparison to the earlier one (Fig. 2.15(a)) that the dynamics of the EMA beam changes to some extent due to the increase in the static and/or dynamic load parameters, particularly in the appearance of the local periodic attractors. For a high value of λ with a low value of p_r (Fig. 2.18(a)), the local periodic attractors are in the development stage leading to period-1 attractors (M, Fig. 2.18(a)) only at higher excitation frequencies. These local period-1 attractors evolve through a stable undeformed state of the EMA beam within a small frequency zone (JM, Fig. 2.18(a)). Now, as the static load parameter increases from p_r=1.05 (Figs. 2.18(a)) to p_r=1.1 (Figs. 2.19(a)), local period-2 attractors also appear through a small critical zone (QR,

Fig. 2.19(a)) where the chaotic oscillations arise similar to the critical zone QR in Fig. 2.15(a). Thus, at a high value of the dynamic load parameter (λ), the local periodic attractors gradually appear with the increase in the static load parameter (p_r). Further, a chaotic attractor is also observed to appear at lower frequencies (KN in Figs. 2.18(a) and 2.19(a)) where the global dynamics of the EMA beam arises. However, from the results in Figs. 2.18 and 2.19, it is clear that the complex motion and the corresponding amplitude of vibration of the EMA beam reduce significantly as the control gain (k_{ed}) increases while the applied electric field (E_z) appears within the reasonable range. Therefore, the extensional mode actuators can also be used for higher values of the static and dynamic load parameters.

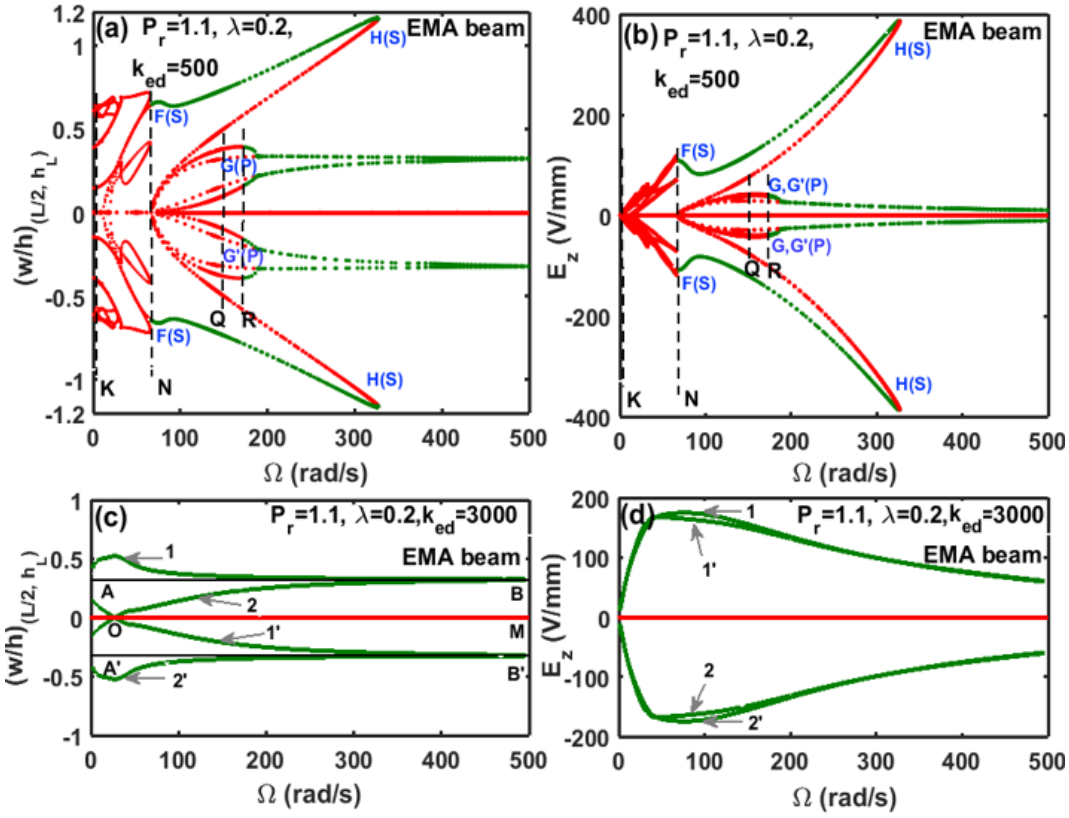

Fig. 2.19. (a), (c) Frequency responses of the EMA beam in its post-buckled state (p_r = 1.1, λ = 0.2, (a) k_{ed} = 500, (b) k_{ed} = 3000); (b), (d) the corresponding variations of the applied electric field ((b) k_{ed} = 500, (d) k_{ed} = 3000).

2.8. Summary

In this chapter, the nonlinear dynamics and active control of smart beams are investigated using the shear mode and extensional mode piezoelectric actuators. The numerical analysis is performed considering two smart beams for separate

use of the two kinds of piezoelectric actuators. These smart beams are considered to operate under the transverse or axial compressive harmonic load while the actuators are activated by supplying the external electric field according to the velocity feedback control law. The dynamics of the smart beams is analysed numerically by deriving the geometrically nonlinear electro-elastic incremental equations of motion in the finite element (FE) framework. The FE equations of motion are solved using Bathe time integration method for evaluation of the transient responses while the frequency responses are evaluated by implementing the harmonic balance method in conjunction with a numerical continuation technique.

The results for the direct excitation of smart beam under transverse harmonic load reveal that the resonant displacement amplitude can be reduced to the desired range by increasing the control gain with a negligibly small change in the externally applied electric field. However, the externally applied electric field significantly increases with the increasing load-amplitude where the applied electric field may appear beyond its permissible value for the piezoelectric actuators. In this concern, the extensional mode actuators are capable of working up to a large extent of the load-amplitude in comparison to that for the shear mode actuators. However, the results for parametric excitation of the smart beams reveal the following observations.

(a) In the pre-buckled state, the parametric instability region can be reduced significantly by increasing the control gain, and this control gain has a minimum value to stabilize the smart beams for a specified axial compressive harmonic load. Beyond this limiting value of the control gain, both the shear mode and extensional mode actuators work well to stabilize the smart beams. But, within the limiting value of the control gain, the shear mode actuator may not be a suitable one as it needs a very high electric field to attenuate the corresponding oscillation (period-2) of the smart beams.

(b) It is observed that the parametric instability of the smart beams is not only confined to the corresponding instability region but also dependent on the external disturbance that ensues transverse deflection of the beams. However, once the dynamic instability arises for any of the reasons, the attenuation of the corresponding oscillation of the smart beams becomes a difficult task to the shear mode actuator as it needs significantly more applied electric field than that for the extensional mode actuator.

(c) With the increase in the control gain at the post-buckled state of the smart beams, first, the global snap-through motion diminishes, and then the chaotic motion reduces to simple period-1 response corresponding to the

buckled equilibrium states. But the corresponding requirement of the external electric field for the shear mode actuator is significantly more than that for the extensional mode actuator. This difference further increases with the increase in the load parameters. So, the shear mode actuator may be utilized for low values of the load parameters while the extensional mode actuator performs well in the reduction of complex motion and also in attenuation of the large amplitude vibration of the smart beams.

Chapter 3

A generalized finite element formulation for nonlinear frequency response analysis of slender viscoelastic beams using harmonic balance method

3.1. Introduction

In the previous chapter, the active control of dynamic instability of a parametrically excited slender beam is investigated using shear mode and extensional mode piezoelectric actuators. Although this study shows a good control capability of the extensional mode piezoelectric actuator in attenuation of complex dynamics of the beam at its pre-buckled or post-buckled state, this kind of actuator cannot be used fruitfully for structural vibration control at a high frequency (Azvine et al., 1995). Moreover, the associated active control system appears with a complex configuration involving sensors, actuators, controllers and external power supply units. So, in the quest for a simpler damping arrangement for controlling parametric instability of beam-like slender structures, the application of CLD treatment has been addressed in a good number of available studies, as presented in Section 1.3.1.

The CLD treatment provides passive damping through a constrained viscoelastic damping layer where the damping layer is constrained between the host structure surface and a stiff constraining layer. Here, the passive damping arises mainly by means of the transverse shear deformation of the constrained viscoelastic layer. So, this damping arrangement appears with a simple configuration, unlike the aforesaid active control system. The available studies (Section 1.3.1) show good damping effectiveness of this CLD treatment for controlling the dynamic instability of slender beams operating under the parametric excitation at the pre-buckled state. However, in practice, the same excitation may also cause various dynamic instabilities and the associated complex motion of the beams once they undergo static instability or buckling. The damping effectiveness of the CLD treatment in attenuation of such complex dynamics of slender beams in the post-buckled state is not yet addressed in the literature to the best knowledge of this researcher. Therefore, an objective of this dissertation is to investigate the effectiveness of the CLD treatment in passive

control of nonlinear dynamics of a parametrically excited beam, especially when it undergoes buckling or static instability.

For this theoretical investigation, one needs to derive mathematical models of the CLD treated beams, where the FE procedure and HBM are presently preferred because of their robustness in the analysis of nonlinear structural dynamics (Section 1.4). Besides, for estimation of accurate damping in the CLD treatment, the viscoelastic material is to be modelled using the advanced viscoelastic constitutive relations like Generalized Maxwell model, Zener model, fractional Zener model, Heredity integral approach, etc. (Hasan et al., 2021; Amabili et al., 2019; Baz, 2019; Galucio et al., 2004; Litewka and Lewandowski, 2017a; McTavish and Hughes, 1992; Zhou et al., 2016). However, these constitutive relations involve temporal derivative/integral of stress/strain. It poses complexity in the derivation of the geometrically nonlinear FE model of viscoelastic structures in conjunction with HBM. In this concern, some studies are available in the open literature (Bilasse et al., 2010; Jacques et al., 2010; Lewandowski and Wielentejczyk, 2017; Litewka and Lewandowski, 2017a, 2017b; Wielentejczyk and Lewandowski, 2019, 2017). Although these available HBM-based FE models can be used for geometrically nonlinear frequency response analysis of viscoelastic structures, the shortcomings are observed as (a) separate FE formulation for each of the viscoelastic constitutive relations and (b) consideration of one or two harmonic terms in the implementation of HBM.

The first shortcoming arises due to the change in the mathematical form from one to another viscoelastic constitutive model. However, it may be tackled by expressing the various viscoelastic constitutive relations in a generalized form for the time-periodic stress/strain. This generalized form of constitutive relation would facilitate a common HBM-based FE formulation for all types of viscoelastic constitutive models.

The second shortcoming appears mainly due to the complexity in handling a long expression of the HBM-based expanded form of the nonlinear stiffness matrix in the FE model. Despite this complexity, one needs to consider a sufficient number of harmonic terms in the implementation of HBM for accurate modelling of nonlinear dynamic characteristics of a viscoelastic structure in the frequency domain. So, the FE formulation would be based on an arbitrary number of harmonic terms in HBM. However, the corresponding formulation may be simplified somewhat by the factorization of the nonlinear strain-displacement matrix in terms of a linear strain-displacement matrix and a nodal displacement matrix/vector. Here, the nodal displacement matrix/vector appears in multiple of the linear strain-displacement matrix so that it would ease the incorporation of

Fourier expansion of nodal displacements towards the derivation of a long and complex expression of the HBM based expanded form of the nonlinear stiffness matrix.

However, the expanded form of the nonlinear stiffness matrix appears with a large number of stiffness terms due to the consideration of an arbitrary number of harmonic terms in HBM. Here, every stiffness term is to be reduced over a time-period according to HBM, where a numerical time-integration method is commonly employed. So, another shortcoming of a high computational time arises due to this time-integration. In this aspect, the analytical method for the time-integration of stiffness terms can be used as addressed in Lewandowski (1997, 1992); however, this analytical approach for time-integration may be a cumbersome one especially for handling a robust FE formulation using a good number of harmonic terms in HBM. Alternatively, in some other studies (Dimitriadis, 2008; LaBryer and Attar, 2010), fast Fourier transform or discrete Fourier transform is utilized where the computational time decreases as compared to that for a conventional numerical time-integration approach. But it requires the evaluation of stiffness terms at a good number of sampling points within the time-period for the computation of Fourier coefficient matrices of the nonlinear stiffness matrix. However, the time-integration of stiffness terms may also be carried out by exploiting the orthogonality of Fourier basis functions. Although this analytical approach is not yet addressed in the literature for the implementation of HBM, it may provide the advantage of simplicity in the time-integration of stiffness terms as well as the reduced computational time.

On the basis of these three newly proposed formulation strategies, an FE formulation in conjunction with HBM is presented in this chapter for the nonlinear frequency response analysis of viscoelastic structures. This formulation is utilized in the subsequent chapters to investigate the damping effectiveness of the CLD treatment for attenuation of the complex dynamics of parametrically excited beams. However, the present HBM-based FE formulation may be called a generalized one since it is not limited to a particular type of viscoelastic constitutive relation. Also, it can be used for an arbitrary number of harmonic terms in HBM.

In the following sections, an FE formulation of a viscoelastic sandwich beam using HBM is presented where all the aforesaid objectives are attained towards a new FE formulation of viscoelastic structures for their nonlinear dynamic analysis in the frequency domain. In Section 3.2, the basic approach of formulating the governing equation of motion is demonstrated. The subsequent formulation is carried out based on the aforesaid objectives, where Section 3.2.1

presents the mathematical formulation for the reduction of various time-domain viscoelastic constitutive models in a generalized form using HBM. Section 3.2.2 illustrates the analytical time-integration by exploiting the orthogonality of Fourier basis functions. Section 3.2.3 presents a special formulation of the nonlinear strain vector in the FE framework to ease the derivation of the nonlinear stiffness matrix and the nonlinear FE equation of motion using HBM with an arbitrary number of harmonic terms. In the next section, i.e. Section 3.4, an FE model of the same viscoelastic sandwich beam is derived in the time-domain based on the fractional Zener constitutive model. This FE model in the time domain is utilized to verify the present FE formulation for viscoelastic structures using HBM, as the corresponding numerical results are presented in Section 3.5.

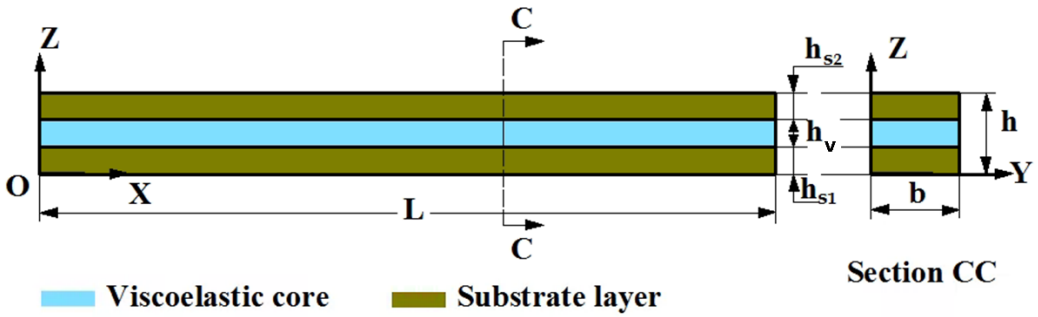

Fig. 3.1. Schematic diagram of a sandwich beam with the viscoelastic core.

3.2. Mathematical modelling of a viscoelastic sandwich beam

Figure 3.1 shows a sandwich beam with the elastic face layers and viscoelastic core. The sandwich beam is represented in a reference Cartesian coordinate system (xyz), where the length, width and thickness of the sandwich beam are denoted by L, b and h, respectively. Within the total thickness (h) of the sandwich beam, the thicknesses of the bottom face layer, top face layer and core layer are denoted by h_{s1}, h_{s2} and h_v, respectively. The material properties of any layer do not vary along the y-direction. Also, there is no externally applied mechanical force on the boundary surfaces parallel to the xz-plane. The ends of the sandwich beam are considered as fully clamped ends, and the beam operates under the transverse mechanical load. Further, there is no body force in any axial direction within the reference coordinate system. So, the sandwich beam is expected to undergo bending deformation in the xz-plane under the plane stress condition. Accordingly, the state of stress and the state of strain at any point in the xz-plane of the sandwich beam can be written, as given in Eq. (2.1).

$$\boldsymbol{\varepsilon} = \{\varepsilon_x \quad \varepsilon_z \quad \gamma_{xz}\}^{\mathrm{T}}, \quad \boldsymbol{\sigma} = \{\sigma_x \quad \sigma_z \quad \tau_{xz}\}^{\mathrm{T}} \tag{2.1}$$

The Green-Lagrange strain-displacement relations at any point in the xz-plane can be written as

$$\boldsymbol{\varepsilon} = (\boldsymbol{\varepsilon}_l + \boldsymbol{\varepsilon}_n)\,,$$

$$\boldsymbol{\varepsilon}_l = \left\{ \frac{\partial u}{\partial x} \quad \frac{\partial w}{\partial z} \quad \frac{\partial w}{\partial x} + \frac{\partial u}{\partial z} \right\}^{\mathrm{T}},$$

$$\boldsymbol{\varepsilon}_n = \left\{ \frac{1}{2}\left(\frac{\partial w}{\partial x}\right)^2 + \frac{1}{2}\left(\frac{\partial u}{\partial x}\right)^2 \quad \frac{1}{2}\left(\frac{\partial w}{\partial z}\right)^2 + \frac{1}{2}\left(\frac{\partial u}{\partial z}\right)^2 \quad \frac{\partial w}{\partial x}\frac{\partial w}{\partial z} + \frac{\partial u}{\partial x}\frac{\partial u}{\partial z} \right\}^{\mathrm{T}} \tag{3.1}$$

where, u and w are the displacements at any point in the xz-plane along the x and z-directions, respectively. The linear ($\boldsymbol{\varepsilon}_l$) and nonlinear ($\boldsymbol{\varepsilon}_n$) strain vectors can also be represented in terms of the displacement vector ($\boldsymbol{d}_s$) as follows

$$\boldsymbol{\varepsilon}_l = \boldsymbol{L}\,\boldsymbol{d}_s\,,\ \boldsymbol{\varepsilon}_n = (1/2)\,\boldsymbol{L}_n(\boldsymbol{d}_s)\,\boldsymbol{d}_s\,,\ \ \boldsymbol{d}_s = \{u \quad w\}^{\mathrm{T}}$$

$$\boldsymbol{L} = \left[(\boldsymbol{L}_x^u)^{\mathrm{T}} \ (\boldsymbol{L}_z^w)^{\mathrm{T}} \ \ (\boldsymbol{L}_x^w + \boldsymbol{L}_z^u)^{\mathrm{T}} \right]^{\mathrm{T}},$$

$$\boldsymbol{L}_n(\boldsymbol{d}_s) = (\boldsymbol{L}_1^u \boldsymbol{d}_s)\,\boldsymbol{L}_x^u + (\boldsymbol{L}_2^u \boldsymbol{d}_s)\,\boldsymbol{L}_z^u + (\boldsymbol{L}_1^w \boldsymbol{d}_s)\,\boldsymbol{L}_x^w + (\boldsymbol{L}_2^w \boldsymbol{d}_s)\,\boldsymbol{L}_z^w\,,$$

$$\boldsymbol{L}_1^u = \left[(\boldsymbol{L}_x^u)^{\mathrm{T}} \ \boldsymbol{O} \ \ (\boldsymbol{L}_z^u)^{\mathrm{T}} \right]^{\mathrm{T}},\,,$$

$$\boldsymbol{L}_1^w = \left[(\boldsymbol{L}_x^w)^{\mathrm{T}} \ \boldsymbol{O} \ \ (\boldsymbol{L}_z^w)^{\mathrm{T}} \right]^{\mathrm{T}},\ \boldsymbol{L}_2^w = \left[\boldsymbol{O} \ \ (\boldsymbol{L}_z^w)^{\mathrm{T}} \ (\boldsymbol{L}_x^w)^{\mathrm{T}} \right]^{\mathrm{T}},$$

$$\boldsymbol{L}_x^u = \{\partial/\partial x \quad 0\}\,,\ \boldsymbol{L}_x^w = \{0 \quad \partial/\partial x\}\,,\ \boldsymbol{L}_z^u = \{\partial/\partial z \quad 0\}\,,\ \boldsymbol{L}_z^w = \{0 \quad \partial/\partial z\} \tag{3.2}$$

In Eq. (3.2), $\boldsymbol{O}$ is the null matrix of size (2×1). However, the sandwich beam is considered to vibrate in the xz-plane under a time-dependent uniformly distributed transverse load (p_{tu})/transverse point-load (p_t) at a point (x_l, z_l) over the top surface of the beam. The corresponding first variations of the total potential energy (δT_p) and the total kinetic energy (δT_t) of the sandwich beam can be written as

$$\delta T_p = \sum_{k=1}^{2} \int_{A^k} \left\langle (\delta\boldsymbol{\varepsilon}_l + \delta\boldsymbol{\varepsilon}_n)^{\mathrm{T}} \boldsymbol{\sigma}^k - (\boldsymbol{l}_t\,\delta\boldsymbol{d}_s|_{z=h})^{\mathrm{T}}\, p_{tu} - (\boldsymbol{l}_t\,\delta\boldsymbol{d}_s|_{(x_l,z_l)})^{\mathrm{T}}\,(p_t/b) \right\rangle b\, dA^k\,,$$

$$\delta T_t = \sum_{k=1}^{2} \int_{A^k} (\delta\dot{\boldsymbol{d}}_s)^{\mathrm{T}} \rho^k\, \dot{\boldsymbol{d}}_s\ b\, dA^k\,,\ \boldsymbol{l}_t = \{0 \quad 1\} \tag{3.3a}$$

$$p_t = p_t^o \cos\Omega t\,,\ \ p_{tu} = p_{tu}^o \cos\Omega t \tag{3.3b}$$

In Eq. (3.3a), the superscript k indicates the material for the elastic face layers or the viscoelastic core according to its value as 1 or 2; A^k represents the area of

the k^{th} material in the xz-plane; ρ^k and $\boldsymbol{\sigma}^k$ are the mass density and stress vector, respectively, at any point in the k^{th} material. However, for the vibration analysis in the frequency domain, the transverse harmonic loads (p_t, p_{tu}) are considered as given in Eq. (3.3b) where p_t^o / p_{tu}^o and Ω are the amplitude and excitation frequency, respectively. Equation (3.3a) is substituted in the extended Hamilton's principle (Eq. (2.9)) to obtain the equation of motion of the sandwich beam, as given in Eq. (3.4).

$$\sum_{k=1}^{2} \int_{A^k} \left\langle \begin{matrix} (\delta \boldsymbol{d}_s)^{\mathrm{T}} \rho^k \ddot{\boldsymbol{d}}_s + (\delta \boldsymbol{\varepsilon}_l + \delta \boldsymbol{\varepsilon}_n)^{\mathrm{T}} \boldsymbol{\sigma}^k \\ -(\boldsymbol{l}_t \, \delta \boldsymbol{d}_s|_{z=h})^{\mathrm{T}} \, p_{tu} - (\boldsymbol{l}_t \, \delta \boldsymbol{d}_s|_{(x_l, z_l)})^{\mathrm{T}} \, (p_t / b) \end{matrix} \right\rangle b \, dA^k = 0 \tag{3.4}$$

Presently, a state of vibration ($\boldsymbol{d}_s$, Ω) of the sandwich beam is expressed with respect to a reference state of vibration (${}^i\boldsymbol{d}_s$, Ω_i) through their increments ($\Delta \boldsymbol{d}_s$, $\Delta\Omega$), as given in Eq. (3.5a). Accordingly, the incremental forms of the strain ($\boldsymbol{\varepsilon}_l$, $\boldsymbol{\varepsilon}_n$) and stress ($\boldsymbol{\sigma}^k$) vectors are given in Eq. (3.5b) where the pre-superscript i denotes a quantity corresponding to the reference state of vibration.

$$\boldsymbol{d}_s = \left({}^i\boldsymbol{d}_s + \Delta \boldsymbol{d}_s \right), \quad \Omega = \left(\Omega_i + \Delta\Omega \right) \tag{3.5a}$$

$$\boldsymbol{\varepsilon}_l = ({}^i\boldsymbol{\varepsilon}_l + \Delta \boldsymbol{\varepsilon}_l), \quad \boldsymbol{\varepsilon}_n = ({}^i\boldsymbol{\varepsilon}_n + \Delta \boldsymbol{\varepsilon}_{n1} + \Delta \boldsymbol{\varepsilon}_{n2}), \quad \boldsymbol{\sigma}^k = ({}^i\boldsymbol{\sigma}^k + \Delta \boldsymbol{\sigma}^k),$$

$${}^i\boldsymbol{\varepsilon}_l = \boldsymbol{L} \; {}^i\boldsymbol{d}_s, \quad \Delta \boldsymbol{\varepsilon}_l = \boldsymbol{L} \; \Delta \boldsymbol{d}_s,$$

$${}^i\boldsymbol{\varepsilon}_n = (1/2) \, {}^i\boldsymbol{L}_n \, {}^i\boldsymbol{d}_s, \quad \Delta \boldsymbol{\varepsilon}_{n1} = {}^i \boldsymbol{L}_n \, \Delta \boldsymbol{d}_s, \; \Delta \boldsymbol{\varepsilon}_{n2} = (1/2) \, \Delta \boldsymbol{L}_n \, \Delta \boldsymbol{d}_s,$$

$${}^i\boldsymbol{L}_n = \boldsymbol{L}_n({}^i\boldsymbol{d}_s), \quad \Delta \boldsymbol{L}_n = \boldsymbol{L}_n(\Delta \boldsymbol{d}_s) \tag{3.5b}$$

Substituting Eqs. (3.5a) and (3.5b) in Eq. (3.4), the incremental equation of motion of the sandwich beam can be obtained as

$$\sum_{k=1}^{2} \int_{A^k} \left\langle \begin{matrix} (\delta \Delta \boldsymbol{\varepsilon}_l + \delta \Delta \boldsymbol{\varepsilon}_{n1} + \delta \Delta \boldsymbol{\varepsilon}_{n2})^{\mathrm{T}} ({}^i\boldsymbol{\sigma}^k + \Delta \boldsymbol{\sigma}^k) + (\delta \Delta \boldsymbol{d}_s)^{\mathrm{T}} \rho^k ({}^i\ddot{\boldsymbol{d}}_s + \Delta \ddot{\boldsymbol{d}}_s) \\ -(\boldsymbol{l}_t \, \delta \Delta \boldsymbol{d}_s|_{z=h})^{\mathrm{T}} \, p_{tu} - (\boldsymbol{l}_t \, \delta \Delta \boldsymbol{d}_s|_{(x_l, z_l)})^{\mathrm{T}} (p_t / b) \end{matrix} \right\rangle b \, dA^k = 0 \tag{3.6}$$

In Eq. (3.6), the strain energy term, i.e. $(\delta \Delta \boldsymbol{\varepsilon}_{n2})^{\mathrm{T}} \, {}^i\boldsymbol{\sigma}^k$ yields the geometric stiffness of the beam; however, it is simplified in a special manner as follows

$$(\delta \Delta \boldsymbol{\varepsilon}_{n2})^{\mathrm{T}} \, {}^i\boldsymbol{\sigma}^k = (\delta \Delta \boldsymbol{\varepsilon}_g^u)^{\mathrm{T}} \, {}^i\boldsymbol{\Gamma}^k \Delta \boldsymbol{\varepsilon}_g^u + (\delta \Delta \boldsymbol{\varepsilon}_g^w)^{\mathrm{T}} \, {}^i\boldsymbol{\Gamma}^k \Delta \boldsymbol{\varepsilon}_g^w,$$

$$\Delta \boldsymbol{\varepsilon}_g^u = \boldsymbol{L}_g^u \, \Delta \boldsymbol{d}_s, \quad \Delta \boldsymbol{\varepsilon}_g^w = \boldsymbol{L}_g^w \, \Delta \boldsymbol{d}_s, \quad \boldsymbol{L}_g^u = \left[(\boldsymbol{L}_x^u)^{\mathrm{T}} \quad (\boldsymbol{L}_z^u)^{\mathrm{T}} \right]^{\mathrm{T}}, \quad \boldsymbol{L}_g^w = \left[(\boldsymbol{L}_x^w)^{\mathrm{T}} \quad (\boldsymbol{L}_z^w)^{\mathrm{T}} \right]^{\mathrm{T}},$$

$${}^i\boldsymbol{\Gamma}^k = \begin{bmatrix} {}^i\sigma_x^k & {}^i\tau_{xz}^k \\ {}^i\tau_{xz}^k & {}^i\sigma_z^k \end{bmatrix} \tag{3.7}$$

Introducing Eq. (3.7) in Eq. (3.6), the incremental equation of motion can be modified as

$$\sum_{k=1}^{2}\int_{A^k}\begin{Bmatrix}(\delta\Delta\boldsymbol{\varepsilon}_l+\delta\Delta\boldsymbol{\varepsilon}_{n1})^{\mathrm{T}}({}^i\boldsymbol{\sigma}^k+\Delta\boldsymbol{\sigma}^k)+(\delta\Delta\boldsymbol{d}_s)^{\mathrm{T}}\rho^k({}^i\ddot{\boldsymbol{d}}_s+\Delta\ddot{\boldsymbol{d}}_s)\\(\delta\Delta\boldsymbol{\varepsilon}_g^u)^{\mathrm{T}}\,{}^i\boldsymbol{\Gamma}^k\Delta\boldsymbol{\varepsilon}_g^u+(\delta\Delta\boldsymbol{\varepsilon}_g^w)^{\mathrm{T}}\,{}^i\boldsymbol{\Gamma}^k\Delta\boldsymbol{\varepsilon}_g^w\\-(\boldsymbol{l}_t\,\delta\Delta\boldsymbol{d}_s\big|_{z=h})^{\mathrm{T}}p_{tu}-(\boldsymbol{l}_t\,\delta\boldsymbol{d}_s\big|_{(x_l,z_l)})^{\mathrm{T}}(p_t/b)\end{Bmatrix}b\,dA^k=0 \tag{3.8}$$

3.3. Present HBM formulation

The nonlinear frequency responses of the sandwich beam under the excitation can be evaluated by implementing HBM, where the periodic response is assumed following the Fourier series with a finite number (H) of harmonic terms as

$$\boldsymbol{d}_s=\boldsymbol{d}_s^o+\sum_{m=1}^{H}\boldsymbol{d}_{sm}^c\cos(m\Omega t)+\boldsymbol{d}_{sm}^s\sin(m\Omega t) \tag{3.9}$$

In Eq. (3.9), $\boldsymbol{d}_s^o$, $\boldsymbol{d}_{sm}^c$ and $\boldsymbol{d}_{sm}^s$ are the displacement amplitude vectors corresponding to the constant, cosine and sine terms, respectively. Accordingly, the periodic solutions for the strain vectors ($\boldsymbol{\varepsilon}_l$, $\boldsymbol{\varepsilon}_n$) appear as

$$\begin{aligned}\boldsymbol{\varepsilon}_l&=(\boldsymbol{\varepsilon}_l)^o+\sum_{m=1}^{H}(\boldsymbol{\varepsilon}_l)_m^c\cos(m\Omega t)+(\boldsymbol{\varepsilon}_l)_m^s\sin(m\Omega t),\\\boldsymbol{\varepsilon}_n&=(\boldsymbol{\varepsilon}_n)^o+\sum_{m=1}^{2H}(\boldsymbol{\varepsilon}_n)_m^c\cos(m\Omega t)+(\boldsymbol{\varepsilon}_n)_m^s\sin(m\Omega t)\end{aligned} \tag{3.10}$$

where, the superscripts o, c and s indicate the strain amplitude vectors corresponding to the constant, cosine and sine terms, respectively. It may be noted here that the nonlinear strain vector ($\boldsymbol{\varepsilon}_n$) appears with $2H$ number of harmonic terms since it is a quadratic function of the displacement vector ($\boldsymbol{d}_s$, Eq. (3.2)).

Generally, for the evaluation of nonlinear frequency responses of elastic structures in the FE framework, the corresponding FE equations of motion are first derived in the time domain. Subsequently, the FE equations of motion are expressed in the frequency domain by implementing the assumed periodic solution (Eq. (3.9)) according to HBM (Blahoš et al., 2020; Chen et al., 2001; MS et al., 2016). However, this procedure is not usually followed for the nonlinear frequency response analysis of a viscoelastic structure because of the temporal derivative/integral of stress/strain in the viscoelastic constitutive relations like Zener model, fractional Zener model, Maxwell model, generalized Maxwell model and hereditary integral approach. In this case of viscoelastic structures, a viscoelastic constitutive relation is first reduced for the periodic stress/strain by

implementing HBM. The subsequent FE formulation is based on this reduced constitutive relation (Lewandowski and Wielentejczyk, 2017; Litewka and Lewandowski, 2017a; Wielentejczyk and Lewandowski, 2019). Now, the reduced form of one type of viscoelastic constitutive relation appears differently from that of another type. So, every type of viscoelastic constitutive relation needs a separate FE formulation, as it is observed in the literature (Jacques et al., 2010; Lewandowski and Wielentejczyk, 2017; Litewka and Lewandowski, 2017a; Wielentejczyk and Lewandowski, 2019). However, presently all the aforesaid viscoelastic constitutive relations are reduced to a generalized form by implementing HBM. It facilitates not only the FE formulation in a uniform manner for all the constitutive relations but also the implementation of the orthogonality of Fourier basis functions, as demonstrated in the following sections.

3.3.1. Reduction of time-domain constitutive relations for periodic stress/strain using HBM

For an isotropic elastic material ($k=1$) in the sandwich beam, the time-domain constitutive relation under the plane stress assumption can be written, as given in Eq. (2.3a).

$$\boldsymbol{\sigma}^k = \boldsymbol{C}^k \boldsymbol{\varepsilon}\,,\ \boldsymbol{C}^k = E^k \boldsymbol{C}_b^k\,,$$

$$\boldsymbol{C}_b^k = \frac{1}{1-(\nu^k)^2}\begin{bmatrix} 1 & \nu^k & 0 \\ \nu^k & 1 & 0 \\ 0 & 0 & (1-\nu^k)/2 \end{bmatrix},\ k=1 \tag{2.3a}$$

Now, for the periodic stress/strain, the constitutive relation (Eq. (2.3a)) can be reduced in a straightforward manner by substituting the periodic solutions of strain vectors (Eq. (3.10)). However, for the viscoelastic core ($k=2$), its time-domain constitutive relation according to the fractional Zener model (Litewka and Lewandowski, 2017a) can be written as

$$\boldsymbol{\sigma}^k + \tau^\alpha (d^\alpha \boldsymbol{\sigma}^k / dt^\alpha) = \boldsymbol{C}^k \left\langle \boldsymbol{\varepsilon} + (E_\infty / E_o)\tau^\alpha (d^\alpha \boldsymbol{\varepsilon} / dt^\alpha) \right\rangle\,,$$

$$\boldsymbol{C}^k = E_o \boldsymbol{C}_b^k\,,\ k=2 \tag{3.11}$$

where, E_o and E_∞ are the relaxed and non-relaxed elastic moduli, respectively; τ is the relaxation time and α represents the fractional-order time derivative. This constitutive relation (Eq. (3.11)) for a viscoelastic material can be reduced by introducing an anelastic strain ($\bar{\boldsymbol{\varepsilon}}$, (Galucio et al., 2004)), as given in Eq. (3.12a) where the anelastic strain vector ($\bar{\boldsymbol{\varepsilon}}$) is defined in Eq. (3.12b).

$$\boldsymbol{\sigma}^k = \boldsymbol{C}^k\,\boldsymbol{\varepsilon}^t\,,\quad \boldsymbol{\varepsilon}^t = (E_\infty/E_o)(\boldsymbol{\varepsilon}-\bar{\boldsymbol{\varepsilon}}) \tag{3.12a}$$

$$\bar{\boldsymbol{\varepsilon}} + \tau^\alpha\,(d^\alpha\bar{\boldsymbol{\varepsilon}}/dt^\alpha) = f\,\boldsymbol{\varepsilon}\,,\quad f = (E_\infty - E_o)/E_\infty \tag{3.12b}$$

Now, the periodic solution for the anelastic strain vector ($\bar{\boldsymbol{\varepsilon}}$) can be assumed similar to that for the other strain vectors ($\boldsymbol{\varepsilon}_l\,,\boldsymbol{\varepsilon}_n$, Eq. (3.10)), as given in Eq. (3.12c).

$$\bar{\boldsymbol{\varepsilon}}_l = (\bar{\boldsymbol{\varepsilon}}_l)^o + \sum_{m=1}^{H}(\bar{\boldsymbol{\varepsilon}}_l)^c_m\cos(m\Omega t) + (\bar{\boldsymbol{\varepsilon}}_l)^s_m\sin(m\Omega t)\,,$$

$$\bar{\boldsymbol{\varepsilon}}_n = (\bar{\boldsymbol{\varepsilon}}_n)^o + \sum_{m=1}^{2H}(\bar{\boldsymbol{\varepsilon}}_n)^c_m\cos(m\Omega t) + (\bar{\boldsymbol{\varepsilon}}_n)^s_m\sin(m\Omega t) \tag{3.12c}$$

Substituting these solutions for the strain vectors ($\boldsymbol{\varepsilon},\bar{\boldsymbol{\varepsilon}}$, Eqs. (3.10) and (3.12c)) in Eq. (3.12b)) and then making the coefficient vectors of all harmonic terms as equal to zero, one can obtain the anelastic strain amplitude vectors ($(\bar{\boldsymbol{\varepsilon}}_l)^o,(\bar{\boldsymbol{\varepsilon}}_l)^c_m,(\bar{\boldsymbol{\varepsilon}}_l)^s_m$, $(\bar{\boldsymbol{\varepsilon}}_n)^o,(\bar{\boldsymbol{\varepsilon}}_n)^c_m,(\bar{\boldsymbol{\varepsilon}}_n)^s_m$, Eq. (3.12c)) in terms of the other strain amplitude vectors ($(\boldsymbol{\varepsilon}_l)^o,(\boldsymbol{\varepsilon}_l)^c_m,(\boldsymbol{\varepsilon}_l)^s_m,(\boldsymbol{\varepsilon}_n)^o,(\boldsymbol{\varepsilon}_n)^c_m,(\boldsymbol{\varepsilon}_n)^s_m$, Eq. (3.10)). The resulting expressions can subsequently be used in Eq. (3.12a) to obtain the constitutive relation by eliminating the anelastic strain amplitude vectors as follows

$$\boldsymbol{\sigma}^k = \boldsymbol{C}^k\,\boldsymbol{\varepsilon}^t\,,\ \boldsymbol{\varepsilon}^t = \boldsymbol{\varepsilon}^t_l + \boldsymbol{\varepsilon}^t_n$$

$$\boldsymbol{\varepsilon}^t_l = (\boldsymbol{\varepsilon}_l)^o + \sum_{m=1}^{H}\left\langle f^c_m(\boldsymbol{\varepsilon}_l)^c_m + f^s_m(\boldsymbol{\varepsilon}_l)^s_m\right\rangle\cos(m\Omega t) + \left\langle f^c_m(\boldsymbol{\varepsilon}_l)^s_m - f^s_m(\boldsymbol{\varepsilon}_l)^c_m\right\rangle\sin(m\Omega t)$$

$$\boldsymbol{\varepsilon}^t_n = (\boldsymbol{\varepsilon}_n)^o + \sum_{m=1}^{2H}\left\langle f^c_m(\boldsymbol{\varepsilon}_n)^c_m + f^s_m(\boldsymbol{\varepsilon}_n)^s_m\right\rangle\cos(m\Omega t) + \left\langle f^c_m(\boldsymbol{\varepsilon}_n)^s_m - f^s_m(\boldsymbol{\varepsilon}_n)^c_m\right\rangle\sin(m\Omega t) \tag{3.13a}$$

$$f^c_m = (E_\infty/E_o)\left[1 - f_m\left\langle 1 + c_l\,(m\Omega\tau)^\alpha\right\rangle\right],\ f^s_m = (E_\infty/E_o)\,f_m\,s_l\,(m\Omega\tau)^\alpha\,,$$

$$f_m = f\Big/\left\{\left\langle 1 + c_l\,(m\Omega\tau)^\alpha\right\rangle^2 + \left\langle s_l\,(m\Omega\tau)^\alpha\right\rangle^2\right\},\ c_l = \cos(\pi\alpha/2),\ s_l = \sin(\pi\alpha/2) \tag{3.13b}$$

It may be noted from Eq. (3.13a) that the parameter f^s_m represents the material damping in the viscoelastic material. The same constitutive relation (Eq. (3.13a)) can also be used for the periodic stress/strain in an elastic material where f^c_m = 1 and f^s_m = 0. However, Eq. (3.13a) may be treated as a generalized form of the viscoelastic constitutive model for the periodic stress/strain, since other commonly used time-domain constitutive models like Kelvin-Voigt model (Baz, 2019), Maxwell model (Baz, 2019), generalized Maxwell model (Amabili et al.,

2019) and Hereditary integral approach (Jacques et al., 2010; Wang and Tsai, 1988) can also be expressed in the similar form (Eq. (3.13a)) for the periodic variation of stress/strain.

For the Kelvin-Voigt model of viscoelastic materials, the time-domain constitutive relation is given by (Baz, 2019),

$$\boldsymbol{\sigma}^k = \boldsymbol{C}^k(\boldsymbol{\varepsilon} + \tau_v \dot{\boldsymbol{\varepsilon}}),\ \boldsymbol{C}^k = E_1 \boldsymbol{C}_b^k,\ k = 2 \tag{3.14a}$$

where, τ_v and E_1 are the relaxation time and stiffness of a viscoelastic material, respectively. Now, to reduce this constitutive relation (Eq. (3.14a)) for the periodic strain, Eq. (3.10) can be utilized, and it yields the resulting constitutive relation in the form of Eq. (3.13a) where the parameters f_m^c and f_m^s appear as

$$f_m^c = 1,\ f_m^s = \tau_v m\Omega \tag{3.14b}$$

For the Maxwell model of viscoelastic materials, the corresponding time-domain constitutive relation is given by (Baz, 2019)

$$\boldsymbol{\sigma}^k + \tau_n \dot{\boldsymbol{\sigma}}^k = \boldsymbol{C}^k \tau_n \dot{\boldsymbol{\varepsilon}},\ \boldsymbol{C}^k = E_n \boldsymbol{C}_b^k,\ k = 2 \tag{3.15a}$$

where, τ_n and E_n are the relaxation time and stiffness of a viscoelastic material, respectively. Now, introducing the periodic solution of strain (Eq. (3.10)), Eq. (3.15a) can be reduced in the same form, as given in Eq. (3.13a) where the parameters $\boldsymbol{\varepsilon}_l^t$, $\boldsymbol{\varepsilon}_n^t$, f_m^c and f_m^s appear as

$$\boldsymbol{\varepsilon}_l^t = \sum_{m=1}^{H} \left\langle f_m^c (\boldsymbol{\varepsilon}_l)_m^c + f_m^s (\boldsymbol{\varepsilon}_l)_m^s \right\rangle \cos(m\Omega t) + \left\langle f_m^c (\boldsymbol{\varepsilon}_l)_m^s - f_m^s (\boldsymbol{\varepsilon}_l)_m^c \right\rangle \sin(m\Omega t)$$

$$\boldsymbol{\varepsilon}_n^t = \sum_{m=1}^{2H} \left\langle f_m^c (\boldsymbol{\varepsilon}_n)_m^c + f_m^s (\boldsymbol{\varepsilon}_n)_m^s \right\rangle \cos(m\Omega t) + \left\langle f_m^c (\boldsymbol{\varepsilon}_n)_m^s - f_m^s (\boldsymbol{\varepsilon}_n)_m^c \right\rangle \sin(m\Omega t)$$

$$f_m^c = (m\Omega\tau_n)^2 \Big/ \left\langle 1 + (m\Omega\tau_n)^2 \right\rangle,\ f_m^s = m\Omega\tau_n \Big/ \left\langle 1 + (m\Omega\tau_n)^2 \right\rangle \tag{3.15b}$$

In the case of the generalized Maxwell model (Amabili et al., 2019) with a finite number (N_l) of Maxwell elements, the stress in a typical (say n^{th}) Maxwell element for the periodic strain can be expressed by Eq. (3.13a) where the parameters $\boldsymbol{\varepsilon}_l^t$, $\boldsymbol{\varepsilon}_n^t$, f_m^c and f_m^s are given in Eq. (3.15b). However, the sum of stresses in all Maxwell elements results in Eq. (3.13a) along with the following expressions for the parameters f_m^c and f_m^s

$$f_m^c = 1 + \sum_{n=1}^{N_l} \left\{ (E_n/E_o)(m\Omega\tau_n)^2 \Big/ \left\langle 1 + (m\Omega\tau_n)^2 \right\rangle \right\},$$

$$f_m^s = \sum_{n=1}^{N_l} \left\{ (E_n/E_o) m\Omega\tau_n \Big/ \left\langle 1 + (m\Omega\tau_n)^2 \right\rangle \right\} \tag{3.16}$$

In the hereditary integral approach, the time-domain constitutive relation is given by Eq. (3.17a) (Jacques et al., 2010; Wang and Tsai, 1988), where Y is the relaxation modulus of a viscoelastic material.

$$\boldsymbol{\sigma}^k = \boldsymbol{C}_b^k \left\langle Y(0)\boldsymbol{\varepsilon} + \int_0^t (dY/d\tau_u)\, \boldsymbol{\varepsilon}(t-\tau_u)\, d\tau_u \right\rangle,\ k=2 \tag{3.17a}$$

However, for the periodic stress/strain, the relaxation modulus (Y) can be obtained from the complex modulus (Eq. (3.17b)) of a viscoelastic material by assuming the harmonic form of strain ($\boldsymbol{\varepsilon} = \boldsymbol{\varepsilon}_0 e^{j\Omega t}$), as given in Eq. (3.17c) where E^R and E^I are the frequency-dependent storage and loss moduli of a viscoelastic material, respectively.

$$E(\omega) = E^R(\Omega) + j\ E^I(\Omega) \tag{3.17b}$$

$$E^R(\Omega) = Y(0) + \int_0^t (dY/d\tau_u)\cos(\Omega\tau_u)\, d\tau_u\ ,$$

$$E^I(\Omega) = -\int_0^t (dY/d\tau_u)\sin(\Omega\tau_u)\, d\tau_u \tag{3.17c}$$

Now, the constitutive relation in Eq. (3.17a) can be reduced in the form of Eq. (3.13a) using the periodic solution of strain vector (Eq. (3.10)) and the relations in Eq. (3.17c), where the parameters f_m^c and f_m^s appear in the form, as given in Eq. (3.17d).

$$f_m^c = E^R(m\Omega)/E_o\ ,\ \ f_m^s = E^I(m\Omega)/E_o \tag{3.17d}$$

In the above derivation, the time-domain viscoelastic constitute models, namely Kelvin-Voigt model, Maxwell model, Zener model, fractional Zener model, generalized Maxwell model and hereditary integral approach are reduced to a generalized form (Eq. (3.13a)) for the periodic stress/strain. It basically removes the requirement of the separate FE formulation of a viscoelastic structure for each of the aforesaid constitutive relations in the geometrically nonlinear frequency response analysis of the viscoelastic structure. This formulation of a generalized constitutive relation also provides an advantage of making a comparison study among the aforesaid different viscoelastic constitutive models in a straightforward manner, particularly for the evaluation of nonlinear frequency responses of a viscoelastic structure. It may also be noted here that the reduced form ($\boldsymbol{\sigma}^k = \boldsymbol{C}^k \boldsymbol{\varepsilon}^t$, Eq. (3.13a)) of the viscoelastic constitutive relations appears similar to that ($\boldsymbol{\sigma}^k = \boldsymbol{C}^k \boldsymbol{\varepsilon}$, Eq. (2.3a)) for the elastic material. So, the aforesaid viscoelastic constitutive relations can be handled easily in the formulation of the governing

equation of motion of a viscoelastic structure for its frequency response analysis, as it is demonstrated in the following sections.

3.3.2. Derivation of the governing equation of motion by exploiting the orthogonality of Fourier basis functions

The Fourier expansion of strain vectors ($^{i}\boldsymbol{\varepsilon}_l$, $\Delta\boldsymbol{\varepsilon}_l$, $^{i}\boldsymbol{\varepsilon}_n$, $\Delta\boldsymbol{\varepsilon}_{n1}$, $\Delta\boldsymbol{\varepsilon}_g^w$, $\Delta\boldsymbol{\varepsilon}_g^u$) appearing in Eqs. (3.5) and (3.7) can be written as

$$
\begin{aligned}
^{i}\boldsymbol{\varepsilon}_l &= (^{i}\boldsymbol{\varepsilon}_l)^o + \sum_{m=1}^{H} (^{i}\boldsymbol{\varepsilon}_l)_m^c \cos(m\Omega t) + (^{i}\boldsymbol{\varepsilon}_l)_m^s \sin(m\Omega t)\,,\\
\Delta\boldsymbol{\varepsilon}_l &= (\Delta\boldsymbol{\varepsilon}_l)^o + \sum_{m=1}^{H} (\Delta\boldsymbol{\varepsilon}_l)_m^c \cos(m\Omega t) + (\Delta\boldsymbol{\varepsilon}_l)_m^s \sin(m\Omega t)\\
^{i}\boldsymbol{\varepsilon}_n &= (^{i}\boldsymbol{\varepsilon}_n)^o + \sum_{m=1}^{2H} (^{i}\boldsymbol{\varepsilon}_n)_m^c \cos(m\Omega t) + (^{i}\boldsymbol{\varepsilon}_n)_m^s \sin(m\Omega t)\\
\Delta\boldsymbol{\varepsilon}_{n1} &= (\Delta\boldsymbol{\varepsilon}_{n1})^o + \sum_{m=1}^{2H} (\Delta\boldsymbol{\varepsilon}_{n1})_m^c \cos(m\Omega t) + (\Delta\boldsymbol{\varepsilon}_{n1})_m^s \sin(m\Omega t)\\
\Delta\boldsymbol{\varepsilon}_g^w &= (\Delta\boldsymbol{\varepsilon}_g^w)^o + \sum_{m=1}^{H} (\Delta\boldsymbol{\varepsilon}_g^w)_m^c \cos(m\Omega t) + (\Delta\boldsymbol{\varepsilon}_g^w)_m^s \sin(m\Omega t)\\
\Delta\boldsymbol{\varepsilon}_g^u &= (\Delta\boldsymbol{\varepsilon}_g^u)^o + \sum_{m=1}^{H} (\Delta\boldsymbol{\varepsilon}_g^u)_m^c \cos(m\Omega t) + (\Delta\boldsymbol{\varepsilon}_g^u)_m^s \sin(m\Omega t)
\end{aligned}
\tag{3.18}
$$

Similarly, using Eqs. (3.5) and (3.13), the stress vectors ($^{i}\boldsymbol{\sigma}^k$ and $\Delta\boldsymbol{\sigma}^k$) at any point in the xz-plane for the k^{th} material can be written, as given in Eq. (3.19a) where f_m^c = 1 and f_m^s=0 for the elastic material ($k=1$).

$$
\begin{aligned}
^{i}\boldsymbol{\sigma}^k &= (^{i}\boldsymbol{\sigma}^k)^o + \sum_{m=1}^{2H} (^{i}\boldsymbol{\sigma}^k)_m^c \cos(m\Omega t) + (^{i}\boldsymbol{\sigma}^k)_m^s \sin(m\Omega t)\,,\\
\Delta\boldsymbol{\sigma}^k &= (\Delta\boldsymbol{\sigma}^k)^o + \sum_{m=1}^{2H} (\Delta\boldsymbol{\sigma}^k)_m^c \cos(m\Omega t) + (\Delta\boldsymbol{\sigma}^k)_m^s \sin(m\Omega t)\,,\\
(^{i}\boldsymbol{\sigma}^k)^o &= \boldsymbol{C}^k(^{i}\boldsymbol{\varepsilon}_l + {}^{i}\boldsymbol{\varepsilon}_n)^o,\ (\Delta\boldsymbol{\sigma}^k)^o = \boldsymbol{C}^k(\Delta\boldsymbol{\varepsilon}_l + \Delta\boldsymbol{\varepsilon}_{n1})^o;\\
(^{i}\boldsymbol{\sigma}^k)_m^s &= \boldsymbol{C}^k\left\langle f_m^c(^{i}\boldsymbol{\varepsilon}_l + {}^{i}\boldsymbol{\varepsilon}_n)_m^s - f_m^s(^{i}\boldsymbol{\varepsilon}_l + {}^{i}\boldsymbol{\varepsilon}_n)_m^c \right\rangle,\\
(^{i}\boldsymbol{\sigma}^k)_m^c &= \boldsymbol{C}^k\left\langle f_m^c(^{i}\boldsymbol{\varepsilon}_l + {}^{i}\boldsymbol{\varepsilon}_n)_m^c + f_m^s(^{i}\boldsymbol{\varepsilon}_l + {}^{i}\boldsymbol{\varepsilon}_n)_m^s \right\rangle,\\
(\Delta\boldsymbol{\sigma}^k)_m^c &= \boldsymbol{C}^k\left\langle f_m^c(\Delta\boldsymbol{\varepsilon}_l + \Delta\boldsymbol{\varepsilon}_{n1})_m^c + f_m^s(\Delta\boldsymbol{\varepsilon}_l + \Delta\boldsymbol{\varepsilon}_{n1})_m^s \right\rangle,\\
(\Delta\boldsymbol{\sigma}^k)_m^s &= \boldsymbol{C}^k\left\langle f_m^c(\Delta\boldsymbol{\varepsilon}_l + \Delta\boldsymbol{\varepsilon}_{n1})_m^s - f_m^s(\Delta\boldsymbol{\varepsilon}_l + \Delta\boldsymbol{\varepsilon}_{n1})_m^c \right\rangle,\ m=1,2,3,...,H\,;\\
(^{i}\boldsymbol{\sigma}^k)_m^s &= \boldsymbol{C}^k\left\langle f_m^c(^{i}\boldsymbol{\varepsilon}_n)_m^s - f_m^s(^{i}\boldsymbol{\varepsilon}_n)_m^c \right\rangle,\ (^{i}\boldsymbol{\sigma}^k)_m^c = \boldsymbol{C}^k\left\langle f_m^c(^{i}\boldsymbol{\varepsilon}_n)_m^c + f_m^s(^{i}\boldsymbol{\varepsilon}_n)_m^s \right\rangle,
\end{aligned}
$$

$$(\Delta\boldsymbol{\sigma}^k)_m^s = \boldsymbol{C}^k \left\langle f_m^c(\Delta\boldsymbol{\varepsilon}_{n1})_m^s - f_m^s(\Delta\boldsymbol{\varepsilon}_{n1})_m^c \right\rangle,$$

$$(\Delta\boldsymbol{\sigma}^k)_m^c = \boldsymbol{C}^k \left\langle f_m^c(\Delta\boldsymbol{\varepsilon}_{n1})_m^c + f_m^s(\Delta\boldsymbol{\varepsilon}_{n1})_m^s \right\rangle, \quad m = H+1,\ H+2,\ldots,2H \tag{3.19a}$$

From Eqs. (3.18) and (3.19a), the Fourier expansion of the products ${}^i\boldsymbol{\Gamma}^k\,\Delta\boldsymbol{\varepsilon}_g^u$ and ${}^i\boldsymbol{\Gamma}^k\,\Delta\boldsymbol{\varepsilon}_g^w$ appearing in Eq. (3.8) can also be obtained as

$${}^i\boldsymbol{\Gamma}^k\,\Delta\boldsymbol{\varepsilon}_g^u = ({}^i\boldsymbol{\Gamma}^k\,\Delta\boldsymbol{\varepsilon}_g^u)^o + \sum_{m=1}^{3H} ({}^i\boldsymbol{\Gamma}^k\,\Delta\boldsymbol{\varepsilon}_g^u)_m^c \cos(m\Omega t) + ({}^i\boldsymbol{\Gamma}^k\,\Delta\boldsymbol{\varepsilon}_g^u)_m^s \sin(m\Omega t),$$

$${}^i\boldsymbol{\Gamma}^k\,\Delta\boldsymbol{\varepsilon}_g^w = ({}^i\boldsymbol{\Gamma}^k\,\Delta\boldsymbol{\varepsilon}_g^w)^o + \sum_{m=1}^{3H} ({}^i\boldsymbol{\Gamma}^k\,\Delta\boldsymbol{\varepsilon}_g^w)_m^c \cos(m\Omega t) + ({}^i\boldsymbol{\Gamma}^k\,\Delta\boldsymbol{\varepsilon}_g^w)_m^s \sin(m\Omega t) \tag{3.19b}$$

Now, the equation of motion of the sandwich beam in the frequency domain can be derived by substituting the expressions of displacement, stress and strain vectors (Eqs. (3.9), (3.10), (3.13), (3.18), (3.19a-b)) in Eq. (3.8), while the resulting expression is to be reduced within a time-period using the Galerkin method. In this conventional procedure, the equation of motion appears with a large number of nonlinear stiffness terms associated with the products of sine and cosine functions. Further, the reduction of the equation of motion within a time-period is commonly carried out using a numerical time-integration method (Blahoš et al., 2020; Chen et al., 2001; MS et al., 2016), which involves a high computational time particularly for the evaluation of nonlinear frequency responses in the FE framework. These two concerns are presently tackled by exploiting the orthogonality of Fourier basis functions, especially to avoid the numerical time-integration and also to reduce the number of terms in the expression of the equation of motion. Here, for the orthogonality of Fourier basis functions, the time-integration of the product of any two Fourier basis functions ($f_j(t)$, Eq. (3.20)) over a time-period (T) can be written as follows

$$\frac{2}{T}\int_0^T f_j(t)\ f_n(t)\ dt = \begin{cases} 0 & j \neq n \\ 1 & j = n\ (j \neq 0, n \neq 0), \\ 2 & j = n = 0 \end{cases} \quad j, n = 0,1,2,\ldots,(2H+1),$$

$$f_0 = 1,\ \ f_m = \cos(m\Omega t),\ \ f_{H+m} = \sin(m\Omega t),\ \ m = 1,2,3,\ldots,H \tag{3.20}$$

According to Eq. (3.20), some terms in the equation of motion corresponding to the multiplication of any two different Fourier basis functions would vanish. Therefore, the expression of the equation of motion is simplified with a reduced number of terms. Also, this reduction of the equation of motion can be carried out without numerical time-integration over the time-period. However, using this

strategy, the incremental governing equation of motion of the sandwich beam can be obtained in the following form

$$\sum_{k=1}^{2}\int_{A^k}\left\{\begin{array}{l} 2\left[\left\langle(\delta\Delta\boldsymbol{\varepsilon}_l+\delta\Delta\boldsymbol{\varepsilon}_{n1})^o\right\rangle^{\mathrm{T}}({}^i\boldsymbol{\sigma}^k+\Delta\boldsymbol{\sigma}^k)^o+(\delta U_g)^o\right] \\ -(\boldsymbol{l}_t\,\delta\Delta\boldsymbol{d}_{s1}^c\big|_{z=h})^{\mathrm{T}}p_{tu}^o-(\boldsymbol{l}_t\,\delta\Delta\boldsymbol{d}_{s1}^c\big|_{(x_l,z_l)})^{\mathrm{T}}(p_t^o/b)+ \\ \sum_{m=1}^{H}\left[\begin{array}{l}\left\langle(\delta\Delta\boldsymbol{\varepsilon}_l)_m^c\right\rangle^{\mathrm{T}}({}^i\boldsymbol{\sigma}^k+\Delta\boldsymbol{\sigma}^k)_m^c+\left\langle(\delta\Delta\boldsymbol{\varepsilon}_l)_m^s\right\rangle^{\mathrm{T}}({}^i\boldsymbol{\sigma}^k+\Delta\boldsymbol{\sigma}^k)_m^s \\ +(\delta U_g)_m^c+(\delta U_g)_m^s \\ -\rho^k(m\Omega_i+m\Delta\Omega)^2\left\langle\begin{array}{l}(\delta\Delta\boldsymbol{d}_{sm}^s)^{\mathrm{T}}({}^i\boldsymbol{d}_{sm}^s+\Delta\boldsymbol{d}_{sm}^s)\\+(\delta\Delta\boldsymbol{d}_{sm}^c)^{\mathrm{T}}({}^i\boldsymbol{d}_{sm}^c+\Delta\boldsymbol{d}_{sm}^c)\end{array}\right\rangle\end{array}\right] \\ +\sum_{m=1}^{2H}\left[\left\langle(\delta\Delta\boldsymbol{\varepsilon}_{n1})_m^c\right\rangle^{\mathrm{T}}({}^i\boldsymbol{\sigma}^k+\Delta\boldsymbol{\sigma}^k)_m^c+\left\langle(\delta\Delta\boldsymbol{\varepsilon}_{n1})_m^s\right\rangle^{\mathrm{T}}({}^i\boldsymbol{\sigma}^k+\Delta\boldsymbol{\sigma}^k)_m^s\right]\end{array}\right\}b\,dA^k=0$$

$$(\delta U_g)_m^s=\left\langle(\delta\Delta\boldsymbol{\varepsilon}_g^u)_m^s\right\rangle^{\mathrm{T}}({}^i\boldsymbol{\Gamma}^k\,\Delta\boldsymbol{\varepsilon}_g^u)_m^s+\left\langle(\delta\Delta\boldsymbol{\varepsilon}_g^w)_m^s\right\rangle^{\mathrm{T}}({}^i\boldsymbol{\Gamma}^k\Delta\boldsymbol{\varepsilon}_g^w)_m^s$$

$$(\delta U_g)_m^c=\left\langle(\delta\Delta\boldsymbol{\varepsilon}_g^u)_m^c\right\rangle^{\mathrm{T}}({}^i\boldsymbol{\Gamma}^k\,\Delta\boldsymbol{\varepsilon}_g^u)_m^c+\left\langle(\Delta\delta\boldsymbol{\varepsilon}_g^w)_m^c\right\rangle^{\mathrm{T}}({}^i\boldsymbol{\Gamma}^k\Delta\boldsymbol{\varepsilon}_g^w)_m^c$$

$$(\delta U_g)^o=\left\langle(\delta\Delta\boldsymbol{\varepsilon}_g^u)^o\right\rangle^{\mathrm{T}}({}^i\boldsymbol{\Gamma}^k\,\Delta\boldsymbol{\varepsilon}_g^u)^o+\left\langle(\delta\Delta\boldsymbol{\varepsilon}_g^w)^o\right\rangle^{\mathrm{T}}({}^i\boldsymbol{\Gamma}^k\Delta\boldsymbol{\varepsilon}_g^w)^o \tag{3.21}$$

In Eq. (3.21), $\Delta\boldsymbol{d}_{s1}^c$ is a coefficient vector in the Fourier expansion of the incremental displacement vector ($\Delta\boldsymbol{d}_s$) corresponding to the m^{th} cosine term ($\cos(m\omega_i t)$, Eq. (3.9)) with $m=1$. It may be noted here that this new formulation would provide lesser computational time than that in the conventional HBM, as it is verified in Section 3.5.2 for the evaluation of nonlinear frequency responses of the sandwich beam in the FE framework.

3.3.3. Derivation of finite element model

For deriving the FE model of the viscoelastic sandwich beam, its xz-plane (Fig. 3.1) is discretized using nine-node isoparametric quadrilateral elements. The edges of a typical element are in parallel to the axes (x and z) of the reference coordinate system. The FE discretization of the xz-plane (Fig. 3.1) is carried out following the inter-phase surfaces of two dissimilar materials so that a typical element is made of either elastic ($k=1$) or viscoelastic material ($k=2$). However, the displacement (${}^i\boldsymbol{d}_s$, $\Delta\boldsymbol{d}_s$, Eq. (3.5a)) and strain (${}^i\boldsymbol{\varepsilon}_l$, $\Delta\boldsymbol{\varepsilon}_l$, ${}^i\boldsymbol{\varepsilon}_n$, $\Delta\boldsymbol{\varepsilon}_{n1}$, $\Delta\boldsymbol{\varepsilon}_g^u$, $\Delta\boldsymbol{\varepsilon}_g^w$, Eq. 3.5b) vectors at any point within a typical element can be expressed in terms of the shape function matrix ($\boldsymbol{N}$) and the elemental nodal displacement vectors (${}^i\boldsymbol{d}^e$

, $\Delta \boldsymbol{d}^e$), as given in Eqs. (3.22a) and (3.22b) where $\boldsymbol{I}_{18}$ is an identity matrix with the size (18×18) and the symbol $\otimes$ represents Kronecker product.

$$ {}^i\boldsymbol{d}_s = \boldsymbol{N}\,{}^i\boldsymbol{d}^e,\ \Delta\boldsymbol{d}_s = \boldsymbol{N}\,\Delta\boldsymbol{d}^e \tag{3.22a} $$

$$ {}^i\boldsymbol{\varepsilon}_l = \boldsymbol{B}_l\,{}^i\boldsymbol{d}^e,\ \ \Delta\boldsymbol{\varepsilon}_l = \boldsymbol{B}_l\,\Delta\boldsymbol{d}^e, $$

$$ {}^i\boldsymbol{\varepsilon}_n = (1/2)\,\boldsymbol{B}_n\,{}^i\boldsymbol{d}_I^e\,{}^i\boldsymbol{d}^e,\ \ \Delta\boldsymbol{\varepsilon}_{n1} = \boldsymbol{B}_n\,{}^i\boldsymbol{d}_I^e\,\Delta\boldsymbol{d}^e, $$

$$ \Delta\boldsymbol{\varepsilon}_g^w = \boldsymbol{B}_g^w\,\Delta\boldsymbol{d}_e,\ \Delta\boldsymbol{\varepsilon}_g^u = \boldsymbol{B}_g^u\,\Delta\boldsymbol{d}_e, $$

$$ \boldsymbol{B}_l = \boldsymbol{L}\,\boldsymbol{N},\ \ \boldsymbol{B}_n = \boldsymbol{B}_1^w\boldsymbol{R}_x^w + \boldsymbol{B}_2^w\boldsymbol{R}_z^w + \boldsymbol{B}_1^u\boldsymbol{R}_x^u + \boldsymbol{B}_2^u\boldsymbol{R}_z^u, $$

$$ \boldsymbol{R}_x^u = \boldsymbol{I}_{18}\otimes\boldsymbol{B}_x^u,\ \ \boldsymbol{R}_z^u = \boldsymbol{I}_{18}\otimes\boldsymbol{B}_z^u, $$

$$ \boldsymbol{R}_x^w = \boldsymbol{I}_{18}\otimes\boldsymbol{B}_x^w,\ \ \boldsymbol{R}_z^w = \boldsymbol{I}_{18}\otimes\boldsymbol{B}_z^w, $$

$$ \boldsymbol{B}_g^u = \boldsymbol{L}_g^u\,\boldsymbol{N},\ \ \boldsymbol{B}_g^w = \boldsymbol{L}_g^w\,\boldsymbol{N},\ \ {}^i\boldsymbol{d}_I^e = {}^i\boldsymbol{d}^e\otimes\boldsymbol{I}_{18}, $$

$$ \boldsymbol{B}_1^u = \boldsymbol{L}_1^u\boldsymbol{N},\ \boldsymbol{B}_2^u = \boldsymbol{L}_2^u\boldsymbol{N},\ \boldsymbol{B}_1^w = \boldsymbol{L}_1^w\boldsymbol{N},\ \boldsymbol{B}_2^w = \boldsymbol{L}_2^w\boldsymbol{N}, $$

$$ \boldsymbol{B}_x^u = \boldsymbol{L}_x^u\boldsymbol{N},\ \boldsymbol{B}_z^u = \boldsymbol{L}_z^u\boldsymbol{N},\ \boldsymbol{B}_x^w = \boldsymbol{L}_x^w\boldsymbol{N},\ \boldsymbol{B}_z^w = \boldsymbol{L}_z^w\boldsymbol{N} \tag{3.22b} $$

It may be noted here that the nonlinear strain vector is expressed in terms of a linear strain-displacement matrix ($\boldsymbol{B}_n$), a nodal displacement matrix (${}^i\boldsymbol{d}_I^e$) and a nodal displacement vector (${}^i\boldsymbol{d}^e$ / $\Delta\boldsymbol{d}^e$, Eq. (3.22b)). This special formulation of nonlinear strain vector yields the nonlinear stiffness matrix in terms of a displacement-independent stiffness coefficient matrix multiplied by the nodal displacement matrix. So, the expression of the overall nonlinear stiffness matrix according to HBM can be obtained in a straightforward manner by replacing the nodal displacement matrix (${}^i\boldsymbol{d}_I^e$) with its Fourier expansion.

However, the Fourier expansion of elemental displacement vectors (${}^i\boldsymbol{d}^e$ / $\Delta\boldsymbol{d}^e$) can be expressed following Eq. (3.9), where the amplitude vectors are denoted by ${}^i\boldsymbol{d}_e^o$ / $\Delta\boldsymbol{d}_e^o$, ${}^i\boldsymbol{d}_{em}^c$ / $\Delta\boldsymbol{d}_{em}^c$ and ${}^i\boldsymbol{d}_{em}^s$ / $\Delta\boldsymbol{d}_{em}^s$ ($m = 1,2,3,...,H$) corresponding to the constant, cosine and sine terms, respectively. Now, using Eq. (3.22b), the strain amplitude vectors (Eq. (3.18)) can be expressed in terms of the displacement vectors (${}^i\boldsymbol{d}_e^o$ / $\Delta\boldsymbol{d}_e^o$, ${}^i\boldsymbol{d}_{em}^c$ / $\Delta\boldsymbol{d}_{em}^c$, ${}^i\boldsymbol{d}_{em}^s$ / $\Delta\boldsymbol{d}_{em}^s$, $m = 1,2,3,...,H$) as follows

$$ ({}^i\boldsymbol{\varepsilon}_l)^o = \boldsymbol{B}_l\,{}^i\boldsymbol{d}_e^o,\ ({}^i\boldsymbol{\varepsilon}_l)_m^c = \boldsymbol{B}_l\,{}^i\boldsymbol{d}_{em}^c,\ ({}^i\boldsymbol{\varepsilon}_l)_m^s = \boldsymbol{B}_l\,{}^i\boldsymbol{d}_{em}^s, $$

$$ (\Delta\boldsymbol{\varepsilon}_l)^o = \boldsymbol{B}_l\,\Delta\boldsymbol{d}_e^o,\ (\Delta\boldsymbol{\varepsilon}_l)_m^c = \boldsymbol{B}_l\,\Delta\boldsymbol{d}_{em}^c,\ (\Delta\boldsymbol{\varepsilon}_l)_m^s = \boldsymbol{B}_l\,\Delta\boldsymbol{d}_{em}^s, $$

$$({}^{i}\boldsymbol{\varepsilon}_n)^o = (1/2)\boldsymbol{B}_n\,\boldsymbol{D}^o\;{}^{i}\boldsymbol{X}^e,\;({}^{i}\boldsymbol{\varepsilon}_n)^c_m = (1/2)\boldsymbol{B}_n\,\boldsymbol{D}^c_m\;{}^{i}\boldsymbol{X}^e,\;({}^{i}\boldsymbol{\varepsilon}_n)^s_m = (1/2)\boldsymbol{B}_n\,\boldsymbol{D}^s_m\;{}^{i}\boldsymbol{X}^e,$$

$$(\Delta\boldsymbol{\varepsilon}_{n1})^o = \boldsymbol{B}_n\,\boldsymbol{D}^o\Delta\boldsymbol{X}^e,\;(\Delta\boldsymbol{\varepsilon}_{n1})^c_m = \boldsymbol{B}_n\,\boldsymbol{D}^c_m\,\Delta\boldsymbol{X}^e,\;(\Delta\boldsymbol{\varepsilon}_{n1})^s_m = \boldsymbol{B}_n\,\boldsymbol{D}^s_m\,\Delta\boldsymbol{X}^e,$$

$$(\Delta\boldsymbol{\varepsilon}^w_g)^o = \boldsymbol{B}^w_g\,\Delta\boldsymbol{d}^o_e,\;(\Delta\boldsymbol{\varepsilon}^w_g)^c_m = \boldsymbol{B}^w_g\,\Delta\boldsymbol{d}^c_{em},\;(\Delta\boldsymbol{\varepsilon}^w_g)^s_m = \boldsymbol{B}^w_g\,\Delta\boldsymbol{d}^s_{em},(\Delta\boldsymbol{\varepsilon}^u_g)^o = \boldsymbol{B}^u_g\,\Delta\boldsymbol{d}^o_e,$$

$$(\Delta\boldsymbol{\varepsilon}^u_g)^c_m = \boldsymbol{B}^u_g\,\Delta\boldsymbol{d}^c_{em},\;(\Delta\boldsymbol{\varepsilon}^u_g)^s_m = \boldsymbol{B}^u_g\,\Delta\boldsymbol{d}^s_{em},$$

$${}^{i}\boldsymbol{X}^e = \{({}^{i}\boldsymbol{d}^o_e)^{\mathrm{T}}\;\;({}^{i}\boldsymbol{d}^c_{e1})^{\mathrm{T}}\;\;({}^{i}\boldsymbol{d}^c_{e2})^{\mathrm{T}}\ldots({}^{i}\boldsymbol{d}^c_{eH})^{\mathrm{T}}\;\;({}^{i}\boldsymbol{d}^s_{e1})^{\mathrm{T}}\;\;({}^{i}\boldsymbol{d}^s_{e2})^{\mathrm{T}}\ldots({}^{i}\boldsymbol{d}^s_{eH})^{\mathrm{T}}\}^{\mathrm{T}}$$

$$\Delta\boldsymbol{X}^e = \{(\Delta\boldsymbol{d}^o_e)^{\mathrm{T}}\;\;(\Delta\boldsymbol{d}^c_{e1})^{\mathrm{T}}\;\;(\Delta\boldsymbol{d}^c_{e2})^{\mathrm{T}}\ldots(\Delta\boldsymbol{d}^c_{eH})^{\mathrm{T}}\;\;(\Delta\boldsymbol{d}^s_{e1})^{\mathrm{T}}\;\;(\Delta\boldsymbol{d}^s_{e2})^{\mathrm{T}}\ldots(\Delta\boldsymbol{d}^s_{eH})^{\mathrm{T}}\}^{\mathrm{T}} \tag{3.23}$$

In Eq. (3.23), the matrices $\boldsymbol{D}^o$, $\boldsymbol{D}^c_m$ and $\boldsymbol{D}^s_m$ ($m=1,2,3,\ldots,2H$) are the coefficient matrices of the Fourier expansion of the product ${}^{i}\boldsymbol{d}^e_I\,{}^{i}\boldsymbol{d}^e$ (Eq. 3.22b) corresponding to the constant, cosine and sine terms, respectively. The simplified expression for the Fourier expansion of the product ${}^{i}\boldsymbol{d}^e_I\,{}^{i}\boldsymbol{d}^e$ is given in the right-hand part of Eq. (3.24), where $({}^{i}\boldsymbol{d}^e_I)^o / {}^{i}\boldsymbol{d}^o_e$, $({}^{i}\boldsymbol{d}^e_I)^s_m / {}^{i}\boldsymbol{d}^s_{en}$ and $({}^{i}\boldsymbol{d}^e_I)^c_m / {}^{i}\boldsymbol{d}^c_{en}$ are the coefficient matrices/vectors corresponding to the constant, sine and cosine terms in the Fourier expansion of ${}^{i}\boldsymbol{d}^e_I / {}^{i}\boldsymbol{d}_e$. The matrices $\boldsymbol{D}^o$, $\boldsymbol{D}^c_m$ and $\boldsymbol{D}^s_m$ can be constructed in terms of these coefficient matrices/vectors by the harmonic balance.

$$\left\langle \boldsymbol{D}^o + \sum_{m=1}^{2H} \boldsymbol{D}^c_m \cos(m\Omega t) + \boldsymbol{D}^s_m \sin(m\Omega t) \right\rangle {}^{i}\boldsymbol{X}^e =$$

$$({}^{i}\boldsymbol{d}^e_I)^o\,{}^{i}\boldsymbol{d}^o_e + \left\{ \begin{array}{l} \displaystyle\sum_{m=1}^{H} \left[\begin{array}{l} \left\langle ({}^{i}\boldsymbol{d}^e_I)^o\,{}^{i}\boldsymbol{d}^c_{em} + ({}^{i}\boldsymbol{d}^e_I)^c_m\,{}^{i}\boldsymbol{d}^o_e \right\rangle \cos(m\Omega t) + \\ \left\langle ({}^{i}\boldsymbol{d}^e_I)^o\,{}^{i}\boldsymbol{d}^s_{em} + ({}^{i}\boldsymbol{d}^e_I)^s_m\,{}^{i}\boldsymbol{d}^o_e \right\rangle \sin(m\Omega t) \end{array} \right] + \\ \displaystyle\sum_{m=1}^{H}\sum_{n=1}^{H} \frac{1}{2} \left[\begin{array}{l} \left\langle ({}^{i}\boldsymbol{d}^e_I)^c_m\,{}^{i}\boldsymbol{d}^c_{en} \right\rangle \left\langle \cos(m+n)\Omega t + \cos(m-n)\Omega t \right\rangle + \\ \left\langle ({}^{i}\boldsymbol{d}^e_I)^s_m\,{}^{i}\boldsymbol{d}^s_{en} \right\rangle \left\langle \cos(m-n)\Omega t - \cos(m+n)\Omega t \right\rangle + \\ \left\langle ({}^{i}\boldsymbol{d}^e_I)^c_m\,{}^{i}\boldsymbol{d}^s_{en} \right\rangle \left\langle \sin(m+n)\Omega t - \sin(m-n)\Omega t \right\rangle + \\ \left\langle ({}^{i}\boldsymbol{d}^e_I)^s_m\,{}^{i}\boldsymbol{d}^c_{en} \right\rangle \left\langle \sin(m+n)\Omega t + \sin(m-n)\Omega t \right\rangle \end{array} \right] \end{array} \right\} \tag{3.24}$$

Now, using Eq. (3.24), the coefficient matrices of the Fourier expansions of the products ${}^{i}\boldsymbol{\Gamma}^k\,\Delta\boldsymbol{\varepsilon}^w_g$ and ${}^{i}\boldsymbol{\Gamma}^k\,\Delta\boldsymbol{\varepsilon}^u_g$ (Eqs. (3.21) and (3.19b)) can be written as given in Eq. (3.25a), where the matrices $(\boldsymbol{\Upsilon}^k_w)^o$, $(\boldsymbol{\Upsilon}^k_w)^c_m$ and $(\boldsymbol{\Upsilon}^k_w)^s_m$ ($m=1,2,3,\ldots,3H$) can be constructed following Eq. (3.25b) similar to the aforesaid construction of $\boldsymbol{D}^o$, $\boldsymbol{D}^c_m$ and $\boldsymbol{D}^s_m$. In Eq. (3.25b), the simplified expression for the Fourier expansion of ${}^{i}\boldsymbol{\Gamma}^k\,\Delta\boldsymbol{\varepsilon}^w_g$ is illustrated in the right-hand part for the construction of $(\boldsymbol{\Upsilon}^k_w)^o$, $(\boldsymbol{\Upsilon}^k_w)^c_m$

and $(\boldsymbol{\Upsilon}_w^k)_m^s$. The Fourier expansion of ${}^i\boldsymbol{\Gamma}^k\,\Delta\boldsymbol{\varepsilon}_g^u$ also appears in a similar manner to construct $(\boldsymbol{\Upsilon}_u^k)^o$, $(\boldsymbol{\Upsilon}_u^k)_m^c$ and $(\boldsymbol{\Upsilon}_u^k)_m^s$ $(m=1,2,3,...,3H)$.

$$({}^i\boldsymbol{\Gamma}^k\,\Delta\boldsymbol{\varepsilon}_g^w)^o=(\boldsymbol{\Upsilon}_w^k)^o\,\Delta\boldsymbol{X}^e,\quad ({}^i\boldsymbol{\Gamma}^k\,\Delta\boldsymbol{\varepsilon}_g^w)_m^c=(\boldsymbol{\Upsilon}_w^k)_m^c\,\Delta\boldsymbol{X}^e,\quad ({}^i\boldsymbol{\Gamma}^k\,\Delta\boldsymbol{\varepsilon}_g^w)_m^s=(\boldsymbol{\Upsilon}_w^k)_m^s\,\Delta\boldsymbol{X}^e$$

$$({}^i\boldsymbol{\Gamma}^k\,\Delta\boldsymbol{\varepsilon}_g^u)^o=(\boldsymbol{\Upsilon}_u^k)^o\,\Delta\boldsymbol{X}^e,\quad ({}^i\boldsymbol{\Gamma}^k\,\Delta\boldsymbol{\varepsilon}_g^u)_m^c=(\boldsymbol{\Upsilon}_u^k)_m^c\,\Delta\boldsymbol{X}^e,\quad ({}^i\boldsymbol{\Gamma}^k\,\Delta\boldsymbol{\varepsilon}_g^u)_m^s=(\boldsymbol{\Upsilon}_u^k)_m^s\,\Delta\boldsymbol{X}^e \tag{3.25a}$$

$$\left\langle(\boldsymbol{\Upsilon}_w^k)^o+\sum_{m=1}^{3H}(\boldsymbol{\Upsilon}_w^k)_m^c\cos(m\Omega t)+(\boldsymbol{\Upsilon}_w^k)_m^s\sin(m\Omega t)\right\rangle\Delta\boldsymbol{X}^e=$$

$$({}^i\boldsymbol{\Gamma}^k)^o\,\boldsymbol{B}_g^w\,\Delta\boldsymbol{d}_e^o+\left\{\begin{array}{l}\displaystyle\sum_{m=1}^{H}\left[\begin{array}{l}\left\langle({}^i\boldsymbol{\Gamma}^k)^o\,\boldsymbol{B}_g^w\,\Delta\boldsymbol{d}_{em}^c+({}^i\boldsymbol{\Gamma}^k)_m^c\,\boldsymbol{B}_g^w\,\Delta\boldsymbol{d}_e^o\right\rangle\cos(m\Omega t)+\\ \left\langle({}^i\boldsymbol{\Gamma}^k)^o\,\boldsymbol{B}_g^w\,\Delta\boldsymbol{d}_{em}^s+({}^i\boldsymbol{\Gamma}^k)_m^s\,\boldsymbol{B}_g^w\,\Delta\boldsymbol{d}_e^o\right\rangle\sin(m\Omega t)\end{array}\right]+\\ \displaystyle\sum_{m=1}^{2H}\sum_{n=1}^{H}\frac{1}{2}\left[\begin{array}{l}\left\langle({}^i\boldsymbol{\Gamma}^k)_m^c\,\boldsymbol{B}_g^w\,\Delta\boldsymbol{d}_{en}^c\right\rangle\left\langle\cos(m+n)\Omega t+\cos(m-n)\Omega t\right\rangle+\\ \left\langle({}^i\boldsymbol{\Gamma}^k)_m^s\,\boldsymbol{B}_g^w\,\Delta\boldsymbol{d}_{en}^s\right\rangle\left\langle\cos(m-n)\Omega t-\cos(m+n)\Omega t\right\rangle+\\ \left\langle({}^i\boldsymbol{\Gamma}^k)_m^c\,\boldsymbol{B}_g^w\,\Delta\boldsymbol{d}_{en}^s\right\rangle\left\langle\sin(m+n)\Omega t-\sin(m-n)\Omega t\right\rangle+\\ \left\langle({}^i\boldsymbol{\Gamma}^k)_m^s\,\boldsymbol{B}_g^w\,\Delta\boldsymbol{d}_{en}^c\right\rangle\left\langle\sin(m+n)\Omega t+\sin(m-n)\Omega t\right\rangle\end{array}\right]\end{array}\right\} \tag{3.25b}$$

Substituting Eqs. (3.19a), (3.19b), (3.23) and (3.25a) in Eq. (3.21), the linearized incremental governing equation of motion of a typical element can be obtained as

$$\boldsymbol{K}_t^e\,\Delta\boldsymbol{X}^e=\boldsymbol{R}^e+\boldsymbol{R}_\Omega^e\,\Delta\Omega$$

$$\boldsymbol{R}^e=\boldsymbol{P}^e\,p_t^o+\boldsymbol{P}_u^e\,p_{tu}^o-\boldsymbol{K}_m^e\,{}^i\boldsymbol{X}^e,\quad \boldsymbol{R}_\Omega^e=-(\partial\boldsymbol{K}_m^e/\partial\Omega_i)\,{}^i\boldsymbol{X}^e,$$

$$\boldsymbol{K}_m^e=\boldsymbol{K}_l^e-\Omega_i^2\boldsymbol{M}^e+(1/2)\boldsymbol{K}_{n1}^e+\boldsymbol{K}_{nt}^e+(1/2)\boldsymbol{K}_{n4}^e,$$

$$\boldsymbol{K}_t^e=\boldsymbol{K}_l^e-\Omega_i^2\boldsymbol{M}^e+\boldsymbol{K}_{n1}^e+\boldsymbol{K}_{nt}^e+\boldsymbol{K}_g^e+\boldsymbol{K}_{n4}^e \tag{3.26}$$

where, the matrices $\boldsymbol{M}^e$, $\boldsymbol{K}_l^e$, $\boldsymbol{P}^e$, $\boldsymbol{P}_u^e$, $\boldsymbol{K}_{n1}^e$, $\boldsymbol{K}_g^e$, $\boldsymbol{K}_{nt}^e$ and $\boldsymbol{K}_{n4}^e$ can be constructed according to Eq. (3.27).

$$(\delta\Delta\boldsymbol{X}^e)^{\mathrm{T}}\boldsymbol{M}^e\Delta\boldsymbol{X}^e=\sum_{m=1}^{H}m^2\left\langle(\delta\Delta\boldsymbol{d}_{em}^c)^{\mathrm{T}}\boldsymbol{M}_s^e\,\Delta\boldsymbol{d}_{em}^c+(\delta\Delta\boldsymbol{d}_{em}^s)^{\mathrm{T}}\boldsymbol{M}_s^e\,\Delta\boldsymbol{d}_{em}^s\right\rangle,$$

$$(\delta\Delta\boldsymbol{X}^e)^{\mathrm{T}}\boldsymbol{K}_l^e\Delta\boldsymbol{X}^e=2(\delta\Delta\boldsymbol{d}_e^o)^{\mathrm{T}}\boldsymbol{K}_{sl}^e\,\Delta\boldsymbol{d}_e^o+\sum_{m=1}^{H}\left\langle\begin{array}{l}(\delta\Delta\boldsymbol{d}_{em}^c)^{\mathrm{T}}\boldsymbol{K}_{sl}^e\,(f_m^c\Delta\boldsymbol{d}_{em}^c+f_m^s\Delta\boldsymbol{d}_{em}^s)+\\ (\delta\Delta\boldsymbol{d}_{em}^s)^{\mathrm{T}}\boldsymbol{K}_{sl}^e\,(f_m^c\Delta\boldsymbol{d}_{em}^s-f_m^s\Delta\boldsymbol{d}_{em}^c)\end{array}\right\rangle,$$

$$(\delta\Delta\boldsymbol{X}^e)^{\mathrm{T}}\boldsymbol{K}_{n1}^e\Delta\boldsymbol{X}^e=\left\{2(\delta\Delta\boldsymbol{d}_e^o)^{\mathrm{T}}\boldsymbol{K}_{sn1}^e\,\boldsymbol{D}^o+\sum_{m=1}^{H}\left\langle\begin{array}{l}(\delta\Delta\boldsymbol{d}_{em}^c)^{\mathrm{T}}\boldsymbol{K}_{sn1}^e(f_m^c\boldsymbol{D}_m^c+f_m^s\boldsymbol{D}_m^s)+\\ (\delta\Delta\boldsymbol{d}_{em}^s)^{\mathrm{T}}\boldsymbol{K}_{sn1}^e\,(f_m^c\boldsymbol{D}_m^s-f_m^s\boldsymbol{D}_m^c)\end{array}\right\rangle\right\}\Delta\boldsymbol{X}^e,$$

$$(\delta\Delta\boldsymbol{X}^e)^{\mathrm{T}}\boldsymbol{K}_{nt}^e\Delta\boldsymbol{X}^e=(\delta\Delta\boldsymbol{X}^e)^{\mathrm{T}}\left\{\begin{array}{l}2(\boldsymbol{D}^o)^{\mathrm{T}}(\boldsymbol{K}_{sn1}^e)^{\mathrm{T}}\Delta\boldsymbol{d}_e^o+\\ \sum_{m=1}^{H}\left\langle\begin{array}{l}(\boldsymbol{D}_m^c)^{\mathrm{T}}(\boldsymbol{K}_{sn1}^e)^{\mathrm{T}}(f_m^c\Delta\boldsymbol{d}_{em}^c+f_m^s\Delta\boldsymbol{d}_{em}^s)+\\ (\boldsymbol{D}_m^s)^{\mathrm{T}}(\boldsymbol{K}_{sn1}^e)^{\mathrm{T}}(f_m^c\Delta\boldsymbol{d}_{em}^s-f_m^s\Delta\boldsymbol{d}_{em}^c)\end{array}\right\rangle\end{array}\right\},$$

$$\boldsymbol{K}_{n4}^e=2(\boldsymbol{D}^o)^{\mathrm{T}}\boldsymbol{K}_{sn4}^e\boldsymbol{D}^o+\sum_{m=1}^{2H}\left\langle\begin{array}{l}(\boldsymbol{D}_m^c)^{\mathrm{T}}\boldsymbol{K}_{sn4}^e(f_m^c\boldsymbol{D}_m^c+f_m^s\boldsymbol{D}_m^s)+\\ (\boldsymbol{D}_m^s)^{\mathrm{T}}\boldsymbol{K}_{sn4}^e(f_m^c\boldsymbol{D}_m^s-f_m^s\boldsymbol{D}_m^c)\end{array}\right\rangle,$$

$$(\delta\Delta\boldsymbol{X}^e)^{\mathrm{T}}\boldsymbol{K}_g^e\Delta\boldsymbol{X}^e=\left\{2(\delta\Delta\boldsymbol{d}_e^o)^{\mathrm{T}}\boldsymbol{K}_g^o+\sum_{m=1}^{H}\left\langle(\delta\Delta\boldsymbol{d}_{em}^c)^{\mathrm{T}}\boldsymbol{K}_{gm}^c+(\delta\Delta\boldsymbol{d}_{em}^s)^{\mathrm{T}}\boldsymbol{K}_{gm}^s\right\rangle\right\}\Delta\boldsymbol{X}^e;$$

$$(\delta\Delta\boldsymbol{X}_e)^{\mathrm{T}}\boldsymbol{P}^e=(\delta\Delta\boldsymbol{d}_{em}^c)^{\mathrm{T}}\boldsymbol{P}_s^e,\ (\delta\Delta\boldsymbol{X}_e)^{\mathrm{T}}\boldsymbol{P}_u^e=(\delta\Delta\boldsymbol{d}_{em}^c)^{\mathrm{T}}\boldsymbol{P}_{su}^e\ \text{ at }\ m=1 \tag{3.27}$$

In Eq. (3.26), the overall elemental stiffness ($\boldsymbol{K}_m^e$) and tangent stiffness ($\boldsymbol{K}_t^e$) matrices are to be constructed through their component matrices, as given in Eq. (3.27). However, the stiffness matrix per unit change of frequency ($\partial\boldsymbol{K}_m^e/\partial\Omega_i$, Eq. (3.26)) can be obtained similar to $\boldsymbol{K}_m^e$ (Eqs. (3.26) and (3.27)), where the coefficient matrices corresponding to the frequency-independent terms are to be omitted, and the parameters f_m^c and f_m^s are to be replaced by $\partial f_m^c/\partial\Omega_i$ and $\partial f_m^s/\partial\Omega_i$, respectively. The different elemental matrices ($\boldsymbol{M}_s^e$, $\boldsymbol{K}_{sl}^e$, $\boldsymbol{K}_{sn1}^e$, $\boldsymbol{K}_g^o$, $\boldsymbol{K}_{gm}^c$, $\boldsymbol{K}_{gm}^s$ and $\boldsymbol{K}_{sn4}^e$) and vectors ($\boldsymbol{P}_s^e$, $\boldsymbol{P}_{su}^e$) appearing in Eq. (3.27) are given in Eq. (3.28) where A^e is the area of a typical element.

$$\boldsymbol{M}_s^e=\int_{A^e}\boldsymbol{N}^{\mathrm{T}}\rho^k\boldsymbol{N}\ b\,dA^e,\ \boldsymbol{K}_{sl}^e=\int_{A^e}(\boldsymbol{B}_l)^{\mathrm{T}}\boldsymbol{C}^k\boldsymbol{B}_l b\,dA^e,$$

$$\boldsymbol{K}_{sn1}^e=\int_{A^e}(\boldsymbol{B}_l)^{\mathrm{T}}\boldsymbol{C}^k\boldsymbol{B}_n b\,dA^e,\ \boldsymbol{K}_{sn4}^e=\int_{A^e}(\boldsymbol{B}_n)^{\mathrm{T}}\boldsymbol{C}^k\boldsymbol{B}_n b\,dA^e,$$

$$\boldsymbol{P}_{su}^e=\int_{A^e}(\boldsymbol{l}_t\boldsymbol{N})^{\mathrm{T}}\Big|_{z=h}b\,dA^e,\ \boldsymbol{P}_s^e=\int_{A^e}(\boldsymbol{l}_t\boldsymbol{N})^{\mathrm{T}}\Big|_{(x_m,z_m)}dA^e,$$

$$\boldsymbol{K}_{gm}^c=\int_{A^e}\left\langle(\boldsymbol{B}_g^w)^{\mathrm{T}}(\boldsymbol{\Upsilon}_w^k)_m^c+(\boldsymbol{B}_g^u)^{\mathrm{T}}(\boldsymbol{\Upsilon}_u^k)_m^c\right\rangle b\,dA^e,$$

$$\boldsymbol{K}_{gm}^s=\int_{A^e}\left\langle(\boldsymbol{B}_g^w)^{\mathrm{T}}(\boldsymbol{\Upsilon}_w^k)_m^s+(\boldsymbol{B}_g^u)^{\mathrm{T}}(\boldsymbol{\Upsilon}_u^k)_m^s\right\rangle b\,dA^e,$$

$$\boldsymbol{K}_g^o=\int_{A^e}\left\langle(\boldsymbol{B}_g^w)^{\mathrm{T}}(\boldsymbol{\Upsilon}_w^k)^o+(\boldsymbol{B}_g^u)^{\mathrm{T}}(\boldsymbol{\Upsilon}_u^k)^o\right\rangle b\,dA^e,\quad m=1,2,...,H \tag{3.28}$$

It may be noted here that the aforesaid elemental matrices are formed in a generalized manner for both the elastic and viscoelastic materials within the sandwich beam, where the values of the parameters f_m^c and f_m^s are 1 and 0, respectively, for an element made of elastic material. However, assembly of the

elemental matrices (Eq. (3.26)) provides the FE equations of motion of the sandwich beam in the frequency domain as follows

$$\boldsymbol{K}_t\,\Delta\boldsymbol{X} = \boldsymbol{R} + \boldsymbol{R}_\Omega\,\Delta\Omega$$

$$\boldsymbol{R} = \boldsymbol{P}\ p_t^o + \boldsymbol{P}_u\ p_{tu}^o - \boldsymbol{K}_m\ {}^i\boldsymbol{X}\,,\ \boldsymbol{R}_\Omega = -(\partial\boldsymbol{K}_m/\partial\Omega_i)\ {}^i\boldsymbol{X}\,,$$

$$\boldsymbol{K}_m = \boldsymbol{K}_l - \Omega_i^2\boldsymbol{M} + (1/2)\boldsymbol{K}_{n1} + \boldsymbol{K}_{nt} + (1/2)\boldsymbol{K}_{n4}\,,$$

$$\boldsymbol{K}_t = \boldsymbol{K}_l - \Omega_i^2\boldsymbol{M} + \boldsymbol{K}_{n1} + \boldsymbol{K}_{nt} + \boldsymbol{K}_g + \boldsymbol{K}_{n4} \qquad (3.29)$$

where, $\boldsymbol{K}_m$ and $\boldsymbol{K}_t$ are the global stiffness and tangent stiffness matrices, respectively; $\boldsymbol{R}$ is the global residue vector; $\boldsymbol{R}_\Omega$ is the global load vector per unit increment of excitation frequency; ${}^i\boldsymbol{X}$ is the global nodal displacement vector and $\Delta\boldsymbol{X}$ is the incremental nodal displacement vector.

However, in the present sandwich beam, the core is made of a soft viscoelastic material so that the viscoelastic core has a negligibly small contribution to the stiffness of the overall structure as compared to the stiff elastic face layers. In this case, the contribution of the viscoelastic material to the geometric stiffness matrix ($\boldsymbol{K}_g^e$, Eq. (3.27)) may be omitted to ease the complex formulation of this matrix ($\boldsymbol{K}_g^e$, Eq. (3.27)) and also to reduce the computational time. This assumption is presently made for the sandwich beam, and its plausibility is verified through numerical experimentation, as presented in Section 3.5.3. However, according to this assumption, the geometric stiffness term ($(\delta\Delta\boldsymbol{\varepsilon}_{n2})^{\mathrm{T}}\,{}^i\boldsymbol{\sigma}^k$, Eq. (3.7)) can be written in the following form

$$(\delta\Delta\boldsymbol{\varepsilon}_{n2})^{\mathrm{T}}\,{}^i\boldsymbol{\sigma}^k = ({}^i\boldsymbol{d}_I^e\,\delta\Delta\boldsymbol{d}^e)^{\mathrm{T}}\,\boldsymbol{K}_{sn3}^e\,\Delta\boldsymbol{d}^e + (1/2)({}^i\boldsymbol{d}_I^e\,\delta\Delta\boldsymbol{d}^e)^{\mathrm{T}}\,\boldsymbol{K}_{sn5}^e\,{}^i\boldsymbol{d}_I^e\,\Delta\boldsymbol{d}^e \qquad (3.30a)$$

$$\boldsymbol{K}_{sn3}^e = \int_{A^e}\left\langle(\boldsymbol{B}_1^u)^{\mathrm{T}}\boldsymbol{C}^k\boldsymbol{B}_l\boldsymbol{R}_x^u + (\boldsymbol{B}_1^w)^{\mathrm{T}}\boldsymbol{C}^k\boldsymbol{B}_l\boldsymbol{R}_x^w + (\boldsymbol{B}_2^u)^{\mathrm{T}}\boldsymbol{C}^k\boldsymbol{B}_l\boldsymbol{R}_z^u + (\boldsymbol{B}_2^w)^{\mathrm{T}}\boldsymbol{C}^k\boldsymbol{B}_l\boldsymbol{R}_z^w\right\rangle b\,dA^e,$$

$$\boldsymbol{K}_{sn5}^e = \int_{A^e}\left\langle\boldsymbol{A}_{1w}^k\boldsymbol{R}_x^w + \boldsymbol{A}_{2w}^k\boldsymbol{R}_z^w + \boldsymbol{A}_{1u}^k\boldsymbol{R}_x^u + \boldsymbol{A}_{2u}^k\boldsymbol{R}_z^u\right\rangle b\,dA^e\,,$$

$$\boldsymbol{A}_{1u}^k = (\boldsymbol{B}_1^u\boldsymbol{R}_x^w)^{\mathrm{T}}\boldsymbol{C}^k\boldsymbol{B}_1^w + (\boldsymbol{B}_1^u\boldsymbol{R}_x^u)^{\mathrm{T}}\boldsymbol{C}^k\boldsymbol{B}_1^u + (\boldsymbol{B}_1^u\boldsymbol{R}_z^w)^{\mathrm{T}}\boldsymbol{C}^k\boldsymbol{B}_2^w + (\boldsymbol{B}_1^u\boldsymbol{R}_z^u)^{\mathrm{T}}\boldsymbol{C}^k\boldsymbol{B}_2^u\,,$$

$$\boldsymbol{A}_{2u}^k = (\boldsymbol{B}_2^u\boldsymbol{R}_x^w)^{\mathrm{T}}\boldsymbol{C}^k\boldsymbol{B}_1^w + (\boldsymbol{B}_2^u\boldsymbol{R}_x^u)^{\mathrm{T}}\boldsymbol{C}^k\boldsymbol{B}_1^u + (\boldsymbol{B}_2^u\boldsymbol{R}_z^w)^{\mathrm{T}}\boldsymbol{C}^k\boldsymbol{B}_2^w + (\boldsymbol{B}_2^u\boldsymbol{R}_z^u)^{\mathrm{T}}\boldsymbol{C}^k\boldsymbol{B}_2^u\,,$$

$$\boldsymbol{A}_{1w}^k = (\boldsymbol{B}_1^w\boldsymbol{R}_x^w)^{\mathrm{T}}\boldsymbol{C}^k\boldsymbol{B}_1^w + (\boldsymbol{B}_1^w\boldsymbol{R}_x^u)^{\mathrm{T}}\boldsymbol{C}^k\boldsymbol{B}_1^u + (\boldsymbol{B}_1^w\boldsymbol{R}_z^w)^{\mathrm{T}}\boldsymbol{C}^k\boldsymbol{B}_2^w + (\boldsymbol{B}_1^w\boldsymbol{R}_z^u)^{\mathrm{T}}\boldsymbol{C}^k\boldsymbol{B}_2^u\,,$$

$$\boldsymbol{A}_{2w}^k = (\boldsymbol{B}_2^w\boldsymbol{R}_x^w)^{\mathrm{T}}\boldsymbol{C}^k\boldsymbol{B}_1^w + (\boldsymbol{B}_2^w\boldsymbol{R}_x^u)^{\mathrm{T}}\boldsymbol{C}^k\boldsymbol{B}_1^u + (\boldsymbol{B}_2^w\boldsymbol{R}_z^w)^{\mathrm{T}}\boldsymbol{C}^k\boldsymbol{B}_2^w + (\boldsymbol{B}_2^w\boldsymbol{R}_z^u)^{\mathrm{T}}\boldsymbol{C}^k\boldsymbol{B}_2^u\,,$$

$$\text{for } k = 1 \qquad (3.30b)$$

Using Eq. (3.30a), the geometric stiffness matrix ($\boldsymbol{K}_g^e$) can be constructed from the following relations

$$\boldsymbol{K}_g^e = \boldsymbol{K}_{n3}^e + (1/2)\boldsymbol{K}_{n5}^e$$

$$(\Delta \boldsymbol{X}^e)^{\mathrm{T}} \boldsymbol{K}_{n3}^e \Delta \boldsymbol{X}^e = \left\{ \begin{array}{l} 2(\delta \Delta \boldsymbol{d}_e^o)^{\mathrm{T}} \boldsymbol{K}_{sn3}^e \boldsymbol{D}^o + \\ \sum_{m=1}^{H} \left\langle (\delta \Delta \boldsymbol{d}_{em}^c)^{\mathrm{T}} \boldsymbol{K}_{sn3}^e \boldsymbol{D}_m^c + (\delta \Delta \boldsymbol{d}_{em}^s)^{\mathrm{T}} \boldsymbol{K}_{sn3}^e \boldsymbol{D}_m^s \right\rangle \end{array} \right\} \Delta \boldsymbol{X}^e ,$$

$$\boldsymbol{K}_{n5}^e = 2(\boldsymbol{D}^o)^{\mathrm{T}} \boldsymbol{K}_{sn5}^e \boldsymbol{D}^o + \sum_{m=1}^{2H} \left\langle (\boldsymbol{D}_m^c)^{\mathrm{T}} \boldsymbol{K}_{sn5}^e \boldsymbol{D}_m^c + (\boldsymbol{D}_m^s)^{\mathrm{T}} \boldsymbol{K}_{sn5}^e \boldsymbol{D}_m^s \right\rangle \tag{3.31}$$

3.4. Governing equation of motion in the time-domain

In order to verify the accuracy of the aforesaid FE formulation using HBM, the steady-state responses of the sandwich beam are also evaluated by deriving the governing equation of motion in the time-domain. For this derivation of the governing equation of motion in the time-domain, the fractional Zener constitutive model (Eq. (3.12a)-(3.12b)) is taken at a discrete time following the Grunwald definition (Galucio et al., 2004) where a time-span of interest is divided into a finite number (N_t) of uniform time steps (Δt). Accordingly, the stress vector ($\boldsymbol{\sigma}_{q+1}^k$, $k=2$) and the anelastic strain vector (Eq. (3.12b)) at any point within the viscoelastic material are given in Eq. (3.32) at the $(q+1)^{th}$ time-step ($q=0,1,2,...,N_t$).

$$\boldsymbol{\sigma}_{q+1}^k = \boldsymbol{C}^k \; f_1^k \, \boldsymbol{\varepsilon}_{q+1} + \boldsymbol{C}^k \, \bar{f}_1^k \sum_{j=1}^{q+1} A_{j+1} \, \bar{\boldsymbol{\varepsilon}}_{q+1-j} ,$$

$$\bar{\boldsymbol{\varepsilon}}_{q+1} = (1-c_b) f \, \boldsymbol{\varepsilon}_{q+1} - c_b \sum_{j=1}^{q+1} A_{j+1} \, \bar{\boldsymbol{\varepsilon}}_{q+1-j} ,$$

$$c_b = \tau^\alpha \Big/ \left\langle \tau^\alpha + (\Delta t)^\alpha \right\rangle , \; A_{j+1} = \frac{j-\alpha-1}{j} A_j ,$$

$$\bar{f}_1^k = c_b \, E_\infty / E_o \; , \; f_1^k = 1 + \left\langle c_b \, (E_\infty - E_o)/E_o \right\rangle \text{ for } k=2 \tag{3.32}$$

In Eq. (3.32), A_j ($j=1,2,....,N_t+1$, $A_j=1$ for $j=1$) are the Grunwald coefficients (Galucio et al., 2004). Equation (3.32) can also be used for the elastic material ($k=1$) in the sandwich beam by taking $\bar{f}_1^k = 0$ and $f_1^k = 1$. However, this constitutive relation (Eq. (3.32)) is introduced in Eq. (3.4) to obtain the governing equation of motion at a discrete-time ($(q+1)^{th}$ time-step), as illustrated in Eq. (3.33). Subsequently, the FE discretization of the displacement and strain vectors

are introduced to obtain the elemental governing equation of motion at a discrete time ($(q+1)^{th}$ time-step), as given in Eq. (3.34a).

$$\sum_{k=1}^{2}\int_{A^k}\left\{\begin{array}{l}\left\langle(\delta\boldsymbol{d}_s)_{q+1}\right\rangle^{\mathrm{T}}\rho^k(\ddot{\boldsymbol{d}}_s)_{q+1}\\ -\left\langle\boldsymbol{l}_t(\delta\boldsymbol{d}_s)_{q+1}\big|_{z=h}\right\rangle^{\mathrm{T}}(p_{tu})_{q+1}-(\boldsymbol{l}_t\,\delta\Delta\boldsymbol{d}_s\big|_{(x_l,z_l)})^{\mathrm{T}}(p_t)_{q+1}\\ +\left\langle(\delta\boldsymbol{\varepsilon}_l+\delta\boldsymbol{\varepsilon}_n)_{q+1})\right\rangle^{\mathrm{T}}\left\langle\boldsymbol{C}^k\,f_1^k\,\boldsymbol{\varepsilon}_{q+1}+\boldsymbol{C}^k\,\bar{f}_1^k\sum_{j=1}^{q+1}A_{j+1}\,\bar{\boldsymbol{\varepsilon}}_{q+1-j}\right\rangle\end{array}\right\}b\,dA^k=0 \tag{3.33}$$

$$\boldsymbol{M}_s^e\,\ddot{\boldsymbol{d}}_{q+1}^e+f_1^k\left\langle\boldsymbol{K}_{sl}^e+(\boldsymbol{K}_{sn}^e)_{q+1}\right\rangle\boldsymbol{d}_{q+1}^e=\boldsymbol{P}_s^e\,(p_t)_{q+1}+\boldsymbol{P}_{su}^e\,(p_{tu})_{q+1}+(\bar{\boldsymbol{P}}_s^e)_{q+1},$$

$$(\boldsymbol{K}_{sn}^e)_{q+1}=(1/2)\left\{\boldsymbol{K}_{sn1}^e(\boldsymbol{d}_I^e)_{q+1}+\left\langle(\boldsymbol{d}_I^e)_{q+1}\right\rangle^{\mathrm{T}}\boldsymbol{K}_{sn4}^e(\boldsymbol{d}_I^e)_{q+1}\right\}+\left\langle(\boldsymbol{d}_I^e)_{q+1}\right\rangle^{\mathrm{T}}(\boldsymbol{K}_{sn1}^e)^{\mathrm{T}},$$

$$(\bar{\boldsymbol{P}}_s^e)_{q+1}=-\int_{A^e}\bar{f}_1^k\left\langle\boldsymbol{B}_l+\boldsymbol{B}_n\,(\boldsymbol{d}_I^e)_{q+1}\right\rangle^{\mathrm{T}}\boldsymbol{C}^k\left(\sum_{j=1}^{q+1}A_{j+1}\,\bar{\boldsymbol{\varepsilon}}_{q+1-j}^e\right)b\,dA^e \tag{3.34a}$$

$$\bar{\boldsymbol{\varepsilon}}_{q+1}^e=f(1-c_b)(\boldsymbol{\varepsilon}_s^e)_{q+1}-c_b\left(\sum_{j=1}^{q+1}A_{j+1}\,\bar{\boldsymbol{\varepsilon}}_{q+1-j}^e\right),$$

$$(\boldsymbol{\varepsilon}_s^e)_{q+1}=\frac{1}{A^e}\int_{A^e}\left\langle\boldsymbol{B}_l+(1/2)\boldsymbol{B}_n\,(\boldsymbol{d}_I^e)_{q+1}\right\rangle\boldsymbol{d}_{q+1}^e\,dA^e \tag{3.34b}$$

In Eq. (3.34a), $\boldsymbol{d}_{q+1}^e$ is the elemental nodal displacement vector at $(q+1)^{th}$ time-step. The elemental matrices ($\boldsymbol{K}_{sl}^e$, $\boldsymbol{K}_{sn1}^e$, $\boldsymbol{K}_{sn4}^e$) and vectors ($\boldsymbol{P}_s^e$, $\boldsymbol{P}_{su}^e$) are defined in Eq. (3.28). Also, $(\bar{\boldsymbol{P}}_s^e)_{q+1}$ represents the elemental memory-load vector at $(q+1)^{th}$ time-step, and it depends on the anelastic strain history ($\bar{\boldsymbol{\varepsilon}}_{q+1-j}^e$, $j=1,2,..,q+1$) where the anelastic strain at a discrete-time is taken by its average value over an element (Eq. (3.34b)). However, by assembling the element matrices in Eq. (3.34a), the FE equation of motion of the sandwich beam at $(q+1)^{th}$ time-step can be obtained as

$$\boldsymbol{M}_s\,\ddot{\boldsymbol{d}}_{q+1}+\left\langle\boldsymbol{K}_{ll}+(\boldsymbol{K}_{nn})_{q+1}\right\rangle\boldsymbol{d}_{q+1}=\boldsymbol{P}_s\,(p_t)_{q+1}+\boldsymbol{P}_{su}\,(p_{tu})_{q+1}+(\bar{\boldsymbol{P}}_s)_{q+1}$$

$$\boldsymbol{K}_{ll}=\sum_{k=1}^{2}f_1^k\boldsymbol{K}_{sl}^k,\;(\boldsymbol{K}_{nn})_{q+1}=\sum_{k=1}^{2}f_1^k(\boldsymbol{K}_{sn}^k)_{q+1} \tag{3.35}$$

where, $\boldsymbol{K}_{sl}^k$ and $(\boldsymbol{K}_{sn}^k)_{q+1}$ are obtained by assembling the elemental matrices $\boldsymbol{K}_{sl}^e$ and $(\boldsymbol{K}_{sn}^e)_{q+1}$, respectively, for the k^{th} material in the sandwich beam. Equation (3.35) is used in conjunction with the Newmark time-integration method to obtain

the steady-state responses of the sandwich beam in the time-domain for the transverse harmonic load.

3.5. Results and discussion

In this section, the numerical results are presented mainly to demonstrate the computational advantages of the present FE formulation for the evaluation of nonlinear frequency responses of a viscoelastic structure using HBM. The length (L), width (b) and thickness (h) of the sandwich beam are considered as 0.4 m, 12 mm and 6 mm, respectively. Within the total thickness (h = 6 mm), the elastic face layers are taken with a thickness ($h_{s1} = h_{s2}$) of 2 mm. The elastic face layers are considered to be made of Aluminum (E = 70.3 GPa, ν = 0.345, ρ =2690 kg/m^3 (Galucio et al., 2004)), and the viscoelastic material for the core layer is taken as 3M ISD 112 (ν = 0.499, ρ =1600 kg/m^3 (Galucio et al., 2004)). Unless otherwise mentioned, the viscoelastic core layer is modelled by the four-parameter fractional Zener model, where the model parameters are E_o = 1.5 MPa, E_∞ = 69.9495 MPa, α = 0.7915 and τ = 0.014052 ms (Galucio et al., 2004). The ends of the sandwich beam are considered as fully clamped ends while it operates under the uniformly distributed transverse harmonic load. Under this dynamic load, the transverse displacement-amplitude (w) at the middle point of the sandwich beam is evaluated within a range of the excitation frequency (Ω), and it is presented in the numerical results.

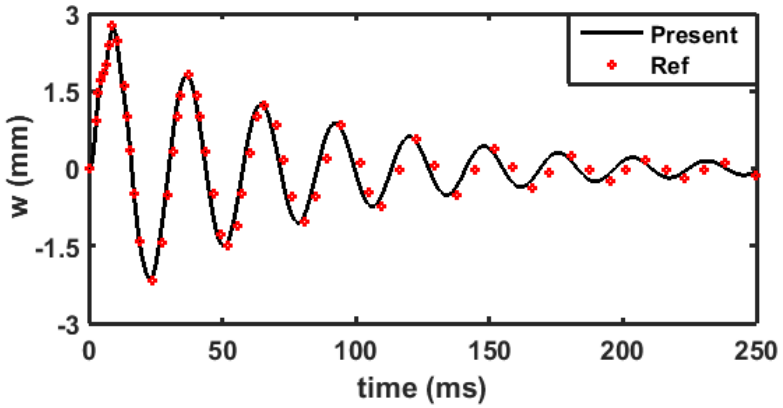

Fig. 3.2. Verification of the present FE code for evaluation of transient responses of the sandwich beam based on the fractional Zener model (Ref. (Galucio et al., 2004)).

3.5.1. Verification of the present FE formulation in the time/frequency domain

Initially, to verify the present FE code for evaluation of responses of the sandwich beam in the time-domain, the beam is considered to operate under a triangular

impulse load at its free end, and the corresponding transient response is illustrated in Fig. 3.2. A similar result for an identical sandwich beam is available in (Galucio et al., 2004), which is also furnished in Fig. 3.2. It may be observed from Fig. 3.2 that the present result is in good agreement with the reference result. This comparison verifies the present FE formulation (Section 3.4) and the implementation of the Newmark time-integration method in the evaluation of transient responses of the sandwich beam based on the fractional Zener model.

Initially, an FE mesh convergence study is performed by evaluating the peak displacement amplitude of the nonlinear frequency response of the sandwich beam with the increasing number of elements. The number of harmonic terms (H) in the HBM and the load-amplitude (p_t^o) are considered as 7 and 4000 N/m^2, respectively. This convergence study shows the sufficient numerical accuracy in the result for the minimum number of elements as 100 (100 element divisions in $x-$direction and one element division in $z-$direction) in each of the elastic layers and 200 (100 element divisions in $x-$direction and 2 element divisions in $z-$direction) in viscoelastic core layer of the sandwich beam. Accordingly, the same FE mesh is considered for evaluation of further numerical results.

In the implementation of HBM for evaluation of nonlinear frequency responses of the viscoelastic sandwich beam, the corresponding periodic solution is assumed according to the Fourier series with a finite number (H) of harmonic terms (Eq. (3.9)). So, first, a convergence study is carried out to decide an appropriate number (H) of harmonic terms for achieving sufficient numerical accuracy in the results. It is carried out by gradually increasing the number of harmonic terms in the assumed solution while a load amplitude (p_t^o) is considered as 4000 N/m^2. The corresponding nonlinear frequency responses of the sandwich beam are illustrated in Fig. 3.3(a), where the governing equation of motion in the frequency-domain (Eq. (3.29)) is solved using a numerical continuation method (Cheung et al., 1990). However, this result suggests at least the first seven harmonic terms (H = 7) in the Fourier expansion of nodal displacements (Eq. (3.9)) for achieving sufficient numerical accuracy in the nonlinear frequency responses of the viscoelastic sandwich beam. It is followed to evaluate the subsequent results.

Further, it is important to observe from Fig. 3.3(a) that the sandwich beam undergoes fundamental as well as superharmonic resonances within the frequency range of interest. Here, the superharmonic resonance does not appear in the frequency response for the consideration of a low or insufficient number of

harmonic terms in the assumed solution. It basically indicates the requirement of a large number of harmonic terms in the assumed solution for a good estimation of nonlinear frequency responses of a viscoelastic structure. In this aspect, the present generalized FE formulation for an arbitrary number of harmonic terms in HBM may be useful in the analysis of a robust viscoelastctic structure, while the available HBM-based FE formulations in this line (Jacques et al., 2010; Lewandowski and Wielentejczyk, 2017; Litewka and Lewandowski, 2017a; Wielentejczyk and Lewandowski, 2019, 2017) are addressed considering one or two harmonic terms.

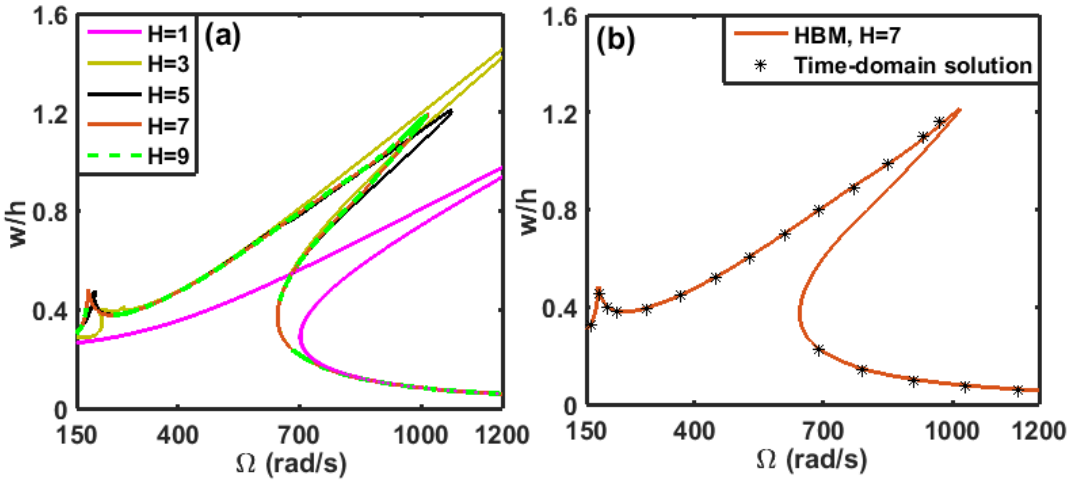

Fig. 3.3. (a) Convergence study for an appropriate number (H) of harmonic terms in implementation of HBM (p_t^o = 4000 N/m²), (b) verification of the present FE formulation for nonlinear frequency response analysis of viscoelastic structures using HBM.

However, the accuracy of the present FE formulation in conjunction with HBM is further verified by evaluating similar frequency responses through the FE formulation of the same problem in the time-domain (Section 3.4). These results are illustrated in Fig. 3.3(b), where it is clear that the solutions obtained from the HBM-based FE formulation are in excellent agreement with similar solutions obtained from the time-domain FE formulation. It may be noted here that the present HBM-based FE formulation for viscoelastic structures is not a conventional one in several aspects, namely (i) reduction of various time-domain viscoelastic constitutive models in a generalized form (Eq. (3.13a)) for the nonlinear frequency response analysis of viscoelastic structures using HBM, (ii) exploitation of orthogonality of Fourier basis functions (Eq. (3.20)-(3.21)) to ease the formulation of the nonlinear stiffness matrix in conjunction with HBM, (iii) avoidance of numerical time-integration over a time-period (Eq. (3.20)-(3.21)) to reduce the computational time in the implementation of HBM and (iv) a special

formulation of the nonlinear strain vector (Eq. (3.22b)) to ease the derivation of the nonlinear stiffness matrix. The implementation of these aspects towards a new FE formulation for viscoelastic structures using HBM is verified through the comparison study in Fig. 3.3(b).

3.5.2. Computational efficiency of present FE formulation using HBM

In the conventional FE formulation of a viscoelastic/elastic structure using HBM, the various system matrices and vectors are first formed in terms of the Fourier expansion of displacement vector (Eq. (3.9)), which are subsequently integrated over a time-period using Galerkin method. This reduction of the system matrices and vectors is commonly carried out by a numerical time-integration method, which involves a high computational time due to a large number of nodal degrees of freedom in the FE model. However, in order to avoid this numerical time-integration towards the reduction of the computational time, presently HBM is implemented prior to the FE discretization using the orthogonality of Fourier basis functions (Eq. (3.20)), as demonstrated in Section 3.3. The corresponding reduction of the computational time is presently verified.

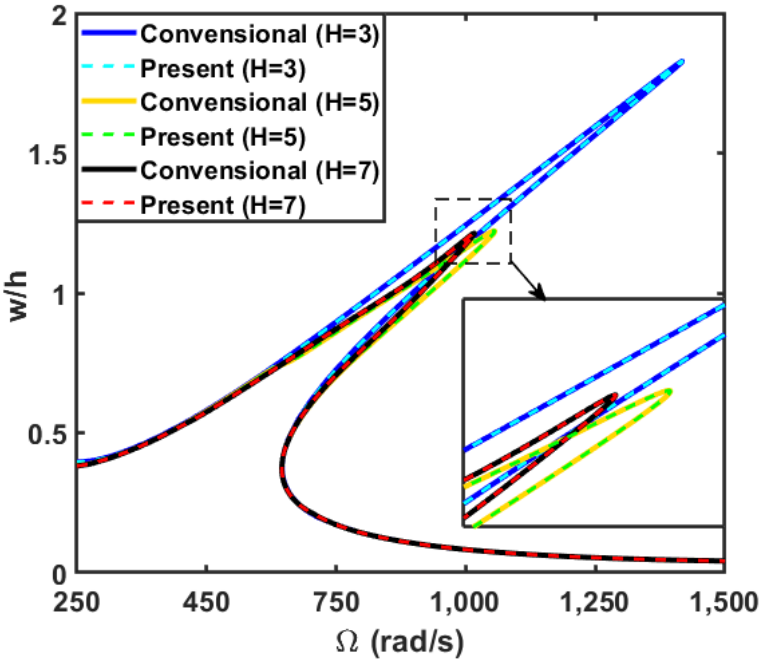

Fig. 3.4. Nonlinear frequency responses of the viscoelastic sandwich beam are evaluated using either conventional or present strategy in the implementation of HBM.

For this verification, the nonlinear frequency responses of the viscoelastic sandwich beam are evaluated for both the conventional and present strategies of implementation of HBM, where the numerical time-integration for conventional strategy is performed using trapezoidal rule with evenly distributed 100

integration points over the time-period. The corresponding nonlinear frequency responses of the viscoelastic sandwich beam are illustrated in Fig. 3.4 for different numbers (H = 3, 5, 7) of harmonic terms in the assumed periodic solution (Eq. (3.9)). For each of these response curves, the computational time is noted in Table 3.1, where the FE codes are written in MATLAB and executed in a CPU with an Octa-Core processor Intel(R) Core(TM) i7-6700 CPU @ 3.4 GHz and RAM of 16 GB. However, for any number (H) of harmonic terms, it may be observed from Fig. 3.4 that the frequency response remains almost the same for both the strategies in the implementation of HBM. However, the present strategy based on the orthogonality of Fourier basis functions (Eq. (3.20)) provides the advantage of significantly less computational time (Table 3.1).

Table 3.1
Computational time for the evaluation of nonlinear frequency responses in Fig. 3.4 using either the present strategy (t_{Pc}) or the conventional strategy (t_{Cc}) in the implementation of HBM.

H	3	5	7
t_{Cc} (hrs)	16.564	41.35	88.38
t_{Pc} (hrs)	4.58	10.14	17.57
$\left(\frac{t_{Cc}-t_{Pc}}{t_{Cc}}\right)\times 100$	72.35	75.48	80.12

3.5.3. Study on the simplified formulation of the tangent stiffness matrix

The nonlinear frequency responses of elastic/viscoelastic structures are commonly evaluated by employing a numerical continuation method where the tangent stiffness matrix is an important parameter in achieving the convergence of solution through Newton-Raphson iteration. Although the inaccurate computation of the tangent stiffness matrix does not produce wrong results, it may lead to more number of Newton-Raphson iterations for the convergence of solution, or even the convergence of solution may fail around the bifurcation points. Therefore, the tangent stiffness matrix would be computed as accurate as possible depending on the geometrical and material complexities in a structural problem. However, in the present case of a viscoelastic sandwich beam, the formulation of the tangent stiffness matrix ($\boldsymbol{K}_t^e$, Eqs. (3.26)-(3.27)) appears in a little complex manner, especially due to the geometric stiffness matrix ($\boldsymbol{K}_g^e$, Eqs. (3.27)-(3.28)) in conjunction with the viscoelastic constitutive relations (Eqs. (3.13)-(3.17)), as demonstrated in Section 3.3. Now, this formulation of the

geometric stiffness matrix ($\boldsymbol{K}_g^e$, Eq. (3.27)-(3.28)) can be simplified by ignoring the viscoelastic part, as illustrated through Eqs. (3.30a), (3.30b) and (3.31). However, the fruitfulness of this simplified formulation of the tangent stiffness matrix is investigated here by evaluating the nonlinear frequency responses of the sandwich structure. These responses are illustrated in Fig. 3.5 for three different thicknesses of the viscoelastic core (h_v) as 2 mm, 4 mm and 6 mm, where the face thickness (h_{s1} , h_{s2}) is considered as 2 mm. It is observed that the ignorance of the viscoelastic part in the formulation of the tangent stiffness matrix does not cause difficulty in the convergence of solution at any point on the response curves for the three different viscoelastic core thicknesses. It may be due to fact that the viscoelastic core has not much contribution to the overall stiffness of the sandwich beam in comparison to that for the elastic face layers.

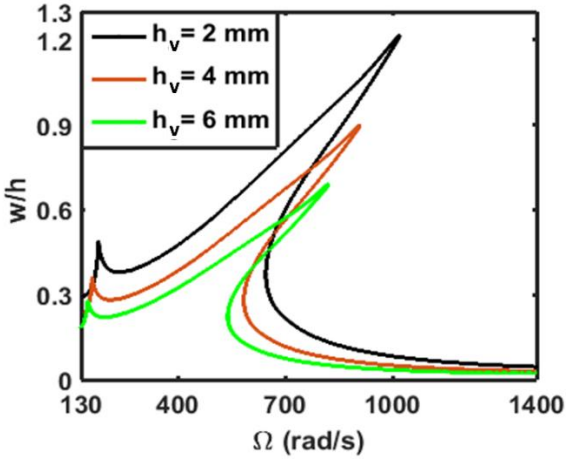

Fig. 3.5. Nonlinear frequency responses of the sandwich beam for three different thicknesses of the viscoelastic core using the simplified formulation of the tangent stiffness matrix (p_t^o = 4000 N/m²).

Table 3.2
Computational time in the evaluation of nonlinear frequency responses (Fig. 3.5) by ignoring the viscoelastic part in the formulation of the tangent stiffness matrix (t_{Fc} for full tangent stiffness matrix; t_{Sc} for simplified tangent stiffness matrix).

h_v (mm)	2	4	6
t_{Fc} (hrs)	18.99	16.43	13.98
t_{Sc} (hrs)	17.26	15.25	12.77
$\left(\frac{t_{Fc}-t_{Sc}}{t_{Fc}}\right)\times 100$	9.12	7.21	8.09

However, this simplification in the computation of the tangent stiffness matrix may also lead to the reduction of the computational time in the evaluation

of nonlinear frequency response curves. So, the computational time for the response curves (Fig. 3.5) is tabulated in Table 3.2. It may be observed from Table 3.2 that the computational time decreases for the aforesaid simplified formulation of the tangent stiffness matrix.

3.5.4. Nonlinear frequency responses of the sandwich beam using different viscoelastic constitutive models

A good number of time-domain viscoelastic constitutive models are available in the literature, where the commonly used ones are the Zener model, fractional Zener model, generalized Maxwell model and hereditary integral approach. However, in the application of these constitutive relations for a viscoelastic material, the corresponding constitutive model parameters are commonly determined from the experimental data for storage and loss moduli of that viscoelastic material within a certain frequency range. In this determination of constitutive model parameters, the sinusoidal variations of the stress and strain are introduced in a time-domain constitutive relation to obtain storage and loss moduli as the functions of constitutive model parameters and frequency. Subsequently, the functional curves of the storage and loss moduli are fitted to the experimental curves for the same moduli within a certain frequency range to obtain the model parameters in the time-domain constitutive relation. Here, curve-fitting is an important concern to achieve accurate values of the model parameters in a time-domain constitutive relation. Practically, accurate fitting of the theoretical curve to the experimental one is not a straightforward task, and the corresponding error varies from one time-domain constitutive relation to another depending on their mathematical forms.

Accordingly, the theoretically estimated dynamic response of a viscoelastic structure may vary as the constitutive relation changes in modelling the viscoelastic material in the structure. It sometimes poses the requirement of evaluation of dynamic responses of a viscoelastic structure using different constitutive relations. In this aspect, the present approach in reduction of various time-domain constitutive models (Eqs. (3.11)-(3.17)) provides an advantage of using any of the aforesaid viscoelastic constitutive models through a common formulation of the equation of motion in the evaluation of nonlinear frequency responses of a viscoelastic structure. For a corresponding demonstration through numerical results, the nonlinear frequency responses of the viscoelastic sandwich beam are evaluated using different constitutive relations and presented in the following results.

$$E^I(\Omega)=\eta E^R(\Omega)\,,\quad \xi=\log_{10}(\Omega)$$

$$\log_{10}\left\langle E^R(\omega)/10^6\right\rangle=-1.751\times10^{-7}\xi^9+2.3469\times10^{-6}\xi^8+1.4\times10^{-5}\xi^7-2.2132\times10^{-4}\xi^6$$
$$-5.2385\times10^{-4}\xi^5+6.5264\times10^{-3}\xi^4+0.014507\xi^3-0.034374\xi^2-0.047775\xi+0.21158$$

,

$$\log_{10}\langle\eta(\Omega)\rangle=-3.2476\times10^{-6}\xi^9+7.2845\times10^{-5}\xi^8-6.2068\times10^{-4}\xi^7+2.3829\times10^{-3}\xi^6$$
$$-1.9425\times10^{-3}\xi^5-1.6785\times10^{-2}\xi^4+0.024351\xi^3+0.031936\xi^2+0.77383\xi-2.2129 \qquad (3.36)$$

Table 3.3
Constitutive model parameters for generalized Maxwell model of the viscoelastic material (3M ISD 112) for different numbers (n) of Maxwell elements (E_o = 1.5 MPa).

n	1	2	3	4
E_n (MPa)	29.9863	50	6.699	1.67853
τ_n (s)	1.37871×10^{-5}	9.63395×10^{-6}	1.182576×10^{-4}	1.50566×10^{-3}

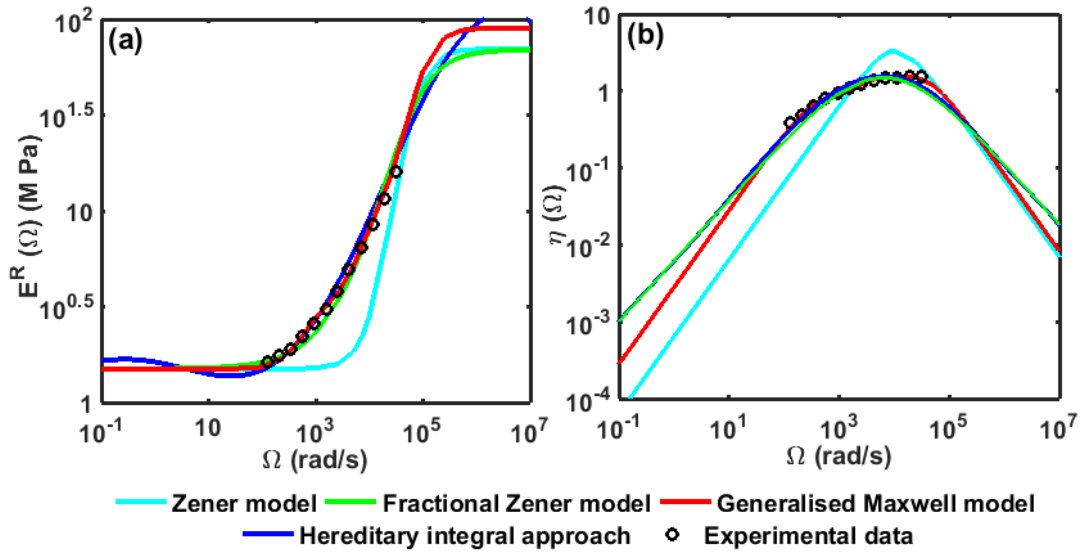

Fig. 3.6. Fitted curves for time-domain viscoelastic constitutive models in the determination of their model parameters from the experimental data (Galucio et al., 2004); (a) storage modulus and (b) material loss factor.

To model the viscoelastic material (3M ISD 112) at the core according to Zener and fractional Zener constitutive relations, the corresponding model parameters are taken from (Galucio et al., 2004). However, for the same viscoelastic material, the model parameters in the generalized Maxwell model (Amabili et al., 2019) are evaluated following the aforesaid curve-fitting approach where the number (n) of Maxwell elements is 4, and the corresponding model

parameters are given in Table 3.3. Next, for the hereditary integral approach, the corresponding frequency-dependent storage ($E^R(\Omega)$) and loss ($E^I(\Omega)$) moduli are also obtained by the curve-fitting approach where the functional forms of the moduli (in N/m^2) are illustrated in Eq. (3.36). However, the fitted curves for all the aforesaid time-domain constitutive relations in the determination of the corresponding model parameters are illustrated in Fig. 3.6.

Using the aforesaid values of model parameters in the reduced form of a time-domain constitutive relation (Eq. (3.13a)), the nonlinear frequency responses of the viscoelastic sandwich beam are illustrated in Fig. 3.7 for the Zener model, fractional Zener model, generalized Maxwell model and hereditary integral approach. Here, it is observed that there is not much variation in the computational time for evaluation of the responses using these constitutive models through the present generalized formulation. However, Fig. 3.7 shows that the responses for the fractional Zener model, generalized Maxwell model and hereditary integral approach appear closely, but the Zener model provides an erroneous result. It may be due to the difference between the theoretically fitted curves and experimental data (Fig. 3.6).

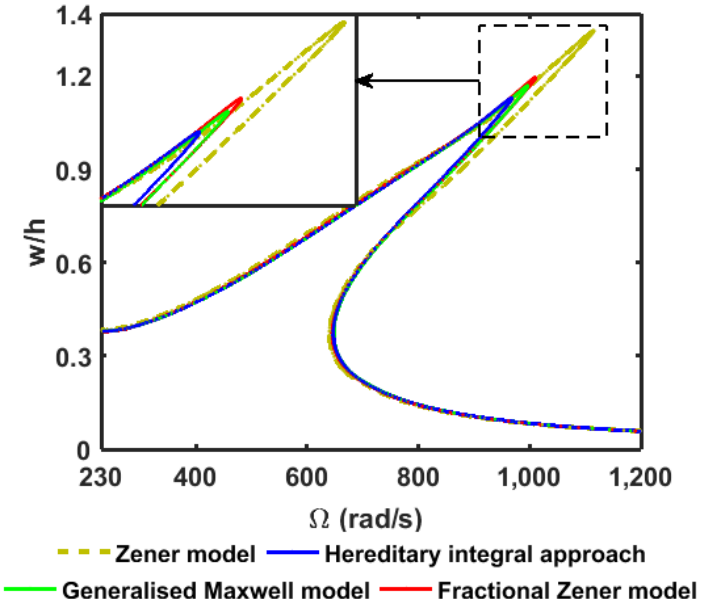

Fig. 3.7. Frequency response of the sandwich beam using different viscoelastic constitutive models for the viscoelastic core (H = 7, p_t^o = 4000 N/m^2).

3.6. Summary

In this chapter, an FE formulation for nonlinear frequency response analysis of viscoelastic structures using HBM is presented by introducing the following three new aspects.

a) The nonlinear strain vector is formulated in terms of a linear strain displacement matrix, a nodal displacement matrix and a nodal displacement vector. It eases the formulation of the HBM based expanded form of nonlinear stiffness matrix in the FE equations of motion of a viscoelastic structure.
b) The orthogonality of Fourier basis functions is exploited for the formulation of the system matrices in conjunction with HBM. It facilitates not only a decreased number of terms in the HBM based expanded form of the system matrices but also a reduced computational time in the evaluation of the nonlinear frequency responses by avoiding the conventional numerical time-integration.
c) Various time-domain viscoelastic constitutive models are reduced into a generalized mathematical form for the time-periodic stress/strain. It facilities the use of different viscoelastic constitutive relations through a common formulation of the equation of motion for the nonlinear frequency response analysis of a viscoelastic structure.

The overall formulation is demonstrated considering a viscoelastic sandwich beam; however, it can be applicable for nonlinear analysis of any other viscoelastic structure because of its generality with respect to the number of harmonic terms in the implementation of HBM. The formulation of the tangent stiffness matrix in conjunction with HBM involves much complexity because of the corresponding geometric stiffness matrix. Although it is tackled by the factorization of nonlinear strain-displcement matix and the exploitation of orthogonality of Fourier basis functions, further simplification in the formulation of the tangent stiffness matrix is introduced by avoiding the viscoelastic counterpart. This simplification is somewhat inaccurate in the computation of the tangent stiffness matrix; however, it is observed that there is no difficulty in the convergence of nonlinear solution through Newton-Raphson iterations for the present problem of a viscoelastic sandwich beam.

Chapter 4

Reduced-order finite element formulation for the geometrically nonlinear dynamic analysis of slender viscoelastic beams

4.1. Introduction

A generalized FE formulation in conjunction with HBM is presented in the previous chapter for the evaluation of nonlinear frequency responses of viscoelastic structures. This formulation is capable of handling an arbitrary number of harmonic terms in HBM. Also, any type of viscoelastic constitutive relation can be used in this HBM-based FE formulation. Therefore, this FE formulation would provide an accurate theoretical estimation of passive damping in a viscoelastic structure and geometrically nonlinear frequency responses. However, the corresponding FE model involves a large number of nodal degrees of freedom, and the number of nodal degrees of freedom further increases in multiple of the number of harmonic terms in HBM. Therefore, high computational time arises in the evaluation of nonlinear frequency responses (Table 3.1). However, in parallel to this FE model in the frequency domain, one needs to derive a similar FE model in the time-domain, especially to trace various dynamic instabilities through the construction of global bifurcation diagrams. This diagram is commonly constructed by evaluating the nonlinear transient responses at different excitation frequencies where the frequency is incremented in a small step within a frequency range of interest. Here, the repetitive evaluation of transient responses using a time-domain FE model usually involves a high computational time mainly because of a large number of nodal degrees of freedom in the FE model.

In this concern of a high computational time for the nonlinear dynamic analysis of viscoelastic structures, the reduction of a full-order FE model into the reduced-order model (ROM) is recommended in the literature. A corresponding literature survey is presented in Section 1.4.2, where it is observed that various approaches, namely ICES, ERM, MSE, MSEC, RKT, FSRK, etc., are proposed for the selection of reduced basis vectors (RBVs) in the derivation of a ROM for viscoelastic structures. But these RBVs are originally proposed for linear dynamic analysis so that they may not provide sufficient accuracy of a nonlinear ROM for

modelling various dynamic instabilities and the associated complex motion of a viscoelastic structure. In this concern, further approach of deriving appropriate RBVs for nonlinear ROM of viscoelastic structures is not yet reported in the literature to the best knowledge of this researcher. Also, a formulation of the nonlinear ROM using the advanced viscoelastic constitutive relations, like fractional Zener model, generalized Maxwell model, etc., is not available in the open literature to date. But this development of nonlinear ROMs would facilitate significantly low computational cost in the nonlinear dynamic analysis of viscoelastic structures. So, this chapter is focused to develop a nonlinear ROM of CLD treated slender beams, while this ROM is utilized in the subsequent chapter for the nonlinear dynamic analysis of similar beams under the parametric excitation.

In this development of a nonlinear ROM, the first objective is to devise a methodology for the derivation of appropriate RBVs to achieve sufficient accuracy of the nonlinear ROM of viscoelastic structures. Here, the strategy is to utilize the aforesaid conventional approaches for derivation of RBVs; however, those are enriched using the concept of static MDs and proper orthogonal decomposition (POD) method. After having these enriched RBVs, the nonlinear ROM can be derived following the conventional formulation procedures (Hollkamp et al., 2005; Jain, 2019; Mignolet et al., 2013). However, for solving the corresponding reduced-order equations of motion through an iterative solution procedure, the reduced-order nonlinear system matrices/vectors are to be formed repeatedly from the corresponding full-order system matrices/vectors. So, the computational time does not decrease appreciably. In this concern, the derivation of the reduced-order system matrices/vectors may be carried out in terms of the reduced coordinates without involving the full-order solution or full-order FE model. A similar derivation for elastic structures was addressed in (Jain, 2015; Touzé et al., 2014), where the formulation of the corresponding nonlinear stiffness matrix is presented in the tensorial form. But, the usual practice in FE formulation is to formulate the system mass, stiffness and damping in the matrix form. So, presently a new formulation technique is introduced by means of a special factorization of nonlinear strain-displacement matrix (Eq. (3.22b)), especially to ease the formulation of reduced-order nonlinear stiffness matrix in the elemental level without involving the full-order FE model.

Apart from the nonlinear stiffness matrix, another nonlinear system parameter in the equation of motion of a viscoelastic structure appears as the nonlinear memory-load vector, since the viscoelastic material is modelled according to the fractional Zener constitutive model. The formulation of the

corresponding reduced-order nonlinear memory-load vector without involving the full-order solution is also introduced at present, in particular, to improve the computational efficiency of the nonlinear ROM in the time domain. Besides this time-domain ROM, a similar formulation for a nonlinear ROM in the frequency domain is also presented based on the HBM and the fractional Zener constitutive model.

The overall formulation is carried out considering a viscoelastic sandwich beam (Fig. 3.1). The nonlinear FE model of this sandwich beam in the frequency-domain and time-domain is derived in 3.3 and 3.4, respectively. The reduction of these full-order FE models is presented in the following sections. First, the derivation of ROM of the sandwich beam in the time domain is presented in Section 4.2. Next, in Section 4.3, HBM based ROM is derived. Section 4.4 presents the methodology for the enrichment of RBVs obtained through MSE/MSEC/MM/ICES/RKT/FSRK, especially for the geometrically nonlinear analysis of the viscoelastic sandwich beam. The numerical results are presented in Section 4.5 to illustrate the accuracy and computational efficiency of the present ROMs.

4.2. Derivation of reduced-order FE model in the time domain

The full-order FE model of the viscoelastic sandwich beam (Fig. 3.1) is derived in Section 3.4, where the nonlinear FE equations of motion are obtained as

$$\boldsymbol{M}_s \ddot{\boldsymbol{d}}_{q+1} + \left\langle \boldsymbol{K}_{ll} + (\boldsymbol{K}_{nn})_{q+1} \right\rangle \boldsymbol{d}_{q+1} = \boldsymbol{P}_s\ (p_t)_{q+1} + \boldsymbol{P}_{su}\ (p_{tu})_{q+1} + (\bar{\boldsymbol{P}}_s)_{q+1}$$

$$\boldsymbol{K}_{ll} = \sum_{k=1}^{2} f_1^k \boldsymbol{K}_{sl}^k\ ,\ (\boldsymbol{K}_{nn})_{q+1} = \sum_{k=1}^{2} f_1^k (\boldsymbol{K}_{sn}^k)_{q+1} \tag{3.35}$$

where, $\boldsymbol{M}_s$ is the global mass matrix; $\boldsymbol{P}_s$ / $\boldsymbol{P}_{su}$ is the global load coefficient vector corresponding to the transversely distributed load/transverse point-load; $(\bar{\boldsymbol{P}}_s)_{q+1}$ is the nonlinear memory-load vector; $\boldsymbol{K}_{sl}^k$ and $(\boldsymbol{K}_{sn}^k)_{q+1}$ are the global linear and nonlinear stiffness matrices, respectively, for the k^{th} material within the sandwich beam. Equation (3.35) can be solved in conjunction with the Newmark time-integration method where the nonlinear solutions at a typical time step can be obtained through the direct iteration method. However, to achieve a reduced computational time in this solution for nonlinear transient responses of the viscoelastic sandwich beam, the full-order FE model (Eq. (3.35)) is now reduced to a nonlinear ROM.

The reduced-order FE model is commonly derived using an admissible reduction basis (RB, $\boldsymbol{\Phi}$) that linearly transforms the nodal displacement vector (

$\boldsymbol{d}_{q+1}$) to the reduced coordinate vector ($\boldsymbol{V}_{q+1}$) according to Eq. (4.1a). The methodology for computation and selection of the RBVs in the reduction basis ($\boldsymbol{\Phi}$) are demonstrated in Section 4.4. However, the linear projection of the system of governing differential equations (Eq. (3.35)) onto the subspace spanned by RB ($\boldsymbol{\Phi}$, Eq. (4.1a)) provides the reduced-order FE model, as given in Eq. (4.1b).

$$\boldsymbol{d}_{q+1} = \boldsymbol{\Phi}\, \boldsymbol{V}_{q+1} \tag{4.1a}$$

$$ {}^{r}\boldsymbol{M}_s \ddot{\boldsymbol{V}}_{q+1} + \left\langle {}^{r}\boldsymbol{K}_{ll} + ({}^{r}\boldsymbol{K}_{nn})_{q+1} \right\rangle \boldsymbol{V}_{q+1} = {}^{r}\boldsymbol{P}_s\,(p_t)_{q+1} + {}^{r}\boldsymbol{P}_{su}\,(p_{tu})_{q+1} + ({}^{r}\bar{\boldsymbol{P}}_s)_{q+1},$$

$$ ({}^{r}\boldsymbol{K}_{nn})_{q+1} = \sum_{k=1}^{2} f_1^k\, ({}^{r}\boldsymbol{K}_{sn}^k)_{q+1}, \quad {}^{r}\boldsymbol{K}_{ll} = \sum_{k=1}^{2} f_1^k\, {}^{r}\boldsymbol{K}_{sl}^k, $$

$$ {}^{r}\boldsymbol{M}_s = \boldsymbol{\Phi}^{\mathrm{T}} \boldsymbol{M}_s \boldsymbol{\Phi}, \quad {}^{r}\boldsymbol{K}_{sl}^k = \boldsymbol{\Phi}^{\mathrm{T}} \boldsymbol{K}_{sl}^k \boldsymbol{\Phi}, \quad ({}^{r}\boldsymbol{K}_{sn}^k)_{q+1} = \boldsymbol{\Phi}^{\mathrm{T}} (\boldsymbol{K}_{sn}^k)_{q+1} \boldsymbol{\Phi}, $$

$$ ({}^{r}\bar{\boldsymbol{P}}_s)_{q+1} = \boldsymbol{\Phi}^{\mathrm{T}} (\bar{\boldsymbol{P}}_s)_{q+1}, \quad {}^{r}\boldsymbol{P}_s = \boldsymbol{\Phi}^{\mathrm{T}} \boldsymbol{P}_s, \quad {}^{r}\boldsymbol{P}_{su} = \boldsymbol{\Phi}^{\mathrm{T}} \boldsymbol{P}_{su} \tag{4.1b}$$

This reduction of the full-order FE model (Eq. (3.35)) would yield less computational time in the evaluation of transient responses of the viscoelastic sandwich beam. However, the reduction of the computational time could not be achieved appreciably, since the computation of the reduced-order system matrices involves full-order system matrices ($\boldsymbol{M}_s, \boldsymbol{K}_{sl}^k, (\boldsymbol{K}_{sn}^k)_{q+1}$) and vectors ($(\bar{\boldsymbol{P}}_s)_{q+1}$, $\boldsymbol{P}_{su}$, $\boldsymbol{P}_s$). Also, the full-order nonlinear stiffness matrix ($(\boldsymbol{K}_{sn}^k)_{q+1}$) and memory-load vector ($(\bar{\boldsymbol{P}}_s)_{q+1}$) are to be computed repeatedly in each iteration for the nonlinear solution at a typical time-step. To avoid this expensive computation due to the formation and reduction of the full-order system matrices/vectors, the reduced-order system matrices/vectors can be formulated at the elemental level by taking the coordinate transformation (Eq. (4.1a)) for a typical element, as given in Eq. (4.2a) where the superscript e indicates the elemental quantity. Using Eq. (4.2a), the strain vector for a typical element can be expressed in terms of the reduced coordinate vector ($\boldsymbol{V}_{q+1}$), as it is illustrated in Eq. (4.2b). Now, using Eqs. (4.2a), (4.2b) and (3.32) in Eq. (3.4) at $(q+1)^{th}$ time-step, the reduced-order system matrices (${}^{r}\boldsymbol{M}_s, {}^{r}\boldsymbol{K}_{sl}^k$, $({}^{r}\boldsymbol{K}_{sn}^k)_{q+1}$, Eq. (4.1b)) and vectors ($({}^{r}\bar{\boldsymbol{P}}_s)_{q+1}$, ${}^{r}\boldsymbol{P}_s$, ${}^{r}\boldsymbol{P}_{su}$, Eq. (4.1b)) can be obtained, as given in Eq. (4.3a). In Eq. (4.3a), a system matrix/vector is first reduced in the elemental level, and then the corresponding reduced-order elemental matrices/vectors for all elements are summed to obtain that system matrix/vector in the reduced form for the overall structure.

$$\boldsymbol{d}^e_{q+1} = \boldsymbol{\Phi}^e \boldsymbol{V}_{q+1} \tag{4.2a}$$

$$\boldsymbol{\varepsilon}_{q+1} = (\boldsymbol{\varepsilon}_l)_{q+1} + (\boldsymbol{\varepsilon}_n)_{q+1},\ (\boldsymbol{\varepsilon}_l)_{q+1} = \boldsymbol{B}_l \boldsymbol{\Phi}^e \boldsymbol{V}_{q+1},$$

$$(\boldsymbol{\varepsilon}_n)_{q+1} = (1/2)\boldsymbol{B}_n \boldsymbol{\Phi}^e_I\ (\boldsymbol{V}_I)_{q+1} \boldsymbol{V}_{q+1},$$

$$\boldsymbol{\Phi}^e_I = \boldsymbol{\Phi}^e \otimes \boldsymbol{\Phi}^e,\ (\boldsymbol{V}_I)_{q+1} = \boldsymbol{V}_{q+1} \otimes \boldsymbol{I}_{N_r} \tag{4.2b}$$

$$({}^r\boldsymbol{K}^k_{sn})_{q+1} = (1/2)\left\{ {}^r\boldsymbol{K}^k_{sn1}(\boldsymbol{V}_I)_{q+1} + \left\langle (\boldsymbol{V}_I)_{q+1} \right\rangle^{\mathrm{T}} {}^r\boldsymbol{K}^k_{sn4}(\boldsymbol{V}_I)_{q+1} \right\} + \left\langle (\boldsymbol{V}_I)_{q+1} \right\rangle^{\mathrm{T}} ({}^r\boldsymbol{K}^k_{sn1})^{\mathrm{T}}$$

$$,\ {}^r\boldsymbol{K}^k_{sl} = \sum_{e \in \boldsymbol{\Xi}^k} (\boldsymbol{\Phi}^e)^{\mathrm{T}} \boldsymbol{K}^e_{sl} \boldsymbol{\Phi}^e,\ {}^r\boldsymbol{K}^k_{sn1} = \sum_{e \in \boldsymbol{\Xi}^k} (\boldsymbol{\Phi}^e)^{\mathrm{T}} \boldsymbol{K}^e_{sn1} \boldsymbol{\Phi}^e_I,$$

$${}^r\boldsymbol{K}^k_{sn4} = \sum_{e \in \boldsymbol{\Xi}^k} (\boldsymbol{\Phi}^e_I)^{\mathrm{T}} \boldsymbol{K}^e_{sn4} \boldsymbol{\Phi}^e_I\ ,\ {}^r\boldsymbol{M}_s = \sum_{e=1}^{n_e} (\boldsymbol{\Phi}^e)^{\mathrm{T}} \boldsymbol{M}^e_s \boldsymbol{\Phi}^e,$$

$${}^r\boldsymbol{P}_s = \sum_{e=1}^{n_e} (\boldsymbol{\Phi}^e)^{\mathrm{T}} \boldsymbol{P}^e_s,\ {}^r\boldsymbol{P}_{su} = \sum_{e=1}^{n_e} (\boldsymbol{\Phi}^e)^{\mathrm{T}} \boldsymbol{P}^e_{su},\ ({}^r\bar{\boldsymbol{P}}_s)_{q+1} = \sum_{e=1}^{n_e} (\boldsymbol{\Phi}^e)^{\mathrm{T}} (\bar{\boldsymbol{P}}^e_s)_{q+1} \tag{4.3a}$$

$$(\bar{\boldsymbol{P}}^e_s)_{q+1} = -\int_{A^e} \bar{f}^k_1 \left\langle \boldsymbol{B}_l + \boldsymbol{B}_n\ (\boldsymbol{d}^e_I)_{q+1} \right\rangle^{\mathrm{T}} \boldsymbol{C}^k \left(\sum_{j=1}^{q+1} A_{j+1} \bar{\boldsymbol{\varepsilon}}^e_{q+1-j} \right) b\, dA^e,$$

$$\bar{\boldsymbol{\varepsilon}}^e_{q+1} = f(1-c_b)(\boldsymbol{\varepsilon}^e_s)_{q+1} - c_b \left(\sum_{j=1}^{q+1} A_{j+1} \bar{\boldsymbol{\varepsilon}}^e_{q+1-j} \right),$$

$$(\boldsymbol{\varepsilon}^e_s)_{q+1} = \frac{1}{A^e} \int_{A^e} \left\langle \boldsymbol{B}_l + (1/2)\boldsymbol{B}_n (\boldsymbol{d}^e_I)_{q+1} \right\rangle \boldsymbol{d}^e_{q+1}\, dA^e \tag{4.3b}$$

The different elemental matrices ($\boldsymbol{M}^e_s$, $\boldsymbol{K}^e_{sl}$, $\boldsymbol{K}^e_{sn1}, \boldsymbol{K}^e_{sn4},$) and vectors ($\boldsymbol{P}^e_s$, $\boldsymbol{P}^e_{su}$) appearing in Eq. (4.3a) are defined in Eq. (3.28) (Section 3.3.3). Further, in Eqs. (4.2b) and (4.3a), $\boldsymbol{I}_{N_r}$ is the unity matrix of size ($N_r \times N_r$); N_r is the number of basis vectors in RB; $\boldsymbol{\Xi}^k$ is a set of elements made of k^{th} material; n_e is the total number of elements. It may be noted from Eq. (4.3a) that a reduced-order system matrix/vector is formulated by avoiding the computation of the corresponding full-order matrix/vector. More importantly, the reduced-order nonlinear stiffness matrix ($({}^r\boldsymbol{K}^k_{sn})_{q+1}$) is formulated in terms of two reduced-order linear stiffness matrices (${}^r\boldsymbol{K}^k_{sn1}, {}^r\boldsymbol{K}^k_{sn4}$) that are to be computed only once before proceeding for solution. It would result reduced computational time while the nonlinear stiffness matrix ($({}^r\boldsymbol{K}^k_{sn})_{q+1}$) is to be computed repetitively for the nonlinear solution at a time step through an iterative solution procedure.

Besides the nonlinear stiffness matrix ($({}^{r}\boldsymbol{K}_{sn}^{k})_{q+1}$), the reduced-order memory load vector ($({}^{r}\bar{\boldsymbol{P}}_{s})_{q+1}$, Eq. (4.3a)) is also to be formed repeatedly in each iteration for the nonlinear solution at a typical time-step. It involves the repetitive computation, reduction and summation of the elemental memory-load vectors ($(\bar{\boldsymbol{P}}_{s}^{e})_{q+1}$, Eq (4.3b)) that are dependent on the elemental nodal displacement vector ($\boldsymbol{d}_{q+1}^{e}$) and anelastic strain history ($\bar{\boldsymbol{\varepsilon}}_{q+1-j}^{e}$) (Eq. (4.3b)). In this connection, the elemental anelastic strain is also to be computed at every time step of the solution. So, for avoiding this expensive computation for the reduced-order memory-load vector ($({}^{r}\bar{\boldsymbol{P}}_{s})_{q+1}$) towards a decrease in the computational time, presently, this load vector ($({}^{r}\bar{\boldsymbol{P}}_{s})_{q+1}$) is expressed in terms of two new force vectors named as reduced-order anelastic forces ($({}^{r}\bar{\boldsymbol{F}}_{s1})_{q+1-j}$, $({}^{r}\bar{\boldsymbol{F}}_{s2})_{q+1-j}$). It is illustrated in Eqs. (4.4a) and (4.4b), where the expression of $(\bar{\boldsymbol{P}}_{s}^{e})_{q+1}$ (Eq. (4.3b)) is substituted in the expression of $({}^{r}\bar{\boldsymbol{P}}_{s})_{q+1}$ (Eq. 4.3a), and the resulting expression is simplified for the reduced-order anelastic forces (Eq. (4.4b)).

$$({}^{r}\bar{\boldsymbol{P}}_{s})_{q+1} = -\left(\sum_{j=1}^{q+1} A_{j+1} ({}^{r}\bar{\boldsymbol{F}}_{s1})_{q+1-j} + \left\langle (\boldsymbol{V}_{I})_{q+1} \right\rangle^{\mathrm{T}} \sum_{j=1}^{q+1} A_{j+1} ({}^{r}\bar{\boldsymbol{F}}_{s2})_{q+1-j} \right) \tag{4.4a}$$

$$({}^{r}\bar{\boldsymbol{F}}_{s1})_{q+1-j} = \sum_{e=1}^{n_e} (\boldsymbol{\Phi}^{e})^{\mathrm{T}} \int_{A^e} \bar{f}_{1}^{k} (\boldsymbol{B}_{l})^{\mathrm{T}} \boldsymbol{C}^{k} \; \bar{\boldsymbol{\varepsilon}}_{q+1-j}^{e} \, b \, dA^{e} \,,$$

$$({}^{r}\bar{\boldsymbol{F}}_{s2})_{q+1-j} = \sum_{e=1}^{n_e} (\boldsymbol{\Phi}_{I}^{e})^{\mathrm{T}} \int_{A^e} \bar{f}_{1}^{k} (\boldsymbol{B}_{n})^{\mathrm{T}} \boldsymbol{C}^{k} \; \bar{\boldsymbol{\varepsilon}}_{q+1-j}^{e} b \, dA^{e} \tag{4.4b}$$

Now, according to Eq. (4.4b), the evaluation of the reduced-order anelastic force history ($({}^{r}\bar{\boldsymbol{F}}_{s1})_{q+1-j}$, $({}^{r}\bar{\boldsymbol{F}}_{s2})_{q+1-j}$) still requires the computation of the elemental anelastic strain history ($\bar{\boldsymbol{\varepsilon}}_{q+1-j}^{e}$). So, by substituting the expression of the elemental anelastic strain (Eq. (4.3b)) in Eq. (4.4b) at $(q+1)^{th}$ time-step, the corresponding reduced-order anelastic forces ($({}^{r}\bar{\boldsymbol{F}}_{s1})_{q+1}$, $({}^{r}\bar{\boldsymbol{F}}_{s2})_{q+1}$) can be obtained as follows

$$({}^{r}\bar{\boldsymbol{F}}_{s1})_{q+1} = (1-c_b) f \, ({}^{r}\boldsymbol{F}_{s1})_{q+1} - c_b \sum_{j=1}^{q+1} A_{j+1} ({}^{r}\bar{\boldsymbol{F}}_{s1})_{q+1-j} \,,$$

$$({}^{r}\bar{\boldsymbol{F}}_{s2})_{q+1} = (1-c_b)\, f\,({}^{r}\boldsymbol{F}_{s2})_{q+1} - c_b \sum_{j=1}^{q+1} A_{j+1}({}^{r}\bar{\boldsymbol{F}}_{s2})_{q+1-j}\,,$$

$$({}^{r}\boldsymbol{F}_{s1})_{q+1} = \bar{f}_1^{k} \left\langle {}^{r}\boldsymbol{K}_{sl}^{k} + (1/2)\,{}^{r}\boldsymbol{K}_{sn1}^{k}(\boldsymbol{V}_I)_{q+1} \right\rangle \boldsymbol{V}_{q+1}\,,$$

$$({}^{r}\boldsymbol{F}_{s2})_{q+1} = \bar{f}_1^{k} \left\langle ({}^{r}\boldsymbol{K}_{sn1}^{k})^{\mathrm{T}} + (1/2)\,{}^{r}\boldsymbol{K}_{sn4}^{k}(\boldsymbol{V}_I)_{q+1} \right\rangle \boldsymbol{V}_{q+1},\ k=2 \qquad (4.5)$$

It may be noted from Eqs. (4.4a) and (4.5) that the reduced-order memory-load vector ($({}^{r}\bar{\boldsymbol{P}}_s)_{q+1}$) can be evaluated using the reduced-order anelastic force history ($({}^{r}\bar{\boldsymbol{F}}_{s1})_{q+1-j}$, $({}^{r}\bar{\boldsymbol{F}}_{s2})_{q+1-j}$) and the reduced coordinate vector ($\boldsymbol{V}_{q+1}$). Here, the computation of the elemental anelastic strain at every time step of solution is avoided. Instead, the reduced-order anelastic forces ($({}^{r}\bar{\boldsymbol{F}}_{s1})_{q+1}$, $({}^{r}\bar{\boldsymbol{F}}_{s2})_{q+1}$), Eq. (4.5)) are computed at each time-step using the reduced-order linear stiffness matrices (${}^{r}\boldsymbol{K}_{sl}^{k}$, ${}^{r}\boldsymbol{K}_{sn1}^{k}$, ${}^{r}\boldsymbol{K}_{sn4}^{k}$) and the reduced coordinate vector ($\boldsymbol{V}_{q+1}$). These linear stiffness matrices (${}^{r}\boldsymbol{K}_{sl}^{k}$, ${}^{r}\boldsymbol{K}_{sn1}^{k}$, ${}^{r}\boldsymbol{K}_{sn4}^{k}$) are already in use for the computation of the linear/nonlinear stiffness matrices. So, the formation of the reduced-order memory load vector ($({}^{r}\bar{\boldsymbol{P}}_s)_{q+1}$) does not involve much computation. However, according to the above formulation, none of the reduced-order system matrices/vectors (${}^{r}\boldsymbol{M}_s$, $\boldsymbol{K}_{sl}^{k}$, $({}^{r}\boldsymbol{K}_{sn}^{k})_{q+1}$, ${}^{r}\boldsymbol{P}_s$, ${}^{r}\boldsymbol{P}_{su}$, $({}^{r}\bar{\boldsymbol{P}}_s)_{q+1}$) involves the computation of the corresponding full-order matrix/vector. Also, all the nonlinear reduced-order system matrices/vectors ($({}^{r}\boldsymbol{K}_{sn}^{k})_{q+1}$, $({}^{r}\bar{\boldsymbol{P}}_s)_{q+1}$) can be computed in the reduced-order scale using the reduced-order linear matrices/vectors (${}^{r}\boldsymbol{K}_{sn1}^{k}$, ${}^{r}\boldsymbol{K}_{sn4}^{k}$, ${}^{r}\boldsymbol{K}_{sl}^{k}$) that are to be formed only once before starting the solution for the nonlinear transient responses of the viscoelastic sandwich beam. The advantage of this formulation in the reduction of the computational time is illustrated through numerical results in Section 4.5.1.

4.3. Derivation of the reduced-order FE model in the frequency domain

The HBM-based FE model of the viscoelastic sandwich beam (Fig. 3.1) is derived in Section 3.3.2. The corresponding incremental governing equation of motion in the frequency-domain is obtained as

$$\sum_{k=1}^{2}\int_{A^k}\left\{\begin{array}{l} 2\left[\left\langle(\delta\Delta\boldsymbol{\varepsilon}_l+\delta\Delta\boldsymbol{\varepsilon}_{n1})^o\right\rangle^{\mathrm{T}}({}^i\boldsymbol{\sigma}^k+\Delta\boldsymbol{\sigma}^k)^o+(\delta U_g)^o\right] \\ -(\boldsymbol{l}_t\,\delta\Delta\boldsymbol{d}^c_{s1}\big|_{z=h})^{\mathrm{T}}\,p^o_{tu}-(\boldsymbol{l}_t\,\delta\Delta\boldsymbol{d}^c_{s1}\big|_{(x_l,z_l)})^{\mathrm{T}}(p^o_t/b)+ \\ \sum_{m=1}^{H}\left[\begin{array}{l}\left\langle(\delta\Delta\boldsymbol{\varepsilon}_l)^c_m\right\rangle^{\mathrm{T}}({}^i\boldsymbol{\sigma}^k+\Delta\boldsymbol{\sigma}^k)^c_m+\left\langle(\delta\Delta\boldsymbol{\varepsilon}_l)^s_m\right\rangle^{\mathrm{T}}({}^i\boldsymbol{\sigma}^k+\Delta\boldsymbol{\sigma}^k)^s_m \\ +(\delta U_g)^c_m+(\delta U_g)^s_m \\ -\rho^k(m\Omega_i+m\Delta\Omega)^2\left\langle\begin{array}{l}(\delta\Delta\boldsymbol{d}^s_{sm})^{\mathrm{T}}({}^i\boldsymbol{d}^s_{sm}+\Delta\boldsymbol{d}^s_{sm}) \\ +(\delta\Delta\boldsymbol{d}^c_{sm})^{\mathrm{T}}({}^i\boldsymbol{d}^c_{sm}+\Delta\boldsymbol{d}^c_{sm})\end{array}\right\rangle\end{array}\right] \\ +\sum_{m=1}^{2H}\left[\left\langle(\delta\Delta\boldsymbol{\varepsilon}_{n1})^c_m\right\rangle^{\mathrm{T}}({}^i\boldsymbol{\sigma}^k+\Delta\boldsymbol{\sigma}^k)^c_m+\left\langle(\delta\Delta\boldsymbol{\varepsilon}_{n1})^s_m\right\rangle^{\mathrm{T}}({}^i\boldsymbol{\sigma}^k+\Delta\boldsymbol{\sigma}^k)^s_m\right]\end{array}\right\}b\,dA^k=0$$

$$(\delta U_g)^s_m=\left\langle(\delta\Delta\boldsymbol{\varepsilon}^u_g)^s_m\right\rangle^{\mathrm{T}}({}^i\boldsymbol{\Gamma}^k\,\Delta\boldsymbol{\varepsilon}^u_g)^s_m+\left\langle(\delta\Delta\boldsymbol{\varepsilon}^w_g)^s_m\right\rangle^{\mathrm{T}}({}^i\boldsymbol{\Gamma}^k\Delta\boldsymbol{\varepsilon}^w_g)^s_m$$

$$(\delta U_g)^c_m=\left\langle(\delta\Delta\boldsymbol{\varepsilon}^u_g)^c_m\right\rangle^{\mathrm{T}}({}^i\boldsymbol{\Gamma}^k\,\Delta\boldsymbol{\varepsilon}^u_g)^c_m+\left\langle(\Delta\delta\boldsymbol{\varepsilon}^w_g)^c_m\right\rangle^{\mathrm{T}}({}^i\boldsymbol{\Gamma}^k\Delta\boldsymbol{\varepsilon}^w_g)^c_m$$

$$(\delta U_g)^o=\left\langle(\delta\Delta\boldsymbol{\varepsilon}^u_g)^o\right\rangle^{\mathrm{T}}({}^i\boldsymbol{\Gamma}^k\,\Delta\boldsymbol{\varepsilon}^u_g)^o+\left\langle(\delta\Delta\boldsymbol{\varepsilon}^w_g)^o\right\rangle^{\mathrm{T}}({}^i\boldsymbol{\Gamma}^k\Delta\boldsymbol{\varepsilon}^w_g)^o \tag{3.21}$$

Now, according to the FE discretization of the sandwich beam (Eq. (3.22)), the displacement and strain vectors $({}^i\boldsymbol{d}_s\,,{}^i\boldsymbol{\varepsilon}_l\,,{}^i\boldsymbol{\varepsilon}_n)$ at the reference state of vibration and the corresponding increments for a typical element are given in Eq. (4.6a). Further, the elemental nodal displacement vectors $({}^i\boldsymbol{d}^e\,,\Delta\boldsymbol{d}^e)$ and matrix $({}^i\boldsymbol{d}^e_I)$ appearing in Eq. (4.6a) can be expressed in terms of the reduced coordinate vector $({}^i\boldsymbol{V}\,/\,\Delta\boldsymbol{V})$, as it is written in Eq. (4.6b).

$${}^i\boldsymbol{d}_s=\boldsymbol{N}\,{}^i\boldsymbol{d}^e,\ \Delta\boldsymbol{d}_s=\boldsymbol{N}\,\Delta\boldsymbol{d}^e,$$

$${}^i\boldsymbol{\varepsilon}_l=\boldsymbol{B}_l\,{}^i\boldsymbol{d}^e,\Delta\boldsymbol{\varepsilon}_l=\boldsymbol{B}_l\,\Delta\boldsymbol{d}^e,\ {}^i\boldsymbol{\varepsilon}_n=(1/2)\,\boldsymbol{B}_n\,{}^i\boldsymbol{d}^e_I\,{}^i\boldsymbol{d}^e,\ \Delta\boldsymbol{\varepsilon}_{n1}=\boldsymbol{B}_n\,{}^i\boldsymbol{d}^e_I\,\Delta\boldsymbol{d}^e,$$

$$\Delta\boldsymbol{\varepsilon}^u_g=\boldsymbol{B}^u_g\,\Delta\boldsymbol{d}^e,\ \Delta\boldsymbol{\varepsilon}^w_g=\boldsymbol{B}^w_g\,\Delta\boldsymbol{d}^e,\ {}^i\boldsymbol{d}^e_I={}^i\boldsymbol{d}^e\otimes\boldsymbol{I}_{18} \tag{4.6a}$$

$${}^i\boldsymbol{d}^e=\boldsymbol{\Phi}^e\,{}^i\boldsymbol{V},\ \Delta\boldsymbol{d}^e=\boldsymbol{\Phi}^e\,\Delta\boldsymbol{V},$$

$${}^i\boldsymbol{d}^e_I\,{}^i\boldsymbol{d}^e=\boldsymbol{\Phi}^e_I\,{}^i\boldsymbol{V}_I\,{}^i\boldsymbol{V},\ {}^i\boldsymbol{d}^e_I\,\Delta\boldsymbol{d}^e=\boldsymbol{\Phi}^e_I\,{}^i\boldsymbol{V}_I\,\Delta\boldsymbol{V},\ {}^i\boldsymbol{V}_I={}^i\boldsymbol{V}\otimes\boldsymbol{I}_{N_r} \tag{4.6b}$$

It may be noted from Eq. (4.6a) that the present factorization $(\boldsymbol{B}_n\,{}^i\boldsymbol{d}^e_I)$ of the nonlinear strain-displacement matrix facilitates the formulation of the reduced-order nonlinear stiffness matrix in terms of the linear stiffness coefficient matrices $({}^r\boldsymbol{K}^k_{sn1}\,,{}^r\boldsymbol{K}^k_{sn4}$, Eq. (4.3a)) multiplied by the reduced coordinate matrix $({}^i\boldsymbol{V}_I)$ similar to Eq. (4.3a). So, the HBM based expanded form of the reduced-order nonlinear

stiffness matrix can be obtained in a straightforward manner by replacing the reduced-coordinate matrix ($^{i}\boldsymbol{V}_I$) with its Fourier expansion.

However, the reduced coordinate vector ($^{i}\boldsymbol{V}$ / $\Delta\boldsymbol{V}$) is expanded in the same form of Eq. (3.9) where the coefficient vectors for constant, cosine and sine terms are denoted by $^{i}\boldsymbol{V}^{o}$ / $\Delta\boldsymbol{V}^{o}$, $^{i}\boldsymbol{V}_m^{c}$ / $\Delta\boldsymbol{V}_m^{c}$ and $^{i}\boldsymbol{V}_m^{s}$ / $\Delta\boldsymbol{V}_m^{s}$ ($m=1,2,3,...,H$), respectively. Substituting this expanded form of the reduced coordinate vector ($^{i}\boldsymbol{V}$ / $\Delta\boldsymbol{V}$) in Eq. (4.6b) and then using the resulting expressions in Eq. (4.6a), the Fourier expansion of the strain vectors ($^{i}\boldsymbol{\varepsilon}_l$, $\Delta\boldsymbol{\varepsilon}_l$, $^{i}\boldsymbol{\varepsilon}_n$, $\Delta\boldsymbol{\varepsilon}_{n1}$, $\Delta\boldsymbol{\varepsilon}_g^{u}$, $\Delta\boldsymbol{\varepsilon}_g^{w}$) can be obtained in terms of the reduced coordinate vector. The corresponding coefficient strain vectors for the constant, cosine and sine terms are illustrated in Eq. (4.7a) by the superscripts o, c and s, respectively.

$$(^{i}\boldsymbol{\varepsilon}_l)^{o}=\boldsymbol{B}_l\,\boldsymbol{\Phi}^{e}\,{}^{i}\boldsymbol{V}^{o},\ (^{i}\boldsymbol{\varepsilon}_l)_m^{c}=\boldsymbol{B}_l\,\boldsymbol{\Phi}^{e}\,{}^{i}\boldsymbol{V}_m^{c},\ (^{i}\boldsymbol{\varepsilon}_l)_m^{s}=\boldsymbol{B}_l\,\boldsymbol{\Phi}^{e}\,{}^{i}\boldsymbol{V}_m^{s},$$

$$(\Delta\boldsymbol{\varepsilon}_l)^{o}=\boldsymbol{B}_l\,\boldsymbol{\Phi}^{e}\Delta\boldsymbol{V}^{o},\ (\Delta\boldsymbol{\varepsilon}_l)_m^{c}=\boldsymbol{B}_l\,\boldsymbol{\Phi}^{e}\Delta\boldsymbol{V}_m^{c},\ (\Delta\boldsymbol{\varepsilon}_l)_m^{s}=\boldsymbol{B}_l\,\boldsymbol{\Phi}^{e}\Delta\boldsymbol{V}_m^{s}$$

$$(^{i}\boldsymbol{\varepsilon}_n)^{o}=(1/2)\boldsymbol{B}_n\boldsymbol{\Phi}_I^{e}\,\boldsymbol{D}^{o}\,{}^{i}\boldsymbol{X},\ (^{i}\boldsymbol{\varepsilon}_n)_m^{c}=(1/2)\boldsymbol{B}_n\boldsymbol{\Phi}_I^{e}\,\boldsymbol{D}_m^{c}\,{}^{i}\boldsymbol{X},$$

$$(^{i}\boldsymbol{\varepsilon}_n)_m^{s}=(1/2)\boldsymbol{B}_n\boldsymbol{\Phi}_I^{e}\boldsymbol{D}_m^{s}\,{}^{i}\boldsymbol{X},$$

$$(\Delta\boldsymbol{\varepsilon}_{n1})^{o}=\boldsymbol{B}_n\boldsymbol{\Phi}_I^{e}\boldsymbol{D}^{o}\Delta\boldsymbol{X},\ (\Delta\boldsymbol{\varepsilon}_{n1})_m^{c}=\boldsymbol{B}_n\boldsymbol{\Phi}_I^{e}\,\boldsymbol{D}_m^{c}\,\Delta\boldsymbol{X},\ (\Delta\boldsymbol{\varepsilon}_{n1})_m^{s}=\boldsymbol{B}_n\boldsymbol{\Phi}_I^{e}\boldsymbol{D}_m^{s}\,\Delta\boldsymbol{X},$$

$$(\Delta\boldsymbol{\varepsilon}_g^{w})^{o}=\boldsymbol{B}_g^{w}\boldsymbol{\Phi}^{e}\Delta\boldsymbol{V}^{o},\ (\Delta\boldsymbol{\varepsilon}_g^{w})_m^{c}=\boldsymbol{B}_g^{w}\boldsymbol{\Phi}^{e}\Delta\boldsymbol{V}_m^{c},\ (\Delta\boldsymbol{\varepsilon}_g^{w})_m^{s}=\boldsymbol{B}_g^{w}\boldsymbol{\Phi}^{e}\Delta\boldsymbol{V}_m^{s},$$

$$(\Delta\boldsymbol{\varepsilon}_g^{u})^{o}=\boldsymbol{B}_g^{u}\,\boldsymbol{\Phi}^{e}\Delta\boldsymbol{V}^{o},\ (\Delta\boldsymbol{\varepsilon}_g^{u})_m^{c}=\boldsymbol{B}_g^{u}\,\boldsymbol{\Phi}^{e}\Delta\boldsymbol{V}_m^{c},\ (\Delta\boldsymbol{\varepsilon}_g^{u})_m^{s}=\boldsymbol{B}_g^{u}\,\boldsymbol{\Phi}^{e}\Delta\boldsymbol{V}_m^{s},$$

$$^{i}\boldsymbol{X}=\{(^{i}\boldsymbol{V}^{o})^{\mathrm{T}}\ \ (^{i}\boldsymbol{V}_1^{c})^{\mathrm{T}}\ \ (^{i}\boldsymbol{V}_2^{c})^{\mathrm{T}}\ldots(^{i}\boldsymbol{V}_H^{c})^{\mathrm{T}}\ \ (^{i}\boldsymbol{V}_1^{s})^{\mathrm{T}}\ \ (^{i}\boldsymbol{V}_2^{s})^{\mathrm{T}}\ldots(^{i}\boldsymbol{V}_H^{s})^{\mathrm{T}}\}^{\mathrm{T}}$$

$$\Delta\boldsymbol{X}=\{(\Delta\boldsymbol{V}^{o})^{\mathrm{T}}\ \ (\Delta\boldsymbol{V}_1^{c})^{\mathrm{T}}\ \ (\Delta\boldsymbol{V}_2^{c})^{\mathrm{T}}\ldots(\Delta\boldsymbol{V}_H^{c})^{\mathrm{T}}\ \ (\Delta\boldsymbol{V}_1^{s})^{\mathrm{T}}\ \ (\Delta\boldsymbol{V}_2^{s})^{\mathrm{T}}\ldots(\Delta\boldsymbol{V}_H^{s})^{\mathrm{T}}\}^{\mathrm{T}} \qquad (4.7a)$$

In Eq. (4.7a), the matrices $\boldsymbol{D}^{o}$, $\boldsymbol{D}_m^{c}$ and $\boldsymbol{D}_m^{s}$ ($m=1,2,3,...,2H$) are the coefficient matrices in the Fourier expansion of the term $^{i}\boldsymbol{V}_I\,{}^{i}\boldsymbol{V}$ (Eq. (4.6b)) corresponding to the constant, cosine and sine terms, respectively. These matrices ($\boldsymbol{D}^{o}$, $\boldsymbol{D}_m^{c}$, $\boldsymbol{D}_m^{s}$) can be constructed using the following relation

$$\left\langle \boldsymbol{D}^{o}+\sum_{m=1}^{2H}\left\{\boldsymbol{D}_m^{c}\cos(m\Omega t)+\boldsymbol{D}_m^{s}\sin(m\Omega t)\right\}\right\rangle {}^{i}\boldsymbol{X}=$$

$$({}^{i}\boldsymbol{V}_I)^o\ {}^{i}\boldsymbol{V}^o + \left\{ \begin{array}{l} \sum_{m=1}^{H} \left[\begin{array}{l} \left\langle ({}^{i}\boldsymbol{V}_I)^o\ {}^{i}\boldsymbol{V}_m^c + ({}^{i}\boldsymbol{V}_I)_m^c\ {}^{i}\boldsymbol{V}^o \right\rangle \cos(m\Omega t) + \\ \left\langle ({}^{i}\boldsymbol{V}_I)^o\ {}^{i}\boldsymbol{V}_m^s + ({}^{i}\boldsymbol{V}_I)_m^s\ {}^{i}\boldsymbol{V}^o \right\rangle \sin(m\Omega t) \end{array} \right] + \\ \sum_{m=1}^{H} \sum_{n=1}^{H} \frac{1}{2} \left[\begin{array}{l} \left\langle ({}^{i}\boldsymbol{V}_I)_m^c\ {}^{i}\boldsymbol{V}_n^c \right\rangle \left\langle \cos(m+n)\Omega t + \cos(m-n)\Omega t \right\rangle + \\ \left\langle ({}^{i}\boldsymbol{V}_I)_m^s\ {}^{i}\boldsymbol{V}_n^s \right\rangle \left\langle \cos(m-n)\Omega t - \cos(m+n)\Omega t \right\rangle + \\ \left\langle ({}^{i}\boldsymbol{V}_I)_m^c\ {}^{i}\boldsymbol{V}_n^s \right\rangle \left\langle \sin(m+n)\Omega t - \sin(m-n)\Omega t \right\rangle + \\ \left\langle ({}^{i}\boldsymbol{V}_I)_m^s\ {}^{i}\boldsymbol{V}_n^c \right\rangle \left\langle \sin(m+n)\Omega t + \sin(m-n)\Omega t \right\rangle \end{array} \right] \end{array} \right\} \qquad (4.7b)$$

where, the right-hand side is the simplified expression of the product of Fourier expansions of ${}^{i}\boldsymbol{V}_I$ and ${}^{i}\boldsymbol{V}$, and the matrices $\boldsymbol{D}^o$, $\boldsymbol{D}_m^c$ and $\boldsymbol{D}_m^s$ ($m = 1,2,3,...,2H$) can be obtained through the harmonic balance. Now, using Eqs. (4.7a) and (3.19a), the coefficient matrices in the Fourier expansions of the terms ${}^{i}\boldsymbol{\Gamma}^k\,\Delta\boldsymbol{\varepsilon}_g^w$ and ${}^{i}\boldsymbol{\Gamma}^k\,\Delta\boldsymbol{\varepsilon}_g^u$ (Eq. (3.21)) can be obtained, as given in Eq. (4.7c). The matrices $(\boldsymbol{\Upsilon}_w^k)^o$, $(\boldsymbol{\Upsilon}_w^k)_m^c$ and $(\boldsymbol{\Upsilon}_w^k)_m^s$ ($m = 1,2,3,...,3H$) in the expanded form of ${}^{i}\boldsymbol{\Gamma}^k\,\Delta\boldsymbol{\varepsilon}_g^w$ can be derived following Eq. (4.7d) through the harmonic balance. The same procedure can also be followed to obtain the matrices ($(\boldsymbol{\Upsilon}_u^k)^o$, $(\boldsymbol{\Upsilon}_u^k)_m^c$, $(\boldsymbol{\Upsilon}_u^k)_m^s$) in the expanded form of ${}^{i}\boldsymbol{\Gamma}^k\,\Delta\boldsymbol{\varepsilon}_g^u$.

$$({}^{i}\boldsymbol{\Gamma}^k\,\Delta\boldsymbol{\varepsilon}_g^w)^o = (\boldsymbol{\Upsilon}_w^k)^o\,\Delta\boldsymbol{X}\ ,\quad ({}^{i}\boldsymbol{\Gamma}^k\,\Delta\boldsymbol{\varepsilon}_g^w)_m^c = (\boldsymbol{\Upsilon}_w^k)_m^c\,\Delta\boldsymbol{X}\ ,\quad ({}^{i}\boldsymbol{\Gamma}^k\,\Delta\boldsymbol{\varepsilon}_g^w)_m^s = (\boldsymbol{\Upsilon}_w^k)_m^s\,\Delta\boldsymbol{X}$$

$$({}^{i}\boldsymbol{\Gamma}^k\,\Delta\boldsymbol{\varepsilon}_g^u)^o = (\boldsymbol{\Upsilon}_u^k)^o\,\Delta\boldsymbol{X}\ ,\quad ({}^{i}\boldsymbol{\Gamma}^k\,\Delta\boldsymbol{\varepsilon}_g^u)_m^c = (\boldsymbol{\Upsilon}_u^k)_m^c\,\Delta\boldsymbol{X}\ ,\quad ({}^{i}\boldsymbol{\Gamma}^k\,\Delta\boldsymbol{\varepsilon}_g^u)_m^s = (\boldsymbol{\Upsilon}_u^k)_m^s\,\Delta\boldsymbol{X}\ ,$$

$$m = 1,2,3,...,3H \qquad (4.7c)$$

$$\left\langle (\boldsymbol{\Upsilon}_w^k)^o + \sum_{m=1}^{3H} \left\{ (\boldsymbol{\Upsilon}_w^k)_m^c \cos(m\Omega t) + (\boldsymbol{\Upsilon}_w^k)_m^s \sin(m\Omega t) \right\} \right\rangle \Delta\boldsymbol{X} = ({}^{i}\boldsymbol{\Gamma}^k)^o\,\boldsymbol{B}_g^w \boldsymbol{\Phi}^e\,\Delta\boldsymbol{V}^o +$$

$$\left\{ \begin{array}{l} \sum_{m=1}^{2H} \left[\begin{array}{l} \left\langle ({}^{i}\boldsymbol{\Gamma}^k)^o\,\boldsymbol{B}_g^w \boldsymbol{\Phi}^e\,\Delta\boldsymbol{V}_m^c + ({}^{i}\boldsymbol{\Gamma}^k)_m^c\,\boldsymbol{B}_g^w \boldsymbol{\Phi}^e\,\Delta\boldsymbol{V}^o \right\rangle \cos(m\Omega t) + \\ \left\langle ({}^{i}\boldsymbol{\Gamma}^k)^o\,\boldsymbol{B}_g^w \boldsymbol{\Phi}^e\,\Delta\boldsymbol{V}_m^s + ({}^{i}\boldsymbol{\Gamma}^k)_m^s\,\boldsymbol{B}_g^w \boldsymbol{\Phi}^e\,\Delta\boldsymbol{V}^o \right\rangle \sin(m\Omega t) \end{array} \right] + \\ \sum_{m=1}^{2H} \sum_{n=1}^{H} \frac{1}{2} \left[\begin{array}{l} \left\langle ({}^{i}\boldsymbol{\Gamma}^k)_m^c\,\boldsymbol{B}_g^w \boldsymbol{\Phi}^e\,\Delta\boldsymbol{V}_n^c \right\rangle \left\langle \cos(m+n)\Omega t + \cos(m-n)\Omega t \right\rangle + \\ \left\langle ({}^{i}\boldsymbol{\Gamma}^k)_m^s\,\boldsymbol{B}_g^w \boldsymbol{\Phi}^e\,\Delta\boldsymbol{V}_n^s \right\rangle \left\langle \cos(m-n)\Omega t - \cos(m+n)\Omega t \right\rangle + \\ \left\langle ({}^{i}\boldsymbol{\Gamma}^k)_m^c\,\boldsymbol{B}_g^w \boldsymbol{\Phi}^e\,\Delta\boldsymbol{V}_n^s \right\rangle \left\langle \sin(m+n)\Omega t - \sin(m-n)\Omega t \right\rangle + \\ \left\langle ({}^{i}\boldsymbol{\Gamma}^k)_m^s\,\boldsymbol{B}_g^w \boldsymbol{\Phi}^e\,\Delta\boldsymbol{V}_n^c \right\rangle \left\langle \sin(m+n)\Omega t + \sin(m-n)\Omega t \right\rangle \end{array} \right] \end{array} \right\} \qquad (4.7d)$$

Now, substituting Eqs. (4.6a), (4.6b), (4.7a) and (4.7c) in Eq. (3.21), the linearized incremental reduced-order FE equation of motion of the sandwich beam in the frequency domain can be obtained as

$$
\begin{aligned}
&{}^{r}\boldsymbol{K}_t\,\Delta\boldsymbol{X} = {}^{r}\boldsymbol{R} + {}^{r}\boldsymbol{R}_{\Omega}\,\Delta\Omega \\
&{}^{r}\boldsymbol{R} = p_t^o\,{}^{r}\boldsymbol{P} + p_{tu}^o\,{}^{r}\boldsymbol{P}_u - {}^{r}\boldsymbol{K}_m\,{}^{i}\boldsymbol{X}\,,\quad {}^{r}\boldsymbol{R}_{\Omega} = -(\partial\,{}^{r}\boldsymbol{K}_m/\partial\Omega_i)\,{}^{i}\boldsymbol{X}\,, \\
&{}^{r}\boldsymbol{K}_m = {}^{r}\boldsymbol{K}_l - \Omega_i^2\,{}^{r}\boldsymbol{M} + (1/2)\,{}^{r}\boldsymbol{K}_{n1} + {}^{r}\boldsymbol{K}_{nt} + (1/2)\,{}^{r}\boldsymbol{K}_{n4}\,, \\
&{}^{r}\boldsymbol{K}_t = {}^{r}\boldsymbol{K}_l - \Omega_i^2\,{}^{r}\boldsymbol{M} + {}^{r}\boldsymbol{K}_{n1} + {}^{r}\boldsymbol{K}_{nt} + {}^{r}\boldsymbol{K}_g + {}^{r}\boldsymbol{K}_{n4} \\
&{}^{r}\boldsymbol{K}_l = \sum_{k=1}^{2}{}^{r}\boldsymbol{K}_l^k\,,\ {}^{r}\boldsymbol{K}_{n1} = \sum_{k=1}^{2}{}^{r}\boldsymbol{K}_{n1}^k\,,\ {}^{r}\boldsymbol{K}_{nt} = \sum_{k=1}^{2}{}^{r}\boldsymbol{K}_{nt}^k\,,\ {}^{r}\boldsymbol{K}_{n4} = \sum_{k=1}^{2}{}^{r}\boldsymbol{K}_{n4}^k
\end{aligned}
\tag{4.8}
$$

where, ${}^{r}\boldsymbol{K}_m$ and ${}^{r}\boldsymbol{K}_t$ are the overall reduced-order stiffness and tangent stiffness matrices, respectively; ${}^{r}\boldsymbol{R}$ is the overall reduced-order residue vector; ${}^{r}\boldsymbol{R}_{\Omega}$ is the overall reduced-order load vector per unit increment of the excitation frequency. The matrices ${}^{r}\boldsymbol{M}$, ${}^{r}\boldsymbol{K}_l^k$, ${}^{r}\boldsymbol{K}_{n1}^k$, ${}^{r}\boldsymbol{K}_g$, ${}^{r}\boldsymbol{K}_{nt}^k$, ${}^{r}\boldsymbol{K}_{n4}^k$ and vectors ${}^{r}\boldsymbol{P}$, ${}^{r}\boldsymbol{P}_u$ appearing in Eq. (4.8) can be constructed according to the following expressions

$$
(\delta\Delta\boldsymbol{X})^{\mathrm{T}}\,{}^{r}\boldsymbol{M}\,\Delta\boldsymbol{X} = \sum_{m=1}^{H} m^2 \left\langle (\delta\Delta\boldsymbol{V}_m^c)^{\mathrm{T}}\,{}^{r}\boldsymbol{M}_s\,\Delta\boldsymbol{V}_m^c + (\delta\Delta\boldsymbol{V}_m^s)^{\mathrm{T}}\,{}^{r}\boldsymbol{M}_s\,\Delta\boldsymbol{V}_m^s \right\rangle,
$$

$$
\begin{aligned}
(\delta\Delta\boldsymbol{X})^{\mathrm{T}}\,{}^{r}\boldsymbol{K}_l^k\,\Delta\boldsymbol{X} = {} & 2(\delta\Delta\boldsymbol{V}^o)^{\mathrm{T}}\,{}^{r}\boldsymbol{K}_{sl}^k\,\Delta\boldsymbol{V}^o + \\
& \sum_{m=1}^{H} \left\langle \begin{matrix} (\delta\Delta\boldsymbol{V}_m^c)^{\mathrm{T}}\,{}^{r}\boldsymbol{K}_{sl}^k\,(f_m^c\Delta\boldsymbol{V}_m^c + f_m^s\Delta\boldsymbol{V}_m^s) + \\ (\delta\Delta\boldsymbol{V}_m^s)^{\mathrm{T}}\,{}^{r}\boldsymbol{K}_{sl}^k\,(f_m^c\Delta\boldsymbol{V}_m^s - f_m^s\Delta\boldsymbol{V}_m^c) \end{matrix} \right\rangle,
\end{aligned}
$$

$$
(\delta\Delta\boldsymbol{X})^{\mathrm{T}}\,{}^{r}\boldsymbol{K}_{n1}^k\Delta\boldsymbol{X} = \left\{ \begin{matrix} 2(\delta\Delta\boldsymbol{V}^o)^{\mathrm{T}}\,{}^{r}\boldsymbol{K}_{sn1}^k\,\boldsymbol{D}^o + \\ \sum_{m=1}^{H} \left\langle \begin{matrix} (\delta\Delta\boldsymbol{V}_m^c)^{\mathrm{T}}\,{}^{r}\boldsymbol{K}_{sn1}^k\,(f_m^c\boldsymbol{D}_m^c + f_m^s\boldsymbol{D}_m^s) + \\ (\delta\Delta\boldsymbol{V}_m^s)^{\mathrm{T}}\,{}^{r}\boldsymbol{K}_{sn1}^k\,(f_m^c\boldsymbol{D}_m^s - f_m^s\boldsymbol{D}_m^c) \end{matrix} \right\rangle \end{matrix} \right\} \Delta\boldsymbol{X}\,,
$$

$$
{}^{r}\boldsymbol{K}_{n4}^k = 2(\boldsymbol{D}^o)^{\mathrm{T}}\,{}^{r}\boldsymbol{K}_{sn4}^k\,\boldsymbol{D}^o + \sum_{m=1}^{2H} \left\langle \begin{matrix} (\boldsymbol{D}_m^c)^{\mathrm{T}}\,{}^{r}\boldsymbol{K}_{sn4}^k\,(f_m^c\boldsymbol{D}_m^c + f_m^s\boldsymbol{D}_m^s) \\ +(\boldsymbol{D}_m^s)^{\mathrm{T}}\,{}^{r}\boldsymbol{K}_{sn4}^k\,(f_m^c\boldsymbol{D}_m^s - f_m^s\boldsymbol{D}_m^c) \end{matrix} \right\rangle,
$$

$$
(\delta\Delta\boldsymbol{X})^{\mathrm{T}}\,{}^{r}\boldsymbol{K}_g\,\Delta\boldsymbol{X} = \left\{ \begin{matrix} 2(\delta\Delta\boldsymbol{V}^o)^{\mathrm{T}}({}^{r}\boldsymbol{K}_{sg})^o + \\ \sum_{m=1}^{H} \left\langle (\delta\Delta\boldsymbol{V}_m^c)^{\mathrm{T}}({}^{r}\boldsymbol{K}_{sg})_m^c + (\delta\Delta\boldsymbol{V}_m^s)^{\mathrm{T}}({}^{r}\boldsymbol{K}_{sg})_m^s \right\rangle \end{matrix} \right\} \Delta\boldsymbol{X}\,,
$$

$$
(\Delta\boldsymbol{X})^{\mathrm{T}}\,{}^{r}\boldsymbol{K}_{nt}^k\Delta\boldsymbol{X} = (\delta\Delta\boldsymbol{X})^{\mathrm{T}} \left\{ \begin{matrix} 2(\boldsymbol{D}^o)^{\mathrm{T}}({}^{r}\boldsymbol{K}_{sn1}^k)^{\mathrm{T}}\,\Delta\boldsymbol{V}^o + \\ \sum_{m=1}^{H} \left\langle \begin{matrix} (\boldsymbol{D}_m^c)^{\mathrm{T}}({}^{r}\boldsymbol{K}_{sn1}^k)^{\mathrm{T}}\,(f_m^c\Delta\boldsymbol{V}_m^c + f_m^s\Delta\boldsymbol{V}_m^s) + \\ (\boldsymbol{D}_m^s)^{\mathrm{T}}({}^{r}\boldsymbol{K}_{sn1}^k)^{\mathrm{T}}\,(f_m^c\Delta\boldsymbol{V}_m^s - f_m^s\Delta\boldsymbol{V}_m^c) \end{matrix} \right\rangle \end{matrix} \right\};
$$

$$(\delta\Delta\boldsymbol{X})^{\mathrm{T}}\ {}^{r}\boldsymbol{P}=(\delta\Delta\boldsymbol{V}_m^c)^{\mathrm{T}}\,{}^{r}\boldsymbol{P}_s\,,\ (\delta\Delta\boldsymbol{X})^{\mathrm{T}}\ {}^{r}\boldsymbol{P}_u=(\delta\Delta\boldsymbol{V}_m^c)^{\mathrm{T}}\,{}^{r}\boldsymbol{P}_{su}\ \text{ at }\ m=1. \tag{4.9a}$$

where, the matrices/vectors ${}^{r}\boldsymbol{M}_s$, ${}^{r}\boldsymbol{K}_{sl}^{k}$, ${}^{r}\boldsymbol{K}_{sn1}^{k}$, ${}^{r}\boldsymbol{K}_{sn4}^{k}$, ${}^{r}\boldsymbol{P}_s$ and ${}^{r}\boldsymbol{P}_{su}$ are defined in Eq. (4.3a), and the other matrices $({}^{r}\boldsymbol{K}_{sg})^{o}$, $({}^{r}\boldsymbol{K}_{sg})_m^s$ and $({}^{r}\boldsymbol{K}_{sg})_m^c$ are as follows

$$({}^{r}\boldsymbol{K}_{sg})^{o}=\sum_{e=1}^{n_e}(\boldsymbol{\Phi}^e)^{\mathrm{T}}(\boldsymbol{K}_{sg}^e)^{o}\ ,\ ({}^{r}\boldsymbol{K}_{sg})_m^c=\sum_{e=1}^{n_e}(\boldsymbol{\Phi}^e)^{\mathrm{T}}(\boldsymbol{K}_{sg}^e)_m^c\,,$$

$$({}^{r}\boldsymbol{K}_{sg})_m^s=\sum_{e=1}^{n_e}(\boldsymbol{\Phi}^e)^{\mathrm{T}}(\boldsymbol{K}_{sg}^e)_m^s\,,$$

$$(\boldsymbol{K}_{sg}^e)_m^c=\int_{A^e}\left\{(\boldsymbol{B}_g^w)^{\mathrm{T}}(\boldsymbol{\Upsilon}_w^k)_m^c+(\boldsymbol{B}_g^u)^{\mathrm{T}}(\boldsymbol{\Upsilon}_u^k)_m^c\right\}b\,dA^e\,,$$

$$(\boldsymbol{K}_{sg}^e)_m^s=\int_{A^e}\left\{(\boldsymbol{B}_g^w)^{\mathrm{T}}(\boldsymbol{\Upsilon}_w^k)_m^s+(\boldsymbol{B}_g^u)^{\mathrm{T}}(\boldsymbol{\Upsilon}_u^k)_m^s\right\}b\,dA^e\,,$$

$$(\boldsymbol{K}_{sg}^e)^{o}=\int_{A^e}\left\{(\boldsymbol{B}_g^w)^{\mathrm{T}}(\boldsymbol{\Upsilon}_w^k)^{o}+(\boldsymbol{B}_g^u)^{\mathrm{T}}(\boldsymbol{\Upsilon}_u^k)^{o}\right\}b\,dA^e\ ,\quad m=1,2,...,H \tag{4.9b}$$

In Eq. (4.8), the overall reduced-order stiffness matrix per unit change of the excitation frequency ($\partial\,{}^{r}\boldsymbol{K}_m/\partial\Omega_i$) can be obtained similar to ${}^{r}\boldsymbol{K}_m$, where the frequency-independent component matrices are to be omitted. Also, the parameters f_m^c and f_m^s are to be replaced by $\partial f_m^c/\partial\Omega_i$ and $\partial f_m^s/\partial\Omega_i$, respectively.

A simplified formulation of the tangent stiffness matrix ($\boldsymbol{K}_t$) was carried out in the previous chapter through Eqs. (3.30a), (3.30b) and (3.31), where the geometric stiffness matrix ($\boldsymbol{K}_g$) is constructed without consideration of its viscoelastic counterpart. This simplification of $\boldsymbol{K}_g$ towards the formulation of $\boldsymbol{K}_t$ for the present viscoelastic sandwich beams provides the advantage of reduced computational time (Table 3.2). Also, it works well to evaluate nonlinear frequency response curves using a numerical continuation method, as verified through the results in Fig. 3.5. So, the same strategy is followed here to simplify the formulation of the reduced-order tangent stiffness matrix ($^{r}\boldsymbol{K}_t$), where the formulation of the reduced-order geometric stiffness matrix ($^{r}\boldsymbol{K}_g$) is simplified using Eq. (3.30b) and the coefficient matrices in the Fourier expansion of the term ${}^{i}\boldsymbol{V}_I\,{}^{i}\boldsymbol{V}$ (Eq. (4.7b)). Accordingly, the expression of ${}^{r}\boldsymbol{K}_g$ can be obtained as follows

$${}^{r}\boldsymbol{K}_g={}^{r}\boldsymbol{K}_{n3}+(1/2)\ {}^{r}\boldsymbol{K}_{n5}$$

$$(\delta\Delta\boldsymbol{X})^{\mathrm{T}}\,{}^{r}\boldsymbol{K}_{n3}^{k}\,\Delta\boldsymbol{X}=\left\{\begin{array}{l}2(\delta\Delta\boldsymbol{V}^{o})^{\mathrm{T}}\,{}^{r}\boldsymbol{K}_{sn3}^{k}\,\boldsymbol{D}^{o}+\\ \sum_{m=1}^{H}\left\langle(\delta\Delta\boldsymbol{V}_{m}^{c})^{\mathrm{T}}\,{}^{r}\boldsymbol{K}_{sn3}^{k}\,\boldsymbol{D}_{m}^{c}+(\delta\Delta\boldsymbol{V}_{m}^{s})^{\mathrm{T}}\,{}^{r}\boldsymbol{K}_{sn3}^{k}\,\boldsymbol{D}_{m}^{s}\right\rangle\end{array}\right\}\Delta\boldsymbol{X}\,,$$

$${}^{r}\boldsymbol{K}_{n5}^{k}=2(\boldsymbol{D}^{o})^{\mathrm{T}}\,{}^{r}\boldsymbol{K}_{sn5}^{k}\,\boldsymbol{D}^{o}+\sum_{m=1}^{2H}\left\langle(\boldsymbol{D}_{m}^{c})^{\mathrm{T}}\,{}^{r}\boldsymbol{K}_{sn5}^{k}\boldsymbol{D}_{m}^{c}+(\boldsymbol{D}_{m}^{s})^{\mathrm{T}}\,{}^{r}\boldsymbol{K}_{sn5}^{k}\,\boldsymbol{D}_{m}^{s}\right\rangle$$

$${}^{r}\boldsymbol{K}_{sn3}^{k}=\sum_{e\in\boldsymbol{\Xi}^{k}}(\boldsymbol{\Phi}^{e})^{\mathrm{T}}\,\boldsymbol{K}_{sn3}^{e}\,\boldsymbol{\Phi}_{I}^{e}\,,\;{}^{r}\boldsymbol{K}_{sn5}^{k}=\sum_{e\in\boldsymbol{\Xi}^{k}}(\boldsymbol{\Phi}_{I}^{e})^{\mathrm{T}}\,\boldsymbol{K}_{sn5}^{e}\,\boldsymbol{\Phi}_{I}^{e}\,,\;k=1 \qquad (4.10)$$

According to Eq. (4.10), the repeated formation of the geometric stiffness matrix (${}^{r}\boldsymbol{K}_{g}$) can be avoided so that none of the component matrices/vectors (${}^{r}\boldsymbol{K}_{sn1}^{k}$, ${}^{r}\boldsymbol{K}_{sn3}^{k}$, ${}^{r}\boldsymbol{K}_{sn4}^{k}$, ${}^{r}\boldsymbol{K}_{sn5}^{k}$, ${}^{r}\boldsymbol{K}_{sl}^{k}$, ${}^{r}\boldsymbol{M}_{s}$) is to be constructed in each Newton-Raphson iteration during the solution of the reduced-order equation of motion. It leads to a decent reduction of the computational time, which is illustrated through numerical results in Section 4.5.1.

4.4. Enrichment of basis vectors

The accuracy of a reduced-order FE model primarily depends on the selection of appropriate RBVs. In this concern, different approaches (MSE, MSEC, MM, ICES, RKT and FSRK) are proposed in the literature for the selection of RBVs. However, these RBVs are originally proposed for linear dynamic analysis of viscoelastic structures. So, these RBVs may not be appropriate ones for accurately modelling various phenomena in nonlinear analysis like bending-stretching coupling, bending-twist coupling, coupling between lower and higher modes, etc. Therefore, the enrichment of these RBVs may be needed for their application in the nonlinear analysis of viscoelastic structures, and it is presently carried out based on the popular concept of modal derivatives (MDs).

For deriving a reduced-order FE model, the common practice is to choose the RBVs as the first few vibration modes (VMs) associated with lower natural frequencies. Although it provides good accuracy in the linear dynamic analysis, enrichment of these RBVs for the nonlinear dynamic analysis can be achieved through MDs (Rutzmoser et al., 2017). These MDs are commonly derived from the vibration modes by differentiating the eigenvalue problem with respect to the reduced coordinates. Now, if these MDs are derived by neglecting the mass matrix, then those are commonly called static MDs (Rutzmoser et al., 2017). However, this methodology for the derivation of static MDs can be followed to enrich not only VMs but also RBVs obtained through any other approach of deriving basis vectors. Here, the resulting vectors are called static derivatives (SDs) (Rutzmoser

et al., 2017). So, for the present case of the dynamic analysis of viscoelastic structures with frequency-dependent material properties, the recommended approaches (MSE/MSEC/MM/ICES/RKT/FSRK) for the RBVs in the linear analysis are utilized; however, these RBVs are enriched with the corresponding SDs especially for the nonlinear dynamic analysis. It may also be noted here that some of the RBVs obtained through the aforesaid approaches lie in the complex domain so that the union of their real and imaginary parts are considered (Kuether, 2019) as RBVs. Further, a static correction vector (Rouleau et al., 2017) is also added in the set of RBVs to account truncated modes. A set of SDs ($\boldsymbol{\varphi}_{pj}$, p or j = 1, 2, 3,..., N_m) for a given set of RBVs ($\boldsymbol{\theta}_p$, p = 1, 2, 3,..., N_m) of a structure oscillating about its static equilibrium position can be evaluated using Eq. (4.11a) (Rutzmoser et al., 2017) where N_m is the number of RBVs ($\boldsymbol{\theta} = [\boldsymbol{\theta}_1 \quad \boldsymbol{\theta}_2 \quad \ldots \quad \boldsymbol{\theta}_{N_m}]$).

$$\boldsymbol{K}\big|_{eq}\,\boldsymbol{\varphi}_{pj} = \left.\frac{\partial \boldsymbol{K}(\boldsymbol{d} = \boldsymbol{\theta}\boldsymbol{v})}{\partial v_j}\right|_{eq} \boldsymbol{\theta}_p \tag{4.11a}$$

In Eq. (4.11a), $\boldsymbol{d}$ is the global nodal displacement vector; $\boldsymbol{\varphi}_{pj}$ is the SD of p^{th} RBV ($\boldsymbol{\theta}_p$) with respect to the j^{th} reduced coordinate; v_j is the j^{th} element of the reduced coordinate vector ($\boldsymbol{v}$); the subscript 'eq' denotes the quantity at the static equilibrium position ($\boldsymbol{d} = \boldsymbol{0}$ or $\boldsymbol{v} = \boldsymbol{0}$); $\boldsymbol{K}$ is the tangent stiffness matrix of the sandwich beam for its static deformation. This tangent stiffness matrix ($\boldsymbol{K}$) can be obtained through the derivation of the strain energy term in Eq. (3.6) considering the constitutive behavior of the viscoelastic material similar to that for an elastic material (Eq. (2.3a)), where the elastic modulus may be taken as the relaxed modulus ($E^k = E_o$, $k = 2$) for the static deformation of the sandwich beam. However, this derivation of the strain energy term (in Eq. (3.9)) by introducing the incremental forms of elemental nodal displacement and strain vectors (Eq. (4.6a)) yields the stiffness matrices $\boldsymbol{K}^e_{sl}$, $\boldsymbol{K}^e_{sn1}$, $\boldsymbol{K}^e_{sn3}$, $\boldsymbol{K}^e_{sn4}$ and $\boldsymbol{K}^e_{sn5}$ (Eqs. (3.28) and (3.30b)) for a typical element. Subsequently, the assembly of these elemental stiffness matrices for the k^{th} material in the sandwich beam provides the component stiffness matrices ($\boldsymbol{K}^k_{sl}$, $\boldsymbol{K}^k_{sn1}$, $\boldsymbol{K}^k_{sn3}$, $\boldsymbol{K}^k_{sn4}$ and $\boldsymbol{K}^k_{sn5}$) in the expression for the tangent stiffness matrix ($\boldsymbol{K}$), as given in Eq. (4.11b) where N_f represents the number of global nodal degrees of freedom and $\boldsymbol{I}_{N_f}$ is the unit matrix of size

($N_f \times N_f$). Now, the derivative of tangent stiffness matrix ($\boldsymbol{K}$) with respect to the reduced coordinate (v_j) can be derived as it is illustrated in Eq. (4.11c).

$$\boldsymbol{K} = \sum_{k=1}^{2} \boldsymbol{K}_{sl}^{k} + (\boldsymbol{K}_{sn1}^{k} + \boldsymbol{K}_{sn3}^{k})\,{}^{i}\boldsymbol{d}_I + ({}^{i}\boldsymbol{d}_I)^{\mathrm{T}}(\boldsymbol{K}_{sn1}^{k})^{\mathrm{T}} + ({}^{i}\boldsymbol{d}_I)^{\mathrm{T}}\left\langle \boldsymbol{K}_{sn4}^{k} + (1/2)\boldsymbol{K}_{sn5}^{k} \right\rangle {}^{i}\boldsymbol{d}_I \,,$$

$${}^{i}\boldsymbol{d}_I = {}^{i}\boldsymbol{d} \otimes \boldsymbol{I}_{N_f} \tag{4.11b}$$

$$\frac{\partial \boldsymbol{K}({}^{i}\boldsymbol{d} = \boldsymbol{\theta}\boldsymbol{v})}{\partial v_j} = \sum_{k=1}^{2} \begin{array}{l} \left\langle \boldsymbol{K}_{sn1}^{k} + \boldsymbol{K}_{sn3}^{k} + ({}^{i}\boldsymbol{d}_I)^{\mathrm{T}}\left(\boldsymbol{K}_{sn4}^{k} + (1/2)\boldsymbol{K}_{sn5}^{k}\right)\right\rangle (\boldsymbol{\theta}_j \otimes \boldsymbol{I}_{N_f}) + \\ (\boldsymbol{\theta}_j \otimes \boldsymbol{I}_{N_f})^{\mathrm{T}} \left\{ (\boldsymbol{K}_{sn1}^{e})^{\mathrm{T}} + \left\langle \boldsymbol{K}_{sn4}^{e} + (1/2)\boldsymbol{K}_{sn5}^{e} \right\rangle {}^{i}\boldsymbol{d}_I \right\} \end{array} \tag{4.11c}$$

The right-hand part of Eq. (4.11a) denotes a pseudo-force vector (say, $\boldsymbol{F}_{pj} = \left\langle \partial \boldsymbol{K}(\boldsymbol{d} = \boldsymbol{\theta}\boldsymbol{v})/\partial v_j \right\rangle\big|_{eq} \boldsymbol{\theta}_p$) that involves the computationally expensive multiplication (Eq. (4.11a) and (4.11c)) of stiffness matrices ($\boldsymbol{K}_{sn1}^{k}$, $\boldsymbol{K}_{sn3}^{k}$, $\boldsymbol{K}_{sn4}^{k}$ and $\boldsymbol{K}_{sn5}^{k}$) and basis vectors ($\boldsymbol{\theta}_p$) at the full-order scale. However, it can also be computed with less computational cost by assembling the corresponding elemental pseudo-force vectors ($\boldsymbol{F}_{ij}^{e}$), as given Eq. (4.11d) where $\boldsymbol{\theta}_p^{e}$ is the p^{th} RBV ($\boldsymbol{\theta}_p$) for a typical element.

$$\boldsymbol{F}_{pj}^{e} = \left.\frac{\partial \boldsymbol{K}^{e}({}^{i}\boldsymbol{d}^{e} = \boldsymbol{\theta}^{e}\boldsymbol{v})}{\partial v_j}\right|_{eq} \boldsymbol{\theta}_p^{e} = \left\{ \begin{array}{l} \boldsymbol{K}_{sn1}^{e} + \boldsymbol{K}_{sn3}^{e} + \\ ({}^{i}\boldsymbol{d}_I^{e})^{\mathrm{T}} \left\langle \boldsymbol{K}_{sn4}^{e} + (1/2)\boldsymbol{K}_{sn5}^{e} \right\rangle \end{array} \right\} (\boldsymbol{\theta}_j^{e} \otimes \boldsymbol{\theta}_p^{e}) +$$
$$(\boldsymbol{\theta}_j^{e} \otimes \boldsymbol{I}_{18})^{\mathrm{T}} \left\{ (\boldsymbol{K}_{sn1}^{e})^{\mathrm{T}} \boldsymbol{\theta}_p^{e} + \left\langle \boldsymbol{K}_{sn4}^{e} + (1/2)\boldsymbol{K}_{sn5}^{e} \right\rangle \left({}^{i}\boldsymbol{d}^{e} \otimes \boldsymbol{\theta}_p^{e} \right) \right\} \tag{4.11d}$$

Thus, the tangent stiffness matrix ($\boldsymbol{K}|_{eq}$, Eq. (4.11a)) at the static equilibrium position ($\boldsymbol{d} = \boldsymbol{0}$) can be derived by substituting ${}^{i}\boldsymbol{d} = \boldsymbol{0}$ in Eq. (4.11b). Whereas pseudo-force vectors ($\boldsymbol{F}_{pj} = \left\langle \partial \boldsymbol{K}(\boldsymbol{d} = \boldsymbol{\theta}\boldsymbol{v})/\partial v_j \right\rangle\big|_{eq} \boldsymbol{\theta}_p$, Eq. (4.11a)) can be derived first by substituting ${}^{i}\boldsymbol{d}^{e} = \boldsymbol{0}$ in Eq. (4.11d) and then by assembling the corresponding elemental pseudo-force vectors.

Now, for a finite number (N_m) of RBVs, there exist $N_m(N_m+1)/2$ number of unique SDs following their symmetry ($\boldsymbol{\varphi}_{pj} = \boldsymbol{\varphi}_{jp}$) (Rutzmoser et al., 2017). Further, these SDs may not be orthogonal to the RBVs. So, the resulting enriched reduction basis may lead to bad conditioning or singularities in the reduced-order FE model. Hence, in this work, the appropriate basis vectors are selected from a

reduction basis ($\boldsymbol{\Theta}_q, q=1, 2,..., N_f$) generated by implementing the proper orthogonal decomposition (POD) over the union of stiffness-normalized RBVs and SDs as

$$\left(\mathfrak{R}-\lambda_q \boldsymbol{I}_{N_f}\right)\boldsymbol{\Theta}_q=0,$$

$$\mathfrak{R}=\frac{1}{N_l}\left(\boldsymbol{\Psi}\,\boldsymbol{\Psi}^T\right),\ \boldsymbol{\Psi}=\left[\Psi_1 \quad \Psi_2 \quad \Psi_3 \quad .... \quad \Psi_{N_l}\right],$$

$$\Psi_s=\Lambda_s\Big/\left\langle(\Lambda_s)^{\mathrm{T}}\,\boldsymbol{K}\big|_{eq}\,\Lambda_s\right\rangle,\ s=1, 2,..., N_l,\ N_l=N_m+\left\langle N_m(N_m+1)/2\right\rangle \tag{4.12}$$

where, Λ_s denotes the s^{th} basis vector from the unified set of RBVs ($\boldsymbol{\theta}_p$) and SDs ($\boldsymbol{\varphi}_{pj}$); $\mathfrak{R}$ is the correlation matrix; λ_q and $\boldsymbol{\Theta}_q$ are the q^{th} proper orthogonal value (POV) and proper orthogonal mode (POM), respectively. So, the enriched reduction basis ($\boldsymbol{\Phi}$) is formed by taking the first few number of basis vectors from a set of POMs that are arranged in descending order of their POVs.

4.5. Results and discussion

The elastic face layers of the viscoelastic sandwich beam are considered to be made of aluminum (E = 70.3 GPa, ν = 0.345, ρ =2690 kg/m^3), while the viscoelastic core is made of 3M ISD 112 (Galucio et al., 2004) (ν = 0.499, ρ =1600 kg/m^3). The viscoelastic material is modelled by fractional Zener viscoelastic constitutive relation where the model parameters (Galucio et al., 2004) are E_o = 1.5 MPa, E_∞ = 69.9495 MPa, α = 0.7915 and $\tau=1.4052\times10^{-5}$ s. The geometrical properties of the sandwich beam (Fig. 3.1) are taken as L = 0.35 m, b = 10 mm, h_{s1} = 5 mm, h_v = 1.5 mm, h_{s2} = 0.5 mm. This beam (Fig. 3.1) is considered to operate under a transverse harmonic point-load or a haversine impulse point-load while the ends of the bottom face layer are considered as fully-clamped ends. The aforesaid point loads are applied at a location $x_l = L/4$, $z_l = 0$ (Eq. (3.3a)). For the transient responses of the sandwich beam under the haversine impulse load, the corresponding transverse displacement (w) is evaluated at the point of loading for presenting the numerical results. Similarly, for the frequency responses of the sandwich beam under the transverse harmonic point-load, the corresponding transverse displacement-amplitude (w) is evaluated at the point of loading and presented in the numerical results.

The amplitude (p_t^o) of the transverse harmonic point-load is considered as 30 N, while the haversine impulse point-load is taken in the form

$p_t(t) = 800 \sin^2(\Omega t/2)$ N with the pulse duration of $2\pi/\Omega$ seconds (Ω =3000 rad/s). The FE mesh for the sandwich beam is considered with 100 elements in each of the elastic layers and 200 elements in viscooelastic core layer following the mesh convergence study in the previous chapter. The corresponding FE codes are written in MATLAB and executed in a CPU with the Octa-Core processor Intel(R) Core(TM) i7-6700 CPU @ 3.4 GHz and RAM of 16 GB. In the case of the computation of transient responses using Newmark method, the value of the time-step is taken as $(\pi/3)\times10^{-5}$ s.

4.5.1. Computational efficiency and accuracy of the present ROMs using enriched RB

Usually, the large-amplitude vibration of a beam element exhibits the bending-stretching coupling phenomenon, and it implies the need of enrichment of RB with the higher-order modes. Therefore, in this subsection, the utility of the aforesaid enrichment of RBVs towards a good accuracy of the ROM in the time/frequency domain is studied with reference to the transient/frequency responses obtained from the previously derived (Chapter 3) full-order FE model. Concurrently, the computational time is also noted in the evaluation of transient/frequency responses through both the reduced-order and full-order FE models especially to illustrate the computational efficiency of the present ROMs.

However, for this computation, the RBVs are considered using the first three complex eigenmodes (say, N_b = 3) that are obtained by the solution of the frequency-dependent complex nonlinear eigenvalue problem in the ICES approach. Additionally, one static correction vector is considered to account for truncated terms in the modal expansion of static solution (Rouleau et al., 2017). Since the eigenmodes are in the complex domain, the RBVs are taken with their real and imaginary parts separately, and thus a total of seven ($2N_b+1$) basis vectors (N_m = 7) appear including a static correction vector. However, the corresponding enriched RB is evaluated by applying POD (Eq. (4.12)) over the union (N_l = 35) of RBVs (N_m =7) and their corresponding SDs (28 vectors), as the corresponding procedure is demonstrated in Section 4.4. Accordingly, the enriched RB ($\boldsymbol{\Phi}$) is constructed by considering the first 35 POMs (N_r = 35).

For the case of the ROM in the time domain, the transient responses of the sandwich beam under the haversine impulse load are obtained by implementing Newmark time-integration method in conjunction with Eq. (4.1b), where all reduced-order matrices/vectors are obtained through element level computation

(Eq. (4.3)). However, as presented in Section 4.2, the computation of the reduced-order memory-load vector can be carried out through the evaluation of either the elemental anelastic strain (Eqs. (4.3a) and (4.3b)) or the reduced-order anelastic forces (Eqs. (4.4a) and (4.5)). For ease in presentation, the ROM with the former strategy of computation of the reduced-order memory-load vector is named as ROM#1, while ROM#2 is identified for the later strategy of computation of the same memory-load vector.

Figure 4.1 shows the comparison of transient responses evaluated through ROM#1 and ROM#2 based on the RBVs with (RB#II) or without (RB#I) enrichment. A similar response obtained from the full-order FE model is also presented in Fig. 4.1. It may be observed that the response evaluated using unenriched RB (RB#I) significantly deviates from the actual response obtained from the full-order FE model. However, the response evaluated using enriched RB (RB#II) is in good agreement with that for the full-order FE model. This observation points to the fruitfulness of the present enriched RB towards the accuracy of the nonlinear ROM in the time domain. Figure 4.1 also shows that the response from ROM#2 is in excellent agreement with that from ROM#1 for both the enriched and unenriched RB. It basically validates the present formulation of the reduced-order anelastic forces (Eqs. (4.4a) and (4.5)).

However, to demonstrate the advantage in the computation of nonlinear transient responses using this new formulation of the reduced-order anelastic forces (Eqs. (4.4a) and (4.5)), the computational time is noted in the evaluation of the responses (Fig. 4.1) using ROM#1, ROM#2 and full-order FE model. These results are illustrated in Table 4.1, where t_r represents the computational time for the evaluation of RB; t_f represents the computational time for the evaluation of linear reduced-order system matrices/vectors (${}^r\boldsymbol{K}_{sn1}^k$, ${}^r\boldsymbol{K}_{sn4}^k$, ${}^r\boldsymbol{K}_{sl}^k$, ${}^r\boldsymbol{M}_s$, ${}^r\boldsymbol{P}_s$, Eq (4.3)) and t_n represents the rest of the computational time for the evaluation of a transient response within the time-span of interest. It may be noted from Table 4.1 that t_n significantly decreases as the ROMs are used instead of the full-order FE model in the evaluation of nonlinear transient response. However, ROM#2 exhibits significantly more computational efficiency than that of ROM#1. This difference appears to be due to the present formulation of the reduced-order anelastic forces to form the memory-load vector by avoiding the repetitive computation of elemental anelastic strain. Table 4.1 also shows that both t_r and t_f increase as the ROM is constructed using enriched RB (RB#II). It occurs due

to the computation of SDs and the corresponding increase in the number of reduced coordinates (Section 4.4).

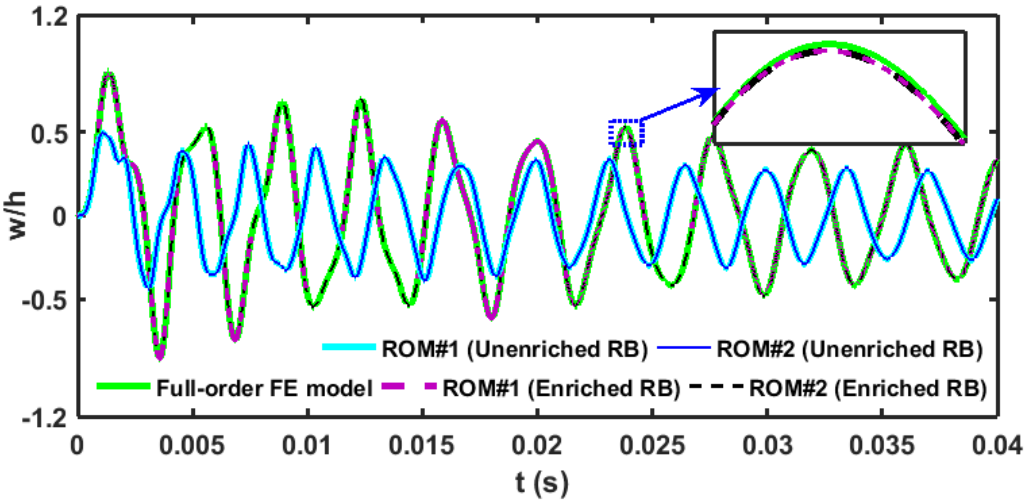

Fig. 4.1. Comparison of nonlinear transient responses evaluated using ROM#1, ROM#2 and full-order FE model.

Table 4.1
Computational time in the evaluation of nonlinear transient responses (Fig. 4.1) using ROM#1, ROM#2 and full-order FE model.

	Full-order FE model	ROM#1		ROM#2	
		RB#I	RB#II	RB#I	RB#II
t_n (min)	252.6	10.734	12.153	0.208	1.53
t_r (min)	---	0.065	0.268	0.065	0.268
t_f (min)	---	0.067	1.691	0.067	1.691

For the case of ROM in the frequency domain, the nonlinear frequency responses of the viscoelastic sandwich beam under the transverse harmonic point-load ($p_t = p_t^o \cos(\omega t)$, p_t^o =30 N) are evaluated by the solution of Eq. (4.8) using a numerical continuation method (Cheung et al., 1990). However, the complex formulation of the corresponding reduced-order tangent stiffness matrix (Eqs. (4.7c), (4.7d), (4.9a) and (4.9b)) is simplified (Eqs. (3.30a), (3.30b) and (4.10)) by avoiding its viscoelastic counterpart, as described in Section 4.3 and section 3.3.3. Although this simplified formulation of the reduced-order tangent stiffness matrix would not affect the accuracy of the nonlinear solution, it may pose difficulty or failure in the convergence of nonlinear solution through Newton-Raphson iteration, especially near the bifurcation points on the response curve. In this concern, the nonlinear frequency responses of the viscoelastic sandwich beam are evaluated with or without simplified formulation of the reduced-order

tangent stiffness matrix, where the ROM is used with the enriched RB. The corresponding responses are illustrated in Fig. 4.2 along with the similar response obtained from the full-order FE model. From these results, it is observed that the simplified formulation of the reduced-order tangent stiffness matrix works well so that there is no shortcoming in the convergence of nonlinear solutions at any point over the response curve.

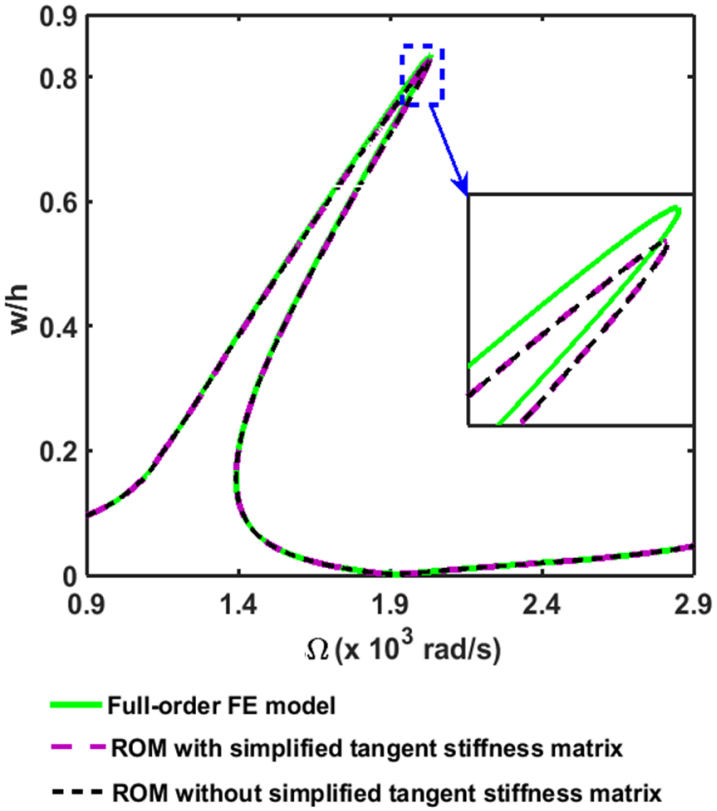

Fig. 4.2. Comparison of frequency responses obtained from full-order FE model and ROM with or without simplified formulation of the tangent stiffness matrix (ROM is taken with the enriched RB (RB#II)).

Table 4.2
Computational time in the evaluation of frequency responses in Fig. 4.2.

	Full-order FE model	ROM without simplified tangent stiffness matrix	ROM with simplified tangent stiffness matrix
t_n (min)	1752.6	122.5	26.8
t_r (min)	---	0.268	0.268
t_f (min)	---	1.717	3.44

However, this simplified formulation of the reduced-order tangent stiffness matrix may also have a certain effect on the computational time in the evaluation of the response curve, as it avoids the repetitive computation of the corresponding reduced-order geometric stiffness matrix ($^r\boldsymbol{K}_g$, Eqs.(4.9a) and (4.9b)) at each iteration. To illustrate it, the computational time is noted and presented in Table

4.2 for the evaluation of the response curves in Fig. 4.2. In Table 4.2, t_r and t_f represent the computational time for the evaluation of RB and linear reduced-order system matrices, respectively, while t_n represents the rest of the computational time in the evaluation of a frequency response curve within the frequency range of interest (Fig. 4.2). It may be observed from this table that t_n decreases significantly as the ROM is used instead of the full-order FE model. Further reduction in the computational time (t_n) is achieved by the aforesaid simplified formulation of the reduced-order tangent stiffness matrix. On the other hand, t_f ($<<t_n$) increases due to the computation of additional linear reduced-order matrices (${}^r\boldsymbol{K}_{sn3}^k$, ${}^r\boldsymbol{K}_{sn5}^k$, Eq. (4.10)) involved in the simplified formulation of the reduced-order tangent stiffness matrix. It may be noted here that a similar verification study was also carried out in the previous chapter (Fig. 3.5, Table 3.2) for the simplified formulation of the tangent stiffness matrix in the full-order FE model.

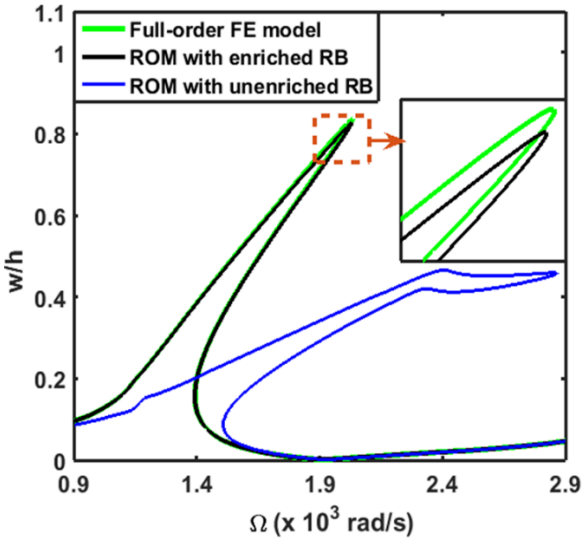

Fig. 4.3. Comparison of frequency responses obtained from full-order FE model and ROM considering unenriched RB (RB#I) or enriched RB (RB#II).

Table 4.3
Computational time in the evaluation of frequency responses (Fig. 4.3**) using the present ROM with the simplified formulation of the tangent stiffness matrix**

	ROM with simplified tangent stiffness matrix	
	RB#I	RB#II
t_n (min)	0.3167	26.8
t_r (min)	0.065	0.268
t_f (min)	0.22	3.44

Presently, the ROM (Eq. (4.8)) in the frequency domain is developed with the enrichment of RB, particularly for the evaluation of nonlinear frequency responses of the viscoelastic sandwich beam with the frequency-dependent material properties. The fruitfulness of this ROM with the enriched RB is clarified through the results in Fig. 4.2, where it is clear that the ROM with the unenriched RB provides inaccurate nonlinear frequency response while the corresponding correction can be made through the enrichment of RB. However, the enrichment of RB includes SDs so that the number of reduced coordinates or degrees of freedom of ROM increases. It results in a little more computational time (t_n, t_r and t_f), as demonstrated in Table 4.3.

4.5.2. Comparative study

Various approaches (MSE/MSEC/MM/ICES/RKT/FSRK) were proposed in the literature to evaluate RBVs in deriving the reduced-order FE model of viscoelastic structures. These RBVs are applicable for linear dynamic analysis of a viscoelastic structure having frequency-dependent material properties. However, the RB in each of the aforesaid approaches is presently enriched (Section 4.4) for its use in the nonlinear analysis of viscoelastic structures, and the accuracy of the corresponding ROM is investigated. It basically addresses a suitable approach in the selection of RB and the corresponding enrichment for the nonlinear analysis of viscoelastic structures with frequency-dependent material properties.

After the evaluation of RBVs through each of the aforesaid approaches, the corresponding enriched RBVs are computed according to the procedure, as described in Section 4.4. However, Table 4.4 illustrates the present consideration in selecting the number of enriched RBVs for different approaches. Initially, for any approach, the RB is taken in the union of the first few (N_b) eigenmodes (columns 1 to 5 of Table 4.4) and one static correction vector, where the total number of RBVs is denoted by N_m (N_m=(N_b+1)). If the eigenmodes are in the complex domain (for MM, FSRK, RKT and ICES approach), then the corresponding RBVs are taken as the real and imaginary parts of the eigenmodes. However, for evaluation of RBVs through MM/FSRK/RKT approach (Jith and Sarkar, 2020; Rouleau et al., 2017; Xie et al., 2018), the selected frequencies (in rad/s) for interpolation/expansion points are given in parenthesis (columns 1 and 2 of Table 4.4). The RBVs are then taken from the eigenmodes (N_b) for all the interpolation/expansion points. Presently, the frequencies are selected around the fundamental natural frequency (1204.5 rad/s) and the impulse excitation frequency (3000 rad/s) to evaluate transient responses under the impulse

excitation. However, similar frequencies for evaluating frequency responses under the transverse harmonic load are considered within the operating frequency range (700 - 4200 rad/s). Further, the number of first few first-order correction vectors considered in the case of MSEC is given in parenthesis (column 4 of Table 4.4). Finally, the number (N_m) of RBVs and the corresponding number (N_r) of enriched RBVs are illustrated in columns 6 and 7, respectively. Presently, a comparative study is carried out by increasing the number of enriched RBVs primarily to address an approach that provides accurate results with less number of RBVs. The corresponding steps in the increment of the number of RBVs are given in the last two columns of Table 4.4, where the number (N_m) of RBVs and the number (N_r) of enriched RBVs are kept constant for all approaches in a typical incremental step.

Table 4.4
Present consideration of the number of enriched RBVs for different approaches (MSE, MSEC, MM, ICES, RKT and FSRK).

MM, FSRK, RKT		ICES	MSEC	MSE	N_m	N_r
ROM in time domain N_b	ROM in frequency domain N_b	N_b	N_b	N_b		
3 (1200)	3 (2450)	3	3 (3)	6	7	12
3 (1200)	3 (2450)	3	3 (3)	6	7	22
4 (1200)	4 (2450)	4	4(4)	8	9	34
4 (500, 1500)	4 (700, 4200)	8	8 (8)	16	17	52
4 (500,1500,3000)	4 (700,4200,2450)	12	12 (12)	24	25	70

Figure 4.4(a) illustrates the comparison of transient responses evaluated using ROM#2 with the enriched RB from different approaches. Here, the number (N_r) of enriched RBVs is taken as 52 (Table 4.4). However, the corresponding displacement errors (D_e) are shown in Fig. 4.4(b), where $D_e = \|\boldsymbol{d} - \boldsymbol{d}_r\|$ and $\boldsymbol{d}$ / $\boldsymbol{d}_r$ is the global nodal displacement vector evaluated with full-order FE model/ROM#2. It can be observed from Figs. 4.4(a)-(b) that the enriched RB obtained through ICES approach yields small displacement error whereas similar enriched RB evaluated through MSE or MSEC yields greater displacement error. It may be due to the fact that the ICES approach accounts the effect of frequency-dependent stiffness/damping of the viscoelastic structure on RBVs, whereas it is completely omitted in the MSE approach and partially considered in MSEC approach. It may also be observed from Figs. 4.4(a)-(b) that the enriched RB

corresponding to MM/RK/FSRK approach provides better accuracy in the result than that for MSE/MSEC approach. This difference appears mainly due to the consideration of complex eigenmodes/Krylov modes in the MM/RK/FSRK approach, which are taken at the selected frequencies within the operating frequency range.

Figure 4.5 illustrates the variation of the mean displacement error (D_e^m) with the increase in the number of enriched RBVs (N_r, Table 4.4) for different approaches. Here, the mean displacement error is defined as $D_e^m = \frac{1}{S}\sum_S \|\boldsymbol{d} - \boldsymbol{d}_r\|$ where S is the total number of responses (S = 3820) corresponding to the time steps ($(\pi/3)\times10^{-5}$ s) within the total time-span (0 to 0.04 s, Fig. 4.4). It may be observed from Fig. 4.5 that the mean displacement error decreases with the increase in the number of enriched RBVs. Here, an RB with an increased number of RBVs accounts higher-order vibration modes that are essential for achieving accurate nonlinear response. It can be obtained through the present approach of enrichment of RBVs using SDs and POD method. However, the deviation in the monotonic decrease of displacement error is observed (Fig. 4.5). It may appear due to the inappropriate selection of relevant higher-order vibration modes from SDs (Section 4.4). From the results in Figs. 4.4 and 4.5, it is clear that ICES approach is better than any other approach in providing an accurate nonlinear response with less number of enriched RBVs.

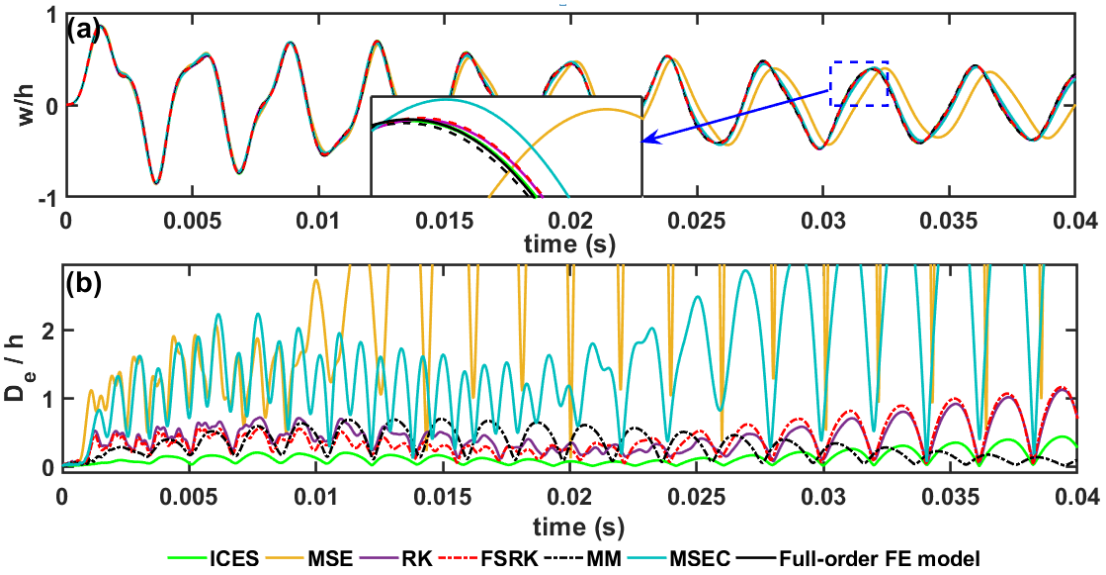

Fig. 4.4. (a) Comparison of transient responses obtained from full-order FE model and ROM#2 considering the number (N_r) of enriched RBVs as 52 from different approaches, (b) corresponding displacement errors with respect to the displacement solution of full-order FE model.

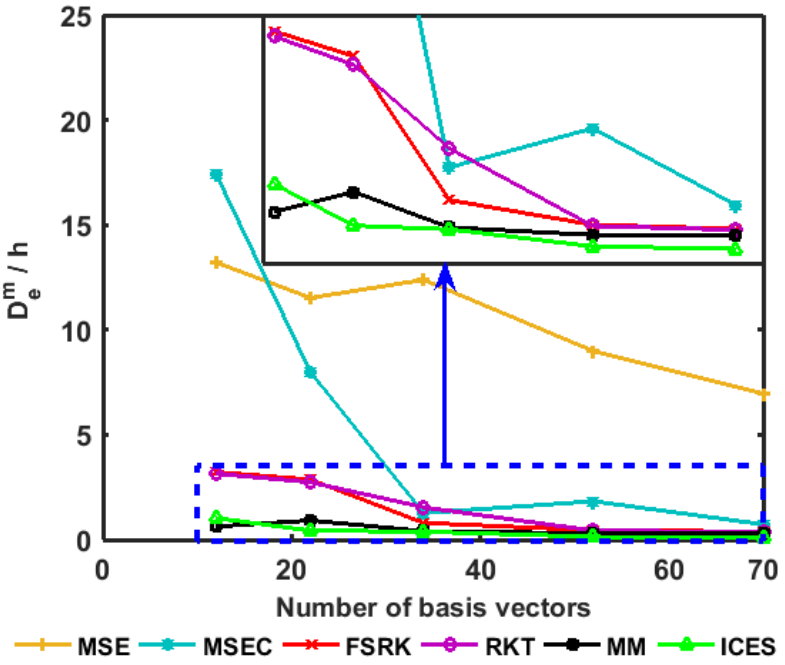

Fig. 4.5. Variation of mean displacement error with the number (N_r) of basis vectors in the enriched RB.

Figure 4.6 illustrates the comparison of nonlinear frequency responses obtained from the present ROM with the enriched RB. The number of enriched RBVs is considered as 52 (Table 4.4) for any of the aforesaid approaches (MSE, MSEC, MM, ICES, RKT and FSRK). The corresponding normalized displacement error ($D_{en} = \|\boldsymbol{d} - \boldsymbol{d}_r\| / \|\boldsymbol{d}\|$) is illustrated in Fig. 4.7. It may be observed from Fig. 4.6 that the shortcoming in the accuracy of the nonlinear frequency response mainly appears near the peak displacement amplitude, where the maximum and minimum error arise for MSE and ICES approaches, respectively. It may be due to the fact that the ICES approach is based on frequency-dependent viscoelastic properties, whereas, in the MSE approach, the dependency of viscoelastic properties on frequency is not accounted in the evaluation of RB. However, MSEC, MM, RKT and FSRK approaches provide better accuracy in the result (Figs. 4.6 and 4.7) as compared to that for MSE approach, since these approaches (MSEC, MM, RKT and FSRK) use some strategies and/or complex eigen modes/Krylov modes at selected frequencies to approximate the effect of frequency-dependent viscoelastic properties on RBVs. Figure 4.8 shows the variation of the mean normalized displacement error ($D_{en}^m = \frac{1}{S}\sum_S \|\boldsymbol{d} - \boldsymbol{d}_r\| / \|\boldsymbol{d}\|$) with the increase in the number of enriched RBVs. Here, S is the total number of responses corresponding to the incremental steps of frequency in the computation of a frequency response curve using a numerical continuation method. It may be observed from Fig. 4.8

that ICES and MM approaches provide almost accurate responses with less number of RBVs as compared to the other approaches.

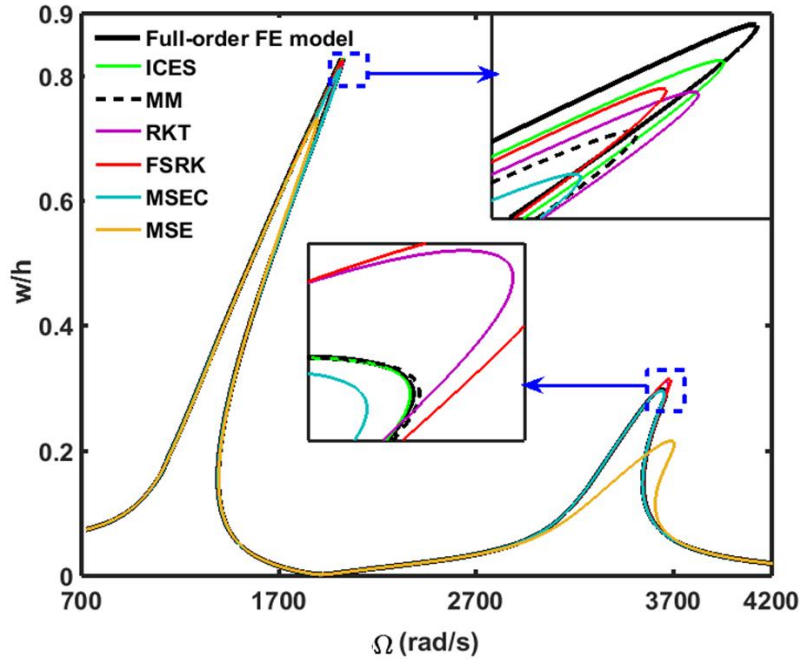

Fig. 4.6. Comparison of nonlinear frequency responses obtained from full-order FE model and ROM considering the number (N_r) of enriched RBVs as 52 through different approaches.

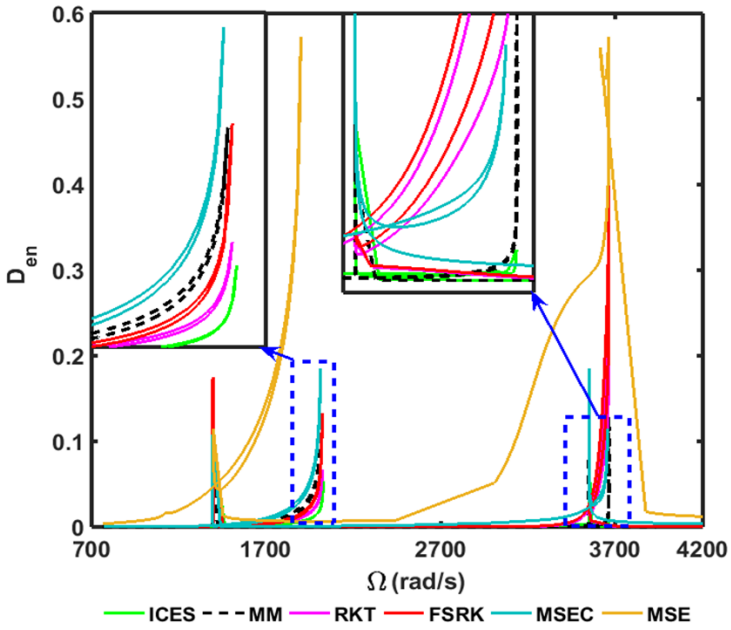

Fig. 4.7. Variation of the normalized displacement error for the nonlinear frequency responses presented in Fig. 4.6.

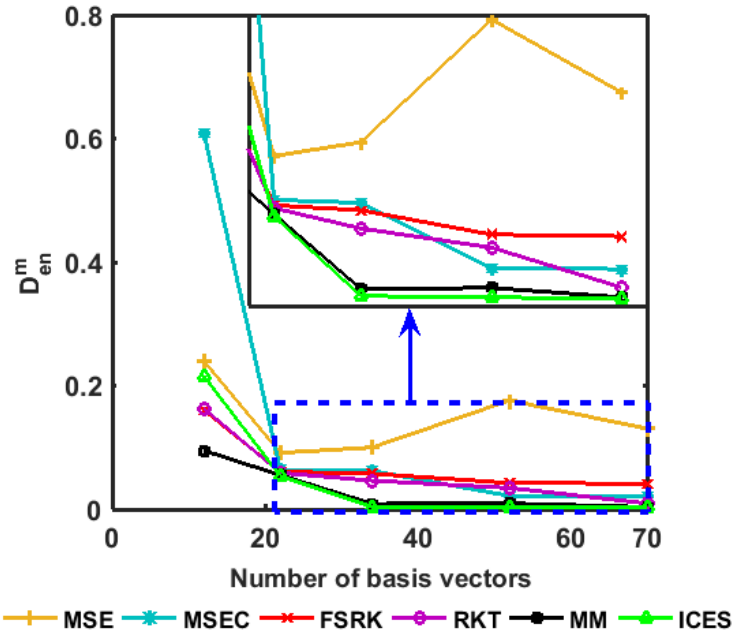

Fig. 4.8. Variation of the mean normalized displacement error with the number (N_r) of basis vectors within the enriched RB.

4.6. Summary

In this chapter, reduced-order models (ROMs) are derived for the geometrically nonlinear FE analysis of viscoelastic structures in the time/frequency domain. The corresponding formulation and fruitfulness of the ROMs are demonstrated considering the large-amplitude vibration of a sandwich beam under the haversine impulse/transverse harmonic point load. The core of this sandwich beam is made of a viscoelastic material that is modelled according to the fractional Zener constitutive relation. The overall study is carried out based on two main concerns of a ROM, which are: (i) proper selection of reduction basis vectors (RBVs) for sufficient accuracy of a nonlinear ROM and (ii) reduction of computational time in the evaluation of nonlinear transient/frequency responses.

In the first concern of the selection of RBVs, the available approaches like MSE, MSEC, MM, ICES, RKT and FSRK are followed. However, these approaches are originally proposed for linear analysis of a viscoelastic structure. So, for the geometrically nonlinear analysis of the same structure, the RBVs obtained from these approaches are presently enriched by means of deriving static derivatives (SDs), where the POD method is utilized over the union of RBVs and SDs to obtain the enriched RBVs. Good accuracy of the present ROMs based on these enriched RBVs is observed in the evaluation of geometrically nonlinear transient/frequency responses of the sandwich beam, where the reference results are taken from the full-order FE model. However, it is found that the required number of enriched RBVs towards the sufficient accuracy in the numerical results varies from one to

another approach, where the present enrichment of RBVs through ICES approach provides the most accurate result with less number of enriched RBVs as compared to the other approaches.

In the second concern of the reduced computational time, a special factorization of the nonlinear strain-displacement matrix is utilized, as it is introduced in the previous chapter. Using this factorization, the reduced-order linear/nonlinear system matrices/vectors are formulated at the elemental level without involving the full-order solution. However, this technique of factorization is not enough to avoid the full-order solution in the derivation of the reduced-order nonlinear memory-load vector appearing in the time-domain ROM, since this nonlinear load-vector involves elemental strain history. So, this reduced-order memory-load vector is presently formulated by introducing two new anelastic nodal forces by avoiding the elemental anelastic strain. However, this novel strategy of formulation of the time-domain ROM of viscoelastic structures eases to form all the reduced-order system matrices and vectors in the elemental level without involving the nodal displacements, where the advantage of a significant reduction of the computational time is achieved in the evaluation of geometrically nonlinear transient responses of the viscoelastic structure.

The equations of motion in the time-domain ROM appear at the discrete-time. So, it is difficult to express this ROM in the frequency domain directly by implementing HBM. So, a separate formulation of ROM in the frequency domain is presented by implementing HBM before the FE discretization. The subsequent formulation of the geometrically nonlinear stiffness matrix appears in a complex manner. Although it is eased by means of the aforesaid factorization of the nonlinear strain-displacement matrix, the nonlinear stiffness matrix appears with a large number of terms associated with the products of sine and cosine functions. The time-integration of these stiffness terms according to HBM poses a high computational cost. It is presently tackled by implementing the orthogonality of Fourier basis functions, while all the reduced-order system matrices and vectors are derived in the elemental level without involving the full-order solution except the reduced-order geometric stiffness matrix. This formulation of ROM in the frequency domain provides significantly reduced computational time in the evaluation of geometrically nonlinear frequency responses of the viscoelastic structure. For further reduction of the computational time, a simplified formulation of the reduced-order tangent stiffness matrix is also presented by omitting the viscoelastic counterpart of geometric stiffness matrix. However, it is applicable for a viscoelastic structure made of elastic and viscoelastic constituent

materials, where the viscoelastic counterpart has a small contribution to the stiffness of the overall structure as compared to that for the elastic counterpart.

Chapter 5

Constrained layer damping treatment of post-buckled beams under parametric excitation: a theoretical study using reduced-order finite element formulation

5.1. Introduction

In the context of passive control of parametrically excited beams, the utilization of viscoelastic materials through the CLD treatment has been addressed in a good number of available studies (Section 1.3.1). In all these available studies, the CLD treatment is applied to control the dynamic instability of beams in the pre-buckled equilibrium state. However, in practice, the operation of a parametrically excited beam may not be confined to the pre-buckled state. In this case, the beam operates in the post-buckled state, where multiple stable and unstable equilibrium states appear simultaneously (Fig. 1.2). It results in complex dynamics along with various dynamic instabilities of the beam, as similar responses are observed in Chapter 2. However, the utility of the CLD treatment in attenuation of this complex dynamics at the post-buckled state of a parametrically excited beam is not yet explored in the open literature to the best knowledge of this researcher. It is attempted in this chapter, where the CLD treatment is configured in different forms of layered beams, and the study is carried out to investigate the suitability of each of the CLD configurations in controlling the complex nonlinear dynamics of the layered beams under the parametric excitation at the post-buckled state.

This theoretical study is performed by deriving a nonlinear ROM of the parametrically excited viscoelastic layered beams, where the reduced-order FE formulation in the previous chapter is followed. Using this ROM, the complex motion along with dynamic bifurcations of the beams is analyzed by evaluating the nonlinear frequency responses and global bifurcation diagrams. However, in this concern of dynamic bifurcation analysis using a nonlinear ROM, the available literature shows the selection of RBVs from proper orthogonal decomposition (POD) modes evaluated through local/global/adaptive POD method (Amsallem et al., 2009; Carlberg, 2015; Lieu and Farhat, 2007; Lu et al., 2019, 2016; Terragni and Vega, 2012; Weickum et al., 2009; Xie et al., 2015). It is observed that POD modes are robust ones in providing sufficient accuracy of a nonlinear ROM for bifurcation analysis (Lu et al., 2019, 2016; Xie et al., 2015). Besides the POD

modes, an alternative approach of the selection of RBVs from the enriched vibration modes (VMs) is introduced in the previous chapter (Section 4.4). These new RBVs work well for the ROM-based analysis of simple nonlinear structural responses, as observed in the previous chapter (Chapter 4). But the suitability of these new RBVs in providing sufficient accuracy of a nonlinear ROM for the dynamic bifurcation analysis of an elastic/viscoelastic structure is not yet verified. Therefore, the present nonlinear ROM for the aforesaid CLD treated beams is derived using these new RBVs, where the above mentioned verification study is carried out before the main objective of investigating the effectiveness of the CLD treatment. The overall study in this chapter is presented in the following manner.

First, the CLD arrangement in three different layered beam configurations is presented in Section 5.2. Next, in Section 5.3, the incremental nonlinear governing equation of motion of the CLD treated beams is derived for an axial compressive harmonic load, where the viscoelastic material in the CLD treatment is modelled using the fractional Zener constitutive model. The subsequent section (Section 5.4) presents the derivation of nonlinear ROM of the CLD treated beams under the parametric excitation. Here, the formulation approach in the previous chapter (Chapter 4) is followed for the derivation of nonlinear ROMs in both the time and frequency domains. However, the numerical results are presented in the subsequent section (Section 5.5), where the appropriateness of the present approach (Section 4.4) of selecting RBVs is first verified for the estimation of complex nonlinear dynamics of the CLD treated beams. Next, the effectiveness of the CLD treatment in passive control of complex dynamics of the parametrically excited layered beams is explored through the numerical results.

5.2. Configuration of layered beams with CLD treatment

The CLD treatment of a beam element is commonly achieved by means of attaching a viscoelastic damping layer on the top/bottom surface of the substrate beam, while this damping layer is constrained by a very thin and stiff constraining layer. This configuration of the CLD treatment is also known as the passive constrained layer damping (PCLD) treatment, as shown in Fig. 5.1(a). However, the available studies in this context reveal that the damping capability of the CLD treatment may improve for the increasing number of constrained viscoelastic layers in the layered configuration (Ray and Kar, 1996; Suzuki et al., 2003). Therefore, besides the PCLD treated beam (Fig. 5.1(a)), the CLD treatment is also configured in three-layered and five-layered beams, as shown in Figs. 5.1(b) and 5.1(c), respectively. The damping layers are made of an isotropic viscoelastic

material, and the substrate/constraining layers are made of an elastic isotropic material. The length, width and thickness of any layered beam are denoted by L, b and h, respectively. However, presently the damping effectiveness of the CLD treatment in attenuation of complex dynamics of the parametrically excited post-buckled beams is studied by taking it (CLD) in three different configurations (Figs. 5.1(a)-(c)) without altering the volumes of viscoelastic and substrate materials. So, the total thickness (h_v) of the viscoelastic layers and the total thickness of the substrate/constraining layers ($h_s + h_c = h_f$) are kept constant for all the layered beams. These layered beams (Figs. 5.1(a)-(c)) are considered to operate under an axial compressive harmonic load (p_a^t) while their ends are taken as fully-clamped ends.

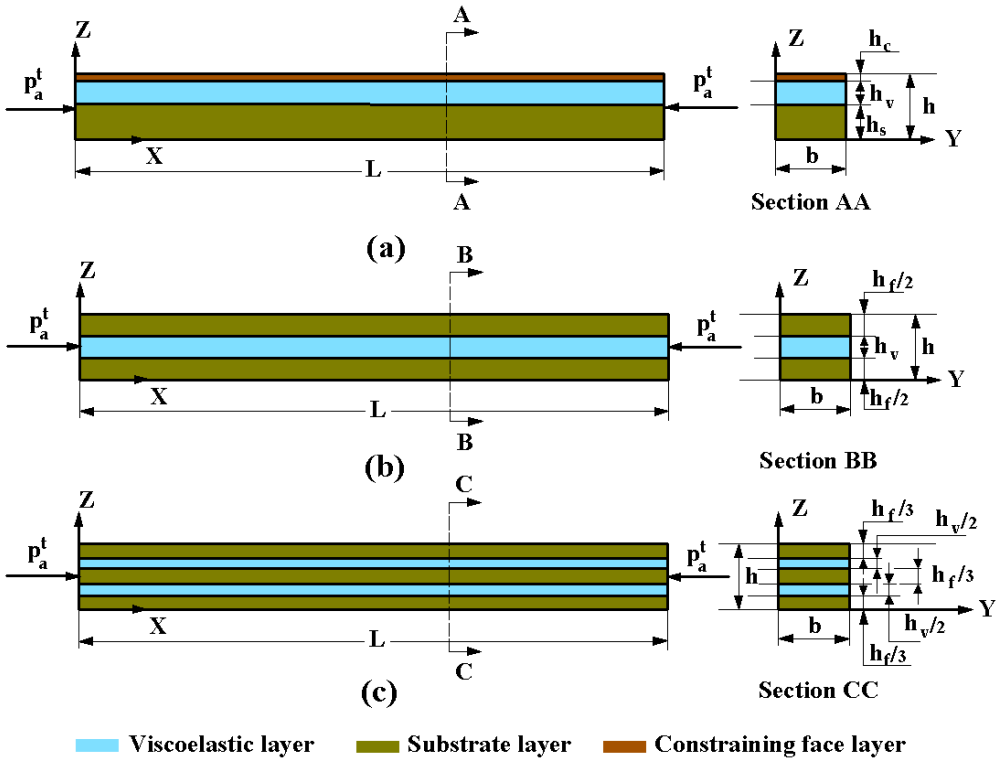

Fig. 5.1. Schematic diagrams of (a) a substrate beam with a PCLD layer, (b) a three-layered beam and (c) a five-layered beam operating under the axial compressive harmonic load (p_a^t).

5.3. Formulation of incremental governing equation of motion

Besides the aforesaid geometrical configurations, material properties and boundary conditions, there is no applied force on the boundary surface in parallel to the xz-plane. Moreover, there is no body force along any axis of the reference coordinate system. So, these layered beams may be treated as plane stress problems in the xz-plane (Dwivedy et al., 2007; Lacarbonara et al., 2007; Ray and

Kar, 1996; Zhu et al., 2018). Accordingly, the state of stress and the state of strain at any point in the xz-plane can be written, as given in Eq. (2.1).

$$\boldsymbol{\sigma} = \{\sigma_x \quad \sigma_z \quad \tau_{xz}\}^{\mathrm{T}}, \quad \boldsymbol{\varepsilon} = \{\varepsilon_x \quad \varepsilon_z \quad \gamma_{xz}\}^{\mathrm{T}} \tag{2.1}$$

The Green-Lagrange nonlinear strain-displacement relations at any point in the xz-plane of a layered beam can be written according to Eq. (3.1).

$$\boldsymbol{\varepsilon} = \boldsymbol{\varepsilon}_l + \boldsymbol{\varepsilon}_n,$$

$$\boldsymbol{\varepsilon}_l = \left\{\frac{\partial u}{\partial x} \quad \frac{\partial w}{\partial z} \quad \frac{\partial w}{\partial x} + \frac{\partial u}{\partial z}\right\}^{\mathrm{T}},$$

$$\boldsymbol{\varepsilon}_n = \left\{\frac{1}{2}\left(\frac{\partial w}{\partial x}\right)^2 + \frac{1}{2}\left(\frac{\partial u}{\partial x}\right)^2 \quad \frac{1}{2}\left(\frac{\partial w}{\partial z}\right)^2 + \frac{1}{2}\left(\frac{\partial u}{\partial z}\right)^2 \quad \frac{\partial w}{\partial x}\frac{\partial w}{\partial z} + \frac{\partial u}{\partial x}\frac{\partial u}{\partial z}\right\}^{\mathrm{T}} \tag{3.1}$$

Further, the linear ($\boldsymbol{\varepsilon}_l$) and nonlinear ($\boldsymbol{\varepsilon}_n$) counterparts of the strain vector ($\boldsymbol{\varepsilon}$) can be written in terms of the displacement vector ($\boldsymbol{d}_s$), as given in Eq. (3.2).

$$\boldsymbol{\varepsilon}_l = \boldsymbol{L}\,\boldsymbol{d}_s, \quad \boldsymbol{\varepsilon}_n = (1/2)\,\boldsymbol{L}_n(\boldsymbol{d}_s)\,\boldsymbol{d}_s, \quad \boldsymbol{d}_s = \{u \quad w\}^{\mathrm{T}}$$

$$\boldsymbol{L} = \left[(\boldsymbol{L}_x^u)^{\mathrm{T}} \; (\boldsymbol{L}_z^w)^{\mathrm{T}} \quad (\boldsymbol{L}_x^w + \boldsymbol{L}_z^u)^{\mathrm{T}}\right]^{\mathrm{T}},$$

$$\boldsymbol{L}_n(\boldsymbol{d}_s) = (\boldsymbol{L}_1^u\boldsymbol{d}_s)\,\boldsymbol{L}_x^u + (\boldsymbol{L}_2^u\boldsymbol{d}_s)\,\boldsymbol{L}_z^u + (\boldsymbol{L}_1^w\boldsymbol{d}_s)\,\boldsymbol{L}_x^w + (\boldsymbol{L}_2^w\boldsymbol{d}_s)\,\boldsymbol{L}_z^w,$$

$$\boldsymbol{L}_1^u = \left[(\boldsymbol{L}_x^u)^{\mathrm{T}} \; \boldsymbol{O} \quad (\boldsymbol{L}_z^u)^{\mathrm{T}}\right]^{\mathrm{T}}, \quad \boldsymbol{L}_2^u = \left[\boldsymbol{O} \quad (\boldsymbol{L}_z^u)^{\mathrm{T}} \quad (\boldsymbol{L}_x^u)^{\mathrm{T}}\right]^{\mathrm{T}},$$

$$\boldsymbol{L}_1^w = \left[(\boldsymbol{L}_x^w)^{\mathrm{T}} \; \boldsymbol{O} \quad (\boldsymbol{L}_z^w)^{\mathrm{T}}\right]^{\mathrm{T}}, \quad \boldsymbol{L}_2^w = \left[\boldsymbol{O} \quad (\boldsymbol{L}_z^w)^{\mathrm{T}} \; (\boldsymbol{L}_x^w)^{\mathrm{T}}\right]^{\mathrm{T}},$$

$$\boldsymbol{L}_x^u = \{\partial/\partial x \quad 0\}, \boldsymbol{L}_x^w = \{0 \quad \partial/\partial x\}, \quad \boldsymbol{L}_z^u = \{\partial/\partial z \quad 0\}, \quad \boldsymbol{L}_z^w = \{0 \quad \partial/\partial z\} \tag{3.2}$$

Generally, the influence of the axial compressive load on the bending deformation of a beam is accounted by means of a pre-stress in the beam (Chen et al., 2002; Ganesan and Kadoli, 2004). This pre-stress corresponds to the axial deformation of the beam under the load. However, the component layers in the present layered beams are made of isotropic materials, and the axial load is applied through the support ends. So, for axial deformation of a layered beam under this load, the corresponding component layers are mainly subjected to the axial stress (σ_x) while the other stress components (σ_z and τ_{xz}) appear with their negligibly small magnitudes. Now, the damping layers are considered to be made of a soft viscoelastic material so that the axial load is mostly sustained by the substrate layers. It leads to a very small axial stress in the viscoelastic layers in comparison to that in the substrate layers. Therefore, the pre-stress in the layered beams under the axial compressive load is presently accounted for the

axial stress (σ_x) in the substrate layers. Moreover, since the layered beams possess a high rigidity against their axial deformation, the linear variation of the axial stress (σ_x) with the applied axial load (p_a^t) may be assumed. Accordingly, the pre-stress matrix ($\boldsymbol{\Gamma}_a^k$) for k^{th} material in a layered beam can be written as

$$\boldsymbol{\Gamma}_a^k = \begin{bmatrix} \sigma_x^k & \tau_{xz}^k \\ \tau_{xz}^k & \sigma_z^k \end{bmatrix} = \boldsymbol{\Gamma}_f^k \, p_a^t ,$$

$$\boldsymbol{\Gamma}_f^k = \begin{bmatrix} -1 & 0 \\ 0 & 0 \end{bmatrix} \frac{r_a^k}{b}, \quad r_a^k = 1/h_f \ \text{ for } k=1 \text{ and } r_a^k = 0 \ \text{ for } k=2 \tag{5.1}$$

where, the superscript k denotes the elastic and viscoelastic materials in the layered beams as per its value as 1 and 2, respectively. Now, for the vibration of the layered beam under the axial compressive harmonic load (p_a^t), the first variations of kinetic energy (δT_t) and potential energy (δT_p) of a layered beam can be written as

$$\delta T_t = \sum_{k=1}^{2} \int_{A^k} (\delta \dot{\boldsymbol{d}}_s)^{\mathrm{T}} \, \rho^k \, \dot{\boldsymbol{d}}_s \, b \, dA^k ,$$

$$\delta T_p = \sum_{k=1}^{2} \int_{A^k} \left\{ (\delta \boldsymbol{\varepsilon}_l + \delta \boldsymbol{\varepsilon}_n)^{\mathrm{T}} \boldsymbol{\sigma}^k + \left\langle (\delta \boldsymbol{\varepsilon}_g^u)^{\mathrm{T}} \boldsymbol{\Gamma}_f^k \boldsymbol{\varepsilon}_g^u + (\delta \boldsymbol{\varepsilon}_g^w)^{\mathrm{T}} \boldsymbol{\Gamma}_f^k \, \boldsymbol{\varepsilon}_g^w \right\rangle p_a^t \right\} b \, dA^k ,$$

$$\boldsymbol{\varepsilon}_g^u = \boldsymbol{L}_g^u \, \boldsymbol{d}_s , \ \boldsymbol{\varepsilon}_g^w = \boldsymbol{L}_g^w \, \boldsymbol{d}_s , \ \boldsymbol{L}_g^u = \begin{bmatrix} (\boldsymbol{L}_x^u)^{\mathrm{T}} & (\boldsymbol{L}_z^u)^{\mathrm{T}} \end{bmatrix}^{\mathrm{T}} , \ \boldsymbol{L}_g^w = \begin{bmatrix} (\boldsymbol{L}_x^w)^{\mathrm{T}} & (\boldsymbol{L}_z^w)^{\mathrm{T}} \end{bmatrix}^{\mathrm{T}} \tag{5.2}$$

$$p_a^t = p_a^o (1 + \lambda \cos \Omega t) \tag{2.7}$$

where, A^k is the area of k^{th} material in the xz -plane; $\boldsymbol{\sigma}^k$ and ρ^k are the stress vector and mass density, respectively, at any point in the k^{th} material. Further, the axial compressive harmonic load (p_a^t) is taken in the form, as given in Eq. (2.7) where p_a^o, λ and Ω are the static counterpart of the axial compressive load, dynamic load parameter and excitation frequency, respectively. Now, substituting Eqs. (5.2) and (2.7) in the extended Hamilton's principle (Eq. (2.9)), the governing equation of motion of a layered beam can be obtained, as given in Eq. (5.3).

$$\int_{t_1}^{t_2} (\delta T_p - \delta T_t) \, dt = 0 \tag{2.9}$$

$$\sum_{k=1}^{2}\int_{A^k}\left\{\begin{array}{l}(\delta\boldsymbol{d}_s)^{\mathrm{T}}\rho^k\ddot{\boldsymbol{d}}_s+(\delta\boldsymbol{\varepsilon}_l+\delta\boldsymbol{\varepsilon}_n)^{\mathrm{T}}\boldsymbol{\sigma}^k+\\ \left\langle(\delta\boldsymbol{\varepsilon}_g^u)^{\mathrm{T}}\boldsymbol{\Gamma}_f^k\boldsymbol{\varepsilon}_g^u+(\delta\boldsymbol{\varepsilon}_g^w)^{\mathrm{T}}\boldsymbol{\Gamma}_f^k\boldsymbol{\varepsilon}_g^w\right\rangle p_a^o(1+\lambda\cos\Omega t)\end{array}\right\}b\,dA^k=0 \tag{5.3}$$

The constitutive relation for an isotropic elastic material ($k=1$) in the layered beam under the plane stress assumption is given in Eq. (2.3a). Also, the constitutive relation for the isotropic viscoelastic material ($k=2$) according to the fractional Zener model (Galucio et al., 2004) is illustrated in Eqs. (3.12a) and (3.12b).

$$\boldsymbol{\sigma}^k=\boldsymbol{C}^k\boldsymbol{\varepsilon},\ \boldsymbol{C}^k=E^k\boldsymbol{C}_b^k,$$

$$\boldsymbol{C}_b^k=\frac{1}{1-(\nu^k)^2}\begin{bmatrix}1 & \nu^k & 0\\ \nu^k & 1 & 0\\ 0 & 0 & (1-\nu^k)/2\end{bmatrix},\ k=1 \tag{2.3a}$$

$$\boldsymbol{\sigma}^k=\boldsymbol{C}^k\boldsymbol{\varepsilon}^t,\quad \boldsymbol{C}^k=E_o\boldsymbol{C}_b^k,\quad \boldsymbol{\varepsilon}^t=(E_\infty/E_o)(\boldsymbol{\varepsilon}-\bar{\boldsymbol{\varepsilon}}) \tag{3.12a}$$

$$\bar{\boldsymbol{\varepsilon}}+\tau^\alpha(d^\alpha\bar{\boldsymbol{\varepsilon}}/dt^\alpha)=f\,\boldsymbol{\varepsilon},\quad f=(E_\infty-E_o)/E_\infty \tag{3.12b}$$

Now, to derive the governing equation of motion in the incremental form, a state of vibration ($\boldsymbol{d}_s$, Ω) is expressed with respect to a reference state of vibration (${}^i\boldsymbol{d}_s$, Ω_i) through their increments ($\Delta\boldsymbol{d}_s$, $\Delta\Omega$), as given in Eq. (3.5a). The corresponding incremental forms of strain vectors ($\boldsymbol{\varepsilon}_l$, $\boldsymbol{\varepsilon}_n$, $\boldsymbol{\varepsilon}_g^u$, $\boldsymbol{\varepsilon}_g^w$) and stress vector ($\boldsymbol{\sigma}^k$) are given in (Eq. (5.4)).

$$\boldsymbol{d}_s={}^i\boldsymbol{d}_s+\Delta\boldsymbol{d}_s,\ \Omega=\Omega_i+\Delta\Omega \tag{3.5a}$$

$$\boldsymbol{\varepsilon}_l=({}^i\boldsymbol{\varepsilon}_l+\Delta\boldsymbol{\varepsilon}_l),\quad \boldsymbol{\varepsilon}_n=({}^i\boldsymbol{\varepsilon}_n+\Delta\boldsymbol{\varepsilon}_{n1}+\Delta\boldsymbol{\varepsilon}_{n2}),\quad \boldsymbol{\sigma}^k=({}^i\boldsymbol{\sigma}^k+\Delta\boldsymbol{\sigma}^k),$$

$$\boldsymbol{\varepsilon}_g^u=({}^i\boldsymbol{\varepsilon}_g^u+\Delta\boldsymbol{\varepsilon}_g^u),\ \boldsymbol{\varepsilon}_g^w=({}^i\boldsymbol{\varepsilon}_g^w+\Delta\boldsymbol{\varepsilon}_g^w),$$

$${}^i\boldsymbol{\varepsilon}_l=\boldsymbol{L}\,{}^i\boldsymbol{d}_s,\ \Delta\boldsymbol{\varepsilon}_l=\boldsymbol{L}\,\Delta\boldsymbol{d}_s,\ {}^i\boldsymbol{\varepsilon}_n=(1/2)\,{}^i\boldsymbol{L}_n\,{}^i\boldsymbol{d}_s,$$

$$\Delta\boldsymbol{\varepsilon}_{n1}={}^i\boldsymbol{L}_n\,\Delta\boldsymbol{d}_s,\ \Delta\boldsymbol{\varepsilon}_{n2}=(1/2)\,\Delta\boldsymbol{L}_n\,\Delta\boldsymbol{d}_s,$$

$${}^i\boldsymbol{\varepsilon}_g^u=\boldsymbol{L}_g^u\,{}^i\boldsymbol{d}_s,\ {}^i\boldsymbol{\varepsilon}_g^w=\boldsymbol{L}_g^w\,{}^i\boldsymbol{d}_s,\ \Delta\boldsymbol{\varepsilon}_g^u=\boldsymbol{L}_g^u\,\Delta\boldsymbol{d}_s,\ \Delta\boldsymbol{\varepsilon}_g^w=\boldsymbol{L}_g^w\,\Delta\boldsymbol{d}_s,$$

$${}^i\boldsymbol{L}_n=\boldsymbol{L}_n({}^i\boldsymbol{d}_s),\ \Delta\boldsymbol{L}_n=\boldsymbol{L}_n(\Delta\boldsymbol{d}_s) \tag{5.4}$$

In Eqs. (3.5a) and (5.4), the pre-superscript '*i*' denotes a quantity corresponding to the reference state of vibration. Substituting Eqs. (3.5a) and (5.4) in Eq. (5.3), the incremental governing equation of motion of a layered beam can be obtained as follows

$$\sum_{k=1}^{2}\int_{A^k}\left\{\begin{array}{l}(\delta\Delta\boldsymbol{\varepsilon}_l+\delta\Delta\boldsymbol{\varepsilon}_{n1})^{\mathrm{T}}({}^i\boldsymbol{\sigma}^k+\Delta\boldsymbol{\sigma}^k)+(\delta\Delta\boldsymbol{d}_s)^{\mathrm{T}}\rho^k({}^i\ddot{\boldsymbol{d}}_s+\Delta\ddot{\boldsymbol{d}}_s)+\\ (\delta\Delta\boldsymbol{\varepsilon}_{n2})^{\mathrm{T}}\,{}^i\boldsymbol{\sigma}^k+\left\langle\begin{array}{l}(\delta\Delta\boldsymbol{\varepsilon}_g^u)^{\mathrm{T}}\boldsymbol{\Gamma}_f^k({}^i\boldsymbol{\varepsilon}_g^u+\Delta\boldsymbol{\varepsilon}_g^u)\\ +(\delta\Delta\boldsymbol{\varepsilon}_g^w)^{\mathrm{T}}\boldsymbol{\Gamma}_f^k({}^i\boldsymbol{\varepsilon}_g^w+\Delta\boldsymbol{\varepsilon}_g^w)\end{array}\right\rangle p_a^o(1+\lambda\cos\Omega t)\end{array}\right\}b\,dA^k=0 \qquad (5.5)$$

In Eq. (5.5), the strain energy term i.e. $(\delta\Delta\boldsymbol{\varepsilon}_{n2})^{\mathrm{T}}\,{}^i\boldsymbol{\sigma}^k$ can be written according to Eq. (3.7). Using Eq. (3.7), the incremental equation of motion (Eq. (5.5)) can be modified, as presented in Eq. (5.6).

$$(\delta\Delta\boldsymbol{\varepsilon}_{n2})^{\mathrm{T}}\,{}^i\boldsymbol{\sigma}^k=(\delta\Delta\boldsymbol{\varepsilon}_g^u)^{\mathrm{T}}\,{}^i\boldsymbol{\Gamma}^k\Delta\boldsymbol{\varepsilon}_g^u+(\delta\Delta\boldsymbol{\varepsilon}_g^w)^{\mathrm{T}}\,{}^i\boldsymbol{\Gamma}^k\Delta\boldsymbol{\varepsilon}_g^w,$$

$${}^i\boldsymbol{\Gamma}^k=\begin{bmatrix}{}^i\sigma_x^k & {}^i\tau_{xz}^k\\ {}^i\tau_{xz}^k & {}^i\sigma_z^k\end{bmatrix} \qquad (3.7)$$

$$\sum_{k=1}^{2}\int_{A^k}\left\{\begin{array}{l}(\delta\Delta\boldsymbol{\varepsilon}_l+\delta\Delta\boldsymbol{\varepsilon}_{n1})^{\mathrm{T}}({}^i\boldsymbol{\sigma}^k+\Delta\boldsymbol{\sigma}^k)+(\delta\Delta\boldsymbol{d}_s)^{\mathrm{T}}\rho^k({}^i\ddot{\boldsymbol{d}}_s+\Delta\ddot{\boldsymbol{d}}_s)+\\ \left\langle\begin{array}{l}(\delta\Delta\boldsymbol{\varepsilon}_g^u)^{\mathrm{T}}\boldsymbol{\Gamma}_f^k({}^i\boldsymbol{\varepsilon}_g^u+\Delta\boldsymbol{\varepsilon}_g^u)\\ +(\delta\Delta\boldsymbol{\varepsilon}_g^w)^{\mathrm{T}}\boldsymbol{\Gamma}_f^k({}^i\boldsymbol{\varepsilon}_g^w+\Delta\boldsymbol{\varepsilon}_g^w)\end{array}\right\rangle p_a^o(1+\lambda\cos\Omega t)\\ +(\delta\Delta\boldsymbol{\varepsilon}_g^u)^{\mathrm{T}}\,{}^i\boldsymbol{\Gamma}^k\Delta\boldsymbol{\varepsilon}_g^u+(\delta\Delta\boldsymbol{\varepsilon}_g^w)^{\mathrm{T}}\,{}^i\boldsymbol{\Gamma}^k\Delta\boldsymbol{\varepsilon}_g^w\end{array}\right\}b\,dA^k=0 \qquad (5.6)$$

5.4. Nonlinear reduced-order FE models in time/frequency domain

The FE model of a layered beam is derived by discretizing its xz-plane using nine-node quadrilateral isoparametric elements, where the edges of a typical element are in parallel to the coordinate axes in the same (xz) plane. The xz-plane of a layered beam is discretized following the inter-layer surfaces so that a typical element is either made of an elastic material ($k=1$) for substrate layer/constraining layer or made of a viscoelastic material ($k=2$) for the constrained damping layer. Now, the incremental forms of displacement vector ($ {}^i\boldsymbol{d}_s$, $\Delta\boldsymbol{d}_s$, Eq. (3.5a)) and strain vectors ($ {}^i\boldsymbol{\varepsilon}_l$, $\Delta\boldsymbol{\varepsilon}_l$, ${}^i\boldsymbol{\varepsilon}_n$, $\Delta\boldsymbol{\varepsilon}_{n1}$, $\Delta\boldsymbol{\varepsilon}_{n2}$, ${}^i\boldsymbol{\varepsilon}_g^w$, $\Delta\boldsymbol{\varepsilon}_g^w$, ${}^i\boldsymbol{\varepsilon}_g^u$, $\Delta\boldsymbol{\varepsilon}_g^u$, Eq. (5.4)) at any point in a typical element can be expressed in terms of the shape function matrix ($\boldsymbol{N}$) and the elemental nodal displacement vector ($ {}^i\boldsymbol{d}^e$, $\Delta\boldsymbol{d}^e$), as given in Eqs. (3.22a) and (5.7) where $\boldsymbol{I}_{18}$ is the unity matrix of size (18×18) and the symbol $\otimes$ represents Kronecker product.

$${}^i\boldsymbol{d}_s=\boldsymbol{N}\,{}^i\boldsymbol{d}^e,\ \Delta\boldsymbol{d}_s=\boldsymbol{N}\Delta\boldsymbol{d}^e \qquad (3.22a)$$

$${}^i\boldsymbol{\varepsilon}_l=\boldsymbol{B}_l\,{}^i\boldsymbol{d}^e,\ \Delta\boldsymbol{\varepsilon}_l=\boldsymbol{B}_l\,\Delta\boldsymbol{d}^e,\ {}^i\boldsymbol{\varepsilon}_n=(1/2)\,\boldsymbol{B}_n\,{}^i\boldsymbol{d}_I^e\,{}^i\boldsymbol{d}^e,$$

$$\Delta\boldsymbol{\varepsilon}_{n1}=\boldsymbol{B}_n\,{}^i\boldsymbol{d}_I^e\,\Delta\boldsymbol{d}^e,\ \Delta\boldsymbol{\varepsilon}_{n2}=(1/2)\,\boldsymbol{B}_n\Delta\boldsymbol{d}_I^e\,\Delta\boldsymbol{d}^e,$$

$$
{}^{i}\boldsymbol{\varepsilon}_g^u = \boldsymbol{B}_g^u\ {}^{i}\boldsymbol{d}^e\ ,\ \ \Delta\boldsymbol{\varepsilon}_g^u = \boldsymbol{B}_g^u\ \Delta\boldsymbol{d}^e\ ,
$$

$$
{}^{i}\boldsymbol{\varepsilon}_g^w = \boldsymbol{B}_g^w\ {}^{i}\boldsymbol{d}^e\ , \Delta\boldsymbol{\varepsilon}_g^w = \boldsymbol{B}_g^w\ \Delta\boldsymbol{d}^e\ ,
$$

$$
\boldsymbol{B}_l = \boldsymbol{L}\,\boldsymbol{N}\ ,\quad \boldsymbol{B}_n = \boldsymbol{B}_1^w\boldsymbol{R}_x^w + \boldsymbol{B}_2^w\boldsymbol{R}_z^w + \boldsymbol{B}_1^u\boldsymbol{R}_x^u + \boldsymbol{B}_2^u\boldsymbol{R}_z^u\ ,
$$

$$
\boldsymbol{B}_g^u = \boldsymbol{L}_g^u\,\boldsymbol{N}\ ,\ \ \boldsymbol{B}_g^w = \boldsymbol{L}_g^w\,\boldsymbol{N}\ ,
$$

$$
\boldsymbol{R}_x^u = \boldsymbol{I}_{18}\otimes\boldsymbol{B}_x^u\ ,\ \ \boldsymbol{R}_z^u = \boldsymbol{I}_{18}\otimes\boldsymbol{B}_z^u\ ,
$$

$$
\boldsymbol{R}_x^w = \boldsymbol{I}_{18}\otimes\boldsymbol{B}_x^w\ ,\ \ \boldsymbol{R}_z^w = \boldsymbol{I}_{18}\otimes\boldsymbol{B}_z^w\ ,
$$

$$
\boldsymbol{B}_1^u = \boldsymbol{L}_1^u\boldsymbol{N}\ ,\ \ \boldsymbol{B}_2^u = \boldsymbol{L}_2^u\boldsymbol{N}\ ,\ \ \boldsymbol{B}_1^w = \boldsymbol{L}_1^w\boldsymbol{N}\ ,\ \ \boldsymbol{B}_2^w = \boldsymbol{L}_2^w\boldsymbol{N}\ ,
$$

$$
\boldsymbol{B}_x^u = \boldsymbol{L}_x^u\boldsymbol{N}\ ,\ \ \boldsymbol{B}_z^u = \boldsymbol{L}_z^u\boldsymbol{N}\ ,\ \ \boldsymbol{B}_x^w = \boldsymbol{L}_x^w\boldsymbol{N}\ ,\ \ \boldsymbol{B}_z^w = \boldsymbol{L}_z^w\boldsymbol{N}\ ,
$$

$$
{}^{i}\boldsymbol{d}_I^e = {}^{i}\boldsymbol{d}^e\otimes\boldsymbol{I}_{18}\,,\ \ \Delta\boldsymbol{d}_I^e = \Delta\boldsymbol{d}^e\otimes\boldsymbol{I}_{18} \tag{5.7}
$$

5.4.1 Computation of reduced basis vectors (RBVs)

For the construction of ROM, the reduction basis ($\boldsymbol{\Phi}$) is computed following the procedure described in Section 4.4. However, this computation of the reduced basis ($\boldsymbol{\Phi}$) needs VMs about a static equilibrium position. To compute this static equilibrium position of the layered beams under the axial compressive load, the corresponding linearized incremental equation of equilibrium for a typical element can be obtained, as given in Eq. (5.8a). Equation (5.8a) is obtained by substituting the discretized forms of displacement/strain vectors (Eqs. (3.22a) and (5.7)) in Eq. (5.6) where the inertia terms and the dynamic counterpart of the axial load are omitted. Here, the constitutive relation for the viscoelastic material is taken similar to that for an elastic material (Eq. (2.3a)), where the elastic modulus is taken as the relaxed modulus ($E^k = E_o,\ k=2$) for the static deformation of the layered beams.

$$
\boldsymbol{K}^e({}^{i}\boldsymbol{d}^e)\,\Delta\boldsymbol{d}^e = \boldsymbol{R}_s^e\,,
$$

$$
\boldsymbol{K}^e({}^{i}\boldsymbol{d}^e) = \boldsymbol{K}_{sl}^e + \boldsymbol{K}_{sn1}^e\,{}^{i}\boldsymbol{d}_I^e + ({}^{i}\boldsymbol{d}_I^e)^{\mathrm{T}}\left\{(\boldsymbol{K}_{sn1}^e)^{\mathrm{T}} + \boldsymbol{K}_{sn4}^e\,{}^{i}\boldsymbol{d}_I^e\right\} + \boldsymbol{K}_{sg}^e + p_a^o\boldsymbol{K}_{sa}^e\,,
$$

$$
\boldsymbol{K}_{sg}^e = (1/2)({}^{i}\boldsymbol{d}_I^e)^{\mathrm{T}}\,{}^{r}\boldsymbol{K}_{sn5}^e\,{}^{i}\boldsymbol{d}_I^e + \boldsymbol{K}_{sn3}^e\,{}^{i}\boldsymbol{d}_I^e\,,\ \ \boldsymbol{R}_s^e = -\boldsymbol{K}_{sm}^e\,{}^{i}\boldsymbol{d}^e\,,
$$

$$
\boldsymbol{K}_{sm}^e = \boldsymbol{K}_{sl}^e + (1/2)\left\{\boldsymbol{K}_{sn1}^e + ({}^{i}\boldsymbol{d}_I^e)^{\mathrm{T}}\boldsymbol{K}_{sn4}^e\right\}{}^{i}\boldsymbol{d}_I^e + ({}^{i}\boldsymbol{d}_I^e)^{\mathrm{T}}(\boldsymbol{K}_{sn1}^e)^{\mathrm{T}} + p_a^o\boldsymbol{K}_{sa}^e \tag{5.8a}
$$

The different elemental matrices ($\boldsymbol{K}_{sl}^e$, $\boldsymbol{K}_{sa}^e$, $\boldsymbol{K}_{sn1}^e$, $\boldsymbol{K}_{sn3}^e$, $\boldsymbol{K}_{sn4}^e$, $\boldsymbol{K}_{sn5}^e$) appearing in Eq. (5.8a) can be obtained according to the following expressions similar to Eqs. (3.28) and (3.30b), where A^e is the area of an element.

$$\boldsymbol{K}_{sl}^{e}=\int_{A^e}(\boldsymbol{B}_l)^{\mathrm{T}}\boldsymbol{C}^k\boldsymbol{B}_l b\,dA^e\,,\ \boldsymbol{K}_{sa}^{e}=\int_{A^e}\left\langle(\boldsymbol{B}_g^u)^{\mathrm{T}}\boldsymbol{\Gamma}_f^k\,\boldsymbol{B}_g^u+(\boldsymbol{B}_g^w)^{\mathrm{T}}\boldsymbol{\Gamma}_f^k\,\boldsymbol{B}_g^w\right\rangle b\,dA^e\,,$$

$$\boldsymbol{K}_{sn1}^{e}=\int_{A^e}(\boldsymbol{B}_l)^{\mathrm{T}}\boldsymbol{C}^k\boldsymbol{B}_n b\,dA^e\,,\ \boldsymbol{K}_{sn4}^{e}=\int_{A^e}(\boldsymbol{B}_n)^{\mathrm{T}}\boldsymbol{C}^k\boldsymbol{B}_n b\,dA^e\,,$$

$$\boldsymbol{K}_{sn5}^{e}=\int_{A^e}\left\langle\boldsymbol{A}_{1w}^k\boldsymbol{R}_x^w+\boldsymbol{A}_{2w}^k\boldsymbol{R}_z^w+\boldsymbol{A}_{1u}^k\boldsymbol{R}_x^u+\boldsymbol{A}_{2u}^k\boldsymbol{R}_z^u\right\rangle b\,dA^e\,,$$

$$\boldsymbol{K}_{sn3}^{e}=\int_{A^e}\left\langle\begin{matrix}(\boldsymbol{B}_1^u)^{\mathrm{T}}\boldsymbol{C}^k\boldsymbol{B}_l\boldsymbol{R}_x^u+(\boldsymbol{B}_1^w)^{\mathrm{T}}\boldsymbol{C}^k\boldsymbol{B}_l\boldsymbol{R}_x^w\\+(\boldsymbol{B}_2^u)^{\mathrm{T}}\boldsymbol{C}^k\boldsymbol{B}_l\boldsymbol{R}_z^u+(\boldsymbol{B}_2^w)^{\mathrm{T}}\boldsymbol{C}^k\boldsymbol{B}_l\boldsymbol{R}_z^w\end{matrix}\right\rangle b\,dA^e\,,$$

$$\boldsymbol{A}_{1u}^k=(\boldsymbol{B}_1^u\boldsymbol{R}_x^w)^{\mathrm{T}}\boldsymbol{C}^k\boldsymbol{B}_1^w+(\boldsymbol{B}_1^u\boldsymbol{R}_x^u)^{\mathrm{T}}\boldsymbol{C}^k\boldsymbol{B}_1^u+(\boldsymbol{B}_1^u\boldsymbol{R}_z^w)^{\mathrm{T}}\boldsymbol{C}^k\boldsymbol{B}_2^w+(\boldsymbol{B}_1^u\boldsymbol{R}_z^u)^{\mathrm{T}}\boldsymbol{C}^k\boldsymbol{B}_2^u\,,$$

$$\boldsymbol{A}_{2u}^k=(\boldsymbol{B}_2^u\boldsymbol{R}_x^w)^{\mathrm{T}}\boldsymbol{C}^k\boldsymbol{B}_1^w+(\boldsymbol{B}_2^u\boldsymbol{R}_x^u)^{\mathrm{T}}\boldsymbol{C}^k\boldsymbol{B}_1^u+(\boldsymbol{B}_2^u\boldsymbol{R}_z^w)^{\mathrm{T}}\boldsymbol{C}^k\boldsymbol{B}_2^w+(\boldsymbol{B}_2^u\boldsymbol{R}_z^u)^{\mathrm{T}}\boldsymbol{C}^k\boldsymbol{B}_2^u\,,$$

$$\boldsymbol{A}_{1w}^k=(\boldsymbol{B}_1^w\boldsymbol{R}_x^w)^{\mathrm{T}}\boldsymbol{C}^k\boldsymbol{B}_1^w+(\boldsymbol{B}_1^w\boldsymbol{R}_x^u)^{\mathrm{T}}\boldsymbol{C}^k\boldsymbol{B}_1^u+(\boldsymbol{B}_1^w\boldsymbol{R}_z^w)^{\mathrm{T}}\boldsymbol{C}^k\boldsymbol{B}_2^w+(\boldsymbol{B}_1^w\boldsymbol{R}_z^u)^{\mathrm{T}}\boldsymbol{C}^k\boldsymbol{B}_2^u\,,$$

$$\boldsymbol{A}_{2w}^k=(\boldsymbol{B}_2^w\boldsymbol{R}_x^w)^{\mathrm{T}}\boldsymbol{C}^k\boldsymbol{B}_1^w+(\boldsymbol{B}_2^w\boldsymbol{R}_x^u)^{\mathrm{T}}\boldsymbol{C}^k\boldsymbol{B}_1^u+(\boldsymbol{B}_2^w\boldsymbol{R}_z^w)^{\mathrm{T}}\boldsymbol{C}^k\boldsymbol{B}_2^w+(\boldsymbol{B}_2^w\boldsymbol{R}_z^u)^{\mathrm{T}}\boldsymbol{C}^k\boldsymbol{B}_2^u \qquad (5.8b)$$

By assembling the elemental matrices and vectors in Eqs. (5.8a) and (5.8b), the linearized incremental equation of equilibrium of the layered beams can be obtained, as given in Eq. (5.9).

$$\boldsymbol{K}({}^i\boldsymbol{d})\,\Delta\boldsymbol{d}=\boldsymbol{R}_s \qquad (5.9)$$

Equation (5.9) can be solved using Newton-Raphson method to obtain the static equilibrium position (${}^i\boldsymbol{d}_{eq}$) of the layered beams for the specified axial compressive load. With reference to this static equilibrium position, VMs and the corresponding enriched RBVs can be computed following the procedure, as demonstrated in Section 4.4.

5.4.2 Derivation of the reduced-order FE model in the time domain

The time-domain ROM of viscoelastic layered beams is derived in Section 4.2 based on the fractional Zener constitutive model. The resulting reduced-order equations of motion at a discrete time (Eq. (4.1a)) can be used in conjunction with the Newmark time-integration method for the evaluation of transient responses. However, this formulation is extended here for the incremental form of the reduced-order equations of motion with the particular interest of using Bathe time-integration method (Bathe, 2006) in the evaluation of nonlinear transient responses of the layered beams.

The fractional Zener constitutive relation (Eqs. (3.12a)-(3.12b)) for viscoelastic materials involves the fractional-order temporal derivative of

stress/strain. It is presently handled using Grunwald definition (Galucio et al., 2004) by discretizing a time-span of interest into a number (N_t) of equal small time steps (Δt). The constitutive relation at a typical time-step (say, $(q+1)^{th}$ time-step) is given in Eq. (3.32). Accordingly, the incremental form of the constitutive equation is given in Eq. (5.10).

$$\boldsymbol{\sigma}_{q+1}^{k} = \boldsymbol{C}^{k}\ f_1^{k}\,\boldsymbol{\varepsilon}_{q+1} + \boldsymbol{C}^{k}\,\bar{f}_1^{k}\sum_{j=1}^{q+1} A_{j+1}\,\bar{\boldsymbol{\varepsilon}}_{q+1-j}\ ,$$

$$\bar{\boldsymbol{\varepsilon}}_{q+1} = (1-c_b)\,f\,\boldsymbol{\varepsilon}_{q+1} - c_b\sum_{j=1}^{q+1} A_{j+1}\,\bar{\boldsymbol{\varepsilon}}_{q+1-j}\ ,$$

$$c_b = \tau^{\alpha}\Big/\left\langle \tau^{\alpha} + (\Delta t)^{\alpha}\right\rangle,\ A_{j+1} = \frac{j-\alpha-1}{j}A_j\ ,$$

$$\bar{f}_1^{k} = c_b\,E_{\infty}/E_o\ ,\ \ f_1^{k} = 1+\left\langle c_b(E_{\infty}-E_o)/E_o\right\rangle \ \text{for}\ k=2 \tag{3.32}$$

$${}^{i}\boldsymbol{\sigma}_{q+1}^{k} + \Delta\boldsymbol{\sigma}_{q+1}^{k} = \boldsymbol{C}^{k}\ f_1^{k}\left\langle \begin{matrix} ({}^{i}\boldsymbol{\varepsilon}_{l} + \Delta\boldsymbol{\varepsilon}_{l})_{q+1} \\ +({}^{i}\boldsymbol{\varepsilon}_{n})_{q+1} + (\Delta\boldsymbol{\varepsilon}_{n1})_{q+1} \end{matrix}\right\rangle + \boldsymbol{C}^{k}\,\bar{f}_1^{k}\sum_{j=1}^{q+1} A_{j+1}\,\bar{\boldsymbol{\varepsilon}}_{q+1-j} \tag{5.10}$$

The ROM in the time-domain can be derived using the RB ($\boldsymbol{\Phi}$) that linearly transforms the nodal displacement vector ($^{i}\boldsymbol{d}_{q+1}, \Delta\boldsymbol{d}_{q+1}$) to the reduced coordinate vector ($^{i}\boldsymbol{V}_{q+1}, \Delta\boldsymbol{V}_{q+1}$) according to Eq. (5.11a). However, presently the ROM is formulated at the elemental level by taking the coordinate transformation (Eq. (5.11a)) for a typical element, as given in Eq. (5.11b), where the superscript e indicates the elemental quantity. Using Eq. (5.11b), the strain vectors (Eq. (5.7)) at $(q+1)^{th}$ time-step can be expressed in terms of the reduced coordinate vector ($^{i}\boldsymbol{V}_{q+1}, \Delta\boldsymbol{V}_{q+1}$), as it is illustrated in Eq. (5.11c).

$${}^{i}\boldsymbol{d}_{q+1} = \boldsymbol{\Phi}\ {}^{i}\boldsymbol{V}_{q+1}\ ,\ \ \Delta\boldsymbol{d}_{q+1} = \boldsymbol{\Phi}\ \Delta\boldsymbol{V}_{q+1} \tag{5.11a}$$

$${}^{i}\boldsymbol{d}_{q+1}^{e} = \boldsymbol{\Phi}^{e}\ {}^{i}\boldsymbol{V}_{q+1}\ ,\ \ \Delta\boldsymbol{d}_{q+1}^{e} = \boldsymbol{\Phi}^{e}\ \Delta\boldsymbol{V}_{q+1} \tag{5.11b}$$

$$({}^{i}\boldsymbol{\varepsilon}_{l})_{q+1} = \boldsymbol{B}_{l}\ {}^{i}\boldsymbol{V}_{q+1},\ (\Delta\boldsymbol{\varepsilon}_{l})_{q+1} = \boldsymbol{B}_{l}\ \Delta\boldsymbol{V}_{q+1},\ ({}^{i}\boldsymbol{\varepsilon}_{n})_{q+1} = (1/2)\,\boldsymbol{B}_{n}\,({}^{i}\boldsymbol{V}_{I})_{q+1}\,{}^{i}\boldsymbol{V}_{q+1},$$

$$(\Delta\boldsymbol{\varepsilon}_{n1})_{q+1} = \boldsymbol{B}_{n}\,({}^{i}\boldsymbol{V}_{I})_{q+1}\,\Delta\boldsymbol{V}_{q+1},\ (\Delta\boldsymbol{\varepsilon}_{n2})_{q+1} = (1/2)\boldsymbol{B}_{n}\,(\Delta\boldsymbol{V}_{I})_{q+1}\,\Delta\boldsymbol{V}_{q+1},$$

$$({}^{i}\boldsymbol{\varepsilon}_{g}^{u})_{q+1} = \boldsymbol{B}_{g}^{u}\ {}^{i}\boldsymbol{V}_{q+1}\ ,\ ({}^{i}\boldsymbol{\varepsilon}_{g}^{w})_{q+1} = \boldsymbol{B}_{g}^{w}\ {}^{i}\boldsymbol{V}_{q+1}, (\Delta\boldsymbol{\varepsilon}_{g}^{u})_{q+1} = \boldsymbol{B}_{g}^{u}\ \Delta\boldsymbol{V}_{q+1},$$

$$(\Delta\boldsymbol{\varepsilon}_{g}^{w})_{q+1} = \boldsymbol{B}_{g}^{w}\ \Delta\boldsymbol{V}_{q+1},$$

$$\boldsymbol{\Phi}_{I}^{e} = \boldsymbol{\Phi}^{e}\otimes\boldsymbol{\Phi}^{e},\ ({}^{i}\boldsymbol{V}_{I})_{q+1} = {}^{i}\boldsymbol{V}_{q+1}\otimes\boldsymbol{I}_{N_r}\ ,\ (\Delta\boldsymbol{V}_{I})_{q+1} = \Delta\boldsymbol{V}_{q+1}\otimes\boldsymbol{I}_{N_r} \tag{5.11c}$$

In Eq. (5.11c), $\boldsymbol{I}_{N_r}$ is the unity matrix of size ($N_r \times N_r$); N_r is the number of basis vectors in RB ($\boldsymbol{\Phi}$). Now, introducing Eqs. (5.11b), (5.11c) and (5.10) in Eq. (5.6) at $(q+1)^{th}$ time-step, the ROM can be derived, as given in Eq. (5.12a).

$$
{}^{r}\boldsymbol{M}_s\,\Delta\ddot{\boldsymbol{V}}_{q+1} + \left\{ {}^{r}\boldsymbol{K}_{sa}\left\langle p_a^o(1+\lambda\cos\Omega_i t)\right\rangle + \left\langle {}^{r}\boldsymbol{K}_{ll} + ({}^{r}\boldsymbol{K}_{nn})_{q+1}\right\rangle \right\}\Delta\boldsymbol{V}_{q+1} = ({}^{r}\boldsymbol{R}_s)_{q+1},
$$

$$
({}^{r}\boldsymbol{K}_{nn})_{q+1} = \sum_{k=1}^{2} f_1^k\,({}^{r}\boldsymbol{K}_{stn}^k)_{q+1}\,,\quad {}^{r}\boldsymbol{K}_{ll} = \sum_{k=1}^{2} f_1^k\,{}^{r}\boldsymbol{K}_{sl}^k\,,
$$

$$
({}^{r}\boldsymbol{K}_{stn}^k)_{q+1} = {}^{r}\boldsymbol{K}_{sn1}^k({}^{i}\boldsymbol{V}_I)_{q+1} + \left\langle ({}^{i}\boldsymbol{V}_I)_{q+1}\right\rangle^{\mathrm{T}}\left\langle ({}^{r}\boldsymbol{K}_{sn1}^k)^{\mathrm{T}} + {}^{r}\boldsymbol{K}_{sn4}^k({}^{i}\boldsymbol{V}_I)_{q+1}\right\rangle + ({}^{r}\boldsymbol{K}_{sg}^k)_{q+1}
$$

$$
,\ ({}^{r}\boldsymbol{K}_{sg}^k)_{q+1} = (1/2)\left\langle ({}^{i}\boldsymbol{V}_I)_{q+1}\right\rangle^{\mathrm{T}}\,{}^{r}\boldsymbol{K}_{sn5}^k({}^{i}\boldsymbol{V}_I)_{q+1} + {}^{r}\boldsymbol{K}_{sn3}^k({}^{i}\boldsymbol{V}_I)_{q+1}\,,
$$

$$
({}^{r}\boldsymbol{R}_s)_{q+1} = ({}^{r}\bar{\boldsymbol{P}}_s)_{q+1} - \left\{ \begin{array}{l} {}^{r}\boldsymbol{K}_{sa}\,p_a^o(1+\lambda\cos\Omega_i t_{q+1}) \\ +\sum_{k=1}^{2} f_1^k\left\langle {}^{r}\boldsymbol{K}_{sl}^k + ({}^{r}\boldsymbol{K}_{sn}^k)_{q+1}\right\rangle \end{array} \right\}{}^{i}\boldsymbol{V}_{q+1} - {}^{r}\boldsymbol{M}_s\,{}^{i}\ddot{\boldsymbol{V}}_{q+1}\,,
$$

$$
({}^{r}\boldsymbol{K}_{sn}^k)_{q+1} = (1/2)\left\{ \begin{array}{l} {}^{r}\boldsymbol{K}_{sn1}^k({}^{i}\boldsymbol{V}_I)_{q+1} + \\ \left\langle ({}^{i}\boldsymbol{V}_I)_{q+1}\right\rangle^{\mathrm{T}}\,{}^{r}\boldsymbol{K}_{sn4}^k({}^{i}\boldsymbol{V}_I)_{q+1} \end{array} \right\} + \left\langle ({}^{i}\boldsymbol{V}_I)_{q+1}\right\rangle^{\mathrm{T}}({}^{r}\boldsymbol{K}_{sn1}^k)^{\mathrm{T}} \qquad (5.12a)
$$

$$
{}^{r}\boldsymbol{K}_{sl}^k = \sum_{e\in\boldsymbol{\Xi}^k}(\boldsymbol{\Phi}^e)^{\mathrm{T}}\boldsymbol{K}_{sl}^e\boldsymbol{\Phi}^e\,,\ {}^{r}\boldsymbol{K}_{sn1}^k = \sum_{e\in\boldsymbol{\Xi}^k}(\boldsymbol{\Phi}^e)^{\mathrm{T}}\boldsymbol{K}_{sn1}^e\boldsymbol{\Phi}_I^e\,,
$$

$$
{}^{r}\boldsymbol{K}_{sn4}^k = \sum_{e\in\boldsymbol{\Xi}^k}(\boldsymbol{\Phi}_I^e)^{\mathrm{T}}\boldsymbol{K}_{sn4}^e\boldsymbol{\Phi}_I^e\,,\ {}^{r}\boldsymbol{K}_{sn5}^k = \sum_{e\in\boldsymbol{\Xi}^k}(\boldsymbol{\Phi}_I^e)^{\mathrm{T}}\boldsymbol{K}_{sn5}^e\boldsymbol{\Phi}_I^e\,,
$$

$$
{}^{r}\boldsymbol{K}_{sn3}^k = \sum_{e\in\boldsymbol{\Xi}^k}(\boldsymbol{\Phi}^e)^{\mathrm{T}}\boldsymbol{K}_{sn3}^e\boldsymbol{\Phi}_I^e\,,\ {}^{r}\boldsymbol{M}_s = \sum_{e=1}^{n_e}(\boldsymbol{\Phi}^e)^{\mathrm{T}}\boldsymbol{M}_s^e\boldsymbol{\Phi}^e\,,\ {}^{r}\boldsymbol{K}_{sa} = \sum_{e=1}^{n_e}(\boldsymbol{\Phi}^e)^{\mathrm{T}}\boldsymbol{K}_{sa}^e\boldsymbol{\Phi}^e \qquad (5.12b)
$$

$$
({}^{r}\bar{\boldsymbol{P}}_s)_{q+1} = -\left(\sum_{j=1}^{q+1} A_{j+1}({}^{r}\bar{\boldsymbol{F}}_{s1})_{q+1-j} + \left\langle ({}^{i}\boldsymbol{V}_I)_{q+1}\right\rangle^{\mathrm{T}} \sum_{j=1}^{q+1} A_{j+1}({}^{r}\bar{\boldsymbol{F}}_{s2})_{q+1-j} \right)
$$

$$
({}^{r}\bar{\boldsymbol{F}}_{s1})_{q+1} = (1-c_b)\,f\,({}^{r}\boldsymbol{F}_{s1})_{q+1} - c_b\sum_{j=1}^{q+1} A_{j+1}({}^{r}\bar{\boldsymbol{F}}_{s1})_{q+1-j}\,,
$$

$$
({}^{r}\bar{\boldsymbol{F}}_{s2})_{q+1} = (1-c_b)\,f\,({}^{r}\boldsymbol{F}_{s2})_{q+1} - c_b\sum_{j=1}^{q+1} A_{j+1}({}^{r}\bar{\boldsymbol{F}}_{s2})_{q+1-j}\,,
$$

$$
({}^{r}\boldsymbol{F}_{s1})_{q+1} = \bar{f}_1^k\left\langle {}^{r}\boldsymbol{K}_{sl}^k + (1/2)\,{}^{r}\boldsymbol{K}_{sn1}^k({}^{i}\boldsymbol{V}_I)_{q+1}\right\rangle{}^{i}\boldsymbol{V}_{q+1}\,,
$$

$$
({}^{r}\boldsymbol{F}_{s2})_{q+1} = \bar{f}_1^k\left\langle ({}^{r}\boldsymbol{K}_{sn1}^k)^{\mathrm{T}} + (1/2)\,{}^{r}\boldsymbol{K}_{sn4}^k({}^{i}\boldsymbol{V}_I)_{q+1}\right\rangle{}^{i}\boldsymbol{V}_{q+1}\,,\ k=2 \qquad (5.12c)
$$

where, $\boldsymbol{\Xi}^k$ is a set of elements made of k^{th} material; n_e is the total number of elements in the FE mesh. The different reduced-order system matrices/vectors (${}^{r}\boldsymbol{M}_s$, ${}^{r}\boldsymbol{K}_{sl}^k$,

${}^{r}\boldsymbol{K}_{sn1}^{k}$, ${}^{r}\boldsymbol{K}_{sn3}^{k}$, ${}^{r}\boldsymbol{K}_{sn4}^{k}$, ${}^{r}\boldsymbol{K}_{sn5}^{k}$, ${}^{r}\boldsymbol{K}_{sa}$) appearing in Eq. (5.12a) are given in Eq. (5.12b). Also, the reduced-order nonlinear memory-load vector (($^{r}\bar{\boldsymbol{P}}_{s}$)$_{q+1}$) is given in Eq. (5.12c). It (($^{r}\bar{\boldsymbol{P}}_{s}$)$_{q+1}$) is derived in terms of the reduced-order anelastic force history (($^{r}\bar{\boldsymbol{F}}_{s1}$)$_{q+1-j}$, ($^{r}\bar{\boldsymbol{F}}_{s2}$)$_{q+1-j}$, Eq. (5.12c)) and the reduced coordinate vector ($\boldsymbol{V}_{q+1}$) following the similar formulation in Section 4.2.

The nonlinear transient responses of the layered beams can be evaluated using the Bathe time integration method (Bathe, 2006) in conjunction with the incremental governing equation of motion (Eq. (5.12a)). It may be noted here that the system matrices/vectors (Eqs. (5.12b) and (5.12c)) are expressed in terms of the reduced-order linear matrices/vectors (${}^{r}\boldsymbol{K}_{sn1}^{k}$, ${}^{r}\boldsymbol{K}_{sn3}^{k}$, ${}^{r}\boldsymbol{K}_{sn4}^{k}$, ${}^{r}\boldsymbol{K}_{sn5}^{k}$, ${}^{r}\boldsymbol{K}_{sl}^{k}$, ${}^{r}\boldsymbol{M}_{s}$, ${}^{r}\boldsymbol{K}_{sa}$). These linear matrices/vectors are to be formed only once before starting the solution of nonlinear transient response. So, it would facilitate reduced computational time to evaluate nonlinear transient responses and global bifurcation diagrams, as illustrated through the numerical results in Section 5.5.1.

5.4.3. Derivation of the reduced-order FE model in the frequency domain

The nonlinear frequency responses of the viscoelastic layered beams are presently computed using the harmonic balance method (HBM). The corresponding nonlinear ROM is derived by modifying the earlier formulation (Section 4.3) due to the change in the type of load/excitation.

According to HBM, the displacements ($\boldsymbol{d}_{s}$) at any point in a layered beam operating under the axial compressive harmonic load (Eq. (2.7)) can be assumed with a finite number (H) of harmonic terms as

$$\boldsymbol{d}_{s} = \boldsymbol{d}_{s}^{o} + \sum_{m=1}^{H} \boldsymbol{d}_{sm}^{c} \cos(m\Omega t/2) + \boldsymbol{d}_{sm}^{s} \sin(m\Omega t/2) \tag{5.13}$$

where, $\boldsymbol{d}_{s}^{o}$, $\boldsymbol{d}_{sm}^{c}$ and $\boldsymbol{d}_{sm}^{s}$ are the displacement amplitude vectors corresponding to the constant, cosine and sine terms, respectively. It may be noted here that the solution (Eq. (5.13)) is assumed similar to that in Eq. (3.9). However, the harmonic components are presently taken with the frequencies in multiple of $m/2$ instead of m, in particular, to capture the sub-harmonic periodic response due to principal primary parametric resonance under the axial compressive harmonic load. Accordingly, the linearized incremental reduced-order FE equation of motion of the layered beams in the frequency domain can be obtained in the similar form,

as given in Eq. (4.8). However, an additional reduced-order geometric stiffness matrix ($^{r}\boldsymbol{K}_{a}$) appears in the governing equation due to the axial compressive harmonic load, as illustrated in Eq. (5.14). This reduced-order geometric stiffness matrix ($^{r}\boldsymbol{K}_{a}$) can be formulated similar to the overall nonlinear reduced geometric stiffness matrix ($^{r}\boldsymbol{K}_{g}$, Eqs. (4.9a), (4.9b), (4.7c) and (4.7d)), where the stress matrix ($^{i}\boldsymbol{\Gamma}^{k}$, Eq. (4.7d)) is to be replaced by the pre-stress matrix ($\boldsymbol{\Gamma}_{a}^{k}$, Eq. (5.1)).

$$
\begin{aligned}
{}^{r}\boldsymbol{K}_{t}\,\Delta\boldsymbol{X} &= {}^{r}\boldsymbol{R} + {}^{r}\boldsymbol{R}_{\Omega}\,\Delta\Omega \\
{}^{r}\boldsymbol{R} &= -{}^{r}\boldsymbol{K}_{m}\,{}^{i}\boldsymbol{X}\,,\; {}^{r}\boldsymbol{R}_{\Omega} = -(\partial\,{}^{r}\boldsymbol{K}_{m}/\partial\Omega_{i})\,{}^{i}\boldsymbol{X}\,, \\
{}^{r}\boldsymbol{K}_{m} &= {}^{r}\boldsymbol{K}_{l} - \Omega_{i}^{2}\,{}^{r}\boldsymbol{M} + (1/2)\,{}^{r}\boldsymbol{K}_{n1} + {}^{r}\boldsymbol{K}_{nt} + (1/2)\,{}^{r}\boldsymbol{K}_{n4} + {}^{r}\boldsymbol{K}_{a}\,, \\
{}^{r}\boldsymbol{K}_{t} &= {}^{r}\boldsymbol{K}_{l} - \Omega_{i}^{2}\,{}^{r}\boldsymbol{M} + {}^{r}\boldsymbol{K}_{n1} + {}^{r}\boldsymbol{K}_{nt} + {}^{r}\boldsymbol{K}_{g} + {}^{r}\boldsymbol{K}_{n4} + {}^{r}\boldsymbol{K}_{a}
\end{aligned}
\tag{5.14}
$$

In Eq. (5.14), $^{r}\boldsymbol{K}_{m}$ and $^{r}\boldsymbol{K}_{t}$ are the overall reduced-order stiffness and tangent stiffness matrices, respectively; $^{r}\boldsymbol{R}$ is the overall reduced-order residue vector; $^{r}\boldsymbol{R}_{\Omega}$ is the overall reduced-order load vector per unit increment of the excitation frequency. The matrices $^{r}\boldsymbol{M}$, $^{r}\boldsymbol{K}_{l}$, $^{r}\boldsymbol{K}_{n1}$, $^{r}\boldsymbol{K}_{g}$, $^{r}\boldsymbol{K}_{nt}$ and $^{r}\boldsymbol{K}_{n4}$ in Eq. (5.14) can be constructed following Eqs. (4.8), (4.9a) and (4.9b), where m or n is to be replaced by $m/2$ or $n/2$ due to the present form of the assumed solution (Eq. (5.13)). Equation (5.14) can be used in conjunction with a numerical continuation method to obtain the nonlinear frequency responses of the parametrically excited layered beams within a frequency range of interest. However, as discussed in the previous chapter (Section 4.3 and 4.5.1), the overall reduced-order geometric stiffness matrix ($^{r}\boldsymbol{K}_{g}$) can be formulated without consideration of its viscoelastic counterpart. It significantly simplifies the formulation of this system matrix ($^{r}\boldsymbol{K}_{g}$) with the additional advantage of reduced computational time.

The above sections (Sections 5.4.2 and 5.4.3) present the formulation of the nonlinear ROMs in the time and frequency domains for the viscoelastic layered beams. However, the corresponding full-order FE models (FOMs) can be obtained using the same formulation by replacing the reduction basis ($\boldsymbol{\Phi}$) with an identity matrix of size ($N_{f} \times N_{f}$).

5.5. Results and discussion

In this section, the numerical results are presented, first, to verify the accuracy and computational efficiency of the presently derived ROMs in the evaluation of complex nonlinear frequency responses/global bifurcation diagrams of the parametrically excited layered beams. Subsequently, the passive damping capability of the CLD treatment in its three different configurations (Figs. 5.1(a)-(c)) is investigated for attenuation of complex dynamics of the layered beams under the parametric excitation in the post-buckled state. In the evaluation of nonlinear frequency responses, the reduced-order governing equation of motion in the frequency domain (Eq. (5.14)) is solved using a numerical continuation method (Cheung et al., 1990). However, Bathe time integration method (Bathe, 2006) is employed to obtain the nonlinear transient responses by the solution of the reduced-order governing equation of motion in the time domain (Eqs. (5.12a), (5.12b) and (5.12c)), where the time-step is taken as $\pi/(40\Omega)$ s. These transient responses are mainly used for the construction of global bifurcation diagrams where the Poincare sections are selected at the intervals of the time period of excitation ($2\pi/\Omega$).

The elastic substrate/constraining layers in the layered beams (Fig. 5.1) are considered to be made of Aluminum (E = 70.3 GPa, ν = 0.345, ρ = 2690 kg/m^3 (Galucio et al., 2004)). The constrained viscoelastic layers are considered to be made of 3M ISD 112 (Galucio et al., 2004) (ν = 0.499, ρ =1600 kg/m^3). The corresponding material parameters according to the fractional Zener viscoelastic constitutive model are E_o = 1.5 MPa, E_∞ = 69.9495 MPa, α = 0.7915 and $\tau = 1.4052\times10^{-5}$ s (Galucio et al., 2004). The length (L) and width (b) of any layered beam (Fig. 5.1) are taken as 0.8 m and 12 mm, respectively. The total thickness (h_f) of elastic layers in any beam is considered as 4 mm. However, in the case of the PCLD treated beam (Fig. 5.1(a)), the thickness (h_f) of the constraining layer is taken as 0.25 mm. So, the thickness (h_s) of the substrate layer appears as 3.75 mm. All beams are considered to operate under the axial compressive harmonic load (Eq. (2.7)), while the boundary conditions over their ends are mentioned in Section 5.2. Under this parametric load, the transverse deflection at the middle point ($L/2, h$) of the layered beams is computed and presented in the numerical results. Initially, a mesh convergence study is performed by evaluating the nonlinear frequency response of sandwich beam using FOM and considering different number of elements in x and z-directions of sandwich beam. Here, the

HBM is implemented with the first seven harmonic terms ($H=7$. Eq. (5.13)). The convergence of peak displacement amplitude for the frequency response of three-layered beam (Fig. 5.1 (b)) and the substrate beam with PCLD layer (Fig. 5.1(a)) is achieved for a minimum 100 elements (100 element divisions in $x-$direction and one element division in $z-$direction) in each elastic layer and 200 elements (100 element divisions in $x-$direction and 2 element divisions in $z-$direction) in viscoelastic core. Further, the convergence of peak displacement amplitude for the frequency response of five-layered beam (Fig. 5.1 (c)) is achieved for 100 elements (100 element divisions in $x-$direction and one element division in $z-$direction) in each layer. The subsequent results are evaluated following this mesh convergence study for each of the layered viscoelastic beams.

5.5.1. Verification of present ROMs in the estimation of complex dynamics

In this section, the accuracy of the presently derived ROMs is verified, particularly for evaluating complex nonlinear dynamics of the viscoelastic layered beams. For this verification study, the three-layered beam (Fig. 5.1(b)) is considered at its pre-buckled and post-buckled equilibrium states. First, this beam (h_v = 2 mm) is taken at its pre-buckled state, and it is considered to undergo principal primary parametric resonance due to the parametric excitation (p_a^o = 100 N and λ = 0.5). The corresponding vibration responses obtained from the time-domain/frequency-domain ROM are illustrated in Fig. 5.2, where the RB is taken with or without enrichment. Similar responses obtained from FOM are also presented in the same figure (Fig. 5.2). Also, the HBM is implemented with the first seven harmonic terms ($H=7$. Eq. (5.13)) to achieve sufficient numerical accuracy in the frequency responses. Further, for ROMs, the unenriched RB is considered to be comprised of the first three VMs obtained through ICES approach (Rouleau et al., 2017). However, the enrichment of these VMs is carried out by the corresponding SDs according to the procedure described in Section 5.4.1 and Section 4.4, where the first twenty POMs are considered in the enriched RB through a convergence study for achieving sufficient numerical accuracy in the results. It may be observed from Fig. 5.2 that the ROMs with the unenriched RB provide inaccurate results as compared to the similar results obtained from FOM. This shortcoming of inaccurate results from the ROMs is mitigated by the enriched RB.

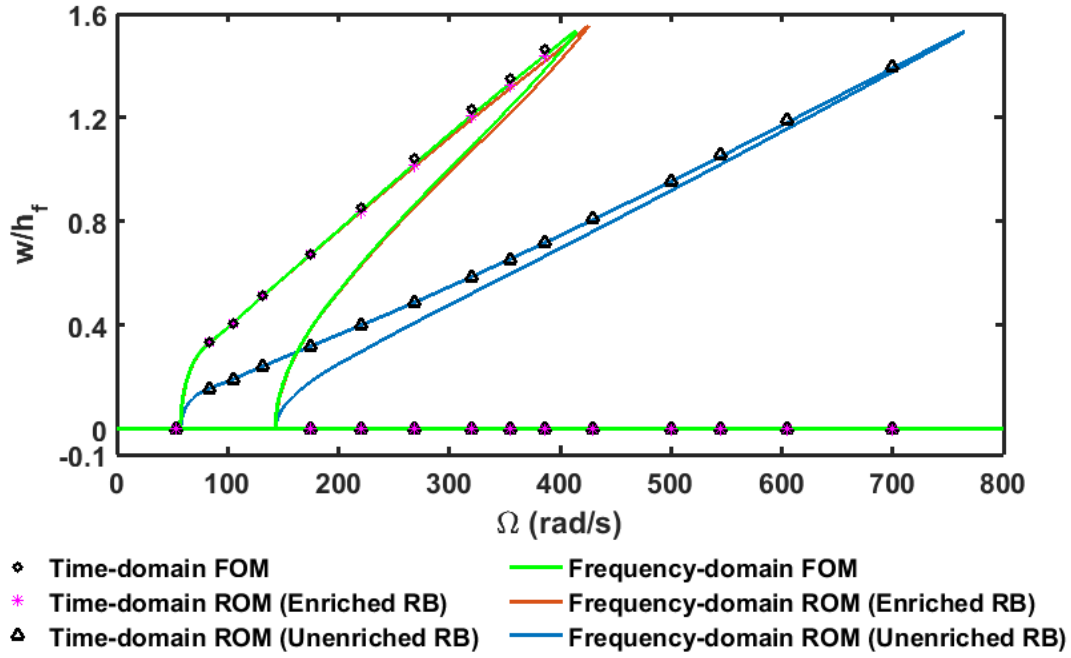

Fig. 5.2. Comparison of frequency responses obtained from the time-domain/frequency-domain FOM and ROM considering unenriched RB or enriched RB.

However, although this comparison study (Fig. 5.2) shows sufficient accuracy of the time-domain/frequency-domain ROM due to the enriched RB, further verification study is also performed to find the appropriateness of this enrichment of RB using VMs, SDs and POD approach (Section 5.4.1 and section 4.4), especially in the estimation of very complex nonlinear dynamic responses. It is carried out, first, by evaluating the complex nonlinear frequency response of the three-layered beam at its post-buckled state where the parametric excitation is considered as p_a^o = 155 N and λ = 0.13. This frequency response obtained from the ROM in the frequency domain is illustrated in Fig. 5.3. A similar result obtained from FOM is also illustrated in the same figure (Fig. 5.3). Here, for the ROM, the first four VMs are considered with reference to the stable buckled equilibrium states, and these VMs are enriched according to the aforesaid procedure (Section 5.4.1 and Section 4.4), where the first 40 POMs are taken in RB through the convergence study for achieving sufficient numerical accuracy in the frequency response (Fig. 5.3). With this modelling approach, the results (Fig. 5.3) show good accuracy of the present ROM with reference to the FOM for evaluation of the complex nonlinear frequency response of the parametrically excited three-layered beam in its post-buckled state. So, the aforesaid enrichment of RB using VMs, SDs and POD approach (Section 5.4.1 and Section 4.4) may be utilized for the estimation of complex nonlinear dynamics of the viscoelastic beams.

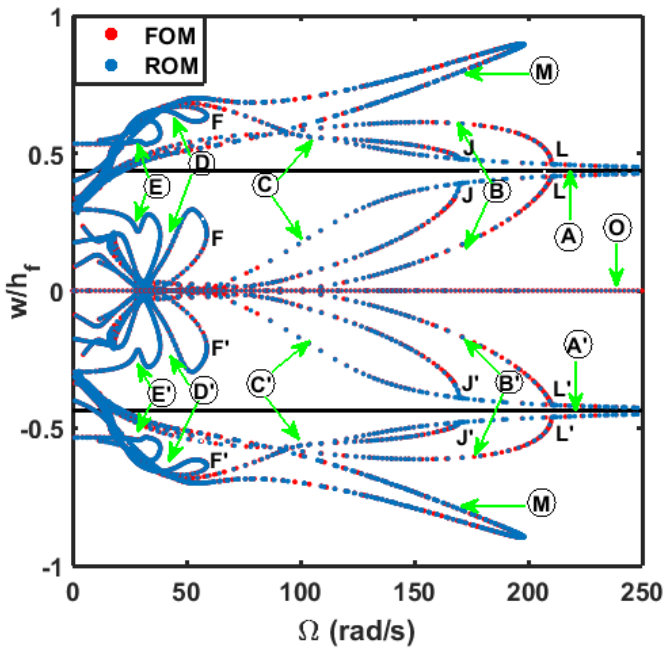

Fig. 5.3. Accuracy of the frequency-domain ROM with reference to the full-order FE model (FOM) in the evaluation of a complex nonlinear frequency response of the thee-layered beam under the parametric excitation in the post-buckled state.

However, this complex frequency response (Fig. 5.3) appears with various dynamic instabilities associated with the complex motion of the three-layered viscoelastic beam. Here, the critical motion of the beam appears with four types of local periodic attractors (B/B', C/C', D/D', E/E') about the buckled equilibria (A/A') and one global periodic attractor (M) with reference to the undeformed state (O). The global periodic attractor involves limit cycle oscillation of the beam about its undeformed state resulting in snap-through motion. The local periodic attractors also involve limit cycle oscillation of the beam about its buckled equilibria, and these local periodic attractors are associated with local principal primary (B/B'), fundamental (C/C') and higher-order parametric resonances (D/D', E/E') at $2\Omega_n$, Ω_n, $\Omega_n/2$, and $\Omega_n/3$, respectively, where Ω_n is the fundamental natural frequency with reference to the buckled equilibria. However, for a clear understanding of various dynamic instabilities appearing in the complex frequency response, one needs to proceed with the corresponding global bifurcation diagram. Now, the construction of this bifurcation diagram using FOM usually involves a high computational time, since this diagram is commonly constructed by the computation of nonlinear transient responses at different frequencies where the frequency is incremented in a small step within a frequency range of interest. In this aspect, the time-domain ROM may be utilized to reduce the computational time. However, it is possible if the time-domain ROM appears

with sufficient accuracy in estimating all kinds of dynamic instabilities within the frequency range of interest.

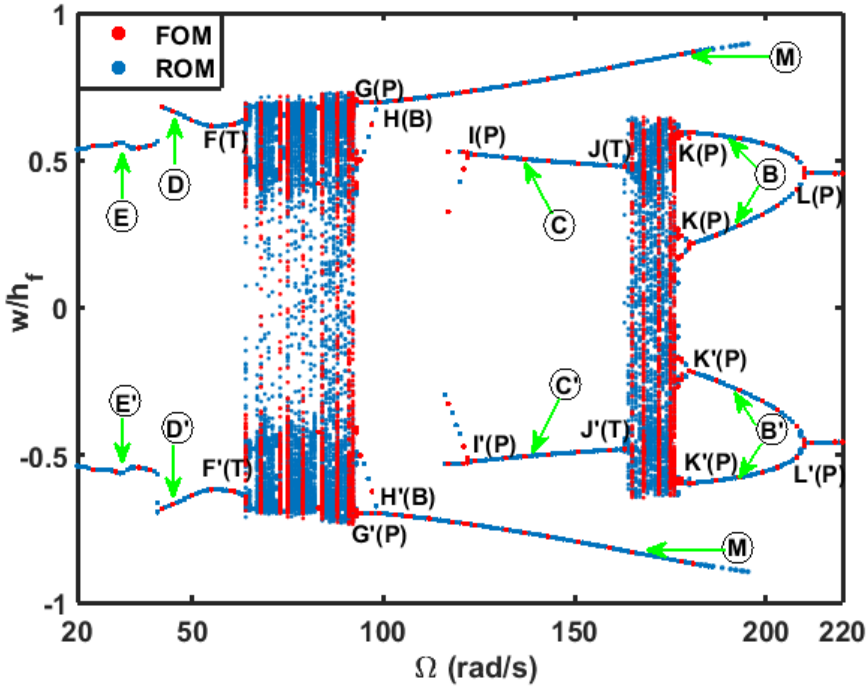

Fig. 5.4. Accuracy of the time-domain ROM with reference to the full-order FE model (FOM) in the evaluation of global bifurcation diagram of the parametrically excited three-layered beam in its post-buckled state.

In this concern, the fruitfulness of the present time-domain ROM with the aforesaid enriched RB is verified by utilizing it to evaluate the global bifurcation diagram within a frequency range (20 rad/s to 220 rad/s) corresponding to the complex frequency response in Fig. 5.3. Figure 5.4 illustrates this bifurcation diagram, where a similar response obtained from FOM is also plotted. It may be observed from Fig. 5.4 that the present ROM in the time-domain has good accuracy with reference to the time-domain FOM in evaluating the global bifurcation diagram. However, to make this comparison precisely, the different types of bifurcations obtained from the time-domain ROM are also compared with those obtained from the time-domain FOM, as described in the following two paragraphs.

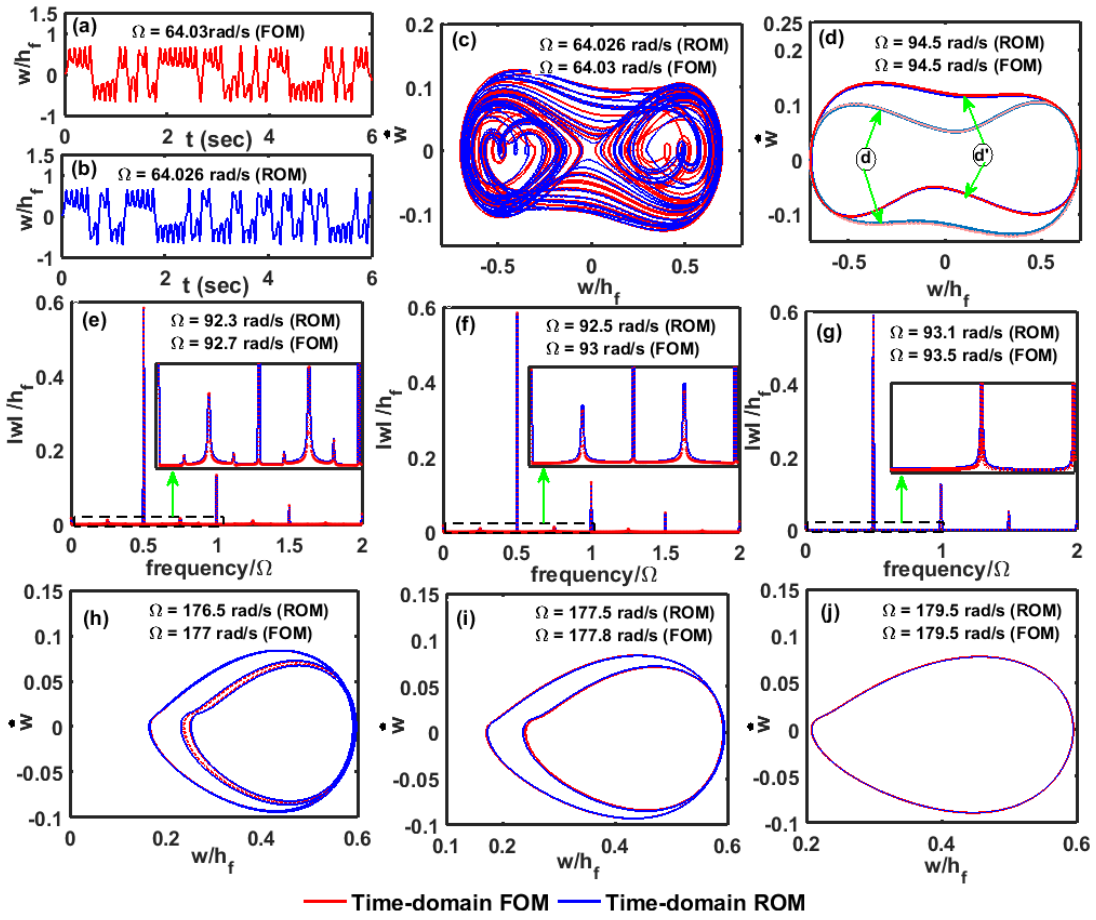

Fig. 5.5. Verification of the present time-domain ROM in the evaluation of different kinds of transient responses with reference to FOM, ((a)-(b) transient responses; (c) phase portraits of chaotic response showing intermittent transition bifurcation; (d) phase portraits for dual period-2 responses; frequency spectrums showing the period-demultiplying bifurcation of global periodic attractors (e) period-8 response, (f) period-4 response, (g) period-2 response; phase portraits showing the period-demultiplying bifurcation of local periodic attractors (h) period-8 , (i) period-4 and (j) period-2 responses).

It can be observed from Fig. 5.4 that period-1 response associated with the local periodic attractors (D/D', E/E') appears at low-frequency range and leads to chaotic motion (FG, F'G', Fig. 5.4) at point F/F' through the intermittent transition bifurcation (T). This type of bifurcation is predicted by ROM at Ω = 64.026 rad/s while similar bifurcation is predicted by FOM at Ω = 64.03 rad/s. The corresponding transient plots (Fig. 5.5(a)-(b)) and a phase plot (Fig. 5.5(c)) also show the accuracy of ROM with reference to FOM. It may also be observed from Fig. 5.4 that the displacement amplitude and frequency range of the chaos obtained from the ROM are very close to that obtained from the FOM. However, in the chaotic region, the transient path obtained from ROM is not exactly aligned with that obtained from FOM (Fig. 5.4). It appears due to the nature of chaos,

where the nonlinear transient response patch is highly sensitive to a very small numerical error (Shinbrot et. al., 1992). This kind of error commonly depends on various factors like computer precession/truncation, selection of RBVs, numerical time-integration method, etc., which differs from one to another method of solution. So, the transient response in the chaotic region obtained from ROM is not exactly aligned with that from FOM. However, with further increase in the excitation frequency, the chaotic motion reduces to a global dual period-2 motion (d, d', Fig. 5.5(d)) through period demultiplying bifurcation (P) around point G/G' (Fig. 5.4). This phenomenon can be seen from frequency spectrums of period-8, period-4 and period-2 responses (Figs. 5.5(e)-(g)) that are depicted through both the time-domain ROM and FOM. However, these responses appear at Ω = 92.3 rad/s, Ω = 92.5 rad/s, Ω =93.1 rad/s for ROM while similar responses through FOM arise at Ω = 92.7 rad/s, Ω = 93 rad/s, Ω = 93.5 rad/s. With the further increase in frequency, the global dual period-2 attractors (d, d', Fig. 5.5(d)) lead to a single global period-2 attractor through inverse symmetry breaking bifurcation (B). However, it arises at Ω = 98.5 rad/s for both the ROM and FOM (Point H, Fig. 5.4).

Besides the snap-through motion due to global period-2 attractor, local period-1 attractors about buckled equilibria evolve at the point I/I' through period demultiplying bifurcation (P) from the local period-2 attractor. It appears at Ω = 122.5 rad/s for ROM and Ω = 122.7 rad/s for FOM. With further increase in the excitation frequency, chaotic motion (JK, J'K', Fig. 5.4) appears at point J/J' due to the appearance of cyclic-fold bifurcation (Fig. 5.3). The corresponding excitation frequency (Ω = 163.5 rad/s) obtained from ROM is very close to that (Ω = 163.7 rad/s) for FOM. However, this chaotic motion reduces to local period-2 attractors about buckled equilibria through period-demultiplying bifurcation around point K/K' (Fig. 5.4). This phenomenon can also be seen from the phase portraits of local period-8, period-4 and period-2 responses (Figs. 5.5(h)-(j)) that are evaluated using both the ROM and FOM. These responses appear at Ω = 176.5 rad/s, Ω = 177.5 rad/s, Ω = 179.5 rad/s for ROM while similar responses arise for FOM at Ω = 177 rad/s, Ω = 177.8 rad/s, Ω = 179.5 rad/s. However, this comparison study (Figs. 5.4 and 5.5) shows good accuracy of the present time-domain/frequency-domain ROM with reference to the time-domain/frequency-domain FOM in the estimation of different kinds of bifurcations and the associated motion of the three-layered beam. Therefore, the subsequent study on the CLD treatment of complex dynamics of the layered beams under the parametric

excitation is carried out using the present ROMs in the time and frequency domains.

With this accuracy of the present ROMs, their main advantage in reducing the computational time is demonstrated in Table 5.1. Presently, the codes for FOM and ROM are written in MATLAB and executed in a CPU with the Octa-Core processor Intel(R) Core(TM) i7-6700 CPU @ 3.4 GHz and RAM of 16 GB. However, in the first row of Table 5.1, the computational time, denoted by t_f, is tabulated for the evaluation of the frequency response (Fig. 5.3) using either FOM or ROM. It may be observed that the computational time significantly reduces for the use of the presently derived ROM instead of FOM. However, in the second row of Table 5.1, the computational time, denoted by t_g, is furnished for the evaluation of nonlinear transient responses from ROM and FOM over 200 cycles of harmonic excitation at a frequency of 110 rad/s. This result also shows the advantage of the reduced computational time for using ROM instead of FOM. It leads to a significant reduction of computational time in the construction of global bifurcation diagrams.

Table 5.1
Computational time in the evaluation of complex frequency response (Fig. 5.3) or transient response (at $\Omega = 110$ rad/s, Fig. 5.4) of the three-layered sandwich beam using the present ROMs and FOMs.

Computational time	FOM	ROM
t_f (hrs)	148.7	6
t_g (hrs)	11.2	0.625

5.5.2. Passive control of nonlinear dynamics of post-buckled beams

In this section, the effectiveness of the CLD treatment in passive control of complex nonlinear dynamics of the parametrically excited post-buckled layered beams (Fig. 5.1) is investigated using the time/frequency domain ROM. The post-buckled equilibrium state of the layered beams arises once they undergo static instability/buckling due to the static counterpart (p_a^o) of the parametric excitation. So, initially, the static instability of the layered beams is analyzed, where the static equilibrium states of a layered beam are evaluated for different values of the static axial load (p_a^o). It is demonstrated in Fig. 5.6 by the variation of transverse deflection of a layered beam with the static axial load (p_a^o), where the total thickness (h_v) of viscoelastic layers in a layered beam is taken as either

0.5 mm or 1.5 mm. It may be observed from Fig. 5.6 that the static instability of the layered beams appears through the pitchfork bifurcation at a certain value of the static axial compressive load (p_a^o), which is commonly called as the critical buckling load (p_{cr}). Through this bifurcation, the initial zero equilibrium state of a layered beam bifurcates to one of the two symmetric buckled equilibrium states (Fig. 5.6). However, from the results in Fig. 5.6, the critical buckling loads for different layered beams are tabulated in Table 5.2. From this result, it is clear that the critical buckling load for the PCLD treated beam (Fig. 5.1(a)) is more than that for the three-layered (Fig. 5.1(b)) or five-layered (Fig. 5.1(c)) beam. Further, the critical buckling load decreases with an increase in the total thickness (h_v) of viscoelastic layers in a layered beam.

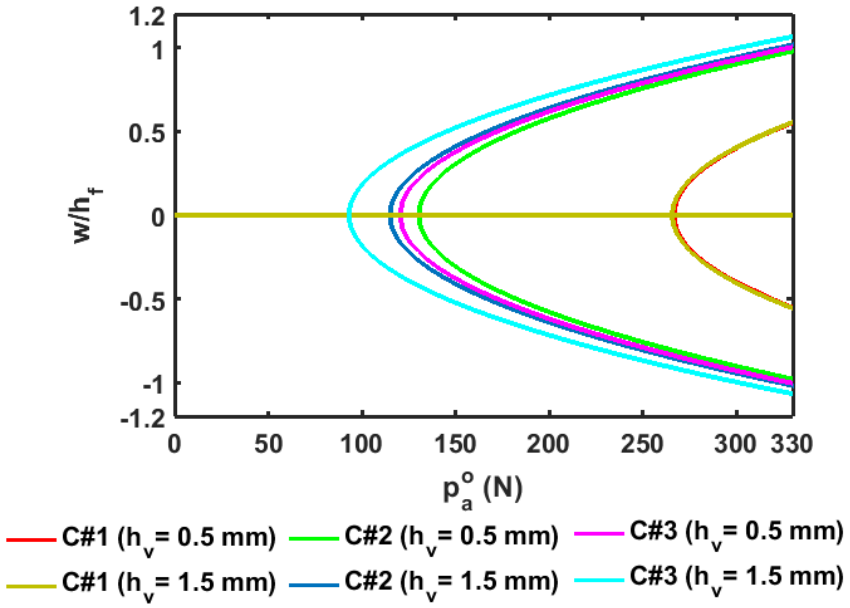

Fig. 5.6. Variation of the transverse deflection of the layered beams with the static counterpart of the parametric load, C#1: PCLD treated beam (Fig. 5.1(a)), C#2: Three-layered beam (Fig. 5.1(b)), C#3; Five-layered beam (Fig. 5.1(c))).

Table 5.2
Critical buckling load (p_{cr}) for the layered beams.

Layered beam	p_{cr} (in N)	
	h_v = 0.5 mm	h_v = 1.5 mm
PCLD treated beam	266.65	265.75
Three-layered beam	130.41	114.96
Five-layered beam	120.32	93.16

Now, to study the dynamics in the post-buckled state of the layered beams under the parametric excitation, first, a value of the static counterpart (p_a^o) of the

excitation is taken as 320 N that is greater than the critical buckling load (p_{cr} , Table 5.2) for all the layered beams. With this value of the static load parameter (p_a^o), the dynamic load parameter (λ) is taken with a value of 0.1. The corresponding frequency response and global bifurcation diagram are illustrated in Figs. 5.7(a) and 5.7(b), respectively, for the PCLD treated beam with the thickness of the constrained viscoelastic layer as 0.5 mm. Similar responses of the PCLD treated beam are also presented in Figs. 5.7(c)-(d) for the thickness of the constrained viscoelastic layer as 1.5 mm. It may be observed from the frequency responses (Figs. 5.7(a) and 5.7(c)) that, at the low-frequency region, the fundamental (C/C') and principal primary parametric (B, B') resonances appear corresponding to the buckled equilibrium states. Additionally, the higher-order parametric resonances (D/D', E/E') are also observed. However, the increase in the thickness of the viscoelastic layer (from h_v = 0.5 mm to h_v =1.5 mm) does not cause a significant change in the dynamics of the PCLD treated beam except a little reduction in the frequency range of the snap-through motion or the global period-2 attractor (M). It may be due to the fact that there is no significant augmentation of damping in the PCLD treated beam with the increased thickness of the constrained viscoelastic layer.

However, the bifurcation diagram (Fig. 5.7(b), for h_v = 0.5 mm) mainly shows two critical zones (FG/F'G' and JK/J'K'), where the chaotic motion of the PCLD treated beam appears. For the first critical zone (FG/F'G'), the chaotic motion appears through the intermittent transition bifurcation (at $\Omega = 48$ rad/s) of local period-1 attractor. It may be due to the appearance of cyclic fold bifurcation in the frequency response associated with the higher-order parametric resonance (D/D', Fig. 5.7(a)). However, this chaotic motion appears with dual chaotic attractors at $\Omega = 130$ rad/s (Fig. 5.7(b)), which reduces to dual global period-2 attractors through period demultiplying bifurcation at G/G' ($\Omega = 131$ rad/s, Fig. 5.7(b)). These dual global period-2 attractors undergo inverse symmetry breaking bifurcation at H/H' ($\Omega = 140$ rad/s, Fig. 5.7(b)), resulting in a single global period-2 attractor. However, with the increase in the frequency of excitation, the local period-1 attractors appear at I/I' ($\Omega = 191$ rad/s, Fig. 5.7(b)) through period demultiplying bifurcation. These local period-1 attractors lead to the second critical zone (JK/J'K', Fig. 5.7(b)) at J/J' ($\Omega =$ 218 rad/s, Fig. 5.7(b)), where the chaotic oscillation of the PCLD treated beam arises. This chaotic motion reduces to local period-2 attractors through the period demultiplying bifurcation at K/K' ($\Omega = 240$ rad/s, Fig. 5.7(b)). However, similar dynamics of the PCLD treated beam

also appears for the higher thickness ($h_v = 1.5$ mm) of the viscoelastic layer, as shown in Fig. 5.7(d).

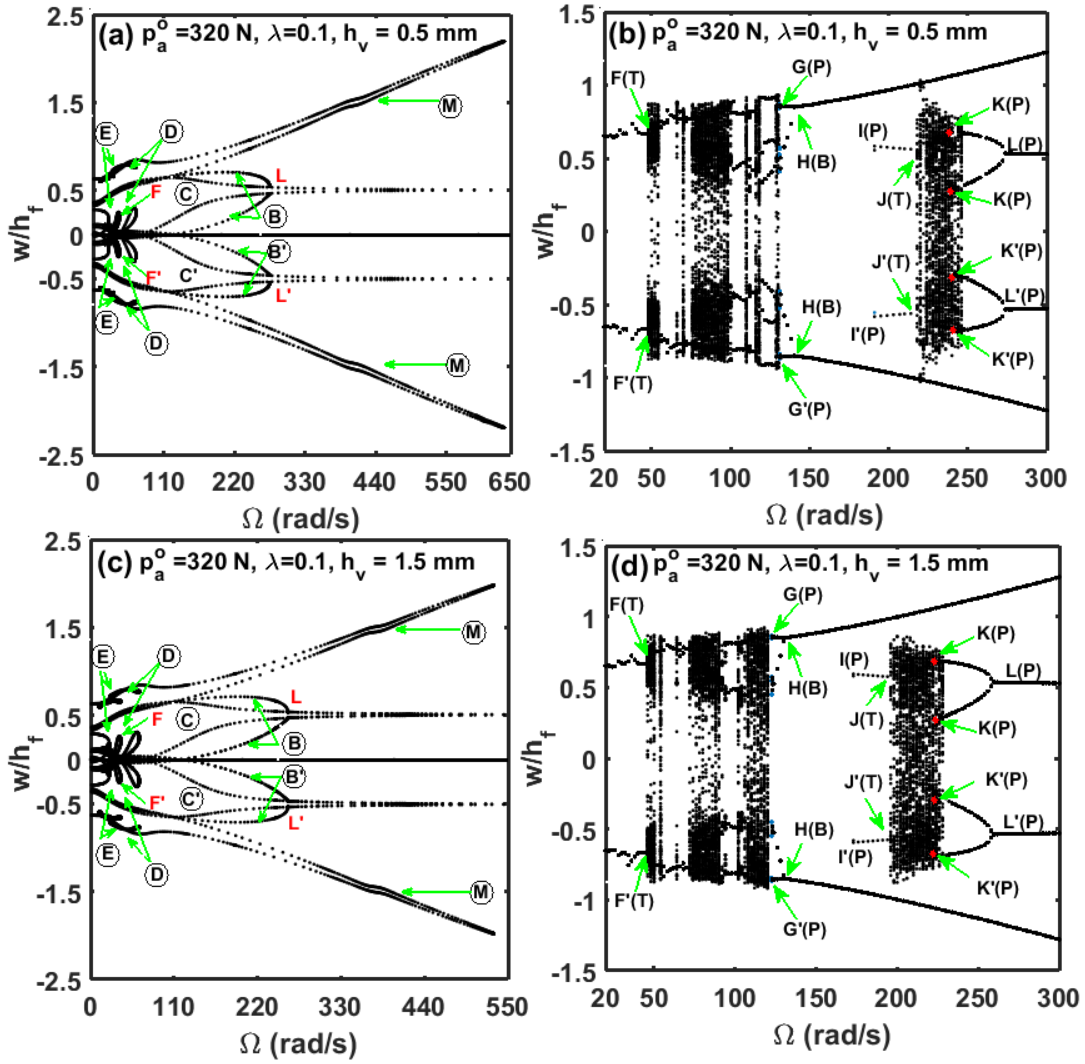

Fig. 5.7. (a), **(b) Nonlinear frequency responses and (b), (d) global bifurcation diagrams of the PCLD treated beam under the parametric excitation (p_a^o = 320 N, λ = 0.1) in the post-buckled state ((a), (b) for h_v = 0.5 mm and (c), (d) for h_v = 1.5 mm).**

For the same parametric excitation (p_a^o = 320 N, λ = 0.1), the dynamics at the post-buckled state of the three-layered beam (Fig. 5.1(b)) is illustrated in Fig. 5.8 for two different values of thickness (h_v = 0.5 mm or h_v =1.5 mm) of the constrained viscoelastic layer. It may be observed from Fig. 5.8 that the dynamics of the three-layered beam mainly appears with the local periodic attractors (B/B', C/C') corresponding to the buckled equilibrium states. The global period-2 attractor (M, Figs. 5.8(a) and 5.8(b)) also appears in a very small frequency range, resulting in the snap-through periodic oscillation of the three-layered beam. But, for an increase in the thickness (h_v =1.5 mm) of the constrained viscoelastic layer,

this global period-2 attractor disappears (Figs. 5.8(c) and 5.8(d)), and the three-layered beam oscillates with local periodic attractors. So, the three-layered beam mainly oscillates about one of the post-buckled equilibrium states, where the peak amplitude of periodic oscillation is significantly lesser than that for the snap-through oscillation (periodic/chaotic motion, Fig. 5.7) of the PCLD treated beam. This reduction of the snap-through oscillation occurs mainly due to the improved damping in the CLD treatment when the PCLD configuration (Fig. 5.1(a)) is altered to the three-layered configuration (Fig. 5.1(b)). Also, the effectiveness of the CLD treatment in the three-layered beam configuration (Fig. 5.1(b)) increases with the increasing thickness of the constrained viscoelastic layer. It may also be noted here that multiple local period-1 attractors (1/1', 2/2', 3/3', 4/4', Figs. 5.8(b) and 5.8(d)) appear simultaneously in a small frequency range near the fundamental resonance (C/C') (Fig. 5.8), where the three-layered beam oscillates with any one of the local period-1 attractors depending on the initial condition.

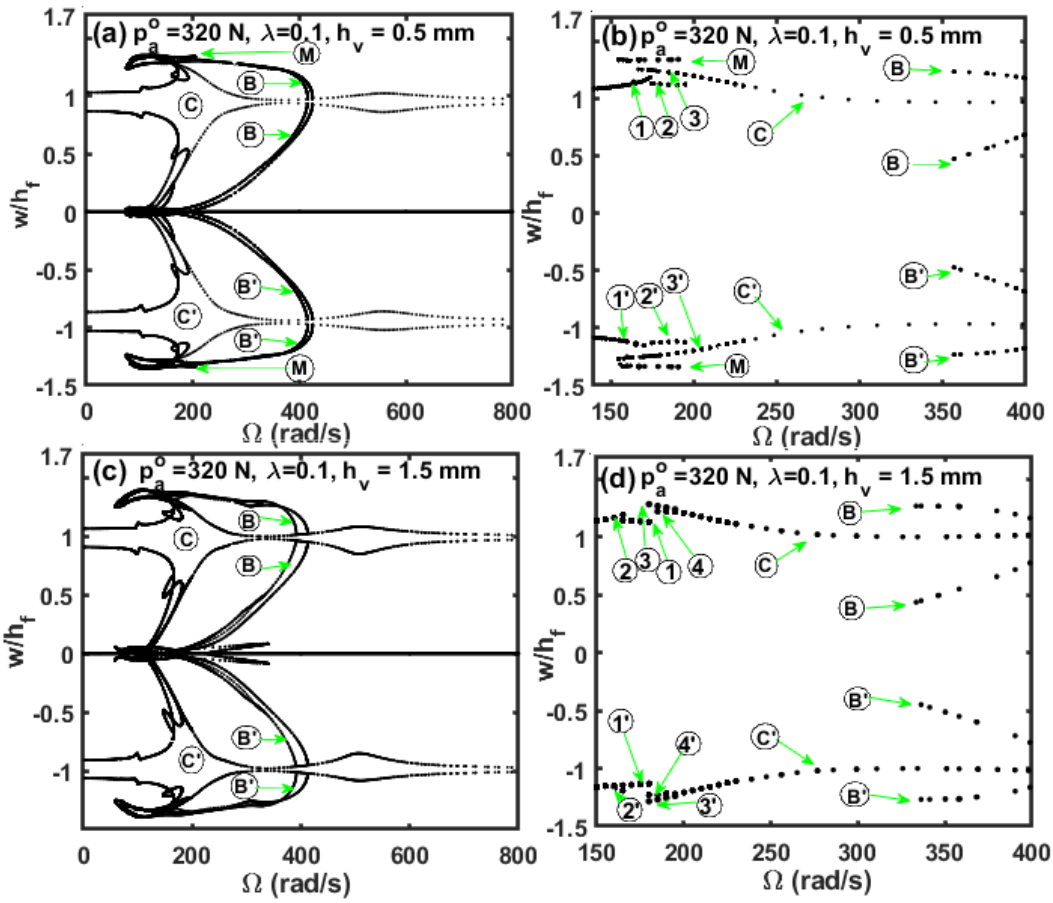

Fig. 5.8. (a), (b) Nonlinear frequency responses and (b), (d) global bifurcation diagrams of the three-layered beam under the parametric excitation (p_a^o = 320 N, λ = 0.1) in the post-buckled state ((a), (b) for h_v = 0.5 mm and (c), (d) for h_v = 1.5 mm).

Next, without alteration of the parametric excitation (p_a^o = 320 N, λ = 0.1), the dynamics at the post-buckled state of the five-layered beam (Fig. 5.1(c)) is illustrated in Fig. 5.9 for two different values of the total thickness (h_v = 0.5 mm and 1.5 mm) of constrained viscoelastic layers. Here, the dynamics of the five-layered beam appears with the local period-1 attractors corresponding to the buckled equilibrium states (Fig. 5.9), where the peak amplitude of periodic oscillation is significantly lesser than that for the snap-through oscillation (periodic/chaotic motions, Fig. 5.7) of the PCLD treated beam. Further, it is observed that the peak amplitude of local periodic oscillation of the five-layered beam is less than that for the three-layered beam.

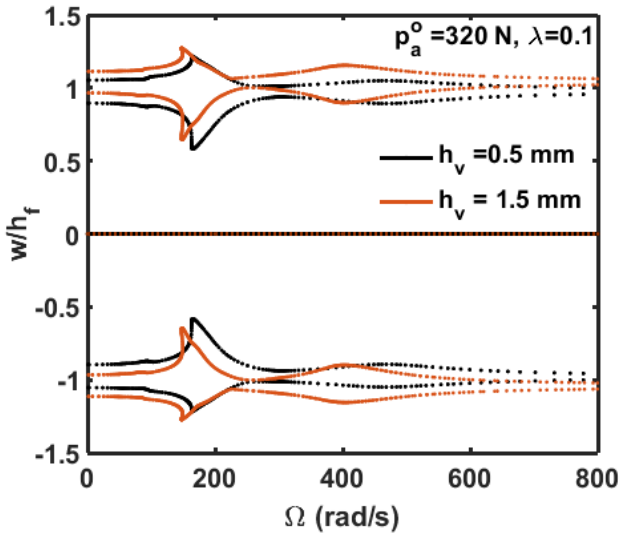

Fig. 5.9. Frequency responses of the five-layered beam under the parametric excitation (p_a^o = 320 N, λ = 0.1) in the post-buckled state ((a), (b) for h_v = 0.5 mm and (c), (d) for h_v = 1.5 mm).

The aforesaid dynamic characteristics (Figs. 5.7, 5.8 and 5.9) of the three different layered beams (Fig. 5.1) are evaluated under the same parametric excitation. Moreover, for a specified value of the total thickness (h_v) of constrained viscoelastic layers, the volumes of viscoelastic and substrate materials are not altered from one to another layered beam, as mentioned in Section 5.2. However, the layered arrangement is varied over the three beams for achieving the CLD treatment in three different configurations, while the investigation of the corresponding damping effectiveness in attenuation of complex dynamics is the main concern. In this issue, the aforesaid results imply that the CLD treatment in the five-layered configuration provides maximum damping to reduce the complex dynamics under the parametric excitation. Also, the effectiveness of the CLD treatment in attenuation of complex dynamics can be augmented by

increasing the thickness of the constrained viscoelastic layers in the three-layered or five-layered configuration. Here, the PCLD configuration is not much effective to attenuate the complex dynamics under the parametric excitation, although this configuration is more stable under the static counterpart of the excitation as compared to the other layered configurations (Table 5.2).

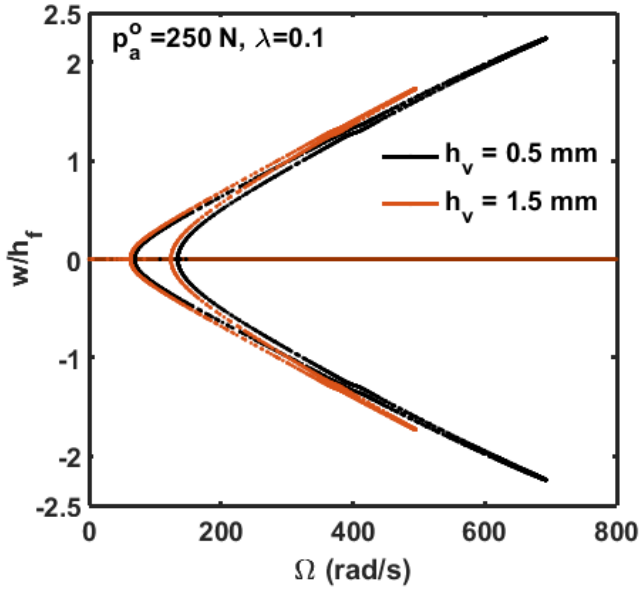

Fig. 5.10. Nonlinear frequency responses of the PCLD treated beam under the parametric excitation (p_a^o = 250 N, λ = 0.1) for two different values of thickness (h_v) of the constrained viscoelastic layer.

With this advantage of better static stability of the PCLD treated beam, it may be preferred for handling the parametric excitation in the pre-buckled equilibrium state. This equilibrium state may facilitate improved damping effectiveness of the PCLD treatment for stabilizing the beam. For an investigation in this issue, the static load parameter (p_a^o) is considered with a value of 250 N, where the PCLD treated beam lies in the pre-buckled state while the three-layered and five-layered beams undergo static instability (Fig. 5.6, Table 5.2). Now, the dynamic load parameter (λ) of the parametric excitation is considered with a value of 0.1. The corresponding frequency response of the PCLD treated beam associated with the principal primary parametric resonance is illustrated in Fig. 5.10 for two different values of thickness (h_v = 0.5 mm and 1.5 mm) of the constrained viscoelastic layer. It may be observed from Fig. 5.10 that the PCLD treated beam oscillates about its initial equilibrium position. But the peak vibration amplitude appears with a high value, although it decreases somewhat for the increase in the thickness of the constrained viscoelastic layer.

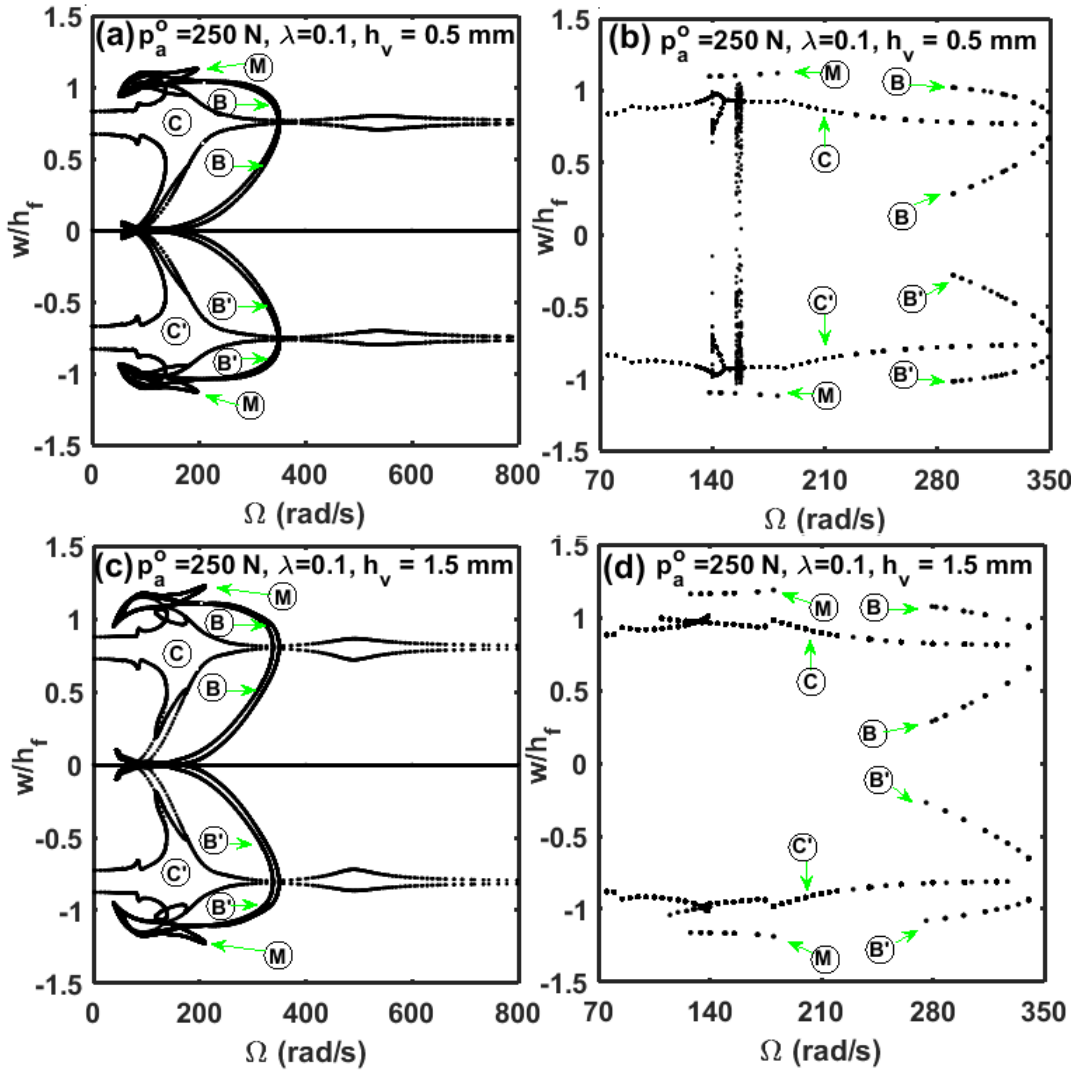

Fig. 5.11. (a), (c) Nonlinear frequency response and (b), (d) global bifurcation diagram of the three-layered beam under the parametric excitation (p_a^o = 250 N, λ = 0.1) for two different values of thickness (h_v) of the constrained viscoelastic layer.

In parallel, for the same loading (p_a^o = 250 N, λ = 0.1), the frequency response and global bifurcation diagram for the three-layered beam are illustrated in Fig. 5.11 considering two different values of thickness (h_v = 0.5 mm and 1.5 mm) of the constrained viscoelastic layer. Here, the three-layered beam undergoes buckling instability, and its dynamics mainly appears with the local periodic attractors corresponding to the buckled equilibrium states similar to the previous result (Fig. 5.8). The corresponding peak amplitude of periodic oscillation (Fig. 5.11(a)) appears with a low value in comparison to that for the periodic oscillation (Fig. 5.10) of the PCLD treated beam. However, in a small frequency region (140

rad/s to 180 rad/s), the global period-2 attractor (M, Figs. 5.11(a) and 5.11(b)) appears, which causes snap-through motion of the three-layered beam. Within the same frequency range, a small critical zone (Ω = 140 rad/s to 141 rad/s) is observed, where the chaotic oscillation appears. This chaotic attractor reduces to local period-2 attractors at $\Omega = 141$ rad/s, and these local period-2 attractors further reduce to local period-1 attractor at $\Omega = 147$ rad/s. However, in parallel to the local period-1 response, a small chaotic region appears between $\Omega = 155$ rad/s and $\Omega = 158$rad/s. Now, for an increase in the thickness (from h_v =0.5 mm to h_v =1.5 mm) of the constrained viscoelastic layer, the critical zone disappears (Figs. 5.11(c) and 5.11(d)) but the global period-2 attractor still remains.

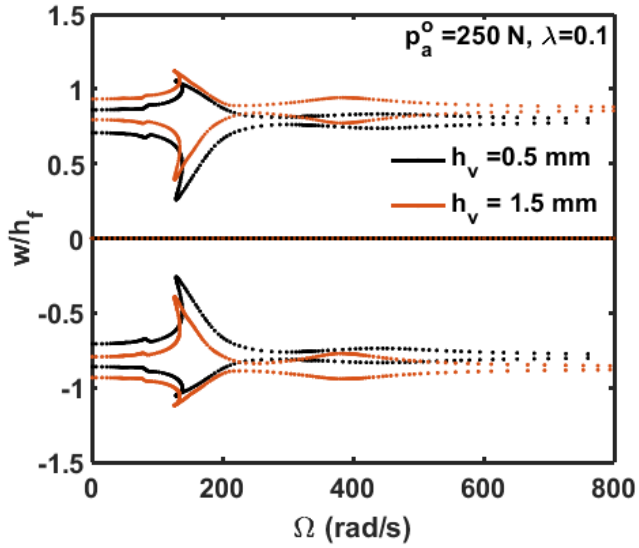

Fig. 5.12. Nonlinear frequency response of the five-layered beam under the parametric excitation (p_a^o = 250 N, λ = 0.1) for two different values of total thickness (h_v) of the constrained viscoelastic layers.

Under the same excitation (p_a^o =250 N, λ =0.1), the frequency response of the five-layered beam is shown in Fig. 5.12. Here, the dynamics of the five-layered beam appears similar to that in Fig. 5.9; however, the difference arises in the amplitude of periodic oscillation and the static equilibrium position of the post-buckled layered beam. From the results in Figs. 5.10, 5.11 and 5.12, it is clear that the PCLD treated beam is more stable under the static counterpart (p_a^o) of the parametric excitation as compared to the three- or five-layered beam. But, the peak amplitude of periodic oscillation of the PCLD treated beam due to the dynamic counterpart (λ) of the same excitation is significantly more than that for the other layered beams. It appears due to the greater damping effectiveness of the CLD treatment for the three- or five-layered configuration. However, this observation implies that the change in the layered configuration of the CLD

treatment towards its greater damping effectiveness may yield the disadvantage of the static instability of the associated beam structure. Now, if the buckled deflection of a CLD treated beam due to the static instability can be accommodated in an application, then this damping treatment may be preferred with the three-layered/five-layered beam configuration for effective vibration attenuation under the parametric excitation.

5.6. Summary

In this chapter, the CLD treatment is taken in three different layered beam configurations. The first one is the PCLD configuration, where a thin elastic layer constrains a viscoelastic damping layer against the top surface of the host beam. The second one is a three-layered sandwich beam with the viscoelastic core, and the third one is a multi-layered beam with two identical constrained viscoelastic layers. All the layered beams are considered to have fixed ends while an axial compressive harmonic load is applied through the support ends. The volumes of viscoelastic layers and substrate/elastic layers do not vary from one to another layered beam. Also, the applied load is kept constant for all the layered beams, and the damping effectiveness of each of the CLD configurations is studied in attenuation of the complex dynamics of the layered beams, mainly in their post-buckled equilibrium state.

This dynamic analysis of the CLD treated beams is performed by deriving reduced-order FE models (ROMs) in the time and frequency domains, where the constrained viscoelastic layer is modelled using the fractional Zener constitutive relation. These ROMs are derived following the similar formulation in Chapter 4, where the only change appears due to the consideration of the parametric excitation instead of the direct excitation. However, for the corresponding RBVs, the ICES approach is utilized to obtain the vibration modes (VMs) about the pre- or post-buckled equilibrium state of the layered beams. These VMs are subsequently enriched using static derivatives (SDs) and proper orthogonal decomposition (POD) method, as the corresponding procedure is detailed in Sections 4.5 and 5.5. The results reveal that these RBVs provide good accuracy of the ROMs for the estimation of very complex motion as well as various dynamic bifurcations of the viscoelastic layered beams, where the reference results are taken from the full-order FE model. Therefore, the present RBVs are robust ones and may be utilized for the nonlinear dynamic analysis of any other viscoelastic structure. However, further study on the passive damping capability of the CLD treatment in attenuation of complex dynamics of the parametrically excited layered beams reveals the following observations.

1. In the post-buckled state, the viscoelastic layered beams undergo very complex motion involving various dynamic instabilities and chaotic oscillation. Besides, the beams also undergo the large-amplitude vibration through the snap-through periodic oscillation with respect to the zero equilibrium state. The CLD treatment is capable of attenuating this complex dynamics as well as large-amplitude vibration through three-layered or five-layered configuration, where the effectiveness of the CLD treatment increases with the increasing thickness of the constrained viscoelastic damping layer. However, the PCLD configuration is not a suitable one for controlling this complex dynamics as its damping effectiveness does not improve effectively with the increase in the thickness of the constrained viscoelastic layer.
2. It is observed that a CLD treated beam is vulnerable to undergo static instability under the parametric excitation as its PCLD configuration is changed to the three-layered or five-layered configuration. In this view, the PCLD configuration may be preferred for the operation of a CLD treated beam under the parametric excitation. However, for a set of values of the static and dynamic load parameters in the parametric excitation, it is found that the amplitude of vibration of the PCLD treated beam for its dynamic instability in the pre-buckled state is significantly more than that of the buckled three/five-layered beam. So, the three-layered or five-layered configuration may be chosen for better control of dynamics of a CLD treated beam if the possible buckled deflection of the beam can be accommodated in an application.

Chapter 6

Nonlinear dynamics of functionally graded pipes conveying hot fluid

6.1. Introduction

In the preceding chapters, the nonlinear dynamics of parametrically excited slender beams is studied with the main concern of controlling their complex dynamics using viscoelastic materials and piezoelectric actuators. It is observed that these active/passive materials work well in attenuation of the complex motion and dynamic instabilities of slender beams. However, this complex dynamics mainly arises once the beam undergoes buckling or static instability. Therefore, it seems that the control of static instability or the operation of the slender beams in the pre-buckled state is a major concern for avoiding complex dynamics. However, the aforesaid active/passive materials commonly work after the onset of motion of the associated structure. So, one needs to look for some alternative way to control the static instability of a slender beam under parametric excitation. In this concern, there may be two ways. The first one is to choose a suitable geometrical configuration of a slender structure, while the other one is to select an appropriate material. For both the cases, the objective is to achieve maximum possible flexural rigidity of a slender structure to avoid its static instability under the parametric excitation.

However, in some applications of parametrically excited slender structures, they appear with a thin-walled cross-section according to their functionality. So, these slender structures are highly flexible ones, and there may not be much scope to change their geometrical configuration or dimensions towards an improved flexural rigidity. In this case, the only option is to choose a suitable material. Further, these flexible slender structures may also operate in the thermal environment, where the static instability commonly occurs at a low value of the static load parameter of the parametric excitation due to the additional thermally-induced compressive stress. So, the material would have temperature resistant property in addition to the sufficient toughness. This circumstance arises in the design of many slender structures like helicopter rotor blades, rotor blades in turbomachinery, industrial robotic arms, pipes conveying hot fluid, etc. However, the present study is performed considering slender pipes conveying hot fluid, as this kind of slender structure are commonly used elements in many

engineering systems, namely steam generators, heat exchangers, liquid propellant rocket engines, etc.

Now, for a slender pipe conveying hot fluid, it is subjected to the thermally-induced compressive stress as well as the similar stress due to the velocity of the internal fluid. Here, the effect of the temperature is indicatively more than that of the flow-velocity in causing the divergence (buckling) of the pipe. So, the pipe may undergo buckling at a very low velocity of the internal hot fluid (Qian et al., 2009), and also it (pipe) may exhibit complex nonlinear dynamics associated with its divergence even at a very low pulsatile velocity of the internal fluid. So, the temperature is the major concern rather than the velocity of the internal fluid in the design of these pipe systems conveying hot fluid.

In practical applications of fluid conveying pipes, they are laid either of the horizontal, vertical and inclined orientations (Alfosail et al., 2017a; Dawson and Paslay, 1984; Lee and Kim, 1999; Lips and Meyer, 2011; Vigneaux et al., 1988; Wang and Bloom, 2001). Here, the static/dynamic behavior of an inclined pipe is somewhat different from that of the vertical pipe mainly because of an initial deflection of the inclined pipe under the gravitational load. It is addressed in a few studies (Gan et al., 2015; Wang and Bloom, 2001, 1999), where the dynamics of inclined cantilever pipes has been analyzed for the steady or pulsatile fluid flow. Although these available studies reveal an indicative effect of the inclination of a pipe on its dynamics, the importance of this geometric parameter (inclination) mainly depends on the rigidity of the pipe. An inclined pipe with high rigidity undergoes a negligibly small initial deflection due to the gravitational load, and thus the corresponding effect on the dynamics of the pipe would not appear in a notable manner. However, due to the temperature of the fluid, the inclination of a pipe may yield a notable thermally induced deflection originated from a very small deflection under the gravitational load. This high initial deflection would pose certain effects on the dynamic characteristics of an inclined pipe operating in the thermal environment although a study in this regard is not yet reported in the literature to the best knowledge of this researcher.

However, in order to alleviate the aforesaid effects of temperature of the internal fluid on the static/dynamic behavior of a pipe system, the pipe can be made of a FGM composed of two isotropic constituent materials, namely metal and ceramic (Koizumi, 1993). Here, the hot surface of the pipe is made of ceramic constituent and the material properties vary gradually from ceramic to metal across the wall-thickness of the pipe. This FGM pipe can withstand against a high temperature of the internal fluid due to the ceramic constituent while its toughness is retained by the metal constituent. So, the stability of the pipe

conveying hot fluid would improve and also it (pipe) can sustain the flow induced vibration. Additionally, the initial thermally induced deflection of the pipe due to its inclination is expected to reduce. However, a few studies on the FGM pipe are available in the literature, as a corresponding literature survey is furnished in Section 1.3.3. In these available studies, the thermo-mechanical stability of FGM pipes is reported, where it is observed that the static stability of a pipe significantly improves for the use of FGM instead of a conventional isotropic material. Also, nonlinear dynamics of FG pipe conveying hot fluid under the forced excitation is investigated, and it is observed that the graded exponent regulates the backbone curve/frequency response. However, further study on the dynamics of FG pipes conveying steady or pulsatile hot fluid is not available in the open literature. Also, the effect of the initial thermally-induced deflection of an inclined pipe on its dynamics is not yet reported in the literature to the best knowledge of this researcher. It is attempted in this chapter considering a pinned-pinned vertical/inclined FG pipe conveying hot fluid with steady or pulsatile flow velocity. Specifically, there are two main objectives of this study. The first one is to investigate the characteristics of divergence (buckling) of the vertical/inclined FG pipe on the basis of variations of some system parameters like inclination angle, temperature of fluid and graded material properties of FGM. The second objective is decided as a thorough investigation on the nonlinear dynamics of the vertical/inclined FG pipe in association with its divergence on the basis of the variations of the aforesaid system parameters and the material damping of FGM. The overall study is presented in the following manner.

First, the geometrically nonlinear governing equation of motion of a pinned-pinned vertical/inclined FG pipe conveying pulsatile hot fluid is derived in Section 6.2. Next, in Section 6.3, the governing equation of motion is first expressed in the form of the nonlinear temporal differential equation using the Galerkin method. Subsequently, the nonlinear temporal differential equation is expressed in the frequency domain by implementing the harmonic balance method (HBM). In Section 6.4, the procedure of local stability analysis of periodic solutions is presented. In Section 6.5, first, the numerical results are presented to explore the dynamic characteristics of vertical FG pipe conveying hot fluid with steady or pulsatile flow-velocity. The subsequent numerical illustrations show the effect of inclination of the FG pipe on its dynamics. Finally, the observations from this study are summarized.

6.2. System model and governing equation of motion

Figure 6.1 shows the schematic diagram of an inclined FG pipe conveying hot fluid with pulsatile flow-velocity. The inner and outer cylindrical surfaces of the pipe are considered to be made of ceramic and metal constituents, respectively, and the material properties smoothly vary from inner ceramic rich surface to outer metal rich surface. The ends of the FG pipe are considered as pinned ends, and the hot fluid is assumed to flow with uniform temperature across the ends of the FG pipe. So, the inner ceramic rich surface of the FG pipe is exposed to a high temperature (T_i) while the temperature of the outer metal rich surface of the same pipe is assumed as room temperature ($T_o = 300$ K).

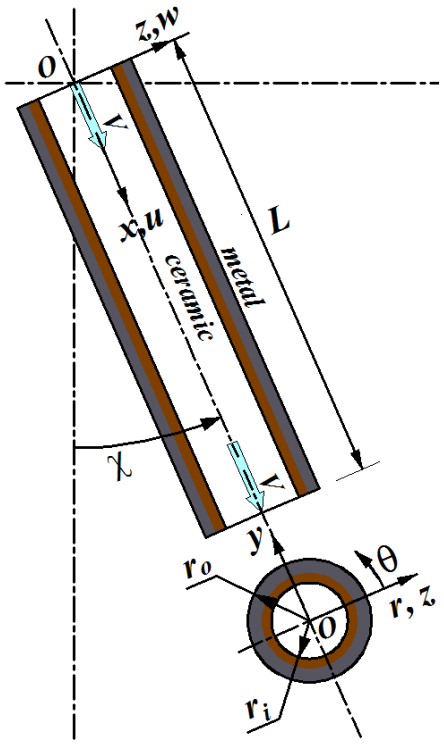

Fig. 6.1. Schematic diagram of an inclined pinned-pinned FG pipe conveying hot fluid.

For the analysis, the reference Cartesian coordinate system (xyz) is attached to the inclined FG pipe such that the origin of the reference coordinate system lies at the center of the circular cross-section at one end of the pipe. The x-axis is lying along the longitudinal direction of the pipe while the z-axis implies the planer motion of the FG pipe in the xz-plane (Fig. 6.1). The inclination of longitudinal (x) axis of the FG pipe with the vertical axis is denoted by the angle χ (Fig. 6.1), and the other geometrical properties like inner radius, outer radius, wall-thickness and length of the FG pipe are symbolized by r_i, r_o, h and L, respectively. Since a slender FG pipe is considered in the present analysis, it is

modeled according to the Euler-Bernoulli beam theory. Moreover, the deformations of the pipe are considered to be restricted to long wavelengths as compared to its radius so that the internal fluid flow is modeled according to the plug flow model.

The uniaxial thermo-elastic constitutive relation of FGM can be written in conjunction with the Kelvin-Voigt model (Findley and Davis, 2013) as,

$$\sigma_x = \left(E + E^* \frac{\partial}{\partial t} \right) (\varepsilon_x - \alpha_T \Delta T), \ \Delta T = T(r) - T_o \tag{6.1}$$

where, σ_x and ε_x are the longitudinal stress and strain, respectively, at any point in the FG pipe ; $T(r)$ is the temperature at a radial point (r) within the thickness of the pipe, and T_o is the reference temperature that is considered as the room temperature ($T_o = 300$ K). The material properties of the FG pipe like Young's modulus (E), viscoelastic dissipation parameter (E^*), density (ρ), thermal conductivity (k) and coefficient of thermal expansion (α_T) are the graded properties according to a power law as (Reddy and Chin, 1998),

$$P(r) = P_m + (P_c - P_m) \left(\frac{1}{2} - \left(\frac{r - r_m}{h} \right) \right)^n \tag{6.2}$$

where, r_m is the mean radius; P_c and P_m are the properties of ceramic and metal constituents, respectively, and n is the power law exponent or graded exponent. The temperature ($T(r)$) at any radial location (r) within the thickness of the FG pipe can be obtained by solving the one-dimensional steady-state heat conduction equation as,

$$-\frac{1}{r}\frac{\mathrm{d}}{\mathrm{d}r}\left(r\,k(r)\frac{\mathrm{d}T(r)}{\mathrm{d}r} \right) = 0 \text{ with } T = T_o \text{ at } r = r_o \text{ and } T = T_i \text{ at } r = r_i \tag{6.3}$$

The solution of Eq. (6.3) can be obtained as (Kadam and Panda, 2014),

$$T(r) = T_i + \frac{T_o - T_i}{D_T} \int_{r_i}^{r} \frac{1}{r\,k(r)}\,dr, \ D_T = \int_{r_i}^{r_o} \frac{1}{r\,k(r)}\,dr \tag{6.4}$$

According to the Euler-Bernoulli beam theory, the displacements at any point in the FG pipe can be written as,

$$u(x,z,t) = u_0(x,t) - z\frac{\partial w_0(x,t)}{\partial x}, \ w(x,z,t) = w_0(x,t) \tag{6.5}$$

where, u_0 and w_0 are the displacements at any point on the middle plane (xy-plane at $z = 0$) of the FG pipe along the x and z directions, respectively. According to this displacement field (Eq. (6.5)), the von Karman nonlinear strain-displacement relation can be written as,

$$\varepsilon_x = \frac{\partial u_0}{\partial x} + \frac{1}{2}\left(\frac{\partial w_0}{\partial x}\right)^2 - z\frac{\partial^2 w_0}{\partial x^2} \tag{6.6}$$

The corresponding total potential energy (T_p) of the inclined FG pipe conveying fluid can be written at any instant of time (t) as,

$$T_p = \frac{1}{2}\int_0^L \int_{r_i}^{r_o} \int_0^{2\pi} (\varepsilon_x \sigma_x) r\, dr\, d\theta\, dx - g(m_f + m_p)\int_0^L \langle (x+u)\cos\chi - w\sin\chi \rangle dx$$
$$-\int_0^L T_{in}\left(\frac{\partial u_0}{\partial x} + \frac{1}{2}\left(\frac{\partial w_0}{\partial x}\right)^2\right) dx,$$
$$m_f = \rho_f\left(\pi r_i^2\right),\ m_p = \int_{r_i}^{r_o}\int_0^{2\pi} \rho(r) r dr d\theta,\ T_{in} = \pi r_i^2 P_{in}(1-2\nu) \tag{6.7}$$

where, ρ_f is the mass density of the fluid; g is the acceleration due to gravity; T_{in} is the axial compressive force per unit length of the pipe due to the internal pressure (P_{in}) of the fluid; m_f / m_p is the mass per unit length of the fluid/pipe. In Eq. (6.7) and also in the subsequent equations, the subscripts p and f indicate the terms related to the material of the pipe and fluid, respectively. Substituting Eqs. (6.1) and (6.6) in Eq. (6.7), the following expression for the total potential energy (T_p) of the FG pipe conveying fluid can be obtained as,

$$T_p = \frac{1}{2}\int_0^L \left[\begin{array}{l} \left(D_p + D_p^*\frac{\partial}{\partial t}\right)\left(\frac{\partial^2 w_0}{\partial x^2}\right)^2 + \left(A_p + A_p^*\frac{\partial}{\partial t}\right)\left(\frac{\partial u_0}{\partial x} + \frac{1}{2}\left(\frac{\partial w_0}{\partial x}\right)^2\right)^2 \\ -(T_{th} + T_{in})\left(\frac{\partial u_0}{\partial x} + \frac{1}{2}\left(\frac{\partial w_0}{\partial x}\right)^2\right) \end{array}\right] dx$$
$$-g(m_f + m_p)\int_0^L ((x+u_0)\cos\chi - w_0\sin\chi) dx,$$
$$D_p = \int_0^{2\pi}\int_{r_i}^{r_o} z^2 E(r) r\, dr\, d\theta,\ D_p^* = \int_0^{2\pi}\int_{r_i}^{r_o} z^2 E^*(r) r\, dr\, d\theta,\ A_p = \int_0^{2\pi}\int_{r_i}^{r_o} E(r) r dr d\theta,$$
$$A_p^* = \int_0^{2\pi}\int_{r_i}^{r_o} E^*(r) r dr d\theta,\ T_{th} = \int_0^{2\pi}\int_{r_i}^{r_o} E(r)\alpha_T(r)\Delta T\, r dr d\theta,\quad z = r\sin\theta \tag{6.8}$$

where, ν is the Poisson's ratio for the material of the pipe; T_{th} is the thermally induced force per unit length of the pipe; D_p / A_p is the flexural/axial stiffness per unit length of the pipe while D_p^* / A_p^* are the similar terms related to the energy dissipation from the pipe. The total kinetic energy (T_t) of the FG pipe conveying fluid with a flow velocity V can be expressed as,

$$T_t=\frac{1}{2}m_f\int_0^L\left[\left(V+\frac{\partial u_0}{\partial t}+V\frac{\partial u_0}{\partial x}\right)^2+\left(\frac{\partial w_0}{\partial t}+V\frac{\partial w_0}{\partial x}\right)^2\right]dx+\frac{1}{2}m_p\int_0^L\left[\left(\frac{\partial u_0}{\partial t}\right)^2+\left(\frac{\partial w_0}{\partial t}\right)^2\right]dx \quad (6.9)$$

The governing differential equation of motion of the FG pipe conveying fluid is derived employing the extended Hamilton's principle as given by Eq. (2.9). Substituting Eqs. (6.8)-(6.9) in Eq. (2.9), two coupled governing differential equations of motion of the overall pipe can be obtained for the arbitrary variations of δu_o and δw_o. Presently, the longitudinal inertia force of FG pipe is ignored for its very small magnitude in comparison to that of the transverse inertia force, and the two coupled governing equations of motion are reduced into one equation in terms of the transverse displacement (w_o) following the same procedure as given in Holmes (1977) and Thomsen (2013). The resulting governing equation of motion of the overall FG pipe can be obtained as given in Eq. (6.10).

$$\int_{t_1}^{t_2}\left(\delta T_t-\delta T_p\right)dt=0 \quad (2.9)$$

$$(m_f+m_p)\frac{\partial^2 w_0}{\partial t^2}+D_p^*\frac{\partial^5 w_0}{\partial x^4\partial t}+2m_fV\frac{\partial^2 w_0}{\partial x\partial t}+D_p\frac{\partial^4 w_0}{\partial x^4}+(m_f+m_p)g\cos\chi\frac{\partial w_0}{\partial x}+$$
$$(m_f+m_p)g\sin\chi+\left[m_fV^2+\left(m_f\frac{\partial V}{\partial t}-(m_f+m_p)g\cos\chi\right)(L-x)+T_{th}+T_{in}-\right.$$
$$\left.\frac{A_p}{2L}\int_0^L\left(\frac{\partial w_0}{\partial x}\right)^2dx-\frac{A_p^*}{L}\int_0^L\left(\frac{\partial w_0}{\partial x}\frac{\partial^2 w_0}{\partial x\partial t}\right)dx\right]\frac{\partial^2 w_0}{\partial x^2}=0 \quad (6.10)$$

The velocity of fluid for pulsatile flow can be expressed as (Jin and Song, 2005),

$$V=V_f\left(1+\lambda\cos(\omega t)\right) \quad (6.11)$$

where, V_f, λ and ω are the mean flow velocity, pulsation velocity-amplitude and pulsation frequency, respectively. For expressing the governing equation of motion (Eq. (6.10)) in the dimensionless form, the following dimensionless quantities (Eq. (6.12)) are introduced where the properties of the metal constituent of the FG pipe at room temperature are considered as the reference material properties that are indicated by the subscript m.

$$\eta=\frac{w_0}{L},\ \xi=\frac{x}{L},\ \bar{t}=\left(\frac{D_m}{m_m+m_f}\right)^{1/2}\frac{t}{L^2},\ v=\left(\frac{m_f}{D_m}\right)^{1/2}VL,\ \gamma=\frac{m_m+m_f}{D_m}gL^3,$$
$$\beta=\frac{m_f}{m_m+m_f},\ k_m=\frac{AL^2}{2I},\ \alpha=\left(\frac{I}{E_m(m_m+m_f)}\right)^{1/2}\frac{E_m^*}{L^2},\ \Omega=\left(\frac{m_m+m_f}{D_m}\right)^{1/2}L^2\omega,$$
$$e_T=E_mA\alpha_T(T_i-T_R)L^2/D_m,\quad \bar{T}_{in}=T_{in}L^2/D_m \quad (6.12)$$

In Eq. (6.12), A and I denote the cross-sectional area of the FG pipe and the area moment of inertia of the same about the y-axis. Introducing the

dimensionless quantities (Eq. (6.12)) in the governing equation of motion (Eq. (6.10)), the following dimensionless equation of motion can be obtained where the superscript ($'$) or ($\cdot$) denotes the differentiation with respect to ξ or $\bar{t}$.

$$M_1\ddot{\eta}+C_1\dot{\eta}''''+C_2\dot{\eta}'+K_1\eta''''+\left[K_2-K_3+K_5(1-\xi)\right]\eta''+K_4\eta'+P_s=0\ ,$$

$$M_1=\left\langle\beta+(1-\beta)\bar{m}_p\right\rangle,\ C_1=\left\langle\overline{D}_p^{*}\,\alpha\right\rangle,\ C_2=\left\langle 2\sqrt{\beta}\,v\right\rangle,\ K_1=\overline{D}_p\ ,$$

$$K_2=\left\langle v^2+\bar{T}_{th}\,e_T+\bar{T}_{in}\right\rangle,\ K_3=\left\langle\bar{A}_p\,k_m\int_0^1(\eta')^2\,d\xi+2\bar{A}_p^{*}\,k_m\,\alpha\int_0^1\eta'\dot{\eta}'d\xi\right\rangle,$$

$$K_4=\left\langle\gamma\cos\chi\left[\beta+(1-\beta)\bar{m}_p\right]\right\rangle,\ K_5=\left\langle\sqrt{\beta}\dot{v}-K_4\right\rangle,\ P_s=\gamma\sin\chi\ ,\ \bar{D}_p=D_p/D_m\ ,$$

$$\bar{D}_p^{*}=D_p^{*}/D_m^{*}\ ,\ \bar{A}_p=A_p/A_m\ ,\ \bar{A}_p^{*}=A_p^{*}/A_m^{*}\ ,\ \bar{m}_p=m_p/m_m\ ,\ \bar{T}_{th}=T_{th}/(T_{th})_m \qquad (6.13)$$

6.3. Solution method

The dimensionless governing equation of motion (Eq. (6.13)) is solved using the Galerkin method where the basis functions (φ_i) are taken as the eigen functions of a pinned-pinned beam. Accordingly, the dimensionless transverse displacement ($\eta(\xi,\bar{t})$) at any point of the FG pipe can be expressed in terms of a number (N_r) of basis functions and the associated generalized coordinates (q_i) as follows,

$$\eta(\xi,\bar{t})=\sum_{i=1}^{N_r}\varphi_i(\xi)\,q_i(\bar{t})=\boldsymbol{\varphi}\,\boldsymbol{q} \qquad (6.14)$$

where, $\boldsymbol{\varphi}$ and $\boldsymbol{q}$ are the vectors of basis functions and generalized coordinates, respectively. Substituting Eq. (6.14) in the Eq. (6.13), the discretized governing equation of motion of the FG pipe conveying hot fluid with pulsatile flow velocity can be obtained as,

$$\boldsymbol{M}_s\,\ddot{\boldsymbol{q}}+\boldsymbol{G}(\Omega,\lambda,\bar{t})\,\dot{\boldsymbol{q}}+\boldsymbol{K}_s(\Omega,\lambda,\bar{t})\,\boldsymbol{q}+2\,\bar{A}_p^{*}\,k_m\,\alpha\,(\boldsymbol{q}^{\mathrm{T}}\boldsymbol{C}\,\dot{\boldsymbol{q}})\,\boldsymbol{C}\,\boldsymbol{q}+$$

$$\bar{A}_p k_m\,(\boldsymbol{q}^{\mathrm{T}}\boldsymbol{C}\,\boldsymbol{q})\,\boldsymbol{C}\,\boldsymbol{q}+P_s\boldsymbol{F}=0\,,$$

$$\boldsymbol{M}_s=M_1\,\boldsymbol{I}_{N_r}\ ,\ \boldsymbol{G}=C_1\,\boldsymbol{\Lambda}+C_2\,\boldsymbol{B}\ ,\ \boldsymbol{K}_s=\left\langle K_1\,\boldsymbol{\Lambda}+K_2\,\boldsymbol{C}+K_5\,(\boldsymbol{C}-\boldsymbol{D})+K_4\,\boldsymbol{B}\right\rangle,$$

$$\boldsymbol{\Lambda}=\int_0^1\boldsymbol{\varphi}^{\mathrm{T}}\boldsymbol{\varphi}''''d\xi\ ,\ \boldsymbol{B}=\int_0^1\boldsymbol{\varphi}^{\mathrm{T}}\boldsymbol{\varphi}'d\xi\ ,\ \boldsymbol{C}=\int_0^1\boldsymbol{\varphi}^{\mathrm{T}}\boldsymbol{\varphi}''d\xi\ ,\ \boldsymbol{D}=\int_0^1\xi\,\boldsymbol{\varphi}^{\mathrm{T}}\boldsymbol{\varphi}''d\xi\ ,$$

$$\boldsymbol{F}=\int_0^1\boldsymbol{\varphi}^{\mathrm{T}}d\xi \qquad (6.15)$$

In Eq. (6.15), $\boldsymbol{I}_{N_r}$ is the unity matrix of size $N_r\times N_r$ and the elements of $\boldsymbol{\Lambda}$, $\boldsymbol{B}$, $\boldsymbol{C}$, $\boldsymbol{D}$ and $\boldsymbol{F}$ are given in Eq. (6.16) where λ_i denotes the i^{th} eigen value corresponding to the basis function ϕ_i.

$$I_{ij}=\begin{cases}0 & i\neq j\\ 1 & i=j\end{cases},\ \Lambda_{ij}=\begin{cases}0 & i\neq j\\ \lambda_i^4 & i=j\end{cases},\ B_{ij}=\begin{cases}\dfrac{2\left\langle -1+(-1)^{i+j}\right\rangle \lambda_i\lambda_j}{\lambda_i^2-\lambda_j^2} & i\neq j\\ 0 & i=j\end{cases},$$

$$C_{ij}=\begin{cases}0 & i\neq j\\ -\lambda_i^2 & i=j\end{cases},\ D_{ij}=\begin{cases}\dfrac{4\left\langle 1-(-1)^{i+j}\right\rangle \lambda_i^3\lambda_j}{(\lambda_i^2-\lambda_j^2)^2} & i\neq j\\ 0.5\,C_{ij} & i=j\end{cases},\ F_i=\left\langle 1-(-1)^i\right\rangle/\lambda_i\ ,$$

$$\text{where } i,j=1,2,3....N \tag{6.16}$$

The nonlinear time-differential equation of motion (Eq. (6.15)) of the FG pipe is solved using the incremental HBM. A pipe conveying pulsatile fluid is usually subjected to the parametric resonance at the frequency of $2\Omega_n/i$ (Paidoussis, 2014), where Ω_n $(n=1,2,3,...)$ is the natural frequency and i is a positive integer. So, the solution $(\boldsymbol{q})$ of the differential equation (Eq. (6.15)) is assumed following the Fourier series with the finite number (H) of harmonics as,

$$\boldsymbol{q}=\boldsymbol{q}^0+\sum_{i=1}^{H}\left\langle \boldsymbol{q}_i^c\cos(i\,\Omega\bar{t}/2)+\boldsymbol{q}_i^s\sin(i\,\Omega\bar{t}/2)\right\rangle \tag{6.17}$$

where, $\boldsymbol{q}^0$, $\boldsymbol{q}_i^c$, $\boldsymbol{q}_i^s$ are the Fourier coefficient vectors corresponding to the constant, cosine and sine terms, respectively. For the convenience of formulation, $\Omega/2$ is represented by $\bar{\Omega}$, and also the differential equation (Eq. (6.15)) is expressed in terms of τ by substituting $\tau=\bar{\Omega}\,\bar{t}$. Accordingly, Eqs. (6.17) and (6.15) can be written in a compact form as,

$$\boldsymbol{q}=\boldsymbol{S}\,\boldsymbol{X}\ ,$$

$$\boldsymbol{S}=\boldsymbol{Q}\otimes\boldsymbol{I}_{N_r},\ \boldsymbol{Q}=\{1\ \ \boldsymbol{Q}_c\ \ \boldsymbol{Q}_s\},\ \boldsymbol{Q}_c=\{\cos\tau\ \cos2\tau\ \ldots\ \cos\mathrm{H}\tau\},$$

$$\boldsymbol{Q}_s=\{\sin\tau\ \ \sin2\tau\ \ldots\ \sin\mathrm{H}\tau\},\ \boldsymbol{X}=\left\{(\boldsymbol{q}^0)^{\mathrm{T}}\ (\boldsymbol{q}^c)^{\mathrm{T}}\ (\boldsymbol{q}^s)^{\mathrm{T}}\right\}^{\mathrm{T}} \tag{6.18}$$

$$\bar{\Omega}^2\,\boldsymbol{M}_s\,\ddot{\boldsymbol{q}}+\boldsymbol{K}_s(\bar{\Omega},\lambda,\tau)\,\boldsymbol{q}+\bar{\Omega}\boldsymbol{G}(\lambda,\tau)\,\dot{\boldsymbol{q}}+2\,\bar{A}_p^*\,k_m\,\alpha\ \bar{\Omega}\ (\boldsymbol{q}^{\mathrm{T}}\boldsymbol{C}\,\dot{\boldsymbol{q}})\boldsymbol{C}\,\boldsymbol{q}+$$

$$\bar{A}_p k_m\ (\boldsymbol{q}^{\mathrm{T}}\boldsymbol{C}\,\boldsymbol{q})\ \boldsymbol{C}\,\boldsymbol{q}+P_s\boldsymbol{F}=0 \tag{6.19}$$

where, $\otimes$ is the Kronecker product.

In order to obtain the linearized incremental governing equation of motion, the state variables $(\boldsymbol{q}\ ,\bar{\Omega}\ ,\lambda)$ are first taken in an incremental form $(\boldsymbol{q}=\boldsymbol{q}_0+\Delta\boldsymbol{q},$ $\bar{\Omega}=\bar{\Omega}_0+\Delta\bar{\Omega},\ \lambda=\lambda_0+\Delta\lambda)$ about a reference state $(\boldsymbol{q}_0,\bar{\Omega}_0,\lambda_0)$ of vibration. Subsequently, the governing differential equation of motion (Eq. (6.19)) is modified keeping the linear incremental terms only as given in Eq. (6.20).

$$\bar{\Omega}_0^2\,\boldsymbol{M}_s\,\Delta\ddot{\boldsymbol{q}}+\boldsymbol{C}_s\,\Delta\dot{\boldsymbol{q}}+\boldsymbol{K}_{st}\,\Delta\boldsymbol{q}=\boldsymbol{R}_s-\boldsymbol{P}_{\Omega}\,\Delta\bar{\Omega}-\boldsymbol{P}_{\lambda}\,\Delta\lambda\ ,$$

$$\boldsymbol{K}_{st} = \boldsymbol{K}_s(\bar{\Omega}_0, \lambda_0, \tau) + \bar{A}_p\, k_m \left\langle (\boldsymbol{q}_0)^{\mathrm{T}} \boldsymbol{C}\, \boldsymbol{q}_0 \boldsymbol{C} + 2\boldsymbol{C}\, \boldsymbol{q}_0 (\boldsymbol{q}_0)^{\mathrm{T}} \boldsymbol{C} \right\rangle$$

$$+2\bar{A}_p^*\, k_m\, \alpha\, \bar{\Omega}_0 \left\langle (\boldsymbol{q}_0)^{\mathrm{T}} \boldsymbol{C}\, \dot{\boldsymbol{q}}_0 \boldsymbol{C} + \boldsymbol{C}\, \boldsymbol{q}_0 (\dot{\boldsymbol{q}}_0)^{\mathrm{T}} \boldsymbol{C} \right\rangle ,$$

$$\boldsymbol{C}_s = \bar{\Omega}_0\, \boldsymbol{G}(\lambda_0, \tau) + 2\bar{A}_p^*\, k_m\, \alpha\, \bar{\Omega}_0\, \boldsymbol{C}\, \boldsymbol{q}_0 (\boldsymbol{q}_0)^{\mathrm{T}} \boldsymbol{C} ,$$

$$\boldsymbol{P}_\lambda = 2\sqrt{\beta} v_f \cos 2\tau\, \boldsymbol{B}\dot{\boldsymbol{q}}_0 + 2\nu v_f \cos 2\tau\, \boldsymbol{C}\boldsymbol{q} - 2\sqrt{\beta}\, v_f \bar{\Omega}_0 \sin 2\tau\, (\boldsymbol{C} - \boldsymbol{D})\boldsymbol{q}_0 ,$$

$$\boldsymbol{P}_\Omega = \boldsymbol{G}(\lambda_0, \tau)\dot{\boldsymbol{q}}_0 - 2\sqrt{\beta} v_f \lambda_0 \sin 2\tau (\boldsymbol{C} - \boldsymbol{D})\boldsymbol{q}_0 + 2\bar{\Omega}_0\, \boldsymbol{M}_s \ddot{\boldsymbol{q}}_0 + 2\bar{A}_b^*\, k_m\, \alpha (\boldsymbol{q}_0)^{\mathrm{T}} \boldsymbol{C}\, \dot{\boldsymbol{q}}_0 \boldsymbol{C}\, \boldsymbol{q}_0 ,$$

$$\boldsymbol{R}_s = P_s\, \boldsymbol{F} - \begin{pmatrix} \bar{\Omega}_0^2 \boldsymbol{M}_s\, \ddot{\boldsymbol{q}}_0 + \boldsymbol{K}_s(\bar{\Omega}_0, \lambda_0, \tau)\, \boldsymbol{q}_0 + \bar{\Omega}_0 \boldsymbol{G}(\lambda_0, \tau)\dot{\boldsymbol{q}}_0 + \bar{A}_p\, k_m\, (\boldsymbol{q}_0)^{\mathrm{T}} \boldsymbol{C}\, \boldsymbol{q}_0 \boldsymbol{C}\, \boldsymbol{q}_0 \\ +2\bar{A}_p^*\, k_m\, \alpha\, \bar{\Omega}_0\, (\boldsymbol{q}_0)^{\mathrm{T}} \boldsymbol{C}\, \dot{\boldsymbol{q}}_0 \boldsymbol{C}\, \boldsymbol{q}_0 \end{pmatrix} \tag{6.20}$$

For expressing the linearized incremental governing equation of motion (Eq. (6.20)) in the frequency-domain, the Galerkin procedure is utilized with the assumed periodic solution (Eq. (6.18)), and the resulting equation is obtained as,

$$\boldsymbol{K}_t\, \Delta\boldsymbol{X} = \boldsymbol{R} - \boldsymbol{R}_\Omega\, \Delta\bar{\Omega} - \boldsymbol{R}_\lambda\, \Delta\lambda ,$$

$$\boldsymbol{K}_t = \int_0^{2\pi} \boldsymbol{S}^{\mathrm{T}} \left(\bar{\Omega}_0^2\, \boldsymbol{M}_s\, \ddot{\boldsymbol{S}} + \boldsymbol{C}_s\, \dot{\boldsymbol{S}} + \boldsymbol{K}_{st}\, \boldsymbol{S} \right) d\tau , \boldsymbol{R} = \int_0^{2\pi} \boldsymbol{S}^{\mathrm{T}}\, \boldsymbol{R}_s\, d\tau ,\ \boldsymbol{R}_\Omega = \int_0^{2\pi} \boldsymbol{S}^{\mathrm{T}}\, \boldsymbol{P}_\Omega\, d\tau ,$$

$$\boldsymbol{R}_\lambda = \int_0^{2\pi} \boldsymbol{S}^{\mathrm{T}}\, \boldsymbol{P}_\lambda\, d\tau \tag{6.21}$$

The solution of Eq. (6.21) within a range of frequency of pulsatile fluid flow provides the frequency response curve of the overall FG pipe.

6.4. Local stability analysis

The local stability of a steady-state nonlinear response can be determined by imposing a small perturbation to it (response). The substitution of this perturbation ($\boldsymbol{q} = \boldsymbol{q}_0 + \Delta\boldsymbol{q}$) in Eq. (6.19) yields the following expression that is similar to Eq. (6.20).

$$\bar{\Omega}_0^2\, \boldsymbol{M}_s\, \Delta\ddot{\boldsymbol{q}} + \boldsymbol{C}_s\, \Delta\dot{\boldsymbol{q}} + \boldsymbol{K}_{st}\, \Delta\boldsymbol{q} = \boldsymbol{R}_s \tag{6.22}$$

where, the steady-state solution ($\boldsymbol{q}_0$) satisfies the governing equation of motion (Eq. (6.19)) for which $\boldsymbol{R}_s = 0$. Equation (6.22) is a second order linear time differential equation (in terms of $\Delta\boldsymbol{q}$) with periodic coefficients, and thus the stability of the nonlinear response can be obtained using Floquet theory by expressing the differential equation (Eq. (6.22)) in the state-space form as,

$$\dot{\boldsymbol{F}} = \boldsymbol{Q}_t(\tau)\, \boldsymbol{F} ,\ \boldsymbol{F} = \{\Delta\boldsymbol{q}\ \ \Delta\dot{\boldsymbol{q}}\}^{\mathrm{T}} ,\ \boldsymbol{Q}_t(\tau) = \begin{bmatrix} \boldsymbol{0} & \boldsymbol{I}_{N_r} \\ -\frac{1}{\bar{\Omega}^2}(\boldsymbol{M}_s)^{-1} \boldsymbol{K}_{st} & -\frac{1}{\bar{\Omega}^2}(\boldsymbol{M}_s)^{-1} \boldsymbol{C}_s \end{bmatrix} \tag{6.23}$$

The stability characteristics of solution can be obtained from the eigen values of the state transition matrix ($\boldsymbol{\phi}$) satisfying $\boldsymbol{F}(\tau+T_m)=\boldsymbol{\phi}\ \boldsymbol{F}(\tau)$, where T_m is the time period (2π) of the system (Eq. (6.23)). If all the moduli of eigen values of $\boldsymbol{\phi}$ are less than 1 then the solution will be stable, otherwise it is unstable. Presently, this state transition matrix ($\boldsymbol{\phi}$) is computed following a procedure proposed by Friedmann et al. (1977), where the transition matrix is evaluated using fourth order Runge-Kutta method and Gill coefficients according to the following expressions,

$$\boldsymbol{\phi}=\sum_{i=1}^{N_t}\boldsymbol{L_t}(T_m-i\,\Delta\tau)\,,$$

$$\boldsymbol{L_t}(\tau)=\boldsymbol{I}+\frac{\Delta\tau}{6}\left(\boldsymbol{Q}_t(\tau)+2\left(1-\frac{1}{\sqrt{2}}\right)\boldsymbol{E_t}(\tau)+2\left(1+\frac{1}{\sqrt{2}}\right)\boldsymbol{F_t}(\tau)+\boldsymbol{G_t}(\tau)\right),$$

$$\boldsymbol{F_t}(\tau)=\left[\boldsymbol{Q}_t\left(\tau+\frac{\Delta\tau}{2}\right)\right]\left(\boldsymbol{I}+\left(-\frac{1}{2}+\frac{1}{\sqrt{2}}\right)\Delta\tau\,\boldsymbol{Q}_t(\tau)+\left(1-\frac{1}{\sqrt{2}}\right)\Delta\tau\,\boldsymbol{E_t}(\tau)\right),$$

$$\boldsymbol{G_t}(\tau)=\left[\boldsymbol{Q}_t\left(\tau+\Delta\tau\right)\right]\left(\boldsymbol{I}-\frac{\Delta\tau}{\sqrt{2}}\boldsymbol{E_t}(\tau)+\left(1+\frac{1}{\sqrt{2}}\right)\Delta\tau\,\boldsymbol{F_t}(\tau)\right),$$

$$\boldsymbol{E_t}(\tau)=\left[\boldsymbol{Q}_t\left(\tau+\frac{\Delta\tau}{2}\right)\right]\left(\boldsymbol{I}+\frac{1}{2}\Delta\tau\,\boldsymbol{Q}_t(\tau)\right) \qquad (6.24)$$

In Eq. (6.24), N_t is the number of time steps; $\Delta\tau\left(=T_m/N_t\right)$ is the time step of the Runge-Kutta numerical integration.

6.5. Numerical results and discussion

In this section, the numerical results are presented to investigate the nonlinear static and dynamic responses of the vertical/inclined FG pipe conveying hot fluid with the steady or pulsatile flow-velocity. The geometrical properties of the pipe are taken as, $r_i=12$ mm, $r_o=13.5$ mm, $L=2$ m. The density of the fluid is considered as 990 Kg/m^3 while it (fluid) flows through the FG pipe with an internal pressure of 4.4 MPa above the atmospheric pressure. The temperature dependent material properties of the metal (Ti-6Al-4V) and ceramic (ZrO_2) constituents of FG material are given in Eqs. (6.25) and (6.26), respectively (Fuchiyama and Noda, 1995; Shen, 2016). The material damping of FGM is considered through its metal constituent only, where the coefficient of viscoelastic dissipation parameter or retardation time (r_τ) is considered as 0.0004 s (Bommakanti et al., 2016) corresponding to the dissipation parameter ($E^*=r_\tau E$) for the metal constituent. With these properties of the constituent materials, the properties at any point in the FG pipe can be determined according to Eq. (6.2), where the temperature-dependent properties of the constituents can be computed

from Eqs. (6.25) and (6.26) in conjunction with the solution for temperature distribution (Eq. (6.4)) across the wall-thickness of the pipe. The Poisson's ratio of FGM is assumed to be constant with the value of 0.3.

$$\begin{gathered} E(T) = (122.14 - 0.055T) \text{ GPa}, \\ \alpha_T(T) = (7.2347 - 0.0071277\,T - 5.2876\times10^{-6}T^2 + 1.2697\times10^{-9})\times10^{-6} \text{ K}^{-1}, \\ k = 7.8 \text{ W m}^{-1}\text{K}^{-1},\ \rho = 4429 \text{ Kg m}^{-3} \end{gathered} \tag{6.25}$$

$$\begin{gathered} E(T) = (235.38 - 0.30377T + 2.6734\times10^{-4}T^2 - 8.17\times10^{-8}T^3) \text{ GPa}, \\ \alpha(T) = (13.628 - 0.018913\,T + 1.2413\times10^{-5}T^2)\times10^{-6} \text{ K}^{-1}, \\ k = 1.8 \text{ W m}^{-1}\text{K}^{-1}, \rho = 3000 \text{ Kg m}^{-3} \end{gathered} \tag{6.26}$$

The static/dynamic responses of the vertical/inclined FG pipe are illustrated on the basis of the variations of the system parameters like inner surface temperature (T_i), graded exponent (n), inclination angle (χ), mean flow velocity (V_f) and pulsation amplitude (λ). The static responses are evaluated by solving Eq. (6.15) without consideration of the time-dependent terms, whereas the dynamic responses in the frequency domain are evaluated by solving Eq. (6.21) in conjunction with the arc-length extrapolation continuation method (Kumar et al., 2015). The dynamic responses of the FG pipe in the time-domain are evaluated by solving Eq. (6.15) using the adaptive Runge-Kutta method especially for the clarification of dynamics of the vertical/inclined FG pipe through the global bifurcation diagram where the Poincare sections are selected based on the time-period ($2\pi/\Omega$) of the excitation frequency (Ω). In all the following numerical results, the responses (η) of the inclined FG pipe are presented corresponding to its middle point ($\xi = 0.5$), and it is denoted by η_m.

Since the present mathematical model of the inclined FG pipe is derived based on the Galerkin discretization and incremental HBM, a convergence study is first carried out where the nonlinear frequency responses of the FG pipe are evaluated by a gradual increase of the number of basis functions in the Galerkin discretization as well as the number of harmonic terms in incremental HBM. It is observed that the results appear with the sufficient numerical accuracy for the first seven basis functions (Eq. (6.14), N_r =7) in the Galerkin discretization and first six harmonic terms (Eq. (6.17), H = 6) in incremental HBM, and thus the same are considered in the present numerical results.

6.5.1. Verification of the present formulation

In order to verify the present formulation for handling the thermo-elastic coupling in the FG pipe, its metal and ceramic constituents are considered as SUS304 and Si_3N_4, respectively, while the FG pipe is taken in vertical orientation ($\chi = 0$) without any fluid flow. Under these conditions, the critical buckling temperature is computed for uniform temperature across the wall-thickness of the FG pipe. These results are illustrated in Table 6.1 for both the temperature-independent and temperature-dependent properties of the constituent materials. Similar results for an identical FG pipe are available in Fu et al. (2015), and the same are also furnished in Table 6.1. It may be observed from Table 6.1 that the present results are in good agreement with the similar results available in Fu et al. (2015) thus verifying the present formulation in handling the thermo-elastic coupling in the FG pipe.

Table 6.1

Comparison of critical buckling temperatures of FG pipe (r_o = 0.5 mm, $r_i = 0.5 r_o$)

Exponent (n)	L/r_o	Temperature dependent		Temperature independent	
		Present	Fu et al. (2015)	Present	Fu et al. (2015)
∞ (SUS304)	25	273.44	273.43	400.23	400.22
4	25	325.64	325.61	499.74	499.74
2	25	353.21	353.19	551.84	551.84
1	25	384.48	384.46	612.12	612.12
0 (Si_3N_4)	25	489.20	489.20	840.35	840.35

The results for nonlinear dynamic response of an inclined FG pipe are not available in the literature, and thus the present formulation in modeling an inclined pipe is verified following the available results in (Alfosail et al., 2017b) for static profile of an inclined submerged pinned-pinned isotropic pipe under an externally applied tensile force. Here, the present governing equation (Eq. (6.10)) is modified slightly by adding the terms corresponding to the applied tensile force (T_e) and the added mass (m_e) for external fluid (submerged) as presented in Eq. (6.27), and the computed static profile of the inclined isotropic pipe at room temperature is plotted in Fig. 6.2(a) together with the similar results available in (Alfosail et al., 2017b). A good agreement of the present results with that in the reference (Alfosail et al., 2017b) can be observed from Fig. 6.2(a), and this comparison verifies the present formulation in handling the inclined pipes.

$$D_p \frac{\partial^4 w_0}{\partial x^4} + \left[m_f V^2 - T_e - \left\langle (m_f + m_p - m_e) g \cos\chi \right\rangle (L-x) - \frac{A_p}{2L} \int_0^L \left(\frac{\partial w_0}{\partial x} \right)^2 dx \right] \frac{\partial^2 w_0}{\partial x^2}$$
$$+ (m_f + m_p - m_e) g \cos\chi \frac{\partial w_0}{\partial x} + (m_f + m_p - m_e) g \sin\chi = 0$$

$$m_e = \rho_e A_e\,,\;\; A_e = \pi r_o^2 \tag{6.27}$$

For the verification of the present incremental HBM formulation and implementation of adaptive Runge-Kutta method in the evaluation of the nonlinear dynamic responses of the FG pipe, similar results are not available in the literature. However, it is carried out by taking a result in reference (Jin and Song, 2005) for nonlinear dynamic response of a vertically oriented ($\chi = 0$) pinned-pinned isotropic pipe conveying pulsatile fluid. This comparison is illustrated in Fig. 6.2(b), where the present results are evaluated through both the incremental HBM formulation and adaptive Runge-Kutta method. It may be observed from Fig. 6.2(b) that the present results are in good agreement with that in the reference (Jin and Song, 2005) thus verifying the present incremental HBM formulation, as well as the present implementation of the adaptive Runge-Kutta method, in evaluating the nonlinear dynamic responses of pipes conveying pulsatile fluid.

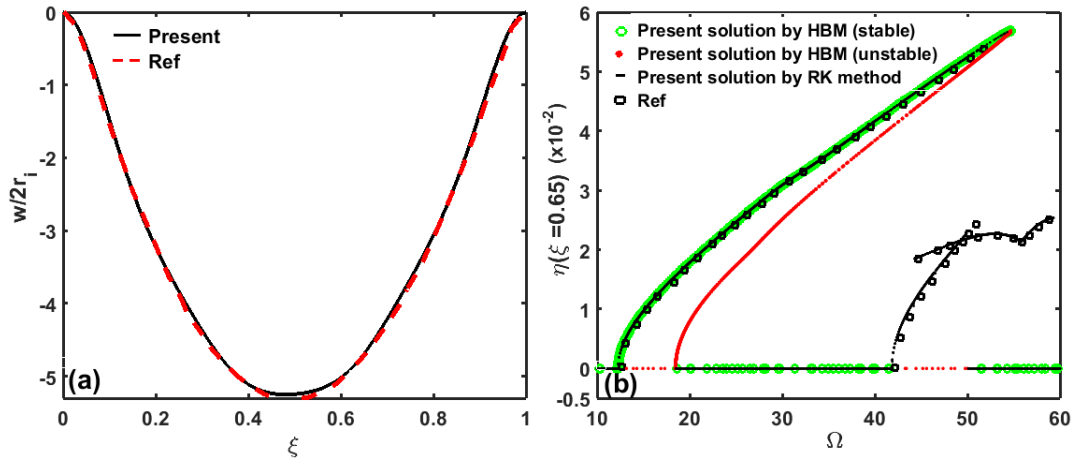

Fig. 6.2. (a) Comparison of the static profile of an inclined isotropic pipe with that for an identical pipe in Ref: (Alfosail et al., 2017b), (b) comparison of nonlinear dynamic response of vertical isotropic pipe conveying pulsatile fluid with the similar response of an identical pipe in Ref: (Jin and Song, 2005). (RK: Runge-Kutta)

6.5.2. Static/dynamic characteristics of the vertical FG pipe conveying hot fluid

In this section, the static instability of the vertical FG pipe conveying hot fluid is first investigated. With reference to this static instability, the pre-buckled and post-buckled equilibrium states of the FG pipe are identified. Subsequently, the nonlinear dynamic characteristics of the fluid conveying FG pipe corresponding to its pre-buckled and post-buckled equilibrium states are investigated. In the last part of this section, the global bifurcation diagrams are presented for analyzing the complex nonlinear dynamics of the fluid conveying FG pipe.

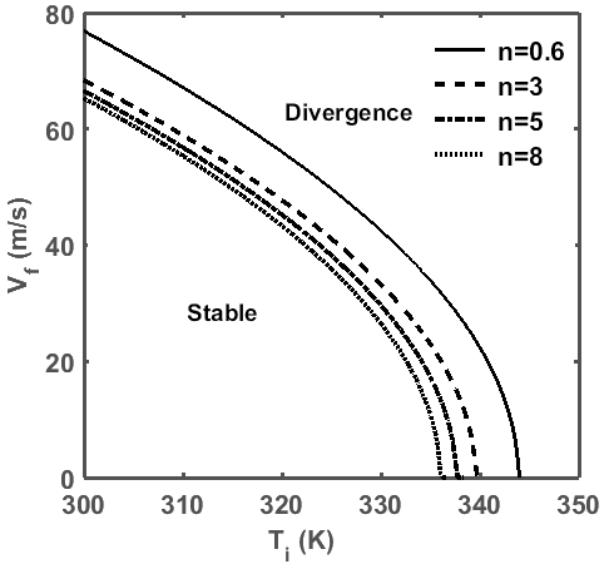

Fig. 6.3. Variation of the constant flow velocity (V_f, $\lambda = 0$) with temperature (T_i) corresponding to the onset of buckling of the vertical FG pipe.

6.5.2.1. Stability of the vertical FG pipe conveying hot fluid with the constant flow velocity

The FG pipe is subjected to the follower compressive force due to the constant flow velocity (V_f, $\lambda = 0$) of the internal fluid. Now, the same FG pipe is also subjected to the thermally induced compressive force because of a high temperature (T_i) at its inner ceramic-rich surface. The combined effect of these compressive forces in the FG pipe on its buckling characteristics is illustrated in Fig. 6.3. For different values of the graded exponent (n) of FGM, Fig. 6.3 illustrates the variation of the flow velocity (V_f, $\lambda = 0$) with temperature (T_i) corresponding to the onset of buckling of the FG pipe. For any value of the graded exponent (n) of FGM, it can be observed from Fig. 6.3 that the buckling of the FG pipe may occur at a low value of flow-velocity (V_f, $\lambda = 0$) for a high temperature (T_i) of the internal fluid. It may also be observed from Fig. 6.3 that the graded exponent (n) of FGM plays an important role in causing the buckling of the FG pipe. For instance, a high value of the graded exponent (n) of FGM causes the buckling of the FG pipe at a low temperature of the internal fluid. In fact, the volume fraction of the ceramic constituent in the FGM decreases for a high value of the graded exponent (n). So, temperature in the FG pipe increases along with its reduced structural rigidity.

6.5.2.2. Parametric instability of the vertical FG pipe conveying hot fluid with pulsatile flow velocity

In this section, the dynamic instability of the FG pipe is investigated when it conveys pulsatile fluid at its pre-buckled equilibrium state. Generally, the dynamic instability of a pipe conveying pulsatile fluid arises through the primary, secondary and combinatory parametric resonances (Paidoussis and Issid, 1974). However, since the present FG pipe possesses high stiffness, it is observed that the combinatory parametric resonance occurs at a very high frequency of pulsatile flow, and this frequency of pulsatile flow may not be feasible in practical applications of the FG pipe. However, among these different kinds of parametric resonances, the most critical one is the principal primary parametric resonance (Bolotin, 1964). So, the dynamic instability of the FG pipe through its principal primary parametric resonance corresponding to the fundamental mode of vibration is investigated at present by means of evaluating the corresponding parametric instability region in the two-dimensional domain of frequency (ω) and amplitude (λ) of pulsatile flow velocity (Pierre and Dowell, 1985).

For different temperatures (T_i) of pulsatile fluid, Figs. 6.4(a)-(d) illustrate the parametric instability regions corresponding to the principal primary parametric resonance at the pre-buckled equilibrium state of the FG pipe. In these results (Figs. 6.4(a)-(d)), the graded exponent (n) of FGM is considered as 5. However, similar results are presented in Figs. 6.4(e)-(g) for different values of the graded exponent (n) of FGM where a temperature of the internal fluid is considered as 335 K. Here, the mean flow velocity (V_f) of pulsatile fluid is considered as 5 m/s. Now, if the internal fluid is considered to flow with a steady flow velocity as 5 m/s ($V_f = 5$ m/s, $\lambda = 0$), then the buckling of the FG pipe appears at a temperature of 337.5 K (Fig. 6.3, $n = 5$). This temperature can be marked as the critical bulking temperature. Following this critical buckling temperature, four different temperatures of the internal fluid are considered for evaluation of the results in Figs. 6.4(a)-(d) corresponding to the pre-buckled equilibrium state of the FG pipe. Similarly, for the results in Figs. 6.4(e)-(g), a temperature (T_i) of the internal fluid is considered as 335 K and three different values of the graded exponent (n) of FGM are taken as 0.8, 1 and 3 in such a manner that the FG pipe remains at its pre-buckled equilibrium state for the constant velocity ($V_f = 5$ m/s, $\lambda = 0$) of the internal fluid.

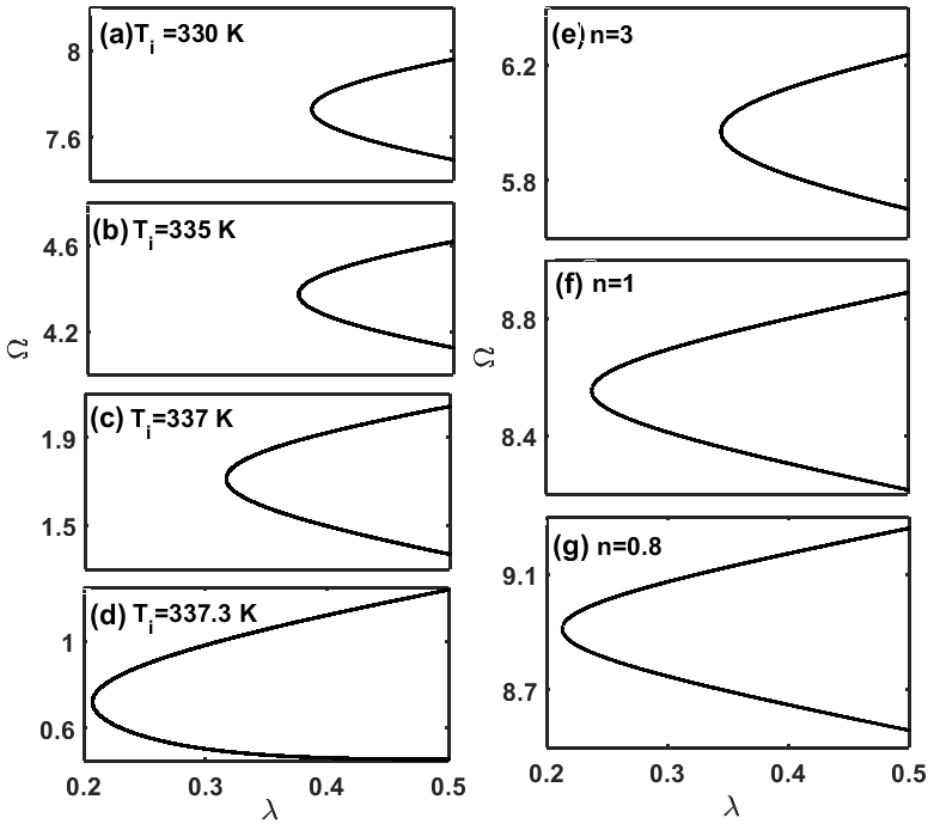

Fig. 6.4. Regions of parametric instability corresponding to the principal primary parametric resonance at the pre-buckled state of the vertical FG pipe ($V_f = 5$ m/s), (a)-(d) for different temperatures (T_i (K), $n = 5$) and (e)-(f) for different values of the graded exponent (n, $T_i =$ 335 K).

Figures 6.4(a)-(d) illustrate that the parametric instability region shifts towards low frequency for an increase of temperature (T_i). It may be due to the fact that the natural frequency of the FG pipe decreases for an increase of temperature (T_i). However, it may be observed from Figs. 6.4(a)-(c) that there is no indicative change in the shape of the parametric instability region for an increase of temperature (T_i). But, the parametric instability region extends towards the low value of pulsatile velocity-amplitude (λ) and the breadth of the same instability region increases for an increase of temperature (T_i). Moreover, it is important to observe from Fig. 6.4(d) that the shape of the parametric instability region changes indicatively when temperature (T_i) of the internal fluid is very close to the critical buckling temperature ($T_i = 337.5$ K). These observations indicate that the parametric instability of the FG pipe at its pre-buckled equilibrium state is indicatively dependent on temperature (T_i) of the internal fluid, especially when this temperature (T_i) is very close to the critical buckling temperature.

However, for a specified temperature (T_i = 335 K) of the internal fluid, Figs. 6.4(e)-(g) illustrate that the breadth of the parametric instability region decreases for an increase of the graded exponent (n) of FGM. It may also be observed from Figs. 6.4(e)-(g) that the parametric instability region shifts towards the high amplitude (λ) of pulsatile flow velocity for an increase of the graded exponent (n) of FGM. This characteristic of the parametric instability region arises mainly due to the improved damping properties of FGM for an increase of its graded exponent (n). In fact, the material damping of FGM appears through its metal constituent and the volume fraction of this metal constituent increases with an increase in the graded exponent (n). So, the material damping in the FGM improves for an increase of the graded exponent (n).

6.5.2.3. Nonlinear frequency responses of the vertical FG pipe conveying pulsatile fluid

The FGM possesses high stiffness because of its ceramic constituent. So, the buckling of the FG pipe occurs at the room temperature (T_i = 300 K) for a very high velocity (V_f , $\lambda = 0$) of the internal fluid (Fig. 6.3). Quantitatively, this velocity of the internal fluid is much higher than that appears in the practical piping systems. However, from the results in Fig. 6.3, it is clear that the buckling of the FG pipe may arise at a feasible velocity of the internal fluid for a high temperature of the fluid, and thus the temperature of the internal fluid is presently taken as the main parameter for identifying the buckling of the FG pipe. With reference to the corresponding critical buckling temperature, the pre-buckled and post-buckled equilibrium states of the FG pipe are recognized, and the nonlinear dynamic characteristics of the FG pipe at these two different static equilibrium states are studied for pulsatile velocity of the internal hot fluid. However, it is important to note here that the FG pipe becomes very flexible at a temperature that is very close to the critical buckling temperature. The high flexibility of the FG pipe leads to its complex dynamic characteristics when the internal fluid flows with pulsatile velocity. In order to illustrate these dynamic characteristics of the FG pipe separately, a transition zone is considered at present following the transition from pre-buckled to post-buckled equilibrium state of the FG pipe corresponding to the increase of temperature around the critical buckling temperature. Within this transition zone, a static equilibrium state of the FG pipe is its pre-buckled or post-buckled equilibrium state at a temperature that is very close to the critical buckling temperature.

6.5.2.3.1. Nonlinear frequency responses of the vertical FG pipe at the pre-buckled equilibrium state

For different temperatures (T_i) of the internal fluid, Fig. 6.5(a) illustrates the frequency responses of the FG pipe (n = 5) corresponding to the principal primary parametric resonance. Here, the FG pipe is in the pre-buckled equilibrium state and the internal fluid flows with the pulsatile velocity (V_f = 5 m/s, λ = 0.5). However, for a constant temperature (T_i = 335 K), similar responses are also shown in Fig. 6.5(b) for different values of the graded exponent (n) of FGM. In these responses and also in the subsequent frequency responses, the stable and unstable solutions over a frequency response curve are indicated by the green and red colour, respectively. However, the parametric resonance evolves through the supercritical and subcritical pitchfork bifurcations, as those are indicated by the points M and N, respectively in Figs. 6.5(a) and 6.5(b). It may be observed from Fig. 6.5(a) that there is no indicative change in the peak displacement-amplitude for the variation of temperature (T_i) of the internal fluid. But, the resonant frequency decreases for an increase of temperature (T_i). It may be due to the fact that the stiffness of the FG pipe decreases with an increase of temperature (T_i). However, for a constant temperature (T_i = 335 K), Fig. 6.5(b) shows that the peak displacement-amplitude decreases indicatively for an increase in the graded exponent (n) of FGM. In fact, the material damping of FGM increases with an increase in the graded exponent (n) and it results in superior attenuation of the peak displacement-amplitude.

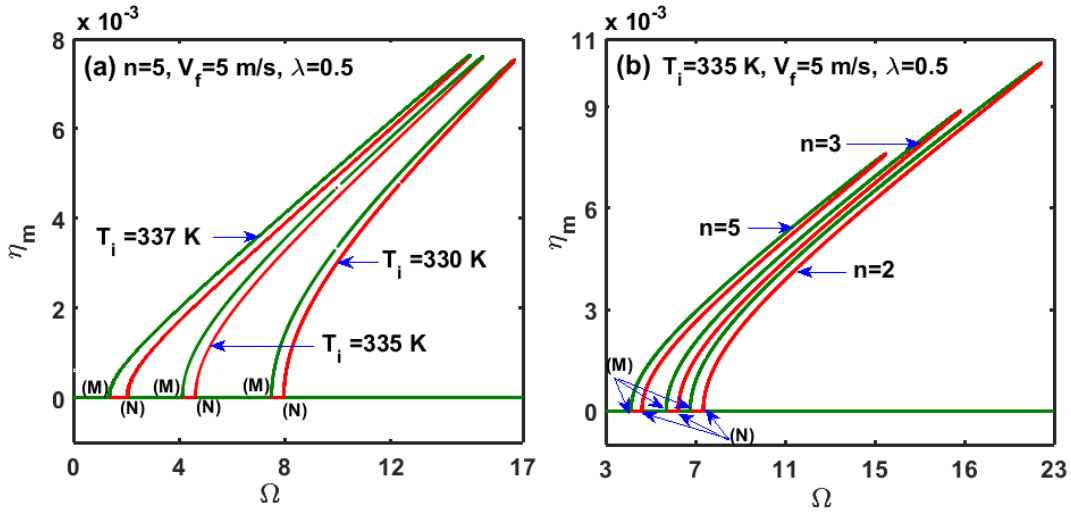

Fig. 6.5. Frequency responses of the vertical FG pipe corresponding to the principal primary parametric resonance when the FG pipe is in its pre-buckled state; (a) for different temperatures (T_i (K), n = 5), (b) for different values of the graded exponent (n, T_i = 335 K) (V_f = 5 m/s, λ = 0.5).

6.5.2.3.2. Nonlinear frequency responses of the vertical FG pipe at the post-buckled state

Following the results in Fig. 6.3, a post-buckled equilibrium state of the FG pipe at a temperature (T_i) of 360 K is considered for the mean flow velocity (V_f) and the graded exponent (n) of FGM as 5 m/s and 5, respectively. Corresponding to this post-buckled equilibrium state, the nonlinear frequency response of the FG pipe is illustrated in Fig. 6.6(a) for the pulsatile fluid flow with a velocity-amplitude (λ) of 0.5. It should be noted here that the transverse deflection of the vertical FG pipe at a post-buckled equilibrium state arises either in the positive or in the negative z-direction. The dynamic characteristics of the FG pipe do not differ if the post-buckled equilibrium state arises in the positive z-direction instead of the negative z-direction or vice versa. So, in Fig. 6.6(a), the frequency response of the FG pipe is presented corresponding to a post-buckled equilibrium state in one of the positive and negative z-directions. Also, the oscillation of the FG pipe at a frequency with reference to an equilibrium position is illustrated by plotting the corresponding maximum and minimum deflections (η_m) of the pipe as well as the mean point of oscillation that is indicated by the black line (Fig. 6.6(a)). This kind of illustration of motion of the FG pipe is also adopted in the subsequent results for its (FG pipe) frequency responses.

Figure 6.6(a) shows that the FG pipe undergoes principal primary and secondary parametric resonances since the corresponding resonant frequencies appear as $2\Omega_n$ and Ω_n, respectively, with reference to the fundamental natural frequency of the FG pipe as Ω_n. Here, the principal primary parametric resonance develops through the period doubling/period demultiplying bifurcation (P) at points J/K and the stable periodic motion evolves at the point R (Fig. 6.6(a)) through the period demultiplying bifurcation. Whereas the principal secondary parametric resonance (Q/L) is associated with the saddle-node bifurcations (S). It may also be observed that the mean point of oscillation varies indicatively near a resonant frequency ($2\Omega_n$ or Ω_n). However, similar frequency responses of the FG pipe are also presented in Figs. 6.6(b) and 6.6(d) for two different temperatures (T_i = 370 K, 380 K). It may be observed from these results (Figs. 6.6(a), 6.6(b) and 6.6(d)) that a resonant frequency ($2\Omega_n$ or Ω_n) increases with the increasing temperature (T_i). More importantly, the principal primary parametric resonance disappears as the temperature of internal fluid increases (Fig. 6.6(d), T_i = 380 K).

Here, the transverse deflection of the post-buckled FG pipe increases for an increase in temperature of the internal fluid. So, the nonlinear stiffness of the FG pipe increases resulting in the disappearance of the principal primary parametric resonance.

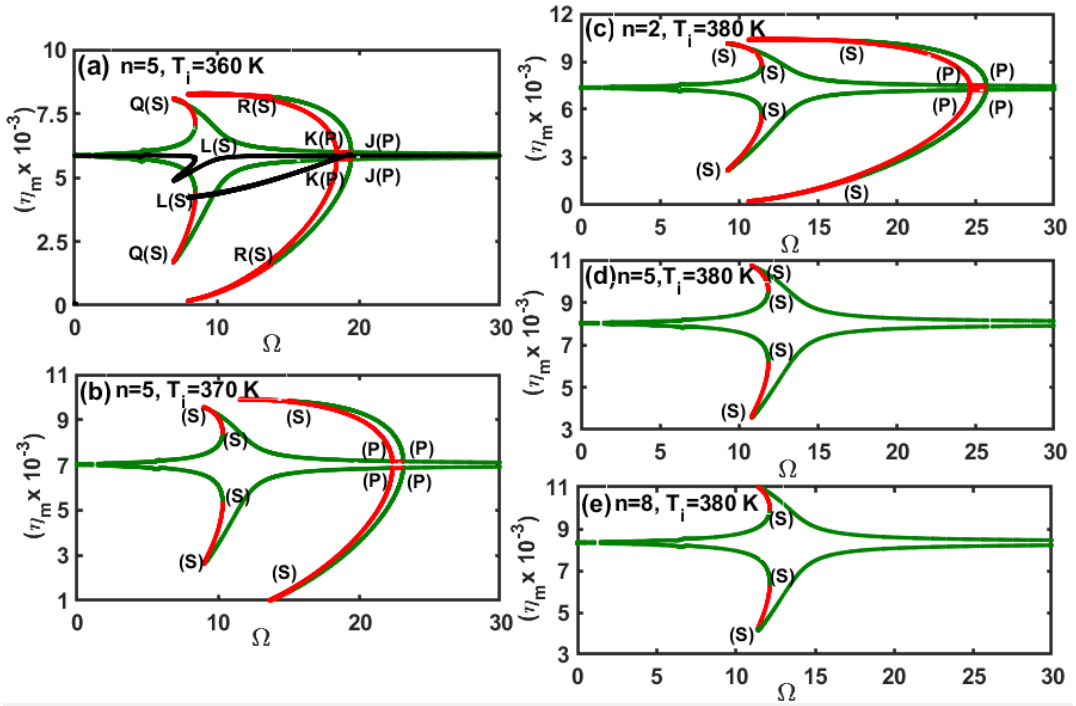

Fig. 6.6. Nonlinear frequency responses of the vertical FG pipe at its post-buckled state, (a), (b), (d) for different temperatures (T_i) ($n=5$), and (c), (d), (e) for different values of the graded exponent (n) ($T_i=380$ K).

Figures 6.6(c)-(e) illustrate the frequency responses of the FG pipe for three different values of the graded exponent (n) of FGM. A temperature of the internal fluid is considered as 380 K and the FG pipe is in the post-buckled equilibrium state. The mean flow velocity and the velocity-amplitude of pulsatile fluid flow are taken as 5 m/s and 0.5, respectively. It may be observed from these results (Figs. 6.6(c), 6.6(d) and 6.6(e)) that the resonant frequency is indicatively dependent on the graded exponent (n) of FGM. The amplitude of vibration of the FG pipe decreases with an increase of the graded exponent (n) of FGM. Also, the principal primary parametric resonance disappears at a high value of the graded exponent (n). There may be two reasons for the disappearance of the principal primary parametric resonance. The first one is the improved material damping of the FGM for a high value of the graded exponent (n). The second one is the increased nonlinear stiffness of the FG pipe since its post-buckled state arises with the greater transverse deflection for an increase in the graded exponent (n).

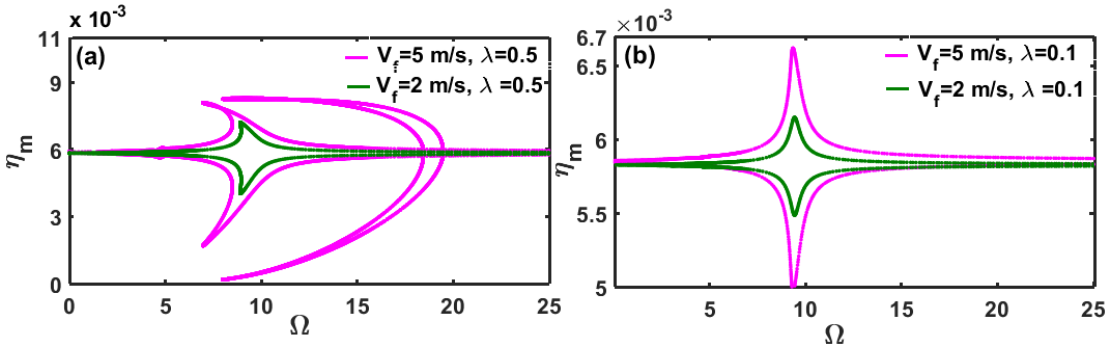

Fig. 6.7. Nonlinear frequency responses of the vertical FG pipe at its post-buckled state ($n=5$, $T_i=360$ K); (a) $V_f=2$m/s or 5 m/s, $\lambda=0.5$; (b) $V_f=2$ m/s or 5 m/s, $\lambda=0.1$.

In order to investigate the effects of the mean flow velocity (V_f) and velocity-amplitude (λ) of pulsatile fluid flow on the nonlinear frequency response of the FG pipe, two different values of the velocity-amplitude (λ) are considered as 0.1 and 0.5. For each of these values of the velocity-amplitude (λ), the mean flow velocity (V_f) is taken either as 2 m/s or as 5 m/s, and the frequency responses of the FG pipe are evaluated as shown in Figs. 6.7(a)-(b). The graded exponent (n) of FGM and temperature (T_i) of the internal fluid are considered as 5 and 360 K, respectively. It may be observed from Figs. 6.7(a)-(b) that the FG pipe undergoes principal secondary parametric resonance for any value ($\lambda=0.1$ or 0.5) of the velocity-amplitude when a low value of the mean flow velocity ($V_f=2$ m/s) is considered. However, if the mean flow velocity (V_f) increases along with a high value of the velocity-amplitude (λ), both the principal primary and secondary parametric resonances appear (Fig. 6.7(a)). These results indicate that the effect of the velocity-amplitude (λ) of pulsatile fluid flow may have an indicative effect on the nonlinear frequency responses of the FG pipe when the pulsatile fluid flows with high mean flow velocity (V_f).

6.5.2.3.3. Nonlinear frequency responses of the vertical FG pipe at the transition state

The temperature (T_i) of the internal fluid is gradually increased within a narrow zone around the critical buckling temperature (337.5 K for $n=5$, $V_f=5$ m/s, Fig. 6.3), and the corresponding changes in the nonlinear dynamic characteristics of the FG pipe are studied. Figure 6.8(a) illustrates the frequency response of the FG pipe at a temperature (T_i = 337.2 K) that is slightly lesser than the critical buckling temperature (337.5 K). This result (Fig. 6.8(a)) clearly shows that the FG pipe

primarily undergoes principal primary parametric resonance. However, the principal secondary parametric resonance and higher-order parametric resonances also appear along with the principal primary parametric resonance. The corresponding resonant frequencies are very close to each other and thus the shape of the parametric instability region changes (Fig. 6.4(d)) (Paidoussis and Issid, 1974). It is interesting to observe from the result in Fig. 6.8(a) that the dual periodic attractors arise through the principal secondary and higher-order parametric resonances. The mean point of oscillation corresponding to each of these dual periodic attractors is also sown in the same figure (Fig. 6.8(a)) by the black line.

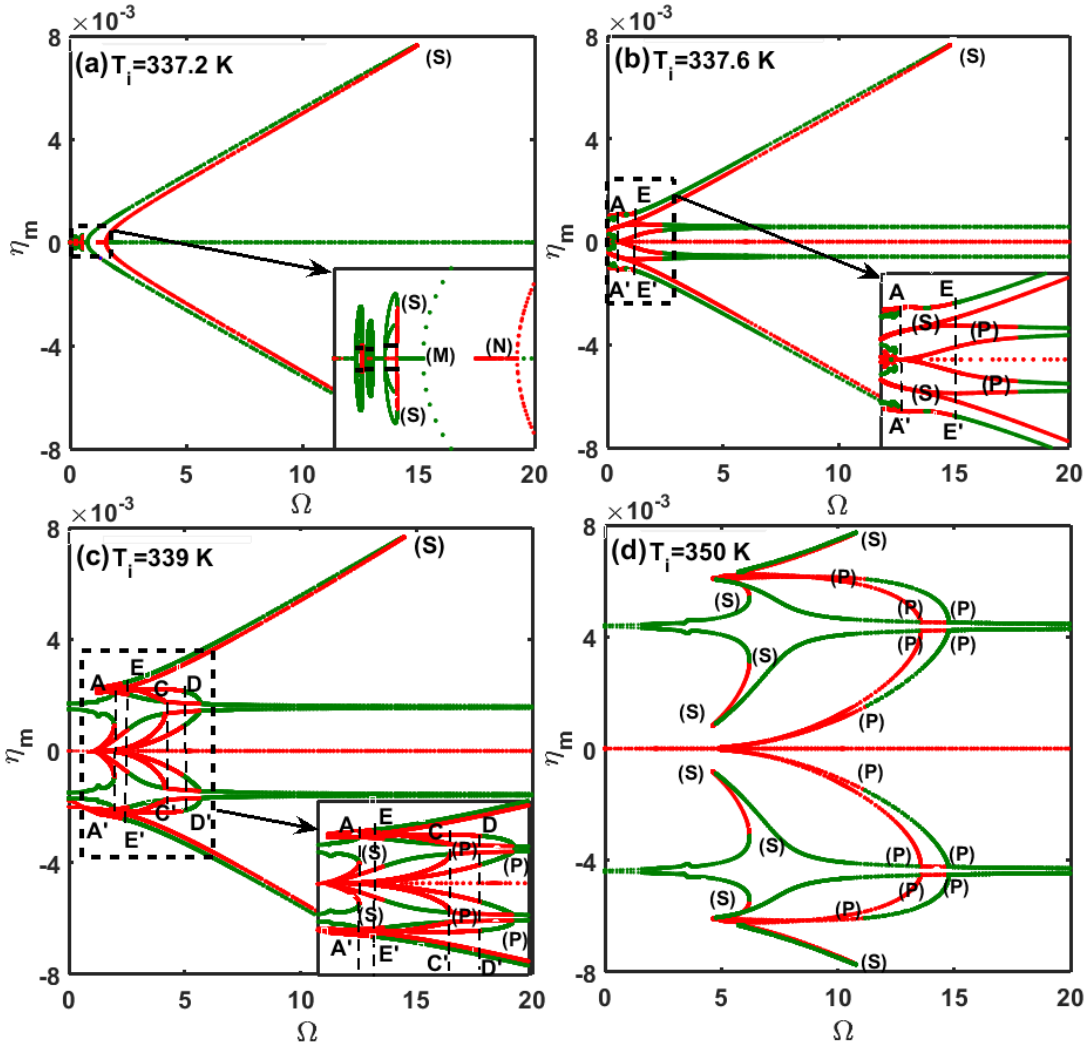

Fig. 6.8. Nonlinear frequency responses of the vertical FG pipe for different temperatures near the critical buckling temperature ($n=5$, $V_f=5$ m/s, $\lambda=0.5$); (a) $T_i=337.2$ K, (b) $T_i=337.6$ K, (c) $T_i=339$ K, (d) $T_i=350$ K.

For further increase of temperature ($T_i=337.6$ K, Fig. 6.8(b)) slightly beyond the critical buckling temperature (337.5 K), multiple stable and unstable dynamic responses of the FG pipe evolve mainly because of the primary and secondary

parametric resonances. Although it is difficult to trace the motion of the FG pipe corresponding to its unstable dynamic responses at the low frequency (Fig. 6.8(b)), mainly two local attractors and one global attractor appear for the stable periodic motion of the FG pipe. A local attractor appears following the post-buckled equilibrium state of the FG pipe. The global attractor continues from the pre-buckled state of the FG pipe, and the corresponding motion of the FG pipe appears as the snap-through periodic motion. For further increase of temperature (T_i), Figs. 6.8(c), 6.8(d) and 6.6(a) show that the global attractor disappears retaining the local attractors. However, the results in Figs. 6.8(b) and 6.8(c) show two critical zones (AE/A'E' and CD/C'D') corresponding to the unstable dynamic responses of the FG pipe. The characteristics of motion of the FG pipe within these critical zones (AE'/A'E' and CD/C'D', Figs. 6.8(b) and 6.8(c)) are investigated in the next section by means of evaluating the global bifurcation diagram.

Figures 6.8(d) and 6.9 illustrate the nonlinear frequency responses of the FG pipe for two different values of the graded exponent ($n=5$ and 8) of FGM. A temperature (T_i) of internal fluid is taken as 350 K and the FG pipe is in the post-buckled equilibrium state. It may be observed from these results (Figs. 6.8(d) and 6.9) that the snap-through motion of the FG pipe disappears for an increase in the graded exponent (n) of FGM. So, the graded exponent of FGM may be treated as a tuning parameter for reducing the complexity in the dynamic characteristics of the FG pipe at its post-buckled equilibrium state.

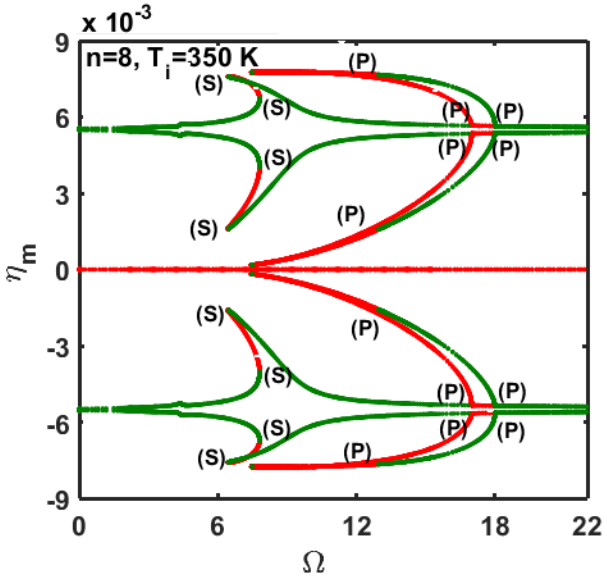

Fig. 6.9. Nonlinear frequency response of the vertical FG pipe at its post-buckled state ($V_f = 5$ m/s, $\lambda = 0.5$, $T_i = 350$ K, $n = 8$).

For a decrease of the mean flow velocity (V_f), the correspodning changes in the nonlinear frequency response of the FG pipe at its post-buckled equilibrium state are illustrated in Figs. 6.8(c) and 6.10(a). A temperature (T_i) of the internal fluid is considered as 339 K and the graded exponent (n) of FGM is taken as 5. It may be observed from these results (Figs. 6.8(c) and 6.10(a)) that the critical zones (AE/A'E' and CD/C'D') corresponding to the unstable dynamic responses of the FG pipe do not appear when the mean flow velocity (V_f) decreases. Also, the peak displacement-amplitude corresponding to the snap-through periodic motion of the FG pipe decreases. If the velocity-amplitude (λ) of the pulsatile fluid flow decreases instead of the mean flow velocity (V_f), then the snap-though motion, as well as the unstable dynamic responses, of the FG pipe may not appear (Figs. 6.8(c) and 6.10(b)). These observations imply indicative effects of the mean flow velocity (V_f) and velocity-amplitude (λ) of pulsatile fluid flow on the nonlinear dynamics of the FG pipe especially when the temperature of the internal fluid is very close to the critical buckling temperature.

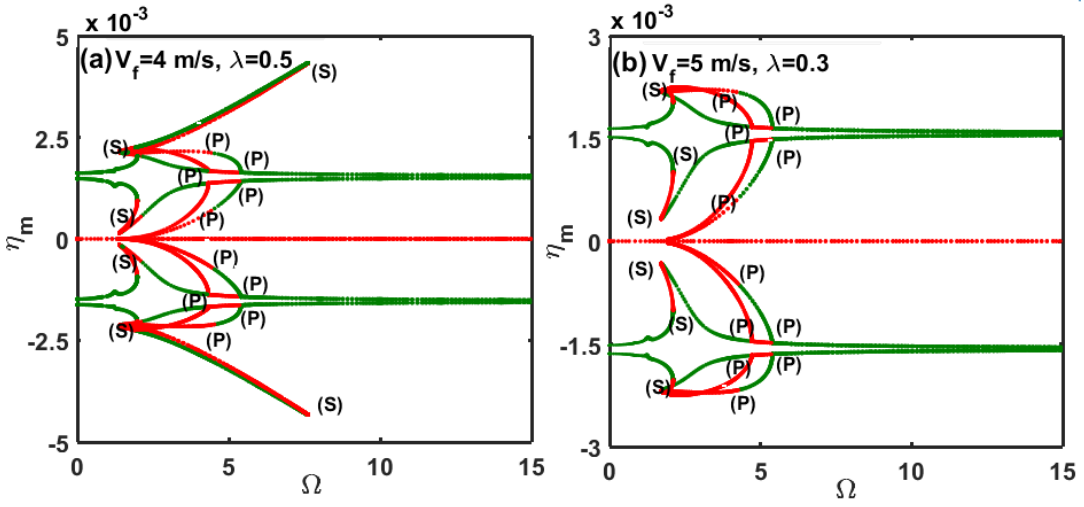

Fig. 6.10. Nonlinear frequency responses of the vertical FG pipe ($n=5$, $T_i=$ 339 K) for different values of the mean flow velocity (V_f) and pulsation velocity-amplitude (λ); (a) $V_f=4$ m/s, $\lambda=0.5$, (b) $V_f=5$ m/s, $\lambda=0.3$.

6.5.2.3.4. Global bifurcation diagrams

In Figs. 6.8(b) and 6.8(c), the unstable dynamic responses of the FG pipe are observed in two zones (AE/A'E' and CD/C'D'). The corresponding motion of the FG pipe is investigated in this section by evaluating the global bifurcation diagrams with respect to the frequency (Ω) or the amplitude (λ) of pulsatile flow velocity.

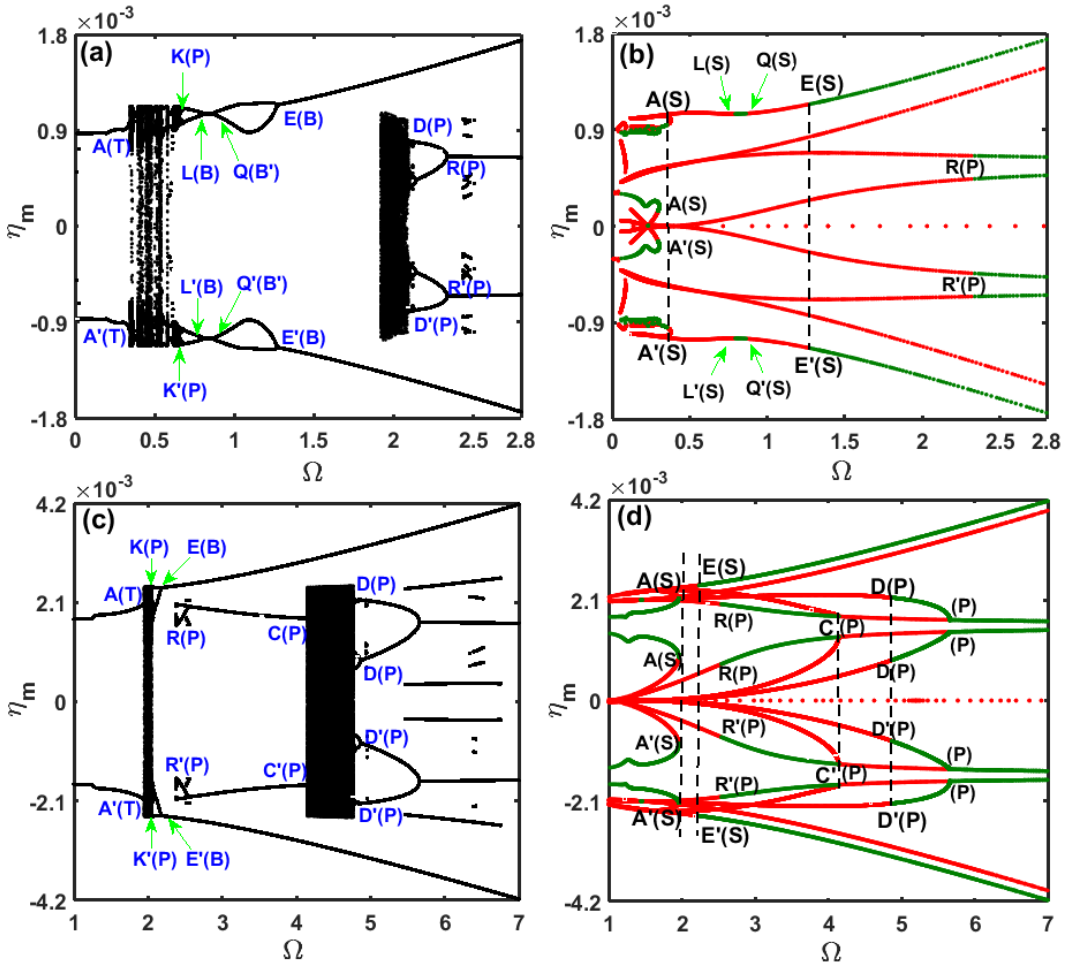

Fig. 6.11. Global bifurcation diagrams with respect to the frequency (Ω) of the pulsating flow velocity of the internal hot fluid ($n=5$, $V_f=5$ m/s, $\lambda=0.5$); (a), (b) for critical zone AB in Fig. 6.8(b) ($T_i=337.6$ K); (c), (d) for critical zones AB and CD in Fig. 6.8(c) ($T_i=339$ K).

6.5.2.3.4.1. Global dynamics of the vertical FG pipe with respect to the frequency of pulsatile flow velocity

For the critical zone AE/A'E' in Fig. 6.8(b), the global bifurcation diagram with respect to the frequency (Ω) of pulsatile fluid flow is illustrated in Fig. 6.11(a). The frequency response of the vertical FG pipe within this critical zone (AE/A'E', Fig. 6.8(b)) is also shown in Fig. 6.11(b). Figure 6.11(c) shows a similar global bifurcation diagram corresponding to the critical zones AE/A'E' and CD/C'D' in Fig. 6.8(c). The frequency responses of the FG pipe in the neighborhood of the critical zones AE/A'E' and CD/C'D' (Fig. 6.8(c)) are shown in Fig. 6.11(d). It may be observed from Figs. 6.11(a)-(b) that two periodic attractors corresponding to the stable periodic motion of the FG pipe appear at the low frequency region and these periodic attractors retain up to the cyclic-fold bifurcation at points A/A' ($\Omega=0.34$). For further increase of the frequency (Ω), the chaotic motion of the FG pipe arises as it is identified through the phase plot and the Poincare map at a

frequency (Ω) of 0.3403 (Figs. 6.12(c) and 6.12(d)). This chaotic motion of the FG pipe develops through the intermittent transition route (T), and the corresponding transient responses of the FG pipe are shown in Figs. 6.12(a) and 6.12(b). This intermittent transition route (T) appears due to the nonexistence of stable periodic attractor beyond the cyclic-fold bifurcation at point A/A' (Fig. 6.11(b)). It is observed that this chaotic motion of the FG pipe mainly involves period-2, period-4 and period-6 attractors; where period-m attractor represents the periodic motion of the FG pipe with the frequency of Ω/m. The period-demultiplying and symmetry-breaking bifurcations are also observed within this chaotic motion of the FG pipe. However, the chaotic motion of the FG pipe continues up to the frequency (Ω) of 0.64 (K/K', Figs. 6.11(a) and 6.12(e)), and dual chaotic attractors (Figs. 6.12(f) and 6.12(g)) evolve for further increase of the frequency (Ω).

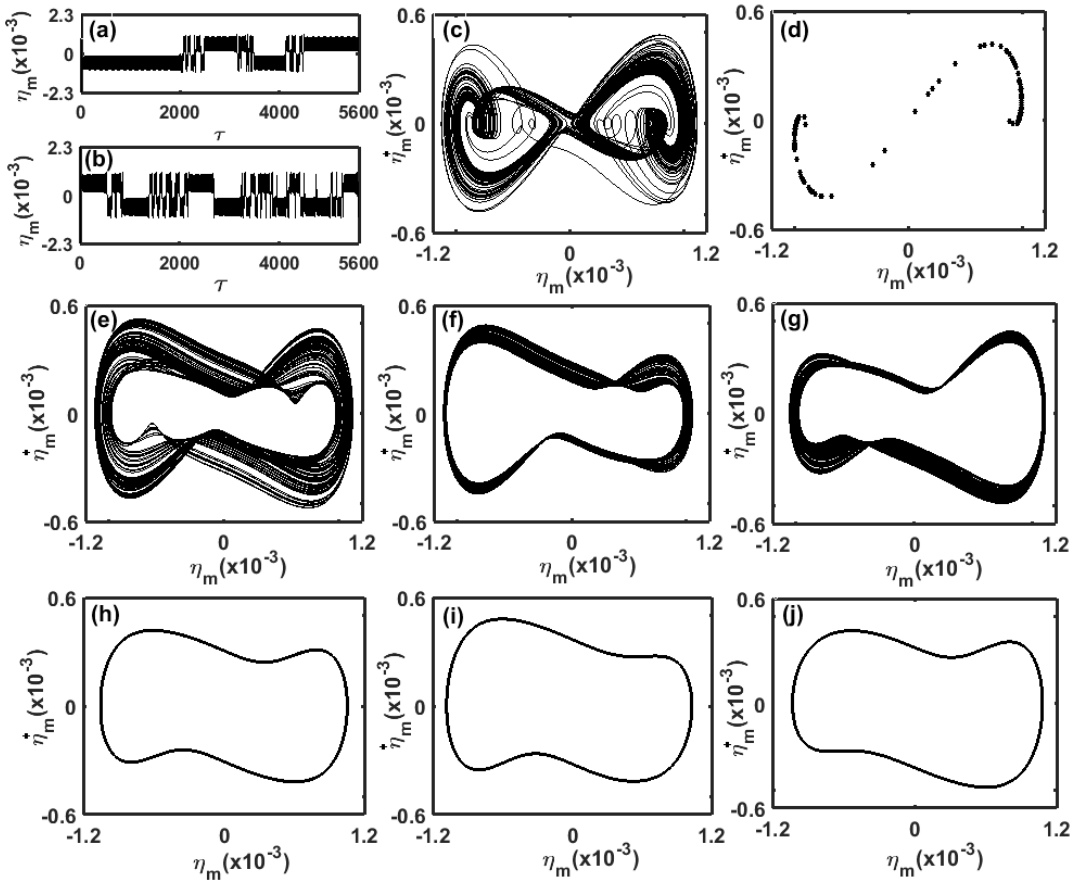

Fig. 6.12. Responses of the veritcal FG pipe at different frequencies ($n=5$, $V_f=5$ m/s, $\lambda=0.5$, $T_i=337.6$ K); transient responses at (a) $\Omega=0.3402$, (b) $\Omega=0.3403$; phase plots at (c) $\Omega=0.3403$, (e) $\Omega=0.64$, (f) $\Omega=0.66$, (g) $\Omega=0.66$, (h) $\Omega=0.85$, (i) $\Omega=0.9$, (j) $\Omega=0.9$; Poincare map at (d) $\Omega=0.3403$.

As the frequency increases, each of the dual chaotic attractors, first, reduces to the period-2 attractor through period-demultiplying bifurcation, and then this periodic motion (period-2) of the FG pipe undergoes the sequence of inverse

symmetry-breaking (B, $\Omega = 0.81$, Fig. 6.11(a)), symmetry-breaking (B', $\Omega = 0.86$, Fig. 6.11(a)) and inverse symmetry-breaking (B, $\Omega = 1.275$, Fig. 6.11(a)) bifurcations at points L/L', Q/Q' and E/E', respectively. The phenomenon of symmetry breaking bifurcation can be observed from Figs. 6.12(h)-(j); where single period-2 attractor (Fig. 6.12(h), $\Omega = 0.85$) reduces to dual period-2 attractors (Fig. 6.12(i)-(j), $\Omega = 0.9$) for an increase of the frequency (from $\Omega = 0.85$ to 0.9). For further increase of the frequency (Ω), a local chaotic attractor appears within a narrow frequency range ($\Omega = 1.92$ to 2.085, Fig. 6.11(a)) and it reduces to the local periodic attractors through the period-demultiplying bifurcation (D/D', Fig. 6.11(a)).

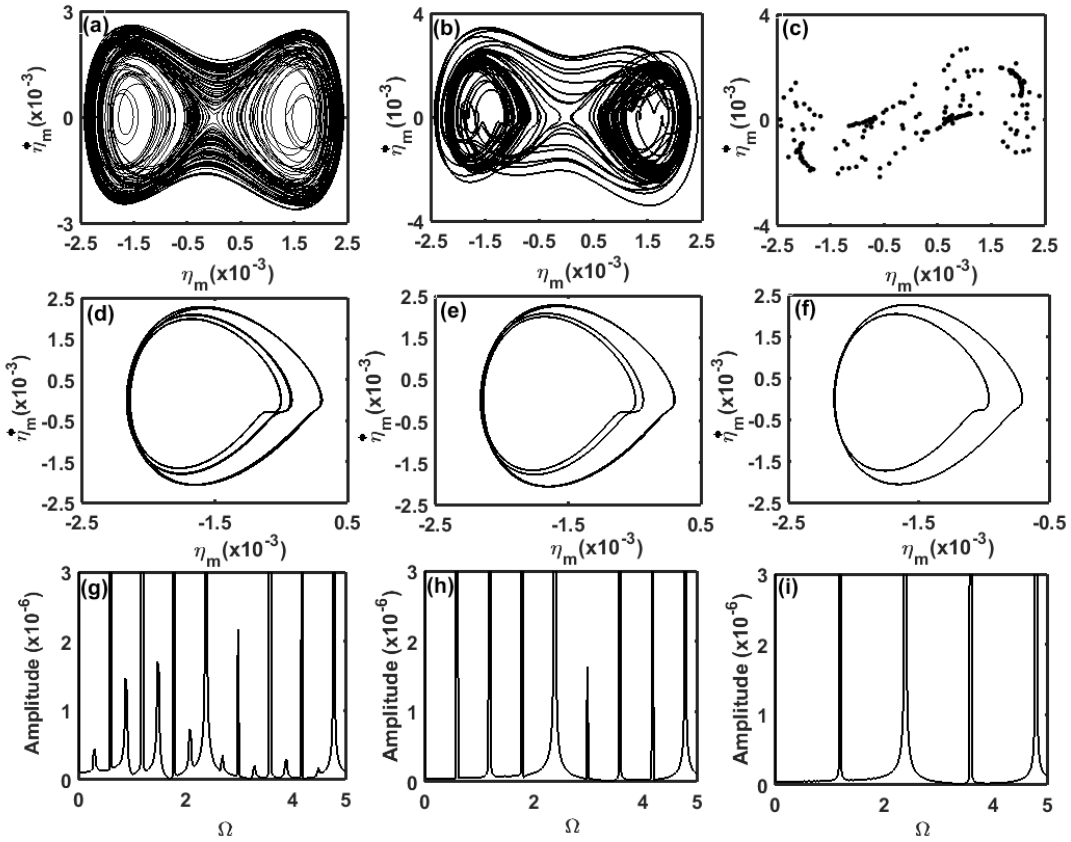

Fig. 6.13. Responses of the vertical FG pipe at different frequencies ($n = 5$, $V_f = 5$ m/s, $\lambda = 0.5$, $T_i = 339$ K); phase plots at (a) $\Omega = 2$, (b) $\Omega = 4.77$, (d) $\Omega = 4.785$, (e) $\Omega = 4.79$, (f) $\Omega = 4.8$; Poincare map at (c) $\Omega = 4.77$; amplitude-frequency spectrums at (g) $\Omega = 4.785$, (h) $\Omega = 4.79$, (i) $\Omega = 4.8$.

For an increase of temperature (T_i) of the internal fluid, the critical zone AE/A'E' shifts towards a high frequency (Ω) (Figs. 6.11(a) and 6.11(c)) and appears within a narrow frequency range. The chaotic motion of the FG pipe arises at any frequency within this critical zone AE as shown in Fig. 6.13(a) at a frequency of Ω = 2. However, as the frequency (Ω) increases, this chaotic

attractor reduces to period-2 attractor through the sequence of period-demultiplying (P, $\Omega = 2.05$ to 2.09) and inverse symmetry-breaking (B, $\Omega = 2.18$) bifurcations at points K/K' and E/E', respectively. The local periodic attractors also evolve through the period-demultiplying bifurcation ($\Omega = 2.57$, Fig. 6.11(c)) at points R/R'. For further increase of the frequency (Ω), these local periodic attractors reduce to the chaotic attractor through the subcritical bifurcation (points C/C', Figs. 6.11(c) and 6.11(d)). The corresponding chaotic motion of the FG pipe is illustrated in Figs. 6.13(b) and 6.13(c) at a frequency (Ω) of 4.77. For a little increase of the frequency (Ω), the period-demultiplying bifurcation arises (points D/D', Fig. 6.11(c)-(d)) where the motion of the FG pipe primarily involves period-16, period-8 and period-4 attractors as shown in Figs. 6.13(d)-(i). However, as the frequency (Ω) increases, this period-demultiplying bifurcation yields period-2 attractor corresponding to the principal primary parametric resonance of the FG pipe at its post-buckled equilibrium state.

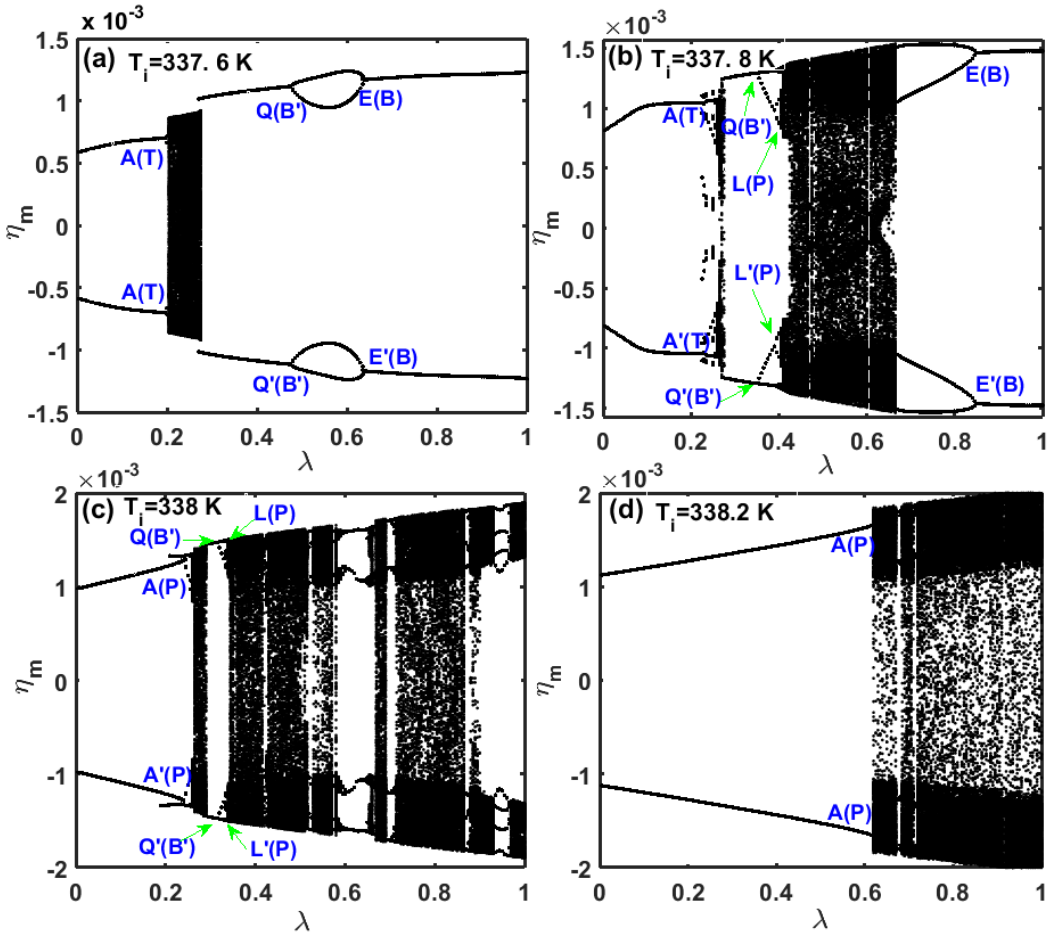

Fig. 6.14. Global bifurcation diagrams with respect to the pulsation velocity-amplitude ($n = 5, V_f = 5$ m/s, $\Omega = 1.23$) at different temperatures, (a) $T_i = 337.6$ K, (b) $T_i = 337.8$ K, (c) $T_i = 338$ K, (d) $T_i = 338.2$ K.

6.5.2.3.4.2 Global dynamics of the vertical FG pipe with respect to the pulsation velocity-amplitude

In order to investigate the effect of velocity-amplitude (λ) of pulsatile fluid flow on the complex dynamic response of the vertical FG pipe, the global bifurcation diagrams with respect to the velocity-amplitude (λ) of pulsatile fluid flow are illustrated in Figs. 6.14(a)-(d) for four different temperatures (T_i = 337.6 K, 337.8 K, 338 K, 338.2 K). The mean flow velocity (V_f) of pulsatile fluid flow and the graded exponent (n) of FGM are taken as 5 m/s and 5, respectively. The frequency (Ω) of pulsatile fluid flow is considered as 1.23 in such a manner that this frequency ($\Omega = 1.23$) lies within the critical zone AB at all temperatures (T_i = 337.6 K, 337.8 K, 338 K, 338.2 K).

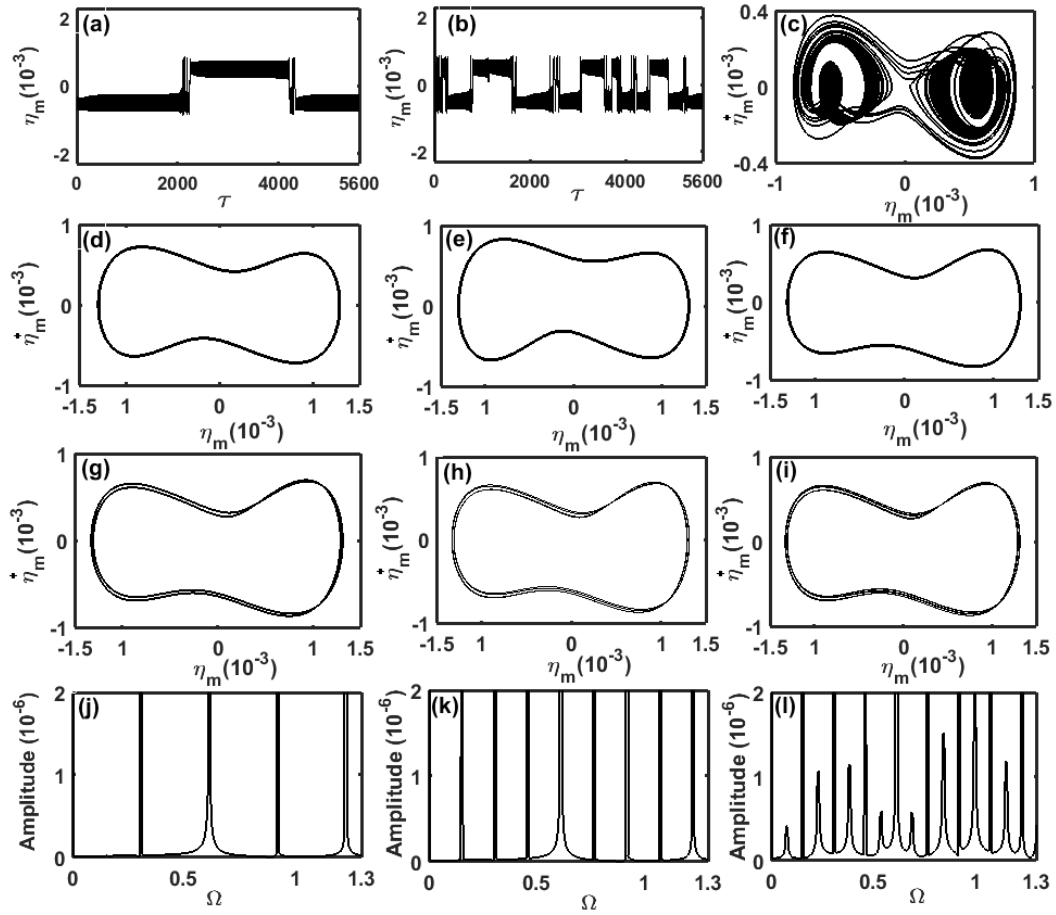

Fig. 6.15. Responses of the vertical FG pipe ($n = 5$, $V_f = 5$ m/s, $\Omega = 1.23$) at different pulsation velocity-amplitudes; time response plots at (a) $\lambda = 0.2025$ ($T_i = 337.6$ K), (b) $\lambda = 0.203$ ($T_i = 337.6$ K), phase plots at (c) $\lambda = 0.203$ ($T_i = 337.6$ K), (d) $\lambda = 0.35$ ($T_i = 337.8$ K), (e) $\lambda = 0.38$ ($T_i = 337.8$ K), (f) $\lambda = 0.38$ ($T_i = 337.8$ K), (g) $\lambda = 0.4$ ($T_i = 337.8$ K), (h) $\lambda = 0.402$ ($T_i = 337.8$ K), (i) $\lambda = 0.403$ ($T_i = 337.8$ K), amplitude-frequency spectrums at (j) $\lambda = 0.4$ ($T_i = 337.8$ K), (k) $\lambda = 0.402$ ($T_i = 337.8$ K), (l) $\lambda = 0.403$ ($T_i = 337.8$ K).

It may be observed from Figs. 6.14(a)-(d) that two periodic attractors arise at low velocity-amplitude (λ) of pulsatile fluid flow. As the velocity-amplitude (λ) increases at low temperature (Figs. 6.14(a)-(b)), the periodic attractors reduce to the chaotic attractor through the intermittent transition route (points A/A', Figs. 6.14(a)-(b)) (Figs. 6.15(a)-(c)). For further increase of velocity-amplitude (λ), one periodic attractor arises (Figs. 6.14(a)-(b)) corresponding to the snap-through motion (period-2) of the FG pipe. However, for a little increase of temperature ($T_i = 338$ K, 338.2 K, Figs. 6.14(c)-(d)), chaotic attractor arises through the period-doubling bifurcation (points A/A', Figs. 6.14(c)-(d)) instead of the intermittent transition route (points A/A', Figs. 6.14(a)-(b)). For an increase of velocity-amplitude (λ) at low temperature ($T_i = 337.6$ K), the snap-through motion may not fall into the chaotic motion again (Fig. 6.14(a)). But, it may appear (Figs. 6.14(b) and 6.14(c)) for a little increase of temperature ($T_i = 337.8$ K, 338 K) where the chaotic attractor appears through the sequence of symmetry-breaking (points Q/Q', Figs. 6.14(b)-(c)) and period-doubling bifurcations (points L/L', Figs. 6.14(b)-(c)). The symmetry-breaking bifurcation is illustrated through the phase plots in Figs. 6.15(d)-(f), where single period-2 attractor (Fig. 6.15(d), $\lambda = 0.35$) reduces to dual periodic attractors (Fig. 6.15(e)-(f), $\lambda = 0.38$) at a temperature (T_i) of 337.8 K. The period-doubling bifurcation is also illustrated through the phase plots in Figs. 6.15(f)-(i), where the period-2 attractor (Fig. 6.15(f), $\lambda = 0.38$) mainly reduces to period-4, period-8 and period-16 attractors (Figs. 6.15(g)-(l)) at a temperature (T_i) of 337.8 K. For further increase of temperature ($T_i = 338.2$ K), the nonlinear stiffness of the FG pipe increases because of its increased transverse deflection corresponding to the post-buckled equilibrium state. So, the periodic attractors remain up to a large value of the velocity-amplitude (λ) before the appearance of the chaotic attractor (points A/A', Fig. 6.14(d)).

6.5.3. Static/dynamic characteristics of the inclined FG pipe conveying hot fluid

In this section, first, the characteristics of divergence (buckling) of the inclined FG pipe conveying hot fluid are investigated based on the variations of inclination angle, temperature and graded material properties of FGM. Subsequently, the nonlinear dynamic responses as well as the corresponding instabilities of the inclined FG pipe are presented. Finally, the effects of the material damping of FGM on the dynamic characteristics of the inclined FG pipe are illustrated.

6.5.3.1. *Nonlinear response of the inclined FG pipe conveying hot fluid with constant flow velocity*

For an inclined pipe, the gravitational load is usually accounted by its two components along the axial and transverse directions to the length of the pipe. The axial component causes a small increase of the axial tension in the pipe, and it lowers the effect of transverse component that causes the transverse deflection of the pipe. However, this initial transverse deflection of the inclined pipe has certain effect on its (pipe) deformation characteristics under the forces associated with the fluid flow (Alfosail et al., 2017a; Gan et al., 2015; Monprapussorn et al., 2007; Wang and Bloom, 2001). So, first, the transverse deflection of the inclined FG pipe under the gravitational load is evaluated at the room temperature ($T_i = T_o = 300$ K). The corresponding static profiles of the FG pipe are illustrated in Fig. 6.16(a) for its different orientation angles (χ) with the vertical axis, where the graded exponent (n) of FGM is taken as 4 and the velocity of the internal fluid is assumed as zero ($V_f = 0$). However, the fluid velocity (V_f) is varied subsequently, and the corresponding variation of the maximum transverse deflection (η_m) of the inclined FG pipe is illustrated in Fig. 6.16(b) for different values of the graded exponent (n) at an inclination angle (χ) of 45^0. It may be observed from Fig. 6.16(a) that the maximum transverse deflection appears at the middle span ($\xi \approx$ 0.5) of the pipe for any inclination angle, and this transverse deflection increases for a higher inclination angle of the FG pipe. If the steady flow-velocity (V_f) of the fluid increases, then Fig. 6.16(b) shows a very small increase in the maximum transverse deflection (η_m) of the FG pipe due to the induced follower compressive force. The corresponding magnitude of static deflection (η) indicates an insignificant effect of the gravitational force on the static deflection of the inclined FG pipe conveying fluid with constant flow velocity, and it appears mainly due to the high stiffness of the FG pipe. However, a different observation is obtained when the inclined FG pipe conveys hot fluid with constant flow velocity as it is presented in the next result.

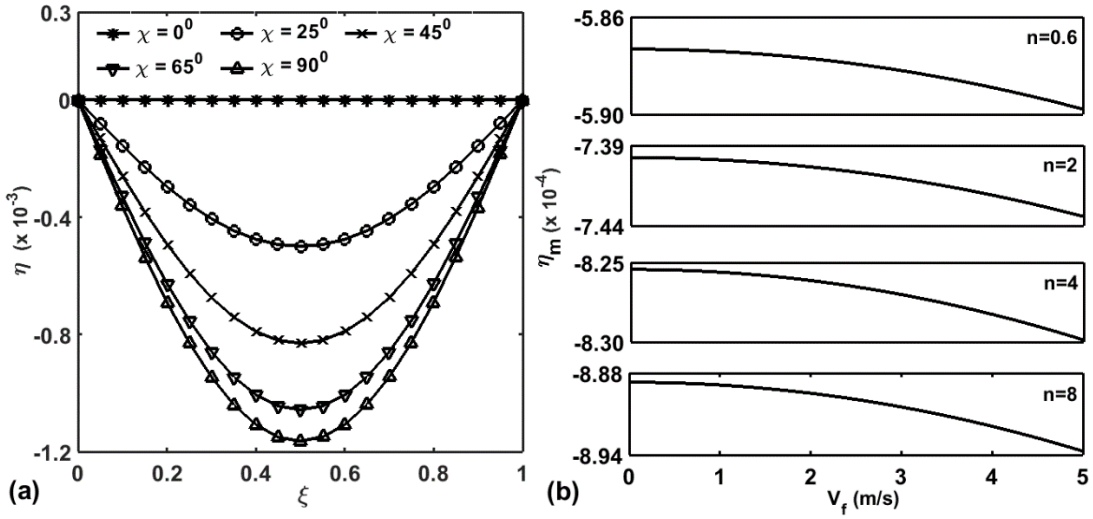

Fig. 6.16. (a) Variation of static profile of FG pipe ($n=4$) having the internal mass of fluid ($V_f=0$) for different values of the inclination angle, (b) variation of maximum transverse deflection (η_m) of the inclined FG pipe ($\chi=45^0$) with the steady flow velocity (V_f) of internal fluid for different values of the graded exponent (n) of FGM ($T_i=T_o=300$ K).

A FG pipe conveying hot fluid is susceptible to undergo the static instability (buckling) due to the combined effect of thermally induced compressive stress and the similar stress due to the flow velocity. However, the thermally induced stress is significantly higher than the stress induced due to the flow velocity (Qian et al., 2009), and thus the temperature in the pipe is more important parameter than the steady flow velocity in concern to its (pipe) static instability or buckling. So, the influence of temperature of hot fluid on the static (divergence) instability of the inclined FG pipe is first investigated through the results in Fig. 6.17. Here, the internal fluid is considered to flow with a steady flow velocity (V_f) of 5 m/s, and the variation of the maximum transverse deflection (η_m) of the FG pipe with the inner wall temperature ($T_i \neq 300$ K, $T_o = 300$ K) is illustrated for different values of the inclination angle (χ) and graded exponent (n) of FGM. For the vertical FG pipe ($\chi=0$), it may be observed from Fig. 6.17 that the divergence of the pipe appears through the pitchfork bifurcation (points P_1 and P_2) at a certain temperature that is called as the critical buckling temperature. The equilibrium state of the vertical FG pipe arrives at any of the two symmetric buckled equilibrium states (positive and negative) beyond the critical buckling temperature where an unstable equilibrium state also appears as indicated by the dotted line (blue dotted lines, Fig. 6.17). However, as the FG pipe becomes inclined one ($\chi \neq 0$), the aforesaid initial transverse deflection of the pipe arises due to the

gravitational load, and it causes the buckling of the FG pipe through the saddle-node bifurcation (points L_1, L_2, L_3, L_4, L_5, L_6, Fig. 6.17). The corresponding critical buckling temperature (at saddle-node bifurcation) is indicatively higher than that (at pitchfork bifurcation) for the vertical FG pipe ($\chi = 0$). Beyond the saddle-node bifurcation, the inclined FG pipe arrives at any of the positive and negative stable equilibrium states while an unstable equilibrium state also appears as it is indicated by the dotted line in Fig. 6.17. It is important to note from the results in Fig. 6.17 that a very small inclination of the FG pipe is sufficient to cause its divergence through the saddle-node bifurcation. However, as the angle of inclination increases, the buckling instability occurs at higher temperature while the corresponding critical buckling temperature decreases with the increase in the graded exponent (n) of FGM (Fig. 6.17).

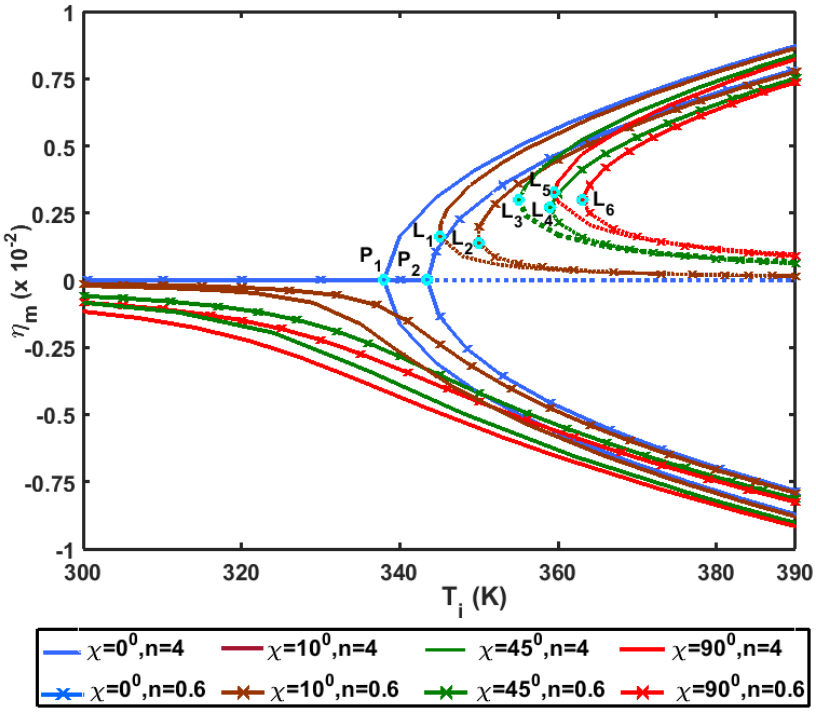

Fig. 6.17. Variation of the maximum transverse deflection (η_m) of the inclined FG pipe with the temperature (T_i) of the internal fluid (V_f = 5 m/s).

6.5.3.2. Nonlinear dynamic response of inclined FG pipe conveying pulsatile hot fluid

As discussed in the earlier section, the divergence of the FG pipe yields its two equilibrium states namely pre-buckled and post-buckled equilibrium states. For each of these equilibrium states of the FG pipe, its dynamic instabilities and the associated motion due to the pulsatile fluid flow are presently analyzed on the basis of the variations of some system parameters, namely temperature (T_i),

graded exponent (n) of FGM, mean flow velocity (V_f), pulsation amplitude (λ) and material damping of FGM.

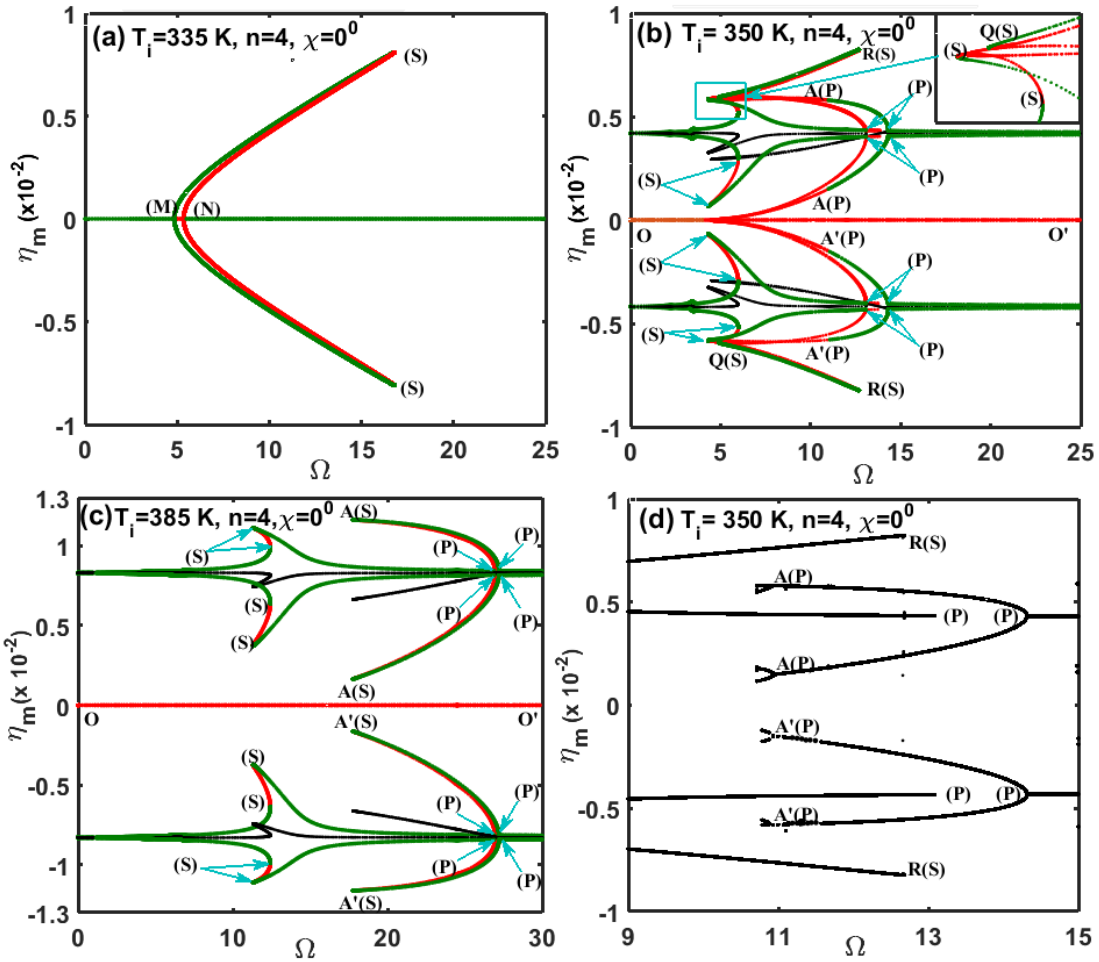

Fig. 6.18. Nonlinear frequency responses of the vertical FG pipe ($\chi = 0$) at its (a) pre-buckled state ($T_i = 335$ K) and (b)-(c) post-buckled state ($T_i = 350$ K, 385 K), (d) global bifurcation diagram with respect to pulsation frequency at the neighborhood of bifurcation points A and A′ in Fig. 18b ($n = 4$, $V_f = 5$ m/s and $\lambda = 0.5$).

6.5.3.2.1. Effect of temperature

The effect of temperature of the internal pulsatile fluid on the dynamics of the vertical FG pipe is investigated and presented in the above sections. This investigation is extended in this section for the inclined orientation of the same FG pipe, where the effect of temperature on the dynamics of the FG pipe is studied starting from the inclination angle as zero. Figure 6.18 illustrates the frequency responses of the FG pipe ($n = 4$) at different temperatures (T_i) when the inclination angle is zero ($\chi = 0$). For the pre-buckled state at a temperature (T_i) of 335 K, Fig. 6.18(a) shows the principal primary parametric resonance through the supercritical and subcritical pitchfork bifurcations (points M and N). However, as

the post-buckled state arises due to an increase in temperature (T_i) from 335 K to 350 K, the principal primary parametric resonance develops through the period doubling/period demultiplying bifurcation. Also, the stable periodic motion evolves (points A or A′ (Fig. 6.18(b)) through the period demultiplying bifurcation, as the corresponding global bifurcation diagram (Fig. 6.18(d)) reveals it to occur within a very small frequency band (near A or A′, Fig. 6.18(d)). However, if the temperature increases in the same (post-buckled) equilibrium state, then this stable periodic motion appears through the saddle-node bifurcation (A, A′, Fig. 6.18(c)). Also, the global periodic oscillation (period-2, QR in Fig. 6.18(b)) of the vertical FG pipe disappears.

The FG pipe is now taken at an inclined orientation ($\chi = 25^{o}$), and its frequency responses in the pre-buckled state are shown in Figs. 6.19(a) and 6.19(b) for two different temperatures (T_i) as 300 K and 335 K, respectively. Comparing the responses at the pre-buckled state of the FG pipe in Figs. 6.18(a) and 6.19(a), the inclination of the FG pipe causes a shift of its static equilibrium position towards the negative side ($\eta_m < 0$) due to the gravitational load. Also, the principal secondary parametric resonance (fundamental resonance) appears along with the principal primary one. Additionally, there is a little shift of the mean point of oscillation (black line, Fig. 6.19(a)) from the static equilibrium point especially when the inclined FG pipe undergoes principal primary parametric resonance. Here, the principal primary parametric resonance appears through the period doubling/period demultiplying bifurcation (Fig. 6.19(a)) instead of the pitchfork bifurcation (Fig. 6.18(a)) in the case of the vertical FG pipe. However, at a higher temperature ($T_i = 335$ K, Fig. 6.19(b)) in the same (pre-buckled) equilibrium state, the transverse deflection of the inclined FG pipe appears indicatively (Fig. 6.17), and thus the softening structural behavior of the FG pipe arises in addition to the hardening one as shown in Fig. 6.19(b) for the response via principal primary parametric resonance. In fact, the mean point of oscillation (black line, Fig. 6.19(b)) shifts towards the zero-line ($\eta_m = 0$), and it results in lesser curvature of the FG pipe at some frequencies leading to the appearance of its (pipe) hardening structural behavior. The corresponding exchange between the hardening and softening behavior of the FG pipe occurs through the saddle node bifurcation (C, D, Fig. 6.19(b)). It may also be observed from Figs. 6.19(a)-(b) that the oscillation of the inclined FG pipe via the fundamental resonance amplifies due to the increase in temperature (T_i) and the corresponding bifurcation (Fig.

6.19(b)) of the stable periodic oscillation occurs through the saddle-node bifurcation.

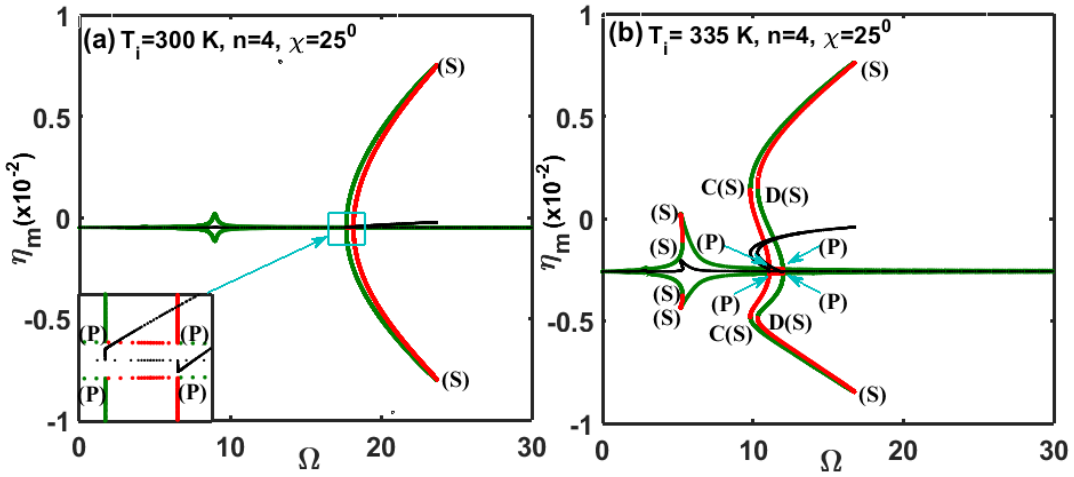

Fig. 6.19. Nonlinear frequency responses of the inclined FG pipe ($n=4$, $\lambda=0.5$, $V_f=5$ m/s, $\chi=25^0$) in the pre-buckled state for different temperatures; (a) $T_i=300$ K, (b) $T_i=335$ K.

As the temperature (T_i) increases, the inclined FG pipe undergoes static instability (buckling). The corresponding frequency response of the inclined FG pipe is illustrated in Fig. 6.20(a) for an inclination angle (χ) of 15^0. In contrast to the similar response of the vertical FG pipe (Fig. 6.18(b)) in the post-buckled state, the response of the inclined FG pipe in Fig. 6.20(a) exhibits unequal amplitudes of oscillation corresponding to its positive and negative buckled equilibrium positions. It appears due to the asymmetric buckled equilibrium positions of the inclined FG pipe with respect to the zero-line ($\eta_m=0$). However, the local primary parametric resonance about the buckled equilibrium positions appears through the period doubling/period demultiplying bifurcation (Fig. 6.20(a)) similar to the response in Fig. 6.18(b). Also, for the response in Fig. 6.20(a), the stable periodic oscillation of the inclined FG pipe corresponding to the local primary parametric resonance arises through the period demultiplying bifurcations at points A and A′ (Fig. 6.20(a)) similar to the response in Fig. 6.18(b). Additionally, similar stable periodic oscillation about the negative buckled equilibrium also arises in a very small frequency region through the saddle-node bifurcation (Point E′, Fig. 6.20(a)). The saddle-node bifurcation appears at all other points of bifurcation (Fig. 6.20(a)) except the point F′ where the period demultiplying bifurcation appears. Similar to the response in Fig. 6.18(b) for the vertical FG pipe, the response (Fig. 6.20(a)) of the inclined FG pipe involves both the global and local motions in a certain frequency range. But, the saddle-node (OO′, Fig. 6.18(b)) in the response of the vertical FG pipe becomes saddle periodic orbit (over OO', Fig. 6.20(a)) due to the

inclination. This saddle periodic orbit shifts towards the positive side ($\eta_m > 0$) from the zero-line ($\eta_m = 0$), and it results in smaller domain of attraction over the positive buckled equilibrium point than that over the negative buckled equilibrium point. It is shown in Fig. 6.20(c) through the plots of the basin of attraction, limit cycle attractors (green closed curves) and saddle periodic orbit (red closed curves) at a frequency of $\Omega = 9$.

For an increase of the inclination angle (χ) from 15^0 to 45^0, the corresponding changes of the frequency response can be observed from Figs. 6.20(a) and 6.20(b), where it is clear that the static equilibrium state of the FG pipe changes from post-buckled to pre-buckled state at the same temperature leading to simpler response. For the response in Fig. 6.20(b) at a higher inclination angle ($\chi = 45^o$) of the FG pipe, the stable periodic motion via principal primary parametric resonance arises through the period doubling/period demultiplying (Points F and B) and saddle-node (Point E) bifurcations. However, the bifurcation of the stable periodic motion via the fundamental resonance occurs through the saddle-node bifurcation (Fig. 6.20(b)). The aforesaid responses (Figs. 6.20(a)-(b)) of the inclined FG pipe show an indicative effect of the inclination angle on its (FG pipe) nonlinear dynamic characteristics.

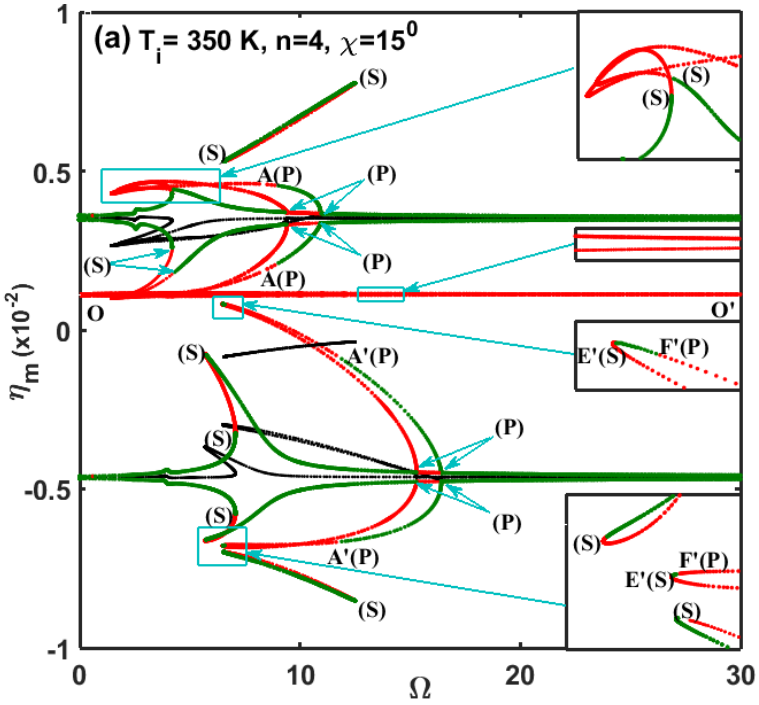

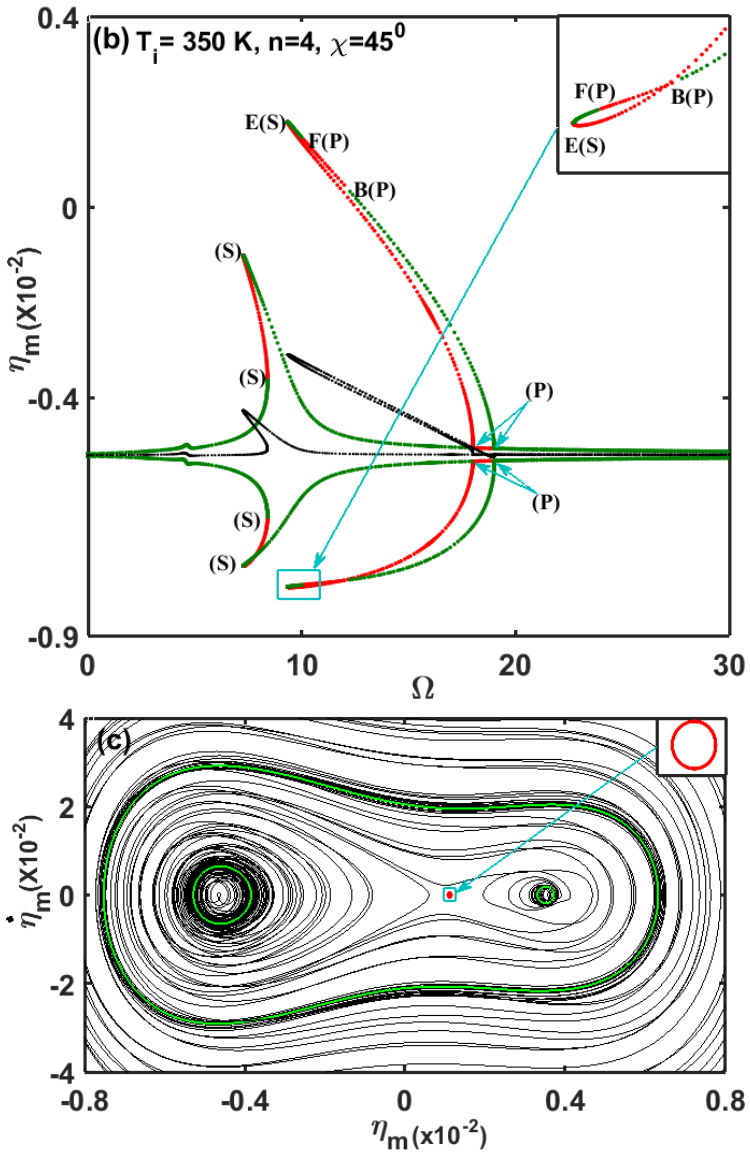

Fig. 6.20. Nonlinear frequency responses of the inclined FG pipe ($n=4$, $\lambda=0.5$, $V_f=5$ m/s) for (a) $\chi=15^0$, $T_i=350$ K and (b) $\chi=45^0$, $T_i=350$ K; (c) basin of attraction at a frequency of $\Omega=9$ corresponding to the frequency response in the case (a).

Figures 6.19(a)-(b) and 6.21(a)-(d) illustrate the changes in the nonlinear dynamic characteristics of the inclined FG pipe ($\chi=25^o$) with the gradual increase of temperature (T_i) as 300 K, 335 K, 344 K, 355 K, 385 K and 390 K. As the temperature increases from the room temperature (300 K) to 335 K or 344 K, the thermal deflection of the inclined FG pipe increases resulting in the simultaneous appearance of hardening and softening structural behavior of the pipe (Figs. 6.19(b) and 6.21(a)). The corresponding exchange between the softening and hardening structural behavior occurs either through the saddle-node bifurcation (Points C and D, Figs. 6.19(b)) or through the period doubling/period

demultiplying bifurcation (Points B and F, Fig. 6.21(a)). However, for further increase of temperature ($T_i = 355$ K, Fig. 6.21(b)), the inclined FG pipe undergoes buckling leading to the nonlinear frequency response, as shown in Fig. 6.21(b). The response in Fig. 6.21(b) is almost similar to that in Fig. 6.20(a); however, the only difference is in the appearance of the global snap-through motion of the FG pipe. It is observed that this global snap-through motion of the FG pipe appears for its low curvature that usually occurs at the post-buckled equilibrium state near the onset of buckling (divergence). However, it is important to notice from Fig. 6.21(b) or Fig. 6.20(a) that the natural frequency and the amplitude of oscillation of the FG pipe do not appear in an equal manner over its two buckled equilibrium states, and it arises due to the difference in the corresponding curvatures of the inclined pipe.

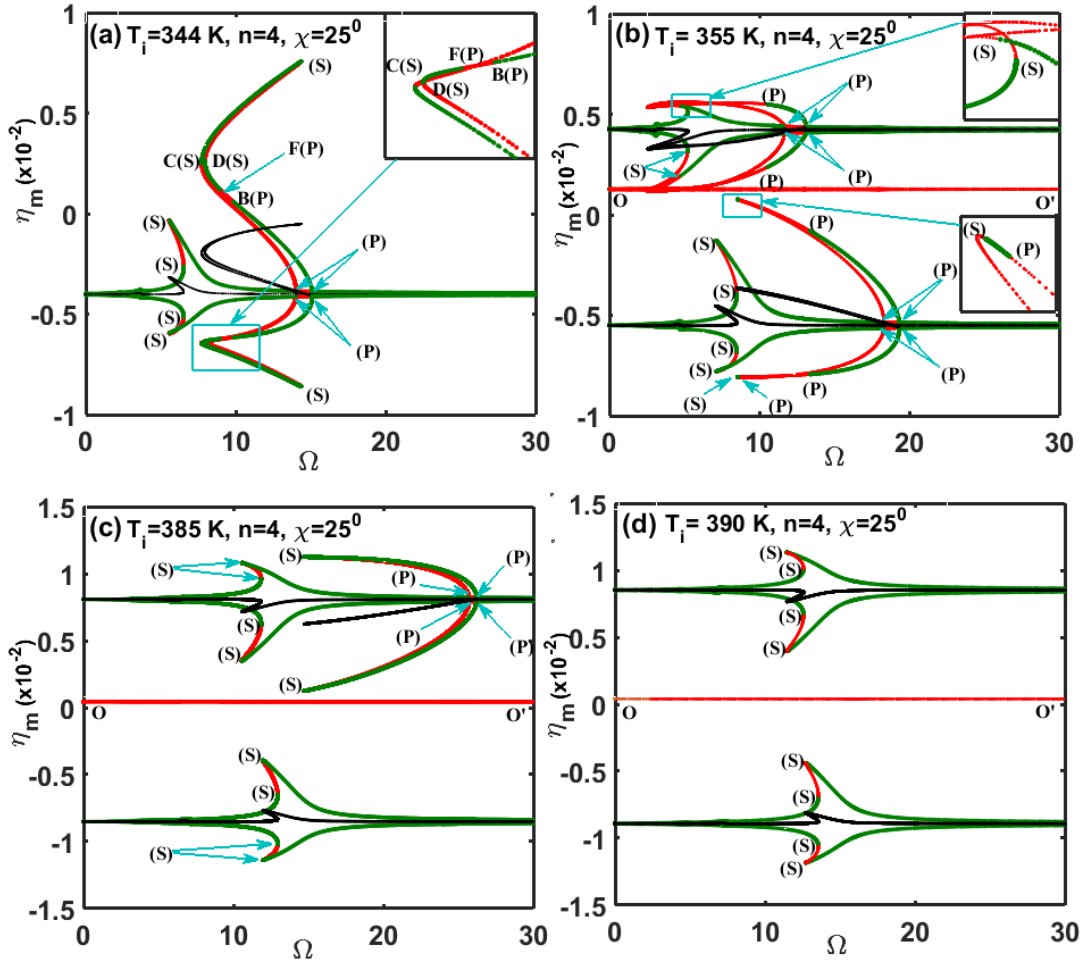

Fig. 6.21. Nonlinear frequency responses of the inclined FG pipe ($n = 4$, $\lambda = 0.5$, $V_f = 5$ m/s, $\chi = 25^0$) for different temperatures; (a) $T_i = 344$ K, (b) $T_i = 355$ K, (c) $T_i = 385$ K and (d) $T_i = 390$ K.

For further increase of temperature ($T_i = 385$K, Fig. 6.21(c)), the local principal primary parametric resonance corresponding to the buckled equilibrium

on the negative side ($\eta_m < 0$) disappears. However, the same also occurs corresponding to the buckled equilibrium on the positive side ($\eta_m > 0$) for a little more temperature ($T_i = 390$ K, Fig. 6.21(d)). This may be due to the fact that the nonlinear stiffness or curvature of the inclined FG pipe increases at a higher temperature (T_i). However, it is important to observe from Fig. 6.21(d) and Fig. 6.18(c) that the frequency response of the inclined FG pipe is almost similar to that for the vertical FG pipe, and it occurs at a high temperature in the post-buckled state of the FG pipe. It may also be observed from Figs. 6.21(b)-(d) that the saddle periodic orbit (OO′) shifts towards the zero-line ($\eta_m = 0$) with the increase in temperature leading to almost equal domains of attraction over the positive and negative post-buckled equilibrium states. It is corroborated in Fig. 6.22 through the plot of the basin of attraction at two different temperatures (T_i = 355 K, $T_i = 385$ K) with $\Omega = 7.5$. From these observations, it may be concluded that the nonlinear dynamic characteristics of the inclined FG pipe at a high temperature in its post-buckled state approach to that of the vertical FG pipe so that the angle of inclination of the FG pipe has minimal effect on its dynamic behavior.

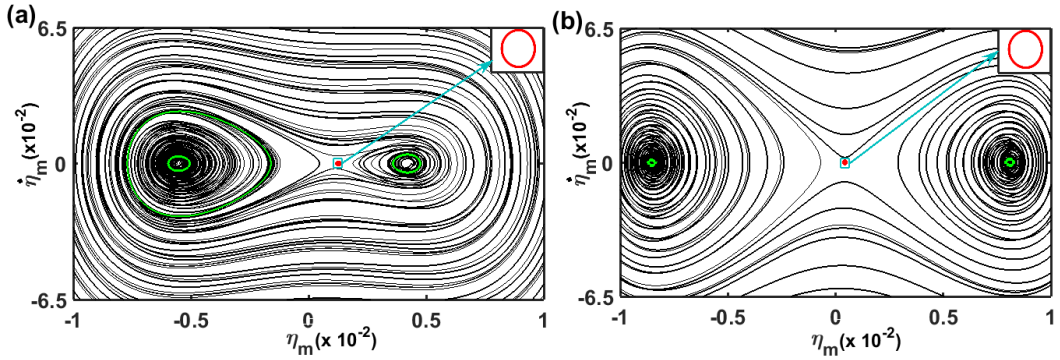

Fig. 6.22. Basin of attraction at a frequency of $\Omega = 7.5$ ($n = 4$, $\lambda = 0.5$, $V_f = 5$ m/s, $\chi = 25^0$) for two different temperatures; (a) $T_i = 355$ K and (b) $T_i = 385$ K (green closed curves are limit cycle attractors and red closed curve is saddle periodic orbit).

6.5.3.2.2. Effect of the graded exponent of FGM

A higher value of the graded exponent (n) of FGM means more volume fraction of the metal constituent resulting in softer FG pipe. Also, the corresponding decrease of the volume fraction of the ceramic constituent yields higher temperature at any point within the wall-thickness of the FG pipe under the specified surface temperatures. These two factors result in higher deflection of the FG pipe for an increase in the graded exponent without any change of the surface temperatures.

Now, at a low temperature, i.e. at the pre-buckled state of the FG pipe, its static profile or curvature appears because of its inclination ($\chi \neq 0$) (Fig. 6.17). This static deflection increases for a higher value of the graded exponent due to the aforesaid reasons. The effect of this greater static deflection on the dynamics of the inclined FG pipe ($\chi = 25^{o}$) conveying pulsatile fluid (V_f = 5m/s, λ = 0.5) is illustrated in Figs. 6.21(a) and 6.23(a) for an increase in the value of the graded exponent from 4 to 8 at a temperature (T_i) of 344 K. These results indicate the disappearance of the hardening structural behavior of the inclined FG pipe for an increase in the graded exponent. In contrast, similar change would not appear for a vertical FG pipe ($\chi = 0^{o}$), where the vertical FG pipe always behaves as a hardening structure since there is no initial static deflection at its pre-buckled state (at a low temperature) (Fig. 6.17).

At the post-buckled state of the inclined FG pipe, the aforesaid result indicates that the two (positive and negative) buckled equilibrium positions of the pipe are not symmetric with respect to the zero-line ($\eta_m = 0$), and it appears due to an inclination angle of the pipe. However, for an increase in the graded exponent (n) at a constant surface temperature (T_i), the curvature of the FG pipe corresponding to its positive/negative post-buckled equilibrium states increases. The corresponding effects on the dynamics of the inclined FG pipe ($\chi = 25^{o}$) at its post-buckled state are illustrated in Figs. 6.23(b) and 6.21(b) for an increase of the graded exponent from 2 to 4. It may be observed from these figures (Figs. 6.23(b) and 6.21(b)) that the global parametric resonance may disappear due to the increased curvature of the FG pipe at a higher value of the graded exponent. Also, for the increase in the graded exponent, the buckled equilibrium positions tends to be symmetric with respect to the zero-line ($\eta_m = 0$) leading to the similar dynamic responses of the inclined FG pipe over its positive and negative post-buckled equilibrium positions. So, a higher value of the graded exponent (n) of FGM yields reduced effect of the inclination angle on the dynamic characteristics of the FG pipe in its post-buckled state.

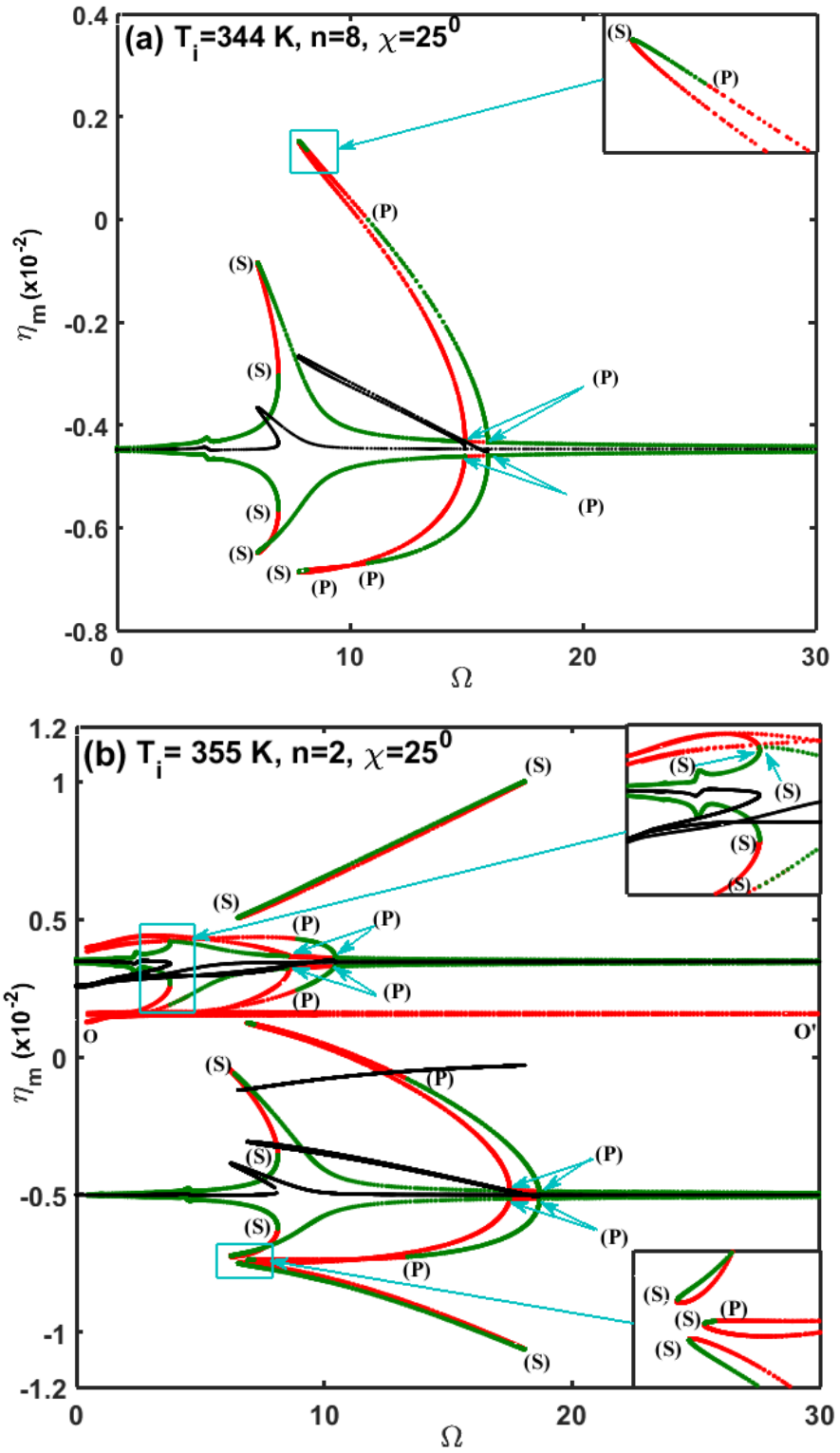

Fig. 6.23. Nonlinear frequency responses of the inclined FG pipe (V_f = 5 m/s, λ = 0.5, χ = 25º) for (a) T_i = 344 K, n = 8 and (b) T_i = 355 K, n = 2.

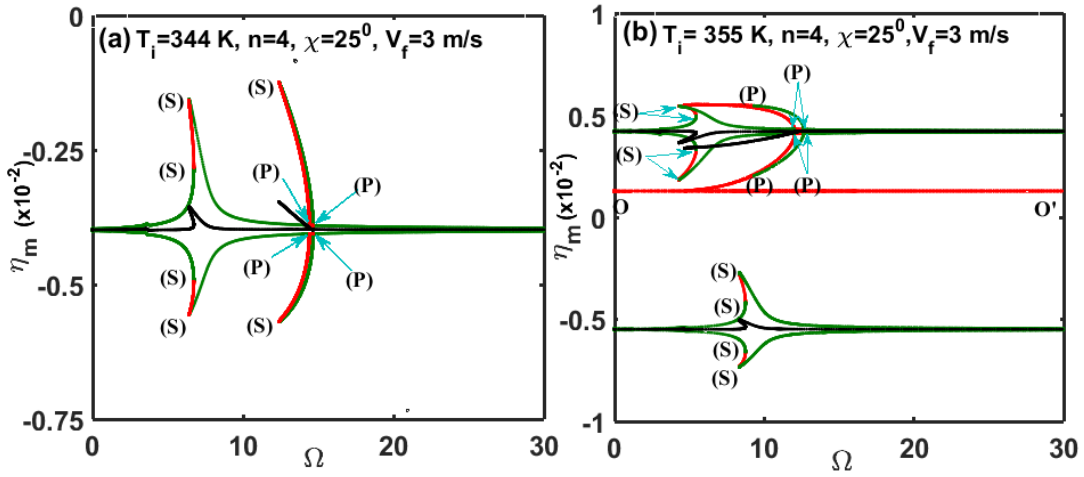

Fig. 6.24. Nonlinear frequency responses of the inclined FG pipe ($n=4$, $\lambda=0.5$, $\chi=25^0$) conveying pulsatile fluid with the flow velocity (V_f) of 3 m/s at two different temperatures; (a) $T_i=$ 344 K and (b) $T_i=$ 355 K.

6.5.3.2.3. Effect of the mean flow velocity and amplitude of the pulsatile fluid

The motion of the inclined pinned-pinned FG pipe arises due to the pulsatile flow of the internal fluid where the excitation parameters are the mean flow velocity (V_f) and the pulsation amplitude (λ). So, the effects of these parameters on the dynamics of the inclined FG pipe are investigated in this section. Figures 6.21(a) and 6.24(a) illustrate the nonlinear frequency responses of the inclined FG pipe ($\chi=25^o$) at its pre-buckled state for two different values of the mean flow velocity (V_f) as 5 m/s and 3 m/s, respectively. It may be observed from these results (Figs. 6.21(a) and 6.24(a)) that the curvature of the inclined FG pipe at its pre-buckled state increases for a higher mean flow velocity since the corresponding compressive stress in the pipe increases. Additionally, a higher mean flow velocity causes the oscillation of the inclined FG pipe with a greater displacement amplitude, where also a greater shift of the mean point of oscillation (black line) towards the zero-line ($\eta_m=0$) appears resulting in the appearance of the hardening structural behavior of the inclined FG pipe. In contrast, the vertical FG pipe has no initial curvature at its pre-buckled state, and thus it always behaves as a hardening structure. However, the amplitude of oscillation of the vertical FG pipe is expected to vary with the change of the mean flow velocity.

For a decrease in the mean flow velocity at the post-buckled state of the inclined FG pipe, Figs. 6.21(b) and 6.24(b) illustrate the corresponding changes in its (FG pipe) nonlinear dynamic behavior. It is clear from these results (Figs. 6.21(b) and 6.24(b)) that the principal primary parametric resonance over the

negative ($\eta_m < 0$) post-buckled equilibrium position disappears for a decrease of the mean flow velocity. Also, the displacement-amplitude of oscillation of the inclined FG pipe decreases. These observations infer simpler dynamics of the inclined FG pipe in its post-buckled state for a low mean flow velocity. Similar changes in the nonlinear dynamic characteristics of the pre or post-buckled inclined FG pipe are also observed for the variation of the pulsation amplitude (λ), and thus these results are not furnished here.

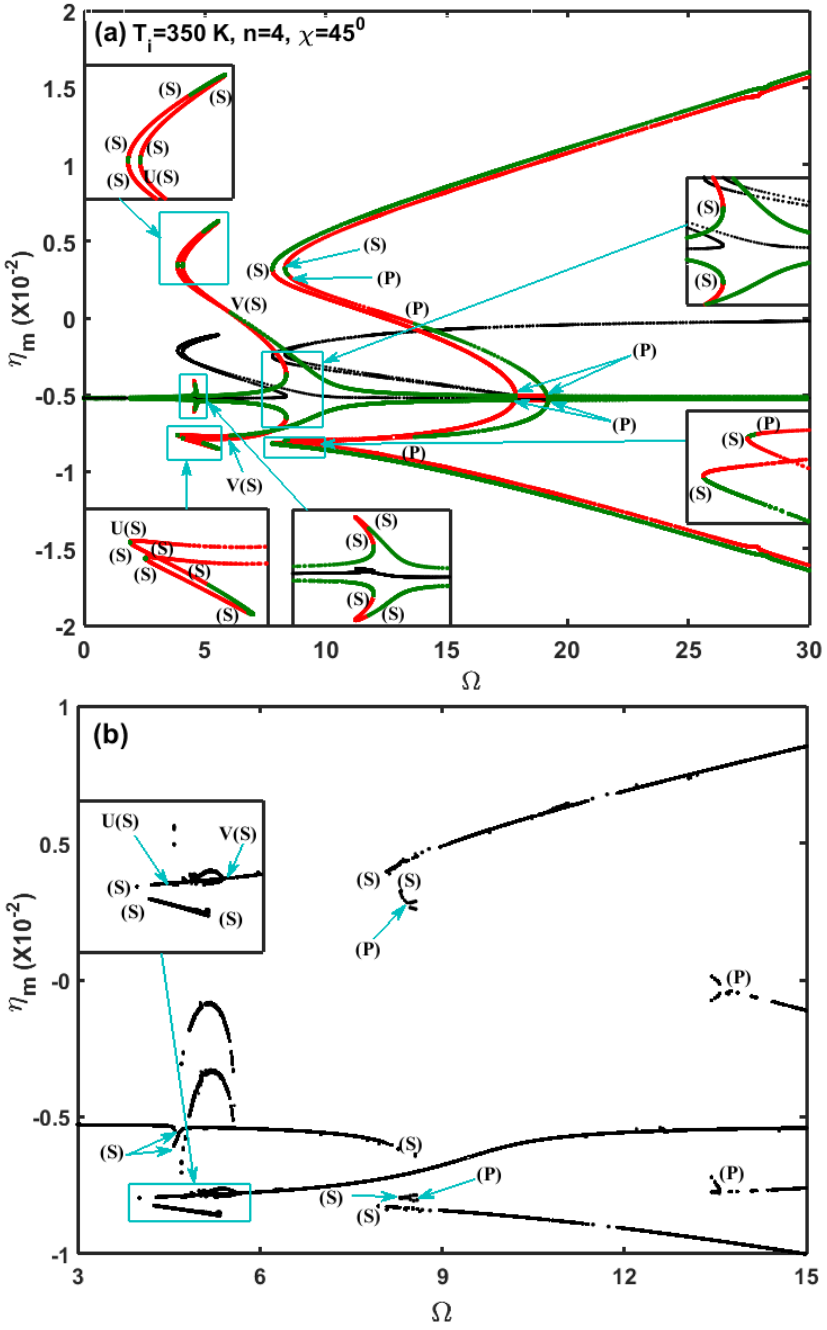

Fig. 6.25. (a) Nonlinear frequency response of the inclined FG pipe at its pre-buckled state (T_i = 350 K, χ = 45⁰) for a low material damping of FGM (r_τ = 0.00004 s, V_f = 5 m/s, λ = 0.5) and (b) the corresponding global bifurcation diagram.

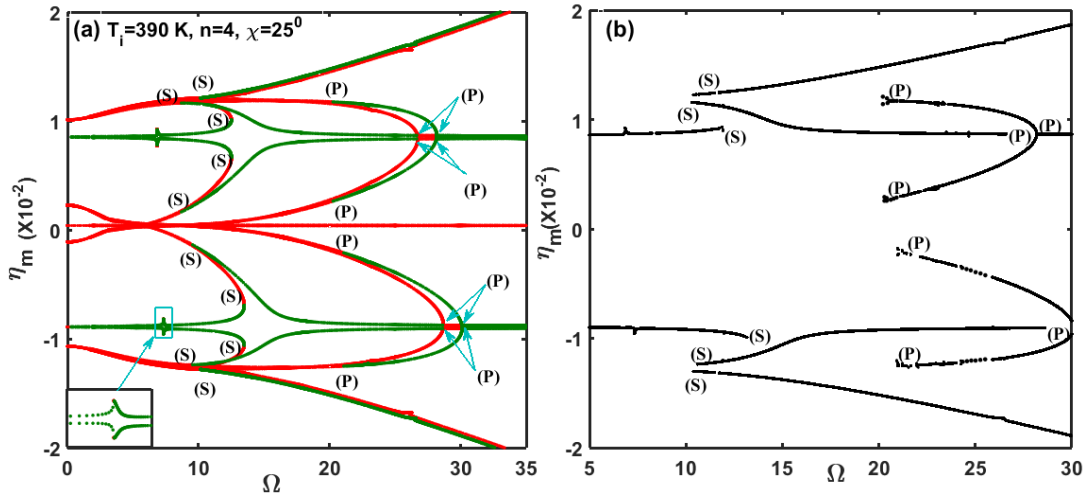

Fig. 6.26. (a) Nonlinear frequency response of the inclined FG pipe at its post-buckled state (T_i = 390 K, χ = 25⁰) for a low material damping of FGM (r_τ = 0.00004 s, V_f = 5 m/s, λ = 0.5) and (b) the corresponding global bifurcation diagram.

6.5.3.2.4. Effect of material damping of FGM

The material damping of the FGM is presently considered through its metal constituent with the assumption of no material damping in the ceramic constituent. The corresponding coefficient of Kelvin-Voigt dissipation parameter or retardation time (r_τ) for the metal constituent is considered as 0.0004 s (Bommakanti et al., 2016) in the evaluation of the aforesaid nonlinear dynamic responses of the FG pipe. However, for investigating the effect of the material damping of FGM on the dynamic behavior of the inclined FG pipe, the same parameter (r_τ) is taken with a lower value as 0.00004 s, and the earlier results in Figs. 6.20(b) and 6.21(d) are reevaluated as presented in Figs. 6.25(a) and 6.26(a).

For the pre-buckled state, it can be observed from Figs. 6.20(b) and 6.25(a) that the oscillation of the inclined FG pipe is amplified indicatively due to its (FG pipe) reduced material damping. Also, the oscillation of the FG pipe via parametric resonances appears in a wide range of frequency. More importantly, the hardening structural behavior of the FG pipe appears along with its softening behavior for both the principal primary and secondary parametric resonances (Fig. 6.25(a)). However, the frequency responses in Figs. 6.20(b) and 6.25(a) indicate a little more complex dynamic behavior of the inclined FG pipe in its pre-buckled state for a decrease of material damping of FGM. For a clarification of the corresponding bifurcation of motion of the inclined FG pipe, the global bifurcation diagram is illustrated in Fig. 6.25(b) for the frequency response in Fig. 6.25(a). It may be

observed from Fig. 6.25(b) that the bifurcation of periodic oscillation via principal primary parametric resonance occurs through period doubling/period demultiplying bifurcation while the bifurcation of similar motion via fundamental resonance occurs through saddle-node bifurcation similar to that for the response in Fig. 6.21(a). However, the higher order parametric resonance is also observed (Fig. 6.25(a)) for the low material damping. In the frequency region between points U and V, a period-4 attractor is also observed (Fig. 6.25(b)) along with the period-1 attractor via the fundamental resonance. These observations indicate the material damping of FGM as an important factor not only to attenuate the oscillation but also to reduce the complex nonlinear dynamic behavior of the FG pipe.

In the post-buckled state of the inclined FG pipe, the changes in its nonlinear dynamics for the aforesaid decrease in the material damping of FGM are clarified though the results in Figs. 6.21(d) and 6.26(a). As displayed in these results (Figs. 6.21(d) and 6.26(a)), the nonlinear dynamic response of the inclined FG pipe appears in a complex manner for a decrease in the material damping of FGM. This complex dynamic behavior of the inclined FG pipe arises mainly due to the extended response of the FG pipe over a wide range of frequency and also due to the appearance of the higher order parametric resonance (zoomed part in Fig. 6.26(a)). However, the corresponding global bifurcation diagram (Fig. 6.26(b)) reveals similar kinds of bifurcations of the periodic motion of the inclined FG pipe as that are observed for the response in Fig. 6.18(b).

6.6. Summary

In this chapter, the nonlinear dynamics of a pinned–pinned FG pipe conveying pulsatile hot fluid is investigated. The FG pipe is comprised of metal and ceramic constituents with the inner ceramic rich surface to withstand a high temperature of the internal hot fluid. The equation of motion of the fluid conveying FG pipe is derived based on the Euler–Bernoulli beam theory and plug-flow model, and that is subsequently solved using Galerkin discretization in conjunction with the incremental harmonic balance/Runge–Kutta method.

First, the static and dynamic characteristics of the fluid-conveying FG pipe are investigated for its vertical orientation. Here, the divergence characteristics revealed that the buckling of the FG pipe arises mainly because of the temperature of the internal fluid. The corresponding critical buckling temperature moderately varies with the graded exponent of FGM. With reference to the critical buckling temperature, the pre-buckled and post-buckled equilibrium states of the FG pipe are identified, and the nonlinear dynamics of the FG pipe is studied based on the

variations of some system parameters namely temperature, graded exponent of FGM, mean flow velocity, amplitude of pulsatile flow velocity and material damping. This study reveals the following observations.

(a) In the pre-buckled state of the vertical FG pipe, it mainly undergoes principal primary parametric resonance while the corresponding instability region shifts towards low velocity–amplitude of pulsatile fluid flow for an increase in temperature of the internal fluid or a decrease in the graded exponent of FGM. The usual shape of the parametric instability region deviates for a temperature of the internal fluid near the critical buckling temperature mainly due to the appearance of additional higher-order parametric resonances.

(b) In the post-buckled equilibrium state of the vertical FG pipe, it mainly undergoes principal primary and secondary parametric resonances. However, the principal primary parametric resonance may disappear at a high temperature of the internal fluid or for a low value of the graded exponent of FGM. If the temperature of the internal fluid decreases towards the critical buckling temperature, the snap-through periodic motion of the vertical FG pipe may also appear. For further decrease in temperature close to the critical buckling temperature, the chaotic motion of the FG pipe may arise through the cyclic-fold bifurcation, intermittent transition route, period-doubling bifurcation and subcritical bifurcation.

Next, the static and dynamic characteristics of the same FG pipe are studied for its inclined orientation. The inclination of the FG pipe causes its static deflection due to the gravity load. This static deflection increases significantly for an increase in the temperature of the internal fluid or the graded exponent of FGM. However, the steady flow velocity of the internal fluid has negligibly small effect on the static deflection of the inclined FG pipe. The inclined FG pipe undergoes buckling at a higher temperature in comparison to that for the vertical FG pipe. Also, the type of bifurcation of the equilibrium state changes from pitchfork to saddle–node bifurcation as the vertical orientation of the pipe is altered to the inclined one. The further study on the dynamic characteristics of the inclined FG pipe conveying hot pulsatile fluid reveals the following observations.

(a) In the pre-buckled state, the inclination causes the appearance of principal primary parametric resonance through the period doubling/period demultiplying bifurcation instead of the pitchfork bifurcation. Further, the principal secondary parametric resonance also appears while the corresponding amplitude of vibration of the FG pipe increases indicatively for

an increase in the temperature/graded exponent of FGM. The FG pipe exhibits either softening or hardening structural behavior during its vibration depending on the deflection of the FG pipe at the mean point of oscillation. The corresponding exchange of structural behavior occurs through the saddle–node/period doubling/period demultiplying bifurcation. The hardening structural behavior of the inclined FG pipe may disappear for an increase in temperature/graded exponent of FGM/ inclination angle.

(b) In the post buckled state, the negative and positive post-buckled equilibrium states are identified according to the deflections of the FG pipe along and opposite to its initial deflection under the gravitational load. However, the saddle periodic orbit is observed instead of the saddle–node associated with the zero equilibrium position. This saddle periodic orbit shifts towards the positive post-buckled equilibrium state due to an increase in the inclination angle or a decrease in the temperature, and it results in unequal domains of attraction or asymmetric dynamic responses over the positive and negative post-buckled equilibrium states.

(c) For an increase in the temperature of the internal fluid from the critical buckling temperature, the principal primary parametric resonance associated with the positive/negative post-buckled equilibrium state disappears. However, the higher order parametric resonances are also observed along with the principal parametric resonances for a low material damping of FGM.

(d) At a very high temperature of the internal fluid, the dynamic responses of the inclined FG pipe at its post-buckled state become similar to that of the vertical FG pipe. More importantly, the chaotic motion of the vertical FG pipe near the critical buckling temperature disappears once the pipe is taken in inclined orientation.

The overall analysis reveals that temperature of the internal pulsatile fluid is the primary concern for complex dynamic response of the FG pipe. However, the graded exponent of FGM and inclination angle may be utilized as the tuning parameters to alleviate the static/dynamic instabilities, as well as the associated complex dynamic responses, of the FG pipe.

Chapter 7

Conclusions and scope for future work

7.1. Conclusions

This dissertation deals with the nonlinear dynamics and active/passive control of parametrically excited beam-like slender structures. The overall study is presented in the preceding six chapters. The first chapter mainly presents a literature review on the (a) nonlinear dynamic characteristics, (b) active/passive control and (c) mathematical modeling of beam-like slender structures under the parametric excitation. A great deal of research towards the exploration of nonlinear dynamic characteristics of parametrically excited slender structures is observed in the open literature. Also, various mathematical modelling approaches are proposed, where most of the theoretical studies are carried out in the Galerkin or FE framework. However, the FE procedure provides the advantage of handling complex geometry and material configuration in a slender structure. But this numerical method of analysis involves a good computational time so that the analysis of nonlinear dynamics of slender structures using reduced-order FE formulation has been focused in the recent literature.

Besides the analysis of nonlinear dynamic characteristics, a good amount of research on the concern of controlling dynamic instabilities and the associated complex motion of parametrically excited slender structures is reported utilizing piezoelectric actuators, viscoelastic damping materials and FGMs. However, the research on the utilization of piezoelectric actuators is limited to extensional mode piezoelectric actuators, where also these actuators are applied to control the dynamic instability in the pre-buckled state of slender structures. In parallel, the utilization of the viscoelastic material is addressed through the CLD treatment; however, the corresponding available studies are limited to the passive control of parametric instability in the pre-buckled state of slender beams. Further, the application of FGMs is reported for improved static/dynamic stability of parametrically excited slender beams and fluid conveying pipes, especially under the thermal environment, where the corresponding available studies are limited to (a) the parametric instability in the pre-buckled state of slender beams and (b) the static stability and dynamics of fluid conveying pipes under the direct excitation.

On the basis of these observations from the literature survey, further research in this dissertation is carried out on the (a) usefulness of shear mode piezoelectric actuators in comparison to the extensional mode actuators for active control of parametrically excited beam-like slender structures, (b) utility of CLD treatment for attenuation of complex nonlinear dynamics of parametrically excited slender beams in the post-buckled state, (c) reduced-order FE modelling of CLD treated slender beams under direct/parametric excitation and (d) effect of graded properties of a vertical/inclined FG pipe on its nonlinear dynamic characteristics while the pipe conveys hot fluid with steady/pulsatile flow velocity. These studies are presented in the subsequent five chapters and summarized here in the following paragraphs.

First, the usefulness of piezoelectric actuators in active control of dynamic instabilities and the associated complex motion of parametrically excited beams is investigated. Both kinds of piezoelectric actuators, namely shear and extensional mode actuators, are used separately by configuring two different smart beams under the direct/parametric excitation. The first smart beam is configured by attaching the extensional mode piezoelectric actuators to the top and bottom surfaces of the host beam. However, the second smart beam is configured as a sandwich beam with a foam core, where shear mode piezoelectric actuator patches are embedded in the core. These smart beams are configured following the working principle of the actuators in control of bending deformation of a beam element, since the instability and the associated motion of the parametrically excited smart beams appear through their bending mode of deformation. The volumes of the actuator patches and the substrate material are kept constant for both kinds of smart beams. Also, both kinds of piezoelectric patches are activated in uniform manner according to the velocity feedback control strategy, especially for making a comparison study on their actuation capabilities in controlling the smart beams under the direct/parametric excitation. The dynamics of the smart beams is studied by deriving closed-loop FE models in the time and frequency domains, where the HBM is employed to convert the FE equations of motion from time to frequency domain. The numerical results reveal the following salient observations.

(i) For a smart slender beam under the forced excitation, the resonant displacement-amplitude can be reduced to the desired range by increasing the control gain, while there is no significant change in the corresponding externally applied electric field to the actuators. However, the externally applied electric field significantly increases with the increasing load-amplitude of the forced excitation. In this concern, the extensional mode

actuators are capable of working up to a large extent of the load-amplitude in comparison to that for the shear mode actuators.

(ii) The parametric instability of the smart beams is not only confined to the corresponding instability region but also dependent on the external disturbance that ensues transverse deflection of the beams. However, once the dynamic instability of a smart beam arises for any of the reasons, the shear mode actuator needs significantly more applied electric field for the attenuation of the corresponding oscillation than that for the extensional mode actuator.

(iii) In the post-buckled state of the smart beams, the complex motion of the beams appears through two local periodic attractors, snap-through periodic motion and the chaotic motion. However, with the increase in the control gain, first, the global snap-through motion diminishes, and then the chaotic motion reduces to simple period-1 response corresponding to the buckled equilibrium states. But the corresponding requirement of the external electric field for the shear mode actuator is significantly more than that for the extensional mode actuator. This difference further increases with the increase in the load parameters.

These observations suggest extensional mode piezoelectric actuator instead of shear mode actuator for controlling complex dynamics of smart beams under direct/parametric excitation. However, the next study is carried out to investigate the usefulness of the CLD treatment in passive control of complex dynamics of a parametrically excited beam. A geometrically nonlinear FE model of the CLD treated beam in the frequency domain is derived using HBM, and the dynamic analysis is performed mainly by evaluating nonlinear frequency responses. However, an FE model of the same beam in the time domain is also derived to construct global bifurcation diagram within a range of excitation frequency, especially to trace various dynamic instabilities/bifurcations.

The HBM-based FE model of the CLD treated beam is formulated by implementing HBM prior to the FE discretization, since the viscoelastic constitutive relations involve temporal derivative/integral of stress/strain. Accordingly, the FE formulation starts with the implementation of HBM over the constitutive relations. However, presently this reduction of viscoelastic constitutive relations using HBM is presented for different constitutive models, namely Kelvin-Voigt model, Zener model, fractional Zener model, Maxwell model, generalized Maxwell model and Hereditary integral approach. All these constitutive models are reduced to a generalized mathematical form for the time-

periodic stress/strain so that there is no need of separate HBM-based FE formulation of a viscoelastic structure when the mathematical form changes from one to another viscoelastic constitutive relation.

However, the HBM-based reduced form of viscoelastic constitutive relations pose the complexity in the subsequent FE formulation, especially for deriving a large expression of the HBM-based expanded form of geometrically nonlinear stiffness matrix with an arbitrary number of harmonic terms. This derivation is presently tackled by introducing a special factorization of nonlinear strain-displacement matrix in terms of a linear strain-displacement matrix and a nodal displacement matrix. However, in the corresponding long expression of the nonlinear stiffness matrix, every stiffness term is composed of a linear stiffness coefficient matrix associated with the product of sine and cosine functions. According to the HBM, these stiffness terms are commonly integrated over a time period using a numerical time-integration method. But it involves high computational time mainly because of a large number of stiffness terms as well as a large number of nodal degrees of freedom in the FE model. So, presently the orthogonally of Fourier basis functions is exploited to perform analytical time-integration towards a reduced computational time. This analytical time-integration strategy also provides an additional advantage of reducing the number of stiffness terms in the HBM-based expanded form of the nonlinear stiffness matrix. However, besides these new strategies in the formulation of HBM-based FE model of CLD treated beams, the numerical results reveal the following observations.

(i) The computational time in the evaluation of nonlinear frequency responses reduces significantly when the present analytical time-integration strategy is used instead of a conventional numerical time-integration method.

(ii) The accuracy in the estimation of nonlinear frequency responses of CLD treated beams varies from one viscoelastic constitutive model to another. In this concern, the present study recommends fractional Zener model, generalized Maxwell model and Hereditary integral approach.

(iii) The formulation of the tangent stiffness matrix may be simplified by avoiding its viscoelastic counterpart. This simplification poses somewhat inaccuracy in the computation of the tangent stiffness matrix; however, it is observed that there is no difficulty in the convergence of nonlinear solution through Newton-Raphson iterations for the present problem of a CLD treated beam. Additionally, this simplified formulation of the tangent stiffness matrix provides the advantage of reduced computational time in the evaluation of nonlinear frequency responses of CLD treated beams.

However, for further reduction of the computational time in the evaluation of nonlinear dynamic responses of CLD treated beams, the aforesaid full-order FE model is reduced to a reduced-order FE model (ROM). For deriving this ROM, the reduced basis vectors (RBVs) may be computed using either of MSE, MSEC, MM, ICES, RKT and FSRK approaches. But these approaches are originally proposed for linear dynamic analysis of viscoelastic structures. So, RBVs computed through these approaches may not provide sufficient accuracy in the nonlinear ROM of a viscoelastic structure. Therefore, for the present nonlinear ROM of CLD treated beams, RBVs obtained through the aforesaid approaches are enriched using static derivatives (SDs). Here, SDs may not be orthogonal to RBVs so that the proper orthogonal decomposition (POD) method is applied over the union of RBVs and SDs. The resulting proper orthogonal modes (POMs) are utilized as the enriched RBVs for the derivation of nonlinear ROM of CLD treated beams. However, the ROM can be formulated following the conventional approaches where the reduced-order system matrices/vectors are derived from the similar matrices/vectors obtained from the full-order FE model. But, in this process, the reduction of the computational time cannot be achieved appreciably due to the involvement of full-order FE model. So, presently a formulation of the nonlinear ROM in the elemental level is introduced without involving the full-order system matrices/vectors.

The nonlinear ROM of the CLD treated beams is derived in both the time and frequency domains based on the fractional Zener constitutive model, where the complexity mainly arises in the derivation of the reduced-order nonlinear system matrices and vectors, namely nonlinear stiffness matrix, tangent stiffness matrix and memory load-vector. The formulation of the reduced-order nonlinear stiffness and tangent stiffness matrices in the elemental level is performed by using the aforesaid factorization of nonlinear strain-displacement matrix. However, the reduced-order nonlinear memory-load vector is formulated in the elemental level by introducing two new anelastic forces. The accuracy of these nonlinear ROMs of CLD treated beams is verified with reference to the full-order FE model. It is observed that the required number of enriched RBVs towards the sufficient accuracy in the numerical results varies from one to another approach (MSE, MSEC, MM, ICES, RKT and FSRK), where the present enrichment of RBVs through ICES approach provides most accurate result with less number of enriched RBVs as compared to the other approaches. It is also observed that the present enriched RBVs and ROMs are capable of estimating very complex nonlinear frequency responses and dynamic bifurcations of CLD treated beams under the parametric excitation. Also, the computational time in the evaluation

of these complex dynamic responses reduces significantly for the formulation of the ROMs in the elemental level.

However, in the subsequent step, these ROMs are utilized to investigate the usefulness of the CLD treatment in passive control of complex dynamics of parametrically excited post-buckled beams. This investigation is carried out by configuring the CLD treatment in three different layered beams. The first one is the PCLD configuration, where a thin elastic layer constrains a viscoelastic damping layer against the top surface of the host beam. The second one is a three-layered sandwich beam with the viscoelastic core, and the third one is a multi-layered beam with two identical constrained viscoelastic layers. All the layered beams are considered to operate under an axial compressive harmonic load applied through the fixed support ends of the beams. The volumes of viscoelastic layers and substrate/elastic layers do not vary from one to another layered beam. Also, the applied load is kept constant for all the layered beams, and the damping effectiveness of each of the CLD configurations is studied in attenuation of the complex dynamics of the layered beams, mainly in their post-buckled equilibrium state. The corresponding numerical results reveal the following observations.

(i) The PCLD treated beam possess greater stability under the static axial compressive load as compared to other two configurations of layered beams. So, the PCLD configuration may be preferred for a CLD treated beam under the parametric excitation. But, it is observed that the amplitude of vibration of the PCLD treated beam corresponding to its dynamic instability in the pre-buckled state is significantly more than that of the buckled three/five-layered beam. Therefore, the three/five layered configuration may be used for better control of dynamics of a CLD treated beam provided that the possible buckled deflection of the beam is to be accommodated in an application.

(ii) In the post-buckled state, the viscoelastic layered beams undergo very complex motion involving various dynamic instabilities and chaotic oscillations. Also, these layered beams undergo the large-amplitude vibration through the snap-through periodic oscillation with respect to the zero equilibrium state. The CLD treatment is capable of attenuating this complex dynamics as well as large-amplitude vibration through three-layered or five-layered configuration. However, the PCLD configuration is not a suitable one for controlling this complex dynamics.

Further study is carried out for investigating the nonlinear dynamics of a pinned-pinned vertical/inclined FG pipe conveying hot fluid with steady/pulsatile flow velocity. The FG pipe is comprised of metal and ceramic constituents with

the inner ceramic rich surface to withstand the high temperature of internal hot fluid. The slender FG pipe is modeled using Euler-Bernoulli beam theory while the fluid flow is modeled by the assumption of plug-flow. The governing equation of motion is derived employing Hamilton's principle, and subsequently it is solved through the Galerkin discretization, where the HBM and adaptive Runge-Kutta method are employed for evaluation of the numerical results in the frequency and time domains, respectively.

First, the effects of the gravitational load and the temperature of the internal fluid on the static deflection of the FG pipe are investigated for its (pipe) different inclination angles with the vertical axis, where the internal mass of fluid is considered with or without steady flow velocity. It is observed that the inclined FG pipe undergoes a very small static deflection (transverse to its length) due to the gravitational load whereas a vertical FG pipe does not have such an initial deflection. Because of this initial small deflection, thermally induced deformation characteristics of the inclined FG pipe differ indicatively from that of the vertical FG pipe like (i) the inclined FG pipe has an indicative thermal deflection at its pre-buckled state whereas a vertical FG pipe does not undergo similar thermal deflection, (ii) the buckling of the inclined FG pipe appears through the saddle-node bifurcation whereas the vertical FG pipe undergoes buckling through the pitchfork bifurcation, (iii) the critical buckling temperature of the FG pipe increases indicatively as its vertical orientation changes to inclined one.

Next, the dynamics of the vertical or inclined FG pipe conveying hot fluid with pulsatile flow velocity is studied, where the temperature of the fluid is increased gradually for investigating the characteristics of motion of the FG pipe corresponding to its pre-buckled and post-buckled equilibrium states. In the pre-buckled state, the vertical FG pipe undergoes principal primary parametric resonance through the pitchfork bifurcation. However, similar resonance in case of the inclined FG pipe evolves through the period doubling bifurcation. The inclination of the FG pipe from the vertical axis may cause the appearance of the principal secondary parametric resonance in the pre-buckled state. As the inclined FG pipe undergoes an indicative thermo-elastic deflection at its pre-buckled state, it mainly behaves as a softening structure. However, a significant change in the mean point of oscillation of the inclined FG pipe is observed during its motion via resonances, and it causes the appearance of hardening structural behavior of the inclined FG pipe at some frequency range. The exchange between the hardening and softening behavior of the inclined FG pipe occurs through saddle-node/period doubling/period demultiplying bifurcation. A higher value of the graded exponent of FGM may cause the disappearance of the hardening

behavior of the FG pipe but it may retain for a higher mean flow velocity or amplitude of pulsating fluid flow.

In the post-buckled state of the vertical/inclined FG pipe, its motion appears with respect to one of the stable post-buckled equilibrium states via the principal primary and secondary parametric resonances, where the stable periodic oscillation of the pipe evolves through the period demultiplying/period doubling/saddle-node bifurcation. Additionally, a stable global periodic oscillation of the FG pipe encircling the post-buckled equilibrium positions (snap-through oscillations) may also appear at the post-buckled state near to the onset of the static instability (buckling). Also, the chaotic motion involving snap-through motion may arise for vertical FG pipe depending on the temperature, pulsatile flow parameters and graded exponent of FGM. Further complexity in the oscillatory motion of the FG pipe via parametric resonances may arise due to the appearance of higher order parametric resonances under the low material damping of FGM. It is observed that the inclination of the FG pipe induces the saddle periodic orbit instead of the saddle node. This saddle periodic orbit shifts towards the one of the stable post-buckled equilibrium states due to the inclination of the FG pipe and temperature, and it results unequal domains of attraction, as well as natural frequencies, over the two stable post-buckled equilibrium positions. This effect of inclination of the FG pipe disappears at a very high temperature and/or at a high value of the graded exponent of FGM so that the dynamic behavior of the inclined FG at its post-buckled state becomes as similar to that of the vertical FG pipe.

These observations indicate that the temperature of the internal pulsatile fluid is the main concern for the complex dynamics of the FG pipe, where the graded exponent of FGM and inclination angle may be utilized as the tuning parameters to alleviate static/dynamic instabilities and the associated complex motion of the FG pipe.

7.2 Scope of future work

Although the preceding chapters of this thesis fulfil the objectives of the present dissertation, some of the future work which may be readily undertaken in line with the present work are as follows.

1. Design of viscoelastic damping treatment for passive control of nonlinear dynamics of fluid conveying pipes.
2. Usefullness of FGM for heat exchanger tubes.

3. FGMs for marine riser in the presence of vortex induced vibration and internal flow.
4. Hybrid damping treatments for control of complex dynamics of slender structures in the post-buckled state.
5. Development of reduced-order FE models in conjuction with corotational formulation.

References

Abou-Rayan, A.M., Nayfeh, A.H., Mook, D.T., Nayfeh, M.A., 1993. Nonlinear response of a parametrically excited buckled beam. Nonlinear Dyn. 4, 499–525.

Ahuja, R., Duffield, R., 1975. Parametric instability of variable cross-section beams resting on an elastic foundation. J. Sound Vib. 39, 159–174.

Alfosail, F.K., Nayfeh, A.H., Younis, M.I., 2017a. Natural frequencies and mode shapes of statically deformed inclined risers. Int. J. Non. Linear. Mech. 94, 12–19.

Alfosail, F.K., Nayfeh, A.H., Younis, M.I., 2017b. An analytic solution of the static problem of inclined risers conveying fluid. Meccanica 52, 1175–1187.

Alhazza, K.A., Daqaq, M.F., Nayfeh, A.H., Inman, D.J., 2008. Non-linear vibrations of parametrically excited cantilever beams subjected to non-linear delayed-feedback control. Int. J. Non. Linear. Mech. 43, 801–812.

Alibeigloo, A., 2010. Thermoelasticity analysis of functionally graded beam with integrated surface piezoelectric layers. Compos. Struct. 92, 1535–1543.

Allen, M.S., Rixen, D., van der Seijs, M., Tiso, P., Abrahamsson, T., Mayes, R.L., 2020. Model reduction concepts and substructuring approaches for nonlinear systems. Substruct. Eng. Dyn. 233–267.

Amabili, M., 2008. Nonlinear vibrations and stability of shells and plates. Cambridge University Press.

Amabili, M., Balasubramanian, P., Breslavsky, I., 2019. Anisotropic fractional viscoelastic constitutive models for human descending thoracic aortas. J. Mech. Behav. Biomed. Mater. 99, 186–197.

An, C., Su, J., 2017. Dynamic behavior of axially functionally graded pipes conveying fluid. Math. Probl. Eng. 6789634.

Anderson, T.J., Nayfeh, A.H., Balachandran, B., 1996. Experimental verification of the importance of the nonlinear curvature in the response of a cantilever beam. ASME. J. Vib. Acoust. 118, 21–27.

Ariaratnam, S.T., Namachchivaya, N.S., 1986a. Dynamic stability of pipes conveying pulsating fluid. J. Sound Vib. 107, 215–230.

Ariaratnam, S.T., Namachchivaya, N.S., 1986b. Dynamic stability of pipes conveying fluid with stochastic flow velocity, Studies in Applied Mechanics. Elsevier, pp. 1–17.

Ariaratnam, S.T., Xie, W.C., Vrscay, E.R., 1989. Chaotic motion under parametric excitation. Dyn. Stab. Syst. 4, 111–130.

Arnau, A., 2004. Piezoelectric transducers and applications. Springer.

Ashley, H., Haviland, G., 1950. Bending vibrations of a pipe line containing flowing fluid, J. Appl. Mech. 17, 229-232.

Askarian, A.R., Haddadpour, H., Firouz-Abadi, R.D., Abtahi, H., 2017. Nonlinear dynamics of extensible viscoelastic cantilevered pipes conveying pulsatile flow with an end nozzle. Int. J. Non. Linear. Mech. 91, 22–35.

Azvine, B., Tomlinson, G.R., Wynne, R.J., 1995. Use of active constrained-layer damping for controlling resonant vibration. Smart Mater. Struct. 4, 1.

Bahraini, S.M.S., Eghtesad, M., Farid, M., Ghavanloo, E., 2012. Comparison of Fractional Kelvin-Voigt and Fractional Zener Models for Large Deflection of Viscoelastic Beams, in: Annual International Conference on Mechanical Engineering-ISME2012. School of Mechanical Eng., Shiraz University, Shiraz, Iran.

Baillargeon, B.P., Vel, S.S., 2005. Active vibration suppression of sandwich beams using piezoelectric shear actuators: experiments and numerical simulations. J. Intell. Mater. Syst. Struct. 16, 517–530.

Balamurugan, V., Narayanan, S., 2002. Finite element formulation and active vibration control study on beams using smart constrained layer damping (SCLD) treatment. J. Sound Vib. 249, 227–250.

Balmes, E., 1997. Model reduction for systems with frequency dependent damping properties. Off. Natl. D ETUDES Rech. Aerosp. ONERA-PUBLICATIONS-TP, proceedings of IMAC, France, February 1997.

Bathe, K. J., 2006. Finite element procedures. Klaus-Jurgen Bathe.

Batra, R.C., Geng, T.S., 2002. Comparison of active constrained layer damping by using extension and shear mode piezoceramic actuators. J. Intell. Mater. Syst. Struct. 13, 349–367.

Baz, A., Imam, K., McCoy, J., 1990. Active vibration control of flexible beams using shape memory actuators. J. Sound Vib. 140, 437–456.

Baz, A.M., 2019. Active and passive vibration damping. John Wiley & Sons.

Belouettar, S., Azrar, L., Daya, E.M., Laptev, V., Potier-Ferry, M., 2008. Active control of nonlinear vibration of sandwich piezoelectric beams: A simplified approach. Comput. Struct. 86, 386–397.

Benjeddou, A., 2007. Shear-mode piezoceramic advanced materials and structures: a state of the art. Mech. Adv. Mater. Struct. 14, 263–275.

Benjeddou, A., Trindade, M.A., Ohayon, R., 1999. New shear actuated smart structure beam finite element. AIAA J. 37, 378–383.

Bian, Z.G., Lim, C.W., Chen, W.Q., 2006. On functionally graded beams with integrated surface piezoelectric layers. Compos. Struct. 72, 339–351.

Bilasse, M., Daya, E.M., Azrar, L., 2010. Linear and nonlinear vibrations analysis of viscoelastic sandwich beams. J. Sound Vib. 329, 4950–4969.

Bilasse, M., Oguamanam, D.C.D., 2013. Forced harmonic response of sandwich plates with viscoelastic core using reduced-order model. Compos. Struct. 105, 311–318.

Blahos, J., Vizzaccaro, A., Salles, L., El Haddad, F., 2020. Parallel harmonic balance method for analysis of nonlinear dynamical systems, in: Turbo Expo: Power for Land, Sea, and Air. American Society of Mechanical Engineers, p. V011T30A028.

Bolotin, V., 1964. The dynamic stability of elastic systems.San Francisco: Holden-Day.

Bommakanti, A., Roy, S., Suwas, S., 2016. Effect of hypoeutectic boron modification on the dynamic properties of Ti-6Al-4V alloy. J. Mater. Res. 31, 2804–2816.

Boumediene, F., Cadou, J.-M., Duigou, L., 2014. A reduction model for eigensolutions of damped viscoelastic sandwich structures. Mech. Res. Commun. 57, 74–81.

Briseghella, L., Majorana, C.E., Pellegrino, C., 1998. Dynamic stability of elastic structures: a finite element approach. Comput. Struct. 69, 11–25.

Cady, W.G., 2018. Piezoelectricity: Volume Two: An Introduction to the Theory and Applications of Electromechanical Phenomena in Crystals. Courier Dover Publications.

Celep, Z., 1985. Dynamic stability of pretwisted columns under periodic axial loads. J. Sound Vib. 103, 35–42.

Chee, C.Y.K., 2000. Static shape control of laminated composite plate smart structure using piezoelectric actuators©. PhD thesis, Univ. Sydney.

Chen, L.-W., Lin, C.-Y., Wang, C.-C., 2002. Dynamic stability analysis and control of a composite beam with piezoelectric layers. Compos. Struct. 56, 97–109.

Chen, L., He, F., Sammut, K., 2009. Vibration suppression of a principal parametric resonance. J. Vib. Control 15, 439–463.

Chen, S.H., Cheung, Y.K., Xing, H.X., 2001. Nonlinear vibration of plane structures by finite element and incremental harmonic balance method. Nonlinear Dyn. 26, 87–104.

Chen, S.S., Jendrzejczyk, J.A., 1985. General characteristics, transition, and control of instability of tubes conveying fluid. J. Acoust. Soc. Am. 77, 887–895.

Chen, S.S., Rosenberg, G.S., 1971. Vibrations and stability of a tube conveying

fluid. Argonne National Lab., III.

Cheung, Y.K., Chen, S.H., Lau, S., 1990. Application of the incremental harmonic balance method to cubic non-linearity systems. J. Sound Vib. 140, 273–286.

Chin, C.-M., Nayfeh, A.H., 1999. Three-to-one internal resonances in parametrically excited hinged-clamped beams. Nonlinear Dyn. 20, 131–158.

Chin, C.-M., Nayfeh, A.H., 1997. Three-to-one internal resonances in hinged-clamped beams. Nonlinear Dyn. 12, 129–154.

Chin, C., Hayfeh, A., Lacarbonara, W., Chin, C., Hayfeh, A., Lacarbonara, W., 1997. Two-to-one internal resonances in parametrically excited buckled beams, in: 38th Structures, Structural Dynamics, and Materials Conference. p. 1081.

Cho, H., Shin, S., Kim, H., Cho, M., 2020. Enhanced model-order reduction approach via online adaptation for parametrized nonlinear structural problems. Comput. Mech. 65, 331–353.

Claeys, M., Sinou, J.J., Lambelin, J.-P., Alcoverro, B., 2014. Multi-harmonic measurements and numerical simulations of nonlinear vibrations of a beam with non-ideal boundary conditions. Commun. Nonlinear Sci. Numer. Simul. 19, 4196–4212.

Cortes, F., Elejabarrieta, M.J., 2007. Homogenised finite element for transient dynamic analysis of unconstrained layer damping beams involving fractional derivative models. Comput. Mech. 40, 313–324.

Czerwinski, A., Luczko, J., 2012. Vibrations of steel pipes and flexible hoses induced byperiodically variable fluid flow. Mech. Control 31, 63–71.

Czerwinski, A., Luczko, J., 2018. Non-planar vibrations of slightly curved pipes conveying fluid in simple and combination parametric resonances. J. Sound Vib. 413, 270–290.

De Lima, A.M.G., Da Silva, A.R., Rade, D.A., Bouhaddi, N., 2010. Component mode synthesis combining robust enriched Ritz approach for viscoelastically damped structures. Eng. Struct. 32, 1479–1488.

Dehrouyeh-Semnani, A.M., Dehdashti, E., Yazdi, M.R.H., Nikkhah-Bahrami, M., 2019. Nonlinear thermo-resonant behavior of fluid-conveying FG pipes. Int. J. Eng. Sci. 144, 103141.

Deng, J., Liu, Y., Zhang, Z., Liu, W., 2017a. Stability analysis of multi-span viscoelastic functionally graded material pipes conveying fluid using a hybrid method. Eur. J. Mech. A/Solids 65, 257–270.

Deng, J., Liu, Y., Zhang, Z., Liu, W., 2017b. Dynamic behaviors of multi-span viscoelastic functionally graded material pipe conveying fluid. Proc. Inst. Mech. Eng. Part C J. Mech. Eng. Sci. 231, 3181–3192.

Detroux, T., Renson, L., Masset, L., Kerschen, G., 2015. The harmonic balance method for bifurcation analysis of large-scale nonlinear mechanical systems. Comput. Methods Appl. Mech. Eng. 296, 18–38.

Dimaggio, O.D., Li, T., 1964. Vibration of a propellant line containing flowing fluid (Transverse vibration of propellant line with internal flowing fluid, using beam approach), in: 5th Annual Structures and Materials Conference. p. 1020.

Dimitriadis, G., 2008. Continuation of higher-order harmonic balance solutions for nonlinear aeroelastic systems. J. Aircr. 45, 523–537.

Dimitriu, G., Ştefanescu, R., Navon, I.M., 2017. Comparative numerical analysis using reduced-order modeling strategies for nonlinear large-scale systems. J. Comput. Appl. Math. 310, 32–43.

Ding, Z., Li, L., Kong, J., Qin, L., 2018. A modal projection-based reduction method for transient dynamic responses of viscoelastic systems with multiple damping models. Comput. Struct. 194, 60–73.

Dodds, H.L., Runyan, H.L., 1965. Effect of high-velocity fluid flow on the bending vibrations and static divergence of a simply supported pipe. National Aeronautics and Space Administration.

Dou, S., Jensen, J.S., 2015. Optimization of nonlinear structural resonance using the incremental harmonic balance method. J. Sound Vib. 334, 239–254.

Dufour, R., Berlioz, A., 1998. Parametric instability of a beam due to axial excitations and to boundary conditions, J. Vib. Acoust. 120, 461-467.

Dunayevsky, V.A., Abbassian, F., Judzis, A., 1993. Dynamic stability of drillstrings under fluctuating weight on bit. SPE Drill. Complet. 8, 84–92.

Dwivedy, S.K., Sahu, K.C., Babu, S., 2007. Parametric instability regions of three-layered soft-cored sandwich beam using higher-order theory. J. Sound Vib. 304, 326–344.

Eftekhari, M., Hosseini, M., 2016. On the stability of spinning functionally graded cantilevered pipes subjected to fluid-thermomechanical loading. Int. J. Struct. Stab. Dyn. 16, 1550062.

El-Bassiouny, A.F., 2006. Nonlinear vibration of a post-buckled beam subjected to external and parametric excitations. Phys. Scr. 74, 39.

Emam, S.A., Abdalla, M.M., 2015. Subharmonic parametric resonance of simply supported buckled beams. Nonlinear Dyn. 79, 1443–1456.

Erturk, A., Inman, D.J., 2011. Piezoelectric energy harvesting. John Wiley & Sons.

Ewins, D.J., Inman, D.J., 2001. Structural Dynamics @ 2000: Current Status

and Future Directions, Engineering dynamics series. Research Studies Press.

Fallah, A., Aghdam, M.M., 2012. Thermo-mechanical buckling and nonlinear free vibration analysis of functionally graded beams on nonlinear elastic foundation. Compos. Part B Eng. 43, 1523–1530.

Fallah, A., Aghdam, M.M., 2011. Nonlinear free vibration and post-buckling analysis of functionally graded beams on nonlinear elastic foundation. Eur. J. Mech. 30, 571–583.

Farokhi, H., Ghayesh, M.H., 2019. A New Geometrically Exact Model for Buckling and Postbuckling Statics and Dynamics of Beams. J. Appl. Mech. 86.

Farokhi, H., Ghayesh, M.H., 2018. Supercritical nonlinear parametric dynamics of Timoshenko microbeams. Commun. Nonlinear Sci. Numer. Simul. 59, 592–605.

Farokhi, H., Ghayesh, M.H., 2016. Size-dependent parametric dynamics of imperfect microbeams. Int. J. Eng. Sci. 99, 39–55.

Fey, R.H.B., Mallon, N.J., Kraaij, C.S., Nijmeijer, H., 2011. Nonlinear resonances in an axially excited beam carrying a top mass: simulations and experiments. Nonlinear Dyn. 66, 285–302.

Firouz-Abadi, R.D., Askarian, A.R., Kheiri, M., 2013. Bending–torsional flutter of a cantilevered pipe conveying fluid with an inclined terminal nozzle. J. Sound Vib. 332, 3002–3014.

Fu, Y., Zhong, J., Shao, X., Chen, Y., 2015. Thermal postbuckling analysis of functionally graded tubes based on a refined beam model. Int. J. Mech. Sci. 96–97, 58–64.

Fuchiyama, T., Noda, N., 1995. Analysis of thermal stress in a plate of functionally gradient material. JSAE Rev. 16, 263–268.

Galucio, A.C., Deu, J.-F., Ohayon, R., 2004. Finite element formulation of viscoelastic sandwich beams using fractional derivative operators. Comput. Mech. 33, 282–291.

Gan, C., Jing, S., Yang, S., Lei, H., 2015. Effects of supported angle on stability and dynamical bifurcations of cantilevered pipe conveying fluid. Appl. Math. Mech. (English Ed. 36, 729–746.

Ganesan, N., Kadoli, R., 2004. A study on the dynamic stability of a cylindrical shell conveying a pulsatile flow of hot fluid. J. Sound Vib. 274, 953–984.

Gao, K., Gao, W., Wu, D., Song, C., 2017. Nonlinear dynamic stability analysis of Euler–Bernoulli beam–columns with damping effects under thermal environment. Nonlinear Dyn. 90, 2423–2444.

Ghandchi Tehrani, M., Kalkowski, M.K., 2016. Active control of parametrically excited systems. J. Intell. Mater. Syst. Struct. 27, 1218–1230.

Gharib, A., Salehi, M., Fazeli, S., 2008. Deflection control of functionally graded material beams with bonded piezoelectric sensors and actuators. Mater. Sci. Eng. A 498, 110–114.

Ghayesh, M.H., Amabili, M., 2015. Nonlinear stability and bifurcations of an axially moving beam in thermal environment. J. Vib. Control 21, 2981–2994.

Ghayesh, M.H., Farokhi, H., 2016. Parametric instability of microbeams in supercritical regime. Nonlinear Dyn. 83, 1171–1183.

Ghayesh, M.H., Farokhi, H., 2015. Chaotic motion of a parametrically excited microbeam. Int. J. Eng. Sci. 96, 34–45.

Ghayesh, M.H., Farokhi, H., Alici, G., 2015. Subcritical parametric dynamics of microbeams. Int. J. Eng. Sci. 95, 36–48.

Ghayesh, M.H., Paidoussis, M.P., Amabili, M., 2013. Nonlinear dynamics of cantilevered extensible pipes conveying fluid. J. Sound Vib. 332, 6405–6418.

Ghayesh, M.H., Paidoussis, M.P., Modarres-Sadeghi, Y., 2011. Three-dimensional dynamics of a fluid-conveying cantilevered pipe fitted with an additional spring-support and an end-mass. J. Sound Vib. 330, 2869–2899.

Ghorbanpour Arani, A.A., Niknejad, S., Abbasian Arani, A.A., 2021. Dynamic Response of Bi-Directional Functionally Graded Materials (BDFGMs) Beams Rested on Visco-Pasternak Foundation Under Periodic Axial Force. J. Solid Mech. 13, 269–285.

Ginsberg, J.H., 1973. The dynamic stability of a pipe conveying a pulsatile flow. Int. J. Eng. Sci. 11, 1013–1024.

Giri, A. M., Ali, S. F., Arockiarajan, A., 2021. Dynamics of symmetric and asymmetric potential well-based piezoelectric harvesters: A comprehensive review. J. Intell. Mater. Syst. Struct. 32, 1881-1947.

Givois, A., Grolet, A., Thomas, O., Deü, J.-F., 2019. On the frequency response computation of geometrically nonlinear flat structures using reduced-order finite element models. Nonlinear Dyn. 97, 1747–1781.

Gorman, D.G., Reese, J.M., Zhang, Y.L., 2000. Vibration of a flexible pipe conveying viscous pulsating fluid flow. J. Sound Vib. 230, 379–392.

Gouskov, A.M., Panovko, G.Y., Voronov, S.A., Sinha, S.C., 2007. Parametric maintenance and control of vibration while deep hole drilling. relation 510, 11.

Gu, J., Dai, B., Wang, Y., Li, M., Duan, M., 2017. Dynamic analysis of a fluid-

conveying pipe under axial tension and thermal loads. Ships Offshore Struct. 12, 262–275.

Gultekin Sinir, B., 2013. Pseudo-nonlinear dynamic analysis of buckled pipes. J. Fluids Struct. 37, 151–170.

Gupta, A., Panda, S., Reddy, R.S., 2020. Improved damping in sandwich beams through the inclusion of dispersed graphite particles within the viscoelastic core. Compos. Struct. 247, 112424.

Gupta, S. K., Wahi, P., 2018. Improving stability of steady drilling using a non-uniform distribution of cutters on the drill-bit. Nonlinear Dynamics and Control of Deep Drilling Systems, Stavanger, Norway, pp. 71.

Gurgoze, M., 1986. Parametric vibrations of a restrained beam with an end mass under displacement excitation. J. Sound Vib. 108, 73–84.

Gutschmidt, S., Gottlieb, O., 2012. Nonlinear dynamic behavior of a microbeam array subject to parametric actuation at low, medium and large DC-voltages. Nonlinear Dyn. 67, 1-36.

Gutschmidt, S., Gottlieb, O. 2010. Bifurcations and loss of orbital stability in nonlinear viscoelastic beam arrays subject to parametric actuation. J. Sound Vib, 329, 3835-3855.

Hasan, M., Patel, B. P., Pradyumna, S., 2021. Influence of cross-sectional velocity profile on flow characteristics of arterial wall modeled as elastic and viscoelastic material. Int. J. Numer. Methods Biomed. 37, e3454.

Heywang, W., Lubitz, K., Wersing, W., 2008. Piezoelectricity: evolution and future of a technology. Springer Science & Business Media.

Hollkamp, J.J., Gordon, R.W., Spottswood, S.M., 2005. Nonlinear modal models for sonic fatigue response prediction: a comparison of methods. J. Sound Vib. 284, 1145–1163.

Holmes, P., Marsden, J., 1978. Bifurcation to divergence and flutter in flow-induced oscillations: an infinite dimensional analysis. Automatica 14, 367–384.

Holmes, P.J., 1978. Pipes supported at both ends cannot flutter. J. Appl. Mech. 45, 619–622.

Holmes, P.J., 1977. Bifurcations to divergence and flutter in flow-induced oscillations: A finite dimensional analysis. J. Sound Vib. 53, 471–503.

Hoseinzadeh, M., Rezaeepazhand, J., 2020. Dynamic stability enhancement of laminated composite sandwich plates using smart elastomer layer. J. Sandw. Struct. Mater. 22, 2796–2817.

Hosseini, M., Fazelzadeh, S.A., 2011. Thermomechanical stability analysis of functionally graded thin-walled cantilever pipe with flowing fluid subjected

to axial load. Int. J. Struct. Stab. Dyn. 11, 513–534.

Housner, G.W., 1952. Bending vibrations of a pipe line containing flowing fluid, J. Appl. Mech. 17, 229-232.

Hu, B.-G., Dokainish, M.A., Mansour, W.M., 1995. A modified MSE method for viscoelastic systems: a weighted stiffness matrix approach, J. Vib. Acoust. 117, 226-231.

Huang, B.W., Kuang, J.-H., 2007a. The parametric resonance instability in a drilling process. ASME J. Appl. Mech. 74, 958–964.

Huang, B.W., Kuang, J.-H., 2007b. The parametric resonance instability in a drilling process, J. Appl. Mech. 74, 958-964.

Huang, Y.M., Yang, M.L., 2009. Dynamic analysis of a rotating beam subjected to repeating axial and transverse forces for simulating a lathing process. Int. J. Mech. Sci. 51, 256–268.

Hyun, S.H., Yoo, H.H., 1999. Dynamic modelling and stability analysis of axially oscillating cantilever beams. J. Sound Vib. 228, 543–558.

Ibrahim, R.A., 2010. Overview of mechanics of pipes conveying fluids—Part I: Fundamental studies. J. Press. Vessel Technol. 132, 034001-1-034001–32.

Iwatsubo, T., Saigo, M., Sugiyama, Y., 1973. Parametric instability of clamped-clamped and clamped-simply supported columns under periodic axial load. J. Sound Vib. 30, 65-IN2.

Iwatsubo, T., Sugiyama, Y., Ishihara, K., 1972. Stability and non-stationary vibration of columns under periodic loads. J. Sound Vib. 23, 245–257.

Iwatsubo, T., Sugiyama, Y., Ogino, S., 1974. Simple and combination resonances of columns under periodic axial loads. J. Sound Vib. 33, 211–221.

Jacques, N., Daya, E.M., Potier-Ferry, M., 2010. Nonlinear vibration of viscoelastic sandwich beams by the harmonic balance and finite element methods. J. Sound Vib. 329, 4251–4265.

Jain, S., 2019. Some Themes in Nonlinear Model Reduction with Applications to Structural Dynamics (Doctoral dissertation, ETH Zurich). PhD thesis.

Jain, S., 2015. Model order reduction for non-linear structural dynamics (Masters dissertation, Delft University of Technology).

Jain, S., Tiso, P., 2018. Simulation-free hyper-reduction for geometrically nonlinear structural dynamics: A quadratic manifold lifting approach. J. Comput. Nonlinear Dyn. 13.

Jayaraman, K., Narayanan, S., 1996. Chaotic oscillations in pipes conveying pulsating fluid. Nonlinear Dyn. 10, 333–357.

Jendrzejczyk, J.A., Chen, S.S., 1985. Experiments on tubes conveying fluid. Thin-Walled Struct. 3, 109–134.

Ji, J.-C., Hansen, C.H., 2000. Non-linear response of a post-buckled beam subjected to a harmonic axial excitation. J. Sound Vib. 237, 303–318.

Jia, Y., Seshia, A.A., 2014. An auto-parametrically excited vibration energy harvester. Sensors Actuators A Phys. 220, 69–75.

Jin, J.D., Song, Z.Y., 2005. Parametric resonances of supported pipes conveying pulsating fluid. J. Fluids Struct. 20, 763–783.

Jith, J., Sarkar, S., 2020. A model order reduction technique for systems with nonlinear frequency dependent damping. Appl. Math. Model. 77, 1662–1678.

Johnson, C.D., Kienholz, D.A., 1982. Finite element prediction of damping in structures with constrained viscoelastic layers. AIAA J. 20, 1284–1290.

Jones, D.I.G., 2001. Handbook of viscoelastic vibration damping. John Wiley & Sons.

Kar, R.C., Sujata, T., 1988. Parametric instability of a non-uniform beam with thermal gradient resting on a Pasternak foundation. Comput. Struct. 29, 591–599.

Karagiannis, D. A., Clayton, G. M., Nataraj, C., 2016. Boundary control of harmonic disturbances on flexible cantilever beams using piezoelectric patch actuators. J. Vib. Control. 22, 3916-3929.

Karkar, S., Cochelin, B., Vergez, C., 2014. A comparative study of the harmonic balance method and the orthogonal collocation method on stiff nonlinear systems. J. Sound Vib. 333, 2554–2567.

Karkoub, M.A., Zribi, M., 2006. Active/semi-active suspension control using magnetorheological actuators. Int. J. Syst. Sci. 37, 35–44.

Kazemirad, S., Ghayesh, M.H., Amabili, M., 2013. Thermo-mechanical nonlinear dynamics of a buckled axially moving beam. Arch. Appl. Mech. 83, 25–42.

Ke, L.L., Yang, J., Kitipornchai, S., 2013. Dynamic stability of functionally graded carbon nanotube-reinforced composite beams. Mech. Adv. Mater. Struct. 20, 28–37.

Ke, L.L., Yang, J., Kitipornchai, S., 2010. An analytical study on the nonlinear vibration of functionally graded beams. Meccanica 45, 743–752.

Kerwin, E., 1965. Macromechanisms of damping in composite structures, in: Internal Friction, Damping, and Cyclic Plasticity. ASTM International.

Kiani, Y., Rezaei, M., Taheri, S., Eslami, M.R., 2011. Thermo-electrical buckling of piezoelectric functionally graded material Timoshenko beams. Int. J.

Mech. Mater. Des. 7, 185–197.

Kitio Kwuimy, C. A., Litak, G., Nataraj, C., 2015. Nonlinear analysis of energy harvesting systems with fractional order physical properties. Nonlinear Dyn. 80, 491-501.

Koizumi, M., 1993. The concept of FGM. Ceram. Trans. Funct. Gradient Mater. 34, 3–10.

Komijani, M., Esfahani, S.E., Reddy, J.N., Liu, Y.P., Eslami, M.R., 2014. Nonlinear thermal stability and vibration of pre/post-buckled temperature- and microstructure-dependent functionally graded beams resting on elastic foundation. Compos. Struct. 112, 292–307.

Kuether, R.J., 2019. Two-tier model reduction of viscoelastically damped finite element models. Comput. Struct. 219, 58–72.

Kumar, A., Panda, S., 2016. Design of a 1-3 viscoelastic composite layer for improved free/constrained layer passive damping treatment of structural vibration. Compos. Part B Eng. 96, 204–214.

Kumar, A., Panda, S., Kumar, S., Chakraborty, D., 2015. A design of laminated composite plates using graded orthotropic fiber-reinforced composite plies. Compos. Part B Eng. 79, 476–493.

Kumar, J. S., Ganesan, N., Swarnamani, S., Padmanabhan, C., 2003. Active control of beam with magnetostrictive layer. Comput. Struct. 81, 1375-1382.

Kumar, R., Gupta, S., Ali, S. F., 2021. Analysis of Stepped Beam Using Reduced Order Models. In Advances in Structural Vibration. Springer, Singapore (pp. 21-33).

Kumar, A., Das, S. L., Wahi, P., Żur, K. K., 2022. On the stability of thin-walled circular cylindrical shells under static and periodic radial loading. J. Sound Vib. 116872.

Kung, S.-W., Singh, R., 1998. Vibration analysis of beams with multiple constrained layer damping patches. J. Sound Vib. 212, 781–805.

LaBryer, A., Attar, P.J., 2010. A harmonic balance approach for large-scale problems in nonlinear structural dynamics. Comput. Struct. 88, 1002–1014.

Lacarbonara, W., Yabuno, H., Hayashi, K., 2007. Non-linear cancellation of the parametric resonance in elastic beams: Theory and experiment. Int. J. Solids Struct. 44, 2209–2224.

Lanc, D., Vo, T.P., Turkalj, G., Lee, J., 2015. Buckling analysis of thin-walled functionally graded sandwich box beams. Thin-walled Struct. 86, 148–156.

Lazarus, A., Thomas, O., Deu, J.-F., 2012. Finite element reduced order models

for nonlinear vibrations of piezoelectric layered beams with applications to NEMS. Finite Elem. Anal. Des. 49, 35–51.

Lee, H.P., 1995. Dynamic stability of spinning pre-twisted beams subject to axial pulsating loads. Comput. Methods Appl. Mech. Eng. 127, 115–126.

Lee, H.P., 1994. Buckling and dynamic stability of spinning pre-twisted beams under compressive axial loads. Int. J. Mech. Sci. 36, 1011–1026.

Lee, U., Kim, J., 1999. Dynamics of branched pipeline systems conveying internal unsteady flow. J. Vib. Acoust. 121, 114–122.

Lee, U., Pak, C.H., Hong, S.C., 1995. The dynamics of a piping system with internal unsteady flow. J. Sound Vib. 180, 297-311.

Lei, S., Zheng, X.Y., Kennedy, D., 2017. Dynamic response of a deepwater riser subjected to combined axial and transverse excitation by the nonlinear coupled model. Int. J. Non. Linear. Mech. 97, 68–77.

Lestari, W., Hanagud, S., 2001. Nonlinear vibration of buckled beams: some exact solutions. Int. J. Solids Struct. 38, 4741–4757.

Lewandowski, R., 1997. Computational formulation for periodic vibration of geometrically nonlinear structures—part 1: theoretical background. Int. J. Solids Struct. 34, 1925–1947.

Lewandowski, R., 1992. Non-linear, steady-state vibration of structures by harmonic balance/finite element method. Comput. Struct. 44, 287–296.

Lewandowski, R., Wielentejczyk, P., 2017. Nonlinear vibration of viscoelastic beams described using fractional order derivatives. J. Sound Vib. 399, 228–243.

Li, F.M., Yao, G., Zhang, Y., 2016. Active control of nonlinear forced vibration in a flexible beam using piezoelectric material. Mech. Adv. Mater. Struct. 23, 311–317.

Li, F., Liu, C., 2012. Parametric vibration stability and active control of nonlinear beams. Appl. Math. Mech. 33, 1381–1392.

Li, H., Wang, Z., Lv, H., Zhou, Z., Han, Q., Liu, J., Qin, Z., 2020. Nonlinear vibration analysis of fiber reinforced composite cylindrical shells with partial constrained layer damping treatment. Thin-Walled Struct. 157, 107000.

Li, Q., Liu, W., Zhang, Z., Yue, Z., 2018. Parametric resonance of pipes with soft and hard segments conveying pulsating fluids. Int. J. Struct. Stab. Dyn. 18, 1850119.

Li, S., Cheng, C., 2009. Free vibration of functionally graded material beams with surface-bonded piezoelectric layers in thermal environment. Appl. Math. Mech. 30, 969–982.

Li, S., Zhang, J., Zhao, Y., 2006. Thermal post-buckling of functionally graded material Timoshenko beams. Appl. Math. Mech. 27, 803–810.

Li, W., Song, Z., Chai, Y., 2015. Discrete singular convolution method for dynamic stability analysis of beams under periodic axial forces. J. Eng. Mech. 141, 4015033.

Li, Y., Yang, Y., 2017. Nonlinear vibration of slightly curved pipe with conveying pulsating fluid. Nonlinear Dyn. 88, 2513–2529.

Lin, R.M., Lim, M.K., 1996. Complex eigensensitivity-based characterization of structures with viscoelastic damping. J. Acoust. Soc. Am. 100, 3182–3191.

Lips, S., Meyer, J.P., 2011. Two-phase flow in inclined tubes with specific reference to condensation: A review. Int. J. Multiph. Flow 37, 845–859.

Litewka, P., Lewandowski, R., 2017a. Nonlinear harmonically excited vibrations of plates with Zener material. Nonlinear Dyn. 89, 691–712.

Litewka, P., Lewandowski, R., 2017b. Steady-state non-linear vibrations of plates using Zener material model with fractional derivative. Comput. Mech. 60, 333–354.

Liu, H.-S., Mote Jr, C.D., 1974. Dynamic response of pipes transporting fluids, J. Eng. Ind. 96, 591-596.

Long Jr, R.H., 1955. Experimental and theoretical study of transverse vibration of a tube containing flowing fluid, J. Appl. Mech. 22, 65-68.

Lu, K., Jin, Y., Chen, Y., Yang, Y., Hou, L., Zhang, Z., Li, Z., Fu, C., 2019. Review for order reduction based on proper orthogonal decomposition and outlooks of applications in mechanical systems. Mech. Syst. Signal Process. 123, 264–297.

Lu, Y., Chen, X., 2020. Nonlinear parametric dynamics of bidirectional functionally graded beams. Shock Vib. 2020.

Luczko, J., Czerwinski, A., 2017. Nonlinear three-dimensional dynamics of flexible pipes conveying fluids. J. Fluids Struct. 70, 235–260.

Luczko, J., Czerwinski, A., 2016. Experimental and numerical investigation of parametric resonance of flexible hose conveying non-harmonic fluid flow. J. Sound Vib. 373, 236–250.

Luczko, J., Czerwinski, A., 2015. Parametric vibrations of flexible hoses excited by a pulsating fluid flow, Part I: Modelling, solution method and simulation. J. Fluids Struct. 55, 155–173.

Lumsdaine, A., Scott, R.A., 1998. Shape optimization of unconstrained viscoelastic layers using continuum finite elements. J. Sound Vib. 216, 29–52.

Lunn, T.S., 1983. Flow-induced Instabilities of Fluid-conveying Pipes (Doctoral dissertation).

Lv, H.W., Li, L., Li, Y.H., 2018. Non-linearly parametric resonances of an axially moving viscoelastic sandwich beam with time-dependent velocity. Appl. Math. Model. 53, 83–105.

Ma, L.S., Lee, D.W., 2012. Exact solutions for nonlinear static responses of a shear deformable FGM beam under an in-plane thermal loading. Eur. J. Mech. 31, 13–20.

Ma, L.S., Lee, D.W., 2011. A further discussion of nonlinear mechanical behavior for FGM beams under in-plane thermal loading. Compos. Struct. 93, 831–842.

Maalawi, K.Y., EL-Sayed, H.E.M., 2011. Stability optimization of functionally graded pipes conveying fluid. World Acad. Sci. Eng. Technol. 79, 374–379.

Mahdiabadi, M.K., Tiso, P., Brandt, A., Rixen, D.J., 2021. A non-intrusive model-order reduction of geometrically nonlinear structural dynamics using modal derivatives. Mech. Syst. Signal Process. 147, 107126.

Mailybaev, A.A., Yabuno, H., Kaneko, H., 2004. Optimal shapes of parametrically excited beams. Struct. Multidiscip. Optim. 27, 435–445.

Majumdar, A., Das, D., 2018. A study on thermal buckling load of clamped functionally graded beams under linear and nonlinear thermal gradient across thickness. Proc. Inst. Mech. Eng. Part L J. Mater. Des. Appl. 232, 769–784.

Manoach, E., Ribeiro, P., 2004. Coupled, thermoelastic, large amplitude vibrations of Timoshenko beams. Int. J. Mech. Sci. 46, 1589–1606.

Marynowski, K., Kapitaniak, T., 2014. Dynamics of axially moving continua. Int. J. Mech. Sci. 81, 26–41.

McClamroch, N.H., Gavin, H.P., 1995. Closed loop structural control using electrorheological dampers, in: Proceedings of 1995 American Control Conference-ACC'95. IEEE, pp. 4173–4177.

Mcdonald, R.J., Namachchivaya, N.S., 2005a. Pipes conveying pulsating fluid near a 0 : 1 resonance : Local bifurcations 21, 629–664.

McDonald, R.J., Sri Namachchivaya, N., 2005b. Pipes conveying pulsating fluid near a 0 : 1 resonance: Global bifurcations. J. Fluids Struct. 21, 665–687.

McTavish, D., Hughes, P., 1992. Finite element modeling of linear viscoelastic structures-the GHM method, in: 33rd Structures, Structural Dynamics and Materials Conference. p. 2380.

Merlette, N., 2006. The use of suitable modal bases for dynamic prediction of structures containing high damping materials. Shock Vib. Dig. 38, 235–

236.

Mignolet, M.P., Przekop, A., Rizzi, S.A., Spottswood, S.M., 2013. A review of indirect/non-intrusive reduced order modeling of nonlinear geometric structures. J. Sound Vib. 332, 2437–2460.

Modarres-Sadeghi, Y., Paidoussis, M.P., 2009. Nonlinear dynamics of extensible fluid-conveying pipes, supported at both ends. J. Fluids Struct. 25, 535–543.

Modarres-Sadeghi, Y., Semler, C., Wadham-Gagnon, M., Païdoussis, M.P., 2007. Dynamics of cantilevered pipes conveying fluid. Part 3: Three-dimensional dynamics in the presence of an end-mass. J. Fluids Struct. 23, 589–603.

Mohanty, S.C., Dash, R.R., Rout, T., 2012. Static and dynamic stability analysis of a functionally graded Timoshenko beam. Int. J. Struct. Stab. Dyn. 12, 1250025.

Mohanty, S.C., Dash, R.R., Rout, T., 2011. Parametric instability of a functionally graded Timoshenko beam on Winkler's elastic foundation. Nucl. Eng. Des. 241, 2698–2715.

Monprapussorn, T., Athisakul, C., Chucheepsakul, S., 2007. Nonlinear vibrations of an extensible flexible marine riser carrying a pulsatile flow. J. Appl. Mech. 74, 754–769.

MS, A.K., Panda, S., Chakraborty, D., 2016. Piezo-viscoelastically damped nonlinear frequency response of functionally graded plates with a heated plate-surface. J. Vib. Control 22, 320–343.

Naguleswaran, S., Williams, C.J.H., 1968. Lateral vibration of a pipe conveying a fluid. J. Mech. Eng. Sci. 10, 228–238.

Namachchivaya, N.S., Tien, W.M., 1989a. Bifurcation behavior of nonlinear pipes conveying pulsating flow. J. Fluids Struct. 3, 609–629.

Namchchivaya, N.S., Tien, W.M., 1989b. Non-linear dynamics of supported pipe conveying pulsating fluid—II. Combination resonance. Int. J. Non. Linear. Mech. 24, 197–208.

Namchchivaya, N.S., 1989. Non-linear dynamics of supported pipe conveying pulsating fluid—I. Subharmonic resonance. Int. J. Non. Linear. Mech. 24, 185–196.

Nayfeh, A.H., 2008. Perturbation methods. John Wiley & Sons.

Nikolic, M., Rajkovic, M., 2006. Bifurcations in nonlinear models of fluid-conveying pipes supported at both ends. J. Fluids Struct. 22, 173–195.

Niordson, Frithiof I., 1953. Vibrations of a cylindrical tube containing flowing fluid. Goteborg :Elanders Boktr.

Olunloyo, V.O.S., Oyediran, A.A., Adewale, A., Adelaja, A.O., Osheku, C.A., 2007. Concerning the transverse and longitudinal vibrations of a fluid conveying beam and the pipe walking phenomenon, in: International Conference on Offshore Mechanics and Arctic Engineering. pp. 285–298.

Oueini, S.S., Nayfeh, H.A., 1999. Single-mode control of a cantilever beam under principal parametric excitation. J. Sound Vib. 224, 33–47.

Oz, H.R., 2001. Non-linear vibrations and stability analysis of tensioned pipes conveying fluid with variable velocity. Int. J. Non. Linear. Mech. 36, 1031–1039.

Padmanabhan, C., Singh, R., 1995. Analysis of periodically excited non-linear systems by a parametric continuation technique. J. Sound Vib. 184, 35-58.

Paidoussis, M.P., 2014. Fluid–structure interactions: slender structures and axial flow, vol. 1. Academic press, London.

Paidoussis, M.P., Issid, N.T., 1976. Experiments on Parametric Resonance of Pipes Containing Pulsatile Flow. J. Appl. Mech. 43, 198–202.

Paidoussis, M.P., Issid, N.T., 1974. Dynamic stability of pipes conveying fluid. J. Sound Vib. 33, 267–294.

Paidoussis, M.P., Li, G.X., 1993. Pipes conveying fluid: A model dynamical problem. J. Fluids Struct. 7, 137-204.

Paidoussis, M.P., Sundararajan, C., 1975. Parametric and Combination Resonances of a Pipe Conveying Pulsating Fluid. J. Appl. Mech. 42, 780–784.

Panda, L.N., Kar, R.C., 2008. Nonlinear dynamics of a pipe conveying pulsating fluid with combination, principal parametric and internal resonances. J. Sound Vib. 309, 375–406.

Panda, L.N., Kar, R.C., 2007. Nonlinear dynamics of a pipe conveying pulsating fluid with parametric and internal resonances. Nonlinear Dyn. 49, 9–30.

Pao, H.P., 1970. Dynamical stability of a towed thin flexible cylinder. J. Hydronautics 4, 144–150.

Parida, R., Dash, P., 2016. Dynamic stability analysis of a circularly tapered rotating beam subjected to axial pulsating load and thermal gradient under various boundary conditions. Int. J. Acoust. Vib 21, 139–144.

Patel, B. P., Ibrahim, S. M., Nath, Y., 2009. Periodic response of nonlinear dynamical system with large number of degrees of freedom. Sadhana. 34, 1033-1037.

Paul, A., Das, D., 2016. Non-linear thermal post-buckling analysis of FGM Timoshenko beam under non-uniform temperature rise across thickness. Eng. Sci. Technol. an Int. J. 19, 1608–1625.

Payette, G.S., Reddy, J.N., 2013. A nonlinear finite element framework for viscoelastic beams based on the high-order Reddy beam theory. J. Eng. Mater. Technol. 135, 11005.

Peletan, L., Baguet, S., Jacquet-richardet, M.T.G., 2013. A comparison of stability computational methods for periodic solution of nonlinear problems with application to rotordynamics 671–682.

Peng, G., Xiong, Y., Gao, Y., Liu, L., Wang, M., Zhang, Z., 2018. Non-linear dynamics of a simply supported fluid-conveying pipe subjected to motion-limiting constraints: Two-dimensional analysis. J. Sound Vib. 435, 192–204.

Peng, G., Xiong, Y., Liu, L., Gao, Y., Wang, M., Zhang, Z., 2019. 3-D non-linear dynamics of inclined pipe conveying fluid, supported at both ends. J. Sound Vib. 449, 405–426.

Pierre, C., Dowell, E.H., 1985. A study of dynamic instability of plates by an extended incremental harmonic balance method. ASME J. Appl. Mech. 52, 693–697.

Piovan, M.T., Machado, S.P., 2011. Thermoelastic dynamic stability of thin-walled beams with graded material properties. Thin-walled Struct. 49, 437–447.

Plouin, A.-S., Balmes, E., 2000. Steel/viscoelastic/steel sandwich shells computational methods and experimental validations, in: International Modal Analysis Conference. pp. 384–390.

Plunkett, R., Lee, C.T., 1970. Length optimization for constrained viscoelastic layer damping. J. Acoust. Soc. Am. 48, 150–161.

Pradhan, M., Dash, P.R., Pradhan, P.K., 2016. Static and dynamic stability analysis of an asymmetric sandwich beam resting on a variable Pasternak foundation subjected to thermal gradient. Meccanica 51, 725–739.

Praveen Krishna, I. R., Padmanabhan, C., 2011. Improved reduced order solution techniques for nonlinear systems with localized nonlinearities. Nonlinear Dyn. 63, 561-586.

Qian, Q., Wang, L., Ni, Q., 2009. Instability of simply supported pipes conveying fluid under thermal loads. Mech. Res. Commun. 36, 413–417.

Qin, Q., 2012. Advanced mechanics of piezoelectricity. Springer Science & Business Media.

Raja, S., Prathap, G., Sinha, P.K., 2002. Active vibration control of composite sandwich beams with piezoelectric extension-bending and shear actuators. Smart Mater. Struct. 11, 63.

Raju, K.K., Rao, G.V., 1984a. Finite element analysis of thermal postbuckling of tapered columns. Comput. Struct. 19, 617–620.

Raju, K.K., Rao, G.V., 1984b. Thermal postbuckling behavior of tapered columns. AIAA J. 22, 1499–1501.

Rao, G.V., Raju, K.K., 1984. Thermal postbuckling of columns. AIAA J. 22, 850–851.

Ray, K., Kar, R.C., 1996a. The parametric instability of partially covered sandwich beams. J. Sound Vib. 197, 137–152.

Ray, K., Kar, R.C., 1996b. Parametric instability of a dual-cored sandwich beam. Comput. Struct. 61, 665–671.

Ray, K., Kar, R.C., 1995. Parametric instability of a sandwich beam under various boundary conditions. Comput. Struct. 55, 857–870.

Rechdaoui, M.S., Azrar, L., 2010. Active control of secondary resonances piezoelectric sandwich beams. Appl. Math. Comput. 216, 3283–3302.

Reddy, J.N., Chin, C.D., 1998. Thermomechanical analysis of functionally graded cylinders and plates. J. Therm. Stress. 21, 593–626.

Reddy, R.S., Panda, S., Gupta, A., 2021. Nonlinear dynamics and active control of smart beams using shear/extensional mode piezoelectric actuators. Int. J. Mech. Sci. 106495.

Ribeiro, P., 2004. Non-linear forced vibrations of thin/thick beams and plates by the finite element and shooting methods. Comput. Struct. 82, 1413–1423.

Rizzi, S.A., Przekop, A., 2008. System identification-guided basis selection for reduced-order nonlinear response analysis. J. Sound Vib. 315, 467–485.

Roslan, S.A.H., Yusof, Z., Rasid, Z.A., Yahaya, M.H., Hassan, M.Z., Mahmud, J., 2019. Dynamic instability response of smart composite material. Materwiss. Werksttech. 50, 302–310.

Rouleau, L., Deu, J.F., Legay, A., 2017. A comparison of model reduction techniques based on modal projection for structures with frequency-dependent damping. Mech. Syst. Signal Process. 90, 110–125.

Rutzmoser, J.B., 2018. Model Order Reduction for Nonlinear Structural Dynamics Simulation-free Approaches (Doctoral dissertation, Technische Universitat Munchen).

Sahoo, S.R., Ray, M.C., 2019. Active damping of geometrically nonlinear vibrations of smart composite plates using elliptical SCLD treatment with fractional derivative viscoelastic layer. Eur. J. Mech. 78, 103823.

Saito, H., Otomi, K., 1979. Parametric response of viscoelastically supported beams. J. Sound Vib. 63, 169–178.

Semler, C., Li, G.X., Paıdoussis, M.P., 1994. The non-linear equations of motion of pipes conveying fluid. J. Sound Vib. 169, 577–599.

Seo, Y.S., Jeong, W.B., Jeong, S.H., Oh, J.S., Yoo, W.S., 2005. Finite element analysis of forced vibration for a pipe conveying harmonically pulsating fluid. JSME Int. J. Ser. C Mech. Syst. Mach. Elem. Manuf. 48, 688–694.

Shastry, B.P., Rao, G.V., 1986. Dynamic stability of columns with two symmetrically placed intermediate supports. J. Sound Vib. 104, 524–527.

Shen, H.S., 2016. Functionally graded materials: nonlinear analysis of plates and shells. CRC press.

Shen, H.S., Lin, F., Xiang, Y., 2017. Nonlinear vibration of functionally graded graphene-reinforced composite laminated beams resting on elastic foundations in thermal environments. Nonlinear Dyn. 90, 899–914.

Sheng, G.G., Wang, X., 2019. Nonlinear forced vibration of functionally graded Timoshenko microbeams with thermal effect and parametric excitation. Int. J. Mech. Sci. 155, 405–416.

Sheng, G.G., Wang, X., 2018. Nonlinear vibration of FG beams subjected to parametric and external excitations. Eur. J. Mech. 71, 224–234.

Shih, Y.S., Yeh, Z.F., 2005. Dynamic stability of a viscoelastic beam with frequency-dependent modulus. Int. J. Solids Struct. 42, 2145–2159.

Shinbrot, T., Grebogi, C., Wisdom, J., Yorke, J. A., 1992. Chaos in a double pendulum. Am. J. Phy. 60, 491-499.

Singh, K., Mallik, A.K., 1979. Parametric instabilities of a periodically supported pipe conveying fluid. J. Sound Vib. 62, 379–397.

Sinha, S.K., 2005. Non-linear dynamic response of a rotating radial Timoshenko beam with periodic pulse loading at the free-end. Int. J. Non. Linear. Mech. 40, 113–149.

Somerset, J.H., Evan-Iwanowski, R.M., 1964. Experiments on parametric instability of columns, in: Proceedings, Second Southeastern Conference on Theoretical and Applied Mechanics. pp. 503–525.

Song, P., Wang, X., Mignolet, M.P., Chen, P.-C., 2016. A Reduced Order Model-Based Nonlinear Damping Model: Formulation and Application to Post Flutter Aeroelastic Behavior, in: 15th Dynamics Specialists Conference. p. 1795.

Sri Namchchivaya, N., Tien, W.M., 1989. Non-linear dynamics of supported pipe conveying pulsating fluid-II. Combination resonance. Int. J. Non. Linear. Mech. 24, 197–208.

Stevens, K.K., Evan-Iwanowski, R.M., 1969. Parametric resonance of viscoelastic columns. Int. J. Solids Struct. 5, 755–765.

Sun, C.T., Zhang, X.D., 1995. Use of thickness-shear mode in adaptive sandwich structures. Smart Mater. Struct. 4, 202.

Sun, Y., Li, S.R., Batra, R.C., 2016. Thermal buckling and post-buckling of FGM Timoshenko beams on nonlinear elastic foundation. J. Therm. Stress. 39, 11–26.

Svensson, I., 2001. Dynamic instability regions in a damped system. J. Sound Vib. 244, 779–793.

Szemplinska-Stupnicka, W., Plaut, R.H., Hsieh, J.-C., 1989. Period doubling and chaos in unsymmetric structures under parametric excitation, J. Appl. Mech. 56, 947-952.

Tabassian, R., Rezaeepazhand, J., 2013. Dynamic stability of smart sandwich beams with electro-rheological core resting on elastic foundation. J. Sandw. Struct. Mater. 15, 25–44.

Tang, Y., Yang, T., 2018. Post-buckling behavior and nonlinear vibration analysis of a fluid-conveying pipe composed of functionally graded material. Compos. Struct. 185, 393–400.

Tang, Y., Zhen, Y., Fang, B., 2018. Nonlinear vibration analysis of a fractional dynamic model for the viscoelastic pipe conveying fluid. Appl. Math. Model. 56, 123–136.

Teunisse, N., Demasi, L., Tiso, P., Cavallaro, R., 2017. Reduced basis methods for structurally nonlinear Joined Wings. Aerosp. Sci. Technol. 68, 486–495.

Tezak, E.G., Mook, D.T., Nayfeh, A.H., 1978. Nonlinear analysis of the lateral response of columns to periodic loads, J. Mech. Des. 100, 651-659.

Thakkar, D., Ganguli, R., 2004. Helicopter vibration reduction in forward flight with induced-shear based piezoceramic actuation. Smart Mater. Struct. 13, 599.

Thompson, J.M.T., Lunn, T.S., 1981. Static elastica formulations of a pine conveying fluid. J. Sound Vib. 77, 127–132.

Thomsen, J.J., 2013. Vibrations and stability: advanced theory, analysis, and tools. Springer Science & Business Media.

Thurman, A.L., Mote Jr, C.D., 1969. Nonlinear oscillation of a cylinder containing a flowing fluid.

Tiso, P., Dedden, R., Rixen, D., 2013. A modified discrete empirical interpolation method for reducing non-linear structural finite element models, in: International Design Engineering Technical Conferences and Computers and Information in Engineering Conference. American Society of Mechanical Engineers, p. V07BT10A043.

Tomlinson, G.R., 1990. The use of constrained layer damping in vibration control. Int. J. Mech. Sci. 32, 233–242.

Touze, C., Vidrascu, M., Chapelle, D., 2014. Direct finite element computation of

non-linear modal coupling coefficients for reduced-order shell models. Comput. Mech. 54, 567–580.

Touze, C., Vizzaccaro, A., Thomas, O., 2021. Model order reduction methods for geometrically nonlinear structures: a review of nonlinear techniques. Nonlinear Dyn. 105, 1141-1190.

Trindade, M.A., 2011. Experimental analysis of active-passive vibration control using viscoelastic materials and extension and shear piezoelectric actuators. J. Vib. Control 17, 917–929.

Trindade, M.A., 2007. Simultaneous extension and shear piezoelectric actuation for active vibration control of sandwich beams. J. Intell. Mater. Syst. Struct. 18, 591–600.

Trindade, M.A., Benjeddou, A., Ohayon, R., 2001. Finite element modelling of hybrid active–passive vibration damping of multilayer piezoelectric sandwich beams—part II: System Analysis. Int. J. Numer. Methods Eng. 51, 855–864.

Trindade, M.A., Benjeddou, A., Ohayon, R., 2000. Modeling of frequency-dependent viscoelastic materials for active-passive vibration damping. J. Vib. Acoust. 122, 169–174.

Trindade, M.A., Benjeddou, A., Ohayon, R., 1999. Parametric analysis of the vibration control of sandwich beams through shear-based piezoelectric actuation. J. Intell. Mater. Syst. Struct. 10, 377–385.

Trindade, M.A., Maio, C.E.B., 2008. Multimodal passive vibration control of sandwich beams with shunted shear piezoelectric materials. Smart Mater. Struct. 17, 55015.

Tsai, X.Y., Chen, L.W., 2002. Dynamic stability of a shape memory alloy wire reinforced composite beam. Compos. Struct. 56, 235–241.

Ungar, E.E., Kerwin Jr, E.M., 1964. Plate damping due to thickness deformations in attached viscoelastic layers. J. Acoust. Soc. Am. 36, 386–392.

Utida, I., Sezawa, K., 1940. Dynamic stability a column under Periodic Longitudinal forces, Report of the Aeronautical Research Institute, Tokyo Imperial University No. 193.

Vasques, C.M.A., Moreira, R.A.S., Rodrigues, J.D., 2010. Viscoelastic Damping Technologies-Part I: Modeling and Finite Element Implementation. J. Adv. Res. Mech. Eng. 1, 76-95.

Vassilev, V.M., Djondjorov, P.A., 2006. Dynamic stability of viscoelastic pipes on elastic foundations of variable modulus. J. Sound Vib. 297, 414–419.

Vigneaux, P., Chenais, P., Hulin, J.P., 1988. Liquid-liquid flows in an inclined pipe. AIChE J. 34, 781–789.

Vizzaccaro, A., Givois, A., Longobardi, P., Shen, Y., Deü, J.-F., Salles, L., Touzé, C., Thomas, O., 2020. Non-intrusive reduced order modelling for the dynamics of geometrically nonlinear flat structures using three-dimensional finite elements. Comput. Mech. 66, 1293–1319.

Vo, T.P., Thai, H.T., Nguyen, T.K., Maheri, A., Lee, J., 2014. Finite element model for vibration and buckling of functionally graded sandwich beams based on a refined shear deformation theory. Eng. Struct. 64, 12–22.

Wang, L., 2009. A further study on the non-linear dynamics of simply supported pipes conveying pulsating fluid. Int. J. Non. Linear. Mech. 44, 115–121.

Wang, L., Jiang, T.L., Dai, H.L., 2017a. Three-dimensional dynamics of supported pipes conveying fluid. Acta Mech. Sin. 33, 1065–1074.

Wang, L., Liu, Z.Y., Abdelkefi, A., Wang, Y.K., Dai, H.L., 2017b. Nonlinear dynamics of cantilevered pipes conveying fluid: towards a further understanding of the effect of loose constraints. Int. J. Non. Linear. Mech. 95, 19–29.

Wang, L., Ni, Q., 2008. Large-amplitude free vibrations of fluid-conveying pipes on a Pasternak foundation. Int. J. Struct. Stab. Dyn. 8, 615–626.

Wang, X., 2003. Instability analysis of some fluid–structure interaction problems. Comput. Fluids 32, 121–138.

Wang, X., Bloom, F., 2001. Stability issues of concentric pipes containing steady and pulsatile flows. J. Fluids Struct. 15, 1137–1152.

Wang, Y., Zhang, Q., Wang, W., Yang, T., 2019. In-plane dynamics of a fluid-conveying corrugated pipe supported at both ends. Appl. Math. Mech. 40, 1119–1134.

Wang, Y., Zhu, W., 2021a. Nonlinear Transverse Vibration of a Hyperelastic Beam Under Harmonically Varying Axial Loading. J. Comput. Nonlinear Dyn. 16, 31006.

Wang, Y., Zhu, W., 2021b. Nonlinear transverse vibration of a hyperelastic beam under harmonic axial loading in the subcritical buckling regime. Appl. Math. Model. 94, 597–618.

Wang, Y.Z., Tsai, T.J., 1988. Static and dynamic analysis of a viscoelastic plate by the finite element method. Appl. Acoust. 25, 77–94.

Wang, Z.M., Liu, Y.Z., 2016. Transverse vibration of pipe conveying fluid made of functionally graded materials using a symplectic method. Nucl. Eng. Des. 298, 149–159.

Warminska, A., Manoach, E., Warminski, J., 2014. Nonlinear dynamics of a reduced multimodal Timoshenko beam subjected to thermal and mechanical loadings. Meccanica 49, 1775–1793.

Weeger, O., Wever, U., Simeon, B., 2014. Nonlinear frequency response analysis of structural vibrations. Comput. Mech. 54, 1477–1495.

Wielentejczyk, P., Lewandowski, R., 2019. Analysis of the Primary and Secondary Resonances of Viscoelastic Beams Made of Zener Material. J. Comput. Nonlinear Dyn. 14, 091003.

Wielentejczyk, P., Lewandowski, R., 2017. Geometrically nonlinear, steady state vibration of viscoelastic beams. Int. J. Non. Linear. Mech. 89, 177–186.

Witteveen, W., Pichler, F., 2014. Efficient model order reduction for the dynamics of nonlinear multilayer sheet structures with trial vector derivatives. Shock Vib. 2014, 913136.

Xie, X., Zheng, H., Jonckheere, S., van de Walle, A., Pluymers, B., Desmet, W., 2018. Adaptive model reduction technique for large-scale dynamical systems with frequency-dependent damping. Comput. Methods Appl. Mech. Eng. 332, 363–381.

Yabuno, H., Ohkuma, M., Lacarbonara, W., 2003. An experimental investigation of the parametric resonance in a buckled beam, in: International Design Engineering Technical Conferences and Computers and Information in Engineering Conference. pp. 2565–2574.

Yabuno, H., Saigusa, S., Aoshima, N., 2001. Stabilization of the parametric resonance of a cantilever beam by bifurcation control with a piezoelectric actuator. Nonlinear Dyn. 26, 143–161.

Yamanouchi, M., Koizumi, M., Hirai, T., Shiota, I., 1990. Proceedings of the first international symposium on functionally gradient materials. Sendai, Japan.

Yao, M., Zhang, W., Yao, Z., 2015. Nonlinear vibrations and chaotic dynamics of the laminated composite piezoelectric beam. J. Vib. Acoust. 137.

Yeh, J.Y., Chen, L.W., 2005. Dynamic stability of a sandwich plate with a constraining layer and electrorheological fluid core. J. Sound Vib. 285, 637–652.

Yeh, J.Y., Chen, L.W., Wang, C.-C., 2004. Dynamic stability of a sandwich beam with a constrained layer and electrorheological fluid core. Compos. Struct. 64, 47–54.

Yeh, Z.-F., Shih, Y.-S., 2006. Dynamic characteristics and dynamic instability of magnetorheological material-based adaptive beams. J. Compos. Mater. 40, 1333–1359.

Yoshizawa, M., NAO, H., Hasegawa, E., Tsujioka, Y., 1985. Buckling and postbuckling behavior of a flexible pipe conveying fluid. Bull. JSME 28, 1218–1225.

Yu, D., Païdoussis, M.P., Shen, H., Wang, L., 2013. Dynamic Stability of Periodic Pipes Conveying Fluid. J. Appl. Mech. 81, 011008.

Yu, D., Wen, J., Zhao, H., Liu, Y., Wen, X., 2008. Vibration reduction by using the idea of phononic crystals in a pipe-conveying fluid. J. Sound Vib. 318, 193–205.

Yun, Y., Temuer, C., 2015. Application of the homotopy perturbation method for the large deflection problem of a circular plate. Appl. Math. Model. 39, 1308–1316.

Yusof, Z., Rasid, Z.A., Hassan, M.Z., Sapuan, S.M., Sarip, S., Yahaya, H., Yakub, F., 2020. The parametric instability improvement of fully anisotropic composite plates with embedded shape memory alloy. Adv. Compos. Lett. 29, 2633366X19899405.

Zahedi, S.A., Babitsky, V., 2016. Modeling of autoresonant control of a parametrically excited screen machine. J. Sound Vib. 380, 78–89.

Zajaczkowski, J., 1981. Destabilizing effect of Coulomb friction on vibration of a beam supported at an axially oscillating mount. J. Sound Vib. 79, 575–580.

Zavodney, L.D., Nayfeh, A.H., 1989. The non-linear response of a slender beam carrying a lumped mass to a principal parametric excitation: theory and experiment. Int. J. Non. Linear. Mech. 24, 105–125.

Zavodney, L.D., Nayfeh, A.H., 1988. The response of a single-degree-of-freedom system with quadratic and cubic non-linearities to a fundamental parametric resonance. J. Sound Vib. 120, 63–93.

Zavodney, L.D., Nayfeh, A.H., Sanchez, N.E., 1990. Bifurcations and chaos in parametrically excited single-degree-of-freedom systems. Nonlinear Dyn. 1, 1–21.

Zavodney, L.D., Nayfeh, A.H., Sanchez, N.E., 1989. The response of a single-degree-of-freedom system with quadratic and cubic non-linearities to a principal parametric resonance. J. Sound Vib. 129, 417–442.

Zghal, S., Bouazizi, M.L., Bouhaddi, N., Nasri, R., 2015. Model reduction methods for viscoelastic sandwich structures in frequency and time domains. Finite Elem. Anal. Des. 93, 12–29.

Zhang, S.H., Chen, H.L., 2006. A study on the damping characteristics of laminated composites with integral viscoelastic layers. Compos. Struct. 74, 63–69.

Zhang, T., Ouyang, H., Zhang, Y.O., Lv, B.L., 2016. Nonlinear dynamics of straight fluid-conveying pipes with general boundary conditions and additional springs and masses. Appl. Math. Model. 40, 7880–7900.

Zhang, W., Wang, F.X., Zu, J.W., 2005. Local bifurcations and codimension-3 degenerate bifurcations of a quintic nonlinear beam under parametric excitation. Chaos, Solitons & Fractals 24, 977–998.

Zhang, X.D., Sun, C.T., 1996. Formulation of an adaptive sandwich beam.

Smart Mater. Struct. 5, 814.

Zhang, Y.L., Chen, L.Q., 2014. Steady-state response of pipes conveying pulsating fluid near a 2:1 internal resonance in the supercritical regime. Int. J. Appl. Mech. 06, 1450056.

Zhang, Y.L., Chen, L.Q., 2013. External and internal resonances of the pipe conveying fluid in the supercritical regime. J. Sound Vib. 332, 2318–2337.

Zhao, D., Liu, J., Wu, C.Q., 2015. Stability and local bifurcation of parameter-excited vibration of pipes conveying pulsating fluid under thermal loading. Appl. Math. Mech. 36, 1017–1032.

Zheng, H., Pau, G.S.H., Wang, Y.Y., 2006. A comparative study on optimization of constrained layer damping treatment for structural vibration control. Thin-Walled Struct. 44, 886–896.

Zhou, K., Ni, Q., Dai, H.L., Wang, L., 2020. Nonlinear forced vibrations of supported pipe conveying fluid subjected to an axial base excitation. J. Sound Vib. 471, 115189.

Zhou, S., Yu, T.J., Yang, X.D., Zhang, W., 2017. Global dynamics of pipes conveying pulsating fluid in the supercritical regime. Int. J. Appl. Mech. 9, 1750029.

Zhou, X.Q., Yu, D.Y., Shao, X.Y., Zhang, S.Q., Wang, S., 2016. Research and applications of viscoelastic vibration damping materials: A review. Compos. Struct. 136, 460–480.

Zhu, B., Dong, Y., Li, Y., 2018. Nonlinear dynamics of a viscoelastic sandwich beam with parametric excitations and internal resonance. Nonlinear Dyn. 94, 2575–2612.

List of Publications

The work presented in this thesis has led to the following publications:

1. Reddy RS, Panda S, Gupta Abhay. Nonlinear dynamics of an inclined FG pipe conveying pulsatile hot fluid. International Journal of Non-Linear Mechanics. 2020; 118:103276.

2. Reddy RS, Panda S, Natarajan, G. Nonlinear dynamics of functionally graded pipes conveying hot fluid. Nonlinear Dynamics. 2020; 99(3):1989-2010.

3. Reddy RS, Panda S, Gupta Abhay. Nonlinear dynamics and active control of smart beams using shear/extensional mode piezoelectric actuators. International Journal of Mechanical Sciences. 2021:106495.

4. Reddy RS, Panda S, Gupta Abhay. A generalized finite element formulation for nonlinear frequency response analysis of viscoelastic structures using harmonic balance method. (Manuscript under preparation)

5. Reddy RS, Panda S, Gupta Abhay. Reduced-order finite element formulation for geometrically nonlinear dynamic analysis of viscoelastic structures. (Manuscript under preparation)

6. Reddy RS, Panda S, Gupta Abhay. Passive control of parametrically excited post-buckled beams with constrained viscoelastic damping layers: a theoretical study using reduced-order FE formulation. (Manuscript under preparation)